R-08-48

Bedrock transport properties Forsmark

Site descriptive modelling SDM-Site Forsmark

James Crawford, Kemakta Konsult AB

October 2008

Svensk Kärnbränslehantering AB
Swedish Nuclear Fuel
and Waste Management Co
Box 250, SE-101 24 Stockholm
Tel +46 8 459 84 00

SKB

ISSN 1402-3091
SKB Rapport R-08-48

Bedrock transport properties Forsmark

Site descriptive modelling
SDM-Site Forsmark

James Crawford, Kemakta Konsult AB

October 2008

Preface

This report consists of several parts for which different authors have contributed material in a collaborative effort. A short description of the main contributors and the relevant parts of this report that they have been involved with follows:

James Crawford, Kemakta Konsult AB (Chapters 1–3, 5–10, Appendices A-L)

Johan Byegård, Eva Selnert, Geosigma AB (Chapter 4)

Eva-Lena Tullborg, Terralogica AB (Chapter 4)

Martin Löfgren, Kemakta Konsult AB (Co-author of Appendix H)

The assistance of Björn Gylling and Håkan Svensson (Napsac simulations) as well as Niko Marsic (ECPM particle tracking simulations using ConnectFlow) from Kemakta Konsult AB is gratefully acknowledged.

Editor: James Crawford

Summary

This report contains a detailed account of the work that has been carried out within the final stage of site descriptive modelling for the Forsmark area (SDM-Site Forsmark) with regard to bedrock transport properties evaluation.

A quantitative assessment is made of flow-related transport properties (the F-factor and advective travel time) within different rock volumes comprising the Forsmark local model area. In this evaluation, the hydrodynamic controls on transport are calculated with the aid of models and data supplied by hydrogeology. The calculations indicate that for similar hydraulic gradients, the properties of the low transmissive rock between deterministic deformation zones should dominate the overall flow-related transport resistance. The conductive flowpaths within this rock volume appear to be rare and when they are encountered they have properties that are broadly consistent with what is expected based upon the distribution of flow transmissivities reported by hydrogeology. Simulations using an equivalent continuous porous medium (ECPM) representation of the Forsmark site where the different hydraulic rock domains, deterministic deformation zones, and shallow bedrock aquifer in the upper 100–150 m of the rock are combined with a set of topologically determined hydraulic boundary conditions have also indicated that a large proportion of the rock volume comprising the hypothetical repository volume should be, for all practical purposes, below the percolation limit and therefore hydraulically non-conductive. The ECPM calculations do indicate, however, that deterministic deformation zones may play a more important role for the overall flowpath transport resistance if additional consideration is given to the higher specific flow-wetted surface in these zones as well as the possibly lower hydraulic gradients in these features relative to the sparsely fractured rock between the zones.

Material properties of the rock governing solute retention as measured in the transport properties laboratory programme have been used to parameterise a semi-quantitative retardation model for the Forsmark site. The effective diffusivity of the rock matrix as given by the formation factor is found to be very similar for different rock types and no strong quantitative basis can be found for distinguishing between the different rock types at the site. Rock matrix within deterministic and probable deformation zones, however, generally has a larger water saturation porosity and greater effective diffusivity than rock matrix residing outside of deformation zones. Although the sample sizes are typically small, there appears to be no systematic difference between the sorptive properties of the different, (hydrothermally unaltered) rock types. The apparent variation of sorptive properties appears to be more strongly related to groundwater composition than the taxonomic identity of the rock. There are also indications that hydrothermally altered material adjacent to fracture surfaces, and more particularly fracture coatings of secondary minerals, may have sorptive and diffusive retention properties that are enhanced relative to that of the unaltered rock matrix.

Simulations of solute transport where material property descriptions are combined with flow-related transport properties suggest that most radionuclides characterised as sorbing have very long residence times. Additionally, it is found that transport models accounting for pseudo-radial diffusion from a narrow flow channel or diffusion to effectively stagnant regions of a flowing fracture may increase radionuclide residence times substantially. Flow channelling therefore may have an overall beneficial effect when fully considered in transport modelling.

Confirmatory tracer tests have been performed in the form of dipole, and single well injection-withdrawal (SWIW) tracer tests. The evaluation of the results gives clear indications of diffusive and sorptive retention processes consistent with the conceptual understanding of solute transport at the Forsmark site. Further analysis suggests that while the retardation of sorbing tracers appears to be governed principally by direct diffusive and sorptive interactions with fracture surface coatings, the retardation of non-sorbing tracers may be more strongly influenced by hydrodynamic effects that have not been fully accounted for in the data evaluation. These additional effects, however, are not thought to be relevant for radionuclide transport at safety assessment timescales.

Sammanfattning

Denna rapport utgör en detaljerad beskrivning av det arbete som utförts inom det avslutande stadiet av den platsbeskrivande modelleringen av Forsmarksområdet med inriktning mot utvärdering av bergets tranportegenskaper.

En kvantitativ bedömning av flödesrelaterade egenskaper (F-faktorer och advektiv transporttid) utförs för de olika bergvolymer som tillsammans utgör det lokala modellområdet i Forsmark. Hydrodynamiska parametrar av vikt för transport beräknas med hjälp av modeller och data som levererats av hydrogeologi. Utvärderingen av dessa beräkningar tyder på att det lågtransmissiva berget mellan deterministiska deformationszoner bör ha en dominerande betydelse för det totala flödesrelaterade transportmotståndet. De konduktiva flödesvägarna är sällsynta i denna bergtyp. I de fall de påträffas överensstämmer dess egenskaper i stort sett med de förväntade baserat på fördelningen av flödestransmissiviteter som rapporterats av hydrogeologi. Simuleringar där Forsmarksområdet representeras av ett ekvivalent kontinuerligt poröst medium (ECPM) har också visat att en stor andel av den föreslagna bergvolym för förvarets placering bör vara hydrauliskt icke-konduktiv. I denna representation kombineras de olika hydrauliska bergdomänerna, deformationszonerna och ytliga vattenbärande skikt i de övre 100–150 m av bergvolymen med en uppsättning av topologiskt bestämda hydrauliska randvillkor. ECPM simuleringarna visar dock att deterministiska deformationszoner kan ha större betydelse för det totala transportmotståndet längs flödesvägarna om hänsyn också tas till de större flödesvätta ytorna och de eventuellt lägre hydrauliska gradienterna i dessa zoner relativt berget mellan zonerna.

Uppmätta materialegenskaper hos berget som bestämmer lösta ämnens retention har använts för att parametrisera en semikvantitativ retardationsmodell för Forsmarksområdet. Den effektiva diffusiviteten i bergmatrisen som ges av formationsfaktorn har visat sig skilja mycket litet mellan olika bergtyper och någon kvantitativ grund för att särskilja olika bergtyper i området har inte kunnat påvisas. Bergmatrisen i deterministiska och troliga deformationszoner har dock generellt en större porositet och större effektiv diffusivitet än bergmatrisen som ligger utanför deformationszoner. Även om antalet bergprover vanligtvis är få verkar det inte finnas någon systematisk skillnad i sorptionsegenskaper mellan de olika (hydrotermiskt oförändrade) bergtyperna. Den märkbara variationen i sorptionsegenskaper verkar vara närmare relaterad till grundvattensammansättningen än till bergtypernas klassificering. Hydotermiskt förändrade zoner nära sprickytor, och särskilt beläggningar av sekundära mineral på sprickytor, verkar ha förhöjda sorptiva och diffusiva retentionskapaciteter jämfört med den ostörda bergmatrisen.

Transportsimuleringar där material- och flödesrelaterade transportegenskaper kombineras tyder på att de flesta sorberande radionuklider har väldigt lång uppehållstid. Det har också visat sig att radionuklidernas beräknade uppehållstid ökar ansenligt med transportmodeller som tar hänsyn till pseudo-radiell diffusion från trånga flödeskanaler eller diffusion till stagnanta zoner i flödande sprickor. Kanalbildningseffekter inkluderade i transportmodeller kan därför ha en gynnsam effekt.

Spårämnesförsök i form av dipol- och enhålstester (SWIW) har utförts med syfte att stärka och verifiera den konceptuella förståelsen av diffusiva och sorptiva retentionsprocesser. Utvärderingen visar tydligt att resultaten stämmer överens med den konceptuella förståelsen av dessa processer i Forsmarksområdet. Utökade analyser tyder på att retardationen av sorberande spårämnen verkar bestämmas av direkt diffusiv och sorptiv interaktion med ytbeläggningar i sprickorna medan retardationen av icke-sorberande spårämnen kan påverkas mer av hydrodynamiska effekter som ej har tagits hänsyn till i utvärderingen av data. Dessa ytterligare effekter tros dock inte ha betydelse för radionuklidtransport i de tidsperspektiv relevanta för säkerhetsanalysen.

Contents

1 Introduction

1.1 Background

The Swedish Nuclear Fuel and Waste Management Company (SKB) is conducting site investigations at two different locations in Sweden (the Laxemar and Forsmark areas) for the purpose of siting a deep geological repository for spent nuclear fuel. The results from the investigations at the sites are used as a basic input to the site descriptive modelling.

A Site Descriptive Model (SDM) is an integrated description of the site and its regional setting, covering the current state of the biosphere as well as ongoing natural processes of importance for long-term safety. The SDM summarises the state of knowledge of the site at the conclusion of the complete site investigation (CSI). It also provides parameters and models to be used in further analyses within safety assessment (SA), repository design, and environmental impact assessment. The present report is produced as the main (level II) reference for the concluding stage of the site descriptive modelling of the Forsmark area (henceforth, SDM-Site Forsmark). The hierarchy of various reports comprising SDM-Site Forsmark are shown in Figure 1-1.

1.2 Scope and objectives

This report provides a detailed account of modelling that has been performed in support of bedrock transport property assessment for SDM-Site Forsmark. The transport site descriptive model presented in this report incorporates both a detailed account of retardation parameters and flow-related transport properties of the rock. The integration of material property data and flow-related transport properties allows the prediction of characteristic transport times for typical transport paths from hypothetical repository depth to the near surface.

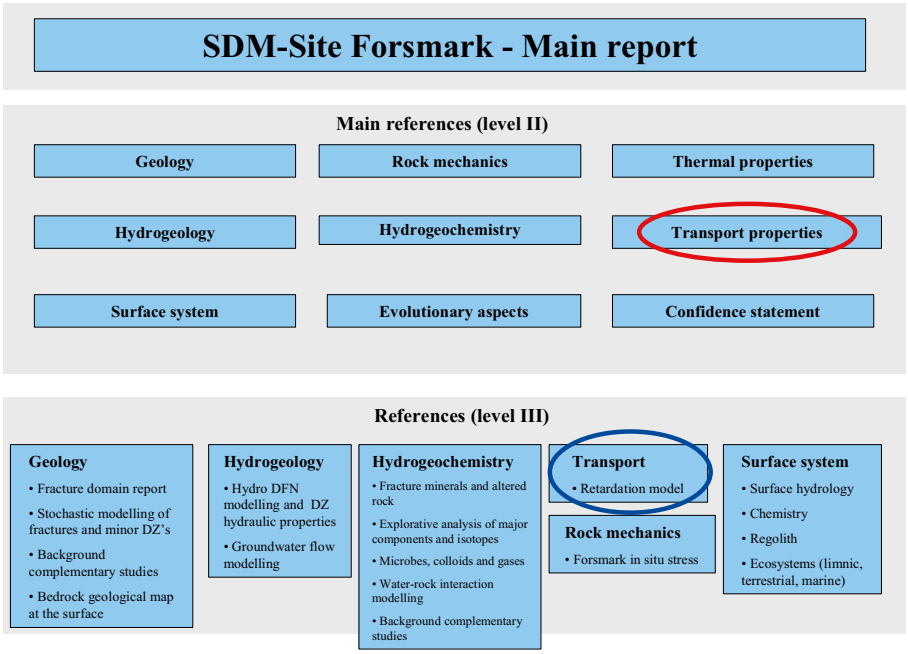

Figure 1-1. *Hierarchy of background reports feeding into the SDM-Site Forsmark main report. The relation of the present level II summary report to the main report is highlighted with a red ellipse, while the level III transport retardation model background report /Byegård et al. 2008/ is highlighted with a blue ellipse.*

The primary objectives of the work are to:

- outline the conceptual understanding of transport processes within the rock encompassing both material property and hydrodynamic aspects controlling solute transport at the Forsmark site,
- provide a summary of quantitative material property data and supporting evidence used to parameterise a retardation model describing the rock matrix as well as typical fracture types and deformation zones encountered in the rock at Forsmark,
- make estimates of the hydrodynamic transport resistance (advective travel time and flow-wetted surface to flow ratio, or F-factor) for typical flowpaths in the target rock volume at Forsmark using data and models supplied by hydrogeology,
- make estimates of travel times for specific solutes investigated in the transport properties laboratory programme for typical flowpaths in the rock at Forsmark without any specific considerations of repository layout or radionuclide release scenarios,
- describe and interpret results of field-scale tracer tests performed at the Forsmark site which are made in support of the site descriptive transport modelling.

A secondary, although no less important goal of this work is also to make a systematic attempt to explain the possible role of flow channelling on the transport of solutes of interest. This includes analyses of the possible impact of channelling phenomena on primary data interpretation as well as possible impacts upon solute migration when considered in flow and transport modelling.

1.3 Hydrogeological and geological setting of the Forsmark site

The Forsmark site is situated in northern Uppland within the municipality of Östhammar about 170 km north of Stockholm. Figure 1-2 illustrates the candidate area with the 12 drill sites that have been the main focus of the subsurface investigations.

Forsmark and the rock domains within it are described in the geology background report /Stephens et al. 2007/. The target volume is a part of the local model area as indicated in Figure 1-3. The target volume is defined as the parts of rock domain RFM029, as well as rock domain RFM045, that are situated north-west of the steeply dipping zone ZFMNE0065 and beneath the gently dipping deformation zones ZFMA2, ZFMA3 and ZFMF1. The rock domains are further subdivided into fracture domains FFM01–FFM06. A fracture domain refers to a rock volume outside deformation zones in which rock units show similar fracture frequency characteristics /Olofsson et al. 2007/.

The subsurface form of the target volume is visualised in Figure 1-4 in three dimensions and shows rock domains RFM029 and RFM045 in relation to the steeply dipping fracture zones ZFM060A, ZFM062A and gently dipping fracture zones ZFMA1 and ZFMA2.

1.4 Hydrogeochemical characteristics of the Forsmark site

The groundwater types represented at the Forsmark site are distinguished largely by way of their salinity and are described as being Fresh, Brackish, or Saline in character. For Brackish type groundwater a further classification is made to distinguish between water of marine and non-marine (deep saline) origin based upon additional indicators such as magnesium content and chloride-bromide ratios. In the hydrogeochemical site descriptive model /Laaksoharju et al. 2008/ the current groundwater types to be found at the site are described in terms of their perceived main origin as can be discerned from hydrogeochemical analysis and modelling interpretation. The so-called “end members” which define the main groundwater types by origin are described in detail by /Gurban 2008/. The present groundwaters have compositions which have been substantially altered by mixing and chemical reactions within the rock although their chemical signatures are still such that we can understand their origin and follow their evolution over long periods of time.

Figure 1-2. *The candidate area for site investigations at Forsmark showing the 12 drill sites that have been the focus of the sub-surface investigations.*

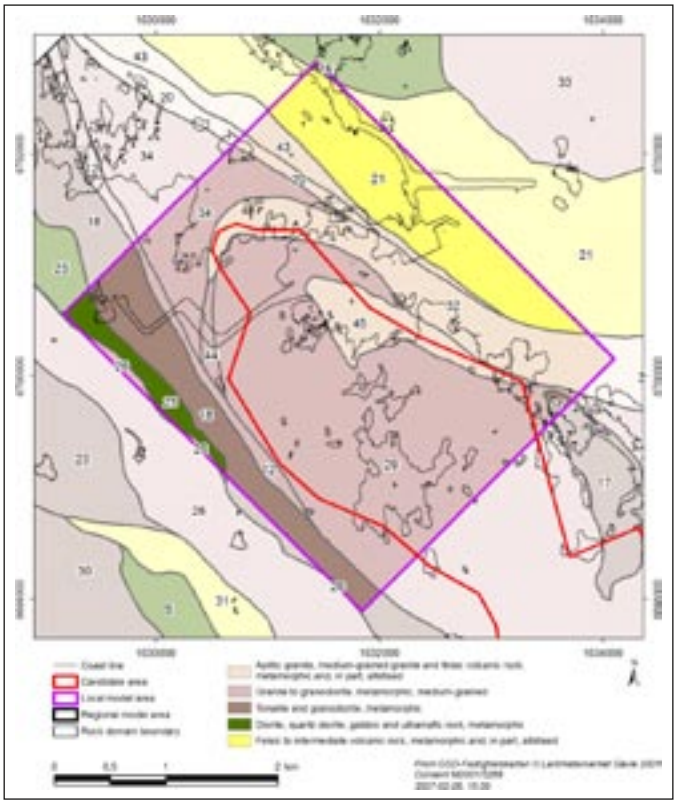

Figure 1-3. *Surface geologic map indicating rock domains inside and immediately around the local model area in Forsmark. Modified after /Olofsson et al. 2007/.*

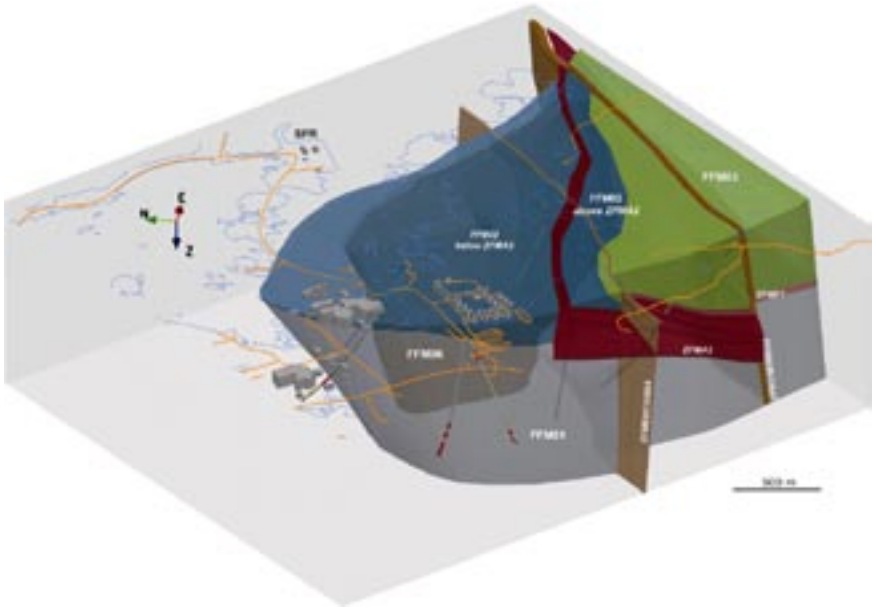

Figure 1-4. *View to the east showing the relationship between the major deformation zones in the target volume (ZFMA2 is shaded red), and the fracture domains FFM01–FFM06. Reproduced from /Olofsson et al. 2007/.*

Past climate changes are recognised as being one of the major driving forces for long term hydrogeochemical changes over periods from hundreds to many thousands of years. The understanding of these changes is therefore of fundamental importance for understanding the evolution and present state of the groundwater within the Fennoscandian crystalline bedrock. Several of the groundwater end members can be associated with past climatic events in the later Pleistocene (i.e. from roughly 100,000 y to 10,000 y before present) including inter-glaciations, glaciations, de-glaciations, and associated shore level displacements in connection with marine/non-marine transgressions and regressions. Among these, the last glaciation and post glacial period is thought to be the most important for the current groundwater state, especially in terms of land uplift, shore-level displacement, and the development of the Baltic basin. In spite of this the hydrogeochemistry of the Forsmark groundwater cannot be satisfactorily explained without including an older relict component (minimum age 1.5 Ma as indicated by ^{4}He and ^{36}Cl concentrations) remaining from previous glacial and interglacial periods. Figure 1-5 shows some of the more recent stages of importance for understanding groundwater chemistry at the Forsmark site.

The primary end members are /Gimeno et al. 2008/:

Altered meteoric: a dilute groundwater ultimately originating from atmospheric precipitation (rainwater) during temperate periods although more particularly during the current interglacial. The composition of this water is influenced by chemical reactions with, for example, calcite and biogenic components accumulated during its movement through surface quaternary deposits.

Glacial: a dilute groundwater originating from the melting of retreating glaciers at the conclusion of the most recent glaciation (18,000–8000 BC). This end member is substantially depleted with respect to the heavy isotopes of oxygen (^{18}O) and hydrogen (^{2}H, Deuterium) indicating a cold climate origin. This end member is defined by analogy with present day glacial melt-waters which have a very low content of dissolved solids (even lower than meteoric water). The end member represents the chemical composition of the water prior to the water rock interaction processes occurring during infiltration into the bedrock. It should be noted that since the glacial water is drastically modified by mixing with waters of other origins, there are essentially no undisturbed glacial melt-water remnants within the bedrock that can be considered as pure glacial mixing components modified only by water-rock interactions.

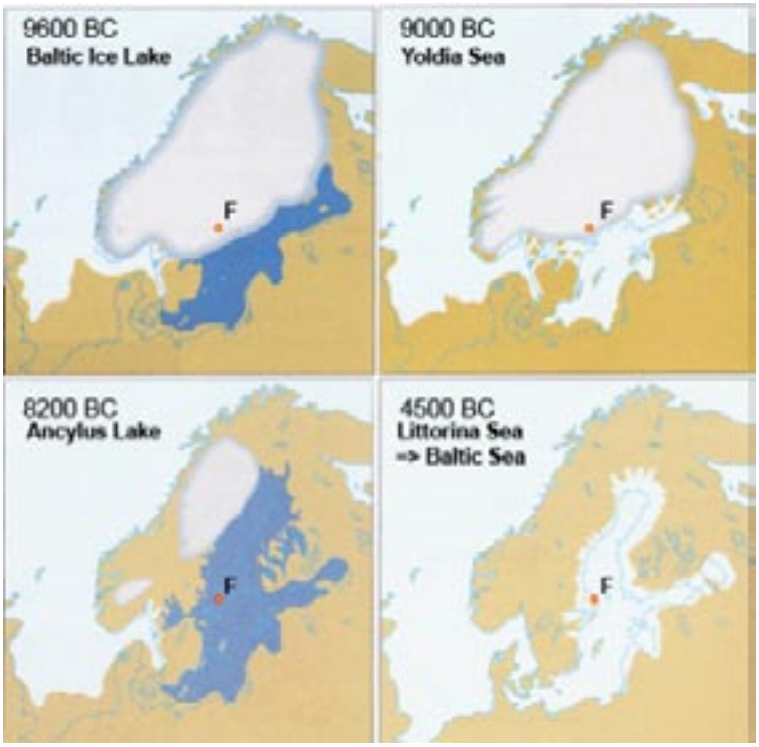

Figure 1-5. *Map of Fennoscandia with some important stages during the Holocene period. Four main stages characterise the development of the aquatic systems in the Baltic basin since the latest deglaciation: the Baltic Ice Lake (13,000–9500 BC), the Yoldia Sea (9500–8800 BC), the Ancylus Lake (8800–7500 BC) and the Littorina/Baltic Sea 7500 BC–present). Fresh water is indicated with dark blue shading and marine/brackish water with light blue. Image taken from /Follin et al. 2008 (article)/. The Forsmark area (annotated "F" in the figure) was probably, at or close to the rim of the retreating ice sheet during the Yoldia Sea stage. (Image taken from /Laaksoharju et al. 2008/).*

Littorina: a brackish, marine groundwater component originating from the period 4,500–3,000 BC and characterised by a salinity (6,500 mg/L Cl) about twice that of the present day Baltic Sea and a relatively high Mg content.

Deep Saline: The chemical composition of this end-member corresponds to the deepest and more saline waters sampled at Forsmark. This water has a salinity of 47,200 mg/L Cl with a predominantly Ca-Na-Cl composition and deviates significantly from the GMWL (Global Meteoric Water Line) in $\delta^{18}O$ vs. $\delta^{2}H$ plots. Although there is some uncertainty concerning the ultimate origin of this water type, the great age of the water (in excess of 1.5 Ma) as estimated from ^{36}Cl data suggests that it is likely to be close to equilibrium with the minerals comprising the bedrock.

The present conceptual model of the evolution of groundwater composition is illustrated schematically in Figure 1-6 for hydraulically conductive zones (i.e. fractures and deformation zones exhibiting flow).

Although the compositional characteristics are thought to be principally determined by mixing of various groundwater end-members, the pH and Eh of the groundwater are determined by chemical reactions (which in turn has consequences for observed distributions of sulphur, iron and carbon species). The pH is mainly controlled by calcite dissolution-precipitation reactions, although aluminosilicate weathering reactions and ion exchange are also thought to play a non-negligible role. Modelling indicates that groundwater at depths greater than about 100 m generally appears to be in equilibrium with calcite. Investigations of fracture minerals show that calcite in fractures is abundant and that no extensive leaching has occurred in response to past glaciation/deglaciation events.

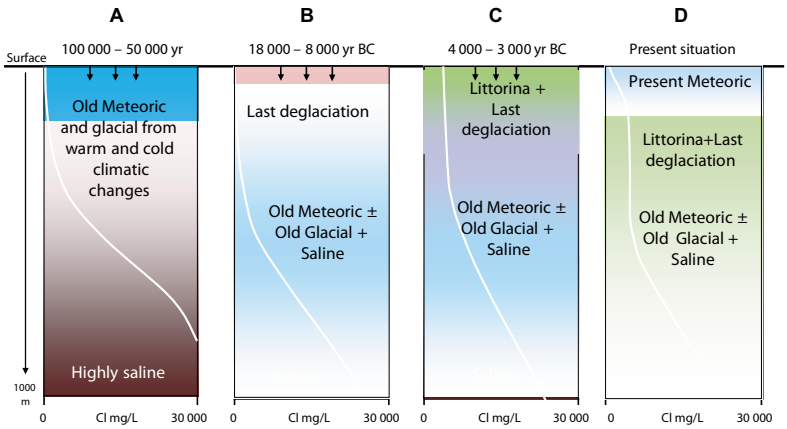

Figure 1-6. *Schematic overview of the current conceptual understanding of late Pleistocene-Holocene groundwater evolution at the Forsmark site showing salinity and groundwater-type distributions versus depth for hydraulically transmissive zones at Forsmark. From left to right these are: A) situation prior to the last deglaciation, B) last deglaciation and intrusion of Late Weichselian meltwater, C) the Littorina Sea water penetration caused by density intrusion, and D) the present day situation. (Image taken from /Laaksoharju et al. 2008/).*

The redox conditions vary considerably with depth although generally appear to be dominated by redox reactions involving various iron and sulphur species. According to data analyses and modelling of the redox system, reducing conditions currently prevail at depths greater than about 20 m. Most of the Eh values determined in brackish groundwaters (at depths between 110 and 646 m) seem to be controlled by the occurrence of an amorphous iron oxyhydroxide with higher solubility than a truly crystalline phase. This indicates that the iron system is disturbed, which also is supported by mineralogical investigations that have identified the presence of fine-grained amorphous to poorly crystalline phases now evolving towards more crystalline phases. At still greater depths the iron system seems to be limited by only crystalline iron hydroxides, mainly hematite. Despite the uncertainty of the measured data (e.g. due to sampling perturbations), the dissolved sulphide concentrations at shallow to intermediate depths are systematically low, possibly due to the precipitation of amorphous Fe(II)-monosulphides, linked to the activity of sulphur-reducing bacteria (SRB). At depths greater than 600 m, the dissolved sulphide concentrations increase, which is consistent with the occurrence of SRB and with the active precipitation of Fe(II)-monosulphides.

The behaviour of uranium is a special case at Forsmark. Elevated concentrations have been detected in groundwaters associated with a Littorina component and the highest concentrations are found in waters in the gently dipping deformation zones south-east of the target volume (i.e. in the hanging wall bedrock of ZFMA2). There are indications that these elevated concentrations are related to easy dissolvable uranium fractions in fracture coatings in contact with these waters. Speciation-solubility calculations support this conclusion and indicate that the high uranium contents are the result of the control exerted by an amorphous (and relatively soluble) uranium phase present in the system, and weakly reducing Eh values which, in combination with the stabilising effect of carbonate, may allow uranium to be periodically and locally mobile to a maximum depth of around 600 m /Laaksoharju et al. 2008/.

Colloid concentrations in Forsmark groundwaters are comparable to those found in other granitic environments and are composed mostly of aluminium, silica, iron and sulphur. Uranium associated to the colloids was found in boreholes KFM02A and KFM06A, in line with the relatively high groundwater uranium concentrations found in these boreholes. The uranium content on the colloids is about 10% of the uranium concentration in the groundwater and colloidal transport is therefore thought to be consequential although not the origin of the high uranium content in the groundwater.

1.5 Relationship to safety assessment

In this report the aim is to provide a comprehensive account of site specific transport properties for the Forsmark site. The broad intention is that this should not only function as an input to safety assessment, but also as an aid to explaining past and predicting future rock-groundwater interactions of relevance to other disciplines such as hydrogeochemistry and hydrogeology. The site specific transport properties are also used as an aid to understanding and quantifying features and processes observed during confirmatory testing.

It is acknowledged that processes observed during field scale tracer tests with a duration of at most a few thousand hours may not necessarily be active over timescales relevant for safety assessment which can encompass timescales of 0.1 to 1 Ma (or perhaps longer). In a practical sense this means that while data derived from interpretation of field tests can be used to corroborate process understanding in a general sense, the transport properties sampled may not be appropriate for application within safety assessment which is associated with entirely different spatial and temporal scales.

The description of the solute transport characteristics of a site is an intermediate step between site characterisation and safety assessment. It represents a diverse mix of site data and partially generic modelling which is used to interpret the consequences of the interactions between hydrogeological and chemical reactive processes in the rock as well as underlying uncertainties.

For safety assessment purposes we are interested in reducing the complexity of the system description sufficiently that well-reasoned estimates of radiological risk can be made. This entails capturing the main physical and chemical properties of the geological formation while seeking to place conservative bounds on processes and parameters that cannot be adequately quantified in a defensible manner. Highly detailed descriptions of transport properties, while useful from the point of view of qualitative process understanding and paleo-hydrogeochemical reconstruction, are less relevant for safety assessment purposes. Field observations and safety assessment requirements are not always easy to reconcile and this report attempts to strike a balance between these different and, at times conflicting, requirements.

1.6 A roadmap to this report

This report is divided up into a number of major sections. To assist the reader, a broad description of the content of each of these sections is briefly described below:

Chapter 1 contains a short background description to the work and the principal aims of this report. In addition, an overview of the Forsmark site including its hydrogeological, geological and hydrogeochemical setting is given.

Chapter 2 gives a summary of the different mechanisms and processes which influence the transport of solutes within fractured rock. It contains a description of the different phenomena of interest for evaluation of flow related transport properties as well as an account of the main chemical and diffusive transport mechanisms which lead to retention of radionuclides in the microporous structures of the rock matrix and consequently retards their transport by flowing groundwater along paths existing in the fracture system. It is in this chapter that the major processes of interest are outlined. Descriptions are given of how these processes are modelled, and what process-descriptive simplifications are necessary in order to establish an internally consistent and accurate model for the purposes of safety assessment.

Chapter 3 contains an account of modelling carried out to determine the flow-related transport properties of the system. It is here the concept of the flow-wetted surface to flow ratio is elaborated and calculations are made to assess its magnitude. This is one of the key parameters influencing the extent of the retardation effect experienced by radionuclides transported with the groundwater and is central to the description of the transport properties of fractured rock.

Chapter 4 contains a description of the material properties of the rock which govern the retention of radionuclides of interest in safety assessment. Different parameters which describe the retention properties of the rock including sorption, diffusion, and porosity are discussed and measurement data from the site descriptive modelling laboratory programme are presented. The chapter concludes with a retardation model describing the retention parameters related to different rock types, fracture types, and various other structural sub-elements in the rock which can be used in a modular fashion to synthesise a model for simulating the transport of radionuclides.

Chapter 5 contains an account of transport modelling which has been carried out with the aim of establishing typical transport times for a selection of radionuclides of interest. It is here the description of flow-related transport properties is brought together with the retardation model in an integrated transport properties model which is used to make predictions of transport times.

Chapter 6 contains an account of a number of field scale tracer tests which have been carried out with the aim of partially validating the existence of postulated retardation mechanisms and models used for their description. This chapter describes each test in detail including major results and discusses the evidence in support of specific retention mechanisms underlying the apparent retardation of tracers transported within the fractured rock.

Chapter 7 contains a broad summary of what has been learned during the process of site descriptive modelling and important conclusions of importance for continued safety assessment studies concerning the Forsmark site. The main conclusions regarding site specific transport properties are also outlined in this chapter. In addition, consequences of various sources of uncertainty and phenomena which can have a strong impact upon the retardation of radionuclide transport are discussed.

As an aid to the reader at the conclusion of each major chapter, a short summary is given of the main findings of interest for the site descriptive model, principal uncertainties identified, and what significance these might have for safety assessment.

1.7 Previous model versions

The main uncertainty identified in earlier Forsmark model versions 1.1 /SKB 2004/ was the lack of site specific transport data. In model version 1.2 /SKB 2005a/ a small amount of matrix porosity and effective diffusivity data was reported. In version 2.1 /SKB 2006a/ a substantially larger data set for matrix porosity and effective diffusivity was reported although still no site specific sorption data was available at that time. This was largely due to the very difficult and time consuming nature of the laboratory techniques used in the measurement of sorption. A large amount of BET surface area data was reported in version 2.1 which is considered to be a reasonable proxy for the qualitative prediction of the relative sorption properties of rock.

Generally, throughout the different iterations of the transport SDM there has been a gradual convergence concerning the overall understanding of the site data. In previous model versions it was beginning to become clear that there were only minor differences in the diffusive and sorptive properties of the major rock types. In line with expectations, the BET surface area data available in model version 2.1 also suggested that the mineral coating present at fracture surfaces should have enhanced retention properties relative to the unaltered rock matrix for most solutes.

These general observations are still considered to be an accurate assessment of the site specific transport properties and there have been no surprise revelations in the continued modelling work. In model version 1.2, a preliminary attempt was made at describing specific fracture types typical of the Forsmark site with individually assigned material properties based upon fracture mineralogy. This concept has been developed further in the present model with the addition of a retardation properties description for structural elements comprising deformation zones.

No predictive modelling of solute transport times was presented in previous model versions; this is an entirely new feature of the SDM-Site transport properties model described in this report.

2 Overview of flow and solute transport properties

The conceptual model underlying the transport properties evaluation in SDM-Site is based upon a description of solute transport in discretely fractured rock. Specifically, the fractured rock is viewed as consisting of mobile and immobile zones. The mobile zones are regions within fractures and deformation zones where groundwater flow and advective transport take place. The immobile zones include the rock mass itself as well as stagnant regions within or immediately adjacent to flowpaths where solutes can be retained (i.e. removed temporarily or permanently from the mobile water) /Berglund and Selroos 2003/.

In the conceptual model, advection is the dominant process for moving solutes in the transport direction, whereas the main role of diffusion is to remove the solutes from the mobile water and transport them within the immobile zones.

The conceptualisation outlined above implies that solute transport takes place along flow paths consisting of connected, hydraulically conductive channels in fractures and deformation zones of different sizes. The fractures and deformation zones reside in rock domains which can contain one or more different rock types. Rock domains are defined in /Stephens et al. 2007/ as rock volumes that show specifically similar composition, grain size, degree of bedrock homogeneity, and degree and style of ductile deformation. A rock volume that shows early-stage alteration (albitisation) is also distinguished as a separate rock domain.

The following sections summarise the conceptual description of flow and solute transport in the bedrock at the Forsmark site.

2.1 Flow related transport properties

In this section the hydrodynamic properties of the hydraulically conductive regions of the rock are discussed. In the site descriptive model, the groundwater system is divided into three different hydraulic domains. These are defined in the hydrogeological background report as /Follin et al. 2007a/:

- HSD, or Hydraulic Soil Domain. This domain comprises the quaternary deposits or soil overlying the bedrock.
- HCD, or Hydraulic Conductor Domain. This domain comprises the deterministically defined deformation zones as defined by geology.
- HRD, or Hydraulic Rock Domain. This domain comprises the fractured bedrock outside of the deformation zones and may include so-called minor deformation zones which are not modelled deterministically.

An illustration of the hydrogeological description of the system is given in Figure 2-1.

Both HCD and HRD domains are hosted within the different geological rock domains as described in section 1.3. A rock domain refers to a rock volume in which rock units that show similar composition, grain size, degree of bedrock homogeneity, and degree and style of ductile deformation have been combined and distinguished from each other. Rock volumes that show early-stage alteration (albitisation) are also distinguished as separate rock domains. The rock domains are labelled RFM*x*, where *x* is an alphanumeric identifier (e.g. RFM029, RFM045, etc).

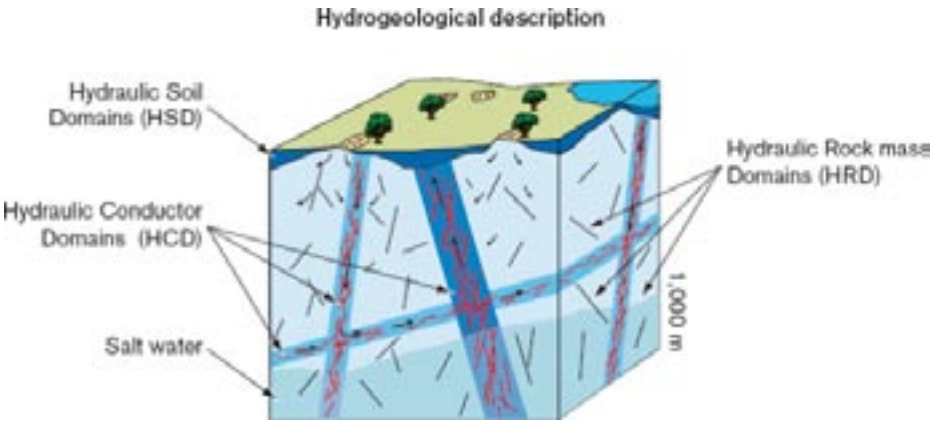

Figure 2-1. *Illustration showing the division of the crystalline bedrock and superficial quaternary deposits into hydraulic domains. Within each domain, the hydraulic properties are represented by equivalent values, or by spatially distributed statistical descriptions. (Image taken from /Rhén et al. 2003/).*

The rock domains are further sub-divided into a number of fracture domains that reflect similar fracture frequency characteristics. The fracture domains are defined on the basis of the single-hole interpretation work and the statistical treatment of fracture populations. Fracture domains are, by definition, considered to be separate entities to deterministic deformation zones, although a single fracture domain can be transected by one or more of these zones. In a similar naming convention as used for rock domains, the fracture domains at Forsmark are referred to as FFM*x*, where *x* is an alphanumeric identifier (e.g. FFM01, FFM02, etc).

It should be remembered that the demarcation of the rock volume into rock domains and fracture domains is a construct based upon the geological characteristics of the rock, whereas the hydraulic rock domains and hydraulic conductor domains are based upon hydrogeological considerations. The various fracture domains comprising the HRD are also divided into a number of sub-units based upon transmissivity characteristics and the intensity of flowing features estimated from borehole hydraulic testing.

In the bedrock transport properties evaluation, we focus primarily upon the properties of the HCD and HRD. The transport properties of the HSD are handled separately within SDM-Site by the surface systems sub-discipline.

2.1.1 Conceptual description of the HCD

Deterministic deformation zones

The Hydraulic Conductor Domain or HCD consists of the set of local major and local minor deformation zones, the orientation, extent and properties of which have been described deterministically in the geology background report /Stephens et al. 2007/. A deformation zone is a general term referring to an essentially 2D structure along which there is a concentration of brittle, ductile or combined brittle and ductile deformation. A brittle deformation zone is further classified as a fracture zone if no specification is given as to whether there has been a shear sense of movement along the zone. A fracture zone that shows a shear sense of movement is referred to as a fault zone. Within the SDM, individual deformation zones are named ZFM*x*, where *x* is an additional alphanumeric identifier specific to individual zones. Generally, the deformation zones at the Forsmark site are further classified according to size. They are referred to as regional (> 10 km), major (1–10 km), and minor deformation zones, or MDZ (< 1 km).

Although modelled as 2D structures, deformation zones are generally made up of swarms of fracture clusters, fracture splays, stepovers and other features that are interpreted en echelon[1] to link up into large heterogeneous structures of common tectonic origin as shown schematically in Figure 2-2. They are identified and modelled on the basis of aerial, surface, and core-borehole geophysical measurements as well as observations at ground surface and in the core-boreholes.

In the conceptual model outlined by /Munier et al. 2003/ deformation zones are depicted as consisting of a heavily fractured core for the most part filled with annealed fractures, breccias and low permeability mylonitic features. Outside the core lies a region of rock with a higher open fracture frequency than the core zone and a consequently higher permeability. Flanking the outer core region is a transition zone with a fracture frequency somewhere in between that of typical rock featuring background fracturing and that of the outer core. Deformation zones are typically formed during repeated cycles of tectonic activity over geological timescales and contain many of the same structures as the HRD although intensely localised along a specific geometric orientation in 3D that defines the deformation zone.

The heterogeneous geological structure of deformation zones implies heterogeneous hydrogeological properties and zones typically exhibit considerable complexity in their flow characteristics. The void space characteristics of individual joints and fault segments comprising the zone, their interconnectivity, and orientation to prevailing stresses are overwhelmingly important for the overall hydraulic properties of the zone. This picture is further complicated by the existence of secondary mineralisations formed during ancient hydrothermal events and contemporary mineral precipitation-dissolution processes. Tectonic processes within deformation zones lead to rock fabric alteration which typically results in the formation of mylonite and cataclasite. The latter of these two is commonly associated with fault breccias (particulate) and gouge material that can have a strong influence on the local hydraulic properties of conductive elements comprising the zones.

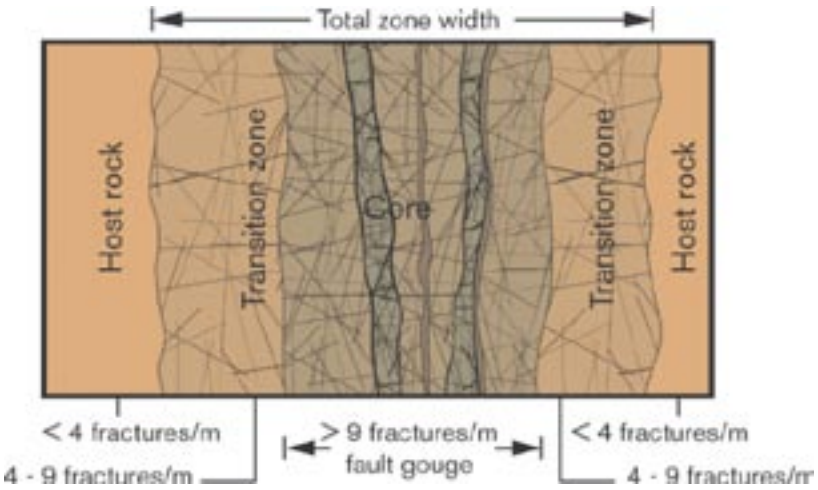

Figure 2-2. *Schematic illustration of the structure of a brittle deformation zone (image taken from /Munier et al. 2003/).*

[1] The geological term “en echelon” is used to describe parallel or subparallel, closely-spaced, overlapping, or step-like minor structural features in rock, such as faults and tension fractures, that are obliquely aligned to the overall structural trend.

At the Forsmark site it is generally observed from flow logs that most flowing features are concentrated to the outer core region of deformation zones and in some cases even concentrated to the outer core/transition zone boundary. In some cases the inner core of deformation zones behaves as an effective hydraulic barrier owing to its low permeability. This was observed, for example, in large-scale hydraulic pumping tests in the Singö zone at Forsmark /Follin et al. 2008/. In this particular case, good hydraulic connectivity was observed between boreholes on the same side of the deformation zone, although relatively poor connectivity between boreholes on opposite sides of the zone.

Deformation zones at the Forsmark site exhibit a large degree of heterogeneity and many bore core intercepts with deformation zones either give very unevenly distributed indications of flow or appear to be completely non-conductive, particularly at greater depths. There are very few instances of flow features evenly and pervasively distributed throughout the thickness of a zone.

Horizontal sheet joints

A number of converging lines of evidence /Follin et al. 2008/ have indicated the existence of a highly conductive, near surface aquifer at the Forsmark site, most particularly in the North-West region of the local model area. The hydrogeological and structural evidence point towards a well connected network of high transmissivity fractures that short circuit the recharge from above as well as the discharge from below thereby giving nearly uniform groundwater levels in the upper 100 m of bedrock (referred to as the "shallow bedrock aquifer"). Chief among the features that are thought to contribute to this effect are the so-called horizontal sheet joints which intersect outcropping deformation zones and single fractures between the deformation zones bounding fracture domain FFM02 /Follin et al. 2008/. The hypothesised location and extent of the feature is shown in Figure 2-3.

Figure 2-3. *The hypothesised horizontal extent of the discrete features as described by /Follin et al. 2008/. The feature approximately covers fracture domain FFM02 and is thought to terminate against the Singö deformation zone to the north (ZFMWNW0001) and ENE0062A to the southeast. The crosses mark the positions of percussion and core-drilled boreholes for which transmissivity measurements are available.*

The conductive structures are heterogeneous although are thought to follow the undulations of the bedrock in such a way that they do not outcrop and stay below the bedrock surface as this dips under the Baltic sea. This feature is considered important for the site specific transport properties at Forsmark since it strongly influences hydraulic gradients within the target volume and governs pathways for solute release at the surface.

2.1.2 Conceptual description of the HRD

The Hydraulic Rock Domain (HRD) is the name given to the relatively sparsely fractured bedrock outside of the deformation zones and is also taken to include minor deformation zones (MDZ) which are not modelled deterministically. As mentioned previously, the rock domains are further sub-divided into six different fracture domains (FFM01–FFM06). This sub-division is based upon fracture frequency characteristics and also reflects the fact that different parts of the HRD have different hydrogeological properties.

The HRD contains many fractures; some open and hydraulically connected to the wider fracture network, some are open although hydraulically isolated, while others may be closed – either tightly sealed by surface asperity contact or annealed by precipitation of minerals. Annealed fractures may be the result of precipitation from saturated hydrothermal fluids or contemporary low temperature groundwater. Annealed fractures may also be reactivated at different times by tectonic stresses.

In the HRD, fractures are considered to span a range of sizes from mm-scale to about 560 m in radial extent which is the lower cut-off for deterministically defined deformation zones /Stephens et al. 2007, Fox et al. 2007/. In the hydrogeological modelling work described in /Follin et al. 2007a/ a circular fracture with a radius of 560 m is taken to be equivalent to a square fracture of side length 1,000 m.

In the geological modelling for SDM-Site it is hypothesised that the frequency of fractures in the HRD is correlated with size by way of a power law (Pareto) distribution which implies a scale-invariant behaviour. This is not the only way to represent the size distribution of the fracture population, but it is mathematically convenient and tends to be supported by observational data at the Forsmark site /Fox et al. 2007/. The larger features, however, are rarely individual fractures and may be considered as linked sets of smaller fractures and minor deformation zones. Deformation zones larger than 1,000 m radius are modelled deterministically in the SDM and are therefore consigned to the HCD.

Generally speaking, dilating parallel fractures in close proximity propagate in such a way that they tend to overlap and converge towards each other owing to the local stress concentrations in the rock. The fractures typically converge “fracture tip to fracture plane” and are interpreted en-echelon as a single feature. The converging parts of the fractures are referred to as “jogs”. For small differential stresses in the rock, there is strong tendency for near lying fractures to interact and converge in this way. For large differential stresses, on the other hand, there is a greater tendency for fractures to overlap for considerable distances without forming connections /NRC 1996/.

Fractures undergoing stress induced shear can interact in complex ways to form minor deformation zones (MDZ). They tend to link up in an en-echelon geometry over a wide range of scales. The so-called “stepover” zones where fault fractures interact tend to be locally very fractured and can form efficient conduits for fluid flow in a perpendicular direction to the shear direction. The permeability of these features may be modified by the precipitation of secondary minerals thereby reducing potential for flow. It is generally thought that the direction of increased permeability in overlapping regions of the en-echelon fractures is oriented in the direction of intermediate principal stress unless completely filled by mineral precipitates /NRC 1996/.

The target volume resides in the bedrock underlying the gently dipping deformation zone ZFMA2 (the so-called "foot wall") and consists of the two rock domains RFM029 and RFM045 as shown in Figure 2-4. The rock domain RFM029 also extends into the rock overlying ZFMA2 (the so-called "hanging wall"), although this is not part of the target volume. The hanging wall of ZFMA2 contains extensive sheet joints and intense fracturing that renders it highly conductive and hydraulically well connected over significant distances (actually, kilometre scale connectivity established on the basis of hydraulic interference tests /Gokall-Norman and Ludvigsson 2007, Gokall-Norman et al. 2005/). This highly conductive near surface zone constitutes the so-called "shallow bedrock aquifer" feature which is characteristic to the Forsmark site.

The fracture domains comprising the HRD are defined in some detail in /Olofsson et al. 2007/, although in summary we can say the following:

- The target volume consists of the three fracture domains FFM01, FFM02, and FFM06 which are resident in rock domain RFM029 and RFM045.
- Fracture domains FFM01 and FFM02 lie in the foot wall of ZFMA2 and are part of rock domain RFM029.
- Fracture domain FFM06 is part of rock domain RFM045.
- Fracture domain FFM03 lies in the hanging wall of ZFMA2 and is part of rock domain RFM029.
- Fracture domains FFM04 and FFM05 are external to the target volume and reside in rock domains RFM012+RFM018 and RFM032+RFM044 respectively.

The layout of the fracture domains relative to the rock domains and ZFMA2 is shown in Figure 2-4.

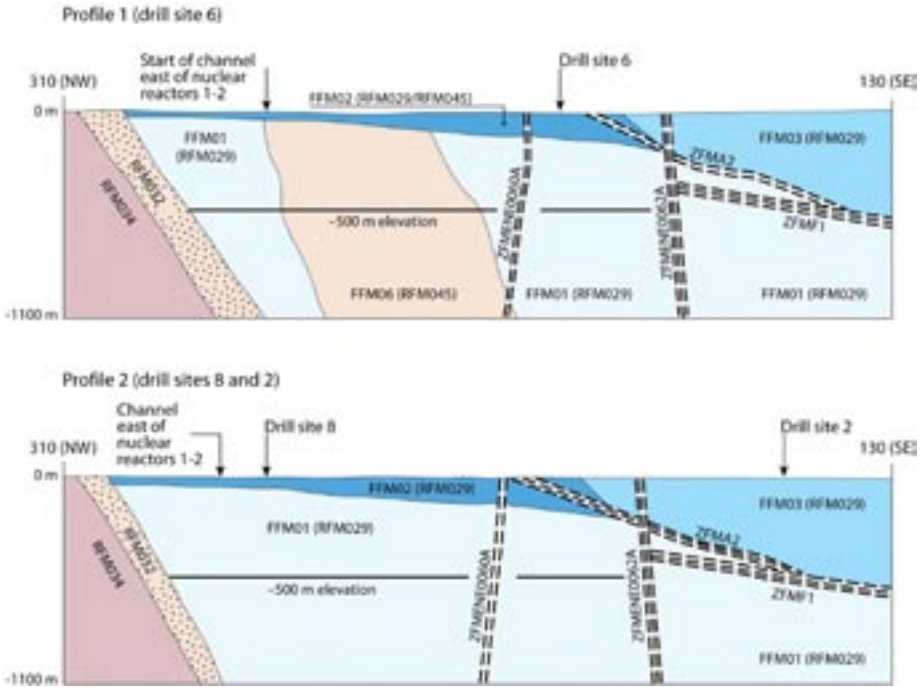

Figure 2-4. *Simplified profiles showing a NW-SE cross-section passing through drill sites 2 and 8 (lower profile) and drill site 6 (upper profile). The labelled fracture domains (FFM01, FFM02, FFM03, and FFM06) occur inside rock domains RFM029 and RFM045. Only the high confidence deformation zones ZFMA2 (gently dipping), ZFM1 (sub-horizontal), and ZFMENE0060A–ZFMENE0062 (steeply dipping) are shown in the figure (image taken from /Olofsson et al. 2007/).*

Most fractures within the target volume are sealed. Based upon the overall statistics of core borehole intercepts at Forsmark, roughly 24% of all mapped fractures are judged to be open and only about 1.7% are associated with flowing features. Of the fractures that are judged to be open, roughly half are considered to be only "possibly open". Detailed statistics of individual deformation zones and fracture domains can be found in the hydrogeology background report /Follin et al. 2007a/. Generally, the overall fracture frequency in the HRD is about one third that found in the HCD, whereas for open fractures the figure is closer to one quarter suggesting that fractures are less likely to be open in the HRD. Taken as a whole, the intensity of flowing features in the HRD is roughly 20% of that in the HCD.

The intensity of fracturing and the frequency of flowing features within the target volume tend to decrease with increasing depth at the Forsmark site while the degree of anisotropy tends to increase somewhat. On average, the open fracture frequency in the upper 200 m of the bedrock is about 2 m^{-1} which falls to 1.1 m^{-1} down to a depth of about 400 m, and about 0.6 m^{-1} below 400 m. The depth trend in frequencies of flowing features is even more marked, and in FFM01 at a depth below 400 m there are only a handful of flowing features to be found outside the deformation zones within the core boreholes.

On the basis of this observation (and in addition to the geological delineation of fracture domains), hydrogeology have introduced further sub-domain volumes where hydrogeological properties differ significantly. These will be discussed in more detail in section 3.2 in connection with the Hydro-DFN model for the HRD.

2.1.3 Flow channelling phenomena

In fractured crystalline rock it is generally thought that flow is heterogeneously distributed and occurs along preferential flowpaths within fractures and deformation zones. This phenomenon is commonly referred to as flow channelling.

In SDM-Site, six principal types of flow channelling have been identified as having relevance for the bedrock transport properties evaluation. These are:

1. Network-scale flow channelling.
2. In-plane flow channelling.
3. Flow channelling at fracture intersections.
4. Flow channelling at geological interfaces.
5. Flow channelling within foliations.
6. Flow channelling within fault stepovers, shears and fracture jogs.

Other, more exotic flow channelling effects are referred to in various discussions in this report. These, however, are considered to be special sub-types of the above listed categories and are not treated explicitly as separate phenomena. Examples are low temperature karstic erosion wormholes in calcite or laumontite annealed fractures, and flow pipes lined with hydrothermal precipitates (e.g. quartz or epidote) as might be found within fault zones that have been subject to aggressive hydrothermal activity.

In the following sections, we shall examine each of the identified six principal types of flow channelling and discuss how they may influence the flow properties of the rock at the Forsmark site. It is noted already here, however, that many aspects of flow channelling are difficult to fully resolve from a surface-based site investigation and may not be possible to properly quantify until the construction of an underground tunnel where more detailed hydrogeological information can be obtained.

Network-scale flow channelling

This type of flow channelling refers to the tendency of heterogeneous fracture networks to exhibit poor hydraulic connectivity and form preferential flowpaths on the scale of the fracture network itself.

When there are large contrasts between transmissivities of individual fractures comprising the network, fluid flow will tend to seek out the path of least hydraulic resistance. If the fracture network is sufficiently poorly connected, this may also give rise to flow compartmentalisation and fractal behaviour. Here, the term fractal is used strictly to describe the spatial distribution of flowing features rather than other scale independent properties such as power law fracture size distributions. We consider network flow channelling processes of this kind to include both regional flow channelling within linked major deformation zones in the HCD as well as on the scale of local fracture clusters within individual deformation zones and the HRD.

For flowing features within the rock to exhibit this behaviour does not necessarily require the fracture network itself to conform to a fractal spatial distribution as this flow characteristic can arise spontaneously in Poissonian fracture networks when close to the percolation threshold /e.g. Follin et al. 2006b/. The impact of fracture network connectivity upon the flow and transport properties of the rock is discussed in more detail in Chapter 3.

In-plane flow channelling

This type of flow channelling refers to the tendency for preferential flowpaths to develop within the plane of individual fractures. It arises due to the variable aperture of the void space between opposing fracture surfaces which results in a spatially variable transmissivity field across the fracture plane.

Although visualised as planar structures, fractures in crystalline rock are typically rough and have highly irregular surfaces. Dilating fractures initially have open, although very slight apertures owing to normal displacement of opposing surfaces. Initially mated, opposing surfaces of such fractures can become mismatched at some length scale due to shear movement relative to the plane of the fracture. When this occurs a somewhat larger void space may emerge where there are regions in which the surfaces are in direct physical contact and regions in which the fracture has a non-negligible aperture /NRC 1996/. Under compression a certain degree of surface asperity contact is usually necessary owing to the need for the fractures to transmit stress. An exception is if the fluid pressure is sufficiently high that the fracture is held completely open. This, however, is highly unusual and such fractures will tend to close again unless held open by mineral precipitates or other detritus in the enlarged void space. There is evidence that the extensive horizontal sheet joints in the near surface (100–150 m) at Forsmark exhibit features consistent with this process that may have occurred during glacial retreat after the last ice age /Follin et al. 2007a/. In this case, clogging by glaciofluvial sediments have resulted in apertures of up to a decimetre or more in these features.

The variable aperture of fractures and the degree of surface asperity contact is dependent upon the effective normal stress perpendicular to the fracture plane. As the hydraulic resistance of a fracture arises due to the viscous forces between the flowing water and the fracture surface, the aperture distribution as well as the existence of flow constrictions and flowpath tortuosity have a very strong influence upon the effective transmissivity of individual fractures.

The aperture and asperity contact area of a fracture tends to vary with applied stress in a complicated fashion. Generally, surface asperity contact area increases approximately linearly with increasing effective normal stress as the rock deforms elastically /e.g. Glover et al. 1998b/. The effective transmissivity of single fractures, however, is known to decrease roughly exponentially with increasing normal stress /NRC 1996/. Substantial shear movements, on the other hand, may cause destruction of asperities and give rise to slickenside striations running parallel to the shear

direction. Repeated loading-unloading cycles and shear reversal as might occur during glaciation-deglaciation also tend to result in hysteresis effects for the relation between transmissivity and stress /NRC 1996/. The overall picture of the effect of *in situ* stress on fracture transmissivity and flow channelling is thus complicated and varies significantly among individual fractures with different tectonic histories. Although the relationship between fracture normal stress and transmissivity is well known for reconfined single fractures described in the scientific literature, it is very difficult to ascertain any universal relationships that are generally applicable for heterogeneous fracture populations. The Forsmark site is no exception in this respect.

A significant concern for flow modelling is that if substantial fractions of fracture surface are in direct physical contact, flow channels may be very narrow and sparsely distributed within individual fractures. In such cases it has been suggested that the frequency of flowing features in the rock may be severely underestimated during flow logging owing to the limited extent of the flow channels and the low probability of intersection with a borehole. A secondary concern is whether the transmissivities of identified flowing features have been assessed correctly given that flow may be strongly channelised over the radius of influence of the measurement. These concerns have been addressed in the present report by way of generic scoping simulations which are described in more detail in section 3.10 and Appendix B.

Flow channelling at fracture intersections

Flow channels arising at the intersection of crossing or terminating fractures have been suggested as possible conduits for fast flow and transport in fractured rock /NRC 1996/. Observations of increased flow at fracture intersections in tunnels constructed in crystalline rock have been reported in the literature /e.g. Abelin et al. 1990, 1991, 1994, Neretnieks 1994/. Some observations of such flow features have also been reported for the Forsmark site by /Carlsson and Olsson 1977/ who studied inflow to tunnels in the vicinity of the nuclear reactor plant in Forsmark. Such features are referred to in this report as fracture intersection zones, or FIZ (using the terminology introduced by /Dershowitz and Klise 2002/). This channelling phenomenon is predicted to occur on the basis of the theoretically reduced viscous resistance for flow parallel to fracture intersections.

For the Forsmark site descriptive modelling, we consider three possible sub-types of flow channels formed at fracture intersections. These are:

A. Simple flow conduits formed at crossing or terminating fracture intersections.

B. Enlarged flow conduits formed due to displacement of block discontinuities.

C. Enlarged flow conduits formed at fracture intersections with enhanced aperture due to spheroidal weathering processes.

These sub-types are illustrated schematically in Figure 2-5.

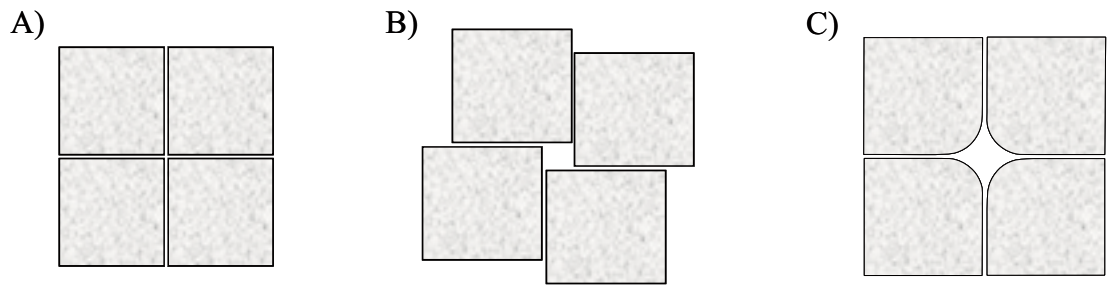

Figure 2-5. *Sketch of different sub-types of flow channelling phenomena potentially occurring at fracture intersections.*

Flow channels characterised as sub-type A for crossing or terminating fracture intersections are ubiquitous within the rock and will exist wherever there is an intersection between two open fractures. From flow modelling of smooth fracture intersections it has been found that the Darcy flux at fracture intersections can be as much as 2-4 times greater than that within the flanking fracture planes if surface roughness is neglected and the applied hydraulic gradient is parallel to the line of fracture intersection (see Appendix A). The enhanced Darcy flux at the intersection will, however, probably not be as great as this in the presence of rough fracture edges, discontinuities and filling materials. Even so, it is possible to discount the influence of such flow channels by consideration of the overall rate of flow. This is discussed in more detail in Appendix A.

Intersection sub-type B is possible where free rock blocks, as might exist in deformation zones, are rotated by shear movement giving rise to an enhanced aperture. In this case it is also possible for stress concentrations at the contacting edges to predispose the corners of the blocks to breakage thereby further enhancing the effective mechanical aperture /Bruines 2003/.

Flow conduits of sub-type C can arise in fractures initially of sub-type A or B as a result of subsequent spheroidal weathering processes. This occurs during geochemical weathering of granitic rock when the formation of secondary minerals in the alteration rim of the fracture weakens its structure. This is particularly the case for oxidative weathering processes where alteration products such as ferric oxy-hydroxides have higher specific volumes than the minerals initially present in the rock matrix. At fracture intersections and block discontinuities weathering is more intense as it can proceed from two adjacent surfaces simultaneously. The combined effect is a tendency for fracture intersections to evolve towards a cuspoid geometry with a substantially enhanced aperture. These types of features are more likely to be found in transmissive deformation zones where hydrothermal alteration has occurred most intensely. At the Forsmark site, roughly 42% of the core borehole intervals within deformation zones exhibit visible signs of oxidative alteration. For the borehole intervals within the fracture domains the figure is only 7% indicating that a large proportion of the oxidative alteration has been restricted to the HCD.

Flow channels corresponding to sub-types B and C present very little viscous resistance to flow and it is possible for very high flow rates to exist in such features. In these cases, fault gouge and fracture filling materials as well as the hydraulic resistance of entry and exit points are the only entities likely to limit flow. In such cases, aperture based analyses of flow resistance may be inaccurate and relations for flow in packed beds of particulates (e.g. the Blake-Kozeny relation /Bird et al. 2002/) may be more appropriate.

Owing to their limited width, it is very difficult to observe such features in boreholes and we can only infer the possibility of their existence from geological argumentation. Although we cannot estimate the spatial frequency or flow properties of these features directly from observational data in boreholes, it is possible to make scoping calculations of the impact that they may have on flow and transport of solutes under different limiting assumptions. This is discussed in more detail in section 3.10 and Appendix D.

Flow channelling at geological interfaces

Here, we consider flow channels that may occur in the vicinity of dykes and other igneous intrusions in the rock. This includes dyke parallel joints and similar geological features, although we extend the definition here to also include regions in the rock where penetration of aggressive hydrothermal fluids have rendered the rock matrix locally more permeable. An example of this at the Forsmark site is the vuggy metagranite formed during quartz dissolution and found in the upper 250–300 m of borehole KFM02A.

Although the increased flow permeability of the rock characterised as vuggy metagranite is well-documented, it is not clear whether dyke parallel joints and similar structures are represented at the Forsmark site. Whatever the case may be, these features are most likely to have

only a limited impact upon flow properties at the site owing to their limited spatial distribution (i.e. they occur only where geological interfaces exist and are atypical for the HRD in general). Such features, if found in the HCD would be internalised as part of the description of specific deformation zones and therefore do not require any special treatment.

Flow channelling within foliations

During ductile deformation, potential flow channels can be created within dilational fractures. These fractures typically form parallel to the fold planes and in the direction of the intermediate stress component /Bruines 2003/. Additional dilational fractures may also form perpendicular to the fold plane in the convex part of the folding structure /NRC 1996/. These features may occur wherever ductile deformation and foliation occurs although are principally thought to be a feature of the HCD.

Flow channelling within fault stepovers, shears and fracture jogs

Overlapping regions of extensional faults or en-echelon fault zones typically host linking structures including fault stepovers, Riedel shears, crush zones, etc that are known to form open conduits for flow that can be oriented in a direction parallel to the intermediate stress vector associated with the formation of the fault /NRC 1996/. These conduits may consist of conductive dilating fractures, fracture clusters, and structural sub-elements such as FIZ (principally sub-type B and C with enlarged apertures). The hydraulic properties of such features are complex and not well understood, although they can potentially host highly transmissive flow channels of limited extent.

Precipitates of secondary minerals such as calcite and quartz from past hydrothermal events can modify the permeability of the flow channels, sometimes effectively propping open the hydraulic aperture to resist subsequent closure during altered stress regimes. The cementation of the flow pore space with precipitates and aggregated breccias can also have consequences for the possibility of detecting such features from borehole investigations as they may be wormhole like (similar to karstic porosity) and hydraulically isolated from nearby open fractures. This is further complicated by the slip of the fault surfaces themselves which can lead to the formation of highly impermeable structures near the core of the deformation zone that can hamper the detection of such features. Low permeability bands can also develop in gouge materials subjected to shear /e.g. Zhang and Tullis 1998, Zhang et al. 1999/. Borehole investigations, however, give no indications of gouge present in the deformation zones at the Forsmark site /Stephens et al. 2008/.

Although such flowing features are probably more likely to occur in the large deformation zones comprising the HCD, similar but less transmissive flow channels could also be hosted in en-echelon, overlapping fractures undergoing dilation (“fracture jogs”) or within minor deformation zones present in the HRD.

Flow conduits of this type within fault stepovers are thought to be very likely in the HCD and the reduced permeability resulting from diagenetic processes cannot be ruled out as a potential problem for the detection of these features from boreholes drilled from the surface. On the other hand, it is not clear whether flow conduits in the simpler structures hosted in the HRD should be more, or less easy to detect than “normal” in-plane flow channels identified from borehole hydraulic testing. Although beyond the scope of what was possible to achieve during this investigation, information contained in the geological site descriptive model could be used to make estimates of the possible biasing effect this might have upon statistics of flowing features identified in the HRD.

2.2 Solute transport

In this section the transport properties of the rock are described. Although the mechanisms and processes that influence transport have relevance for many different environmental solutes, we place particular emphasis upon the migration of radionuclides from a hypothetical repository to the ground surface.

In crystalline rock such as granite, all long range transport occurs by way of advectively channelised flow. Owing to the low permeability of the rock, the water residing in the porosity of the rock matrix is considered to be immobile and long range transport through the rock mass itself can be neglected over the timescales relevant for safety analysis. There are a number of processes which act to retard the transport of solutes in such a way that they are transported at a slower rate than the groundwater within which they are carried. These processes are described in the following sections.

2.2.1 Fractured rock microstructure and the conceptual understanding of solute transport

In the event of deposition canister failure, radionuclides may escape and migrate to the surrounding rock through the bentonite buffer or backfilling material surrounding the canister emplacement. The radionuclides may then be transported into fractures intersecting the deposition hole, into the disturbed zone around the excavated volume, and into fractures intersecting the tunnels.

Radionuclides that reach the rock volume are transported by the groundwater flowing in fractures within the rock. Certain radionuclides may sorb on the surface of the fractures through which they are transported. From the fractures they may also migrate into the rock matrix by molecular diffusion. As flow is commonly channelised, there may be regions of stagnant water within the fractures into which nuclides can migrate by molecular diffusion and then subsequently migrate into the rock matrix. The interior of the rock matrix contains stagnant "porewater" and micro-surfaces upon which the radionuclides can sorb.

An illustration of a typical open fracture likely to be found in the fracture domains at Forsmark is shown in Figure 2-6. Open, water bearing fractures generally feature a thin coating of secondary mineralisation typically consisting of chlorite, calcite, and mixed layer clay minerals. Smaller amounts of other minerals such as hematite, prehnite, epidote, and individual pyrite mineral grains may also be present (see section 4.2.1). It is frequently found that the mineral coatings exhibit a discontinuous structure rather than forming distinct layers. Single mineral phases such as calcite can therefore be found in direct contact with both the fracture surface and flowing water in the fracture and are interspersed with, for example, chlorite in a patchwork like arrangement. There may be an alteration rim of limited thickness, which may or may not be made visible by red staining (due to the presence of hematite microprecipitates), adjacent to the fracture surface and extending a short distance into the rock. A statistically significant number of open fractures have been identified at the Forsmark site that lack surface mineralisations possibly indicative (although not necessarily) of geologically recent formation. These are discussed in more detail in Chapter 4.

Fractures may have been formed at different times, been reactivated, and undergone both hydrothermal and low temperature alteration processes giving rise to different fracture filling materials. In borecores taken from the Forsmark site, younger fractures containing filling materials formed at low temperature are frequently seen to transect older fractures annealed with filling materials of hydrothermal origin. This is illustrated in Figure 2-6 by the diagonally crossing fracture filled with, what could be assumed to be, hematite stained adularia based upon coloration. The depicted open fracture is what customarily is referred to as a "background fracture" to distinguish it from structures such as minor deformation zones which exhibit substantially greater microstructural complexity.

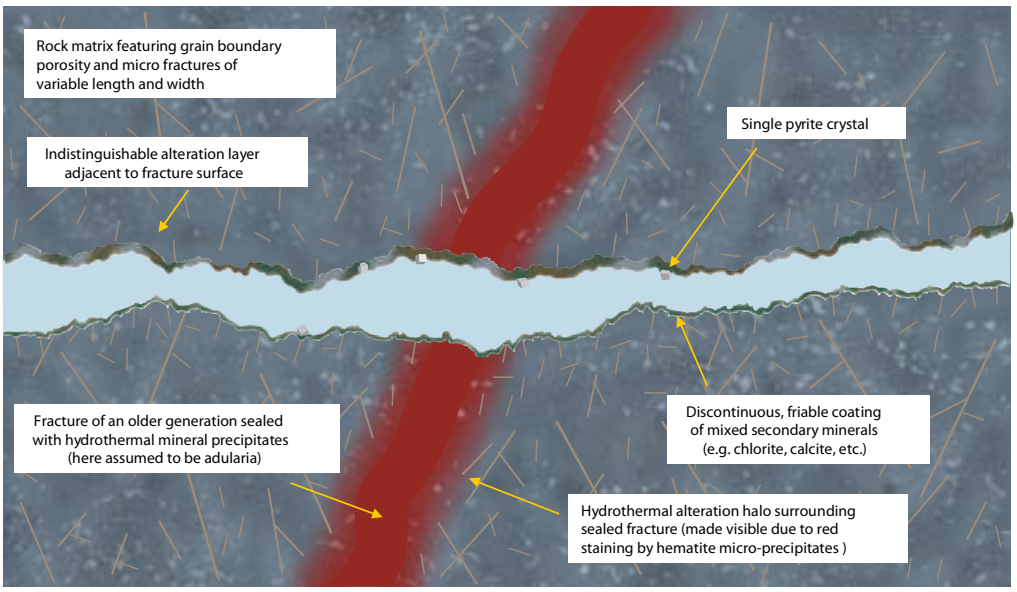

Figure 2-6. *Schematic illustration of a transport path in cross-section. The pathway is characteristic of a typical fracture with a discontinuous coating of secondary minerals. A mix of discontinuous chlorite and calcite coatings are shown in the figure with the occasional pyrite mineral grain. A typical sealed fracture of an older generation is shown transecting the open fracture section. The sealed fracture filling is a hydrothermally precipitated mineral such as adularia with red hematite staining. A reddish hydrothermal oxidation halo is also shown at the interface between the fracture filling and surrounding rock matrix.*

Eight different fracture types have been identified at the Forsmark site. These differ only in the types of secondary minerals present in the fracture coating and the estimated thickness of the alteration rim. The classification is based partly upon the different historical epochs of alteration that are thought to have occurred at the site, and partly upon the potential for the different secondary minerals to influence transport processes. By far the most common fracture mineral is chlorite, often found in combination with calcite and occasionally other clay minerals. The different fracture types are discussed in more detail in section 4.5.2.

In principal, we conceptualise the fractures comprising deformation zones to be similar to the background fractures in the fracture domains, although with added microstructural complexity and with different proportions of type-fractures. Fractures within deterministic deformation zones comprising the HCD are considered to have layers of hydrothermal and sometimes tectonic alteration that extend from the fracture surface to some distance within the host rock. In some cases, the rock between successive fractures is completely altered leaving no intervening unaltered rock whatsoever. During the evolution of the rock, the fractures may have been sealed by secondary mineral precipitates and reactivated in different cycles. The fracture coatings therefore are not necessarily distributed evenly on both surfaces of the fracture.

In the conceptual model, advection within flow channels is the dominant process for long range transport, whereas the main role of diffusion is to remove the radionuclides from the mobile zone and transport them within the immobile zones where they may sorb on mineral surfaces and be sequestered in the water filled porosity of the rock matrix. In the following sections these processes will be discussed in more detail.

It should be noted that this conceptual model and the methodology for site descriptive modelling in general are, to a large extent, based on previous experience from experiments at Stripa /e.g. Birgersson et al. 1992/ as well as from the Äspö Hard Rock Laboratory (HRL). The conceptual model illustrated in Figure 2-6 is derived primarily from the TRUE project /Winberg et al. 2000, Poteri et al. 2002/ carried out at the Äspö HRL, although is considered applicable to the transport conditions in the Forsmark area.

Matrix diffusion

Matrix diffusion is considered to be a major mechanism for the transport retardation of radionuclides released from a repository /Neretnieks 1980/. Put simply, it describes the tendency for solutes to be transported by random molecular movement from regions of high concentration to regions of low concentration within the immobile zone. Diffusion in the rock matrix takes place within the connected microporosity of the rock. The microporosity consists mainly of grain boundary pores and micro-fractures. Additional pore types that can exist are sheet silicate pores (the inter-layer regions of clay minerals) and solution pores or fluid inclusions /Möri et al. 2003/.

Grain boundary porosity has been found to be the most abundant pore type in low porosity (< 1%), unaltered rock at Forsmark. This has been established using autoradiograph measurements of core sample impregnation with ^{14}C-labelled poly-methylmethacrylate (^{14}C-PMMA) /Penttinen et al. 2006/. Altered core samples featuring high porosities, on the other hand, have been found to be dominated by intragranular porosity (i.e. microfractures). Samples taken close to water bearing fractures tend to be highly porous (as much as 10%) for a depth of several cm into the rock matrix. This also tends to be dominated by micro-fracture porosity although weathered mineral grains with internal porosities of up to 20% have also been identified in the PMMA studies.

It is difficult to obtain fully representative samples from bore cores owing to stress relaxation and mechanical damage incurred during core excavation and sample preparation. This generally results in dilation of the existing pore spaces and the formation of additional micro-fractures that increase the porosity of samples used in laboratory measurements.

In the rock mechanics laboratory programme, the volumetric strain response of rock during hydrostatic triaxial compression was measured for matrix core samples taken from KFM01A and KFM02A at Forsmark (sampling elevations from –200 m to –600 m) /Jacobsson 2007/. From this data, it would appear that stress release could account for a considerable proportion of the total, unstressed porosity of matrix core samples from Forsmark. These measurements were performed on large core samples with a diameter of 51 mm and length of 130 mm so may not be representative of samples which have been sawn into smaller pieces. Independent measurements made by comparison of water loss in original and re-saturated 120 mm core samples from KFM01D during the matrix porewater characterisation have also indicated the possibility of a stress-release related dilation of matrix pore spaces (as much as 50%) during and after core sample retrieval /Waber and Smellie 2007/.

Laboratory through diffusion and electrical resistivity measurements are typically made on core samples 1–3 cm in length. The results obtained for samples of different length generally show reasonable agreement, although artefacts related to core damage and stress-release cannot be entirely ruled out.

Under increasing *in situ* stresses, the pore spaces may become compressed resulting in reduced effective diffusivity. Since the stress magnitude in the target volume (i.e. FFM01 –400 m to –600 m) is relatively large /Glamheden et al. 2007/, we expect a non-negligible compression of the micro-porosity in the rock matrix *in situ*. An additional complicating factor is the highly anisotropic nature of the stress field within the target volume, which has an unknown effect upon the pore closure. The rock matrix directly adjacent to open fractures and flowing features, on the other hand, may be less affected by *in situ* pore compression owing to locally relieved stress conditions and locally more intense micro-fracturing.

It has been hypothesised /Löfgren 2004/ that grain boundary pores should be ubiquitous throughout the rock mass. The reasoning for this is as follows: When rock magma crystallises at great depths, the grain boundary porosity is virtually non-existent and individual crystals are as closely packed as possible. As the rock is uplifted (which occurred during Proterozoic times in the case of the Fennoscandian shield), the temperature decreases, mineral grains become increasingly rigid and the pressure decreases. As different minerals have different thermal expansion coefficients and bulk moduli of expansion, some grains expand while others contract during this process. This uneven change in mineral volume gives rise to a void surrounding individual grains. Above a certain temperature, void creation is likely to be counteracted by

re-crystallisation and other processes associated with metamorphism. At some point during the uplift, metamorphism ceases due to low temperature conditions. Uplift from these depths may create the grain boundary porosity observed today within the rock matrix around repository depth. The differential expansion of mineral grains may also induce strains that result in intragranular micro-fracturing as an additional mechanism for the formation of porosity.

The process of grain boundary expansion is such that we might expect connectivity of grain boundary pores to extend throughout the entire rock mass in a pervasive manner. It should be remembered, however, that this is purely a hypothesis at present and would need to be confirmed by microscopic characterisation and thermal modelling. It is also possible that the pressure field *in situ* doesn't allow for the relatively small thermal expansion differences to manifest beyond the vicinity of the fracture zones and in the form of microfractures. This could also mean that grain boundary pores may only occur in de-stressed core samples where significant decompaction of the mineral crystals forming the rock matrix has occurred.

Studies of *in situ* rock resistivity, as described in section 4.3, lend strong support to the concept of matrix pore connectivity over large distances into the rock matrix. There are also a number of examples of long stretches of rock within boreholes which exhibit (*in situ* measured) diffusive properties roughly equal to the site average although without a single mapped open fracture for up to 10–15 m (see Appendix H). The existence of diffusive exchange over many tens of metres and very long time scales is also strongly supported by the signatures of paleo-hydrogeochemical markers found in the porewater of the rock matrix at the Forsmark site /Laaksoharju et al. 2008/. Specifically, the fact that sampled matrix pore water many tens of metres distant from the nearest identifiable flowing fracture contains relict groundwater signatures is a strong indication of an essentially unlimited matrix penetration depth regardless of how fast the process is thought to occur.

Matrix diffusion is customarily considered to involve diffusion in the stagnant pore water that saturates the microporous system of the rock matrix. Diffusion from flowpaths to stagnant water volumes, however, can also occur in fault gouge, fracture coatings and in stagnant water lying within the fracture plane itself. Diffusion in water-bearing, although hydraulically non-conductive fractures which incidentally intersect advective transport paths may also be significant for retention if the fracture frequency is sufficiently high. Diffusion within the in-plane stagnant zones of an advective fracture as well as subsidiary stagnant water-filled fractures may have important consequences for solute transport when consideration is also given to the additional matrix surface area potentially available for solute interaction /Neretnieks 2006a/.

The rate of diffusive transport in the rock matrix is (in addition to the concentration gradient) determined by:

- The intrinsic diffusivity of the solute species in the pore water.
- Sorption reactions (discussed in the following subsection).
- The geometry of the porous system (the formation factor).
- Non-partitioning interactions between solutes and mineral surfaces (e.g. anion exclusion, diffusion of cations in the electrical double layer).

Often the diffusivity of a species in the pore water is approximated as the diffusivity of the species at infinite dilution. This is inexact and in certain circumstances additional consideration needs to be given to multicomponent effects and the possible influence of the electrical double layer (EDL) within the limited pore space of the rock matrix. For very dilute solutes multicomponent effects can be largely neglected, although they may be of some importance when consideration is given to the transport of major solutes that determine the porewater chemistry. Electrical double layer effects may need to be considered during different scenarios of repository evolution where anion exclusion and EDL-mediated surface diffusion may have a non-negligible impact upon the effective diffusion properties of the rock matrix. The intrinsic diffusivity of solutes is also influenced by the temperature of the porewater which varies with depth from the ground surface. The effect, however, is small and relatively simple to correct for.

Partitioning is discussed in the following subsection although it can be mentioned already here that the immobilisation of solutes at mineral surfaces within the rock matrix decreases their apparent diffusivity (i.e. depth of penetration). On the other hand, it also enables greater amounts of solutes to be transported into the rock matrix as free concentrations in the pore water are kept low for longer periods of time thereby substantially enhancing transport retardation.

There are four main entities associated with the geometry of the porous system that affect the diffusive transport. These are; the porosity, the constrictivity, the tortuosity, and the pore connectivity. The combined effect on the effective diffusivity from the porosity, tortuosity, and constrictivity is internalised in the formation factor. As transport can only occur in the pore water and generally not through mineral lattices themselves, the volume available for transport is restricted. The connected porosity can be divided into transport porosity and "dead-end" porosity (also called storage porosity). Non-connected porosity, such as fluid inclusions, is believed to be of no importance for matrix diffusion.

Sorption

The term "sorption" is a broad concept that describes the processes by which dissolved solutes are sorbed (adsorbed or absorbed) on or in another substance /IUPAC 1997/. Although sorption can also include Van der Waals interactions, in the context of radionuclide transport we mainly consider adsorption to mineral surfaces by way of electrostatic and covalent chemical bonding. In this report we use the terms sorption and adsorption interchangeably.

Sorption can take place on the external fracture surfaces in contact with flowing water or within the microporous structure of the rock matrix itself. Since the diffusion-accessible mineral surface area within the rock matrix can be orders of magnitude greater than that of the external fracture surfaces in contact with flowing water, the sorption of radionuclides can give an enormously increased retardation effect over that of matrix diffusion alone.

Transported radionuclides are usually in the form of ionic, charged species and will tend to sorb upon mineral surfaces that possess a net charge of opposite sign. Such interactions are well described in the scientific literature /e.g. Stumm and Morgan 1996/ and the most important mechanisms for this interaction are thought to be ion-exchange and surface complexation. The surface charge of minerals is usually described as having a *permanent* component which is independent of solution composition, and a *variable* component which changes with the solution composition /Langmuir 1997/. Permanent charge arises due to so-called isomorphous substitutions within mineral crystal lattices as well as lattice imperfections or defects. This is a negative charge as elements within the crystal lattice are replaced by elements with a higher number of valence electrons (e.g. Al^{3+} replaced by Fe^{2+} or Mg^{2+}). The variable charge largely occurs at crystal edges where oxide groups can interact with various aqueous species present in solution.

For phyllosilicate minerals, which includes biotite, chlorite, and smectite clay minerals, the charge is dominated by the permanent component and there is only minor variation with solution composition. For non-phyllosilicate minerals (such as silica, hematite, and feldspar minerals), the charge is dominated by the variable component. The variable surface charge is sensitive to the pH of the solution since it derives from ionisation or reaction of surface oxide groups. These processes give rise to surface "functional groups" such as O^{2-}, OH^{-}, OH_2^{+} which possess charge. From the surface chemistry literature /e.g. Stumm and Morgan 1996/ it is evident that most of the minerals that comprise granitic rock will have negatively charged surfaces at all reasonable groundwater pH values.

Figure 2-7 illustrates the principle of the association of ionic solutes with a charged mineral surface.

Non-hydrated cations form so-called "inner-sphere" surface complexes and are thought to be covalently bound to the functional groups at the mineral surface (the inner sphere complex is indicated as a single grey sphere at the surface in Figure 2-7). These are considered so closely

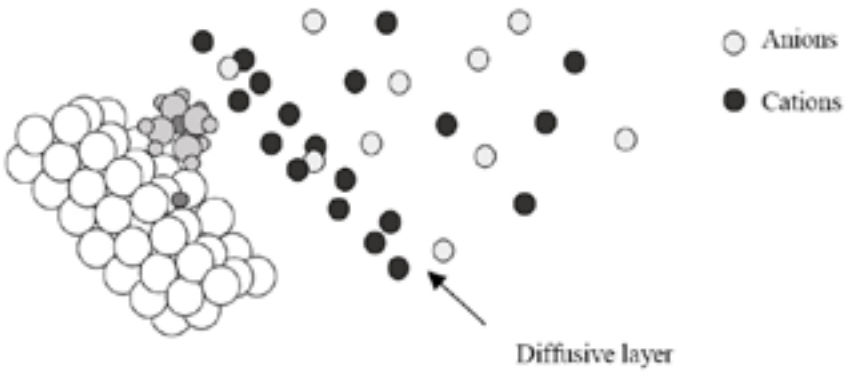

Figure 2-7. *Conceptual illustration of solutes at a mineral surface. Image taken from /Löfgren and Neretnieks 2002/ and adapted from /Stumm and Morgan 1996/. The negatively charged mineral surface is shown to the left of the image (white spheres), while the solution containing ionic solutes is shown to the right (shaded spheres).*

bound to the surface that they are immobile. Inner sphere complexes do not generally balance the entire negative surface charge of mineral surfaces and as a result there are other hydrated cations bound by electrostatic forces to the surface as "outer-sphere" complexes (shown by the grey sphere surrounded by water molecules in Figure 2-7). Although less strongly bound than inner sphere complexes, due to their close proximity to the mineral surface they are considered to be more or less bound to specific functional groups and their mobility is considerably reduced.

In many cases, the inner and outer sphere complexes cannot completely balance the total negative charge of the surface and therefore other cations in solution are attracted towards the surface. At some distance the more closely bound cations shield the residual charge of the surface from less closely bound cations to such an extent that only the potential gradient normal to the surface limits the movement of the less closely bound cations. For these cations, transport parallel to the surface is relatively unhindered while movement normal to the surface is restricted by electrostatic forces. The volume these cations occupy is referred to as the diffuse double layer or electrical double layer (EDL) /Stumm and Morgan 1996/.

Whereas surface complexing solutes associate with reactive functional groups at the mineral surface, exchangeable solutes reside at the mineral surface in close association with permanently charged sites. This interaction is purely electrostatic in nature. Different solutes have different hydrated charge densities and therefore can associate more or less closely with these charged sites thereby giving rise to different affinities for association amongst different solution components. Although they are treated differently in sorption models, it is noted that outer sphere complexes are identical to, and are generally considered to be, ion exchangers /e.g. Bradbury and Baeyens 2005/. Ion-exchange in the context of solute transport in geological media refers to the tendency of certain cations to replace others electrostatically bound to charged sites at the mineral surface due to the differences in sorption affinity.

2.2.2 Modelling approach

In the safety assessment framework that provides the basis for identification of retention parameters in the site descriptive models, retention is assumed to be caused by diffusion and equilibrium sorption /e.g. Berglund and Selroos 2003/. For modelling purposes these processes are usually assumed to be reversible and linear. In safety assessment modelling, diffusive transport of solute within the rock matrix is typically characterised by an effective diffusivity, D_e that can vary spatially depending upon the local microstructural properties of the rock. The effective diffusivity of specific solutes in the rock depends upon the geometric structure and connectivity of the rock matrix porosity which as already discussed can consist of both microfractures

and grain boundary pores. The effect of pore space geometry, specifically the tortuosity and constrictivity of the pores, is formalised in the definition of the formation factor, F_f which is independent of the identity of the diffusing species (see Appendix H). Additional effects such as anion exclusion which can act to reduce the effective diffusivity of specific solutes are typically internalised in the effective diffusivities used in safety assessment calculations by way of an additional correction factor.

The sorption of specific solutes on mineral surfaces is characterised by a linear partitioning coefficient, K_d that describes the equilibrium relation between sorbed and aqueous solute concentrations. While the effective diffusivity is relatively insensitive to the identity of the diffusing species, the sorptivity of different solutes can vary over many orders of magnitude, ranging from very weak sorption in the case of certain ion-exchanging solutes to very strong sorption in the case of trivalent actinides and lanthanides. Some solutes such as tritium, Cl^- and I^- have little or no perceptible sorption at all and their rate of uptake to the rock matrix is governed by the effective diffusivity and storage porosity of the rock matrix.

The sorption of solutes on specific rock types is related to the distribution of minerals in the rock as different solutes exhibit varying affinities for different mineral phases. This is connected to both the surface area and site density of permanent charge and surface reactive groups on individual mineral grains. Sorption is strongly influenced by the composition of the groundwater. The ionic strength, pH, Eh (redox), and presence of various complexing agents can all modify the strength of sorption and have a very strong influence upon the mobility of specific solutes. It is frequently the case that the apparent sorptive variability between different rock types is less than that observed within rock types due to the acute sensitivity of sorption for minute changes in groundwater composition and experimental conditions between different experiments.

All sorptive variability is internalised in the K_d values used in safety assessment by measuring the sorption of radionuclides of concern on different representative rock types in contact with site specific water compositions selected to mirror the likely groundwater chemistry to be found at the site over the relevant timescales.

It is thought that radionuclides will principally be transported via a sequence of pathways featuring successively increasing flow in the HRD until they encounter flowpaths in the HCD from where they may be transported to the near surface. Implicit in this conceptual model is the conjecture of transport in a dual porosity system where there is a clear demarcation between advective and diffusive domains. This is a modelling simplification. In reality, a hierarchy of scales exist for transport within the rock which results in a continuum of behaviours spanning the different size realms.

The use of a Fickian model for solute diffusion in combination with a linear model of sorption (as implied by the K_d concept) are modelling simplifications of what is in reality a complex, coupled reactive transport process. Generally, such simplifications are justified on the basis that the transported radionuclides are considered to be extremely dilute, trace components within the groundwater. There is a broad scientific consensus, however, that provided appropriate parameter values are selected for the prevailing conditions the use of these modelling simplifications is adequate for the goals of safety assessment /see e.g. NEA 1999, Alexander et al. 2003, McKinley and Scholtis 1993/. With regard to sorption, the use of a constant K_d value is contingent upon the following conditions being fulfilled /Crawford et al. 2006/:

- The modelled process is a true equilibrium sorption process.
- The water chemistry, mineralogy, and physical state of the rock are identical to those used in partitioning coefficient data acquisition and do not vary in time and space.
- The solute concentration range encountered along the transport path (for the radionuclide of interest) must not invalidate the fundamental assumption of sorption linearity.

The mechanisms by which radionuclides are postulated to interact with the rock matrix (i.e. diffusion and sorption) are also applicable to the transport of other solutes dissolved in the groundwater and are considered to be part of the suite of chemical reactive processes that affect groundwater composition. For groundwater constituents that are present in sufficiently high concentrations that they themselves exert an influence upon the groundwater hydrogeochemistry, simplifications such as those outlined above cannot be used and more sophisticated reactive transport models must generally be employed.

2.2.3 Alternative processes and process models

Alternative conceptual models for transport could involve additional processes or more refined descriptions of the presently considered processes. In the transport site descriptive model presented in this report, a number of additional mechanisms have been included in the transport modelling of specific radionuclides that have not been previously considered. Specifically, the impact of diffusion into in-plane stagnant zones from narrow flow channels has been considered as well as the consequences of diffusive uptake into the rock matrix in a 2D radially symmetric mode rather than a 1D linear mode as is typically assumed in safety assessment modelling. In both cases, the scoping calculations made for a set of model alternatives incorporating reasonable assumptions give indications that substantial enhancement of radionuclide transport retardation is possible (see Chapter 5) if these mechanisms were to be fully considered in safety assessment.

For radionuclide retention, consideration of more refined representations of radionuclide sorption (process-based, thermodynamic sorption models) and additional retention processes (e.g. precipitation and co-precipitation) are of particular interest. Modelling activities involving process-based models of sorption have been initiated and are ongoing /SKB 2007a/. Although not intended to supercede the use of simplified linearised approaches for transport modelling in the short to medium term, they will play an increasingly significant role in the selection of K_d data appropriate for specific scenarios and partial validation of modelling simplifications used in safety assessment modelling.

Similarly, more detailed consideration of surface mediated transport processes such as anion exclusion and surface diffusion of cations is envisaged as an aid to selection of appropriate data for matrix diffusivities in future safety assessment. Although anion exclusion is an important phenomenon which may decrease uptake of anionic species to the rock matrix, enhanced diffusion of cations in the electrical double layer is currently thought to be of relevance only for very weakly sorbing solutes (more specifically, cations that sorb by ion-exchange). The possibility of more detailed models of matrix diffusion incorporating multiple rates of mass transfer in heterogeneously distributed porosity, and possibly also process based description of diffusion (i.e. Maxwell-Stefan) are possible avenues for future work, although it is not yet clear whether they will provide significantly improved models and insights for safety assessment applications.

3 Flow related transport properties model

As mentioned in previous sections, solute transport in fractured rock is thought to occur primarily along advective flow paths hosted within fractures and deformation zones. Matrix diffusion coupled with sorption has also been identified as the main retardation process that limits the rate at which solutes are transported along these flowpaths. In general, the greater the surface area in contact with flowing water (the so called "flow-wetted surface", or *FWS*) for a given water flowrate, the greater the interaction will be with both the fracture surface itself and the rock matrix. Within SDM-Site the flow-wetted surface to flow ratio is referred to as the "F-factor" /Andersson et al. 1998/ or "hydrodynamic transport resistance". The F-factor is a key parameter governing the transport of radionuclides within fractured rock.

The conceptual understanding and modelling of channelised flow within the rock are central for the prediction of radionuclide transport retardation. In this chapter, the analysis of hydrodynamic controls on radionuclide transport is presented. Here, this takes the form of a simplified conceptual model for transport from a canister position to the near surface via flowpaths of sequentially increasing transmissivity. The focus is upon identifying the flow related transport properties of typical flowpaths within the rock. Using the data and models supplied by hydrogeology for the target volume at the Forsmark site, predictions of F-factors and advective travel times are made according to this conceptual model and a set of assumed boundary conditions. The estimated F-factors and advective travel times are then used as the basis for calculations presented in Chapter 5 where the transport times of representative radionuclides are estimated for site specific conditions at Forsmark.

3.1 Overall modelling strategy

The repository siting concept includes a respect distance /Munier and Hökmark 2004/ of a minimum of 100 m between any given canister emplacement and regional deformation zones with trace length above 3,000 m. These zones are primarily avoided for mechanical protection, although it may also be noted that such zones usually have a high transmissivity and therefore potentially fast transport paths to the biosphere are avoided concomitantly by this choice. In addition to this, the locations of individual canister holes are chosen both to avoid fractures along which sufficient seismic movement can occur that would jeopardise canister integrity as well as to minimise the possibility of buffer erosion from the deposition hole during potential post glacial episodes of increased water flow. The fractures which are likely to intersect a canister position may therefore not be representative of the HRD as a whole and thus should be treated separately in any consideration of typical flowpaths from the repository to the near surface.

In the modelling work presented in this report, we conceptualise transport to occur along advective flowpaths in a multi-compartment system. This is illustrated schematically in Figure 3-1.

The three compartments assumed in the transport model are:

1. The non-engineered near field (NNF).
2. The immediate far field (IFF).
3. The distant far field (DFF).

In this model, the non-engineered near field (NNF) is assumed to comprise approximately the first 10 m or so from a canister position intersected by one or more low transmissivity fractures to the nearest large conductive structure within the HRD. The distance of 10 m is arbitrary although thought to be not an unreasonable order of magnitude estimate of the average distance for a "typical" transport path in the NNF.

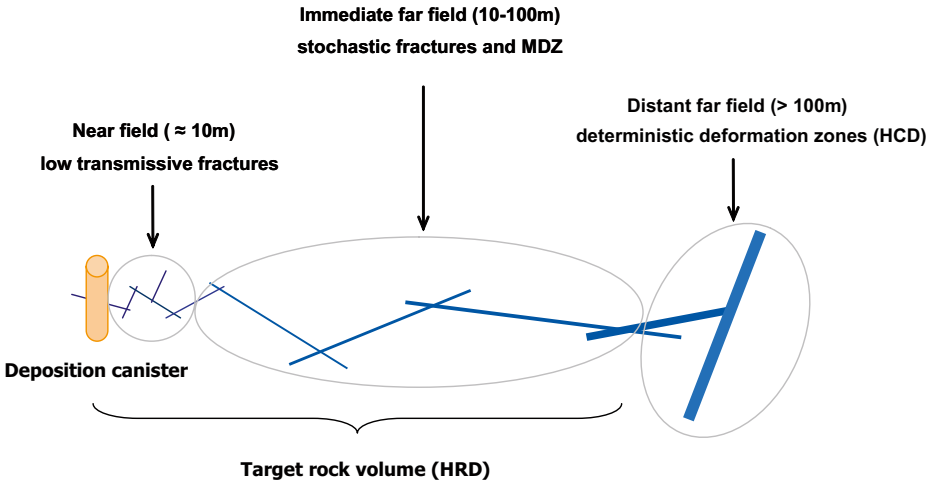

Figure 3-1. *Illustration of a potential flowpath from a hypothetical repository to the near surface. Transport is conceptualised to occur along a sequence of flowpaths featuring increasing transmissivity.*

The immediate far field (IFF) is assumed to comprise the first 10–100 m in the HRD. This distance is also arbitrary, although motivated by consideration of the respect distance to the transition region of large deformation zones. Since fractures featuring high transmissivities are likely to be avoided when selecting canister deposition holes, typical flowpaths within the IFF should, on average, have higher transmissivities than flowpaths within the NFF.

The distant far field in the present context is taken to comprise the deformation zones residing in the HCD. In all, some 131 deformation zones have been modelled deterministically in the hydrogeology SDM for Forsmark /Follin et al. 2007a/. These deformation zones are visualised in Figure 3-2.

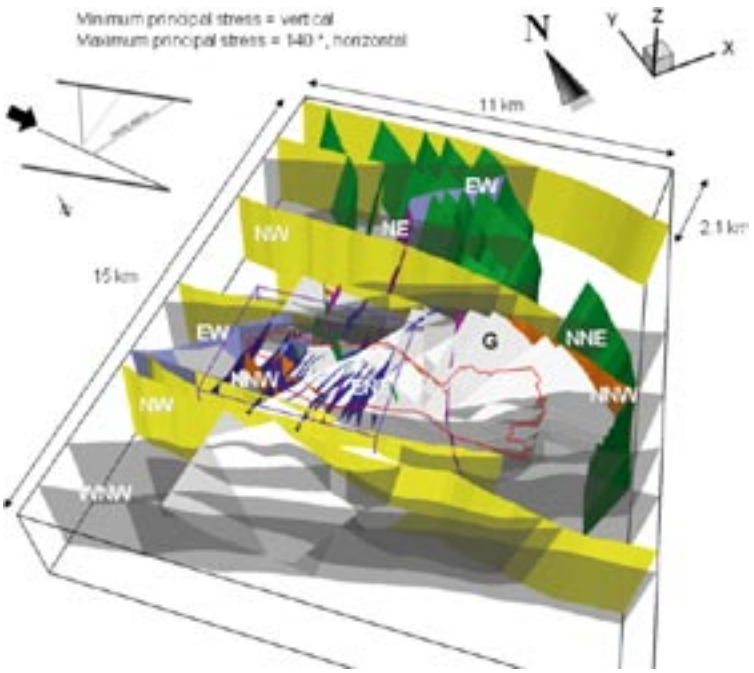

Figure 3-2. *3D visualisation of the 131 deformation zones modelled deterministically in the hydro-geological SDM for Forsmark. The steeply-dipping deformation zones (107 in number) are shaded in different colours and labelled with regard to their principal direction of strike. The gently-dipping zones are shaded in pale grey and denoted by a G. The border of the candidate area is shown in red and the regional and local model domains in black and purple, respectively. The image is modified from /Follin et al. 2007a/.*

The description of transport in the HCD is simplified by considering only those deformation zones in the analysis that are thought to have the most dominant role in forming flowpaths from a repository to the near surface. These pathways are indicated in Figure 3-3.

Although issues concerning the specific layout of the repository are not considered within the SDM, it is assumed that the bulk of a hypothetical repository would lie somewhere in the vicinity of the steeply-dipping zones ZFMENE0060A and ZFMENE0062A, and the gently-dipping zone ZFMA2. For the analyses of Hydrodynamic transport resistance presented here, we consider transport from a hypothetical repository at elevation –450 m to the near surface which is taken to be at an elevation of –100 m. Most of the hydrodynamic transport resistance is encountered at greater depths within the HCD, so the neglection of the highly transmissive features (e.g. horizontal sheet joints) in the upper reaches of the bedrock does not substantially influence the estimated F-factors.

Within safety assessment, alternative scenarios of radionuclide transport are considered. One of these is the possibility of a deliberate or accidental anthropogenic intrusion as illustrated in Figure 3-3. In such a situation, transport via the HCD may be bypassed completely. Although this is discussed briefly in the following sections in the context of the connectivity of the fracture network comprising the HRD, we do not make any specific calculations for such flowpaths as these are considered to be more of a safety assessment character and not strictly part of an SDM.

In the overall modelling strategy, F-factor estimations are made for each sub-compartment of the hypothetical transport path assuming a pre-defined set of reference conditions. In the calculations presented in this chapter, a local hydraulic gradient of 1% is assumed as a reference condition for each sub-compartment. This allows comparisons to be made of the relative importance of different compartments given different scenarios for the local hydraulic gradient.

The cumulative F-factor for the complete transport path is given by:

$$F = \left(\frac{i_0}{i_{NNF}}\right) F_{NNF_0} + \left(\frac{i_0}{i_{IFF}}\right) F_{IFF_0} + \left(\frac{i_0}{i_{DFF}}\right) F_{DFF_0} \qquad 3\text{-}1$$

Here, the terms F_{NNF_0}, F_{IFF_0} and F_{DFF_0} refer to the F-factor (y/m) calculated for each compartment under the reference hydraulic gradient, i_0 (m/m). As the F-factor is inversely proportional to the hydraulic gradient, the numeric value for each compartment can then be easily rescaled for different scenario-specific values i_{NNF}, i_{IFF}, and i_{DFF} (m/m).

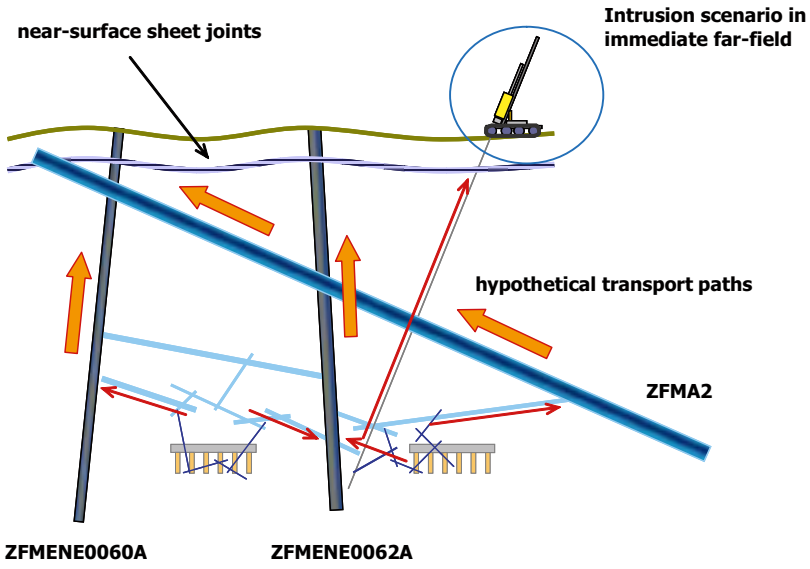

Figure 3-3. *Illustration of the main flowpaths through the HCD considered most likely for transport from a hypothetical repository.*

It should be noted that the calculation procedure represented by Equation 3-1 makes no à priori consideration of flowpath "persistence" /e.g. Painter and Cvetkovic 2005/ which may need to be considered if realistic distributions of F-factors are to be estimated for the multi-compartment system. By flowpath persistence we refer to the tendency of fast flowpaths in one compartment to be associated with fast flowpaths in subsequent compartments. In this report we consider the sum of median F-factors obtained for each compartment to be approximately representative of the composite transport path and make estimates of the overall F-factor accordingly.

It should be noted, however, that the demarcation of the transport system into a three-stage compartment is used here purely for illustrative purposes and for making scoping calculations to account for where the main hydrodynamic transport resistances are encountered in the rock. In SR-Site, the hydrogeological models comprising the HRD and HCD are used directly in an integrated model where flowpath persistence arises naturally.

3.2 Overview of input from hydrogeology

The main source of input data used as a basis for the calculations presented in this chapter is the hydrogeology background report /Follin et al. 2007a/. The overall approach to modelling the site specific hydrogeological properties combines a deterministic representation of the major deformation zones residing in the HCD with a stochastic representation of the less fractured rock outside these zones residing in the HRD. For the fracture domains comprising the HRD, the stochastic description is based upon a discrete fracture network (DFN) representation conditioned to borehole observational data. In SDM-Site this is referred to as the hydrogeological DFN, or Hydro-DFN for short. The description of the HCD, on the other hand, is based upon a 2D representation of deformation zone structures incorporating a simplified model of lateral and depth dependent transmissivity variation, conditioned to borehole observational data.

The various models and input data supplied by hydrogeology are described in the following sections.

3.2.1 Hydrogeological data

A detailed account of the hydrogeological input data gathered for the Forsmark site is given in the hydrogeology SDM /Follin et al. 2007a/ and only a brief overview is given here.

The methods used for hydraulic characterisation of the bedrock differs according to the drill technique employed. The shallow, percussion-drilled (HFM) boreholes are 140 mm in diameter and typically less than 200 m deep. These are investigated using the HTHB method which combines pumping and impeller flow logging. HTHB measurements generally have a measurement threshold corresponding to a fracture transmissivity of about 10^{-6} m^2/s and therefore can only be used to characterise structures featuring relatively high flow rates.

For the core-drilled (KFM) boreholes, both the Posiva Flow Log (PFL) and Pipe String System (PSS) methods have been used for hydraulic characterisation. The PFL method can be used in two different modes (PFL-s and PFL-*f*) as described in e.g. /Rouhiainen and Sokolnicki 2005/. In this report, however, we generally refer to PFL-f measurements which are intended to detect individual fractures on a dm scale spatial resolution. The measurements are made at steady state flow conditions after roughly a week of pumping the entire borehole at different drawdowns. The flow itself is measured by a thermal pulse or thermal dilution method for a packed off section of 0.5 m length sealed with rubber discs. The probe is winched in increments through the borehole to obtain a detailed map of borehole inflows. By measuring the ratio of flows at two different drawdowns, the background head can be calculated and, assuming approximately radial flow conditions, the transmissivity can be estimated. The quantitative transmissivity threshold for the measurement method varies depending upon the field conditions, although typically it is on the order of 10^{-9} m^2/s for the Forsmark site. Qualitative indications of flow can be found at transmissivities nearly an order of magnitude less than the quantitative limit.

The PSS measurement system is based upon a constant head, double-packer injection method. In this case, the packed section is pressurised rather than the entire borehole and the transient flow vs. time curve is interpreted to give a best estimate transmissivity in addition to an assumed steady state value obtained after 20 minutes of injection. The PSS method has a measurement threshold of roughly 6.7×10^{-10} m^2/s which is lower than PFL-*f* although the interpretation is complicated by the possibility of transient effects in isolated fracture clusters masquerading as connected fractures of low transmissivity as well as locally connected fractures short circuiting with the borehole above or below the packed-off section thus giving false indications of hydraulic connectivity. For these reasons, the Hydro-DFN produced by hydrogeology is largely based upon PFL-*f* measurement data. The consequences of this are discussed in the hydrogeology background report /Follin et al. 2007a/ although will be discussed in more detail in section 3.6 in the context of low transmissive fractures intersecting individual canister positions.

3.2.2 Hydrogeological description of the HRD

Fracture set orientations

In the geology SDM, fractures are classified into different sets based upon similar strike and dip as measured from core-borehole intercepts. Classifying the observed fractures into different sets allows the anisotropy of preferred orientation to be represented in a relatively straight-forward manner. For the Forsmark site it has also been found that the symmetrical Fisher distribution /Fisher 1953/ can be used successfully to represent the orientations of fracture poles within individual sets. The symmetrical Fisher distribution models the distribution of fracture poles as a Gaussian cluster around a specific preferred orientation. It is the equivalent of the symmetric bivariate normal distribution extended to a spherical surface. The resulting discrete fracture network (DFN) model represents a synthesis of data from all boreholes and is intended to represent the average properties of the fractured rock within the investigated rock volume.

In the DFN model produced for SDM-Site by hydrogeology, the membership of fracture sets is determined on the basis of "hard sector" divisions where fractures are clearly demarcated into specific sets depending upon whether they fall within or outside predefined boundaries in a stereonet plot of projected fracture poles. The hard sector division is based upon that previously used in the Forsmark 1.2 SDM. The DFN model produced by geology, on the other hand differs slightly in that it represents a mixture of hard and soft sector sets and there is thus some overlap of the fracture pole clusters. This, however, has been judged by hydrogeology to give only minor differences as both models represent a best estimate fit to the observational data /Follin et al. 2007a/. The fracture sets used by hydrogeology are named after the orientation of the mean fracture strike direction and consist of a NS, NE, NW, EW, and a horizontal (HZ) set.

Fracture intensity

The volumetrically normalised total area of fracture planes in the rock volume is called the fracture intensity or P_{32} (m^2/m^3) and can be estimated from the borehole fracture intersection frequency, P_{10} (1/m) after correction for orientation bias in the observational data /Terzaghi 1965/. Details of the correction procedure can be found in the hydrogeology background report /Follin et al. 2007a/.

Whether or not a fracture is mapped as open or closed in the geological interpretation does not say a lot about its hydraulic aperture. Fractures that are hydraulically closed by surface asperity contact although non-sealed (i.e. that physically part the borecore) will be mapped as open if the fracture is judged to be genuine. Since fracturing can occur during drilling and bore core extraction, this is a judgment that relies on physical examination of the borecore fracture surface. As the evidence is frequently ambiguous, the interpretation is assigned a confidence level in the Sicada database (open-certain, open-probable, open-possible).

By and large, only completely sealed fractures that do not part the bore core or sealed fractures that have clearly been broken open during drilling and core extraction are mapped as closed-certain in the geological interpretation. Most sealed fractures that have been broken during drilling are mapped as closed-probable or closed possible which reflects the uncertainty of actually determining if they are pre-existing or incurred during drilling.

Fractures are mapped as partly open if there is clear evidence for open sections within an unbroken borecore. These are typically fractures that only partly penetrate the borecore or sealed fractures that host visibly permeable structures. In the Hydro-DFN model, the fracture intensity (P_{32}) is estimated on the basis of open and partly open fracture statistics within the core boreholes. The geological DFN, on the other hand, considers all fractures both open and closed. An implicit assumption in the hydrogeological modelling is that the fractures are assumed to be either geologically open across their full extent, or closed (annealed) across their full extent. The validity of this assumption will be discussed later in the context of channelling effects although it can be noted already here that it is an assumption that is central to the estimation of the flow wetted surface within the rock.

Fracture size distributions

Although the open fracture areal intensity (P_{32o}) in the rock can be readily estimated from 1-dimensional statistics of fracture-borehole intersection, the distribution of fracture sizes within the rock is a much more difficult parameter to quantify. In the geology SDM, statistics of fracture trace length on surface outcrops are measured for fractures on the scale of metres to tens of metres. In addition to this, there is also information available for lineaments on the scale of 1 km to several kilometres. A significant problem is that there is a substantial gap in the data for fractures in the size range, from tens of metres to 1 km (i.e. side length).

There are a number of different alternative models that can be used to represent the distribution of fractures sizes, including the lognormal, exponential, gamma, and power law distributions /e.g. Bonnet et al. 2001/. Some of these are discussed in the geology discrete fracture modelling background report /Fox et al. 2007/ and the geological SDM strategy documents /Munier 2004/. A commonly used assumption is one of a mode of fracturing that spans all scales in a continuous manner (the so-called "tectonic continuum" hypothesis). In keeping with this hypothesis, each fracture set in the Hydro-DFN is assigned a frequency-size distribution that is modelled as a power law (Pareto) distribution which is inherently scale invariant. The key parameters for the power law distribution are the so-called shape parameter, k_r (the power law exponent) and the location parameter, r_0 (essentially the smallest fracture size considered in the model).

For the purposes of synthesising a hydrogeological DFN model, it is thought that trace lengths on surface outcrops are not relevant for parameterising the fracture network at repository depth owing to differences in the mechanisms of their formation (so-called "fracture genetics"). An alternative procedure is therefore used for estimating the appropriate fracture parameters, r_0 and k_r. The method employed is based upon an iterative simulation procedure coupled with an analysis of open fracture connectivity and is described in the following sections.

Spatial distribution of fractures

Although fractures within the HRD at first glance appear to be distributed in a random fashion, this is not always the case and the variation of fracture intensity and preferred orientation can vary as a function of depth, lithology, influence of tectonic processes, or other geological factors. In SDM-Site Forsmark, a large proportion of the fracture orientation variability is accounted for by dividing up the rock into different fracture domains. For the Hydro-DFN, additional sub-divisions within fracture domains are proposed in order to account for depth variation of hydrogeological properties. Even after accounting for these coarse scale variations, there are frequently regions that show indications of spatial clustering.

If the locations of fracture centroids are completely independent, constant, and uniform (isotropic) over a rock volume, then the system is said to be random /Munier 2004/ and the spatial distribution is described as being Poissonian. A direct and testable consequence of a Poissonian spatial structure is that the frequency of fracture intercepts observed in a borehole should be approximately constant (i.e. showing no trend or structure) and their spacing should follow an exponential distribution. Using different geostatistical methods, this analysis can also be extended to fracture trace centres identified on surface outcrops as described in /Munier 2004/ and the geology SDM /Fox et al. 2007/.

Frequently, however, the distribution of fracture centroids has an intrinsic, non-random structure that is described as being fractal in nature. For a Poissonian distribution of fracture centres we would expect the fracture intensity to scale with the Euclidean dimension; double the volume of the rock, for example, and the total number of fractures should also double. For a system which exhibits fractal clustering, on the other hand, this may not be the case.

From analysis of borehole and surface outcrop data it has been argued in the geology SDM that the spatial distribution of fractures in the HRD at Forsmark is indeed best described as being Poissonian over the length scales of interest. A similar conclusion was also reached by /Darcel et al. 2006/, where only very weak support for a fractal spatial distribution was found and the observational data were reasonably consistent with a Euclidean scaling regime.

As the Hydro-DFN produced by hydrogeology is based exclusively upon core borehole data, there is not sufficient data to argue convincingly in favour of a Fractal spatial distribution or indeed any other kind of spatial model. The simplest spatial model, however, is Poissonian and on the basis of the geological argumentation in favour of this, it has been assumed in the hydrogeological modelling work. It should be noted that this does not imply that the distribution of flowing features also exhibits Poissonian spatial structure. As mentioned previously in section 2.1.3, fractal clustering of flowing features can arise spontaneously in a Poissonian fracture system if it is close to the percolation threshold /Follin et al. 2006b/.

Resultant Hydrogeological DFN model

The modelling procedure used for obtaining Hydro-DFN parameters for each of the fracture domains comprising the HRD is described in detail in the hydrogeology background report /Follin et al. 2007a/. The main steps required in constructing such a model are illustrated in Figure 3-4.

A key assumption in the Hydro-DFN modelling work is the hypothesis of a correlation between fracture size and transmissivity. The reasoning behind the hypothesis of a size-transmissivity relation is two-fold. Firstly, we can infer the existence of a correlation owing to the fact that large joints and fault fractures are also commonly associated with larger dilation and shear movement than smaller features. Indeed, the strategy for identifying and avoiding deposition positions in unfavourable locations is based upon an inferred relationship between fracture size and potential for shear movement during deglaciation (see e.g. /Munier and Hökmark 2004/ and /Cosgrove et al. 2006/). It is not unreasonable to anticipate therefore that the mean hydraulic transmissivity of such features is also correlated with size. The second argument relates to the fact that deformation zones are often comprised of a number of smaller elements interpreted en-echelon as a single feature. Larger fractures and minor deformation zones are also more likely to feature greater microstructural complexity than smaller single fractures in the rock. For this reason we can also suspect that larger features have greater potential for hosting fast flow channels of greater transmissivity than smaller features.

As it is not possible to observe these correlations in a quantitative fashion directly in the field, three different size-transmissivity models have been used in the Hydro-DFN modelling. These three models are thought to represent the approximate range of possibilities for the Forsmark site.

As discussed in /Follin et al. 2007a/, two extreme assumptions are to assume either a direct correlation between fracture size and transmissivity or to assume there is no correlation. These are referred to as the correlated (or fully correlated, FC) and uncorrelated (or non-correlated, NC) cases, respectively. A third possibility, the semi-correlated case (SC), assumes a partial correlation between fracture size and transmissivity with a stochastically distributed variation around a size-correlated mean value. This is thought to be the most realistic scenario as we would almost always expect some stochastic variation in a heterogeneous system.

In the Hydro-DFN modelling the correlation between size and transmissivity is assumed to either take the form of a power law (FC) or a log-normal distribution (NC). The semi-correlated model (SC), on the other hand, assumes a combination of these. It is noted that there are other

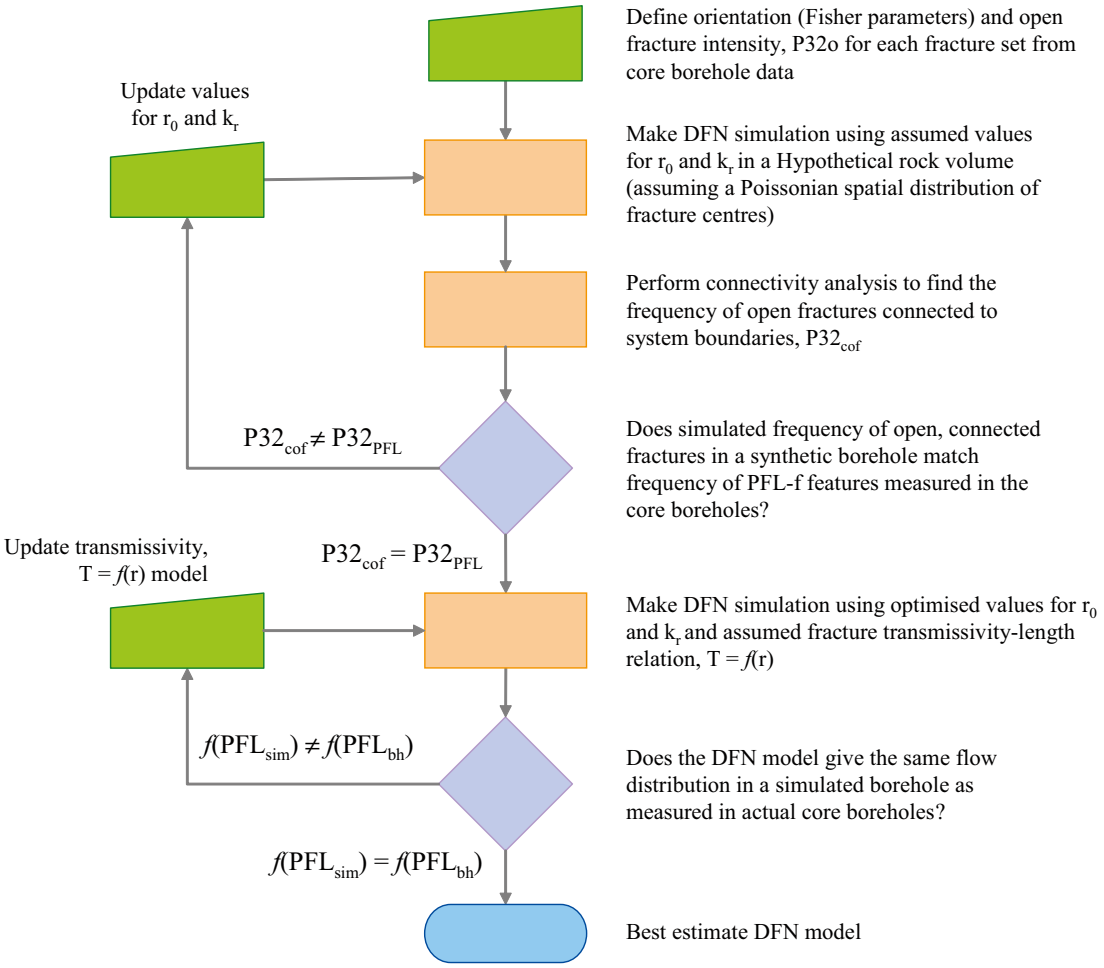

Figure 3-4. *Flowchart showing procedure for obtaining optimised Hydro-DFN parameters using an iterative simulation fitting procedure.*

alternatives that have not been explored such as a uniform log-normal or a stochastic power law distribution (see e.g. /Gustafson and Fransson 2006/). The choice of models actually used in the modelling work, however, is thought to be reasonable given the sparsity of data and should reproduce the flow characteristics of the system with realistic efficacy. Details of the three transmissivity models are given in Table 3-1.

It should be noted that the modelling procedure outlined above does not directly consider flow channelling phenomena apart from network scale flow channelling effects which arise naturally due to fracture connectivity issues. There therefore exists the possibility that there are inbuilt biases in the resulting Hydro-DFN. There are a number of issues that need to be considered in relation to this. These are discussed more fully in section 3.10.

Owing to the depth dependency apparent in the field measurement data, fracture domain FFM01 was broken up into several sub volumes and parameterised separately. Two different alternatives are described in the hydrogeology background report /Follin et al. 2007a/ where FFM01 is divided up into two, respectively three sub-volumes. In this report we focus upon the three part model which was parameterised according to Table 3-2.

Since FFM02 is limited to the upper section of the rock above –200 m, a single volume was found to be sufficient to describe the hydrogeological properties of the rock. The parameters for FFM02 are given in Table 3-3.

For FFM03, a model based upon two sub-volumes above and below –400 m was proposed. The parameters for FFM02 are given in Table 3-4.

Table 3-1. Different transmissivity models used in Hydro-DFN modelling (adapted from Follin et al. 2007a). The variable T (m^2/s) is the transmissivity; adjustable parameters in the various models are a, b, μ, and σ; the symbol R_n (0,1) represents a normal random deviate with mean zero and variance of unity.

Type	Description	Relation
Semi Correlated (SC)	lognormal distribution about a power-law correlated mean	$\log_{10} T = \log_{10}(a) + b\log_{10}(r) + \sigma R_n(0,1)$
Correlated (FC)	1:1 power law relation	$\log_{10} T = \log_{10}(a) + b\log_{10}(r)$
Uncorrelated (NC)	lognormal distribution about a constant mean	$\log_{10} T = \mu + \sigma R_n(0,1)$

Table 3-2. Hydro-DFN parameters for FFM01 with depth dependency (a) above –200 m, (b) –200 m to –400 m, and (c) below –400 m (adapted from /Follin et al. 2007a/).

Fracture domain	Fracture set name	Orientation set pole: (trend, plunge), conc.	Size model, power-law (r_0, k_r) (m, –)	Intensity, (P_{32}), valid size interval: (r_0, 560 m) (m^2/m^3)	Transmissivity model Eq. type, constants T (m^2/s)
FFM01a > –200 m	NS	(87, 2) 21.7	(0.04, 2.50)	0.073	Semi-Correlated: (*a,b,σ*) (6.3×10^{-9}, 1.3, 1.0);
	NE	(135, 3) 21.5	(0.04, 2.70)	0.319	
	NW	(41, 2) 23.9	(0.04, 3.10)	0.107	Correlated: (*a,b*) (6.7×10^{-9}, 1.4);
	EW	(190, 1) 30.6	(0.04, 3.10)	0.088	
	HZ	(343, 80) 8.2	(0.04, 2.38)	0.543	Uncorrelated: (*μ, σ*) (–6.7, 1.2)
FFM01b –200 m to –400 m	NS	(87, 2) 21.7	(0.04, 2.50)	0.142	Semi-Correlated: (*a,b,σ*) (1.3×10^{-9}, 0.5, 1.0);
	NE	(135, 3) 21.5	(0.04, 2.70)	0.345	
	NW	(41, 2) 23.9	(0.04, 3.10)	0.133	Correlated: (*a,b*) (1.6×10^{-9}, 0.8);
	EW	(190, 1) 30.6	(0.04, 3.10)	0.081	
	HZ	(343, 80) 8.2	(0.04, 2.38)	0.316	Uncorrelated: (*μ, σ*) (–7.5, 0.8)
FFM01c < –400 m	NS	(87, 2) 21.7	(0.04, 2.50)	0.094	Semi-Correlated: (*a,b,σ*) (5.3×10^{-11}, 0.5, 1.0);
	NE	(135, 3) 21.5	(0.04, 2.70)	0.163	
	NW	(41, 2) 23.9	(0.04, 3.10)	0.098	Correlated: (*a,b*) (1.8×10^{-10}, 1.0);
	EW	(190, 1) 30.6	(0.04, 3.10)	0.039	
	HZ	(343, 80) 8.2	(0.04, 2.38)	0.141	Uncorrelated: (*μ, σ*) (–8.3, 1.0)

Table 3-3. Hydro-DFN parameters for FFM02 (adapted from /Follin et al. 2007a/).

Fracture domain	Fracture set name	Orientation set pole: (trend, plunge), conc.	Size model, power-law (r_0, k_r) (m, –)	Intensity, (P_{32}), valid size interval: (r_0, 560 m) (m^2/m^3)	Transmissivity model Eq. type, constants T (m^2/s)
FFM02	NS	(87, 2) 21.7	(0.04, 2.75)	0.342	Semi-Correlated: (*a,b,σ*) (9.0×10^{-9}, 0.7, 1.0);
	NE	(135, 3) 21.5	(0.04, 2.62)	0.752	
	NW	(41, 2) 23.9	(0.04, 3.20)	0.335	Correlated: (*a,b*) (5.0×10^{-9}, 1.2);
	EW	(190, 1) 30.6	(0.04, 3.40)	0.156	
	HZ	(343, 80) 8.2	(0.04, 2.58)	1.582	Uncorrelated: (*μ, σ*) (–7.1, 1.1)

Table 3-4. Hydro-DFN parameters for FFM03 with depth dependency (a) above –400 m, and (b) below –400 m (Adapted from /Follin et al. 2007a/).

Fracture domain	Fracture set name	Orientation set pole: (trend, plunge), conc.	Size model, power-law (r_0, k_r) (m, –)	Intensity, (P_{32}), valid size interval: (r_0, 560 m) (m^2/m^3)	Transmissivity model Eq. type, constants T (m^2/s)
FFM03a > –400 m	NS	(87, 2) 21.7	(0.04, 2.60)	0.091	Semi-Correlated: (a,b,σ) (1.3×10^{-8}, 0.4, 0.8);
	NE	(135, 3) 21.5	(0.04, 2.50)	0.253	
	NW	(41, 2) 23.9	(0.04, 2.55)	0.258	Correlated: (a,b) (1.4×10^{-8}, 0.6);
	EW	(190, 1) 30.6	(0.04, 2.40)	0.097	
	HZ	(343, 80) 8.2	(0.04, 2.55)	0.397	Uncorrelated: (μ, σ) (–7.2, 0.8)
FFM03b < –400 m	NS	(87, 2) 21.7	(0.04, 2.60)	0.102	Semi-Correlated: (a,b,σ) (1.8×10^{-8}, 0.3, 0.5);
	NE	(135, 3) 21.5	(0.04, 2.50)	0.247	
	NW	(41, 2) 23.9	(0.04, 2.55)	0.103	Correlated: (a,b) (7.1×10^{-9}, 0.6);
	EW	(190, 1) 30.6	(0.04, 2.40)	0.068	
	HZ	(343, 80) 8.2	(0.04, 2.55)	0.250	Uncorrelated: (μ, σ) (–7.2, 0.8)

3.2.3 Hydrogeological description of the HCD

In the hydrogeology background report /Follin et al. 2007a/ a large amount of hydrogeological data is tabulated relating to interpreted borehole intercepts with deterministically modelled deformation zones. The data correlates specific deformation zones with elevation (of borehole measurement intervals) and measured transmissivity. The measurement data indicate a substantial depth trend and a considerable variation dependent upon zone orientation. This is illustrated in Figure 3-5 for three main groupings of zone orientation; zones with an ENE strike, gently dipping zones, and zones with other orientations.

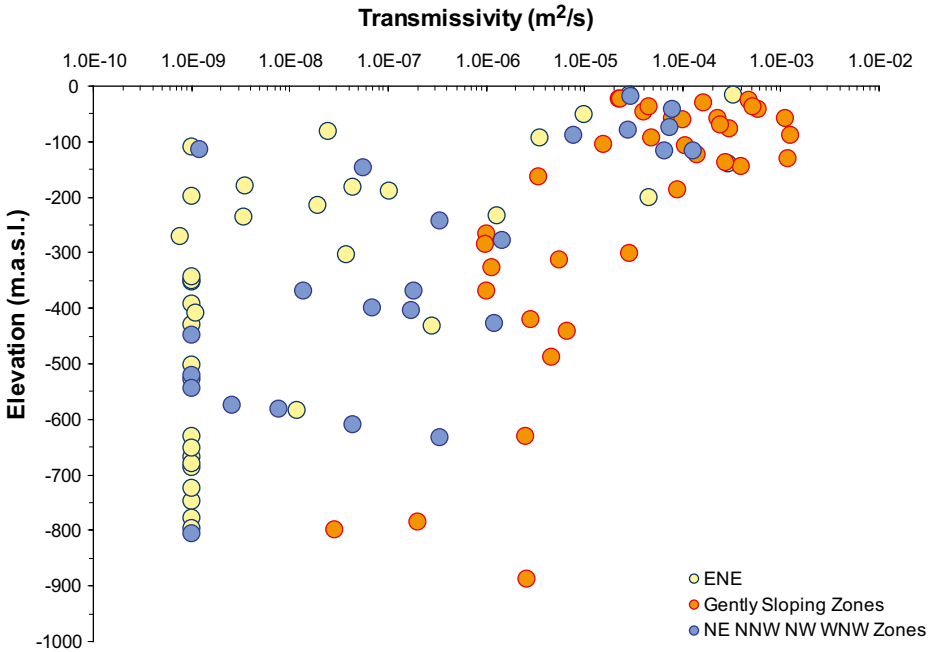

Figure 3-5. *Variation of transmissivity with depth for deformation zones belonging to different orientation categories.*

As can be seen from the figure, the gently dipping zones appear to be most transmissive with a relatively narrow range of lateral heterogeneity and moderate depth trend. Deformation zones with an ENE strike and other orientations (NE, NNW, NW, WNW) are collectively referred to as steeply dipping zones. Such zones are generally less transmissive, have a substantially larger lateral heterogeneity, and a very strong decrease in transmissivity with increasing depth. The relation between orientation and the hydrogeological properties of deformation zones is not fully understood at the Forsmark site /Follin et al. 2007a/. In spite of this it is noted that the zones denoted WNW and G (gently dipping) are largely parallel to the current direction of principal stress whereas zones with an ENE strike are orthogonal to the current direction of principal stress.

In /Follin et al. 2007a/ an exponential decay model is suggested for the depth trend. The hypothesis of an exponential decay with increasing depth is generally supported by other studies in the literature (see for example, the meta-analysis by /Stober and Bucher 2007/) and it is also consistent with the way in which transmissivity of single fractures is thought to vary with the increasing normal stress at increasing depth. In the hydrogeological description a distinction is made between two different kinds of lateral heterogeneity:

- *Intra-category lateral heterogeneity*, concerning the differences in transmissivity observed between all deformation zones belonging to a particular category of deformation zones, e.g. all deformation zones with an ENE strike.
- *Intrinsic lateral heterogeneity*, concerning the spatial variability in transmissivity observed within a single (specific) deformation zone and elevation.

Owing to their favourable orientation relative to the ground surface, certain gently dipping zones (ZFMA2 in particular) are intercepted by a number of boreholes. For these deformation zones we have a number of independent measurements of transmissivity that give us a reasonable idea of the balance between depth-dependent and lateral variability as shown in Figure 3-6.

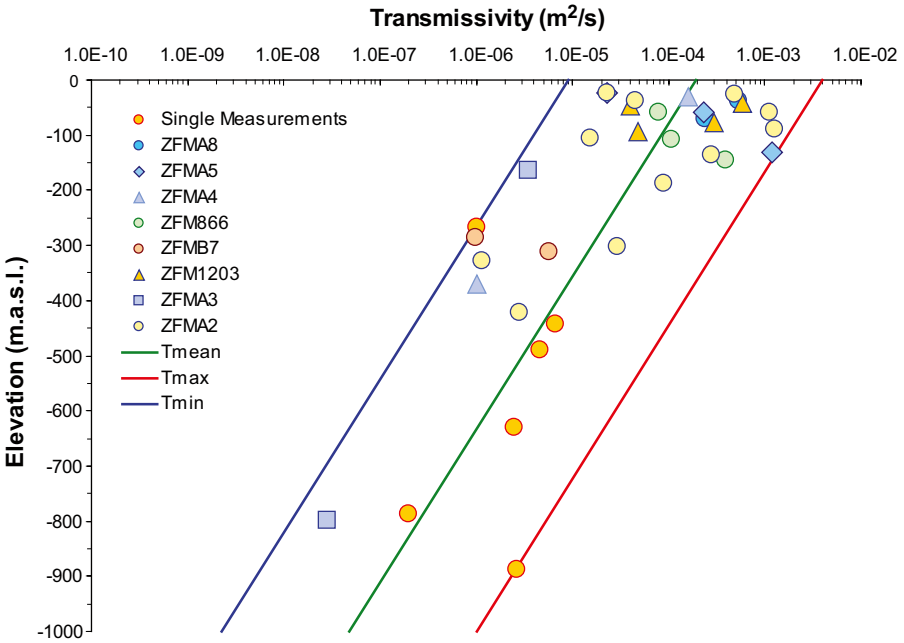

Figure 3-6. *Variation of transmissivity with depth for gently dipping deformation zones. The approximate range of transmissivities for all deformation zones within the category is the area bounded by the blue and red curves (assumed to be limiting cases). The mean transmissivity vs. depth trend is shown as a green curve.*

For the steeply dipping zones, there are few multiple borehole intercepts and there is consequently a poorer understanding of the relation between depth dependency and lateral variability as shown in Figure 3-7 and Figure 3-8.

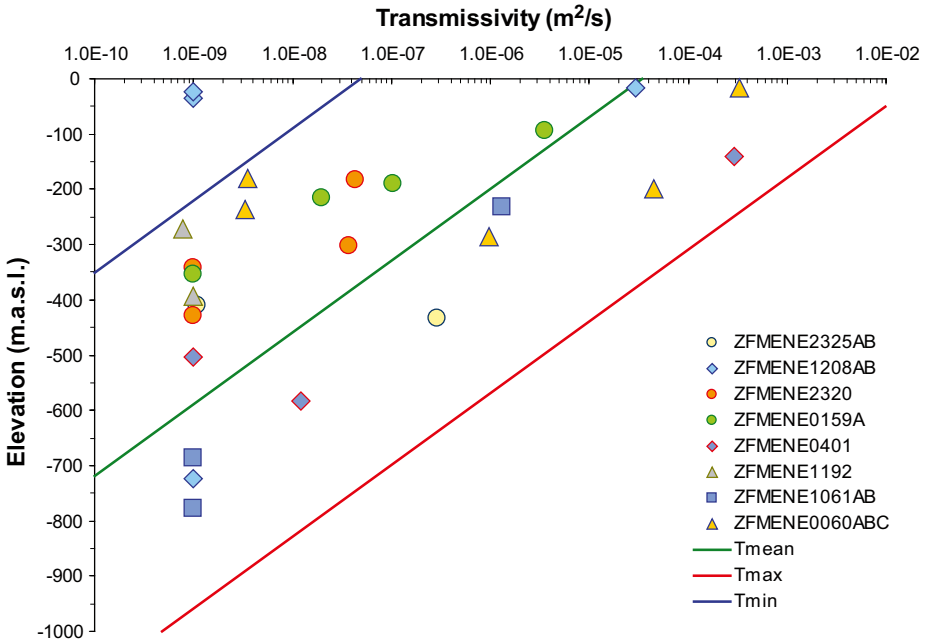

Figure 3-7. *Variation of transmissivity with depth for steeply dipping deformation zones with an ENE strike. The approximate range of lateral transmissivity is the area bounded by the blue and red curves (assumed to be limiting cases). The mean transmissivity vs. depth trend is shown as a green curve.*

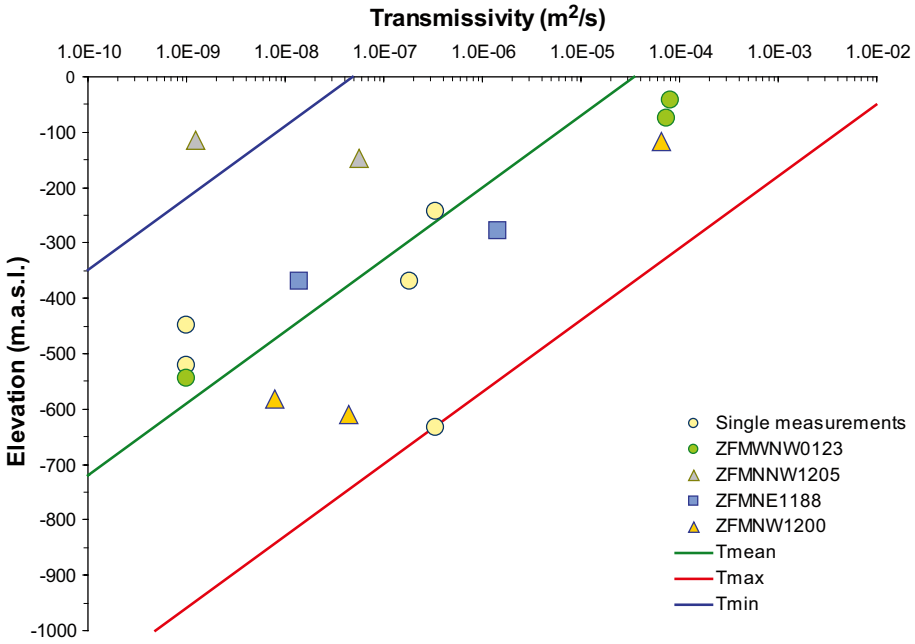

Figure 3-8. *Variation of transmissivity with depth for steeply dipping deformation zones with a NE, NNW, NW, or WNW strike. The approximate range of lateral transmissivity is the area bounded by the blue and red curves (assumed to be limiting cases). The mean transmissivity vs. depth trend is shown as a green curve.*

The exponential model for transmissivity is defined in /Follin et al. 2007a/ as:

$$T(z) = \exp\left(\frac{z-m}{k}\right) \qquad 3\text{-}2$$

Where the parameters k and m are constants and z is elevation (metres above sea level). Equation 3-2 can also be written in a more physically meaningful form as:

$$T(z) = T(0)\exp\left(\frac{z}{k}\right) \qquad 3\text{-}3$$

Where $T(0)$ is the expected value of the transmissivity at zero elevation and $1/k$ is derived from the slope for the line of best fit to the data when plotted on semi-logarithmic axes (as in the previous Figures).

As can be readily appreciated from the scatter of data points in Figure 3-7 and Figure 3-8, there is simply not enough measurement data for individual deformation zones to differentiate properly between intra-category and intrinsic lateral variability. For this reason we consider all steeply dipping zones to have a similar depth dependency relation and consequently, a dominant intrinsic lateral variability component. This is a simplification that is used in the present report to make estimates of flow related transport properties that are partially generic in nature (i.e. they can apply equally well to all deformation zones of a particular class).

It is possible that by lumping the hydrogeological properties of different deformation zones together in this fashion, a bias may be introduced whereby the modelled properties represent the central tendency of the aggregate data set while failing to represent local extremes of behaviour. For the calculations presented in this report, the data set was considered sufficiently sparse that it was not possible to consider individual deformation zones separately in a rigorous fashion with the possible exception of ZFMA2. In the case of ZFMA2, the proposed transmissivity depth model is broadly compatible with the data set including the other gently dipping deformation zones and therefore does not need to be considered in isolation. It should be noted, however, that in the regional hydrogeological modelling for SDM-Site Forsmark a procedure of local conditioning was used to assign transmissivity-depth trends for specific deformation zones /Follin et al. 2007b, 2008/ to give agreement with borehole observations and hydrogeochemical measurement data.

In /Follin et al. 2007a/ it is recommended that lateral heterogeneity should be modelled without any spatial correlation as a first approximation (owing to a lack of measurement data to suggest otherwise). In addition, two simple models are proposed for the non-correlated lateral transmissivity variability.

Alternative 1 assumes a log-uniform distribution of transmissivities[2]:

$$\log T(x,y,z) = \log T(0) + \frac{z}{k} + \log(D)\left(R_0^1 - 0.5\right) \qquad 3\text{-}4$$

Where, R_0^1 is a uniform random deviate in the interval [0,1] and D is the ratio between the upper and lower bounds of the distribution (i.e. the red and blue curves for T_{max} and T_{min} in the previous Figures).

Alternative 2 assumes a log-normal distribution of transmissivities:

$$\log T(x,y,z) = \log T(0) + \frac{z}{k} + \sigma_T R_n(0,1) \qquad 3\text{-}5$$

Where, $R_n(0,1)$ is a normal random deviate with a mean of zero and variance of unity, and σ_T is the lateral variability of the distribution. If we make the assumption that the ratio D is a reasonable approximation of the 95% confidence interval for log T /Follin et al. 2007a/, the standard deviation σ_T of the distribution can be estimated to be:

$$\sigma_T \approx \frac{\log(D)}{2\times 1.96} \qquad 3\text{-}6$$

[2] All logarithms are natural $\log_e$ unless otherwise specified.

Table 3-5. Deformation zone transmissivity model parameters used in transport calculations presented in this report. Parameter values are based upon the limiting transmissivity cases (blue, green, and red curves) shown in the previous figures.

ZFM Category	m	k	D
Gently dipping zones (G)	666 (T_{max}) 1,033 (T_{mean}) 1,400 (T_{min})	120.6	4.42×10^{2}
Steeply dipping zones (ENE, NE, NNW, NW, WNW)	210 (T_{max}) 580 (T_{mean}) 950 (T_{min})	56.4	4.98×10^{5}

A summary of the parameter values used for the transport modelling calculations presented in this report are given in Table 3-5.

In section 3.7 the impact of spatial correlation for lateral transmissivity variation is explored using a set of case studies in a simplified sensitivity analysis.

3.3 Model volume description and boundary conditions

For modelling the flow related transport properties of the HRD, we consider a hypothetical cubic volume of rock with dimensions 100 m×100 m×100 m. As mentioned previously, this size is chiefly motivated by consideration of the respect distance to the transition region of large deformation zones. The layout of the modelled rock volume relative to the hypothetical repository, the HCD, and an assumed local hydraulic gradient is illustrated schematically in Figure 3-9. The general modelling approach is broadly similar to that used previously in /Crawford 2006/ as well as /Painter 2006/, /Cvetkovic et al. 2004/ and /Outters 2003/ for generic modelling of fractured rock transport properties.

As a first approximation, we consider a local hydraulic gradient applied parallel to the simulation axes. To account for directional anisotropy in the hydrogeological properties of the HRD, calculations are made for a hydraulic gradient applied over different directions corresponding to the three principal axes of the model (i.e. North-South, East-West, and Vertical).

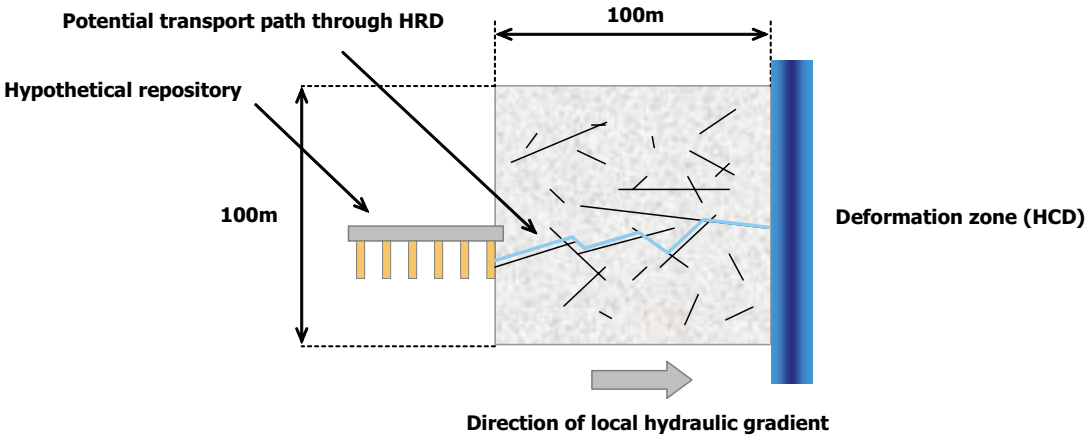

Figure 3-9. *Illustration of HRD model volume showing the relation between the hypothetical repository, a steeply dipping deformation zone in the HCD, and the prevailing local hydraulic gradient.*

The continental hydraulic gradient in Sweden is taken to be roughly the height of the tallest features within the Scandinavian mountains (≤ 2,500 m) over the average distance to the Baltic sea (~ 400–500 km). Although only a very rough estimate, it gives an idea of the order of magnitude of the super-regional hydraulic gradient relevant for the Forsmark area. The hydraulic gradient calculated in this fashion is in the range 0.5%–0.6% (0.005–0.006 m/m).

On a regional scale and assuming that the groundwater approximately follows the landscape topography[3], we estimate a groundwater hydraulic gradient in the near surface on the order of 0.3%–0.7% (0.003–0.007 m/m). This corresponds to a difference in groundwater surface elevation of about 10–25 m over a 3–4 km distance from inland to the Baltic coast at Forsmark.

Additional complicating factors are site scale, lateral and depth dependent variations in salinity and temperature which have the potential to influence flow patterns by way of buoyancy effects. Generally there is a consistent depth dependent variation of both of these parameters within the local model area /Laaksoharju et al. 2008, Sundberg et al. 2008/ and any lateral variations appear to be sufficiently small that they should not have an appreciable impact upon contemporary hydraulic gradients.

In any case, given the uncertainty in assigning an appropriate representative hydraulic gradient based upon topographical considerations, we make the assumption of 1% (0.01 m/m) in the transport properties evaluation. This is the reference hydraulic gradient used for subsequent calculations of flow related transport properties. Furthermore, it must be remembered that the estimates provided in this report are only intended to be indicative. A comprehensive assessment of the flow and flowpaths from the actual repository layout is to be made within the framework of long term safety assessment (e.g. SR-Site).

A large number of *in situ* measurements of flow under approximately background hydraulic conditions have been made in the Forsmark area as part of the site investigation. Some of these have been performed in permanently instrumented boreholes /Wass 2006, 2007, 2008/, while others have been performed in conjunction with tracer tests for the purpose of characterising individual flowing features /Gustafsson et al. 2005, 2006ab, Wass and Andersson 2006/. These tests are based upon a tracer dilution method, where the groundwater flow is fitted to the measured decrease in tracer concentration with time using a mixed tank reactor model. The method is extremely sensitive and can measure flow rates substantially lower than that possible using standard flow logging methods thus enabling the method to be used to measure flow under relatively natural (i.e. non-pumped) conditions.

By combining these measurements with the estimated transmissivities of the specific borehole sections obtained independently, the apparent background hydraulic gradient can be estimated. A compilation of the site specific data is given in Figure 3-10 (data compiled by /Nordqvist et al. 2008/) where the apparent gradient is plotted as a function of fracture transmissivity and measurement elevation.

As can be seen from the figure there is a large spread in the measurement data around the estimated reference hydraulic gradient (horizontal broken line). In spite of the large variability in the data, however, there does appear to be a non-negligible inverse correlation with transmissivity as indicated by the power law regression curve in the Figure (orange line). There is a predominance of high transmissivity features in the upper parts of the target volume (specifically within the percussion-drilled, HFM boreholes) although it is not clear whether there is any particular depth trend of the hydraulic gradient for transmissivities less than about 10^{-5} (m^2/s).

The existence of the inverse correlation between gradient and transmissivity is qualitatively consistent with expectations based upon flow modelling calculations described in Appendix C. The magnitude of the apparent background hydraulic gradient, on the other hand, appears to

[3] This is not necessarily a good assumption at Forsmark owing to the near surface shallow bedrock aquifer feature as discussed in /Follin et al. 2007a/. It does, however, allow the calculation of an approximate upper limit to the regional scale hydraulic gradient.

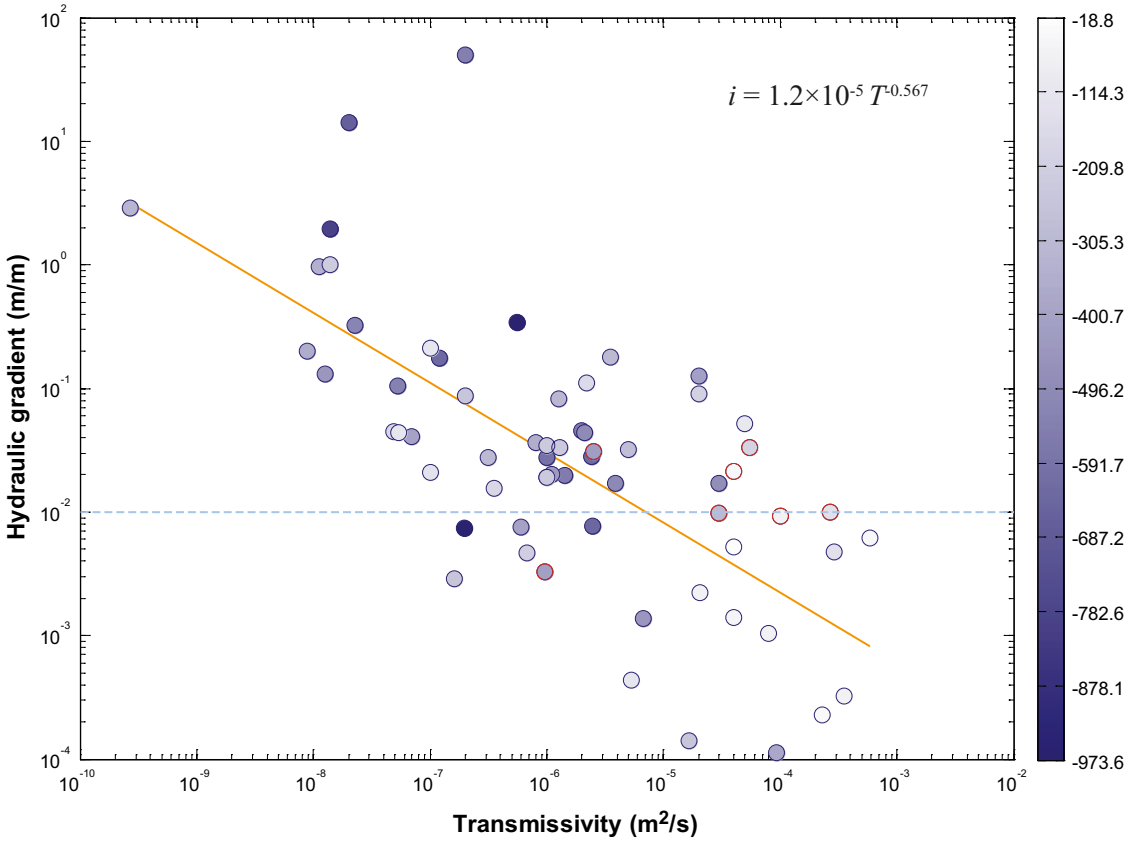

Figure 3-10. *Apparent hydraulic gradients measured at the Forsmark site as a function of fracture transmissivity (x-axis) and measurement elevation (shading). The horizontal broken line corresponds to the reference hydraulic gradient of 1%. The orange line represents a linear regression curve for the power law given in the figure. Symbols with a red outline are measurements specific to ZFMA2. The colourbar to the far right indicates elevations (m) corresponding to the shading of markers in the figure.*

be considerably greater than what seems reasonable in comparison to the estimated reference gradient for the site. In the scoping simulations, the local hydraulic gradient in any individual network element is rarely more than about an order of magnitude higher than the reference gradient and, in most cases, substantially lower for 2D and 3D flow regimes. Larger gradients may possibly be found in extreme cases of 1D flow connectivity for flow channels with a power law distribution of lengths and size-correlated transmissivities. In Figure 3-10 the empirically derived, apparent local gradients are up to three orders of magnitude higher than the reference level. To obtain such gradients in the field would require a very unusual flow connectivity that may be unrealistic for the Forsmark site. This apparent discrepancy has also been remarked in a more detailed analysis of the Forsmark site data by /Nordqvist 2008/.

It is possible that the apparent hydraulic gradient estimated from site data are biased upwards due to the combining of data obtained using different methods that may not be entirely compatible. The measurement method used for estimating transmissivity in the core-boreholes, for example, is based upon a transient analysis of flow injection in a pseudo radial-spherical flow regime. The measurement method using tracer dilution does not involve any pumping, is "nominally" at steady-state, and the flow regime determined by the local or regional hydraulic boundary conditions is principally linear in character.

The assumption of a steady state flow condition, however, is not entirely realistic since much of the hydraulically connected fracture system at Forsmark has very high hydraulic diffusivity (i.e. low storativity) /Follin et al. 2007b/. This means that measurements are extremely sensitive to small disturbances at the site due to activities in other boreholes or even in some cases disturbances due to rainfall (e.g. Appendix G in /Follin et al. 2007b/) and tidal effects (Figure 8-19

in /SKB 2005a/). Measurements made in boreholes at different times have also shown flowrate variability of as much as an order of magnitude /Wass 2008/ possibly due to these effects, which could easily give rise to a bias of the same magnitude in the estimated hydraulic gradient.

In addition, since we know very little about the actual distribution of flow space within the conductive features tested, the estimated transmissivity of the active flow channels could easily be underestimated by as much as an order of magnitude or greater (see Appendix B for further discussion). A further possibility raised in the report by /Nordqvist et al. 2008/ is that the correction factor for distortion of the flow field is underestimated and it is speculated that the correction factor could be as much as 1–5 times greater than the correction factor of 2 typically assumed.

Since we suspect the magnitude of the estimated hydraulic gradient to be an artefact, we recommend against use of the power law indicated in Figure 3-10 for directly assigning local hydraulic gradients to the different compartments in the flow related transport properties model. In the calculations presented in the following sections for the NFF, we assume hydraulic gradients in the range 0.1%–10% which is thought to be more reasonable for the site. In order to examine the impact of possible inverse correlation between transmissivity and hydraulic gradient, we additionally make calculations assuming a power law relation with the same exponent as in Figure 3-10, although with magnitude reduced by a factor of 100. This modification gives a maximum gradient of slightly less than 10% for the least transmissive fractures.

It should be clearly noted that the forgoing discussion concerning uncertainty of local hydraulic gradients does not affect the larger regional scale simulations where the hydraulic boundary conditions are well characterised. In these simulations, spatially variable local gradients arise naturally due to the distribution of differently conductive elements in the hydrogeological model.

3.4 Modelling strategy for the HRD

3.4.1 The non-engineered near field (NNF)

For the non-engineered near field (NNF), we are interested in assessing the F-factor for the first cluster of connected, low-transmissive background fractures that connect a typical deposition hole with a typical major flowpath within the HRD.

In the analysis by /Cosgrove et al. 2006/ the critical radius for a fracture that intersects a canister position is given as 50 m based upon seismic considerations. If we were to assume hypothetically that this represents a lower size limit for fractures allowed to intersect canister positions, it is possible to estimate how frequently such features should be expected to occur on average in the repository volume. From the Hydro-DFN model for FFM01c (< –400 m) provided by hydrogeology it is relatively straight forward to estimate the average distance between potentially hydraulically conductive features with a radius greater than 50 m within the HRD. To do this we can calculate the truncated P_{32c} for the size range 50 m to 560 m and estimate the average spatial separation of such fractures. Using the parameters in Table 3-2, this separation distance is calculated to be on the order of about 100 m if we consider open fracture frequencies. If, on the other hand, we were to consider purely the flowing fracture frequency (P_{10PFL} = 0.004 /Follin et al. 2007a/) we would estimate that there was a flowing feature about once every 250 m.

On the basis of the above discussion, we could speculate that such features are relatively rare in the HRD and most canister positions will probably be located sufficiently distant that they can be discounted from contributing significantly to radionuclide fluxes in the far-field. Although this may be the case for a large proportion of canister positions, it is still necessary to make estimates of F-factors for "typical" flowpaths. The question then becomes; what would a typical distance be for radionuclide transport from a canister position to a major flowpath?

Here we have to consider a number of issues. Firstly, a typical distance in this context does not necessarily imply average distance since a damaged canister in close proximity to a major flowpath can be expected to have a much greater impact upon far-field radionuclide release

rates than a damaged canister located further away, all other things being equal. We also have to consider what respect distance is to be applied for large fractures that, although not actually intersecting the deposition hole, may be sufficiently close to cause concern with regard to radionuclide transport potential. It is likely to be canister positions with closest proximity to these features that have the greatest potential to influence the far field release. An additional consideration is the possibility that the repository itself, including the excavation damaged zone (EDZ) will connect and activate flowpaths that otherwise would be isolated in the virgin rock.

Most of these considerations, however, are strongly coupled to repository layout and design criteria and as such are more of a safety assessment character. For this reason and owing to the dominant role of canister positions in close proximity to major flowpaths, we shall make the assumption of an approximately 10 m transport distance for the NNF. By assuming this respect distance what we are actually saying is that large conductive features ($\geq$ 50 m radius) lying closer than this to individual canister positions will likely be identified from geophysical measurements and other geological clues and therefore will be avoided. Large features lying 10 m or more away from a canister hole may not be seen and therefore could well exist somewhere in the repository volume. These features and the canister deposition holes in closest proximity will then probably dominate the radionuclide flux from the repository. We note, however, that the assumption of 10 m transport distance is very pessimistic and could be considered as more or less a worst case scenario for the NNF.

For a single hypothetical pathway connecting a deposition hole with a major flow path in the HRD, the F-factor is given by /SKB 2005b/:

$$F = \frac{2L_p}{Ti} \tag{3-7}$$

Where, L_p is the NNF flowpath length, T is the flowpath transmissivity, and i is the hydraulic gradient.

If we assume that any fracture less than 50 m in radius intersecting a deposition hole is accepted, the cut-off transmissivity for such features could be anywhere between about 10^{-8} and 10^{-10} m^2/s depending upon which size-transmissivity model is used in the calculation (see Table 3-1). Since we are considering local pathways rather than an entire rock volume, we also have to consider carefully what is an appropriate hydraulic gradient for such a background fracture or fracture cluster comprising the NNF. Owing to this uncertainty, estimates of the F-factor were made for possible hydraulic gradients in the range 0.1%–10% as well as for the special case where the local hydraulic gradient is correlated with feature transmissivity using the empirically derived result in Figure 3-10.

3.4.2 The immediate far field (IFF)

As discussed in section 3.3, the immediate far-field is simulated as a 100 m×100 m×100 m cubic volume (referred to as a "voxel") with a hydraulic potential difference applied over opposing faces. To account for directional anisotropy in the Hydro-DFN model, simulations are also made along the different axes of the model. Consideration is therefore given to transport parallel to the x-axis (EW direction), y-axis (NS direction), and z-axis (vertical direction).

The aim of the simulations is not to model the actual F-factor distribution for transport of radionuclides from an individual canister position, but rather to give an indication of F-factors associated with typical flowpaths in the HRD. This is important to bear in mind as an individual canister hole presents a cross-sectional area considerably less than the 10,000 m^2 face of the simulation volume. Transport from any particular canister location is therefore strongly dependent upon additional considerations of local fracture network connectivity and represents a sub-sampling of the typical F-factor distributions calculated for the rock volume as a whole. The simulation results presented in this chapter are based upon average properties of the rock volume and do not specifically consider these additional stochastic aspects that are more of a safety assessment character. In addition to F-factors for typical flowpaths in the rock, an assessment is also made

as to the frequency with which they can be expected to occur. This is an important measure of transport potential in the HRD as it reflects directly upon the number of canister positions that we can expect to be in near contact with major flowpaths.

Initially it was intended to use the Hydro-DFN produced by hydrogeology directly in the Napsac/ConnectFlow numerical code /Serco Assurance 2007/ for the simulation of flow related transport properties within the HRD. This was the simulation tool used for the investigation of fracture domains FFM02, FFM03, and the upper parts of FFM01 (i.e. FFM01a–b, above –400 m). Owing to the low intensity of connected features within FFM01c at repository depth (below –400 m), however, very few simulated fracture networks are found to be hydraulically connected. Use of the Napsac simulation tool for such sparsely fractured volumes is inefficient and a novel approach implemented within the Matlab program /Mathworks 2005/ was therefore devised for the assessment of flow related transport properties in this volume. This procedure is described in the following paragraphs.

Modelling strategy for FFM01c (< –400 m)

As an initial modelling step for FFM01c (< –400 m), 1,000 stochastic DFN realisations were generated using the Hydro-DFN parameters given in Table 3-2 and subjected to a connectivity analysis using graph theory. The fracture radius (size) distribution was truncated to the range of 1–560 m and the connectivity analysis was performed for different boundary plane separation distances in the range 10–100 m, and along the three principal axes of the simulation volume (see Figure 3-11). The aim was to identify candidate realisations that exhibit potential hydraulic connectivity between boundary planes within the simulated rock volume and how this connectivity can be expected to vary with hypothetical distance (i.e. respect distance between a notional repository and the HCD). The fractures were generated in a volume region significantly larger than the simulation volume in order to avoid edge truncation effects and fracture network thinning at the system boundaries.

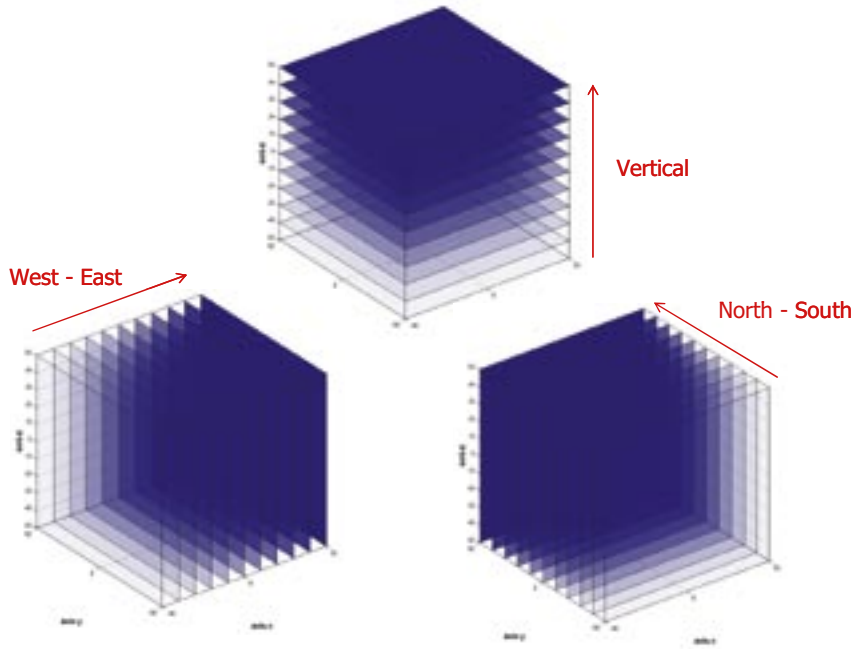

Figure 3-11. *Illustration of modelling strategy for FFM01c (< –400 m). The connectivity of individual DFN realisations was assessed for different hypothetical transport distances in the range 10–100 m and along the different principal axes of the simulation volume. Hypothetical boundary planes for the different transport distances are depicted as shaded polygons in the figure.*

For each realisation found to be hydraulically connected, the Hydro-DFN was converted to an equivalent pipe network representing the connectivity of individual fractures comprising the network. In this approximate method, midpoints of fracture intersections are considered to be mixing nodes and pair-wise pipe connections are made between nodes residing in individual fracture planes. The conductance of individual pipe elements within a fracture plane is proportional to the transmissivity of the fracture hosting the connection and the distance between the mixing nodes. In this fashion, the hydraulic connectivity and relative transmissivity of different pathways through the system can be honoured. The overall approach is a similar although simplified version of that used in the PAWorks package for flow simulation in discrete fracture networks /Dershowitz et al. 2004/.

Although this approximation gives an acceptable representation of the hydraulic properties of the rock (hydrological responses), the transport pathways are not altogether realistic as the model does not capture the intricacies of mass transfer interactions between interconnected flow channels in the plane of fractures. For this reason we do not use particle tracking methods to calculate solute transport as this would likely give physically non-meaningful results. Instead, we use the weighted adjacency matrix of the resultant pipe network to calculate a hypothetical path of least transport resistance (PLTR) using graph theory. From the known lengths and conductances of individual pipe elements comprising the PLTR a notional F-factor for this pathway can be calculated in a relatively straight forward manner for an assumed hydraulic gradient. The method is based upon a Matlab version of Dijkstra's algorithm /Cormen et al. 2001/ as implemented within the Boost Graph Library /Gleich 2006/. Since we are considering a substantially larger volume of rock than that considered for the NNF, the assumption of the regional hydraulic gradient of 1% is probably not unreasonable as a boundary condition for this calculation. The implications of this will need to be fully investigated within safety assessment using detailed simulations of radionuclide transport from the repository to the HCD.

Using an equivalent pipe network representation of the fracture network makes it possible to investigate the impact of hydraulically conductive fracture intersection zones (FIZ) in a rudimentary fashion. For systems with neutrally conductive FIZ, there is little tendency for flow to occur along the line of fracture intersection. Equivalent pipe connections made between the midpoints of fracture intersections can therefore be taken to represent an approximate, average trajectory for fluid flow in the system. For highly conductive FIZ (Type B and C as illustrated in Figure 2-5), on the other hand, there is a strong tendency for flow to occur along the path of least resistance which includes the line of fracture intersection. In the limiting case of zero hydraulic resistance in the FIZ, pipe connections are made between the points of closest approach of the fracture intersection line segments. This scheme is illustrated in Figure 3-12.

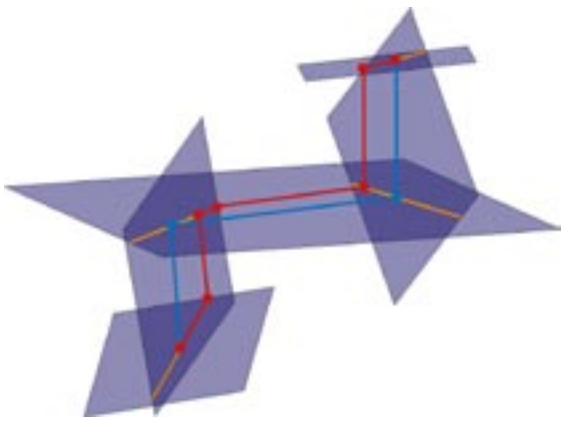

Figure 3-12. *Illustration of equivalent 3D pipe network concept for the case of neutrally conductive FIZ (blue nodes and pipes connecting fracture intersection midpoints) and for highly conductive FIZ (red nodes and pipes connecting fracture intersection points of closest approach). Fractures are visualised as blue polygons and fracture intersections are indicated as orange line segments.*

The treatment of conductive FIZ in this fashion represents a worst case scenario for the transport modelling as no account is made of filling materials, discontinuities and roughness in the fracture intersections that would reduce the potential for preferential flow to occur. The F-factor estimates for the Hydro-DFN incorporating conductive FIZ therefore constitute an approximate upper bound for the detrimental impact that such features can have upon the transport resistance in the system, all other things being equal.

Using the simulation technique described above, the PLTR was calculated for the limiting cases of neutrally- and highly conductive FIZ and the different size-transmissivity models described in section 3.2.2. Although the DFN connectivity analysis considers 10 m intervals in the range 10 m to 100 m, F-factor estimates were made only for 25 m, 50 m, 75 m, and 100 m transport distances owing to the numerically intensive nature of the calculations.

In the calculations, the same hydraulic gradient was applied in each case. For the 100 m transport distance, for example, the hydraulic potential difference was 1 m. In a similar fashion for the 25 m, 50 m, and 75 m cases, the hydraulic potential difference was set to 0.25 m, 0.5 m, and 0.75 m respectively. The results reported for each transport distance therefore represent individually applied boundary conditions rather than an F-factor reported at a check-point (control plane) within a larger simulation.

The reason for performing the calculation in this way is because the heterogeneous population of single penetrating fractures and fracture network clusters exhibit different connectivity characteristics over different length scales. Given that the Hydro-DFN also incorporates length transmissivity relations for fractures it is reasonable to expect that the transmissivity of typical flowpaths is also a function of boundary plane separation. By applying the same hydraulic gradient in each case, it was possible to quantify the properties of typical flowpaths for different distances separating the notional boundary planes in a comparable fashion. Although no specific calculations concerning intrusion scenarios have been made in this report, these comparisons are also relevant for scoping estimation of the flow related transport properties for short transport distances between a hypothetical repository and an intruding borehole.

A detailed account of the modelling procedure for FFM01c (< –400 m) can be found in Appendix D.

Modelling strategy for FFM01a–b, FFM02, FFM03

For the remaining fracture domains, the intensity of fracturing is sufficiently high that simulations could be carried out effectively using the Napsac/ConnectFlow program. In these cases, the Hydro-DFN was implemented directly in the program using the parameters given in Table 3-2, Table 3-3 and Table 3-4. For these cases, realisations were made for each transport direction and size-transmissivity model considering a transport distance of 100 m only. As previously, the fracture radius distribution was truncated to the range of 1–560 m and a total of 20 DFN realizations were made for each case. It should be noted, however, that a proportion of the fracture networks generated exhibited zero connectivity and the statistics for the F-factors of typical flowpaths are therefore not always based upon a full complement of 20 realisations.

Napsac calculates flow using a finite element method applied directly to the fracture network in 3D. F-factor estimates were made for each connected DFN realisation using the particle tracking algorithm in Napsac. Unlike the F-factor estimates for FFM01c (< –400 m), the results here represent the ensemble average for 1,000 released particles. As particles can take different routes through the system, a distribution of F-factors is obtained.

3.5 Modelling strategy for the HCD

In the regional flow modelling report /Follin et al. 2007b/ deformation zones comprising the HCD are notionally assumed to be planar structures featuring an exponentially decreasing transmissivity with increasing depth. It should be remembered that there is no requirement for flowing features comprising deformation zones in the HCD to be planar and in reality we can probably expect a very complex system of preferential flowpaths that follow a convoluted path in three-dimensional space. The individual flow path elements comprising the zones may be short and highly interconnected, long and poorly interconnected or some combination in between. In cross-section, a deformation zone may look something like that illustrated schematically in Figure 3-13.

Having said this it is also a matter of practicality that, given the scarcity of detailed hydrogeological data for individual zones, it is hardly possible to give a more detailed description of these flow features. In the calculations made for the HCD in this report it is therefore assumed that the flow and transport properties of deformation zones can be approximately represented as flow channels distributed in an approximately planar structure. Here, we assume that the transmissivity estimated from borehole hydraulic measurements can be used directly to represent the transmissivity of individual flow channel elements. Since both the flow-wetted surface and the flow in an individual channel is proportional to the flow channel width, the unknown channel width is cancelled out when taking the ratio of these two entities and therefore does not need to be considered explicitly.

Although we know this to be a physically inaccurate description, we think that the description is cautious in that it will tend to overestimate flowpath connectivity and possibly underestimate the available flow wetted surface for a given flowrate through the zone. This would result in lower F-factor estimates than what would be obtained with a more detailed three-dimensional model of a deformation zone where the same flow is distributed over a larger flow-wetted surface area. The accuracy of this assumption, however, depends upon whether the transmissivity of individual flow channels is properly assessed from borehole data. Since the surfaces of natural open fractures are not generally parallel plates, both the transmissivity and flow-wetted surface of the flow channels can differ from that implicit in the above model formulation.

If we assume an approximately planar structure for deformation zones in the HCD, we can formulate the transport problem for a zone of arbitrary orientation and dip as shown in Figure 3-14.

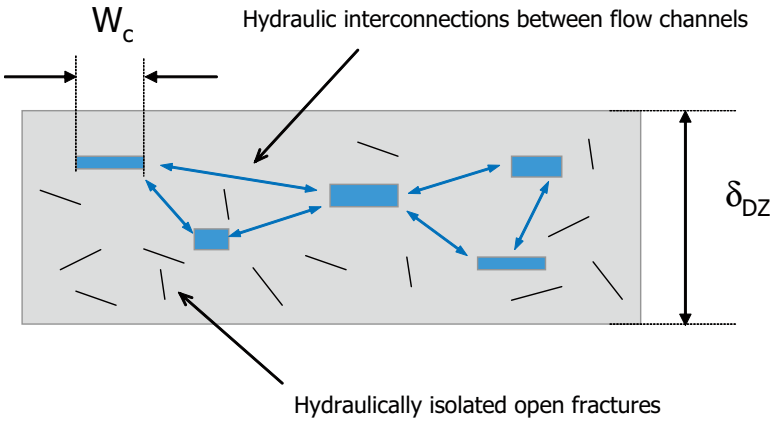

Figure 3-13. *Cross section of a hypothetical deformation zone with flow channels oriented into the plane of the page. The flow channels may have varying widths and hydraulic apertures and follow convoluted pathways through the interpreted deformation zone. Although typically modelled as a planar feature there is no requirement for this to be the case.*

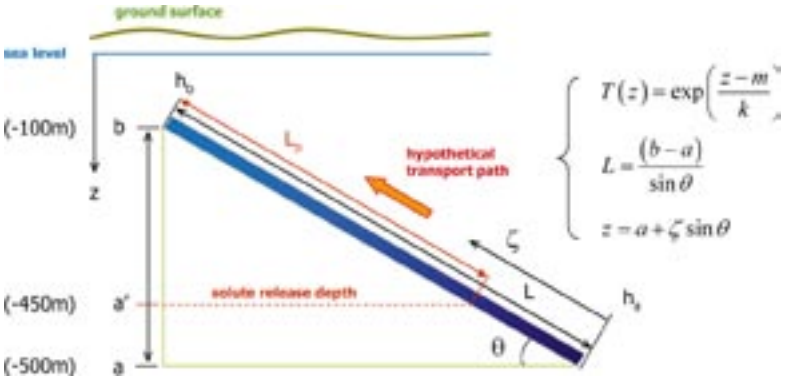

Figure 3-14. *Conceptual illustration of transport within a deformation zone of arbitrary orientation and dip (θ). A hydraulic gradient is assumed to exist across the zone that causes flow from depth to the surface through flow channels of steadily increasing transmissivity. In the hypothetical scenario for transport, the applied hydraulic gradient is assumed to extend from –500 m to roughly –100 m elevation with solute release at –450 m.*

The magnitude of flow through the zone is dependent upon the effective transmissivity of the system over the length of the applied hydraulic head differential. Using the exponential decay model for zone transmissivity, the effective transmissivity can be shown to be:

$$T_{eff} = \frac{1}{\frac{1}{L}\int_0^L \frac{1}{\exp\left(\frac{z-m}{k}\right)} d\xi} = \frac{(b-a)/k}{\exp\left(\frac{-a+m}{k}\right) - \exp\left(\frac{-b+m}{k}\right)} \qquad (3\text{-}8)$$

For solute release at some depth a' in the elevation interval $[a,b]$, the F-factor can be calculated analytically as:

$$F = \frac{2L_p}{T_{eff}\, i} = \frac{2L_p}{T_{eff}\left(\frac{h_a - h_b}{L}\right)} = \frac{2k(b-a')}{\Delta h\left(\sin^2\theta\right)}\left(\exp\left(\frac{-a+m}{k}\right) - \exp\left(\frac{-b+m}{k}\right)\right) \qquad (3\text{-}9)$$

Although an analytical estimate of the F-factor can be easily made using Equation 3-9, additional numerical simulations were carried out to investigate the effect that different transmissivity correlation models have upon the F-factor of typical flowpaths through the deformation zone. For this purpose a simple 2D channel network model implemented in Matlab was used for the numerical simulations. The transmissivity field for the channel network was generated by overlaying a 2D Gaussian correlated random field onto the depth dependent mean transmissivity model. A full account of the simulation procedure can be found in Appendix E. Seven different transmissivity model variants incorporating spatial correlation were investigated as sensitivity case studies (with horizontal and vertical correlation lengths of L_x and L_y relative to the plane of the deformation zone). These were:

1. log-normally distributed transmissivities with an isotropic Gaussian correlation structure and exponential depth trend (correlation lengths: L_x = 20 m, L_y = 20 m),
2. log-normally distributed transmissivities with an isotropic Gaussian correlation structure and exponential depth trend (correlation lengths: L_x = 5 m, L_y = 5 m),
3. log-normally distributed, spatially non-correlated transmissivities with exponential depth trend,
4. log-normally distributed transmissivities with an anisotropic Gaussian correlation structure and exponential depth trend (correlation lengths: L_x = 5 m, L_y = 20 m),
5. log-normally distributed transmissivities with an anisotropic Gaussian correlation structure and exponential depth trend (correlation lengths: L_x = 20 m, L_y = 5 m),

6. log-uniform distributed, spatially non-correlated transmissivities with exponential depth trend,
7. log-normally distributed transmissivities with an "extreme" anisotropic Gaussian correlation structure and exponential depth trend (correlation lengths: L_x = 10 m, L_y = 100 m).

For each of these calculations a regional hydraulic gradient of 1% was assumed.

3.6 Transport properties of the HRD

3.6.1 The non-engineered near field (NNF)

The F-factor for a single pathway in the non-engineered near field (NNF) was calculated as a function of flowpath transmissivity using Equation 3-7. The flowpath transmissivity was taken to be approximately the same as the assumed tolerable range for flowing fractures intersecting canister positions. The results of these calculations are shown in Figure 3-15 for an assumed transport distance of 10 m and different hydraulic gradients.

As can be seen from the figure, the assumed hydraulic gradient can have a large impact upon the results particularly if an inverse correlation is assumed between fracture transmissivity and local hydraulic gradient. If there is no relation between gradient and transmissivity we would expect canister positions intersected by low transmissivity fractures to not contribute appreciably to the radionuclide release rate. If, on the other hand, there is an inverse relation of the kind postulated in section 3.3, the low transmissive fractures may play a more important role than initially suspected. This possibility must be investigated more fully within safety assessment.

It should also be noted that the hydraulic gradient correlation used in the calculations shown Figure 3-15 is purely speculative since the pre-factor in the power law expression is reduced by two orders of magnitude relative to that which was estimated on the basis of the empirical data analysis presented previously in Figure 3-10. The rationale for this is given in section 3.3 and the results shown in the figure above are intended to be interpreted only as a tentative, "what if" analysis.

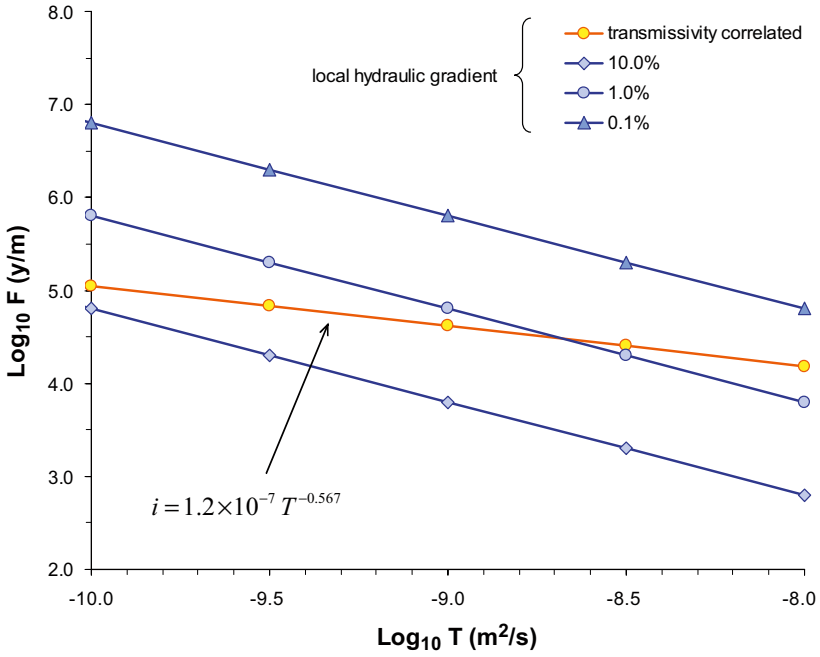

Figure 3-15. *F-factors for typical flowpaths as a function of flowpath transmissivity in the non-engineered near field (NNF). The calculations consider a transport distance of 10 m and a range of hypothetical hydraulic gradients (blue curves). F-factors corresponding to the special case of an inverse correlation between transmissivity and hydraulic gradient are also shown (orange curve).*

3.6.2 The immediate far field (IFF)

Results for FFM01c (< –400 m)

The results of the connectivity analysis for FFM01c (< –400 m) are shown in Figure 3-16 where the percolation probability is plotted as a function of the boundary plane separation distance in the simulations. The results are based upon the probability of existence of at least one percolating structure spanning the modelled domain for 1,000 stochastic realisations of the Hydro-DFN considering fractures in the size range 1 m to 560 m.

The results of the connectivity analysis indicate that the probability of forming a hydraulically connected fracture cluster over the respect distance of 100 m from the repository is very low. Indeed, the probability of any individual realisation exhibiting overall hydraulic connectivity is 4% or less for this rock volume (2.6% for EW connectivity, 3.7% for NS connectivity, and 1.4% for vertical connectivity). The Hydro-DFN model displays slightly greater hydraulic connectivity in the NS direction than EW, although the difference is quite small. The system is clearly less well connected along the vertical axis than for the horizontal directions. For the realisations that are connected over a 100 m transport distance, about 50–70% (EW 69%, NS 54%, Vertical 50%) are single fractures that penetrate the entire simulation volume. The remaining realisations exhibiting connectivity generally consist of small clusters of 2–6 large intersecting fractures. None of the realisations contain pervasive clusters of small, connected fractures.

A visualisation of the path of least transport resistance, PLTR is shown in Figure 3-17 for the case of neutrally conductive FIZ and in Figure 3-18 for highly conductive FIZ. It is interesting to note that the PLTR trajectory is very different in both cases. It is also noteworthy that the flowpath for the neutrally conductive FIZ case, although dominated by four prominent fractures also contains two flow bottlenecks in the form of small linking fractures highlighted with yellow ellipses in Figure 3-17. In Figure 3-18 the FIZ flow conduits are coloured orange and account for roughly 60% of the total flow path length.

If we assume that the probability of encountering a connected fracture cluster is proportional to the surface area of the hypothetical boundary plane, we can estimate the probability of a direct hydraulic connection for an individual deposition hole. Given that the simulation volume has boundary planes with an area of 10,000 m^2, the overall probability of a randomly located deposition hole forming a direct connection with a hydraulically connected cluster (100 m in

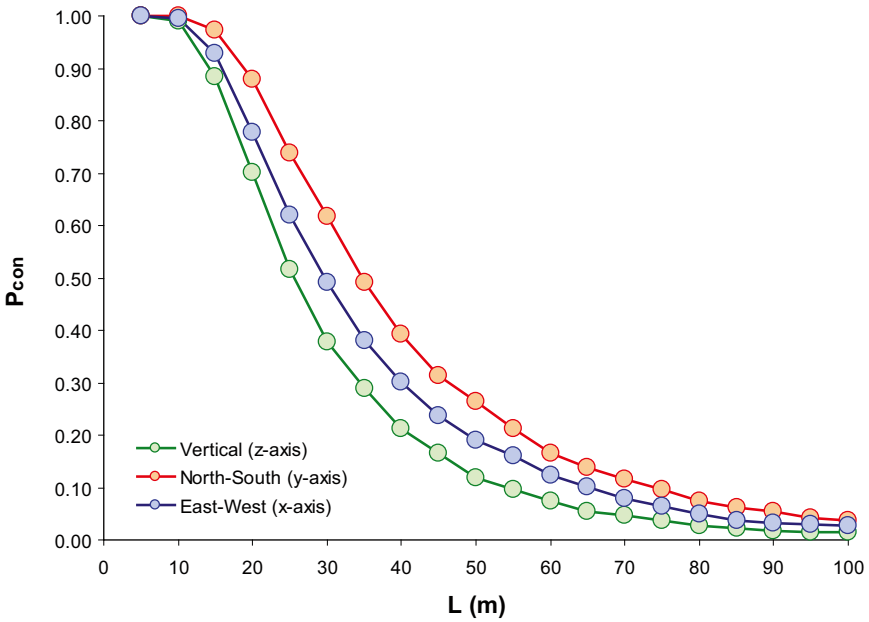

Figure 3-16. *Results of connectivity analysis for FFM01c (< –400 m) based upon 1,000 stochastic realisations of the Hydro-DFN model. The percolation probability is plotted as a function of distance for the three principal axes of the model.*

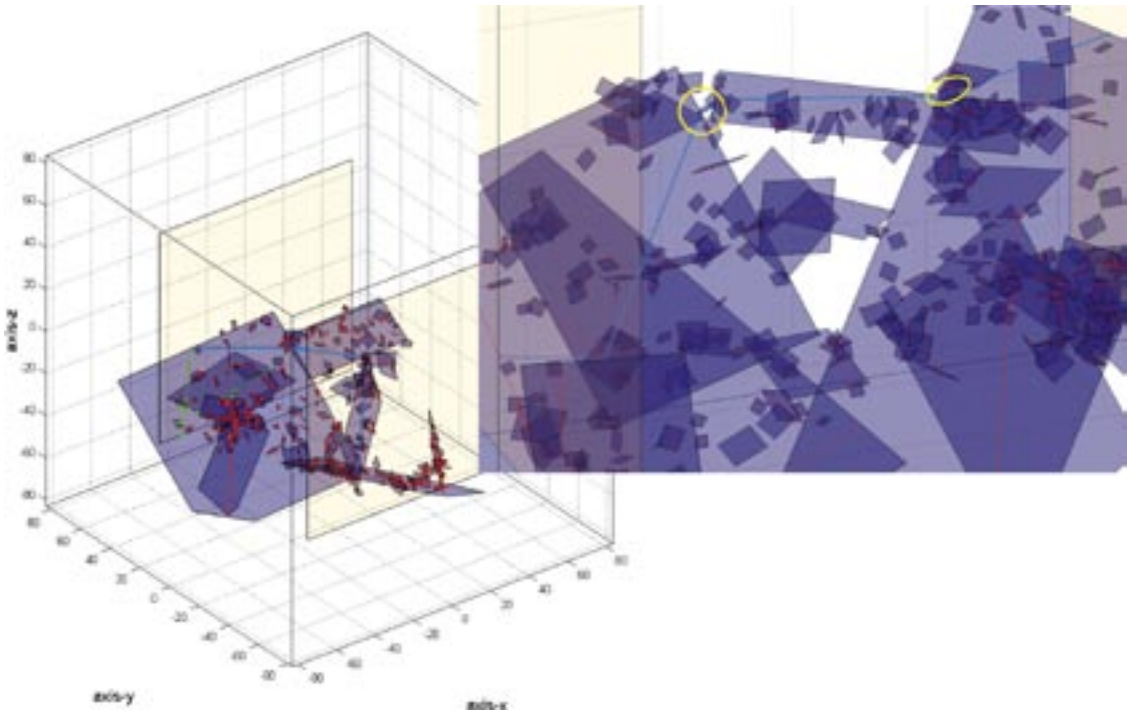

Figure 3-17. *Trajectory of calculated path of least transport resistance, PLTR (light blue pipes) for a typical realisation assuming neutrally conductive FIZ and a NS hydraulic gradient for a transport distance of 100 m (only hydraulically connected fractures are shown). Note the two flow "bottlenecks" highlighted with yellow ellipses in the rotated close-up image on the right hand side.*

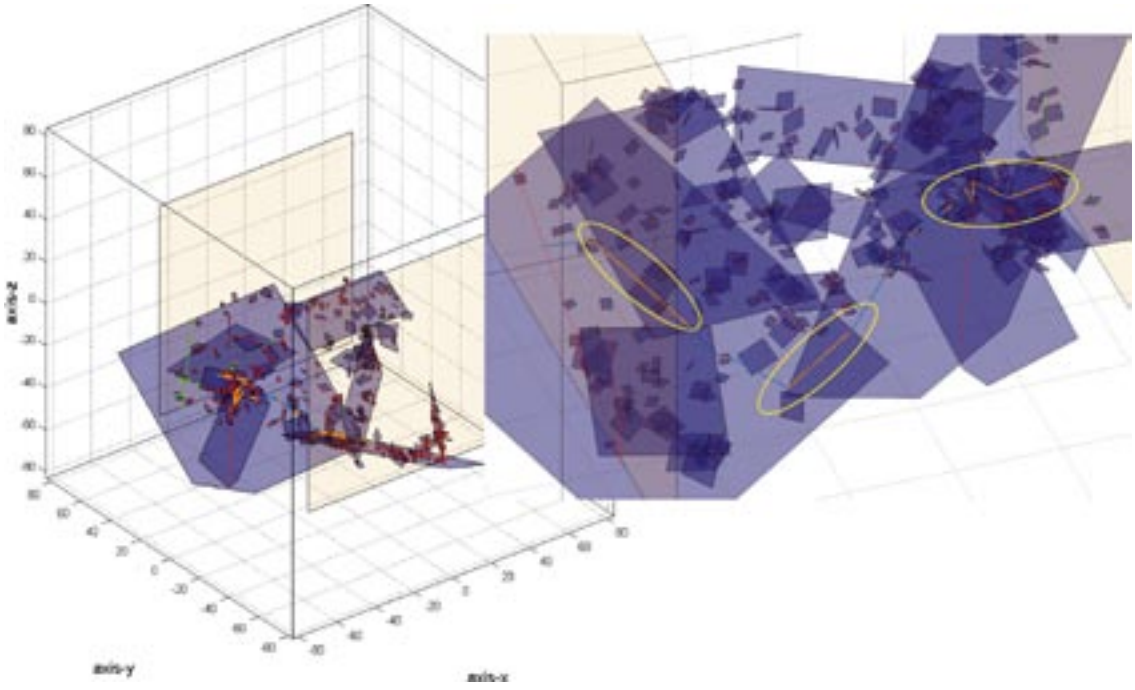

Figure 3-18. *Trajectory of calculated path of least transport resistance, PLTR (light blue and orange pipes) for a typical realisation assuming highly conductive FIZ and a NS hydraulic gradient for a transport distance of 100 m (only hydraulically connected fractures are shown). Some of the larger FIZ flow conduits (orange pipes) are highlighted with yellow ellipses in the rotated close-up image on the right hand side.*

extent) is on the order of 2×10^{-4} if we additionally assume that a deposition hole has an effective cross-sectional area of about 50 m^2. This estimate is very rough, however, as it considers a canister in isolation and does not account for the effect of surrounding canister holes or the deposition tunnel on the connectivity of the rock close to the repository, nor does it consider the preferential orientation of fracture sets. It is purely meant to be an illustration of how poorly connected the fracture network in the target volume appears to be.

The percolation threshold for the system seems to occur at a boundary plane separation distance of about 25–35 m. Here, we use the same operational definition employed by /Mourzenko et al. 2004, 2005/ where the percolation threshold is defined as the distance at which the percolation probability is exactly 50% (i.e. half of all realisations exhibit no connectivity). This definition considers the fact that when the largest fractures are of the same size or larger than the system itself, the percolation probability can never completely vanish as there is always a slight probability of a single fracture spanning the entire modelled volume. Since the largest fractures in the DFN model have a radius of 560 m this is why the percolation probability shown in Figure 3-16 undergoes a smooth sigmoid transition with a connection probability gradually tapering off with increasing boundary separation distances. The long tailing-off of the percolation probability curve to the right hand side of the theoretical percolation threshold is also consistent with what would be expected when using a power law distribution of fracture sizes.

Hydraulically connected DFN realisations were converted to an equivalent pipe network and the path of least transport resistance, PLTR was calculated for each realisation using Dijkstra's algorithm /Cormen et al. 2001/ for the case of neutrally conductive FIZ as well as highly conductive FIZ. A full account of the modelling procedure and results can be found in Appendix D. An example of typical F-factor ranges calculated using this method is given in Figure 3-19 for a NS oriented hydraulic gradient and the semi-correlated (SC), fracture size-transmissivity model.

The resultant F-factor distributions represent the aggregate data set of 1,000 realisations and therefore should be interpreted as a probability distribution for the singular F-factor corresponding to the path of least transport resistance in each realisation. This should not be confused with the ensemble average F-factor distribution for transport in an individual DFN realisation where consideration is also given to advective dispersion processes. This is what would be obtained with a particle tracking algorithm such as that employed in the Napsac/ConnectFlow simulation tool.

Summary statistics for the PLTR within FFM01c (< –400 m) are given in Table 3-6 for the case of neutrally conductive FIZ, and in Table 3-7 for highly conductive FIZ.

The median F-factor obtained in the simulations is on the order of about 10^6 y/m for 100 m transport in the NS direction and a 1% hydraulic gradient (semi-correlated transmissivity model). The results obtained for the different horizontal transport directions are very similar and the median F-factor differs by a small amount between the NS and EW transport cases. There is a slightly larger difference for transport in the vertical direction where the median F-factor is about 40% higher than that calculated in the NS case. The presence of conductive FIZ does not appear to have a great impact upon the results and F-factors estimated in these cases are only about 30–60% less (in arithmetic units) than for the neutrally conductive FIZ cases. This is explained by the fact that it is very unlikely for the FIZ flow conduits themselves to form a contiguous flowpath through the system and there are almost always intervening flowpath segments of lower transmissivity in the form of in-plane flow channels. It is these discontinuous, low transmissivity segments that tend to determine the overall F-factor for the flowpath in such cases. The conductive FIZ were assumed to possess zero flow resistance and an effective flow-wetted surface 1% of that for a "normal" in-plane flow channel.

Overall, the estimated F-factor distribution appears to be most strongly influenced by the assumed fracture size-transmissivity model which can account for variation as great as 1–2 orders of magnitude. The FC model tends to give the lowest median F-factor values while the SC model gives the highest values. F-factors calculated for the SC and NC cases exhibit the greatest spread with a variation of approximately two orders of magnitude separating the 10% and 90% quantiles. The

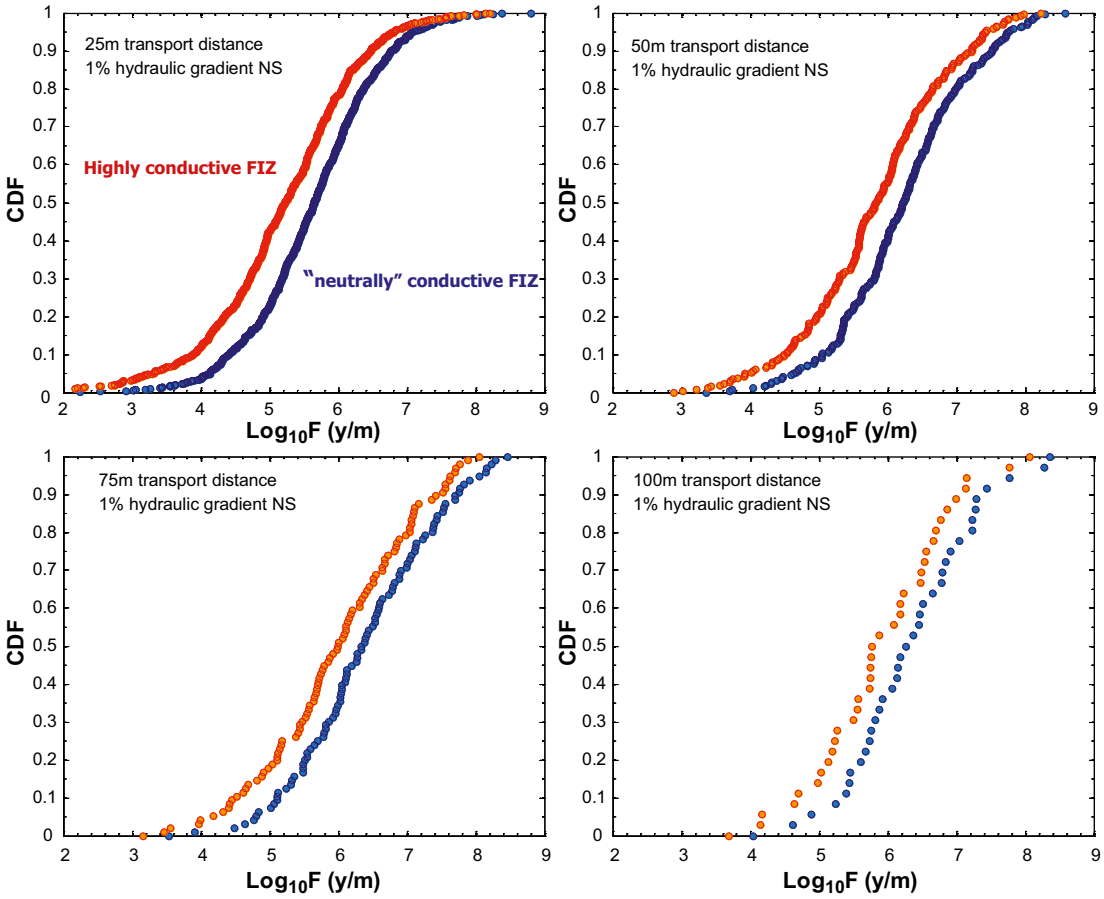

Figure 3-19. Typical F-factor ranges for paths of least transport resistance, PLTR in the immediate far-field (IFF) based upon the results of 1,000 realisations of the Hydro-DFN for FFM01c (< –400 m). The calculations consider different transport distances, an assumed hydraulic gradient of 1% applied along the North-South axis, and a semi-correlated fracture length-transmissivity (SC) model. Results are given for the case of neutrally conductive FIZ (blue markers) and for highly conductive FIZ (orange markers) and are plotted as cumulative distribution probability curves.

Table 3-6. Summary statistics for the F-factor (log_{10} units) corresponding to the path of least transport resistance (PLTR) estimated for FFM01c (< –400 m) assuming neutrally conductive FIZ, a nominal transport distance of 100 m, and a hydraulic gradient of 1%. Results are given for the three different principal transport directions and the three different transmissivity models.

Transmissivity model	Fully Correlated (FC)			Semi-Correlated (SC)			Non-Correlated (NC)		
Gradient direction	EW	NS	V	EW	NS	V	EW	NS	V
Mean	4.78	4.83	4.96	6.37	6.32	6.28	5.41	5.31	5.21
Median	4.74	4.82	4.90	6.31	6.26	6.41	5.47	5.33	5.11
5th percentile	4.21	4.26	4.63	4.80	4.71	4.71	4.11	3.93	4.04
10th percentile	4.40	4.46	4.67	5.27	5.27	4.90	4.73	4.16	4.39
25th percentile	4.59	4.65	4.69	5.89	5.72	5.22	5.14	4.72	4.68
75th percentile	4.92	5.02	5.05	7.02	6.94	6.95	5.66	5.68	5.60
90th percentile	5.24	5.13	5.47	7.43	7.41	7.47	6.11	6.50	6.36
95th percentile	5.30	5.27	5.60	8.04	8.10	8.28	6.51	7.32	6.68
Std. deviation	0.32	0.28	0.32	0.92	0.95	1.12	0.61	0.90	0.77
Variance	0.10	0.08	0.10	0.85	0.91	1.25	0.38	0.82	0.59
Min value	4.16	4.16	4.62	4.31	4.04	4.66	3.68	3.65	3.94
Max value	5.49	5.39	5.64	8.46	8.36	8.51	6.68	7.40	6.76
Fraction connected (%)	2.6	3.7	1.4	2.6	3.7	1.4	2.6	3.7	1.4

Table 3-7. Summary statistics for the F-factor (log_{10} units) corresponding to the path of least transport resistance (PLTR) estimated for FFM01c (< –400 m) assuming highly-conductive FIZ, a nominal transport distance of 100 m, and a hydraulic gradient of 1%. Results are given for the three different principal transport directions and the three different transmissivity models.

Transmissivity model	Fully Correlated (FC)			Semi-Correlated (SC)			Non-Correlated (NC)		
Gradient direction	EW	NS	V	EW	NS	V	EW	NS	V
Mean	4.50	4.39	4.66	6.09	5.90	5.98	5.12	4.88	4.93
Median	4.47	4.41	4.63	6.13	5.77	6.18	5.27	4.81	4.86
5th percentile	3.78	3.71	4.09	4.51	4.15	4.37	3.71	3.48	3.73
10th percentile	3.94	3.86	4.22	5.12	4.65	4.53	4.52	3.72	4.06
25th percentile	4.33	4.19	4.38	5.43	5.23	4.92	4.72	4.14	4.22
75th percentile	4.76	4.73	4.79	6.73	6.59	6.66	5.47	5.31	5.46
90th percentile	4.99	4.79	5.21	7.17	7.11	7.27	5.83	6.04	6.18
95th percentile	5.05	4.85	5.33	7.74	7.55	7.96	6.21	6.99	6.36
Std. deviation	0.36	0.36	0.36	0.92	0.99	1.14	0.68	0.95	0.80
Variance	0.13	0.13	0.13	0.84	0.98	1.30	0.47	0.90	0.64
Min value	3.74	3.64	4.06	4.10	3.69	4.33	3.07	3.26	3.63
Max value	5.22	5.06	5.36	8.25	8.06	8.16	6.54	7.05	6.41
Fraction connected (%)	2.6	3.7	1.4	2.6	3.7	1.4	2.6	3.7	1.4

FC model, on the other hand, exhibits only 0.5–1.0 orders of magnitude variation for the same quantile range. The smaller number of points comprising the F-factor probability distributions at greater transport distances directly reflects the reduced connectivity of the system over increasing length scales.

Results for FFM01a–b, FFM02, and FFM03

Results of F-factor estimations for the other rock sub-volumes comprising the HRD are given in the following tables. These data are based upon 20 Napsac/ConnectFlow realisations of the Hydro-DFN model for each sub-volume. The results are not directly comparable to those given in the previous section as they consider an ensemble average of 1,000 released particles in each simulation instead of the global path of least transport resistance, PLTR for each individual simulation. The summary statistics represent a pooling of all particle tracking results. The F-factor distributions should therefore not be seen as a true distribution of values for solute transport within the rock volume, but interpreted rather as a probability distribution for typical transport paths within the rock. The F-factor for transport from any given canister location would then correspond to a sub-sampling of these distributions. Since it is not possible to simulate highly-conductive FIZ in any simple fashion using Napsac/ConnectFlow, the results consider only the base case of neutrally conductive FIZ.

Summary statistics for the estimated F-factor for typical flowpaths within FFM01a (> –200 m) are given in Table 3-8 and for the depth interval (–200 m to –400 m) in Table 3-9.

Table 3-8. Summary statistics for the F-factor (log_{10} units) corresponding to the pooled particle residence time distribution data for FFM01a (> –200 m) assuming neutrally conductive FIZ, a nominal transport distance of 100 m, and a hydraulic gradient of 1%. Results are given for the three different principal transport directions and the three different transmissivity models.

Transmissivity model	Fully Correlated (FC)			Semi-Correlated (SC)			Non-Correlated (NC)		
Gradient direction	EW	NS	V	EW	NS	V	EW	NS	V
Mean	2.80	2.96	3.80	2.89	2.48	3.93	3.60	3.37	4.37
Median	2.79	2.88	3.82	2.94	2.79	3.68	3.38	3.24	4.47
5th percentile	1.49	1.70	2.26	1.27	0.34	2.58	2.51	1.69	2.92
10th percentile	1.74	1.80	2.79	1.72	0.64	2.77	2.71	2.05	3.21
25th percentile	2.40	2.46	3.17	2.39	1.76	3.29	2.98	2.81	3.67
75th percentile	3.23	3.44	4.51	3.43	3.32	4.32	4.07	3.84	4.90
90th percentile	3.69	3.86	4.86	4.06	3.89	5.26	4.98	4.80	5.38
95th percentile	4.03	4.57	5.01	4.24	4.36	6.56	5.90	5.35	5.74
Std. deviation	0.69	0.84	0.82	0.86	1.39	1.05	1.09	1.00	0.83
Variance	0.48	0.70	0.68	0.74	1.93	1.10	1.18	0.99	0.69
Min value	1.34	1.41	2.20	0.66	–2.51	2.34	0.68	1.46	2.70
Max value	6.81	7.13	6.89	5.86	6.57	8.50	8.16	8.00	7.35
Recovered particles (%)	88	100	50	100	98	85	100	100	85

Table 3-9. Summary statistics for the F-factor (log_{10} units) corresponding to the pooled particle residence time distribution data for FFM01b (–200 m to –400 m) assuming neutrally conductive FIZ, a nominal transport distance of 100 m, and a hydraulic gradient of 1%. Results are given for the three different principal transport directions and the three different transmissivity models.

Transmissivity model	Fully Correlated (FC)			Semi-Correlated (SC)			Non-Correlated (NC)		
Gradient direction	EW	NS	V	EW	NS	V	EW	NS	V
Mean	4.64	4.70	5.20	5.30	5.02	5.60	4.72	4.50	5.07
Median	4.64	4.69	5.03	5.26	5.10	5.54	4.66	4.47	4.87
5th percentile	3.62	3.81	4.20	3.87	3.38	4.37	3.73	3.10	4.13
10th percentile	3.84	4.00	4.31	4.48	3.88	4.48	3.82	3.49	4.28
25th percentile	4.19	4.27	4.65	4.78	4.58	4.91	4.08	3.94	4.47
75th percentile	5.11	5.02	5.81	5.86	5.73	6.11	5.24	5.07	5.50
90th percentile	5.36	5.42	6.19	6.33	6.09	6.79	5.79	5.52	6.23
95th percentile	5.53	5.71	6.41	6.45	6.35	7.34	6.01	5.89	6.49
Std. deviation	0.58	0.55	0.72	0.74	1.07	0.88	0.80	0.80	0.83
Variance	0.34	0.30	0.52	0.55	1.15	0.77	0.64	0.64	0.69
Min value	3.57	3.59	3.85	3.57	–0.01	3.67	3.05	2.34	3.56
Max value	7.21	7.97	7.94	8.22	9.07	9.41	8.31	11.36	9.20
Recovered particles (%)	75	100	40	90	90	80	95	95	70

Summary statistics for the estimated F-factor for typical flowpaths within FFM02 (> –200 m) are given in Table 3-10.

Summary statistics for the estimated F-factor for typical flowpaths within FFM03a (> –400 m) are given in Table 3-11 and for depth (< –400 m) in Table 3-12.

Table 3-10. Summary statistics for the F-factor (log_{10} units) corresponding to the pooled particle residence time distribution data for FFM02 (> –200 m) assuming neutrally conductive FIZ, a nominal transport distance of 100 m, and a hydraulic gradient of 1%. Results are given for the three different principal transport directions and the three different transmissivity models.

Transmissivity model	Fully Correlated (FC)			Semi-Correlated (SC)			Non-Correlated (NC)		
Gradient direction	EW	NS	V	EW	NS	V	EW	NS	V
Mean	3.37	3.33	3.59	3.88	3.72	4.19	3.79	3.884	4.31
Median	3.33	3.35	3.65	3.84	3.77	4.18	3.86	3.917	4.33
5th percentile	2.42	2.43	2.48	2.84	2.71	2.69	2.34	2.772	3.02
10th percentile	2.54	2.54	2.69	2.96	2.83	3.18	2.81	2.975	3.36
25th percentile	2.88	2.86	3.18	3.31	3.18	3.59	3.27	3.353	3.84
75th percentile	3.78	3.75	4.00	4.23	4.19	4.70	4.35	4.386	4.83
90th percentile	4.27	4.07	4.31	4.80	4.57	5.21	4.74	4.711	5.21
95th percentile	4.65	4.31	4.53	5.59	4.84	5.83	5.00	4.914	5.47
Std. deviation	0.69	0.59	0.61	0.74	0.67	0.86	0.83	0.674	0.76
Variance	0.48	0.34	0.38	0.54	0.45	0.74	0.69	0.455	0.58
Min value	0.69	1.84	1.96	2.36	2.17	1.91	1.38	2.074	1.99
Max value	7.76	5.98	7.53	7.23	6.43	7.90	8.80	7.372	7.70
Recovered particles (%)	100	100	100	100	100	95	100	100	100

Table 3-11. Summary statistics for the F-factor (log_{10} units) corresponding to the pooled particle residence time distribution data for FFM03a (> –400 m) assuming neutrally conductive FIZ, a nominal transport distance of 100 m, and a hydraulic gradient of 1%. Results are given for the three different principal transport directions and the three different transmissivity models.

Transmissivity model	Fully Correlated (FC)			Semi-Correlated (SC)			Non-Correlated (NC)		
Gradient direction	EW	NS	V	EW	NS	V	EW	NS	V
Mean	4.04	4.22	3.97	4.83	4.77	4.61	4.28	4.60	4.05
Median	4.06	4.23	3.96	4.74	4.76	4.68	4.31	4.61	4.04
5th percentile	3.35	3.53	3.15	3.87	3.09	3.43	3.18	3.44	2.78
10th percentile	3.47	3.64	3.37	4.03	4.11	3.76	3.36	3.80	3.02
25th percentile	3.71	3.94	3.57	4.36	4.33	4.13	3.83	4.22	3.56
75th percentile	4.32	4.46	4.27	5.10	5.26	5.14	4.75	5.10	4.51
90th percentile	4.56	4.72	4.61	5.85	5.66	5.48	5.09	5.48	5.04
95th percentile	4.71	4.92	4.87	6.22	5.90	5.62	5.27	5.63	5.34
Std. deviation	0.44	0.42	0.51	0.69	0.71	0.74	0.66	0.75	0.76
Variance	0.19	0.18	0.26	0.47	0.51	0.55	0.43	0.57	0.57
Min value	3.16	3.20	3.04	3.58	2.88	2.50	2.66	1.94	2.42
Max value	6.69	7.11	7.19	8.45	7.98	7.16	7.77	7.14	6.83
Recovered particles (%)	100	85	95	80	75	80	95	95	95

Table 3-12. Summary statistics for the F-factor (log_{10} units) corresponding to the pooled particle residence time distribution data for FFM03b (< –400 m) assuming neutrally conductive FIZ, a nominal transport distance of 100 m, and a hydraulic gradient of 1%. Results are given for the three different principal transport directions and the three different transmissivity models.

Transmissivity model	Fully Correlated (FC)			Semi-Correlated (SC)			Non-Correlated (NC)		
Gradient direction	EW	NS	V	EW	NS	V	EW	NS	V
Mean	4.36	4.62	4.36	4.80	4.83	4.70	4.47	4.54	4.20
Median	4.39	4.54	4.31	4.75	4.73	4.64	4.30	4.59	4.28
5th percentile	3.58	3.84	3.47	4.11	4.26	3.35	3.46	3.57	3.07
10th percentile	3.80	3.96	3.69	4.16	4.37	3.71	3.63	3.70	3.30
25th percentile	3.95	4.17	3.94	4.43	4.57	4.25	3.88	4.19	3.75
75th percentile	4.67	4.98	4.64	5.11	5.10	5.00	4.92	4.93	4.70
90th percentile	4.98	5.52	5.16	5.47	5.37	5.85	5.69	5.14	4.98
95th percentile	5.13	5.69	5.45	5.75	5.50	6.13	5.89	5.32	5.16
Std. deviation	0.47	0.59	0.58	0.51	0.39	0.84	0.75	0.53	0.67
Variance	0.22	0.34	0.34	0.26	0.15	0.70	0.56	0.28	0.45
Min value	3.44	3.49	3.34	3.80	4.14	3.07	3.33	3.41	2.46
Max value	6.75	7.32	7.58	7.04	6.69	8.18	8.00	7.18	7.58
Recovered particles (%)	80	65	75	55	35	50	70	65	80

In general it appears that the fracture domains FFM01a/b, FFM02, and FFM03a/b are associated with lower F-factors for typical flowpaths than the range predicted for FFM01c in the previous section. The hydrodynamic transport resistance of typical flowpaths within FFM01c therefore appears to be considerably larger than for the other sub-volumes investigated.

3.7 Transport propeties of the HCD

Using the analytical model described in Equation 3-9, F-factors for typical flowpaths within the HCD have been calculated for an assumed hydraulic gradient of 1%. Here, we also assume that the dip of zone ZFMA2 (24°) is representative of the gently dipping zones likely to be encountered by radionuclides transported in the distant far field. Similarly, for the steeply dipping zones we assume a dip corresponding to that of ZFMA0060A (85°) in the calculations. The results of these calculations are given in Table 3-13.

It is clear from these calculations that radionuclides transported in the gently dipping zones will be subject to lower F-factors than for those escaping via the steeply dipping zones. For the assumed transmissivity-depth model, the difference is on the order of two orders of magnitude. It is interesting to note that the path length (L_p) for the transport scenario as envisaged for the gently dipping zone is over 860 m whereas for the steeply dipping zone it is only 350 m.

Table 3-13. F-factor estimates for transport within the HCD using analytical result given in Equation 3-9 and an assumed 1% hydraulic gradient.

ZFM Category	θ (deg.)	T_{eff} (m^2/s)	log_{10} F (y/m)
Gently dipping zones (G)	24° (ZFMA2)	2.2×10^{-4} (max) 1.0×10^{-5} (mean) 5.0×10^{-7} (min)	1.4 2.7 4.0
Steeply dipping zones (ENE, NE, NNW, NW, WNW)	85° (ZFM0060A)	2.4×10^{-5} (max) 3.4×10^{-8} (mean) 4.9×10^{-11} (min)	2.0 4.8 7.7

A typical set of results for the numerical simulations using the 2D channel network model are shown in Figure 3-20 and Figure 3-21. The particular realisation shown here as an example assumes a lognormally distributed transmissivity field with exponential depth trend and an isotropic Gaussian correlation structure (with a correlation length of 20 m). The F-factor distribution is calculated by particle tracking with release of particles as a line source at an elevation of –450 m.

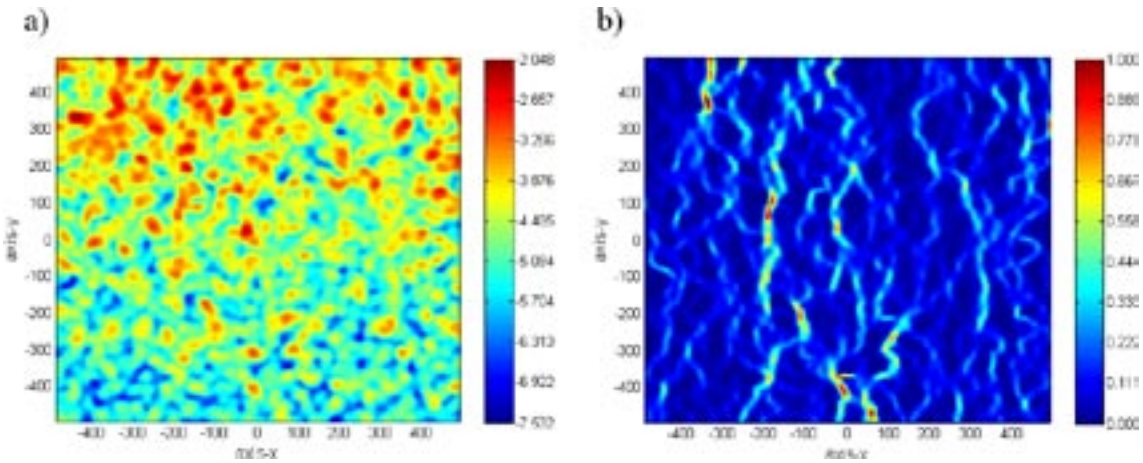

Figure 3-20. *a) lognormally distributed transmissivity field for a gently dipping zone with an isotropic, Gaussian spatial correlation and exponential depth trend (L_x = 20 m, L_y = 20 m). The data are given as log_{10} values for the transmissivity (m^2/s) projected onto a 2D plane; b) corresponding flow field (normalised values) simulated with a 2D channel network model.*

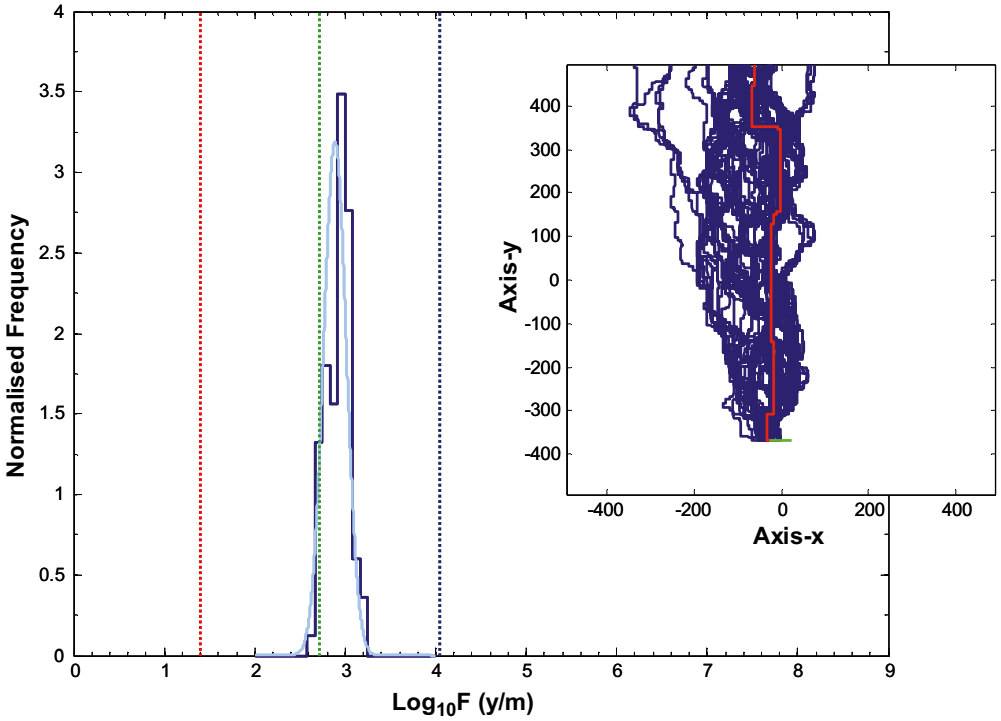

Figure 3-21. *Corresponding F-factor distribution calculated using 2D channel network model and (inset) trajectory of 100 particles released as a line source at –450 m elevation (the red trajectory corresponds to the path of least transport resistance). The vertical broken lines in the main figure indicate the analytically estimated F-factor for the minimum (blue), mean (green), and maximum (red) transmissivity trend. The simulated data are shown as a dark blue outline histogram and the light blue curve represents a fitted lognormal distribution to the simulated data.*

A full account of the simulation procedure and results can be found in Appendix E. Generally it was found that the results were only weakly influenced by the choice of correlation structure even for the very anisotropic spatial correlation fields provided the correlation length is substantially less than the dimensions of the system being modelled. If the simulated transmissivity fields were to exhibit spatial correlations greater than the scale of the modelled transport distance, we may expect to find fast flow channels with reduced F-factors /Neuman 2005/. The mean F-factor in all cases modelled was very close to that calculated using the analytical model and mean transmissivity-depth trend curve.

In a recent numerical study by /Boadu 2000/ it was shown that there is an empirical relationship between fracture permeability (and porosity) and P-wave velocity ratio derived from reflection seismology measurements. Although we have not had the opportunity to compare the effective transmissivities calculated here with estimates based upon seismic measurements, we note this as a possible independent means of cross-checking the results that might be worth investigating further.

3.8 Advective transport time and the F-factor

One of the parameters of interest for safety assessment is the advective transport time for the network of fractures forming conductive pathways from the repository to the near surface. This is also referred to as the water "residence time" in the scientific literature /e.g. Neretnieks 1980/. The advective transport time can be important for the transport of colloids and non-sorbing solutes in flowpaths featuring very low F-factors. Generally, for sorbing solutes the advective transport time is very small in comparison to the matrix retention time and can be neglected in radionuclide transport calculations if the F-factor is sufficiently high /Neretnieks and Moreno 2003, Cvetkovic et al. 2004/. In the following sections we discuss some of the theoretical aspects related to evaluation of the advective transport time and its relation to the F-factor and other variables. Based upon the data available from hydrogeology /Follin et al. 2007a/, scoping calculations are made of the advective transport time. We also make an attempt to reconcile the theoretical predictions of the F-factor in previous sections with first-order estimates based upon raw data derived from hydraulic tests.

3.8.1 Theoretical considerations

The F-factor for a particular flowpath, the advective travel time, and the mean transport aperture are coupled by the relation:

$$F = \frac{2t_w}{\bar{\delta}_t} = \int_0^{L_p} \frac{2}{v(\zeta)\delta_t(\zeta)} d\zeta \qquad (3\text{-}10)$$

This means that the advective travel time and the F-factor are highly correlated by way of their mutual dependency upon the velocity field /Cvetkovic et al. 1999/.

In the field it is relatively straight forward to measure *in situ* flow rates and drawdowns using hydraulic testing. On the other hand, the fracture aperture or flow-wetted surface generally cannot be determined by non-destructive means /Neretnieks 2007/. Although the fracture aperture may be accessible locally where a borehole intercepts a fracture plane, this does not say a great deal about the average properties of the kinematic porosity or its spatial variation. It is also very difficult to measure *in situ* fracture apertures on a sub-millimetre scale using borehole cameras. For these reasons, the estimation of parameters such as transport aperture or flow-wetted surface needs to be addressed indirectly by way of modelling.

For the fracture aperture, there are basically two problems: 1) finding an appropriate measure of effective macroscopic aperture for "real" fractures; and, 2) finding a phenomenologically consistent description of how the flowrate (or flow velocity) varies as a function of this aperture.

A great deal of effort has been made in the past decade to create high fidelity models of fracture aperture variation that can be used to make pore-scale simulations of flow and transport /e.g. Brown 1995, Glover et al. 1998a, Drazer and Koplik 2002, Ogilvie et al. 2006/. It is generally thought that if the physical fracture aperture can be resolved in sufficient detail then the Reynolds approximation for the Navier Stokes equations gives a reasonably accurate representation of the flow dynamics in the fracture /Brown 1987, Zimmerman et al. 1991/. This is generally what is referred to as the local cubic law, or LCL /e.g. Berkowitz 2002/ in the hydrogeology literature (it is also commonly referred to as the Hagen-Poiseuille law for parallel-plate flow). This simplification is used in many modelling tools /e.g. Moreno et al. 1988, Cvetkovic et al. 1999, Miller 2002/ and is reasonably accurate for low Reynolds number flow in most practical situations /e.g. Koyama et al. 2008/.

In this report, we differentiate between the use of the cubic law to describe flow properties on the pore-scale (LCL) and the use of the cubic law to describe flow on the scale of an entire fracture using a calculated mean fracture aperture. Here, we refer to this upscaled version of the LCL as the macroscopic cubic law, or MCL. The fracture aperture referred to by the MCL is simply the equivalent aperture of a parallel plate fracture that would exhibit the same transmissivity as the actual fracture.

It has been shown previously in a forward modelling perspective that fracture to fracture variability tends to dominate the statistics of the F-factor distribution and internal fracture heterogeneity plays a subordinate role /e.g. Painter 2006/. This is because flow tends to seek out the path of least hydraulic resistance and within a variable aperture fracture featuring many parallel-connected flowpaths the most transmissive paths therefore tend to control the flow characteristics of the fracture. Indeed for an open, variable aperture without significant asperity contact, the effective hydraulic aperture as defined by the MCL is reasonably well approximated by the geometric mean of the aperture distribution provided the aperture variation is not too large /Silliman 1989, Auradou et al. 2006/.

Deviations from the pore-scale LCL are well known in the scientific literature /e.g. Brown et al. 1995, Mourzenko et al. 1995, Ge 1997, Oron and Berkowitz 1998, Konzuk and Kueper 2004/. It has also been shown that deviation from the LCL should also intensify with increasing fracture compression /Sisavath et al. 2003/. These deviations have a number of origins. Chief among these relates to the definition of aperture itself on pore-scale resolution. Different definitions such as the vertical aperture, normal-to-local-centreline aperture, or the “ball” aperture described by /Mourzenko et al. 1995/ are all valid representations of the local fracture aperture, although each of these tend to give deviations from what would be predicted using a fully three-dimensional description based upon the Navier Stokes equation or Lattice Boltzmann modelling approach. This is due to the fact that the Reynolds approximation is only strictly valid for smoothly varying surfaces and is not altogether appropriate for self-affine fracture surfaces possibly featuring mismatched surface displacements, anisotropic discontinuities, and out of plane tortuosity. The approach simply cannot capture the full dynamics of flow within such complex geometries. Other non-linear flow effects can also play a role, although these are probably only of relevance during hydraulic testing when flowrates may be sufficiently high that inertial effects and other unusual flow phenomena may need to be considered close to the borehole or at fracture intersections /e.g. Kosakowski and Berkowitz 1999, Lage and Antohe 2000, Park et al. 2003, Zimmerman et al. 2004/.

The deviation from cubic behaviour on the scale of the MCL approximation is a more general problem as it relates to the ability of a simply abstracted mean aperture to correctly represent the properties of what in reality may be a very complex structure on the pore scale. It is also easy to forget that much of the discussion in abovementioned references centres on assumptions of flow in fractures featuring variable apertures with well defined mathematical-stochastic spatial structure. As pointed out by /Neretnieks 2002/ this is not necessarily always the case and it is quite feasible for other macroscopic laws to more correctly describe the physics of flow. A more general formulation for the flow would be:

$$Q = k_{+}\delta_{t}^{n} \tag{3-11}$$

Where, k_+ is a proportionality constant, δ_t is the average "mechanical" aperture (in this case taken to be equal to the mean transport aperture), and the exponent n depends upon the flow regime that dominates within the flowpath under consideration. As discussed by /Neretnieks 2002/, the exponent n can vary anywhere from $n = 0$ in the case of a fracture where the flow is dominated by local flow "pinch points" or "bottlenecks", $n = 1$ for a pathway filled with particulate matter, to $n = 3$ in the case of true parallel plate flow. In a similar analysis /Nolte et al. 1989/ found that the n exponent for highly compressed fractures in Stripa granite could be as great as $n = 7.6–9.8$ owing to flowpath tortuosity and constrictivity effects. Essentially, Equation 3-11 accounts for the difficulty in characterising an appropriate average aperture that can be related to the macroscopic flow properties.

For true parallel plate flow (MCL), the transport aperture is equal to hydraulic aperture and can be given in terms of the flow channel, or fracture transmissivity as:

$$\delta_t \approx \delta_h = \left(\frac{12\mu_w}{\rho_w g_c} T \right)^{1/3} \tag{3-12}$$

In field experiments which typically involve clusters of interconnected fractures, the MCL has been shown to severely under-predict advective travel times when tracer test results are considered together with effective apertures derived from hydraulic data /Tsang 1992/. Put another way, calculations based upon effective hydraulic apertures tend to give higher flow velocities and shorter advective transport times than are actually observed in field tracer experiments. This does not necessarily mean that the MCL is incorrect, since it can be shown theoretically that the effective transport aperture, δ_t (or "mass balance aperture" using the terminology of /Tsang 1992/) should differ from the hydraulic aperture, δ_h by way of the relation /Gelhar 1993/:

$$\delta_t = \delta_h \exp\left(\sigma_g^2/2\right) \tag{3-13}$$

This relation simply reflects the difference between the mean aperture (transport) and median aperture (hydraulics) of a fracture assuming a lognormally distributed, heterogeneous aperture distribution. In a practical sense this means that the relative variation of both hydraulic and transport aperture may still be consistent with an underlying cubic law, although they can differ in absolute value. This suggests that we could make a more accurate estimate of the transport aperture by combining Equation 3-12 and 3-13 to give:

$$\delta_t = \exp\left(\sigma_g^2/2\right)\left(\frac{12\mu_w}{\rho_w g_c} T \right)^{1/3} \tag{3-14}$$

A meta analysis carried out by /Guimera and Carrera 2000/ identified a moderate level of support for the MCL in field tests carried out in range of different fractured rock types. Although there are large uncertainties in the reinterpreted data sets, they also propose that site-specific deviations from the MCL could, in principal, be explained by local variations in the logarithmic fracture aperture variance, σ_g^2.

If a flowpath hosted in a fracture or enlarged fracture intersection is filled or even only partially filled with particulate matter, its flow properties may be more accurately determined by the Blake-Kozeny equation /Bird et al. 2002/ in which case the apparent hydraulic aperture will reflect the properties of the interstitial pore space of the particulates. In highly compressed fractures with substantial surface asperity contact areas, the hydraulic aperture may be biased by pinch points at entry and exit locations or even due to the tortuosity and constrictivity of the flow space itself thus giving an apparent hydraulic aperture substantially less than its transport aperture.

In a study carried out at the Kamaishi mine in Japan, /Sawada et al. 2000, 2001/ a quadratic relation for the variation of fracture transmissivity with transport aperture was proposed (henceforth referred to as the macroscopic quadratic law, MQL). This relation was found to give better agreement with transport apertures estimated from tracer tests using non-sorbing tracers. In another study carried out at the Äspö HRL, /Uchida et al. 1994/ found that the relationship between hydraulic diffusivity and transmissivity could be best described using a quadratic

law which also implies a quadratic relation between storativity and transmissivity. Since storativity is essentially a measure of the volume of a fracture, it is closely related to the transport aperture. If we neglect the fact that stagnant volumes are also included in the hydraulic diffusivity measured by transient hydraulic testing, the local transport aperture, δ_t (m) can then be shown to be approximately proportional to the square root of the fracture transmissivity, T (m^2/s):

$$\delta_t = a_t \sqrt{T} \tag{3-15}$$

Based upon the data from Kamaishi experiment, the empirical constant, a_t ($s^{1/2}$) was estimated to be in the range 1–10. In the Äspö study by /Uchida et al. 1994/, a value of $a_t \approx 0.5$ was found to give the best agreement with tracer test data.

In /Uchida et al. 1994/ it is suggested that a storativity that varies as a function of the square root of transmissivity is consistent with the notion of flow in a "pipe-bundle" within individual fractures. As it is stated, however, this explanation does not seem to fully explain the empirical relation since the functional dependency of transmissivity upon aperture can be shown from consideration of the Hagen-Poiseuille equation to be consistent with the cubic law and not different to the corresponding relation for a narrow slit, or parallel plate model of flow within a fracture (see Appendix F).

An internally consistent and independently verifiable explanation for the empirical Equation 3-15 does not appear to be currently available. Nevertheless, we can speculate upon the origin of the phenomenon by first noting that the MQL describing the relation between transmissivity and transport aperture on the level of the fracture population does not necessarily contradict the MCL on the level of individual fractures.

This could arise, for example, due to a statistical drift in the properties of the underlying population of flowing features sampled in hydraulic and tracer tests. One way this could happen would be if the flowing features at the lower end of the transmissivity range were to have a different aperture variance, σ_g^2 to those features at the top end of the transmissivity range. To obtain the same behaviour as the MQL relation described by Equation 3-15 would require low transmissive fractures to have an aperture variance substantially less than that for highly transmissive fractures.

We have no empirical supporting evidence to suggest why there should be a systematic drift in fracture properties across the transmissivity range. On the basis of the 2D simulations of in-plane flow channelling in Appendix B, however, we can speculate that fractures featuring low aperture variance will tend to exhibit lower relative transmissivities for a given surface area contact fraction (f_c) arising due to compression under *in situ* stress. Fractures with larger aperture variances, on the other hand, seem to be associated with greater relative transmissivities for the same surface contact area. We can also speculate that a proportion of the more transmissive hydraulic features may take the form of enlarged flow channels hosted within FIZ or fault stepovers whereas the low transmissive features may be dominated by in-plane flow channels. Flow channels hosted within enlarged fracture intersections and fault stepovers could exhibit considerably larger disparities between transport and hydraulic aperture owing to flow restrictions (pinch-points) at flow entry and exit points.

It has been shown in a number of recent studies /e.g. Cvetkovic et al. 1999, Cheng et al. 2003, Cvetkovic et al. 2004/ that the statistical distribution of the F-factor is partially correlated with the advective travel time:

$$F \sim t_w^{\alpha} \tag{3-16}$$

Where, the exponent α is an empirically derived constant derived from Hydro-DFN simulations. Based upon a DFN model representing the geometric and hydraulic properties of the prototype repository and the TRUE Block Scale site at the Äspö Hard Rock Laboratory, /Cvetkovic et al. 2004/ obtained values for α ranging from 1.4 (MCL-assumption) to 1.6 (MQL-assumption). We mention this because, in theory, it would allow the approximate prediction of the F-factor distribution from knowledge of the statistics of advective travel times in the system.

3.8.2 Estimated advective travel times for safety assessment conditions

Using either the MCL or MQL it is possible make scoping estimates of advective travel times under the same conditions assumed for the F-factor calculations presented in previous sections.

For the HRD, we consider the same model volume and local hydraulic gradient as described in section 3.3 and illustrated in Figure 3-9. If we make the further assumption that potential flow-paths in the system are hosted predominantly in sub-horizontal fractures, the minimum fracture radius that could give a hydraulically connected flowpath is roughly 50 m. On the other hand, since a fracture radius cut-off of 560 m has been assumed in the definition of the HRD, this constitutes the upper limit to the hydraulically connected fracture sizes likely to be encountered. For a flowpath of length, L_p (m) and hydraulic gradient i (m/m) the advective travel time within the HRD can then be given as:

$$t_w = \frac{V}{Q} = \frac{L_p \bar{\delta}_t}{T\, i} \approx \begin{cases} \dfrac{L_p}{i}\left(\dfrac{12\mu_w}{\rho_w g_c}\right)^{1/3} T^{-2/3} & \text{(MCL)} \\ \dfrac{a_t L_p}{i} T^{-1/2} & \text{(MQL)} \end{cases} \qquad (3\text{-}17)$$

Assuming a 100 m long flowpath and the reference hydraulic gradient of 1%, we can estimate likely advective travel times within the different fracture domains using Equation 3-17. The results of these calculations are shown in Table 3-14 for the different fracture domains parameterised in section 3.2.2 assuming $a_t = 0.5$.

Table 3-14. Estimated advective travel times for fracture domains resident in the HRD assuming two different models (MCL and MQL) for transport aperture scaling as a function of transmissivity. Here, a flowpath length, L_p = 100 m and a hydraulic gradient of 1% has been assumed in parity with the previous F-factor calculations.

Fracture domain	T-model	Transmissvity range (radius 50 m–560 m) T (m²/s)	Advective travel time range (100 m path length) t_w (y), MCL	t_w (y), MQL
FFM01a > –200 m	SC	1.0×10^{-6}–2.4×10^{-5}	4.4×10^{-3}–0.036	0.032–0.16
	FC	1.6×10^{-6}–4.7×10^{-5}	2.8×10^{-3}–0.027	0.023–0.13
	NC	2.0×10^{-7}	0.11	0.35
FFM01b –200 m to –400 m	SC	9.2×10^{-9}–3.1×10^{-8}	0.37–0.83	0.9–1.7
	FC	3.7×10^{-8}–2.5×10^{-7}	0.092–0.33	0.32–0.83
	NC	3.2×10^{-8}	0.36	0.89
FFM01c < –400 m	SC	3.7×10^{-10}–1.3×10^{-9}	3.1–7.1	4.4–8.2
	FC	9.0×10^{-9}–1.0×10^{-7}	0.17–0.84	0.5–1.7
	NC	5.0×10^{-9}	1.3	2.2
FFM02	SC	1.4×10^{-7}–7.6×10^{-7}	0.044–0.14	0.18–0.42
	FC	5.5×10^{-7}–9.9×10^{-6}	7.9×10^{-3}–0.054	0.05–0.21
	NC	7.9×10^{-8}	0.20	0.56
FFM03a > –400 m	SC	6.2×10^{-8}–1.6×10^{-7}	0.12–0.23	0.39–0.64
	FC	1.5×10^{-7}–6.2×10^{-7}	0.050–0.13	0.20–0.41
	NC	6.3×10^{-8}	0.23	0.63
FFM03b < –400 m	SC	5.8×10^{-8}–1.2×10^{-7}	0.15–0.24	0.46–0.66
	FC	7.4×10^{-8}–3.2×10^{-7}	0.078–0.21	0.28–0.58
	NC	6.3×10^{-8}	0.23	0.63

Table 3-15. Advective travel time estimates for transport within the HCD using the analytical expression given in Equation 3-19 (MCL and MQL) and an assumed hydraulic gradient of 1%.

ZFM Category	Properties	t_w (y), MCL	t_w (y), MQL
Gently dipping zones (G) e.g. ZFMA2	L_p = 860 m T_{eff} = 1.0×10^{-5} m^2/s (mean) θ = 24°	0.085	0.63
Steeply dipping zones (ENE, NE, NNW, NW, WNW) e.g. ZFM0060A	L_p = 350 m T_{eff} = 3.4×10^{-8} m^2/s (mean) θ = 85°	2.8	12

For advective travel times within the deformation zones in the HCD, we assume the same conceptual model for transport as illustrated in Table 3-15. Since the transmissivity of deformation zones within the HCD decays exponentially with depth, we need to consider this explicitly in the calculation. Using the nomenclature already established in section 3.5, the advective travel time along a flowpath of length L_p in the HCD can be shown to be:

$$t_w = \frac{V}{Q} = \frac{1}{T_{eff} i}\int_{L-L_p}^{L} \delta_t(\xi)\,d\xi \approx \begin{cases} \dfrac{1}{T_{eff} i}\left(\dfrac{12\mu_w}{\rho_w g_c}\right)^{1/3}\displaystyle\int_{L-L_p}^{L} T(\xi)^{1/3}\,d\xi & \text{(MCL)} \\ \dfrac{a_t}{T_{eff} i}\displaystyle\int_{L-L_p}^{L} T(\xi)^{1/2}\,d\xi & \text{(MQL)} \end{cases} \tag{3-18}$$

Using the exponential model for transmissivity decay with depth (Equation 3-2), this can be simplified to:

$$t_w \approx \begin{cases} \dfrac{3k}{T_{eff} i \sin(\theta)}\left(\dfrac{12\mu_w}{\rho_w g_c}\right)^{1/3}\left(\exp\left(\dfrac{b-m}{3k}\right)-\exp\left(\dfrac{a'-m}{3k}\right)\right) & \text{(MCL)} \\ \dfrac{2a_t k}{T_{eff} i \sin(\theta)}\left(\exp\left(\dfrac{b-m}{2k}\right)-\exp\left(\dfrac{a'-m}{2k}\right)\right) & \text{(MQL)} \end{cases} \tag{3-19}$$

Where, the effective transmissivity, T_{eff} is defined by Equation 3-8, m and k are the parameters of the transmissivity model, θ is the dip angle of the deformation zone in radians, and a' and b are the release and recovery elevations for the hypothetical solute transport path.

Based upon the deformation zone transmissivity model parameters given in Table 3-5 and the reference hydraulic gradient of 1%, we can estimate the advective travel time for the HCD using Equation 3-18 assuming the same path lengths (L_p) as used previously for the calculation of F-factors in the HCD. Here, as previously we assume a value for a_t of 0.5.

In the case of the gently dipping zone, ZFMA2 the advective travel time is calculated to be on the order of 0.085–0.6 y for the 860 m path length from –450 m to –100 m elevation depending upon which aperture-transmissivity model is used. For the less transmissive, steeply dipping zones as exemplified by ZFM0060A, the advective travel time is substantially larger and in the range 2.8–12 y. The path length in this case is roughly 350 m for the same notional release and recovery elevations.

3.8.3 Direct estimation of the F-factor from borehole measurement data

To provide a reality check on F-factor ranges obtained from detailed hydrogeological modelling, it is possible to use borehole hydraulic data directly to give an order of magnitude estimate of representative F-factors characterising the HRD and HCD.

One way of making such an estimate is to focus on the level of individual flowing features identifiable from borehole hydraulic measurements. Here, we consider what the theoretical transport resistance would be if the flowing feature sampled in a borehole were to correspond to a typical flowpath. For this purpose, the most appropriate conditions for comparison with safety assessment conditions would be those corresponding to the natural background hydraulic gradients at the site.

As already discussed in section 3.3, there are a large number of *in situ* measurements of flow under approximately background hydraulic conditions which could, in principle, be used to make such a calculation. These measurements take the form of tracer dilution tests performed in permanently instrumented boreholes /Wass 2006, 2007, 2008/ and borehole sections used in conjunction with SWIW tests /Gustafsson et al. 2005, 2006ab, Wass and Andersson 2006/.

In order to use these measurements to derive a raw-data based estimate of a site specific F-factor, we need to make the following assumptions:

1) The hydraulic conditions are representative for the undisturbed background hydraulic gradient and are similar to those that would be encountered under safety assessment conditions.
2) The flow measured in a tracer dilution test, after correction for distortion of flow caused by the borehole, is representative of a flowpath of width at least equal to the borehole diameter, W_{bh}.
3) The flowpath length, L_p is the same as that used for the calculation of F-factors (with the hydrogeological model) upon which the comparison is based, i.e.:

   100 m for the HRD (i.e. the same as in the voxel calculations for FFM01-3)
   860 m for gently dipping deformation zones in the HCD (e.g. ZFMA2)
   350 m for steeply dipping deformation zones in the HCD (e.g. ZFM060A)
4) The flow-wetted surface of the sampled flowpath is equal to, or greater than twice the product of borehole diameter and flowpath length.

Based upon these assumptions, we define the F-factor as:

$$F \approx \frac{2W_{bh}L_p}{Q_{bh}/\alpha_{corr}} \geq \frac{4W_{bh}L_p}{Q_{bh}} \qquad (3\text{-}20)$$

With regard to assumption 1, we can say that although tracer dilution tests are carried out in the absence of pumping in the measurement borehole itself, it is known that there is often considerable hydraulic interference from other activities occurring at the site. These undesirable influences are exacerbated at Forsmark due to the very high hydraulic diffusivity of the connected fracture system (as already discussed in section 3.3). Consequently, assumption 1 described above is not reliable and measured flowrates therefore are probably not representative of the regional hydraulic gradient. In all likelihood this would mean a bias towards higher measured flowrates and consequently lower F-factors than would be representative of the true regional gradient.

The flow distortion introduced by the borehole depends on the permeability of the borehole section itself (effectively infinite) relative to that of the surrounding aquifer including any disturbed zone. In the interpretation of tracer dilution tests, a value for the correction factor of $\alpha_{corr} = 2$ is generally assumed in calculations /e.g. Nordqvist et al. 2008/. This is what would be expected for a simple fracture aligned orthogonally to the borehole. Since the actual geometry and complexity of the flowing feature is not known accurately, this should be considered to be only a rough estimate. A fracture inclined at an angle of 45° to the borehole, for example, would give a correction factor roughly 41% greater.

The presence of a zone of altered permeability, referred to as a skin zone, may give greater or less distortion than that predicted purely by consideration of the fracture orientation relative to the borehole. The borehole skin may be positive thereby indicating a decreased permeability

near the borehole, or negative, indicating an increased permeability near the borehole. Positive skin may arise due to clogging of the fracture with infill material (giving a correction factor less than 2), while negative skin may reflect local erosion of fracture infill material or redistribution of stress near the borehole (giving a correction factor greater than 2). Also /Bidaux and Tsang 1991/ investigated the impact of an excess fracture permeability assumed to decay exponentially with distance from a borehole (referred to as a "complex skin"). In that study it was found that the correction factor could be as great as 10 or more for a range of negative skin factors depending upon the assumed radius of penetration of the increased permeability zone from the borehole.

Provided assumption 2 (above) is reasonable, then the result given by the right-hand side Equation 3-20 should constitute a lower bound for the F-factor. For flow correction factors greater than 2 and greater flow channel widths, the F-factor may therefore be larger than this simple estimate suggests. In /Follin et al. 2008/ a cumulative distribution of skin factors is compiled for Forsmark based upon 550 PSS measurements in 5 m test sections. Roughly 80% of the tested borehole sections gave indications of negative skin factors with 50% having skin factors less than –2.5 thereby suggesting that Equation 3-20 will tend to underestimate the effective F-factor of the sampled flow path if the measured flow rate is deemed representative.

Since the F-factor is not a directly measurable quantity, it is probably more enlightening to recast Equation 3-20 to give the hypothetical flowrate required to attain a specified F-factor since this can then be compared directly with the borehole measurement data. The results of this calculation are shown in Figure 3-22 for the reference flowpath lengths described above.

In the methodological description for tracer dilution tests /Gustafsson 2002/, the detection limit is given in terms of the Darcy velocity as being in the range 4×10^{-11} to 6×10^{-12} m/s if an error margin of up to 10% is acceptable. This limit is based upon consideration of the flow rate where the rate of advective transport is only 10 times greater than the hypothetical rate of transport by diffusion into a stagnant water-filled fracture. For a 1 m borehole section, this would correspond to a flowrate in the approximate range of 10^{-11} to 10^{-12} m^3/s. This, however, is a best case for a short borehole section with a small mixing volume. In reality, many of the tested borehole

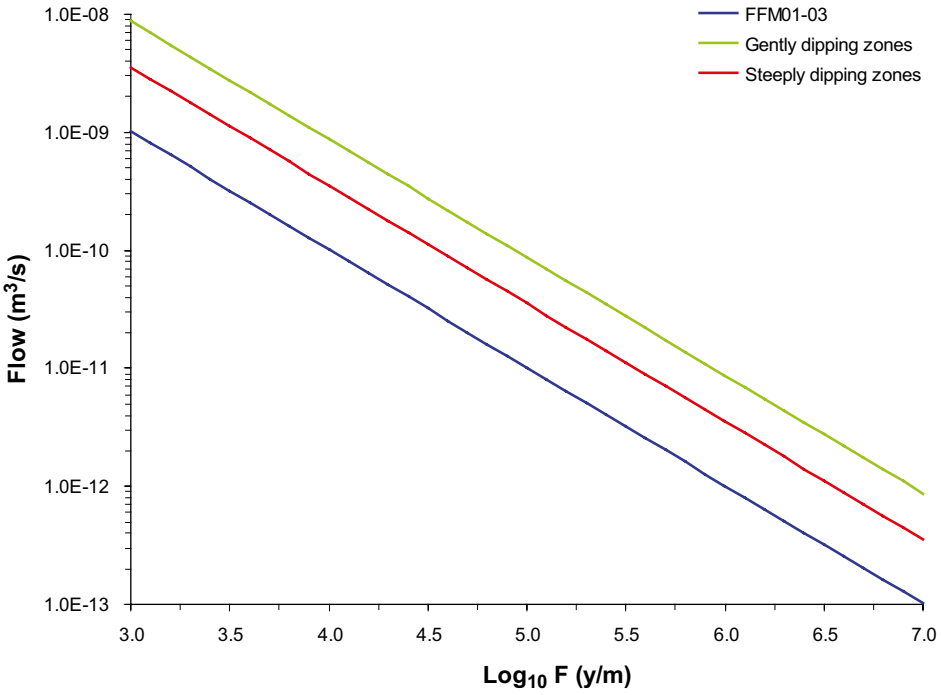

Figure 3-22. *Magnitude of flowrate theoretically required to attain a specified F-factor for the assumed flowpath lengths (100 m for FFM01–3, 860 m for gently dipping deformation zones, and 350 m for steeply dipping deformation zones).*

sections are significantly longer than 1 m. For the permanently instrumented boreholes, for example, it is not uncommon for the tested sections to be anywhere from 5 m to 30 m in length. Such long borehole intervals contain significant dead volumes (even with volume reducer inserts) and therefore can be expected to have considerably higher detection limits.

The actual background flows measured at the Forsmark site using the tracer dilution method are shown in Figure 3-23.

From Figure 3-23 it can be seen that there is only one data point available for FFM01c at repository depth. This measurement was made over a 1 m borehole interval in KFM01D at an elevation of –446.6 m and indicated a flowrate of 2.5×10^{-10} m^3/s. Using Equation 3-20 gives an F-factor of roughly 4×10^3 y/m which is somewhat lower than expected for this volume.

Although there are few tracer dilution test data available for FFM01 at repository depth, there are a number of measurements available for the elevation interval from –200 m to –400 m. In Figure 3-24 a comparison has been made between the F-factors calculated by the empirical relation given in Equation 3-20 and those calculated by Napsac/ConnectFlow using the Hydro-DFN calibrated for this elevation interval (i.e. FFM01b, see Table 3-9).

As can be seen from Figure 3-23 and Figure 3-24, the measured background flowrates differ significantly from what is required to give the same F-factors predicted by the hydrogeological model for this fracture domain and elevation interval.

The difference between the empirically derived estimates and those simulated using the Hydro DFN seem large, although upon consideration of probable biases inherent in the analysis it is possible that the empirically derived F-factors might be unreasonably low. It is also plausible that flow dilution tests have only been made in borehole sections featuring relatively high flowrates that may not be completely representative of the site in general. It therefore cannot be entirely ruled out that there are flows in non-tested borehole sections that are at or below the detection limit of this method and therefore the plotted values (given as an interpolated, cumulative distribution of percentiles in Figure 3-24) may represent a biased snapshot of flow statistics for the intermediate depth zone of fracture domain FFM01b (–200 m to –400 m).

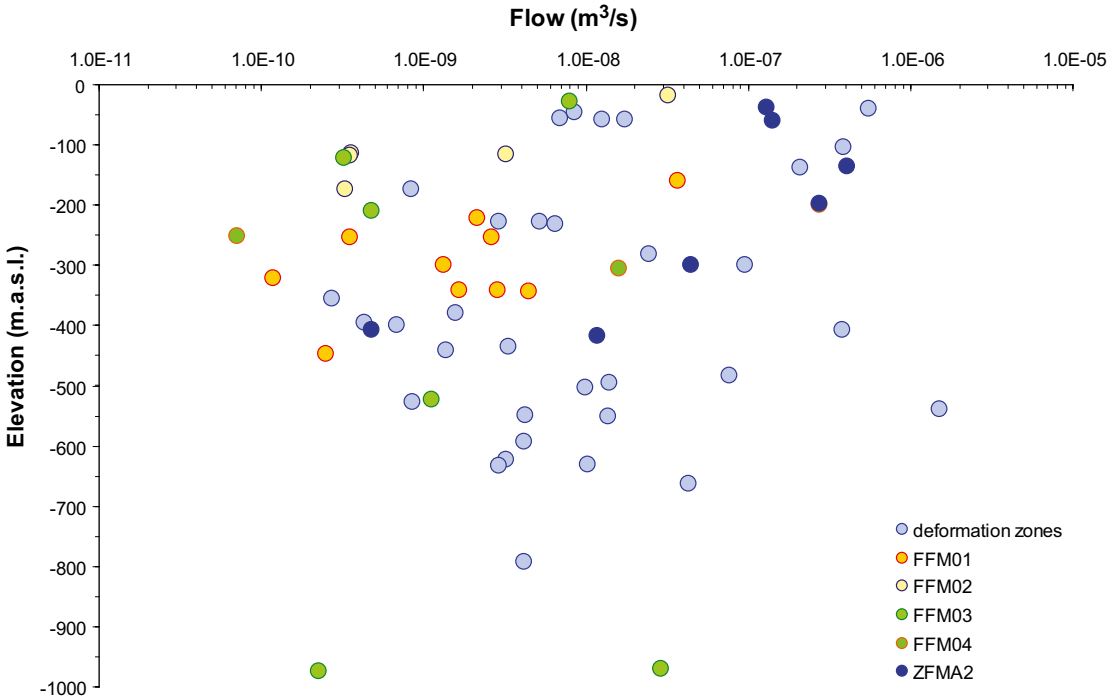

Figure 3-23. *Background flowrates measured in hydraulically conductive borehole sections using the tracer dilution method. The data are categorised according to whether the measurements were made within fracture domains, ZFMA2, or other non-specified deformation zones.*

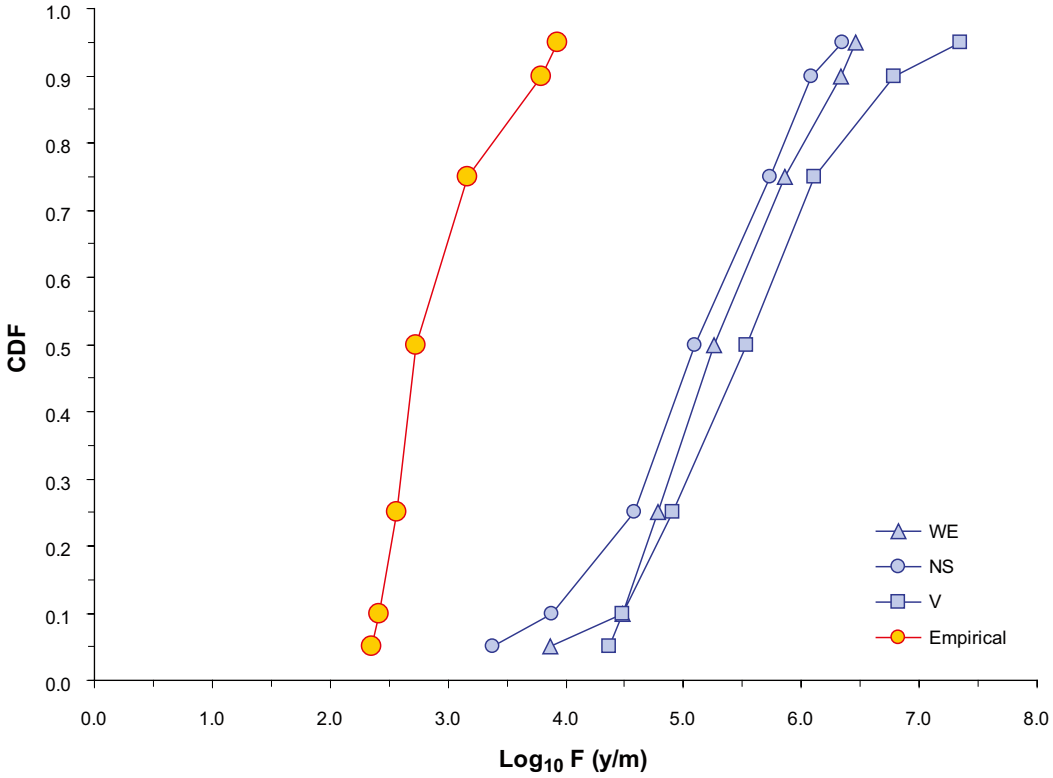

Figure 3-24. *Comparison of F-factors calculated using Napsac/ConnectFlow for FFM01b (–200 m to –400 m) and corresponding estimated F-factors based upon borehole flow measurement data and the same transport path length. The data are given as an interpolated cumulative probability distribution curve for the empirical borehole data (the curve with red-orange markers to the left) and simulated data assuming the semi-correlated transmissivity-length distribution (curves with blue markers to the right) where transport along the three principal directions has been considered.*

In addition, there are indications from the Hydro-DFN modelling work that point-sampled hydrogeological properties used to make estimates of the F-factor according to Equation 3-20 may not be fully representative of the flowpath integrated F-factor obtained by considering hydrodynamic transport properties along an entire particle trajectory. For the particular Hydro-DFN model used in Figure 3-24, for example, it is found that the F-factor obtained using the initial properties of the transport paths at the particle release locations gives F-factor estimates, on average, about 2–3 orders of magnitude less than those obtained by correct integration of flow velocity and fracture aperture along the flowpath (i.e. using Equation 3-10). Qualitatively similar results have been reported by /Cvetkovic and Cheng 2008/ in single fracture modelling interpretations of the TRUE-1 tracer tests and by /Cvetkovic et al. in prep./ in connection with Hydro DFN modelling of the TRUE Block Scale experiments carried out at the Äspö HRL.

Further analysis is needed to identify the source of this apparent discrepancy. One possible way to check the consistency of the hydrogeological modelling predictions would be to directly simulate the conditions of a tracer dilution test using the regional scale Hydro-DFN model and compare simulated borehole flow statistics with the site measurement data. This would need to be done using the Hydro-DFN directly rather than the equivalent continuous porous medium (ECPM) analogue used in the regional scale hydrogeological simulations since we are interested in flow magnitudes on the scale of individual conductors rather than averages for larger volumes of rock. Since the Hydro-DFN is conditioned upon data obtained from essentially the same bore-holes, it should in principle also be able to correctly predict the flow characteristics of the same transmissive features under altered hydraulic conditions.

3.9 ECPM simulations of the regional flow model

Within the hydrogeology site descriptive modelling, flow and transport simulations were carried out with the intention of testing the hydrostructural model developed for the Forsmark candidate area against site scale measurement data including environmental "point-water heads" and drawdowns obtained during hydraulic interference tests. An additional aim of this work was to increase the understanding of paleo-hydrogeochemical conditions and reconstruction of groundwater evolution during the Holocene (i.e. the last 10,000 years). This work is extensively detailed in the background report by /Follin et al. 2008/.

Within the hydrogeological modelling work, an additional analysis was also carried out involving particle tracking from a hypothetical repository loosely based upon the D1 layout described in /Brantberger et al. 2006/. One aim of this particular calculation was to ascertain potential radionuclide release locations as an input for surface systems modelling and for safety assessment.

The following sub-sections of this chapter contain a detailed account of these particle tracking results for solute release at –450 m elevation within the target volume. The aim is to compare the simulation results with the scoping calculations presented in previous sections in order to gain a greater understanding of the flow-related transport properties of the target volume. The main difference in the calculations presented here is that we attempt to incorporate an accurate set of topographically determined, hydraulic head boundary conditions and an appropriate three-dimensional integration of the different hydrogeological elements comprising the HRD and HCD, which in previous sections have been considered as separate compartments.

3.9.1 Flow related transport properties for solute release at –450 m

A particle tracking simulation was made using the ConnectFlow program and the Base Case flow model developed by hydrogeology and described in the report by /Follin et al. 2008/. The ConnectFlow simulations are based upon an equivalent continuous porous medium (ECPM) representation of the combined HRD and HCD hydrostructural models.

The geometry of the particle release area and number of released particles were the same as that used in the hydrogeology site descriptive modelling. However, for reasons of consistency with the previously presented scoping calculations for the HCD (described in section 3.5), the calculation was carried out for solute release at –450 m elevation rather than –500 m as considered in the hydrogeological modelling work. The particle tracking simulations consider a flow field taken from the final time step of the paleo-hydrogeochemical simulations and "frozen" in time. This means that although the flow field is not strictly in a steady state configuration, it is assumed constant for the purposes of the particle tracking simulations.

The particle release area was defined by a square region with an edge length of 2,140 m. A total of 11,236 particles were released on a regular grid with a 20 m spacing between particle release locations. The actual grid of particle release locations in relation to prominent deformation zones is illustrated as a 2D projection in Figure 3-25. Since the deformation zones are actually curved and comprised of a mosaic of triangulated surfaces, the visualised trace lines for deformation zone intersection with the release plane were estimated using a PCA (principal component analysis), best fit plane to the surfaces defined for the target volume. This was implemented in Matlab using an algorithm described by /Peyré 2004/. On the scale of the repository volume, this was found to be a sufficiently accurate representation for visualisation purposes.

Solely for the purpose of the visualisations presented in this section, the initial x- and y- coordinates of the system (RT90) were transformed to a more convenient local set with an origin defined as the centre of the particle release polygon (x = 1631530, y = 6700002). Elevations, however, are retained in the RHB 70 standard for consistency with the hydrogeological modelling report and all other site descriptive modelling reports /Follin et al. 2008/. The reason for the coordinate transformation is to render the scale of the relative transport distances more straightforward to interpret from the image axes.

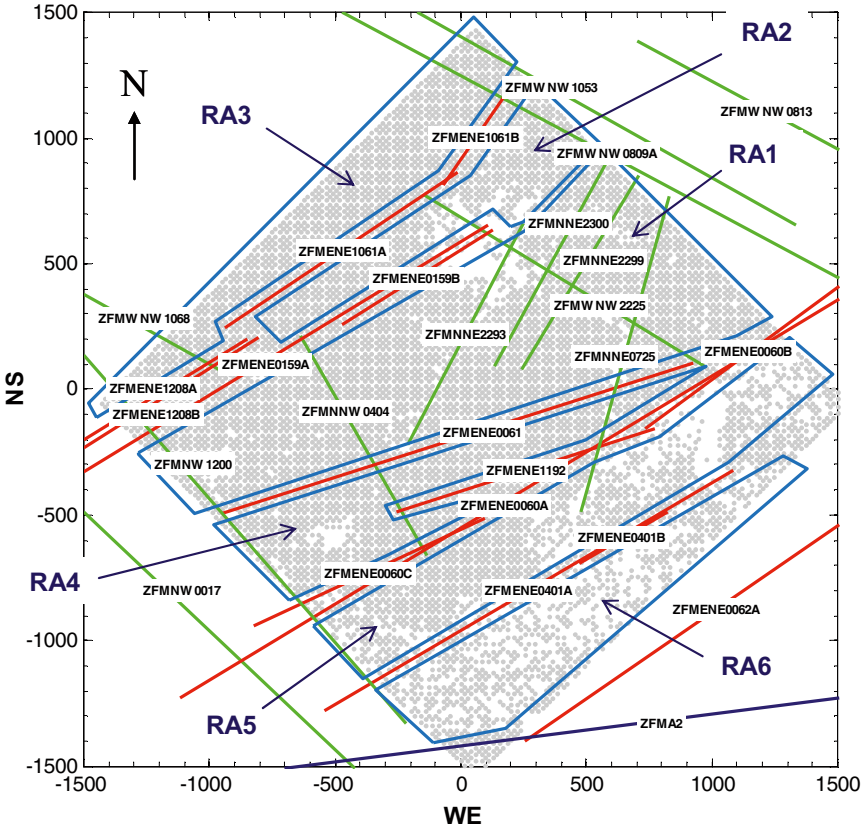

Figure 3-25. *Visualisation of particle release locations (grey markers) divided up into six major release areas, RA1–RA6 (mauve-blue coloured polygons) based upon boundaries with major deformation zones featuring ENE strike (red traces). Other significant deformation zones with NNE, WNW, NW orientation are indicated (green traces) as well as the gently dipping ZFMA2 zone (dark blue). The axis scaling is based upon a coordinate transformation with origin at the centre of the particle release grid.*

As can be seen from Figure 3-25 there are a number of missing ("blanked out") particles clustered around some of the deformation zones to the north and south-eastern areas of the repository. These correspond to particles which were "lost" in the simulation by becoming trapped at the bottom of the simulation volume. This appears to be due to numerical issues associated with the coupling of the transient salt transport and density dependent flow models which is handled as a 1-step, non-iterative coupled flow and transport calculation. It is thought, however, that this should not affect the results for the majority of particles released from the repository nor the overall accuracy of the simulations. These particles are also flagged for removal prior to visualisation and before calculation of the statistical data for typical transport paths.

The particle tracks for a subset of migration paths originating in release area, RA1 are visualised in Figure 3-26. Here, particles are illustrated for a regular grid with a 40 m separation between individual release locations to reduce clutter in the image. The markers signifying the surface exit locations of the particles are coloured according to the cumulative flowpath F-factor (in $\log_{10}$ units).

As discussed in /Follin et al. 2008/ many of the short transport paths are associated with release from the western side of the repository volume where the particles travel upwards until they reach the near surface sheet joint features from where they track laterally in a predominantly north-east arc until they discharge close to the Singö deformation zone. Other particles on the eastern side of the repository were found to move horizontally or downward until they encounter the gently dipping zones that slope in a south-east direction from where they are transported to the surface and discharged eastwards within the Baltic sea. These paths are generally associated with substantially longer transport distances with larger F-factors and advective transport times. For safety assessment purposes, the particles belonging to the former group may be more significant since they are characterised by shorter, more direct transport paths to the surface and have smaller F-factors and advective transport times.

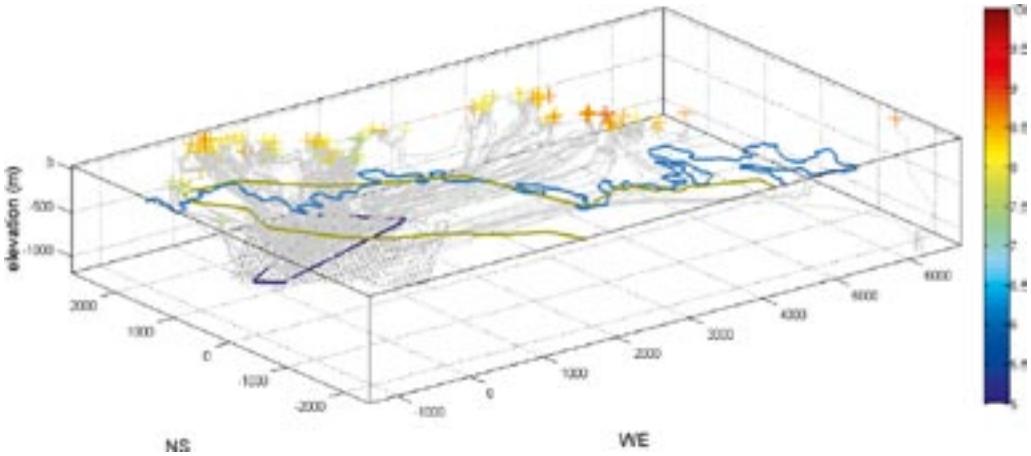

Figure 3-26. *Visualisation of surface exit locations for a subset of particles transported from release area, RA1 (the dark blue outline in the centre left of the image). The candidate area for the Forsmark site investigation is depicted as the green outline and light blue curve indicates the present day shoreline. The particle tracks are visualised as grey curves, with coloured markers indicating the actual exit locations. Exit markers are coloured according to cumulative F-factor (y/m) with log_{10} colour indexing as indicated by the colour bar on the right hand side of the figure.*

The same subset of surface exit locations are visualised in Figure 3-27 from an overhead perspective. The single particle track (#228) highlighted in Figure 3-27 with a red coloured trajectory is a typical example of one of the shorter transport paths taken from the hypothetical release area. It has an integrated F-factor that is approximately representative of the lower 10% of the ensemble distribution of transport paths that discharge near the Singö deformation zone (i.e. 90% of particles discharging near the Singö zone are associated with larger F-factors and advective travel times).

The particle release locations within RA1 are shown in Figure 3-28 where individual release points are coloured according to the cumulative flowpath F-factor accumulated at the surface exit location (log_{10} colour indexing). In this case, the particle release locations are shown for the grid with 20 m spacing.

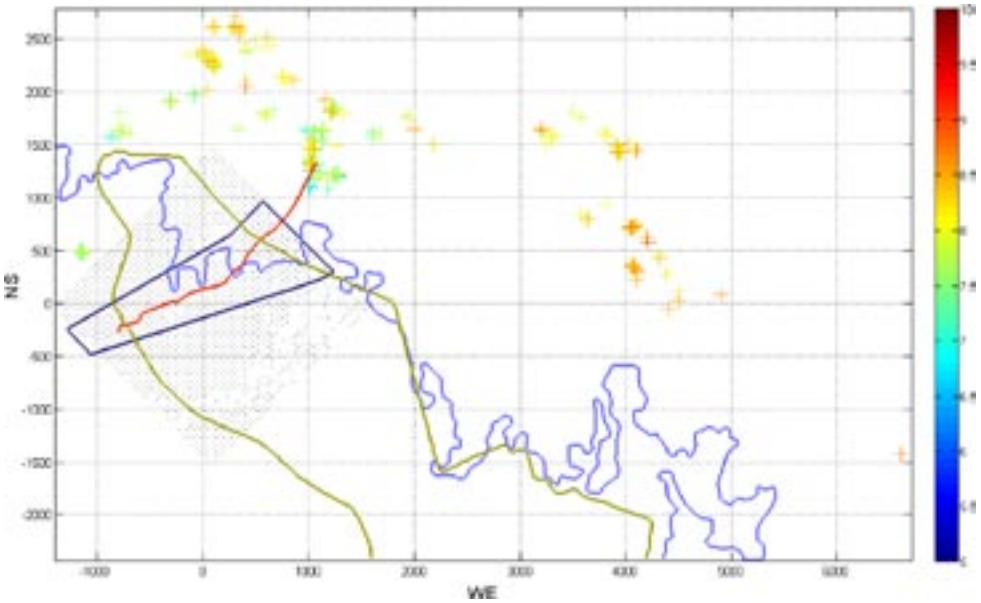

Figure 3-27. *Visualisation of surface exit locations for a subset of transported particles coloured according to cumulative F-factor (y/m) and with log_{10} colour indexing as indicated by the colour bar on the right hand side of the figure. The exit locations and other details in the figure are the same as those shown in the previous figure.*

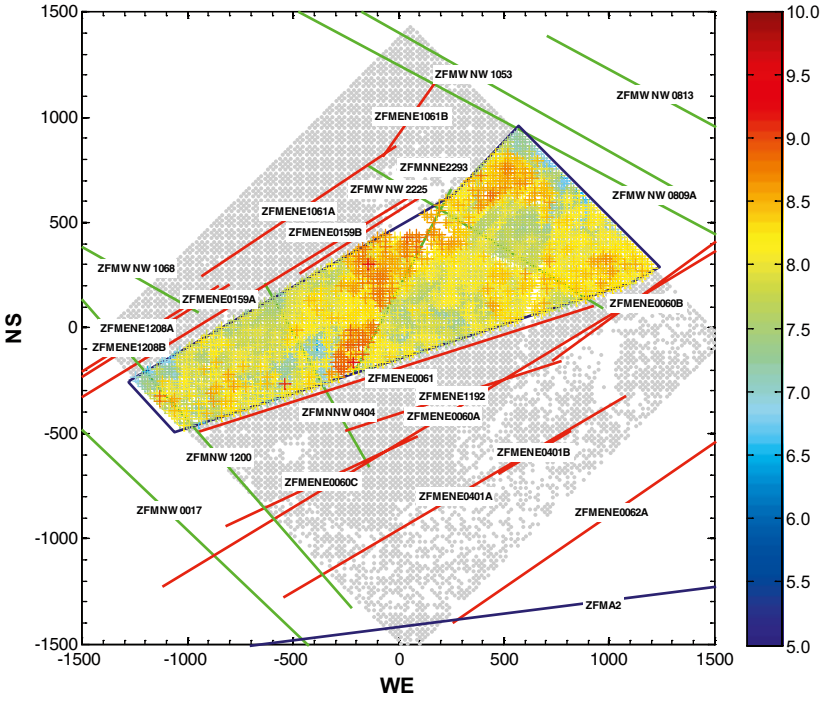

Figure 3-28. *Visualisation of the full set of particle release locations within RA1 coloured according to cumulative F-factor (y/m) at exit location (log_{10} colour indexing). Some of the more prominent deformation zones transecting the hypothetical repository are indicated.*

An interesting feature in Figure 3-28 is the apparent disparity in F-factors for particles released on opposite sides of deformation zone ZFMNNE2293 in the central area. Particles released directly to the western side of this zone are associated with clearly higher F-factors than particles released to the east of this zone.

The distribution of F-factors for particles released in the central area, RA1 are given in Figure 3-29 for the particles which arrived at the surface exit locations. The corresponding distribution of advective travel times for the released particles and the transport distance from release location to surface exit points are given in Figure 3-30 and Figure 3-31.

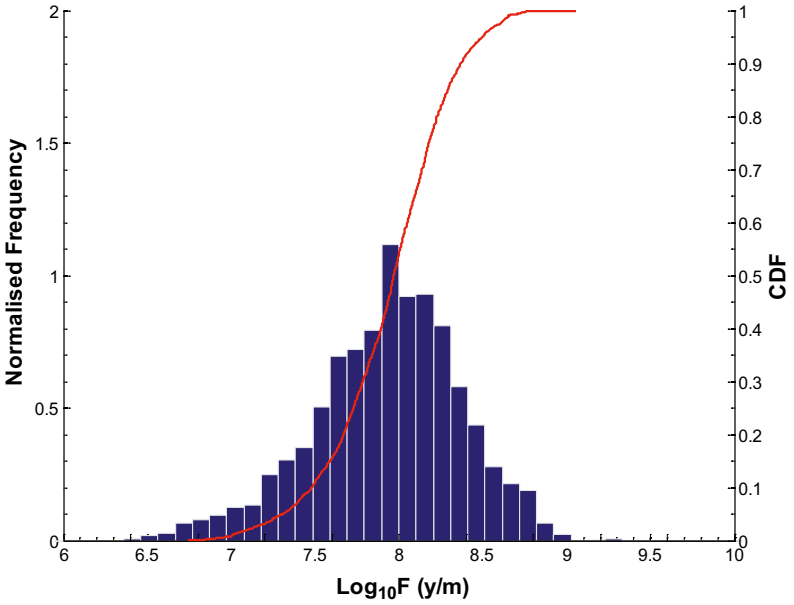

Figure 3-29. *F-factor distribution calculated with ConnectFlow for solute release at –450 m elevation within the target volume release area, RA1. The simulated data are shown as a histogram and empirical cumulative distribution function (CDF).*

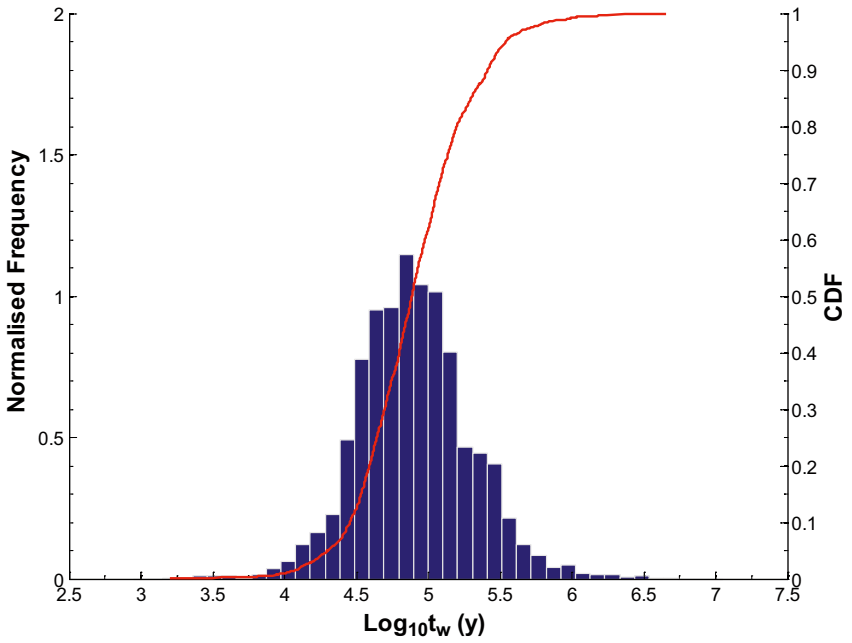

Figure 3-30. *Advective travel time, t_w distribution calculated using ConnectFlow for solute release at –450 m elevation within the target volume release area, RA1. The simulated data are shown as a histogram and empirical cumulative distribution function (CDF).*

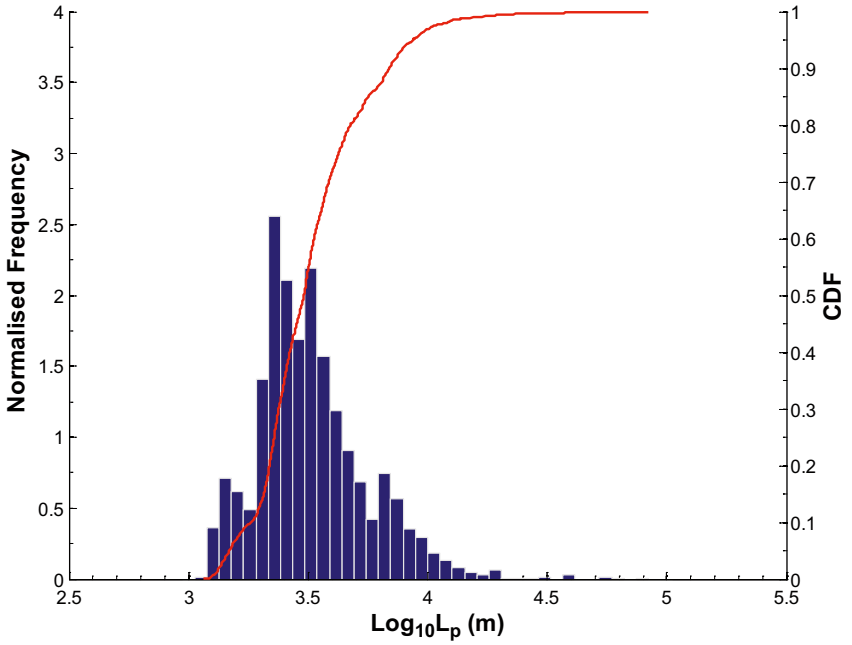

Figure 3-31. *Travel distance, L_p distribution calculated using ConnectFlow for solute release at –450 m elevation within the target volume release area, RA1. The simulated data are shown as a histogram and empirical cumulative distribution function (CDF).*

A cross-plot of the F-factor vs. advective travel time as well as F-factor vs. travel distance can be found in Figure 3-32 and Figure 3-33.

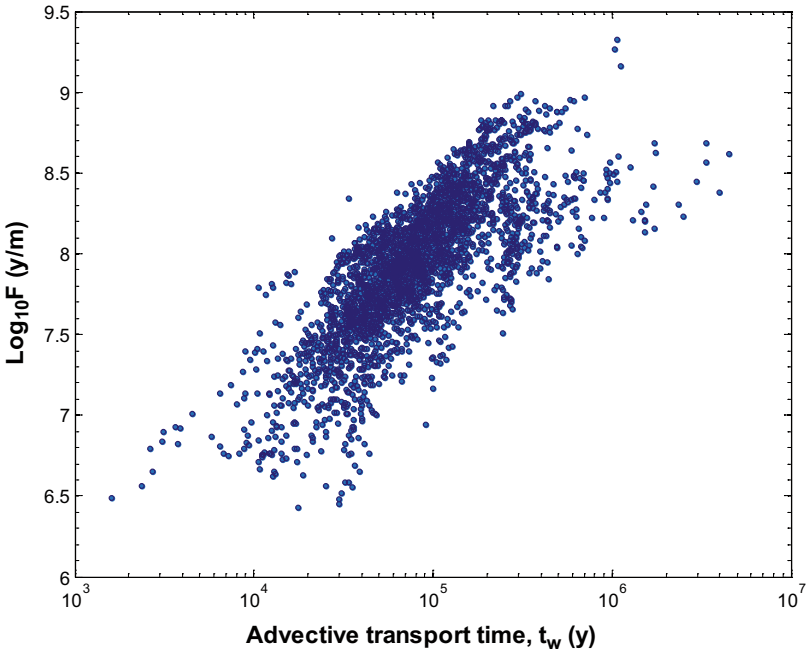

Figure 3-32. *Cross plot of F-factor vs. advective travel time, t_w calculated using ConnectFlow for solute release at –450 m elevation within the target volume release area, RA1.*

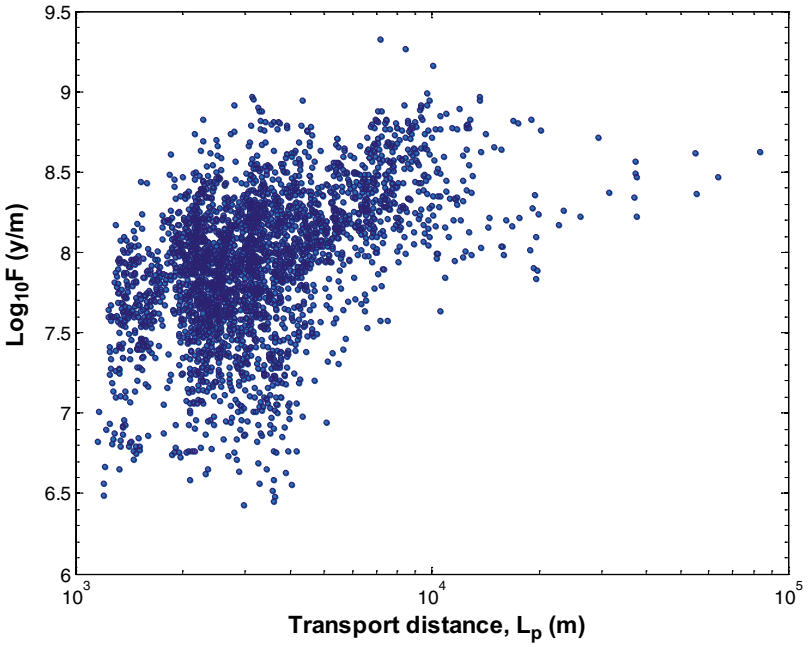

Figure 3-33. *Cross plot of F-factor vs. travel distance, L_p calculated using ConnectFlow for solute release at –450 m elevation within the target volume release area, RA1.*

It is noted here that a small number of the particle tracks at the upper end of the distribution shown in Figure 3-31 and Figure 3-33 appear to be excessively long (up to 80 km). This seems to affect only a small number of particles and may be related to particle being trapped in local regions where the flow solution is not entirely convergent. Summary statistics for the F-factor, advective travel time and transport path length are given in Table 3-16:

Table 3-16. Summary statistics for flow related transport properties calculated using ConnectFlow for solute release over a planar surface at –450 m within the target volume. Results are given for the F-factor (F), advective travel time (t_w), and transport distance (L_p).

Parameter	$\log_{10}F$ (y/m)	$\log_{10}t_w$ (y)	$\log_{10}L_p$ (m)
Mean	7.93	4.90	3.51
Median	7.96	4.89	3.48
5th percentile	7.14	4.31	3.17
10th percentile	7.35	4.46	3.26
25th percentile	7.66	4.64	3.36
75th percentile	8.22	5.14	3.63
90th percentile	8.46	5.41	3.84
95th percentile	8.62	5.54	3.94
Std. deviation	0.44	0.39	0.23
Variance	0.19	0.15	0.05
Min value	6.43	3.20	3.06
Max value	9.32	6.66	4.92
Skew	–0.39	0.24	1.02
Kurtosis	3.23	4.09	5.12
# Released particles	3,014	3,014	3,014

As can be seen from the summary statistics given in Table 3-16, the mean F-factor for particle transport from release area, RA1 is on the order of about 8.5×10^7 y/m while the mean advective transport time is just short of 80,000 years. The mean transport distance is about 3.2 km. In comparison with previous scoping calculations these results seem very high; the mean F-factor, for example is about 2 orders of magnitude higher than what was taken to be a reasonable average value in the calculations presented in previous sections for typical transport paths in fracture domain FFM01c (< –400 m). Similarly, the advective travel time is at least three orders of magnitude greater than that predicted for the summed HRD and HCD advective travel times estimated on the basis of the macroscopic quadratic law (MQL) discussed in section 3.8.

In agreement with previous investigations, the cross-plots of F-factor against advective travel time show a relatively strong positive correlation whereas the cross-plot of F-factor against transport distance exhibit only very weak positive correlation for long transport distances. It should be remembered that the particle tracking simulations are based upon a steady state flow field "frozen in time" at the conclusion of the paleo simulations for hydrochemistry. The shoreline displacement and distribution of salinity in the system are therefore assumed to be constant for the particle tracking simulations, which may not be strictly accurate for the very long advective transport times predicted.

From Figure 3-29, there are small number of fast flowpaths featuring F-factors on the order of about 2×10^6 y/m, although these are generally associated with the edge areas where particles discharge directly to deformation zones. The majority of the transport paths, however, appear to be associated with large F-factors, on average about two orders of magnitude greater than those predicted in the scoping calculations detailed in sections 3.4 to 3.6. An interesting question which arises from this comparison is whether the calculation results and associated assumptions discussed in section 3.4, in particular, are excessively pessimistic and substantially underestimate the flow related transport properties of the HRD or whether the ECPM simulations made using ConnectFlow are overly optimistic. These possibilities are examined in detail in the following sections.

3.9.2 Theoretical analysis of the ECPM calculations

In order to fully understand the reasons why the ConnectFlow simulations predict much higher F-factors than the previous scoping calculations, it is necessary to consider how the F-factor for a transport path is calculated in the ECPM-based (equivalent continuum porous medium) modelling approach used by the program. In the ECPM method, the calculation of the F-factor is similar in many respects to a stream tube approximation, where the F-factor is given by:

$$F = \frac{V_p a_R}{Q} = \frac{A_{xs} L_p a_R}{Q} \tag{3-21}$$

Here, V_p (m^3) is the volume of the stream tube, a_R (m^2/m^3) is the specific flow-wetted surface, and Q (m^3/y) is the flowrate. For a stream tube of length L_p (m), the volume is given by the product of path length and cross-sectional area, A_{xs} (m^2) of the stream tube. The notion of a stream tube is illustrated in Figure 3-34:

For an equivalent porous medium, the flowrate through the rock is given by Darcy's law:

$$Q = K_m A_{xs} i \tag{3-22}$$

Where K_m is the mean hydraulic conductivity (m^2/s) and i (m/m) is the hydraulic gradient. In the ECPM modelling approach, however, we have the additional complication that the hydraulic conductivity does not need to be the same in different directions. In ConnectFlow, the hydrogeological anisotropy of the flowing fracture network is internalised in the permeability tensor which can be derived directly from the geometry and hydraulic properties of the fractures contained within the discretised volume elements of the model. The permeability tensor is calculated using the Oda method /Oda 1985/ for deriving ECPM properties and is based upon anunderlying realisation of the Hydro-DFN made within the Napsac program. For the ConnectFlow simulations discussed in this chapter, a truncated fracture radius distribution in the range 5.64–560 m was assumed for the fracture domains.

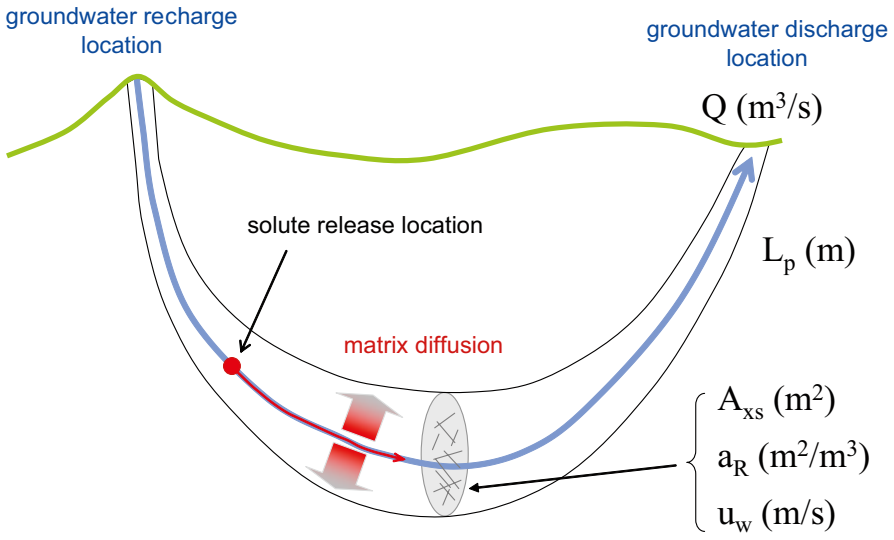

Figure 3-34. *Illustration of the concept of a stream tube. Mass can enter and exit at inlet and outlet locations only, but not over the boundaries of the stream tube. The flowrate (Q) is constant in the stream tube, although the cross-sectional area (A_{xs}), water velocity (u_w), and specific flow-wetted surface (a_R) can all vary as a function of stream tube length (L_p). Adapted from /RETROCK 2004/.*

Although the hydraulic conductivity can vary in different directions, it is possible to make scoping calculations using mean conductivity values to check the results of the ECPM calculations made using ConnectFlow. The F-factor is given by combining Equation 3-21 and 3-22 to give /e.g. Andersson et al. 1998/:

$$F = \frac{L_p a_R}{K_m i} \tag{3-23}$$

This approach has been previously used to make estimates of site specific F-factors in /Crawford 2006/. In order to use Equation 3-23 to make scoping calculations, it is necessary to have a representative set of parameters describing the flow-wetted surface, mean hydraulic conductivity, and flowpath length. Fortunately, the first two of these items can be obtained directly from the hydrogeological SDM background report /Follin et al. 2007a/ where two different alternatives are given for the parameterisation of FFM01.

One of these modelling alternatives is based upon a division into a transmissivity interval above and below –400 m (referred to here as Case B). The other is based upon a division into three transmissivity intervals > –200 m, –200 m to –400 m, and < –400 m (referred to as Case A). The Case A model alternative is that which was used for the calculations presented in 3.6 in the present report and the ConnectFlow simulations described in /Follin et al. 2008/. Data for both modelling alternatives are illustrated in Figure 3-35:

Specific inflow is defined as the pumping flowrate (m^3/s) divided by the drawdown (m) in the borehole. It should also be noted that the specific inflows, Q/s (m^2/s) given in the Figure are normalised with respect to the elevation interval considered. The Q/s data for Case B therefore represents weighted averages of the data for Case A rather than simply the sum of Q/s values.

The mean hydraulic conductivity can be estimated by rearranging Thiems equation describing steady-state radial flow:

$$K_m \approx \frac{(Q/s)\log(r_0/r_{bh})}{2\pi\ L_{bh}} \tag{3-24}$$

For the repository volume, we calculate K_m to be roughly 6×10^{-11} m/s using Equation 3-24 and assuming $r_0/r_{bh} \approx 500$ as in /Rouhiainen and Pöllänen 2003/. This corresponds to a permeability of about 7.6×10^{-18} m^2/s at an *in situ* temperature of 12°C.

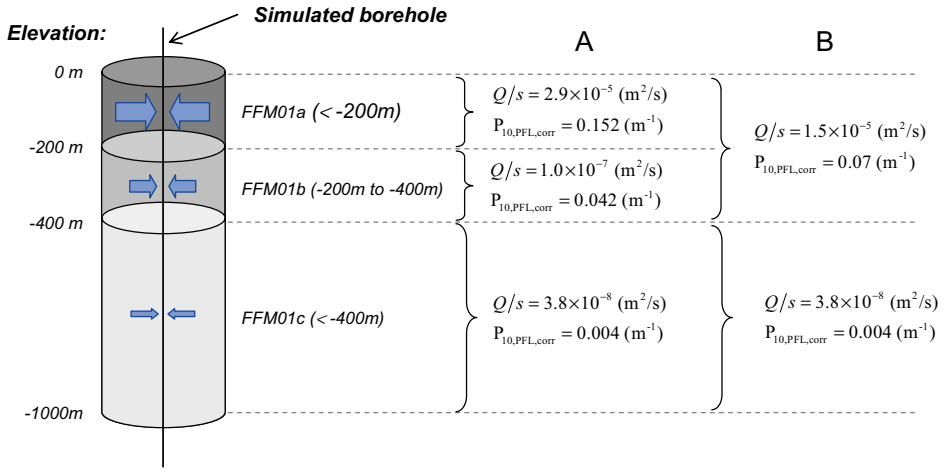

Figure 3-35. *Illustration of simulated borehole and measurement data used for determination of flow properties in the Hydro-DFN modelling work /Follin et al. 2007a/. To the right of the figure are the normalised specific inflows to boreholes within FFM01 and Terzaghi-corrected $P_{10,PFL}$ measurement data for the two models with elevation subdivisions as described in the text; A) three intervals with boundaries at –200 m and –400 m, B) two intervals above and below –400 m.*

We can estimate the specific flow-wetted surface (m^2/m^3) using the relation given by /Moreno et al. 1997, Andersson et al. 1998/:

$$a_R = 2C_p \cdot C_{FF} \approx \begin{cases} 2P_{10,PFL} & \text{(parallel fractures)} \\ 4P_{10,PFL} & \text{(isotropic random fractures)} \end{cases} \quad (3\text{-}25)$$

Here, C_p is a correction factor used to relate the conductive fracture frequency, C_{FF} to the true specific flow-wetted surface area and is a function of relative fracture and borehole orientations. In many cases it has been found that C_p is quite close to 2 /e.g. Geier et al. 1992/ which can be theoretically shown to be the case for an isotropically random orientation of flowing channels.

Since many of the flowing features at the Forsmark site have preferential orientation, this assumption is not entirely accurate. In the hydrogeological modelling work described in /Follin et al. 2007a/, it was found that the Terzaghi corrected intensity of connected open fractures, P_{10cof} (m^{-1}) identified in many of the Forsmark boreholes was approximately equal (numerically) to the estimated volumetric surface area intensity, P_{32} (m^2/m^3) of open fractures. This implies properties similar to the parallel fracture case in Equation 3-25.

Based upon the corrected $P_{10,PFL}$ data reported in /Follin et al. 2007a/ and given in Figure 3-35, we therefore estimate the specific flow-wetted surface of the rock to be on the order of 0.008 m^2/m^3 using Equation 3-25 and assuming $C_p \approx 1$.

If we neglect the negligible role that the horizontal sheet joint features should play for the accumulation of hydrodynamic transport resistance along the flowpath, we could guess that a typical transport path length from release depth to the near surface is at least 450 m possibly extending to somewhat more than 1 km. Using Equation 3-23 with this range of path lengths, the estimated hydraulic conductivity, a characteristic hydraulic gradient of not more than about 1% (see discussion in section 3.3) and a specific flow-wetted surface of 0.008 m^2/m^3, should give F-factors on the order of just over 10^5 y/m.

The advective travel time can be obtained simply from a mass balance of water in the stream tube:

$$t_w = \frac{V_p \theta_f}{Q} \approx \frac{L_p \theta_f}{K_m i} \quad (3\text{-}26)$$

The kinematic porosity, θ_f in Equation 3-26 can be shown to be equal to the product of transport aperture and specific flow-wetted surface:

$$\theta_f = \overline{\delta_t} \cdot a_R \quad (3\text{-}27)$$

For an average fracture aperture of 1 mm, for example, we would calculate an equivalent kinematic porosity of 8×10^{-6} and an advective transport time of 200–400 y for the transport path considered here.

It is possible, however, to estimate an average transport aperture using, for example, the macroscopic quadratic law (MQL) and the relation between fracture transmissivity (m^2/s) and hydraulic conductivity (m/s) of an equivalent porous medium:

$$K_m = T_f \cdot C_{FF} \quad (3\text{-}28)$$

Assuming the MQL (Equation 3-15), the transport aperture can then be estimated as:

$$\overline{\delta_t} \approx a_t \sqrt{T_f} = a_t \sqrt{\frac{2C_p K_m}{a_R}} \quad (3\text{-}29)$$

For the parameter values considered in this section, we calculate an average transport aperture of 6×10^{-5} m. This would imply a kinematic porosity of 5×10^{-7} and consequently an advective transport time of approximately 10–30 y.

As is clearly obvious from the above results, the first order estimation of F-factors and advective transport times given here for a stream tube approximation gives results that are reasonably in parity with those predicted using the scoping calculations described in previous sections although still some orders of magnitude less than the values predicted by ConnectFlow. The reasons for this lie not in the ECPM modelling approach itself, but rather in the parameter values used in the model. This will be discussed in the following section.

3.9.3 Detailed profile of a typical short migration path

The migration path for particle #228, previously illustrated in Figure 3-27, is shown from a perspective view in Figure 3-36.

The cumulative F-factor as a function of transport path length is shown in Figure 3-37 where the different structural elements encountered by the particle are colour coded and labelled individually.

In the case of the particle track visualised in Figure 3-37, the bulk of the hydrodynamic transport resistance appears to be encountered in the first 80 m, or so of the release location. This corresponds to the target volume within fracture domain FFM01 where the flowrates are thought to be exceptionally low.

The cumulative advective travel time for the same particle is shown in Figure 3-38.

From a comparison of Figure 3-37 and Figure 3-38, transport within FFM01 accounts for about 80% of the overall F-factor achieved by the particle although only about 30% of the advective transport time for which the deformation zones and horizontal sheet joints play a more dominant role.

To explain the reasons for such high F-factors and advective transport times it is useful to make plots of the various parameters that are directly used in their calculation (and written to an output file by ConnectFlow). Figure 3-39 shows the local hydraulic conductivity encountered by the particle along its transport path plotted as a function of transport path length.

As can be seen from Figure 3-39, the particle is released in a zone where the hydraulic conductivity for the first 80 m is effectively equal to that of the background rock matrix and nearly an order of magnitude less than that estimated from raw borehole data in section 3.9.2 (estimated to be 6×10^{-11} m/s using Equation 3-24). The rock matrix conductivity is given by the permeability cut-off level used in the ECPM simulations and corresponds to a hydraulic conductivity of 7.92×10^{-12} m/s at an assumed *in situ* temperature of 12°C.

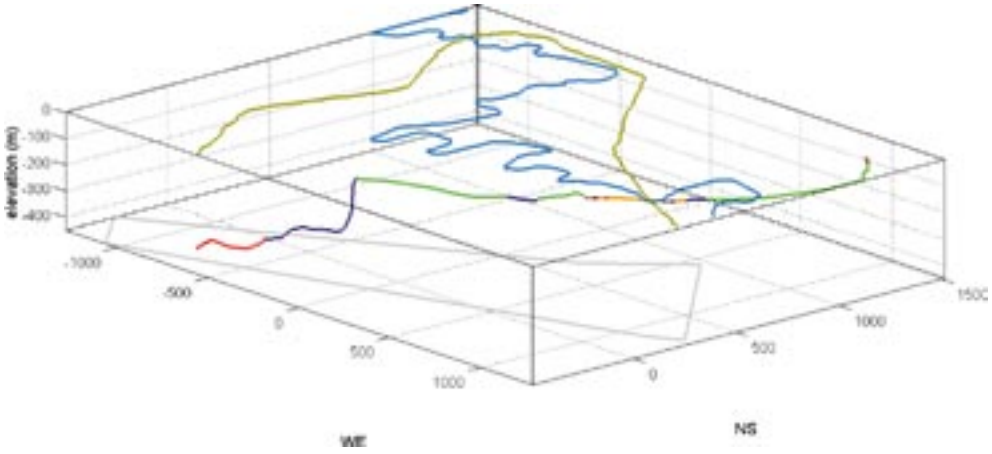

Figure 3-36. *The transport path taken by particle #228 in perspective view from a NE vantage point. The path line is coloured with regard to structural elements that the particle encounters on its way to the surface exit location, i.e. red for fracture domain FFM01, orange for FFM06, dark blue for the various deterministic deformation zones, green for near surface sheet joint features, and brown for Quaternary deposits.*

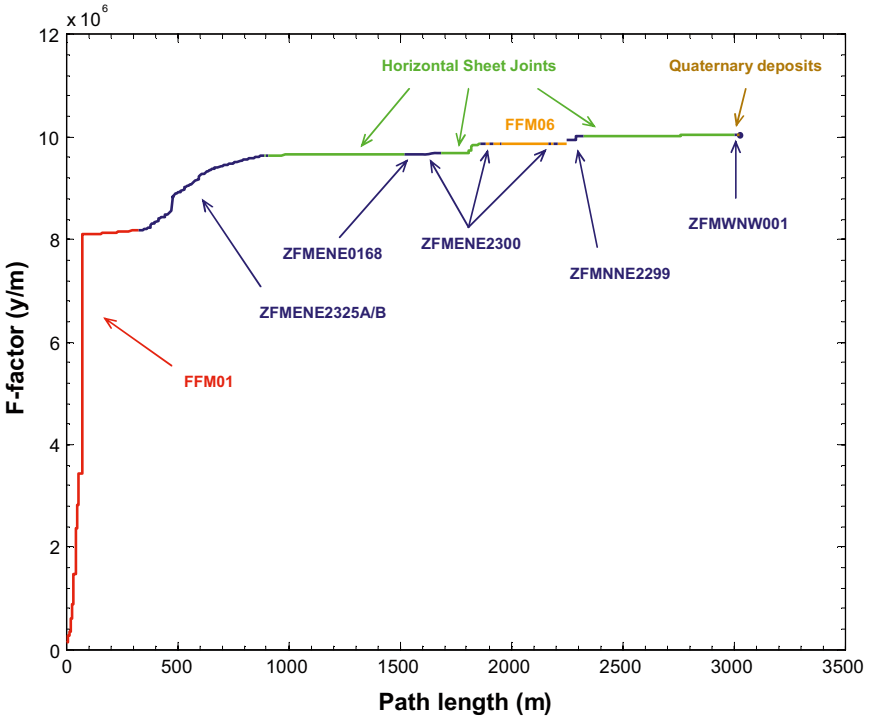

Figure 3-37. *Cumulative F-factor (y/m) as a function of transport path length for particle #228. The cumulative F-factor at the surface exit location is characteristic of the lower 10% percentile of "fast" transport paths discharging near the Singö deformation zone.*

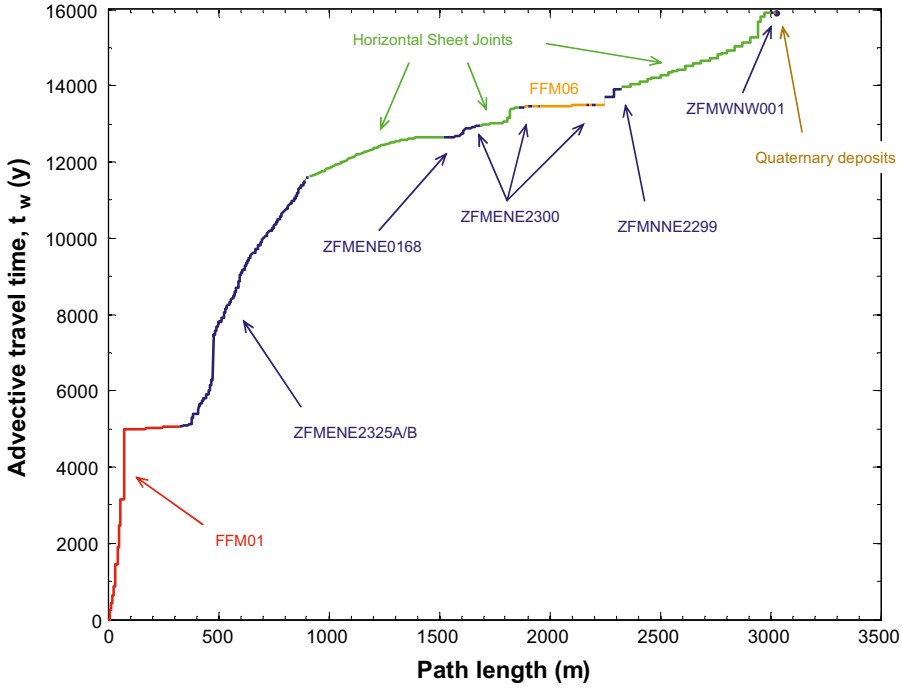

Figure 3-38. *Cumulative advective transport time (y) as a function of transport path length for particle #228.*

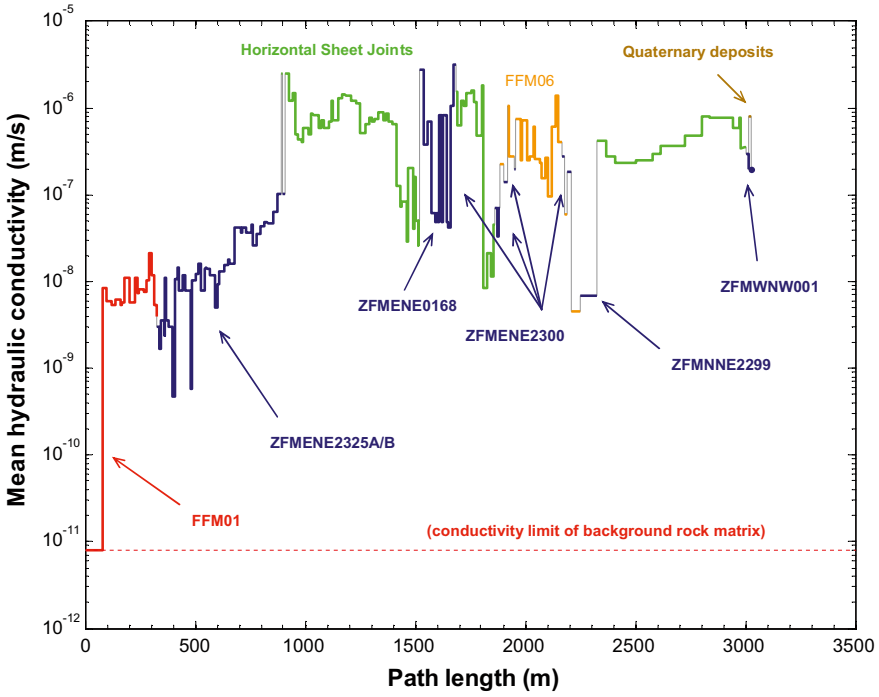

Figure 3-39. *Mean hydraulic conductivity (m/s) as a function of transport path length for particle #228. The broken horizontal line at the bottom of the figure represents the limit of hydraulic conductivity for the rock matrix itself assuming an in situ temperature of 12°C (this is defined as a permeability cut-off in ConnectFlow). The grey coloured segments represent discontinuities in the parameter value when the particle passes from one structural feature to another.*

From a cursory inspection of Figure 3-39, the sudden increase in conductivity encountered by the particle after a transport distance of about 80 m could be taken as being indicative of the particle passing from a lower depth zone of FFM01 to an upper depth zone (where the rock has a generally higher conductive fracture frequency and less favourable hydraulic properties). Examination of the particle tracking data, however, shows that this does not appear to be the case and the particle is always below an elevation of –400 m while within the confines of FFM01. The reason for the sudden increase in hydraulic conductivity after 80 m (–430 m elevation) from the matrix cut-off level to roughly 7×10^{-9} m/s is simply a transition from a very poorly conductive part of the rock to a more conductive region. It should also be noted that the mean hydraulic conductivity experienced by the particle for the subsequent 246 m of the transport path through FFM01, is about two orders of magnitude greater than the estimated average for this elevation interval within the fracture domain.

Figure 3-40 shows the local hydraulic gradient experienced by particle #228 along its transport path. Figure 3-41 immediately following shows a scatter plot of the hydraulic gradient plotted against the local mean hydraulic conductivity. The markers in the scatter plot are shaded with regard to elevation in a similar fashion to the empirical data previously presented in Figure 3-10 (and Appendix C).

It is interesting to note that the data are qualitatively similar to those presented in Appendix C where a channel network model was used to assess the apparent inverse correlation of empirically estimated hydraulic gradients versus transmissivity. Similarly to the scoping calculations detailed in Appendix C, we find that the hydraulic gradient generally does not exceed the estimated regional hydraulic gradient for the site. Although only shown for a single particle in Figure 3-41, this has been found to be largely true for all particles that have been examined. The local hydraulic gradients along the visualised transport path vary from a minimum of about 2×10^{-5} in parts of the near surface horizontal sheet joints to a maximum of roughly 7×10^{-3} in FFM01 near the particle release point. The upper limit of the hydraulic gradient is very close to the estimate given in section 3.3 based upon approximate consideration of the regional topography.

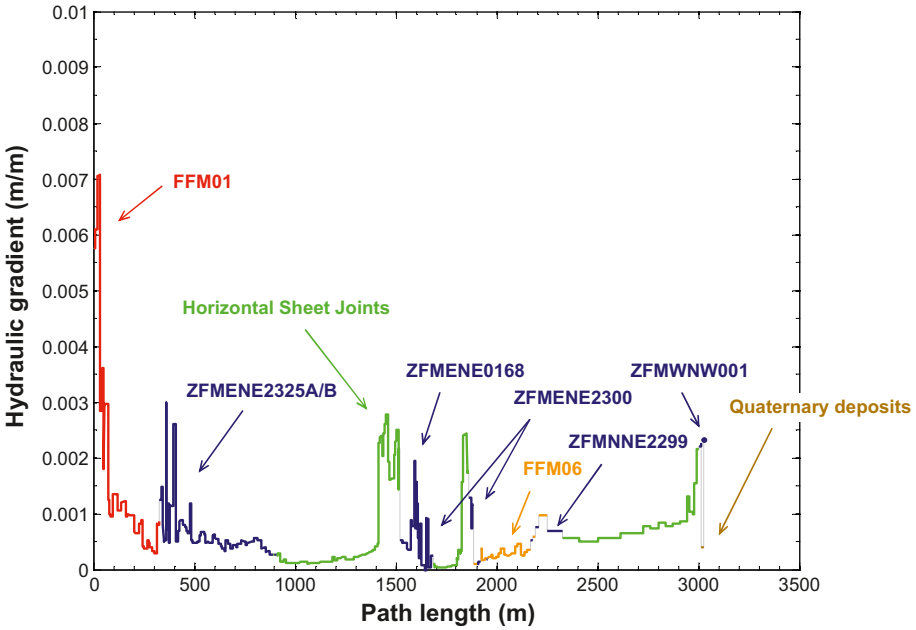

Figure 3-40. *Local hydraulic gradient (m/m) plotted as a function of transport path length for particle #228.*

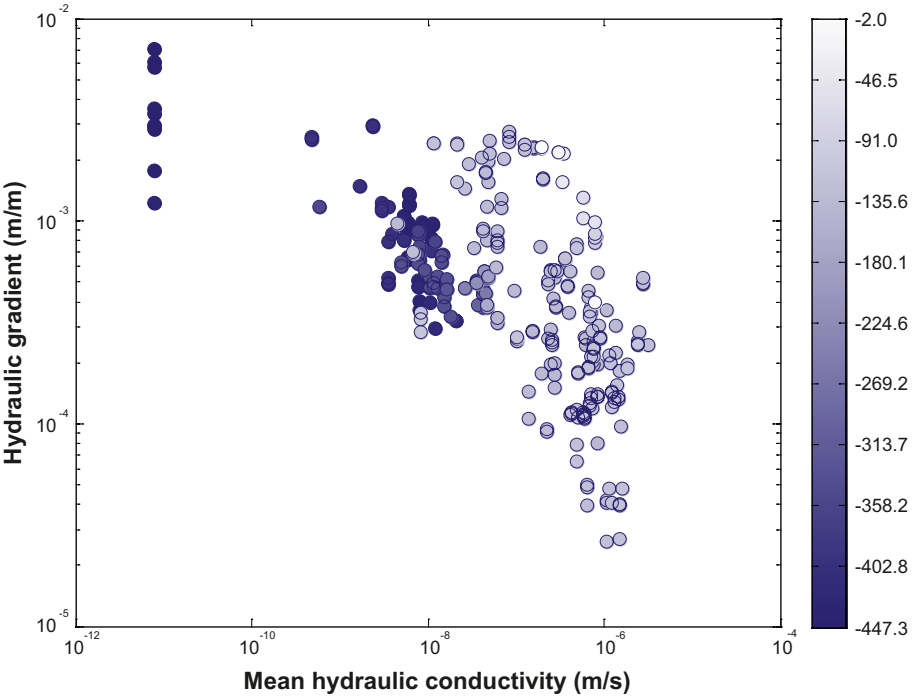

Figure 3-41. *A scatter plot of the local hydraulic gradient (m/m) experienced by particle #228 along its transport path versus the mean hydraulic conductivity of the rock at that location. The symbols are shaded according to elevation (m) as specified in the colour bar on the right-hand side of the figure.*

The specific flow-wetted surface used in the ECPM calculations is plotted in Figure 3-42 and shows that the specific flow-wetted surface of the flowpath initially encountered by particle #228 is on the order of 3–15 times larger that that estimated on the basis of Terzaghi corrected PFL flow frequencies measured in the investigation boreholes. As previously discussed in section 3.9.2, the best estimate specific flow-wetted surface is roughly 0.008 m^2/m^3 for FFM01

at repository depth. For the deformation zones and horizontal sheet joints, the specific flow wetted surface used in the ECPM model ranges from about 0.06 m^2/m^3 to a maximum of 1.0 m^2/m^3.

As discussed previously, the local equivalent transport aperture (m) is given by the ratio of kinematic porosity and specific flow-wetted surface ($\overline{\delta}_t = \theta_f / a_R$) and is shown in Figure 3-43 as a function of the transport path length.

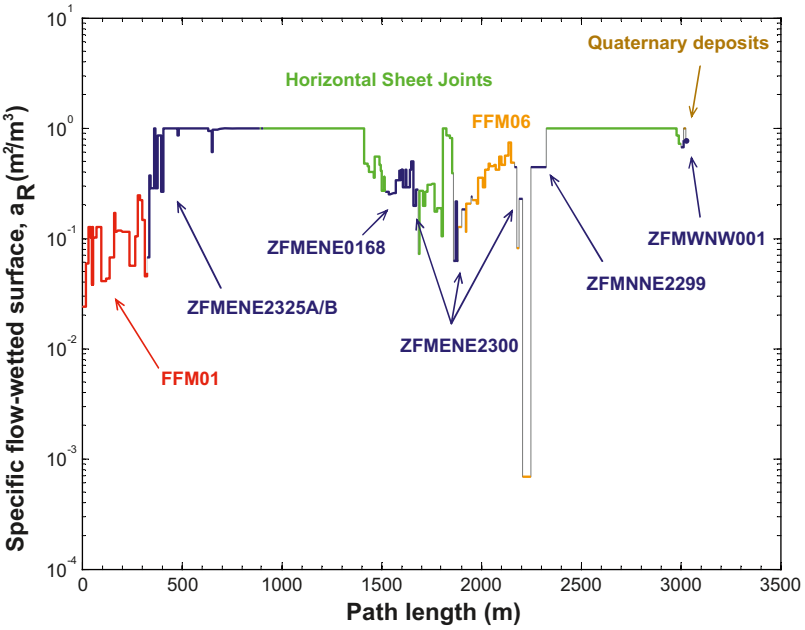

Figure 3-42. *Local specific flow-wetted surface, a_R (m^2/m^3) encountered by particle #228 and plotted as a function of transport path length.*

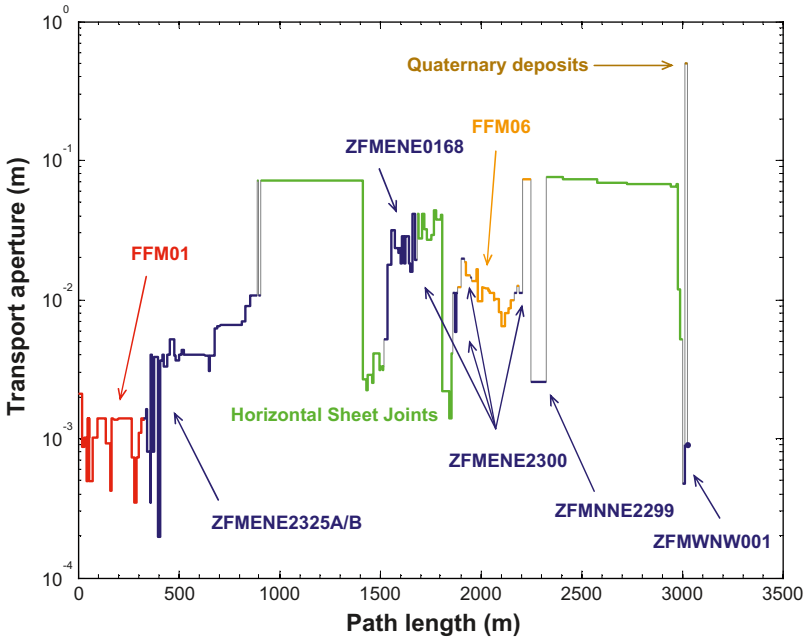

Figure 3-43. *Local effective transport aperture (m), calculated as the ratio of kinematic porosity and specific flow-wetted surface, encountered by particle #228 and plotted as a function of transport path length.*

Since flow is conceptualised to occur within discrete fractures rather than in a true porous medium, the transport aperture gives a more physically meaningful measure of the advective pore space volume than kinematic porosity.

As can be seen from Figure 3-43, the transport aperture is relatively high in the ECPM simulations, amounting to an average of about 1 mm within FFM01 and several mm to cm within the deterministic deformation zones. The average transport aperture encountered in the near surface sheet joints is slightly less than a dm for most of the time although there are localised regions where it is somewhat less than this.

3.9.4 Discussion concerning the reasonableness of calculation results

At face value, it appears that the simulation results are consistent with the physics of the system "as it is modelled" and the particular parameter values used in the calculations. The step-wise F-factors calculated by ConnectFlow for the ECPM simulations and those estimated using the stream tube approximation are shown in Figure 3-44 for particle #228 in the form of a cross plot and shows reasonable (although not exact) agreement. The stream tube data are calculated using the individual parameter values plotted in section 3.9.3 and Equation 3-23. The question, however, remains; are the results reasonable and why do they differ so much from the scoping calculation results presented in sections 3.6–3.8?

First and foremost, in this particular case it should be acknowledged that the particle transport within the first 80 m of the release location in FFM01 may not be an appropriate representation of transport in the fractured rock. Here, it is clear that the particle has been released in an ECPM voxel with properties corresponding to the rock matrix itself and cannot be taken to represent the "true" hydrogeological properties of this fracture domain. Although there is no reason why radionuclide transport cannot occur by way of a slow seepage flux through the rock matrix, the F-factor is not strictly defined for this case and as such, is not physically meaningful. Furthermore, the cut-off permeability used in the ECPM simulations may be as much as 1–2 orders of magnitude higher than the "actual" matrix permeability existing under *in situ* stresses (see, for example, Figure H-2 in Appendix H). This would mean that the rate of radionuclide transport via this mechanism may be significantly overestimated.

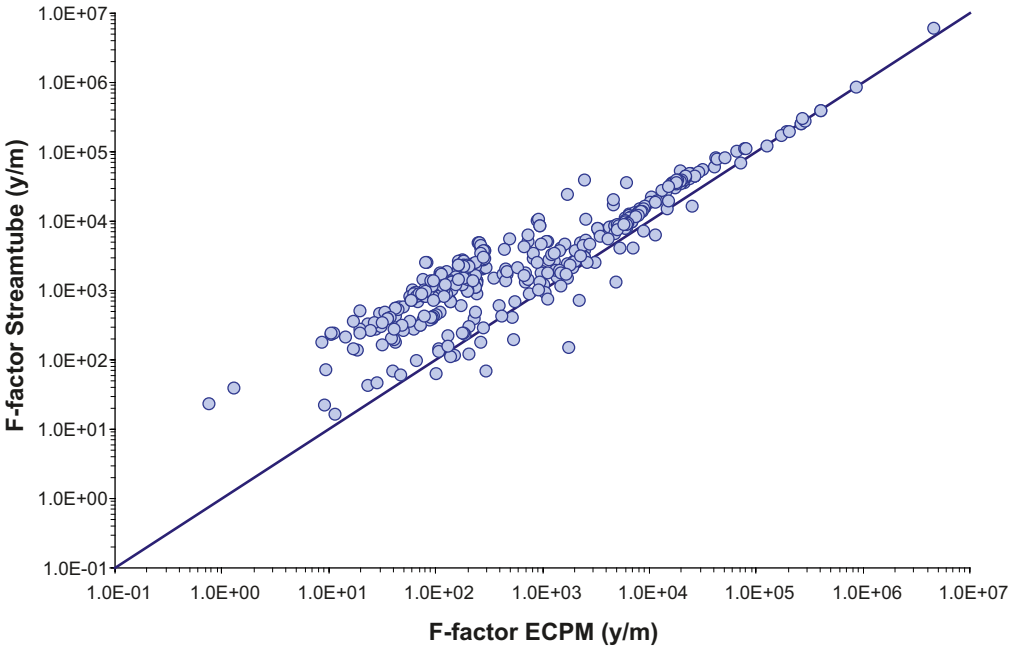

Figure 3-44. *Cross-plot of stepwise F-factors calculated using the stream tube approximation (Equation 3-23) versus F-factor calculated by the ECPM implemented in ConnectFlow for particle #228.*

The relatively high hydraulic conductivity (7×10^{-9} m/s) experienced by the particle over the subsequent 246 m of its transport path, although seemingly much higher than the borehole estimated average for this elevation interval FFM01 can also be explained in terms of the properties of the underlying Hydro-DFN used to generate the ECPM representation. Depending on the random location of transmissive structures in the Hydro-DFN, we expect most voxels within fracture domain FFM01 at this depth to be either non-conductive or relatively strongly conductive owing to the presence of one or more large fractures that can persist for distances up to the maximum fracture size (in this case, fractures with a 560 m radius).

This has already been discussed in section 3.6.2 where it was found that most randomly generated Hydro-DFN realisations for this elevation zone of FFM01 were either below the percolation limit or hydraulically conductive with properties roughly corresponding to the largest fractures transecting the particular voxel. Consequently, we should only expect the average hydraulic conductivity of the rock to approach that estimated by Equation 3-24 on support scales of sufficient size that the effect of locally high transmissive features is diluted by the much larger volume of essentially impermeable rock. The relatively high conductivity in the local sub region of FFM01 sampled by particle #228 may therefore not be entirely unreasonable.

From the total of 517 particles that are tracked from release area RA1 using the 40 m grid, 384 (74%) discharge via short pathways to the north-east near the Singö deformation zone. Of these, only 136 (35%) are actually released within fracture domain FFM01, 77 (20%) within FFM06, while the remainder are found to exit directly to the various deterministic deformation zones (34%) and other fracture domains (11%) intersecting the RA1 footprint.

Of the particles that are released within FFM01 itself, 11 encounter an initially transmissive region. However, 7 of these subsequently "wander" advectively into the rock matrix, leaving only 4 that are transported without advection in the rock matrix at any point along their migration path. Particles that are initially released in conductive regions although later migrate advectively through the rock matrix are taken to be indicative of hydraulic compartmentalisation. If conductive voxels are hydraulically isolated in this fashion, the only way for particles to escape is by an advective pathway through the rock matrix itself.

Effectively, this means that 97% of the particles released may be considered to be either fully encapsulated within the rock matrix or released in conductive, although hydraulically isolated regions of the rock. Particle track #228 initiates in the rock matrix itself and only encounters conductive features after the first 80 m of advective transport, so cannot be taken to be representative of a realistic transport path through the rock.

Of the 77 particles released within FFM06, 22 encounter an initially transmissive region although 15 of these subsequently advect through the rock matrix as described previously for FFM01. This leaves only 7 particles that are transported without advection in the rock matrix at any point along their migration path. For FFM06, this means that 90% of the particles released may be considered to be initially encapsulated or released within hydraulically isolated compartments.

Interestingly, of the 130 particles released directly to deterministic deformation zones only 10 (8%) are transported without advection in the rock matrix at any point along their migration path. It is also found in many cases that the F-factors accumulated in the deterministic deformation zones are higher than for transport within the fracture domains (some additional particle tracking examples are given in Appendix G).

Although there are no measurement data compiled in /Follin et al. 2007a/ for the specific zones encountered by particle #228, a plot of the site wide statistics of PFL features in deterministic and possible deformation zones is given in Figure 3-45. Examination of the data histogram in comparison with the data given in Figure 3-42 (assuming the relation between $P_{10,PFL}$ and a_R given by Equation 3-25) reveals that the specific flow-wetted surface assumed for these structures in the ECPM are probably not unreasonable and in a statistical sense may even be an underestimate of the flow wetted surface potentially available within the zones.

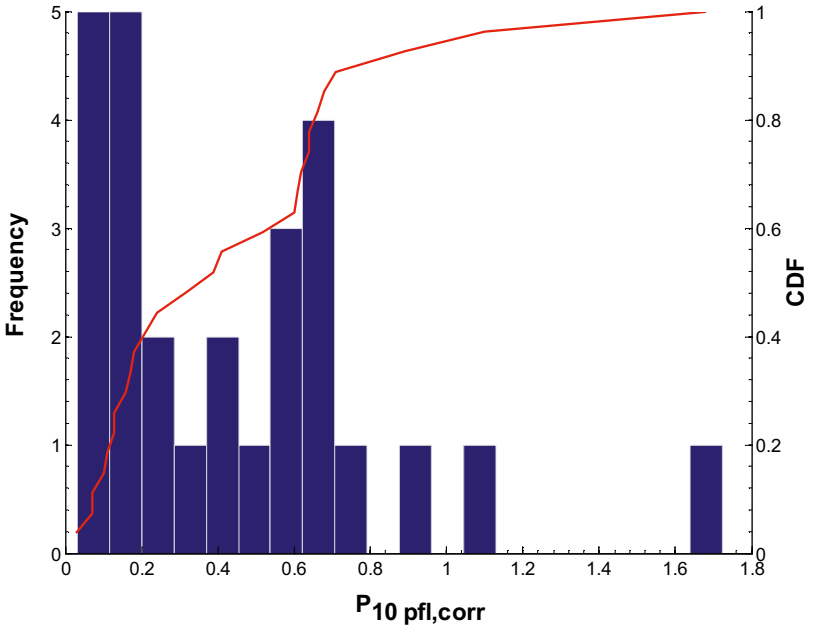

Figure 3-45. *Terzaghi corrected intensity of flowing features identified by PFL measurements within deterministic and possible deformation zones at the Forsmark site (Data are taken from Table 10-7 in /Follin et al. 2007a/). The data are given both as a histogram (blue bars) and an empirical cumulative distribution function, CDF (red curve) and exclude deformation zones with no discernable flow.*

The effective transport apertures reported for particle #228 and plotted in Figure 3-43 are substantially higher than those predicted using the macroscopic cubic law (MQL). In the ECPM model, the path length averaged transport aperture is found to be 3.5 cm. The MQL, on the other hand, predicts a transport aperture of roughly 0.5–0.7 mm (calculated using Equation 3-29 and point values of hydraulic conductivity and specific flow-wetted surface logged along the migration path). This implies an increase in advective travel time of 50–70 times for the ECPM simulations over that given by the MQL.

In /Follin et al. 2008/ it is stated that the kinematic porosity was globally increased by a factor of about 10 to obtain a match to the hydrogeochemistry data for a subset of boreholes in the candidate area. If we consider the increased hydraulic apertures in the ECPM simulations together with the fact that the average hydraulic gradient is as little as 5–10% of the assumed reference gradient in the scoping calculations (presented in section 3.8.2), the difference in estimated advective travel times seems explicable.

3.10 Impact of flow channelling

In this report we have attempted to characterise flow channelling in the context of both the interpretation of primary data (inverse modelling) as well as likely consequences when propagated forward in models (forward modelling). We therefore aim to answer the questions:

- *What significance does flow channelling have for the interpretation of field data? Is there evidence, for example, that our models of flow and transport contain inherent biases accrued during data acquisition owing to the inability of borehole investigations to adequately discriminate, characterise, or identify relevant hydrogeologic features in the rock?*
- *What significance does flow channelling have for the migration of solutes in fractured crystalline rock when included in models of flow and transport in safety assessment?*

In this chapter we deal primarily with the first of these questions and the second is dealt with later in Chapter 5 where the impact of flow channelling on solute transport is investigated in more detail.

In terms of data interpretation, there are two main issues that need to be considered. One of these is whether or not the true frequency of flowing features in the rock is underestimated owing to the possibility that low permeable structures and surface asperity contacts in fracture planes conceal them from detection by borehole hydraulic testing. This is referred to here as a "Type 1" flow censoring effect. The other issue is whether the transmissivity models used in the hydrogeological site description are somehow biased by the presence of flow channels in the rock. This is referred to here as a "Type 2" flow censoring effect. Both of these issues are, however, interrelated since the calibration of the transmissivity models for the fracture domains in the HRD is based upon conditioning to give the same numbers of flowing features (i.e. above the detection threshold) and flowrate magnitudes as observed in the field.

On the one hand we have the possibility that the true frequency of flowing features is underestimated and those detected are characterised with flowrates that might not be representative of the feature. This might occur if flow is highly channelised in pipe-like features and there are significant issues relating to the permeability of the structures in which they are hosted (due to, for example, accretions of fracture filling materials). Even if hydraulic testing successfully detects the nearby presence of a flow conduit, the borehole is unlikely to intersect it directly and therefore the transmissivity of the structure may be substantially underestimated.

On the other hand, it is well known from previous experiences at the Äspö HRL /e.g. Black and Hodgkinson 2005/ that even very well constrained Hydro-DFN models appear to give greater flow connectivity and less flow compartmentalisation than what is actually observed in the field. This is particularly the case for larger features interpreted en-echelon as single structures in the Hydro-DFN models. Assumptions of equidimensioned fractures in Hydro-DFN models may also play a role in this /e.g. Black et al. 2007/, although the existence of fractures with large major/minor axis aspect ratios is highly speculative.

It is difficult to predict what consequence this would have for the transmissivity models used in the Hydro-DFN since many of these factors may be mutually interdependent. The fact that Hydro-DFN models assume flow over the entire fracture surface, for example, may introduce a bias by forcing artificially low transmissivities in the model to match the observational data. The result of this would be that both the true frequency and transmissivity of flowing features may be higher than what we think.

Generalised radial flow analysis of PSS hydraulic responses in packed off borehole sections /Follin et al. 2006/ suggest that most flowing features (70–80%) are associated with flow dimensions greater than 1.5, although a significant fraction (on the order of 20–30%) exhibit smaller flow dimensions symptomatic of approximately linear flow channelling. Although it is likely that some flow channels are missed, this result is generally consistent with the notion of a hydraulically well-connected flow space within the fractures. Furthermore, in the transient analysis of PSS tests reported by /Hjerne et al. 2008/, only a very small proportion of tested sections gave indications of constant head boundary characteristics. Since such behaviour would be strongly indicative of strongly transmissive flow channels hosted in otherwise poorly transmissive features, it is possible to conclude that Type 2 flow censoring effects, as described above, are not strongly evident in the available data set.

Scoping calculations described in detail in Appendix B have also shown that most flowing features should theoretically be identifiable from borehole investigations even in the presence of highly channelised flow arising due to surface asperity contacts. The reason for this is that fracture planes need to support a certain level of in-plane connectivity in order for flow to exist at all in very sparsely fractured rock. This is particularly the case where fracturing is sufficiently sparse that pipe-like flow channels of limited extent such as fracture intersection zones (FIZ) or fast flow channels hosted in fault stepovers, cannot form contiguous pathways through the rock. While the possible existence of fast and persistently compartmentalised flowpaths is conceivable for the large and intensely fractured deformation zones comprising the HCD, this seems less likely for the smaller structures located in the HRD.

The scoping calculations show that for modest surface contact fractions of up to at least 30%, fractures should be sufficiently well connected hydraulically that detection of in-plane flow channels is almost certain provided that the borehole at least partially intersects an open region of the fracture and assuming fracture filling materials do not fill the pore space. Moreover, the transmissivity correction factor for the space filling effects of asperity contact appears to be relatively small for modest surface contact fractions meaning that transmissivities may not be greatly underestimated for this type of flow-channelling effect at least amongst the more transmissive fractures.

For surface contact fractions on the order of about 40% and upwards, however, hydraulic compartmentalisation may occur which reduces the chances of a positive identification depending upon where the borehole intersects the fracture plane in relation to the flowing feature. Fractures become essentially non-conductive for surface contact fractions above about 50% which is the theoretical percolation limit for 2D bond percolation networks. This implicitly assumes that the longest correlation length (or equivalent spectral measure) for pore space aperture variation is substantially less than the size of the fracture under consideration.

Further it should be considered that the most transmissive fractures are also likely to be the least compressed and should only exhibit small surface area contact fractions. The least transmissive fractures, on the other hand, are likely to exhibit greater a degree of surface contact possibly rendering their transmissivity at or below the level of instrumental detection, even if the flow space is nominally connected. This means that we would expect a larger biasing effect for fractures belonging to the lower end of the transmissivity spectrum. As such we can speculate that although Type 1 flow censoring effects are probably present they most likely will not have a great impact on the more transmissive features to be found within the HRD.

An exception to this may be karstic erosion features in fractures containing large amounts of readily solubilised calcite precipitates. Owing to their wormhole-like structure within low-permeable features, these may not be readily detectable from borehole intersects with fracture planes. Similar features could exist in the deterministic deformation zones comprising the HCD; the existence of rhomboidal-shaped veins of precipitated calcite or quartz in fault stepovers, for example, is well documented in the literature /NRC 1996/ and strongly indicates the prior existence of flow pipes. The hydrothermal processes which led to the formation of the vuggy granite found in KFM02A would have mobilised large amounts of quartz which may have precipitated within or adjacent to flow channels at other locations, possibly not far from where it was initially dissolved. Consideration of such processes is therefore relevant for the Forsmark site.

Under modern environmental conditions, however, calcite is the principle mineral, the distribution of which could be substantially influenced by precipitation-dissolution processes. Generally, we would expect calcite to be mobilised downwards within the fractured rock at Forsmark under the influence of infiltrating meteoric water with elevated carbonate concentrations. Owing to the non-linear solubility curve for calcite in a closed system, spatially separate water flows saturated at different carbon dioxide partial pressures (pCO_2) become undersaturated upon mixing and once again can aggressively dissolve calcite /e.g. Langmuir 1997/. This is a well-known mechanism for karst formation referred to as “mischungskorrosion” (mixing corrosion) /EPA 2002/. Additionally, for downward flowing water it is also possible to predict a gradual precipitation of calcite mobilised from shallower depths owing to the increase of temperature with increasing depth at the site (since the solubility of calcite decreases with increasing temperature /e.g. Langmuir 1997/).

It is stated in /Sandström et al. 2008/ that only a small number of fractures with laumontite fracture coatings are found to be transmissive at the Forsmark site. It is also speculated that the near complete absence of laumontite in transmissive fractures may be due to the dissolution of this mineral (which is considered to be easily weathered) in reactivated older fractures. Although there is no direct evidence from borehole data for karstic erosion features involving fractures filled with this mineral, the possibility of this cannot be excluded at this stage.

The impact of calcite dissolution and precipitation on flow channelling is difficult to predict à priori as it is highly dependent upon dissolution kinetics and diffusion in a non-linear fashion.

Reaction instabilities arising due to the complicated feedback between permeability and mineral dissolution may also lead to fingering phenomena /e.g. Steefel and Lasaga 1994, Lichtner 1996/ which is the defining characteristic of karstic wormhole formation. This is further complicated by the effects of *in situ* normal stresses which will attempt to close fractures as mineral precipitates lining the fracture are dissolved /e.g. Verberg and Ladd 2002/. Mineral grains at asperity contacts with high stress concentrations are thermodynamically predisposed to greater dissolution than mineral grains at lower stress locations which can lead to a redistribution of fracture minerals in a process known as pressure solution /NRC 1996/. These coupled phenomena will be particularly important if the pore space is propped open by contact bridges of secondary mineralisation. The dynamics of these processes are sufficiently complex that spontaneous switching from increasing to decreasing permeability under the influence of infiltrating fluids is not unknown /e.g. Polak et al. 2004, Yashuhara et al. 2006/.

Although much of the research reported in the literature concerns sedimentary formations, many of the processes will have analogues in crystalline rock fractures filled with calcite deposits and so are considered relevant for these discussions. In summary, however, it is not currently clear how these phenomena should affect the permeability of fractures owing to the possibility of both positive and negative feedbacks for the evolving transmissivity of the flow system. Given the high *in situ* stresses at Forsmark, however, it seems likely that fractures might evolve towards lower permeability under the influence of these combined processes.

Based upon the available data it is not clear whether karstic erosion features are common in the HRD, although they cannot either be completely ruled out as a possible concern. Calcite is present in roughly half of the open fractures found at repository depth and, based upon the statistical data reported by /Löfgren and Sidborn 2008/, the fracture coatings are estimated to have an arithmetic average thickness on the order of 0.05 mm. Since there is a very low probability of direct borehole intersection with karstic erosion features in annealed fractures, these are generally not observed in the site investigation boreholes.

Scoping calculations based upon solution of the Navier-Stokes equations for flow in crossing or terminating fracture intersections (FIZ sub-type A) indicate that FIZ features will not contribute significantly to flow channelling phenomena in the rock. The impact of highly conductive FIZ (sub-type B and C) has also been demonstrated by way of scoping calculations using the existing Hydro-DFN model for FFM01c (< –400 m) and assuming fracture traces with negligible flow resistance. Details of these calculations can be found in Appendix A and Appendix D. In the calculations it is shown that even if highly conductive FIZ features comprise up to ~ 50% of the typical flowpaths in the HRD, they should not have a significant deleterious impact upon the F-factor for transport of solutes. This, however, is contingent upon the open fracture intensity being sufficiently low that they do not form contiguous pathways through the rock.

3.11 Summary of main findings

In summary, the key findings of this chapter include:

- Transport from a repository through the geosphere to the near surface is proposed to occur via a sequence of advective pathways featuring progressively increasing flow and transmissivity. For the purpose of making scoping calculations of hydrodynamic transport resistance, the conceptual flow system was therefore sub-divided into three serially connected compartments:
  a) The non-engineered near field (NNF) comprising the network of poorly transmissive flow channels linking canister deposition holes with typical flowpaths in the HRD featuring relatively high flowrates.
  b) The immediate far-field (IFF) comprising the relatively transmissive flowpaths within the HRD which can persist for several hundred metres distance through the rock until encountering deformation zones in the HCD.
  c) The distant far field (DFF) comprising very transmissive flowpaths hosted in deformation zones within the HCD which provide fast conduits for flow to the near surface.

- F-factors for the NNF are difficult to evaluate as they are highly dependent upon selection/rejection criteria for transmissive fractures intersecting the deposition holes. Typical F-factors in the range of about 10^3–10^7 y/m are calculated for fractures in the transmissivity range from 10^{-8}–10^{-10} m^2/s depending upon the underlying assumptions, which include typical path lengths and representative hydraulic gradients.
- Owing to the poor connectivity of open fractures at repository depth within FFM01c (< –400 m), a modelling strategy based upon identifying the path of least transport resistance (in a large number of realisations of the Hydro-DFN) was used to estimate F-factors for "typical" flowpaths in the IFF. Median F-factors on the order of 10^6 y/m were found to be the norm for this fracture domain over a simulated cubic volume of 100 m×100 m× 100 m and different transport directions assuming a semi-correlated fracture size-transmissivity relation.
- Less than 4% of the Hydro-DFN realisations for FFM01c (< –400 m) exhibited hydraulic connectivity of any kind and about half of those that did were usually associated with a single large fracture penetrating the entire simulation voxel. The remaining simulations featuring hydraulic connectivity were the result of mutual intersection of a small number (2–6) large fractures forming hydraulic connections. No realisations exhibited pervasive clusters of hydraulically connected small fractures. The probability of a realisation featuring connectivity was found to be slightly less in the vertical direction than in the principal horizontal directions considered (North-South and East-West).
- Probability of hydraulic connectivity decreases rapidly with increasing respect distance from a hypothetical repository as different fracture size classes make active connections at different distances of notional hydraulic boundary separation.
- Simulations of other fracture domains (upper regions of FFM01, FFM02, and FFM03) using Napsac/ConnectFlow give indications of clearly reduced hydrodynamic transport resistance as compared to FFM01 at repository depth.
- Using the exponential decay model of deformation zone transmissivity provided by hydrogeology it is possible to calculate a simple analytical value for typical F-factors in the HCD for a set of well-defined boundary conditions. We find that typical flowpaths within gently dipping zones typified by ZFMA2 are associated with F-factors of less than 10^3 y/m for transport from repository depth to the near surface indicating relatively poor hydrodynamic transport resistance. Steeply dipping deformation zones on the other hand (ZFM0060A as an example) are found to have F-factors on the order of 10^5 y/m. Numerical simulations considering different transmissivity spatial correlation structures generally give results that are consistent with the analytical model and do not differ strongly from the predicted central value provided the largest spatial correlation length is substantially less than the transport distance modelled. Given that we expect hydraulic gradients to be somewhat lower than the regional average (1%) in the more transmissive regions of the rock, these F-factors may be underestimated.
- Particle tracking calculations for solute transport from repository depth to the surface have been made using the Base Case model developed by hydrogeology and an ECPM representation simulated with ConnectFlow. The simulations predict mean F-factors of about 2 orders of magnitude higher than that calculated using the simplified models developed for the purpose of flow-related transport property evaluation in this report. Advective transport times are found to be about 3–4 orders of magnitude greater than expected. Reasons for the discrepancy are given below:

  The high F-factors can be partially attributed to the fact that most particles appear to be released either directly within the rock matrix or within regions that are transmissive although hydraulically isolated. These particles must be transported advectively through the rock matrix in order to reach conductive features that communicate with the near surface aquifers. Cumulative F-factors associated with such flowpaths are not physically meaningful and can therefore be discounted.

F-factors for particles that are not transported advectively through the rock matrix are approximately consistent with the scoping calculations made using the 3 compartment approximation. Any residual discrepancies appear to be related to lower hydraulic gradients and higher specific flow-wetted surfaces in the ECPM representation which are deemed to be not unfeasible. The ECPM simulations also suggest that the deterministic deformation zones may play a more important role for the overall transport resistance in the system than the 3-compartment scoping calculations would otherwise suggest.

The discrepancy in advective travel times appears to be related to the abovementioned factors as well as a kinematic porosity roughly an order of magnitude larger than that predicted using the macroscopic quadratic law (MQL). The larger kinematic porosity was necessary to obtain a model fit with the measured hydrogeochemical profiles in the paleo-hydrogeochemical simulations.

- Six different sub-classes of flow channelling have been identified as being potentially important for the Forsmark site and have been considered in the analyses presented in this chapter. Flow channelling may have an impact upon interpretation of borehole data by way of censoring effects leading to the underestimation of the frequency of flowing channels within the rock. Some channels may be very narrow in width and unlikely to be intersected directly by a borehole and therefore the permeability of the surrounding fracture pore space becomes very important for identification of these features and interpretation of their hydraulic properties. The uncertainties introduced by certain forms of flow channelling appear to be reasonably well constrained by scoping simulations. The overall effect of flow-channelling doesn't appear to be sufficiently severe at present that it would cast considerable doubt on the utility of the hydrogeological models produced within SDM Site, although further justification of this will need to be made during safety assessment. It should also be acknowledged that there is a limit to the extent to which we can constrain the impact of flow channelling from surface based investigations. The full hydraulic impact of fracture filling minerals and the possible existence of pipe-like flow channels can only be fully gauged during the construction phase of the repository where these features may be directly observable from tunnels.

4 Bedrock retardation model

The bedrock retardation model is one of the key elements of the overall site descriptive model contained in this report. Essentially the retardation model is comprised of the following sub-elements:

- a qualitative identification and description of "typical" geological materials, fracture types and deformation zones to be found at the Forsmark site with regard to processes of relevance for transport of environmental solutes and radionuclides,
- quantitative data describing material properties of the different geological materials comprising the rock matrix as well as relevant alteration types and secondary minerals found in association with fractures and deformation zones,
- quantitative data concerning the relative abundance and spatial distribution of different minerals to be found in association with fractures and deformation zones,
- an abstracted model of material properties recommended for describing the transport of solutes at the Forsmark site. This also includes a set of "Type" fractures and structural elements of deformation zones which can be assembled in a modular fashion for application within numerical transport codes.

The methods used in the transport programme produce primary data on the retardation properties of the rock. The main parameters of interest are the immobile zone porosity, θ_m, the effective diffusivity, D_e and the linear equilibrium sorption coefficient, K_d. These retardation parameters are evaluated, interpreted and presented in the form of a retardation model; the strategy for laboratory measurements, data evaluation and development of retardation models is described by /Widestrand et al. 2003/. In the three-dimensional spatial representation of the Forsmark site, the retardation model is used to parameterise the various geological elements described in the geological site-descriptive model. These elements consist of the rock mass itself containing varying proportions of different site specific rock types, key fracture classes characteristic of the Forsmark site, and various deformation zone microstructural components.

The retardation model combines material properties data for the major rock types and their various alteration states with a description of various fracture sub-classes and deformation zone structural elements typical for the Forsmark site investigation area. This is intended to form a basis for the parameterisation of models used within safety assessment. The integration of the material properties parameterisation with the flow-related transport properties provides a basis for solute transport modelling and scale-up of flow path retention properties.

The different methods used in the laboratory programme are described in /Widestrand et al. 2003/. The primary data evaluation is made in the transport properties evaluation background report by /Byegård et al. 2008/. This chapter is a summary of that report.

4.1 Description of input data

The development of the retardation model relies to a large extent on interaction with other disciplines; primarily geology and hydrogeochemistry. Specifically, geology provides lithological and structural models where the rock types, fractures and deformation zones are described, as well as the mineralogical compositions of intact and altered materials. Hydrogeochemical information is used as a basis for the selection of water compositions in laboratory measurements of retardation parameters. Furthermore, hydrogeochemical data together with results from mineralogical and geochemical analyses of fracture materials are important inputs to the conceptual development of the site specific retardation model and the description of the understanding of the retention processes at the site.

The input data for the retardation model consist of laboratory and *in situ* measurements of material properties from the transport properties laboratory programme as well as supporting information from other disciplines. The available site investigation data on transport properties are summarised in /Selnert et al. 2008/. Transport data obtained from the laboratory programme include effective diffusivities and formation factors for diffusive solute transport in the rock matrix, matrix porosities, specific surface areas of rock, cation exchange capacities (CEC), and sorption properties of rock in contact with synthetic groundwater of varying composition. Field data is also available in the form of roughly 100,000 *in situ* measurements of the rock formation factor obtained from high resolution geophysical logging in the site investigation boreholes.

4.2 Data and models from other disciplines

Supporting descriptive data from the combined geological/hydrogeochemical interpretations of fracture mineralogy and wall rock alteration data are provided by /Sandström et al. 2008/. Other geological, hydrogeological, and hydrogeochemical inputs were obtained from the relevant SDM modelling background reports as well as detailed studies of specific features (e.g. deformation zones /Nordgulen and Saintot 2006/).

4.2.1 Summary of supporting geological data

For the transport properties site descriptive modelling, attention has focused upon the rock domains RFM029 (dominant) and RFM045 (subordinate) as these are volumetrically the most significant domains both in the local model volume as well as the target volume.

A full account of the proportions of different rock types and classes of alteration can be found in the geology SDM background report /Stephens et al. 2008/. A brief summary of the rock types and corresponding codes referred to in this report, however, is given in Table 4-1 together with the different proportions of each rock type comprising RFM029 and RFM045.

The approximate volume fractions of the different rock types based upon the geological interpretation of borehole data are visualised in Figure 4-1.

Table 4-1. Rock names and SKB codes for major and most common subordinate rock types found within rock domain RFM029 and RFM045. Approximate proportions (vol%) for each rock type is also given for both rock domains.

Rock name	SKB code	RFM029	RFM045
Granite to granodiorite, metamorphic, medium-grained	**101057**	73.6	18.0
Pegmatite, pegmatitic granite	**101061**	13.3	13.9
Granite, granodiorite and tonalite, metamorphic, fine- to medium-grained	**101051**	4.6	9.0
Granite, metamorphic, aplitic	**101058**	1.2	49.3
Amphibolite	**102017**	4.4	6.3
Granite, fine- to medium-grained	**111058**	1.5	1.3
Felsic to intermediate volcanic rock, metamorphic	**103076**	0.4	1.2
Calc-silicate rock (skarn)	**108019**	0.3	0.2
Quartz-dominated hydrothermal vein/segregation	**8021**	0.2	0.2
Diorite, quartz diorite and gabbro, metamorphic	**101033**	0.2	0.2

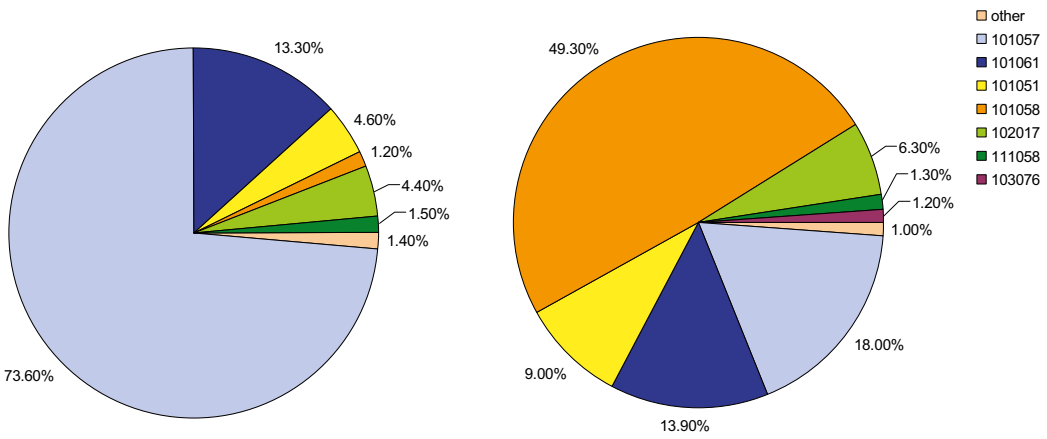

Figure 4-1. *Quantitative estimates (vol%) of the proportions of different rock types found in rock domain RFM029 (left) and RFM045 (right).*

For the purposes of parameterising the material properties of the rock, however, we can say that the rock in RFM029 is dominated by granite to granodiorite, metamorphic, medium grained (101057) with smaller amounts of subordinate rock types (101061, 101051, and 102017). The most abundant types of rock alteration in RFM029 is oxidation (associated with hematite) and albitisation. Zones of quartz dissolution and vuggy rock are also present, often localised to upper reaches of RFM029.

Rock domain RFM045 is dominated by Na-K altered (albitised) and metamorphosed granitic rocks of which the most common is granite, metamorphic, aplitic (101058), although a smaller amount of the granitic rock type 101057 is also present. Modal analyses indicate that Na-K alteration gives rise to an increase in the quartz content and a marked decrease in the content of K-feldspar, relative to the equivalent unaltered rocks. The albitisation is not pervasive throughout the domain and fresh rock is also present. Compared with domain RFM029, there is a somewhat higher proportion of the alteration referred to as oxidation outside deformation zones. Subordinate rock types include pegmatite and pegmatitic granite (101061), fine- to medium-grained metagranitoid (101051) and amphibolite (102017). These rock types occur mainly in the form of isolated minor bodies or lenses and dykes. All occur, however, with a greater frequency than what is observed in domain RFM029 (see Figure 4-1).

RFM012, RFM018, RFM032 and RFM044 are marginal rock domains; i.e. rock domains not included in the target volume. These domains are generally affected by strong ductile deformation and also show an increased frequency of fractures or possible deformation zones. These have not been included in the parameterisation of the retardation model presented in this chapter.

There is a clear tendency for an increased extent of alteration within deformation zones. The major mineralogical changes in oxidized (hematite disseminated) rock are the almost complete hydrothermal alteration (saussuritization) of plagioclase feldspar, chloritization of biotite and a fine dissemination of hematite microprecipitates inside the altered plagioclase grains and along grain boundaries. An increase in the porosity is also associated with this type of alteration /Sandström and Tullborg 2006/. Analysis of oxidation along the cored boreholes demonstrates that it occurs independently of elevation, it is not related to near-surface processes and it is an inherent feature of deformation zones (although with a non-pervasive distribution). In albitised rock there is a redistribution of sodium and potassium; producing a fine-grained quartz-plagioclase feldspar-(biotite) rock in especially granitic rocks, with a significant loss of K-feldspar compared with the unaltered rocks. According to borehole data, albitisation is not confined to deformation zones. Virtually all occurrences of vuggy rock are found within or immediately adjacent to possible deformation zones within the single hole interpretations and deterministically modelled deformation zones from the SDM-Site geological model.

The statistical occurrence of different alteration types is given in Figure 4-2 for RFM029 and Figure 4-3 for RFM045.

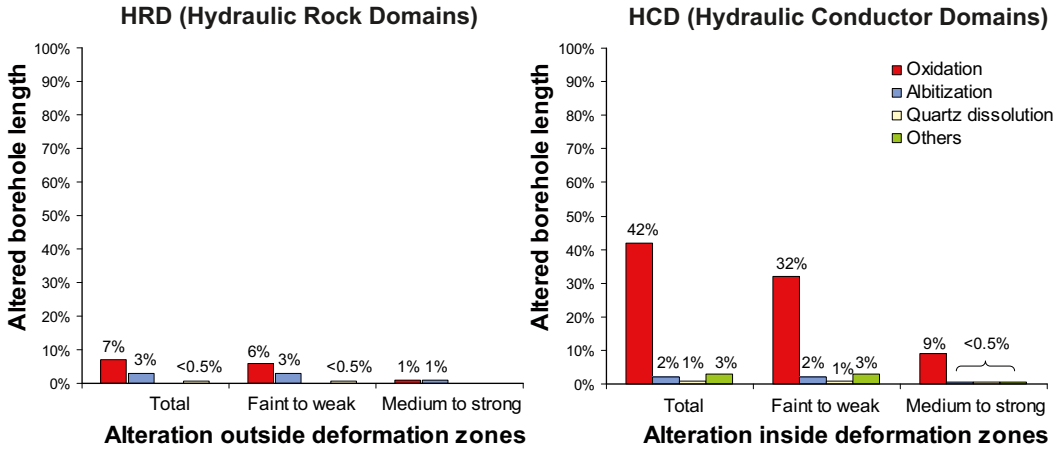

Figure 4-2. *Quantitative estimates (vol%) of the type and degree of alteration found in rock domain RFM029 within the HRD (left) and HCD (right).*

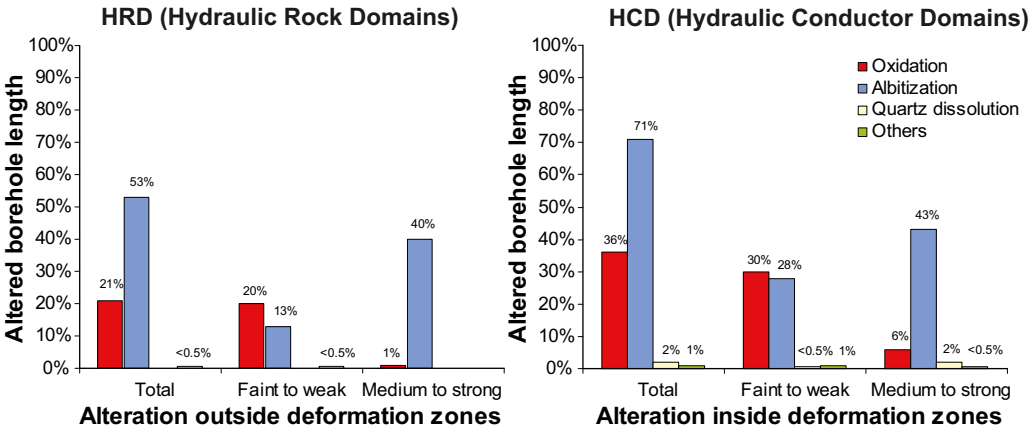

Figure 4-3. *Quantitative estimates (vol%) of the type and degree of alteration found in rock domain RFM045 within the HRD (left) and HCD (right).*

Fracture types

Most fractures within the target volume are sealed. There is greater intensity of open and partly open fractures in the upper reaches of the rock although this decreases strongly with increasing depth, particularly in the foot wall of ZFMA2. The majority of fractures were initiated 1.75–1.9 Ga (during the Svecokarelian to Palaeozoic period) and many show signs of later reactivation. These are described below as being Generation 1–3. There is no evidence of the sub horizontal fractures being younger than the vertical sets although they may have been reactivated at different times. Four distinct generations of fracture mineralisation formed at different times have been distinguished at Forsmark /Sandström et al. 2008/. The defining features of these are summarised below:

Generation 1; consists of epidote, quartz and Fe-rich chlorite in fractures and as sealing in brittle-ductile cataclasites. The minerals precipitated under hydrothermal conditions at temperature > 150–200°C. Generation 1 minerals are conspicuous in sub-horizontal and gently dipping fractures or in steep, WNW-ESE to NW-SE fractures. However, they are also present along fractures in other steeply dipping sets. This generation formed between 1.8 and 1.1 Ga, and is possibly related to the late Svecokarelian and/or Gothian tectonothermal events.

Generation 2; consists of a sequence of hydrothermal fracture minerals precipitated at temperatures between ~ 150–280°C and are dominated by adularia, albite, laumontite, prehnite, calcite, chlorite and hematite. Generation 2 minerals are particularly common along steep, ENE-WSW

to NNE-SSW and NNW-SSE fractures. $^{40}Ar/^{39}Ar$ ages from adularia indicate a major influence of early Sveconorwegian tectonothermal activity at 1.1 to 1.0 Ga on the development of fracture systems that are coated or filled by generation 2 minerals. Both reactivation of older fractures and formation of new fractures are inferred during the Sveconorwegian tectonothermal event. Dissolution of fracture minerals occurred before the formation of generation 3 minerals.

Generation 3; consists of minerals precipitated under low temperature conditions during the Palaeozoic. The most abundant minerals are calcite, quartz, pyrite, corrensite and asphaltite. The formation fluid was influenced by organic material, which may have emanated from an overlying sedimentary cover. The orientation of fractures with generation 3 minerals suggests reactivation of fractures filled with older minerals but new fractures were also formed.

Generation 4; is dominated by chlorite/clay minerals and thin precipitates of calcite in predominantly hydraulically conductive fractures and fracture zones. These minerals are prominent along sub-horizontal and gently dipping fractures, but are also present in different sets of steeply dipping fractures. It is inferred that most of the hydraulically conductive fractures are hosted in ancient structures (Proterozoic-Palaeozoic) and precipitation of generation 4 minerals has most likely occurred over a long period of time.

Based upon the characterisation of different fracture mineralisations and theoretical potential for influencing transport properties, eight major fracture types have been identified. These are summarised in Table 4-2 and typical examples are shown in Figure 4-4.

Table 4-2. Classification of basic fracture types within retardation model.

Type	Fracture coating	Thickness	Wall rock alteration
A	***Chl+Ca***	≤ 0.5 mm	Fresh
B	***Chl+Clay*** ± *Ep* ± *Pr* ± *Ca*	~1 mm	Altered (~1 cm)
C	***Chl+Hm*** ± *Other*	< 0.5 mm (0.1 mm)	Altered (0.5 cm)
D	***Chl*** ± *other*	< 0.5 mm (0.1 mm)	Fresh
E	***Lau*** ± *Ca* ± *Chl*	0.1–2 mm	Altered (1–5 cm)
F	***Ca*** ± *Qz* ± *Py* ± *other*	0.1–2 mm	Fresh
G	***Clay*** ± *other*	1–5 mm	Altered (≥ 5 cm)
H	***No mineral***		Fresh

Notes: fracture mineral abbreviations are: chlorite (Chl), calcite (Ca), epidote (Ep), hematite (Hm), laumontite (Lau), prehnite (Pr), pyrite (Py), quartz (Qz).

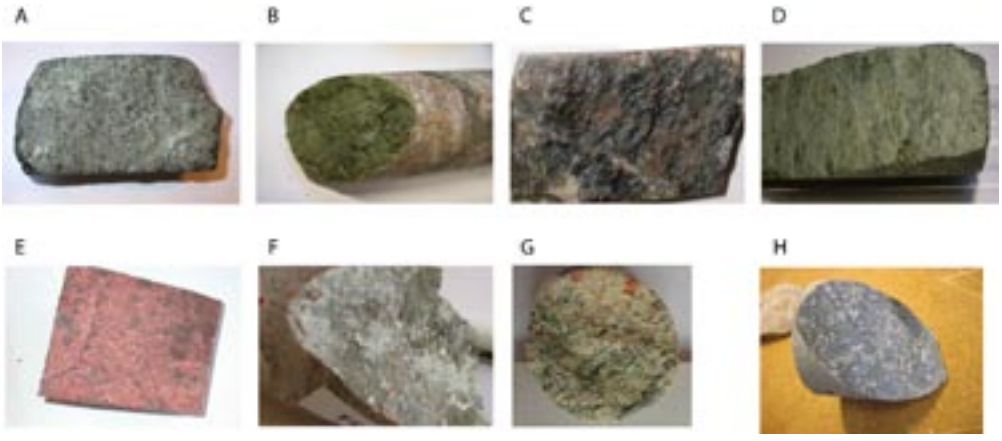

Figure 4-4. *Typical appearance of the surface coating minerals associated with the basic fracture types considered in the retardation model.*

Based upon detailed studies of fracture mineralogy and wall rock alteration /Sandström et al. 2008/, the relative abundance of fracture minerals at Forsmark can be summarised as: calcite and chlorite/corrensite > laumontite > quartz, adularia, albite, clay minerals > prehnite, epidote > hematite and pyrite. With the exception of asphaltite and goethite which are almost exclusively associated with FFM02, roughly the same mineralogy is found in FFM01, FFM02, FFM03, and FFM06 although the proportions of the different minerals may vary.

Chlorite and calcite are the most frequent fracture coating/filling minerals, occurring either exclusively or together with other minerals. Chlorite and calcite are present in about 34% of the mapped open fractures and 38% of the transmissive fractures. According to boremap data, chlorite together with clay (mainly corrensite) is present in about 7% of the open fractures. Detailed fracture mineralogical studies /Sandström et al. 2008/, however, show that corrensite is common in fractures with chlorite and it can therefore not be excluded that the frequency might be somewhat underestimated.

Calcite also occurs together with quartz, pyrite and other minerals in about 15% of the open fractures and 19% of the transmissive fractures.

Clay minerals as illite, smectite and mixed layer clay (smectite/illite) are found in association with at least 3% of the open fractures. Most of these fractures are found in the upper 100–150 m which may be of importance considering their increased sorption capacity. Other clay minerals such as corrensite (swelling mixed layer clay) generally occur together with chlorite and are present in about 7% of the open fractures. The latter fracture type is not restricted to any particular depth but constitute a larger proportion, about 10–20% of the total number of open fractures at repository depth.

Laumontite (± calcite ± chlorite) is a common fracture mineral in open fractures (~ 14%) as well as in sealed fracture networks. Laumontite is, however, unusual in fractures associated with identified (PFL) flowing features, where it occurs with frequency of about 1%. It is difficult to determine whether these fractures are originally open or sealed (i.e. reactivated during core retrieval). This means that the frequency of open, laumontite coated fractures might be uncertain. According to PMMA measurements of sealed fracture networks /Penttinen et al. 2006/, laumontite has an increased porosity of approximately 3%.

About 6% of all open fractures are mapped without any minerals. These fractures are to a great extent horizontal to subhorizontal in orientation (i.e. with a dip < 25°). The frequency with which they occur is roughly 50% greater amongst the horizontal-subhorizontal features as compared to the total set of open fractures. The majority of these fractures also seem to occur in the upper 400 m of the investigatory boreholes.

A visualisation of the relative abundance of different fracture types is given in Figure 4-5.

For generation 1 and 2 fractures, hydrothermal reddening normally extends a few centimetres perpendicularly out from fracture surfaces. The alteration, in particular for chloritization, extends further into the rock than the reddening suggests and the amount of rock mapped as “oxidised” should therefore be seen as a minimum value of the true amount of altered rock (see following section on Deformation zones). An increase in the connected porosity in the altered rock can be seen, most likely due to the chloritization of biotite and an increase in the intensity of micro-fracturing.

Most of the single fractures at the Forsmark area at elevations less than –500 m exhibit low transmissivity, although open and semi-open fractures are mapped throughout the entire drill-cores. It is believed that the mineralogical composition of the fracture coatings is important as well as the presence or absence of an altered zone in the wall rock adjacent to the conductive fractures as these constitute potential diffusive pathways within the rock.

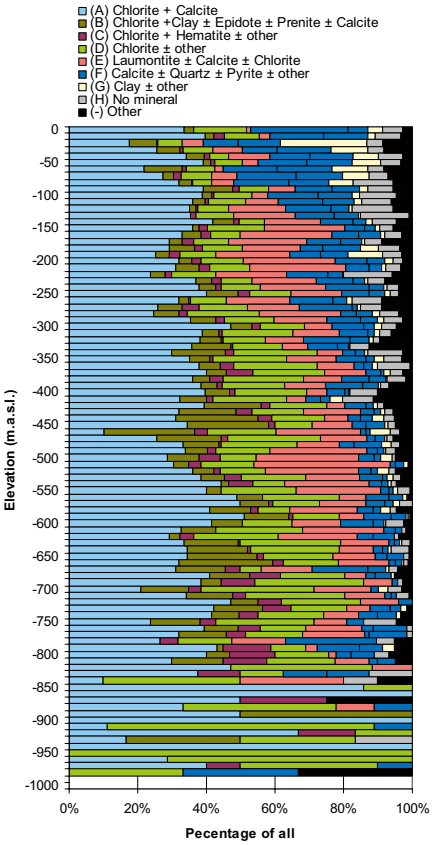

Figure 4-5. *Relative abundance of different fracture types at various depths at the Forsmark site (based on boremap data in Sicada considering all cored boreholes). It should be noted that the apparent discontinuous statistical distribution at depths > 850 m reflect a greater sparsity of data rather than a true change in the distribution of fracture types.*

Concerning the mineralogy in transmissive fractures, the dominating fracture assemblages are chlorite + calcite, chlorite ± others and calcite ± quartz ± pyrite ± other (i.e. fracture types A, D and F), although fractures completely lacking secondary minerals are also relatively common (fracture type H).

Only a small number of fractures with laumontite appear to be currently hydraulically conductive. The absence of laumontite in transmissive fractures, however, may be due to dissolution of this easily weathered mineral in reactivated older fractures. This has already been discussed in the context of possible flow channelling effects in section 3.10. Fracture transmissivities are relatively broadly spread for all fracture types and generally range between 10^{-10} to 10^{-5} m^2/s, excluding fracture type H (i.e. with no mineral coating) which have maximum transmissivity values (single fractures) of up to 10^{-3} m^2/s.

Deformation zones

Deformation zones are structurally very heterogeneous and it is very difficult to exactly delineate their extent and internal structure from a small number of borehole intercepts. Figure 4-6 illustrates conceptually how a deformation zone might appear from interpretation of a borehole intercept and how the actual extent and geometrical shape of the zone may actually vary.

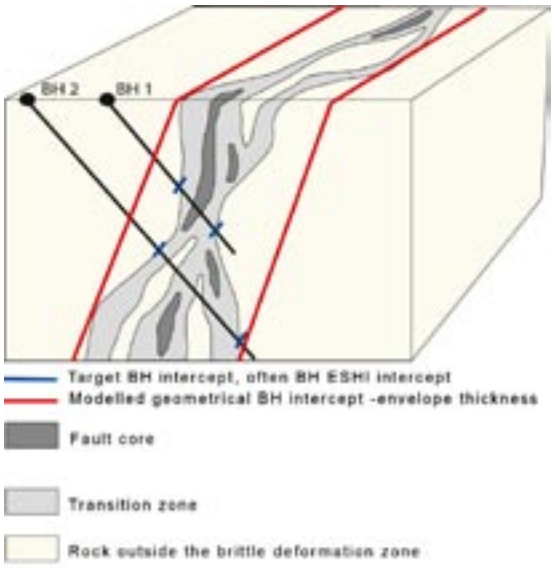

Figure 4-6. *Three-dimensional conceptual illustration of brittle deformation zone geometry typical for Forsmark (redrawn after /Caine et al. 1996/). Hypothetical borehole intercepts are indicated by the diagonal black lines in the figure.*

The transition zone can range in thickness from a few metres to several tens of meters. This part of the zone has an increased fracture frequency together with a more extensive alteration compared to the surrounding bedrock. The transition zone, however, can contain segments that are unaffected with respect to fracture frequency and alteration. The core of the deformation zone is usually thinner than the transition zone and its thickness can vary from a few centimetres to a few metres. The core has even higher fracture frequency and is often composed of sealed fractures (mainly in sealed fracture networks), fault breccia or cataclasite (often cohesive). The boundaries between the host rock, transition zone and core are commonly diffuse and difficult to demarcate.

The deformation zones within the local model area at the Forsmark site are numerous and are described individually as deterministic features in both the geological /Stephens et al. 2008/ and hydrogeological /Follin et al. 2008/ site descriptive models. The existence of certain zones is not confirmed in a deterministic sense (i.e. established from multiple, independent geophysical investigations). These are referred to as “possible” deformation zones in the site descriptive models and their existence is predicated upon indications in the extended single hole interpretation (ESHI) data which may include borehole logs of fracture frequency, alteration, and focussed resistivity geophysical measurements. The single hole interpretation data is also used to delineate cores, transition zones, as well as important structural elements such as sealed fracture networks and crushed rock within the deterministically confirmed deformation zones.

Generally, the deformation zones at Forsmark can be divided into four distinct sets based upon orientation:

- Vertical and steeply, SW-dipping deformation zones with sub-sets referred to as WNW and NW. These zones contain mylonites, cataclastic rocks and cohesive breccias, and are dominated by sealed fractures. They initiated their development in the ductile regime but continued to be active in the brittle regime, i.e. they are composite structures. Epidote, quartz, chlorite and calcite are conspicuous along the fractures in these zones (generation 1 mineral paragenesis). Regional zones that are longer than 10 km (e.g. Forsmark, Singö and Eckarfjärden deformation zones) are restricted to this set.
- Gently dipping fracture zones that formed in the brittle regime and, relative to all the other sets, contain a higher frequency of open fractures and incohesive crush material. Chlorite, calcite and clay minerals are conspicuous along the fractures in these zones. Locally, epidote,

quartz, adularia, hematite, prehnite, laumontite, pyrite and asphaltite are also present. It is apparent that these zones include minerals from all four mineral parageneses and it is inferred that fluid movement has occurred along these zones at several times during geological history.

- Vertical and steeply dipping fracture zones with sub-sets referred to as ENE (NE) and NNE. These zones formed in the brittle regime and are dominated by sealed fractures. Hematite-stained adularia, laumontite, chlorite and calcite are conspicuous along the fractures in these zones (generation 2 mineral paragenesis). The generation 1 mineral epidote, however, is locally present along fractures with steep ENE to NNE orientation in these zones.
- Vertical and steeply dipping fracture zones that are referred to as the NNW set. These zones formed in the brittle regime and are dominated by sealed fractures. Fillings and coatings along the fractures in these zones are similar to those observed in the ENE to NNE set. Clay minerals are also present along steeply dipping fractures with NNW strike in some zones. On the basis of their low frequency of occurrence, the NNW set is judged to be of lower significance at the Forsmark site, relative to the other three sets.

The major mineralogical changes in the altered rock are an almost complete saussuritisation of plagioclase, chloritization of biotite, and some hematisation of magnetite. The plagioclase of oligoclase composition has been replaced by a mineral assemblage consisting of albite, adularia, sericite, epidote, hematite and calcite. The red-tinged colouration of the rock is due to the dissemination of hematite with sub-microscopic hematite grains within and along the grain boundaries of the saussuritised plagioclase.

For each of the possible deformation zones identified in the cored boreholes (i.e. from single hole- and extended single hole interpretations, SHI and ESHI), an analysis of the mineralogy has been carried out. Since fractures with different orientations are present within a zone, an important task has been to establish how the different fracture minerals are distributed according to fracture orientation. The minerals asphaltite, calcite, chlorite, clay minerals, epidote, hematite/adularia, laumontite, prehnite, pyrite, quartz, and others that occur in different mineral generations, have been addressed in the investigation. Additionally, the occurrence of hematite staining adjacent to fractures (so-called oxidised walls) and the occurrence of fractures where no mineral filling or coating has been identified were also included. Data from open and partly open fractures are distinguished from sealed fractures. Transmissive fractures, if any, are frequently found in the transition zone.

As mentioned previously, almost all occurrences of vuggy rock are to be found either within or in near association (i.e. in proximity to one side of the zone) with deterministic deformation zones. It is inferred that the vuggy rock represents channels within deformation zones along which, at some time (or times) during geological history, aggressive hydrothermal fluids have flowed and induced changes in the quartz content of the bedrock.

Fault gouge has not been detected during the mapping of drillcores or during the detailed characterisation of deformation zones. A loss of drill core has been documented, however, along 35 borehole sections of which 23 lie along possible deformation zones. It appears that the most frequent cause of drill core loss is related to drilling induced damage of the intact rock. It has been noted that at least one section may have contained incohesive material containing fault gouge which was flushed out with the drilling fluid.

For the purpose of developing a retardation model, four different kinds of altered bedrock have been distinguished as recurrent elements within, or in close association with deformation zones in addition to the single fractures described in the previous section. The recognition of these elements is based on macroscopic observations of altered parts of the retrieved drill cores during the initial phase of rock sampling for the laboratory program (discussed in section 4.3). Furthermore, these structural elements can occur individually, or together within a deformation zone and are considered as distinct from the single fracture types which also populate the deformation zones. These structural elements are described in Table 4-3.

Table 4-3. Main identified structural elements residing in deformation zones that have been included in the retardation model.

1)	Strongly altered (tectonised and partly incohesive) wall rock described in this report as “fault rock”. Altered rock fragments with varied mineralogy dependent on host rock. Chlorite, saussurite, and clay are generally present.	
2)	Sealed fracture networks mainly consisting of breccia and cataclasite. Different fracture fillings such as laumontite + calcite, epidote, chlorite.	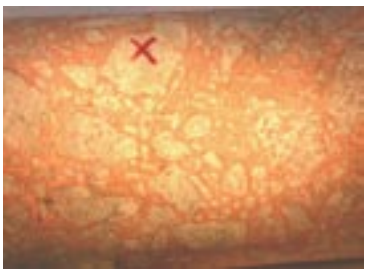
3)	Quartz dissoluted rock (vuggy rock).	
4)	Oxidised wall rock (mainly medium or strong degree of alteration).	

Synthesis of a generalised model for deformation zones is difficult owing to their complexity and extraordinary spatial variability. This is further complicated by the fact that their structure is usually only known from a small number of one-dimensional borehole intercepts. Much of the complexity of deformation zones arises through cycles of reactivation during different geological events. They therefore display a wide spectrum of alteration types, as well as brittle and ductile features accrued at different stages of their geological history.

An important concern during the modelling work has been to establish a level of appropriate microstructural detail that is both physically realistic and adequate for the purposes of safety assessment and other transport modelling. Typical questions that arose during this work included whether retention parameters should be given to the zone in its entirety or whether it is more appropriate to parameterise the different structural elements of the zone separately (i.e. fractures, altered bedrock, etc) including dividing the deformation zone into high transmissive and low transmissive sub-structures. A number of different ways to deal with these questions are illustrated in Figure 4-7.

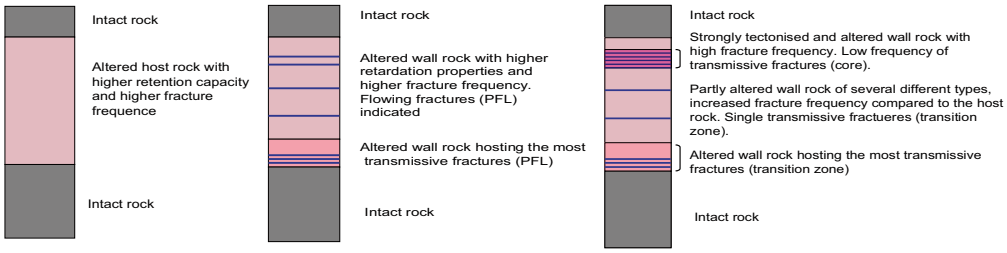

Figure 4-7. *Schematic illustration of different alternatives for describing a deformation zone retardation model; a) deformation zone considered as a single unit with higher retention capacity than the surrounding bedrock, b) deformation zone divided up into a high transmissive and a low-transmissive unit, c) variation including core and transition zone, the latter divided into a high and low transmissive unit.*

As illustrated in Figure 4-6, a deformation zone might be intersected by several boreholes and yet, exhibit dissimilar microstructural properties in each intersection. The core and transition zone in a deformation zone may contain one or more of the four structural elements described above and in Table 4-3. In addition, the fracture frequency and fracture mineralogy can be expected to vary throughout the zone as well.

As far as retention properties are concerned (i.e. for sorption, porosity, and effective diffusivity), there may be a considerable diversity between the different segments, single fractures and combinations thereof which comprise the complete deformation zone.

4.2.2 Summary of supporting hydrogeochemical data

The groundwaters at Forsmark are characterised by compositions that range in salinity from fresh (< 200 mg/L Cl) to saline water (~ 15,000 mg/L). Components of meteoric waters from cold and temperate climates as well as marine and deep saline groundwaters have also been identified. The following division into different water types have been applied for the description of the hydrogeochemistry at the Forsmark site /Laaksoharju et al. 2008/:

Fresh: (< 200 mg/L Cl; < 1.0 g/L TDS); Mainly meteoric in origin, i.e. Na(Ca)-$HCO_3(SO_4)$-(Cl) in type, $\delta^{18}O$ = –11 to –12 ‰ SMOW[4].

Brackish Marine: (2,000–6,000 mg/L Cl; 3.5–10 g/L TDS; Mg > 100 mg/L); Variable Littorina Sea component (± modern Baltic Sea) + Last Deglaciation melt water ± Saline component; Na-Ca-Mg-Cl-SO_4; $\delta^{18}O$ = –11.5 to –8.5 ‰ SMOW

Brackish to Saline Non-marine: Brackish to Saline Non-marine (4,000–15,000 mg/L Cl; 8.5–16 g/L TDS; Mg < 25 mg/L); Old Meteoric ± Old Glacial ± Last Deglaciation melt water ± Saline component, i.e. Ca-Na-Cl in type, $\delta^{18}O$ = –16 to –10.5‰ SMOW.

In the upper part of the bedrock (50–150 m depth) mixing between Fresh and Brackish Marine waters is common. This mixing may be natural as well as anthropogenic and partly due to sampling in relatively long borehole sections, mainly from percussion boreholes.

Another example of natural and/or anthropogenic mixing is the waters sampled in the transition zone between Brackish Marine and Brackish Non-marine groundwaters. These waters range from 4,000–6,500 mg/L Cl and from 25–100 mg/L in Mg.

The conceptual model of the hydrogeochemistry (Figure 4-8) shows the distribution of these groundwater types along a WNW-ESE cross section.

[4] Deviations in oxygen and hydrogen isotope ratios are given in parts per thousand and are related to the SMOW reference (Vienna Standard Mean Oceanic Water) as defined by the International Committee for Weights and Measures (CIPM).

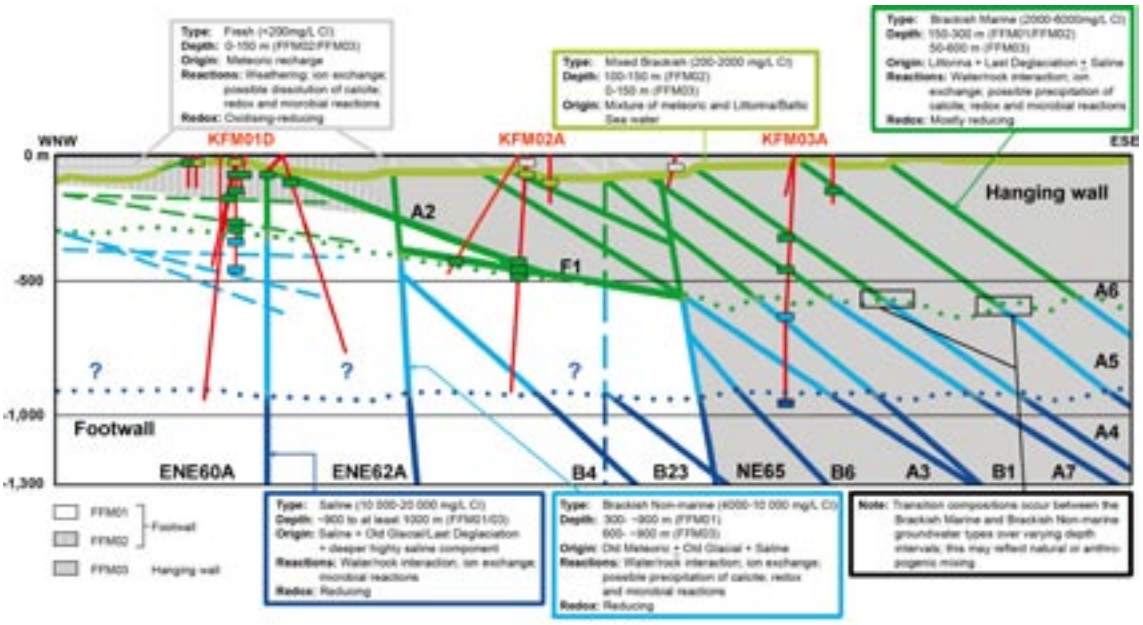

Figure 4-8. *WNW-ESE cross-section and site descriptive model along the central part of the candidate volume showing the groundwater types and their properties (salinity, origin, major reactions and redox conditions). The footwall (FFM01 and FFM02) and hanging wall (FFM03) are indicated, separated by the major, gently-dipping deformation zones ZMFA2 and F1 /from Laaksoharju et al. 2008/.*

For the laboratory measurements of transport properties it has been important to choose experiment waters that reflects the present water composition at repository depth but also to represent wider ranges of compositions that cover potential variations in groundwater compositions during the future phases of the potential repository.

For the batch sorption measurements especially, the water chemistry plays an important role and four different groundwater compositions have therefore been selected:

I. Fresh diluted Ca-HCO_3 water; groundwater now present in the upper 100 m of the bedrock, but also a water type that can be found at greater depths during late phases of glacial periods.

II. Groundwater with marine character, Na-(Ca)-Mg-Cl (5,000 mg/L Cl); This constitutes a large portion of the groundwaters found at 150 to 600 m depth at Forsmark. It is assumed to originate from the Littorina stage of the postglacial Baltic Sea.

III. Saline groundwater of Na-Ca-Cl type (5,400 mg/L Cl); this is a water with higher Ca and lower Mg compared to the Type II water.

IV. Brine type water of very high salinity, Ca-Na-Cl type water with Cl content of 45,000 mg/L; during a glacial period, brine type waters can be forced to more shallow levels than at present.

Water of salinity close to the one measured at repository depth has been used for the diffusivity measurements. A water composition (described as Type II) was chosen for use in the experiments although only the major components (i.e. Ca^{2+}, Na^{+}, Cl^{-} and SO_4^{2-}) were included in the synthetic groundwater formulation.

The compositions of these groundwater types are specified in Table 4-4, referring to specific sampling intervals in the boreholes.

Table 4-4. Groundwater compositions used in the transport properties evaluation laboratory programme for the Forsmark site; concentrations are given in mg/l.

	Type I (HSH02 0–200 m) Fresh water	Type II (KFM02A 509–516 m) Groundwater with marine character (Present groundwater at repository level)	Type III (KFM03 639–646 m) Saline groundwater	Type IV (KLX02 1,383–1,392 m) Brine type water of very high salinity
Li^+	0.016	0.051	0.028	4.85
Na^+	127	2,120	1,690	7,450
K^+	2.16	33.3	14.2	32.6
Rb^+	(0.0252)[A]	0.0628	0.0393	0.178
Cs^+	(1.17×10^{-3})[A]	1.79×10^{-3}	7.09×10^{-4}	0.0186
NH_4^+	(0.0947)[A]	0.04	0.204	0.56
Mg^{2+}	1.43	232	52.7	1.2
Ca^{2+}	5.21	934	1,470	14,800
Sr^{2+}	0.0695	7.95	16.9	253
Ba^{2+}	(1.29)[A]	0.188	0.0907	0.024
Fe^{2+}	(0.364)[C]	1.20	0.233	3.45
Mn^{2+}	0.02	2.12	0.318	1.11
F^-	3.03	0.9	0.204	(1.6)[D]
Cl^-	21.5	5,150	5,190	36,800
Br^-	(0.2)[B]	22	38.9	509
SO_4^{2-}	8.56	510	195	1,210
Si(tot)	6.56	5.2	6.28	2.6
HCO_3^-	252	124	21.9	42
S^{2-}	(0.01)[B]	0.05	0.0295	0.05
pH	8.58	7.1	7.55	6.8

[A)] No measurements available, data imported from KSH01 #5263.
[B)] Based on detection limit.
[C)] Based on the Fe-tot measurement.
[D)] No measurements available, data imported from KLX02 #2731

4.3 Overview of transport property data

This section consists of two parts. The first part comprises a description of the main methods and techniques used in the laboratory programme for acquisition of transport property data (also referred to as material properties data in this report) as well as a general overview of issues related to data interpretation. The second part is a detailed description of the experimental data obtained from the laboratory investigations. These are presented in the form of material property tables for each relevant parameter and material type under specified conditions.

4.3.1 Methods and parameters

The main parameters used in the retardation model are the total storage porosity, θ_m (–), the effective diffusivity, D_e (m^2/s), and the linear equilibrium sorption coefficient, K_d (m^3/kg). The different laboratory techniques used for obtaining data and evaluating these parameters are described in the following sections.

Porosity

In the context of the retardation model described in this report, the porosity refers to the volume of the rock that is filled with water and available for both storage and transport of solutes (θ_m). Here, we make a theoretical distinction between the total storage porosity, θ_m of the rock and the transport porosity, θ_p which only considers the connected pore space available for diffusive through-transport.

Although very heterogeneously distributed on a microscopic to cm- or perhaps dm-scale, for the purposes of transport modelling the porosity is considered to be homogeneously distributed in the rock matrix on the macroscopic scale relevant for solute transport calculations.

The porosity data used in the site descriptive transport modelling has mainly been obtained from measurements performed on rock samples intended for diffusion and sorption studies. The method used for determination of the porosity (SS-EN 1936) is a gravimetric technique based upon water re-saturation of the sample, followed by a drying step. There are indications from pore water studies reported by /Waber and Smellie 2007/ that the water re-saturation technique might overestimate the porosity under *in situ* conditions by as much as 50% owing to stress release and core damage effects (this is discussed in more detail in Appendix H and Appendix L).

Estimations of the porosity for the deformation zone elements have been found to be difficult owing to the general heterogeneity of samples combined with problems of sample cohesion. For this reason, the porosity measurement based upon water saturation has been complemented with measurements based upon a PMMA-impregnation technique (Polymethylmethacrylate) /Penttinen et al. 2006/. This technique is a very valuable method for studying the spatial distribution and modality of porosity in samples on a microscopic scale.

Effective diffusivity

The effective diffusivity is frequently given in terms of the formation factor, F_f; a dimensionless number which is defined as the ratio of the effective diffusivity, D_e of a solute in the rock to that of the solute in water at infinite dilution, D_w. Theoretically, the formation factor is a geometrical factor that includes the effect of transport porosity, θ_p as well as pore tortuosity, τ^2 and constrictivity δ /e.g. Löfgren and Neretnieks 2003/. Typically, it is defined as:

$$F_f = \frac{D_e}{D_w} = \theta_p \frac{\delta}{\tau^2} \qquad (4\text{-}1)$$

The effective diffusivity can also be defined in terms of a pore diffusivity, D_p which internalises the transport tortuosity-constrictivity term in its definition:

$$D_e = D_p \theta_p \qquad (4\text{-}2)$$

The transport porosity, θ_p should theoretically be lower than the total accessible porosity, θ_m which also includes dead-end pores that do not contribute directly to the diffusive flux. Since the transport porosity is already internalised in the measurement of the effective diffusivity (or formation factor), it is generally not necessary to evaluate this separately for the purposes of transport modelling within safety assessment. In the Forsmark site descriptive modelling θ_p and θ_m are, for all practical purposes, considered to be identical.

Although strictly a geometrical parameter, measurement of the formation factor is influenced by other non-geometrical artefacts such as surface diffusion and anion exclusion effects. Operationally, however it is still defined as the ratio of effective and free diffusivity. For this reason, laboratory measurements of the formation factor using electrical resistivity are customarily carried out on materials that have been pre-equilibrated with high ionic strength water ($\geq$ 1.0 M) so as to not be excessively influenced by surface conduction artefacts (a more detailed discussion of this can be found in Appendix H). From the formation factor, approximate effective diffusivities can be calculated for all solutes of interest using solute-specific, free diffusivities from the literature /Widestrand et al. 2003/.

Formation factors can be obtained by a variety of different methods. The main laboratory methods used within the transport programme are through-diffusion tests and electrical resistivity measurements on slices of bore core samples. Through-diffusion tests are made using a two-compartment measurement cell where a tracer (tritiated water in the current laboratory programme) is allowed to diffuse through a 1–3 cm long bore core sample from a high concentration compartment to a low concentration compartment, initially free of tracer. The effective diffusivity and capacity factor are then obtained by fitting a theoretical model of diffusion to the breakthrough data for the measurement cell /e.g. Ohlsson and Neretnieks 1995/.

The through-diffusion tests used in the laboratory programme are based upon the use of tritiated water (HTO) as a tracer substance which for all practical purposes can be considered to be non-interacting. In previous investigations, uranine and iodide (I^-) were frequently used as tracers. Anion exclusion effects relating to the thickness of the electrical double layer (EDL) relative to the pore diameter, however, compromise the applicability of results obtained using these solutes for cation diffusion (although more so at low ionic strengths) and therefore they have not been used in the current site investigation. The choice of HTO as a reference tracer is motivated by the wish to obtain a quantification of the geometrical formation factor with a minimum of additional interacting processes that are strongly dependent on pore water chemistry /Widestrand et al. 2003/. Anion exclusion, however, may be important for transport processes of anions at low ionic strength in certain safety assessment scenarios.

Laboratory electrical resistivity measurements are performed also using 1–3 cm long drill core pieces and the formation factor is obtained as the ratio between the pore water resistivity and that of the (typically) brine saturated rock. This is possible owing to the analogy between diffusivity and ionic mobility as formalised in the Einstein relation /e.g. Atkins 1999/. Both alternating (AC) and direct (DC) current can be used for these measurements, although AC is frequently preferable owing to electrode polarisation effects arising when using DC methods. AC current also allows phase angle measurements to be made which can be helpful for identifying the presence of conductive minerals such as magnetite or excessive amounts of clay minerals which can lead to anomalous results /Thunehead 2005ab, 2007ab/.

Laboratory resistivity measurements can be performed relatively quickly, which enables testing of large numbers of samples. Thus, the majority of the laboratory formation factor data are from resistivity measurements. Electrical resistivity can also be measured by *in situ* methods using a resistivity logging tool /Löfgren 2004/. In laboratory measurements of resistivity, the rock samples are firstly saturated with a solution of known salinity (typically, $\geq$ 1 M NaCl), whereas *in situ* measurements rely upon accurate characterisation of the matrix porewater. This is typically done using flowing water in fractures as a proxy, although this implicitly assumes diffusive equilibrium between the matrix porewater and that sampled in the borehole. It is also possible to leach porewater from retrieved bore core samples to estimate the composition of the native porewater /Waber and Smellie 2008/. The *in situ* method can only be used for parts of the borehole where sufficiently strong saline conditions prevail that surface conduction artefacts are not an issue for result interpretation. The utility of this method and various issues related to its reliability are discussed in detail in Appendix H.

Sorption

The notion of sorption in the context of the site descriptive modelling relates to the adsorptive interaction of radionuclides with the surfaces of geological materials. As already discussed in section 2.2 this occurs principally by way of the association of ionic solutes with charged mineral surfaces. In the simplified approach to sorption modelling adopted within the site descriptive model, sorption processes are considered to be linear (no intrinsic concentration dependency) as well as being fast and reversible (chemical kinetics are not considered). The concept is the same as that described in the strategy report by /Widestrand et al. 2003/.

Within the laboratory programme the equilibrium sorption distribution coefficient, K_d is measured by batch sorption tests on crushed rock and unconsolidated fracture-filling materials. These measurements are performed in contact with different water compositions intended to

cover the range of groundwater chemistries likely to be encountered by transported solutes. As the crushing of rock samples results in the formation of additional sorption surface area that may not be representative of the *in situ* rock, sorption data for different size fractions can be used to extrapolate estimates for the sorption coefficient for the internal surfaces of the crushed rock material.

In the original strategy for laboratory methods to be used in the transport properties evaluation /Widestrand et al. 2003/, an extrapolation technique based upon linear regression of sorption measurement data for different crushed rock size fractions was recommended for the evaluation of the sorption on internal surfaces of the rock matrix. Specifically, the evaluation technique attempts to distinguish sorption on internal and external surfaces by relating the apparent partitioning ratio, R_d (m^3/kg) to the mass-based sorption coefficient on internal surfaces, K_d (m^3/kg) and surface area normalised sorption coefficient, K_a (m) for sorption on the external surfaces of crushed particles /Widestrand et al. 2003/:

$$R_d \approx K + \frac{6K_a}{\rho_{bm} d_p} \tag{4-3}$$

The values of K_a and K_d and their error estimates can be obtained by linear regression when data for more than one particle size fraction are available if it is additionally assumed that different particle size fractions have identical surface roughness/sphericity and are not fractionated with respect to mineral content. The characteristic particle size, d_p (m) is customarily assumed to be the volumetric mean size based upon the upper and lower sieve sizes bracketing the sample /e.g. Byegård and Larsson 2004/, while ρ_{bm} (kg/m^3) is the bulk density of the rock.

Owing to problems associated with the extrapolation of data, this technique was found to be unreliable, and a different strategy was adopted for SDM-Site Forsmark based upon direct application of the distribution coefficient measured for the largest size fraction (1–2 mm) at the longest contact time (180 days). Since the surface areas measured for particles in this size range are reasonably close to that measured for monolithic core samples thought to be representative of the *in situ* rock (see section 4.4.3), this is thought to be the most appropriate alternative evaluation method.

Association of transported radionuclides with secondary minerals at the fracture surfaces is typically assumed to be sufficiently fast at safety assessment timescales, that their diffusive properties do not need to be considered explicitly. These surface reactions are therefore considered to be independent of the flow related transport properties and are described as an instantaneous, equilibrium partitioning process. In the retardation model developed for the Forsmark site, these processes are described in terms of an equilibrium surface sorption coefficient, K_a (m) for the fracture coating. This is typically internalised in transport models in the form of a retardation coefficient, defined as:

$$R_a = 1 + \frac{2K_a}{\delta_t} \tag{4-4}$$

Where δ_t is the transport aperture governing the advective travel time within the flowing water.

Assuming fast diffusive equilibrium, the retardation coefficient for direct sorption at the fracture surface can also be defined in terms of the sorptivity (K_{ds}) of the fracture coating, its bulk density (ρ_{bs}), porosity (θ_s), and thickness (δ_{fs}) relative to the transport aperture:

$$R_a = 1 + \left(\theta_s + K_{ds}\rho_{bs}\right)\frac{2\delta_{fs}}{\delta_t} \tag{4-5}$$

For loose, unconsolidated particulates residing in the fracture such as fault gouge or breccia, the retardation coefficient can also be defined in terms of the corresponding material properties of the particulates (i.e. K_{dg}, ρ_{bg}, θ_g) and the relative void fraction, β_g they occupy in the fracture:

$$R_a = 1 + \left(\theta_g + K_{dg}\rho_{bg}\right)\left(\frac{\beta_g}{1-\beta_g}\right) \tag{4-6}$$

BET surface area and CEC

Since the sorption of radionuclides is a surface mediated process, the quantification of mineral surface area within the rock matrix and fracture coatings is a valuable proxy for understanding sorption property variability. The sorption of many radionuclides has been observed to be strongly correlated with mineral surface area /e.g. Bertetti et al. 1996, 1998, Pabalan et al. 1998, Prikryl et al. 2001/. The correlation is expected to be quite strong for radionuclides that sorb mostly by way of a surface complexation mechanism and to some extent independent of the type of mineral phases present /Turner and Pabalan 1999/. This is thought to be because the variably charged, surface functional groups of most silicate materials are similar and consist of a mixture of amphoteric silanol and aluminol reactive sites /Bradbury and Baeyens 1997/. Sorption is not restricted to silicate minerals, however, and the different ferric oxides which may be present in the rock as oxidation products can strongly sorb cations that form surface complexes /e.g. Jakobsson 1999/. This is partly to do with their large surface area, but also due to the fact that they generally function as much stronger surface ligands than the corresponding reactive sites on silicate minerals.

For permanently charged sites that are known to be important for ion-exchange, there is also a correlation between sorptivity and surface area although the correlation is less strong owing to the fact that not all minerals sorb equally well. It is well known for example that mica minerals such as biotite and its alteration product chlorite can have a disproportionate effect upon the sorption of ion exchangers in granitic rocks /e.g. Torstenfelt et al. 1982/. The sorption of ion exchangers is sometimes more closely related to the cation exchange capacity, CEC of the rock than the surface area.

The surface area of mineral phases within the rock available for sorption is measured using the BET method /Brunauer et al. 1938/ which is based upon the adsorption of gas probe molecules to a surface. Although it is difficult to establish a direct quantitative relationship between bulk surface area and sorption site density for a mixed mineral system, the results of BET surface measurements are included in the retardation model as a qualitative proxy for sorption that is useful for understanding observed sorption processes.

BET measurements have been performed on site-specific materials according to the ISO 9277 standard method. Three types of measurements have been performed for the Forsmark site specific material.

For drill core samples, crushing and sieving was performed. The particle size fractions 63–125 μm and 2–4 mm were measured in duplicate samples for each fraction. A simple linear extrapolation technique was used to distinguish internal and external surface area in a similar fashion to that used for sorption data (analogous to Equation 4-3):

$$A_{BET} = A_{INT} + A_{EXT} = A_{INT} + \frac{6\lambda}{\rho_b d_p} \qquad (4\text{-}7)$$

Here, A_{BET} (m^2/g) is the total surface area measured using the BET method, A_{INT} (m^2/g) is the surface area of internal microsurfaces within the particle, A_{EXT} (m^2/g) is the external surface area of the particle, and λ (m^2/m^2) is the so-called surface roughness of the particle which is an empirical factor that takes into account both the true surface roughness of the particle and deviation from sphericity ($\lambda = 1$ for a sphere). The linear extrapolation procedure implicitly assumes that the A_{INT} and λ are constant across different size fractions.

For natural fracture samples, surface material was abraded by scraping the fracture surfaces. The size fraction < 125 μm was then isolated by sieving of the abraded material and measured in duplicate samples.

In addition to these measurements, an attempt was also made to measure the BET surface area for a small number of monolithic samples thought to be representative of the intact rock.

The method (ISO 13536) employed for CEC measurement, although thought to be very reliable for soil investigations, was found to be less useful for crushed rock samples owing to their relatively low exchange capacities. For this reason, the CEC values presented in the property tables should be considered to be only semi-quantitative estimates.

4.3.2 Data from the laboratory programme

The laboratory investigations have been designed with the aim of providing site-specific data for storage porosity, sorption, and diffusive properties of different rock types and geologic materials associated with fracture surfaces. Bore core samples for these measurements have been selected from several boreholes in accordance with the guidelines described in /Widestrand et al. 2003/. Since the laboratory measurements of diffusion and sorption are very time consuming, a majority of the rock samples are collected from the first five cored boreholes investigated (KFM01A–KFM06A). In order to describe the spatial heterogeneity of the retardation parameters as well as possible effects of stress release, rock samples were selected from a range of different depths in the boreholes. In order that the material properties data reflect the properties of flowing features as far as possible, the selection of samples from open fractures was directed by indications of water flow as recorded in flow logs when available. For deformation zones, indications of both water flow and wall rock alteration were considered during the selection of representative samples. An overview of the available transport laboratory data can be found in Table 4-5.

Since the geological model was updated continually during the site investigations it has not been possible to include rock core samples selected on the basis of the last stages of the geological and hydrogeological modelling work. Notwithstanding this, the sample set has been found to be representative for the target volume with respect to the major (101057) and minor rock types, different fracture classes as well as structural elements sampled from important transmissive deformation zones such as ZFMA2. Consequently, there is a good representation of samples from rock domain RFM029, although RFM045 is relatively poorly represented. A few rock samples, for example from a tonalitic rock type (101054), are not directly representative of the target volume since the rock domain where the sample was taken from (RFM017) is excluded from the present focused area.

Table 4-5. Rock sample data included in the retardation model. Note that a rock sample is considered as one sample-ID; e.g. KFM01A_103 m. BET and CEC measurements are performed on two different crushed size fractions. Batch sorption measurements are performed on two different size fractions for a number of different radionuclides and water types.

Method	Total samples	Number of rock type samples	Number of fracture type samples	Number of samples representative of deformation zones
Porosity (water saturation)	211	182	–	29
PMMA	13	5	1**	6
Electric resistivity (lab)	163	142	–	21
Through diffusion	72	50	–	22
BET (crushed rock)	46	29	12	5
BET (whole core)	4	4	–	–
CEC	9	4	2(3)	3
Batch sorption (crushed rock)	17	6	6	4
Batch sorption (whole core)	4	4	–	–

* Including rock samples with faint to weak oxidation.
** Porosity measured orthogonally across an annealed fracture surface.

4.4 Material properties data

In this section the material properties data used to parameterise the retardation model are discussed.

4.4.1 Porosity

The results of the porosity measurements are summarised in Table 4-6. The detailed geological characterisation performed using a binocular microscope found several samples to have small cracks 3–15 mm in length and with a width of ≤ 0.5 mm, in both fresh and altered rock samples. These cracks are larger than intragranular micro cracks /Stråhle 2001/, and cut through mineral grains. Comparison of the porosities determined for samples with and without observable micro cracks (as described in Table 4-6), indicates that these cracks give rise to an apparently higher porosity.

The samples have been further categorised with respect to whether they originate in deformation zones (DZ), or not (N). The results indicate virtually no difference in the median values of the porosity measured for the two sample sub-categories. There is, however, some indications that there is an over-representation of the highest porosity amongst the samples from deformation zones.

Table 4-6. Porosities (vol%) of different rock types from the Forsmark area considering only samples without visible open fractures. Data are given as the arithmetic mean (± standard deviation), median, minimum, and maximum values for the specified numbers (n) of samples involved in the study. The entries in the column labelled DZ identifies whether the corresponding rows of data are based upon deformation zone (DZ) materials or non-deformed host rock (N).

Rock type (SKB code)	All rock samples						Rock samples without visible open fractures fractures				
	DZ	Mean ± σ	Median	Min.	Max.	n	Mean ± σ	Median	Min.	Max.	n
Granite, granodiorite and tonalite, metamorphic, fine- to medium-grained (101051)	N	0.23 ± 0.09	0.22	0.10	0.54	26	0.23 ± 0.09	0.22	0.10	0.54	25
	DZ	0.55 ± 0.54	0.38	0.13	1.6	6	0.32 ± 0.20	0.28	0.13	0.59	4
Granite to granodiorite, metamorphic, medium-grained, vuggy rock samples excluded. (101057)	N	0.24 ± 0.13	0.22	0.03	0.89	108	0.23 ± 0.11	0.22	0.03	0.89	106
	DZ	0.9 ± 2.2	0.24	0.17	9.19	33	1.0 ± 2.4	0.22	0.17	9.19	27
Pegmatite, pegmatitic granite (101061)	N	0.4 ± 0.25	0.27	0.24	0.68	3	0.32	–	–	–	1
Amphibolite (102017)	N	0.16 ± 0.10	0.10	0.08	0.30	5	0.16 ± 0.10	0.10	0.08	0.30	5
	DZ	5.15 ± 6.8	5.15	0.34	9.95	2	0.30	–	–	–	1
Granodiorite, metamorphic (101056)	DZ	0.34 ± 0.21	0.34	0.19	0.48	2	0.34 ± 0.21	0.34	0.19	0.48	2
Felsic to intermediate volcanic rock, metamorphic (103076)	N	0.36	–	–	–	1	0.36	–	–	–	1
	DZ	0.78	–	–	–	1	0.78	–	–	–	1
Tonalite to granodiorite, metmorphic (101054)	N	0.16 ± 0.03	0.16	0.11	0.19	4	0.16 ± 0.03	0.16	0.11	0.19	4
Granite, metamorphic, aplitic (101058)	N	0.22 ± 0.06	0.22	0.18	0.26	2	0.22 ± 0.06	0.22	0.18	0.26	2
Granite, fine to medium-grained (111058)	N	0.32 ± 0.06	0.32	0.28	0.36	2	0.32 ± 0.06	0.32	0.28	0.36	2

For the 101057 rock type, an additional categorisation has been performed in which the visible alteration of the samples has been used as a distinguishing parameter for the porosity interpretation. The results shown in Table 4-7 indicate, not surprisingly, that there is a much higher representation of strongly and medium altered rock in the deformation zones compared to the non deformation zone samples. The porosities of the altered samples taken from deformation zones are also higher than for the samples without visible traces of strong or medium alteration. A similar comparison between samples from non-deformation zones, however, shows no significant increase in porosity for the altered samples. It should be remembered that this comparison (particularly the latter) is based on a quite limited number of samples and may not be statistically significant.

Porosity measurements were performed on samples representing the four different deformation zone structural elements discussed in section 4.2.1. The results are presented in Table 4-8 and can be summarised as:

For the Fault rock, (strongly tectonised and partly incohesive material), an average porosity of ~ 10% has been estimated using the PMMA technique. The porosity is, however, heterogeneously distributed and less altered grains may have a porosity < 2%.

The sealed fracture network sample (breccia/cataclasite) was found to have an average porosity of 3%, determined by the PMMA technique. A very pronounced heterogeneity of the porosity distribution is found with the large grains having low porosity and the interspersed, more fine-grained matrix having regions of very high porosity.

The strongly altered vuggy rock samples show a very significant increase in porosity compared to all other rock types included in this study. This is due to the quartz dissolution that this type of rock has undergone; resulting in “porosity” with mm-scale voids heterogeneously distributed in the rock. This rock type is considered as a deformation zone element, since it is known to be only associated with deformation zones.

For the oxidized wall rock (medium and strong alteration), the reported porosity is based upon samples of the metagranite rock type 101057 which, in the stereo microscope investigation, were found to be strongly or medium altered.

Table 4-7. Porosities (vol%) of different sample categories from the Forsmark area for the 101057 rock type based on the alteration of the samples. The entries in the column labelled DZ identifies whether the corresponding rows of data are based upon deformation zone (DZ) materials or non-deformed host rock (N). The alteration analyses based on the binocular inspection of the individual drill core samples. Samples having observable open fractures have also been excluded.

Sample category	DZ	Mean ± σ	Median	Min.	Max.	n
All samples	N	0.23 ± 0.11	0.22	0.03	0.89	106
With observation of medium or strong alteration	N	0.24 ± 0.06	0.26	0.15	0.29	4
Without observation of medium or strong alteration	N	0.23 ± 0.12	0.22	0.03	0.89	102
All samples	DZ	1.0 ± 2.4	0.22	0.17	9.19	27
With observation of medium or strong alteration	DZ	2.5 ± 3.8	0.54	0.18	9.19	9
Without observation of medium or strong alteration	DZ	0.25 ± 0.10	0.22	0.17	0.62	18

Table 4-8. Porosities (vol%) of different deformation zone structural elements from the Forsmark area. Data are given as the arithmetic mean (± standard deviation), median, minimum, and maximum values for the specified numbers (n) of samples involved in the study.

Structural element	All rock samples					Comments
	Mean ± σ	Median	Min.	Max	n	
Fault rock (breccia and cataclasite)	10	10	–	–	1	Determined by PMMA-impregnation /Penttinen et al. 2006/
Sealed fracture network	3	3	–	–	1	Determined by PMMA-impregnation (very heterogeneously distributed porosity) /Penttinen et al. 2006/
Vuggy rock (101057)	13 ± 6	16.28	2.36	19.33	16	Water saturation measurement
Oxidised wall rock (medium and strong alteration)	2.5 ± 3.8	0.54	0.18	9.19	9	Water saturation measurement. (selected from the medium and strongly altered samples of rock type 101057 located in deformation zones)

4.4.2 Effective diffusivity

Through-diffusion measurements

The measurements of effective diffusivity using the through-diffusion measurement technique indicate formation factors in the range of 1.0×10^{-4} to 1.5×10^{-4} for the major rock types (101057 and 101051). Exceptions are amphibolite (102017) which seems to have a somewhat lower diffusivity, and Felsic to intermediate volcanic rock, metamorphic (103076) which has a higher porosity than average and is also associated with higher diffusivity. It is noted, however, that with the exception of the more frequently occurring rock types (101057 and 101051) the number of samples are low and the statistical basis for differentiating the diffusive properties of these rock types is questionable.

Table 4-9. Formation factors (F_f) of different rock types from the Forsmark area determined from the through-diffusion experiments and electrical resistivity measurements (red text). The arithmetic mean (± standard deviation), median, minimum, maximum values are given for the specified numbers (n) of samples involved in the study. The entries in the column labelled DZ identifies whether the corresponding rows of data are based upon deformation zone (DZ) materials or non-deformed host rock (N).

Rock type	DZ	Mean ± σ	Median	Min.	Max.	n
Granite, granodiorite and tonalite, metamorphic, fine- to medium-grained (101051)	N	$(1.0 \pm 0.8)\times10^{-4}$	1.0×10^{-4}	4.1×10^{-5}	1.6×10^{-4}	2
	DZ	$(2.3 \pm 2.1)\times10^{-4}$	1.5×10^{-4}	1.0×10^{-4}	7.6×10^{-4}	12
Granite to granodiorite, metamorphic, medium-grained, vuggy rock samples excluded. (101057)	N	$(1.6 \pm 1.5)\times10^{-4}$	1.2×10^{-4}	4.7×10^{-5}	6.8×10^{-4}	18
	N	$(3.2 \pm 3.2)\times10^{-4}$	2.5×10^{-4}	6.6×10^{-5}	2.8×10^{-4}	83
	DZ	$(1.1 \pm 1.0)\times10^{-4}$	5.2×10^{-5}	2.5×10^{-5}	3.6×10^{-4}	14
	DZ	$(2.0 \pm 1.2)\times10^{-4}$	1.5×10^{-4}	4.1×10^{-5}	4.0×10^{-4}	14
Deformation zone, category 3, Vuggy rock (101057)	DZ	$(1.2 \pm 0.8)\times10^{-2}$	1.5×10^{-2}	5.2×10^{-4}	2.3×10^{-2}	12
Amphibolite (102017)	N	2.9×10^{-5}	2.9×10^{-5}	–	–	1
	DZ	2.3×10^{-5}	2.3×10^{-5}	–	–	1
Felsic to intermediate volcanic rock, metamorphic (103076)	N	5.7×10^{-4}	5.7×10^{-4}	–	–	1
Tonalite to granodiorite, metmorphic (101054)	N	$(7.8 \pm 7.4)\times10^{-4}$	8.1×10^{-5}	7.0×10^{-5}	8.3×10^{-5}	3
Granite, metamorphic, aplitic (101058)	N	$(1.8 \pm 1.7)\times10^{-4}$	1.8×10^{-4}	6.2×10^{-5}	3.0×10^{-4}	2

An attempt has been made to study the influence of the porosity on the formation factor. The different formation factors determined by through diffusion experiments are presented in Figure 4-9 as of function of their porosity as measured by the water saturation technique. When considering the complete data set including highly porous samples, an approximate fit could be interpreted from the data. At the very low porosities characteristic of the bulk of the measurements, however, the utility of the Archie's law relation can be questioned for the description of the macroscopic diffusive properties of the different rock types. The large scatter of data at low porosities (< 1%) seems to indicate that the effective tortuosity/constrictivity of the diffusion paths is highly variable and may determine the magnitude of the formation factor to a greater extent than the total porosity of the sample. A greater proportion of the total porosity being in the form of dead-end pores which do not actively contribute to the diffusion of tracer could also be inferred from the results.

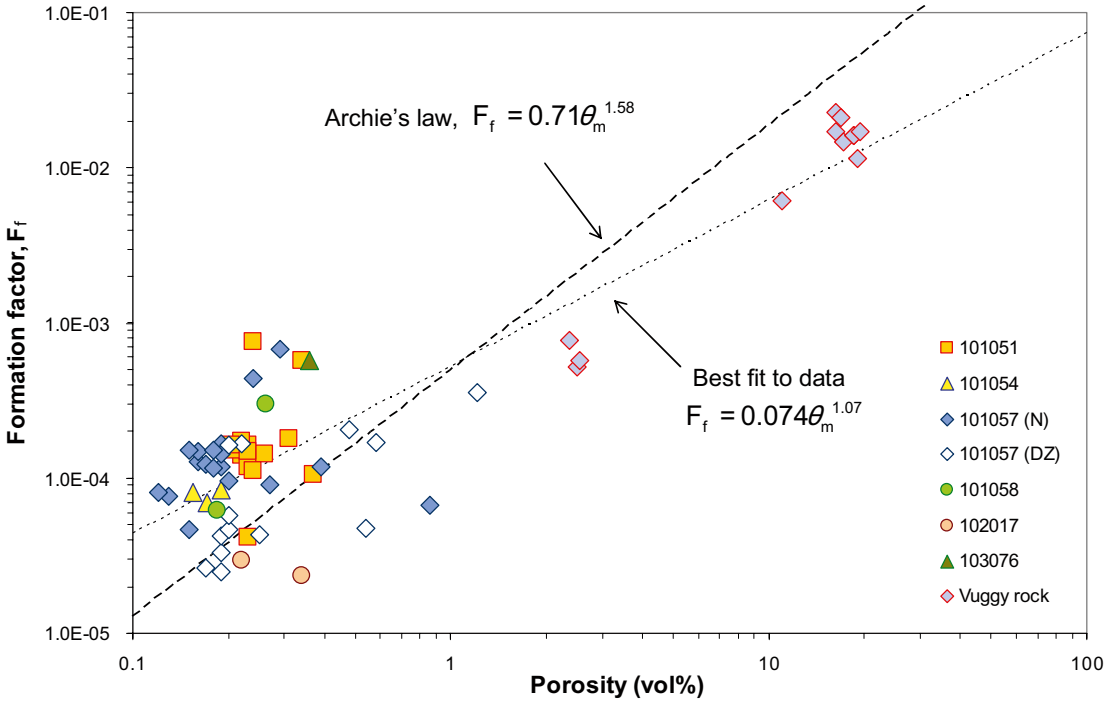

Figure 4-9. *Formation factor determined from through diffusion measurements vs. porosity measured by the water saturation method (SS-EN 1936). A comparison is made to the relation known as Archie's law /Parkhomenko 1967/ and a similar power law fit to the actual measurement results obtained in this investigation.*

Electrical resistivity measurements

A summary of the results of electrical resistivity measurements used to estimate formation factors is provided in Table 4-9. Some general observations based upon these results are presented in the following paragraphs.

An investigation has been made where the formation factors of 31 samples, previously used for through diffusion experiments, were measured using the electrical resistivity method. The results shown in Figure 4-10 indicates that the laboratory-based, electrical resistivity method tends to give higher formation factors than those obtained using the through diffusion method. There are, however, large variations in the results. The ratio between the resistivity measurement and the through diffusion measurement has been found to be in the range 2.2 ± 1.2. At the present time a cogent explanation for this deviation is not available, although it is highly consistent with results of previous studies indicating a physical mechanism that is conserved between different investigations. Further discussion concerning this can be found in Appendix H.

This trend is also consistent with the finding of the difference of the formation factors for the 101057 rock type (Table 4-9) where ratios of 2.1 and 2.9 between the median values for the non deformation zone samples and the deformation zone samples are found.

Comparisons have also been made between the samples used for through diffusion experiments and the results of the in situ resistivity measurements for the exact location of the sample used in the laboratory investigation. The results show that, unlike the laboratory resistivity measurements, the in situ resistivity measurements are associated with significantly lower formation factors as compared to the data obtained from through-diffusion measurements.

Formation factors which are presented in the retardation model tables (section 4.5) in this report are based upon both measurement techniques. The only exception is for rock type 101061 (Pegmatite, pegmatic granite) where only laboratory resistivity measurements were available. In that particular case, the formation factor from the resistivity measurement, 4.4×10^{-4} was divided by a factor of 2.2 derived from the comparative measurements to account for the empirical measurement bias, thereby giving a formation factor of 2×10^{-4}.

It could be argued that the through-diffusion technique is the method that best simulates the actual physical process aimed to be studied (i.e. solute diffusion in the porewater) and that the electrical resistivity technique may be influenced by artefacts that are not, as yet fully understood which give rise to the empirical deviation of roughly a factor of two. It is noted, however, that the empirically observed deviation is so consistent and conserved between different investigations that there are good arguments for using a simple empirical correction even in the absence of a full mechanistic explanation of the effect. A detailed discussion concerning the issues related to use of the electrical resistivity measurement technique can be found in Appendix H where the use of *in situ* formation factors derived from borehole resistivity logging is discussed. A large amount of data derived from the *in situ* measurements is also presented there and sorted according to rock type for comparative purposes.

A cross-plot of formation factors as determined by resistivity measurements and through-diffusion measurements is given in Figure 4-10. As can be seen from the Figure, resistivity measurements made in the lab have a tendency to estimate formation factors about double that of the through-diffusion method. The formation factor given by the nearest comparable *in situ* resistivity measurement, on the other hand, typically gives values that are less than the through-diffusion method. As discussed in detail in Appendix H, formation factors derived from laboratory resistivity measurements of core samples are typically about an order of magnitude higher than the corresponding *in situ* resistivity measurement values for the same locations in the borehole.

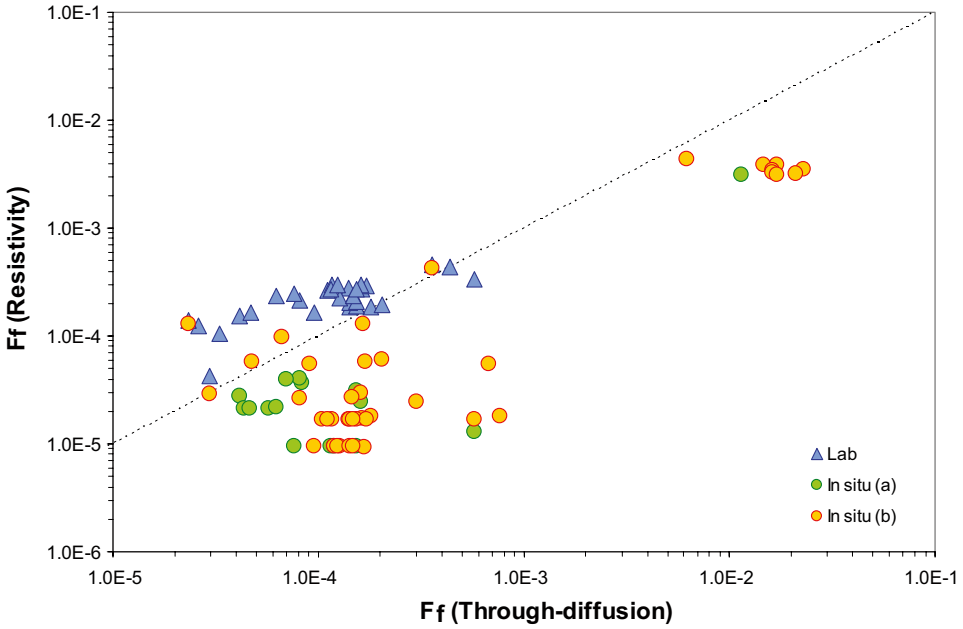

Figure 4-10. *Cross-plot comparison of the formation factor determined by the electrical resistivity method (vertical axis) vs. through diffusion (horizontal axis). The results from the in situ resistivity measurements have been divided into two groups of measurements; a) measurement points in proximity (≤ 0.5 m) to known open fractures and, b) measurement points distant (≥ 0.5 m) from known open fractures.*

4.4.3 BET surface area

As described previously, drill core samples were firstly crushed and sieved and then the BET surface area of the size fractions 0.063–0.125 mm and 2–4 mm was measured in duplicate samples for each size fraction. The extrapolation technique described in section 4.3.1 (Equation 4-7) was employed to estimate the inner surface BET area of the samples. The results of these measurements are given in Table 4-10.

Samples of loose fracture surface coatings were obtained by mechanical abrasion and the < 125 µm fraction was isolated through sieving of the collected material. The BET surface area was then measured in duplicate samples. The results of these measurements are given in Table 4-11 without extrapolation since they are already in a friable condition which is considered to be their natural state.

Comparison of the results for different rock types

The results of the BET surface area measurement are presented in Table 4-10 and Table 4-11. The major finding is the large difference between the non-altered samples compared to altered rock and fracture surfaces.

The latter group tends to be over-represented by small size fractions which, for geometrical reasons, is presumed to give higher BET surface areas. Nevertheless, comparison of the results within the smaller size fraction cohort (see Figure 4-11) shows that fracture filling material in several cases has surface areas ~ 50 times higher than the major rock type 101057. From these results alone it can be deduced that the rock material in, or adjacent to the fractures could, if sufficiently thick, constitute a non-negligible sink for retention of radionuclides in safety assessment. This would give enhanced retardation of radionuclide transport for early solute breakthrough compared to that achieved if only the unaltered rock matrix is considered.

Table 4-10. Measured BET surface area (m^2/g) of crushed rock samples for the size fractions 0.063–0.125 mm and 2–4 mm. The arithmetic mean (± standard deviation), median, minimum, maximum values are given for the specified numbers (n) of samples involved in the study. The entries in the column labelled DZ identifies whether the corresponding rows of data are based upon deformation zone (DZ) materials or non-deformed host rock (N).

Rock type (SKB code)	DZ	Size fraction	Mean ± σ	Median	Min.	Max.	n
101051	N	0.063–0.125 mm	0.22 ± 0.12	0.24	9×10^{-3}	0.34	14
	N	2–4 mm	0.023 ± 0.014	0.024	2×10^{-3}	0.048	14
101057	N	0.063–0.125 mm	0.19 ± 0.16	0.19	0.07	0.29	27
	N	2–4 mm	0.025 ± 0.015	0.026	3×10^{-4}	0.058	27
101057 (medium alteration)	N	0.063–0.125 mm	0.74 ± 0.01	0.738	0.732	0.745	2
	N	2–4 mm	0.342 ± 0.01	0.342	0.335	0.349	2
101054	N	0.063–0.125 mm	0.27 ± 0.03	0.27	0.25	0.29	2
	N	2–4 mm	0.043 ± 0.01	0.042	0.036	0.049	2
101061	N	0.063–0.125 mm	0.307 ± 0.02	0.307	0.296	0.318	2
	N	2–4 mm	0.052 ± 0.005	0.052	0.048	0.055	2
	DZ	0.063–0.125 mm	0.23 ± 0.01	0.233	0.227	0.239	2
	DZ	2–4 mm	0.025 ± 0.007	0.028	0.0205	0.03	2
102017	N	0.063–0.125 mm	0.051 ± 0.05	0.052	7×10^{-3}	0.095	4
	N	2–4 mm	$(2.5 \pm 2.1)\times10^{-4}$	2.5×10^{-4}	1×10^{-4}	4×10^{-4}–	2
	DZ	0.063–0.125 mm	0.316 ± 0.02	0.316	0.304	0.327	2
	DZ	2–4 mm	0.0385 ± 0.001	0.0385	0.038	0.039	2
101058	DZ	0.063–0.125 mm	0.183 ± 0.0014	0.183	0.182	0.184	2
	DZ	2–4 mm	0.052 ± 0.004	0.052	0.049	0.055	2
1013076	N	0.063–0.125 mm	0.205 ± 0.003	0.205	0.203	0.207	2
	N	2–4 mm	0.047 ± 0.006	0.047	0.042	0.051	2

Table 4-11. Measured BET surface area (m^2/g) of mineral coatings associated with fracture types and deformation zone material. Data are given for the crushed rock size fractions 0.063–0.125 mm and 2–4 mm where available. For material that is initially in a disaggregated state, only the smaller size fraction is given. The arithmetic mean (± standard deviation), median, minimum, maximum values are given for the specified numbers (n) of samples involved in the study.

Description	Size fraction	Mean ± σ	Median	Min.	Max.	n
Fracture type A	0.063–0.125 mm	0.49 ±	0.49	0.41	0.56	2
Fracture type B	0.063–0.125 mm	10.3 ±	10.3	10.0	10.6	2
Fracture type C	0.063–0.125 mm	2.3 ± 0.6	2.4	1.7	2.9	3
Fracture type D	0.063–0.125 mm	5.1 ± 2.2	4.0	3.7	7.7	3
Fracture type E	0.063–0.125 mm	0.42 ± 0.02	0.43	0.09	0.43	6
	2–4 mm	$(2.5 \pm 2.1)\times10^{-4}$	2.5×10^{-4}	1×10^{-4}	4×10^{-4}	2
Fracture type F	0.063–0.125 mm	2.2 ± 1.1	2.0	1.2	3.3	3
	2–4 mm	2.98	2.98	–	–	1
Fracture type G	0.063–0.125 mm	4.3 ± 1.4	4.3	3.3	5.3	2
	2–4 mm	1.67 ± 0.01	1.67	1.66	1.68	2
DZ (Category 1) Fault rock	0.063–0.125 mm	5.6 ± 2.3	5.6	3.6	7.6	4
	2–4 mm	1.98 ± 0.06	1.98	1.94	2.02	2
DZ (Category 2) Sealed fracture network	0.063–0.125 mm	0.64 ± 0.04	0.64	0.61	0.67	2
	2–4 mm	0.78 ± 0.14	0.78	0.69	0.88	2
DZ (Category 3) Vuggy rock	0.063–0.125 mm	1.58 ± 0.01	1.58	1.57	1.59	2
	2–4 mm	0.27 ± 0.01	0.27	0.26	0.28	2
DZ (Category 4) Oxidised wall rock	0.063–0.125 mm	0.77 ± 0.01	0.77	0.76	0.78	2
	2–4 mm	0.196 ± 0.01	0.195	0.189	0.202	2

BET surface area vs particle size

It is thought that crushing of samples can give rise to as much as 1–2 orders of magnitude increase in surface area as compared to undisturbed rock /e.g. Crawford et al. 2006/. Since sorption is strongly related to surface area, the additional surfaces created in the crushing process may give strongly biased overestimates of the sorption capacity of the rock. One of the main purposes of the BET surface area measurements was therefore to ascertain how much new surface area is created in the crushing process that is non-representative of the intact, *in situ* rock.

In the laboratory strategy document /Widestrand et al. 2003/ for the batch sorption experiment, it is suggested that if the largest size fraction of crushed rock has a surface area > 75% of that of the smallest fraction, then the creation of new surfaces during crushing can be assumed to be negligible. In this case, to avoid diffusive disequilibrium effects, it is recommended the smallest size fraction is used and the solute distribution coefficient (R_d) thus obtained used directly as the K_d for the *in situ* rock.

If, on the other hand, the BET-measurements show the surface area of the largest size fraction is < 75% of that measured for the smallest size fraction it can be concluded that a significant fraction of the surface area of the smaller fraction is created during the crushing of the rock material and the crushed rock is therefore not representative for the intact rock. In this case, the measured solute distribution coefficient is taken to be equal to the sum of the sorption on internal surfaces (deemed relevant for *in situ* conditions) and sorption on external particle surfaces (not representative of intact rock).

In order to differentiate between the sorption on internal and external surfaces, it was proposed that three different size fractions should be used for the batch sorption experiment (0.045–0.090 mm, 0.25–0.5 mm, 1–2 mm) and extrapolation of the results should be made in accordance with Equation 4-3.

As can be seen in Figure 4-11 and Figure 4-12 there is a clear and significant increase of the total specific surface area with decreasing particle size. It appears that the increase is proportionately greater for the crushed fresh rock material than for fracture material and altered rock material.

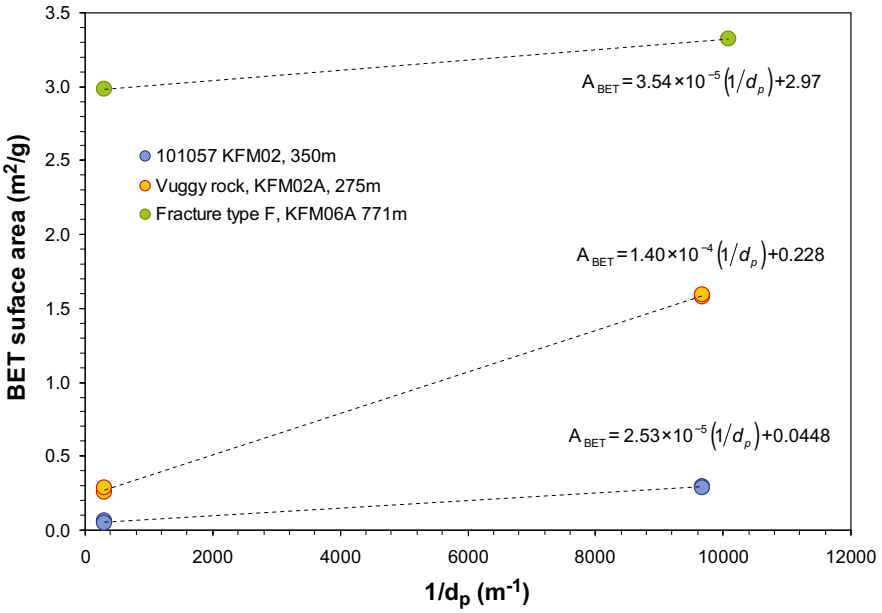

Figure 4-11. *Examples of BET surface areas as a function of the inverse of the particle size (volumetric mean of bracketing sieve sizes) of the rock material used.*

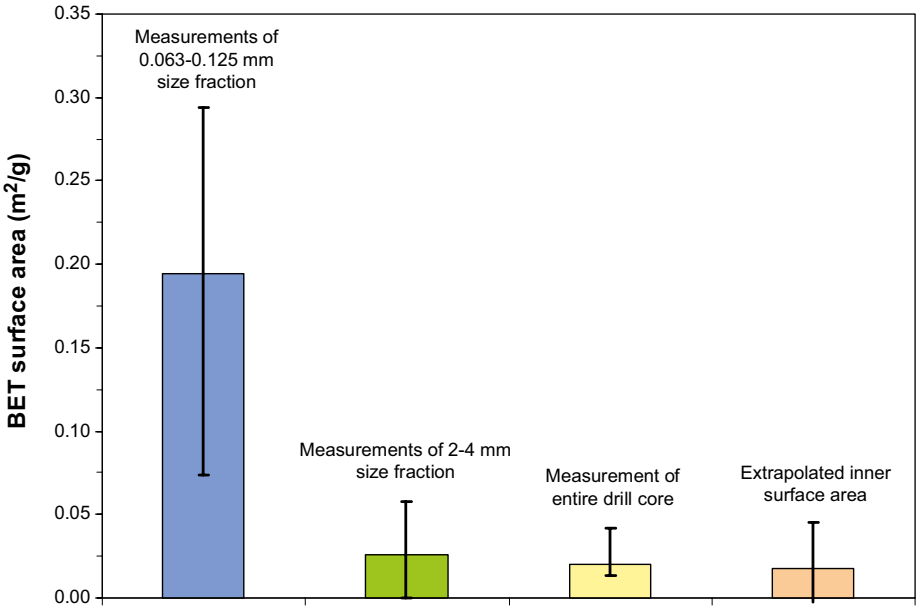

Figure 4-12. *Comparison between the results of the total number of BET surface area measurement of the 101057 rock type. The illustrated values refer to the median values and the error bars give the uncertainty represented by the minimum and maximum values obtained for all the measurements.*

The increase, however, is generally lower than what would be expected for ideally spherical shaped particles since a strictly geometrical model would yield an increase of the specific surface area by a factor of roughly 32 from the 2–4 mm size fraction to the 0.063–0.125 mm size fraction. For the non-altered metagranite rock type (101057), for example, the increase in surface area is roughly a factor of 7 which could be regarded as an indication a significant fraction of sampled surface area in the larger size fraction being in the form of "inner surfaces".

When considering the comparatively large number of samples investigated belonging to the main metagranite rock type (101057), a large variation is nevertheless observed. This observation concerns both the measured replicate values within the individual size fractions as well as for the ratios between the two measured size fractions. Provided that the BET surface measurement procedure gives reliable values, this could be an indication of a considerable heterogeneity even within what is identified as a single rock type. The large BET-surface area measured for the strongly altered 101057 rock type (~ 5–10 times higher than for the corresponding non-altered rock), could indicate that there will be an influence of alteration on the BET surface area even at levels of alteration barely observable by visual inspection.

A comparative measurement campaign was performed in which the BET surface area of crushed material in the size fractions 0.063–0.125 mm, 2–4 mm and intact drill core samples of diameter 56 mm were compared. The results shown in Figure 4-12 indicate that a reasonable agreement is obtained (given the uncertainties) for the larger size fraction, the intact drill core, and the inner surface area extrapolated from the data for each size fraction using Equation 4-7.

From this finding it is postulated that the sorption measured for the largest size fraction should give results that are most representative of the intact, *in situ* rock assuming that the measured sorption occurs upon inner surfaces of the mineral grains accessible by diffusion.

4.4.4 Sorption

The results for the sorption coefficients selected from the large database of measurement results reported in Sicada are presented in Table 4-12 to Table 4-22. Sorption coefficients are thus presented for the different groups of geological materials, sorted according to:

- Major rock types.
- Different fracture types.
- Four different deformation zone structural elements.

Some general comments can be made concerning the results:

For the Sr(II) tracer, the sorption loss from the aqueous phase can only be statistically verified for the fresh groundwater (with a few exceptions). For the other groundwater types, the high salinity promotes a strong competition for the sorption sites, giving very low adsorption. This can be seen in the minimum values, which can include negative values, indicating that the sorptive effect is smaller than the standard deviation of the measurement for the blank solution.

Similarly to Sr(II), the sorption behaviour of both Ra(II) and Cs(I) was strongly influenced by the water composition. This is to be expected from their cationic exchange behaviour, which results in decreasing sorptivity with increasing salinity owing to competition for sorption sites.

In the laboratory programme, Am(III) and in some cases Eu(III) were used as model substances to simulate the sorption of the trivalent actinides and lanthanides which are loosely referred to in this report as Ac-Ln(III) (this abbreviation should not be taken to specifically mean either actinium or lanthanum). These substances were found to sorb very strongly. Even in the blank sample for groundwater without any geological material present, a strong loss of the tracer can be observed which is thought to be the result of adsorption on test tube walls or possibly the formation of so-called “intrinsic” colloids (i.e. microprecipitation of hydrolysed solute species in suspension). Thorough investigations of these samples have, however, shown that in samples with rock material present, the amount of tracer associated the test tube walls is negligible compared to the sorption on the rock material.

Salinity does not appear to strongly influence the sorption of the trivalent Ac-Ln(III) tracer, the redox sensitive elements U and Np, nor Ni(II). This is expected behaviour since the major sorption mechanism for these tracers is thought to be surface complexation rather than cation exchange.

The sorption of the redox sensitive elements Np and U is comparatively low indicating the presence of the oxidized Np(V) and U(VI) species, respectively. For some of the measurements, a pronounced increase of the sorption can be found for the smallest size fraction. The increase is much higher than what should be expected from the relative BET surface areas of the different size fractions. A possible explanation for this is that minerals having enhanced reducing capacity have been enriched in the smaller size fraction during the crushing and sieving process. It is also possible that the increased surface area of the small particle size fraction results in an increased rate of weathering reactions involving Fe(II)-containing silicate minerals. These processes could result in the reduction of Np and U species to Np(IV) and U(IV) in these samples. Since the redox status is not well known for these solutes in the batch sorption experiments, they are listed in the data Tables as Np(IV/V) and U(IV/VI) to make this uncertainty clear to the reader.

The time dependence of tracer loss in the aqueous phase can, in a number of cases, be potentially interpreted as the result of solute diffusion within the internal microporosity of the crushed particles. The magnitude of the tracer loss time dependency is consistent with a spherical diffusion model /Crank 1975/ assuming effective diffusivities similar to those predicted for the rock matrix. There are, however, additional uncertainties in the data analysis which makes this interpretation speculative. The different processes which may contribute to the apparent time dependency of solute uptake will be examined in more detail during the selection of data for SR-site.

Sorption properties of specific rock types

Table 4-12. Measured sorption coefficients, R_d (m^3/kg) for rock type 101057 (unaltered) based upon the 1–2 mm size fraction and a contact time of 180 days. The arithmetic mean (± standard deviation), median, minimum, maximum values are given for the specified numbers (n) of samples involved in the study.

Solute		Groundwater type			
		Marine	Saline	Fresh	Brine
Cs(I)	mean ± σ	$(3.6 \pm 2.5)\times10^{-3}$	$(4.0 \pm 1.6)\times10^{-3}$	$(1.9 \pm 0.7)\times10^{-2}$	$(1.8 \pm 0.6)\times10^{-3}$
	median	2.5×10^{-3}	3.1×10^{-3}	1.7×10^{-2}	1.7×10^{-3}
	max.	8.6×10^{-3}	7.3×10^{-3}	3.1×10^{-2}	2.8×10^{-3}
	min.	9.8×10^{-4}	1.5×10^{-3}	1.2×10^{-2}	1.1×10^{-3}
	n	12	17	11	11
Sr(II)	mean ± σ	$(3.8 \pm 16.0)\times10^{-4}$	$(2.4 \pm 8.1)\times10^{-4}$	$(4.6 \pm 3.2)\times10^{-3}$	$(2.1 \pm 6.5)\times10^{-4}$
	median	2.8×10^{-5}	9.2×10^{-5}	3.8×10^{-3}	2.5×10^{-5}
	max.	3.4×10^{-3}	2.0×10^{-3}	1.1×10^{-2}	2.1×10^{-3}
	min.	-1.3×10^{-3}	-8.0×10^{-4}	7.0×10^{-4}	-5.0×10^{-4}
	n	12	17	11	11
Ln-Ac(III)	mean ± σ	$(8.4 \pm 9.7)\times10^{-1}$	$(5.6 \pm 2.3)\times10^{-1}$	$(1.3 \pm 1.3)\times10^{-1}$	$(3.9 \pm 2.2)\times10^{-1}$
	median	4.1×10^{-1}	5.2×10^{-1}	7.6×10^{-2}	3.9×10^{-1}
	max.	3.2	1.2	3.8×10^{-1}	8.2×10^{-1}
	min.	3.3×10^{-2}	1.3×10^{-1}	3.3×10^{-2}	5.7×10^{-2}
	n	12	17	11	11
Ra(II)	mean ± σ	$(1.7 \pm 0.9)\times10^{-2}$	$(6.5 \pm 1.2)\times10^{-3}$	$(9.3 \pm 2.1)\times10^{-2}$	$(2.1 \pm 0.7)\times10^{-4}$
	median	1.2×10^{-2}	6.8×10^{-3}	9.3×10^{-2}	2.1×10^{-4}
	max.	2.7×10^{-2}	7.7×10^{-3}	1.1×10^{-1}	2.6×10^{-4}
	min.	1.0×10^{-2}	5.1×10^{-3}	7.8×10^{-2}	1.6×10^{-4}
	n	3	5	2	2
Ni(II)	mean ± σ	$(2.5 \pm 0.4)\times10^{-2}$	$(2.2 \pm 0.4)\times10^{-2}$	$(6.5 \pm 0.9)\times10^{-2}$	$(3.3 \pm 0.3)\times10^{-3}$
	median	2.7×10^{-2}	2.0×10^{-2}	6.5×10^{-2}	3.3×10^{-3}
	max.	2.7×10^{-2}	2.7×10^{-2}	7.1×10^{-2}	3.6×10^{-3}
	min.	2.1×10^{-2}	1.8×10^{-2}	5.9×10^{-2}	3.1×10^{-3}
	n	3	5	2	2
Np(IV/V)	mean ± σ	$(1.4 \pm 1.7)\times10^{-3}$	$(3.0 \pm 3.9)\times10^{-4}$	$(1.3 \pm 0.2)\times10^{-3}$	$(-1.9 \pm 0.1)\times10^{-3}$
	median	6.0×10^{-4}	1.4×10^{-3}	1.3×10^{-3}	-1.9×10^{-3}
	max.	3.4×10^{-3}	8.1×10^{-4}	1.4×10^{-3}	-1.8×10^{-3}
	min.	3.3×10^{-3}	-4.0×10^{-5}	1.1×10^{-3}	-2.0×10^{-3}
	n	3	5	2	2
U(IV/VI)	mean ± σ	$(2.9 \pm 0.4)\times10^{-3}$	$(7.8 \pm 3.6)\times10^{-4}$	$(1.0 \pm 0.2)\times10^{-3}$	$(1.9 \pm 0.5)\times10^{-3}$
	median	2.7×10^{-3}	6.0×10^{-4}	1.0×10^{-3}	1.9×10^{-3}
	max.	3.3×10^{-3}	1.2×10^{-3}	1.2×10^{-3}	2.3×10^{-3}
	min.	2.6×10^{-3}	4.7×10^{-4}	8.7×10^{-4}	1.6×10^{-3}
	n	3	5	2	2

Notes: Entries given as ”n/a” in the table signify data “not available”.

Table 4-13. Measured sorption coefficients, R_d (m^3/kg) for rock type 101051 (unaltered) based upon the 1–2 mm size fraction and a contact time of 180 days. The arithmetic mean (± standard deviation), median, minimum, maximum values are given for the specified numbers (n) of samples involved in the study.

Solute		Groundwater type			
		Marine	Saline	Fresh	Brine
Cs(I)	mean ± σ	$(2.1 \pm 0.1)\times10^{-3}$	$(2.9 \pm 0.3)\times10^{-3}$	$(7.9 \pm 1.7)\times10^{-3}$	n/a
	median	2.1×10^{-3}	3.1×10^{-3}	7.4×10^{-3}	n/a
	max.	2.2×10^{-3}	3.1×10^{-3}	9.8×10^{-3}	n/a
	min.	2.0×10^{-3}	2.6×10^{-3}	6.5×10^{-3}	n/a
	n	3	3	3	n/a
Sr(II)	mean ± σ	$(1.7 \pm 0.2)\times10^{-4}$	$(2.8 \pm 1.3)\times10^{-4}$	$(2.9 \pm 0.1)\times10^{-4}$	n/a
	median	1.7×10^{-4}	3.0×10^{-4}	2.9×10^{-3}	n/a
	max.	1.9×10^{-4}	4.0×10^{-4}	3.0×10^{-3}	n/a
	min.	1.4×10^{-4}	1.4×10^{-4}	2.7×10^{-3}	n/a
	n	3	3	3	n/a
Ln-Ac(III)	mean ± σ	$(2.9 \pm 0.4)\times10^{-1}$	$(3.9 \pm 0.6)\times10^{-1}$	$(1.3 \pm 0.2)\times10^{-1}$	n/a
	median	2.9×10^{-2}	3.8×10^{-1}	1.1×10^{-1}	n/a
	max.	3.2×10–2	4.5×10–1	1.5×10^{-1}	n/a
	min.	2.5×10^{-2}	3.4×10^{-1}	1.1×10^{-1}	n/a
	n	3	3	3	n/a

Notes: Entries given as ”n/a” in the table signify data “not available”

Table 4-14. Measured sorption coefficients, R_d (m^3/kg) for rock type 101054 (unaltered) based upon the 1–2 mm size fraction and a contact time of 180 days. The arithmetic mean (± standard deviation), median, minimum, maximum values are given for the specified numbers (n) of samples involved in the study.

Description		Groundwater type			
		Marine	Saline	Fresh	Brine
Cs(I)	mean ± σ	$(4.8 \pm 0.7)\times10^{-3}$	$(8.4 \pm 0.2)\times10^{-3}$	$(1.8 \pm 0.2)\times10^{-2}$	n/a
	median	4.6×10^{-3}	8.4×10^{-3}	1.9×10^{-2}	n/a
	max.	5.6×10^{-3}	8.6×10^{-3}	1.9×10^{-2}	n/a
	min.	4.3×10^{-3}	8.2×10^{-3}	1.6×10^{-2}	n/a
	n	3	3	3	n/a
Sr(II)	mean ± σ	$(3.4 \pm 0.4)\times10^{-4}$	$(0.1 \pm 2.2)\times10^{-4}$	$(4.1 \pm 0.1)\times10^{-3}$	n/a
	median	3.5×10^{-4}	1.0×10^{-5}	4.2×10^{-3}	n/a
	max.	3.6×10^{-4}	2.7×10^{-4}	4.2×10^{-3}	n/a
	min.	2.9×10^{-4}	-8.4×10^{-5}	4.1×10^{-3}	n/a
	n	3	3	3	n/a
Ln-Ac(III)	mean ± σ	$(3.5 \pm 0.2)\times10^{-2}$	$(8.2 \pm 1.4)\times10^{-1}$	$(2.1 \pm 0.3)\times10^{-1}$	n/a
	median	3.7×10^{-2}	8.4×10^{-1}	2.2×10^{-1}	n/a
	max.	3.7×10–2	9.5×10–1	2.3×10^{-1}	n/a
	min.	3.3×10^{-2}	6.7×10^{-1}	1.8×10^{-1}	n/a
	n	3	3	3	n/a

Notes: Entries given as ”n/a” in the table signify data “not available”.

Sorption properties of fracture types

In the following tables the sorption properties for surface coating minerals associated with different fracture types are presented. Measurement data are available for all fracture types with the exception of fracture type A (chlorite + calcite) and C (chlorite + hematite ± other) owing to the difficulty of obtaining sufficient quantity of representative samples using the surface abrasion technique in these particular cases. The sorptive properties of fracture type H (no mineral coating) is taken to be the same as the unaltered rock (101057).

Table 4-15. Measured sorption coefficients, R_d (m^3/kg) for fracture coating materials associated with Fracture Type B (KFM03A 643.8 m). Data are based upon the < 0.125 mm size fraction and a contact time of 180 days. The arithmetic mean (± standard deviation), median, minimum, maximum values are given for the specified numbers (n) of samples involved in the study.

Solute		Groundwater type			
		Marine	Saline	Fresh	Brine
Cs(I)	mean ± σ	n/a	$(1.6 \pm 0.08)\times10^{-1}$	1.5 ± 0.16	$(4.8 \pm 0.39)\times10^{-2}$
	median	n/a	1.6×10^{-1}	1.5	4.8×10^{-2}
	max.	n/a	-	-	-
	min.	n/a	-	-	-
	n	n/a	1	1	1
Sr(II)	mean ± σ	n/a	n/a	$(2.0 \pm 0.43)\times10^{-1}$	$(-1.3 \pm 1.6)\times10^{-3}$
	median	n/a	n/a	2.0×10^{-1}	-1.3×10^{-3}
	max.	n/a	n/a	-	-
	min.	n/a	n/a	-	-
	n	n/a	n/a	1	1
Ln-Ac(III)	mean ± σ	n/a	$(7.5 \pm 1.7)\times10^{-2}$	$(1.0 \pm 0.45)\times10^{-1}$	$(8.6 \pm 0.95)\times10^{-1}$
	median	n/a	7.5×10^{-2}	1.0×10^{-1}	8.6×10^{-1}
	max.	n/a	–	-	-
	min.	n/a	-	-	-
	n	n/a	1	1	1

Notes: For single meeasurements, uncertainty is given as an estimate based on radiometric counting statistics; entries given as ”n/a” in the table signify data “not available”.

Table 4-16. Measured sorption coefficients, R_d (m^3/kg) for fracture coating materials associated with Fracture Type D (KFM01B 418.29 m). Data are based upon the < 0.125 mm size fraction and a contact time of 180 days. The arithmetic mean (± standard deviation), median, minimum, maximum values are given for the specified numbers (n) of samples involved in the study.

Solute		Groundwater type			
		Marine	Saline	Fresh	Brine
Cs(I)	mean ± σ	$(4.1 \pm 0.5)\times10^{-3}$	n/a	$(6.4 \pm 1.3)\times10^{-2}$	$(1.2 \pm 0.3)\times10^{-3}$
	median	4.1×10^{-3}	n/a	6.4×10^{-2}	1.2×10^{-3}
	max.	–	n/a	–	–
	min.	–	n/a	–	–
	n	1	n/a	1	1
Sr(II)	mean ± σ	$(3.7 \pm 4.5)\times10^{-4}$	n/a	$(3.7 \pm 1.1)\times10^{-1}$	$(-3.0 \pm 4.9)\times10^{-4}$
	median	3.7×10^{-4}	n/a	3.7×10^{-1}	-3.0×10^{-4}
	max.	–	n/a	–	–
	min.	–	n/a	–	–
	n	1	n/a	1	1
Ln-Ac(III)	mean ± σ	2.4 ± 0.5	n/a	1.5 ± 0.3	2.8 ± 0.6
	median	2.4	n/a	1.5	2.8
	max.	–	n/a	–	–
	min.	–	n/a	–	–
	n	1	n/a	1	1

Notes: For single meeasurements, uncertainty is given as an estimate based on radiometric counting statistics; entries given as ”n/a” in the table signify data “not available”.

Table 4-17. Measured sorption coefficients, R_d (m^3/kg) for fracture coating materials associated with Fracture Type E (KFM04A 377.16 m, KFM05A 611.68 m). Data are based upon the < 0.125 mm size fraction and a contact time of 180 days. The arithmetic mean (± standard deviation), median, minimum, maximum values are given for the specified numbers (n) of samples involved in the study.

Solute		Groundwater type			
		Marine	Saline	Fresh	Brine
Cs(I)	mean ± σ	$(1.6 \pm 0.24)\times10^{-2}$	$(1.6 \pm 0.3)\times10^{-2}$	$(2.9 \pm 1.4)\times10^{-1}$	$(4.1 \pm 0.4)\times10^{-3}$
	median	1.4×10^{-2}	1.6×10^{-2}	2.2×10^{-1}	4.1×10^{-3}
	max.	1.8×10^{-2}	1.8×10^{-2}	4.4×10^{-1}	–
	min.	1.4×10^{-2}	1.4×10^{-2}	2.0×10^{-1}	–
	n	3	2	3	3
Sr(II)	mean ± σ	$(1.3 \pm 3.8)\times10^{-4}$	$(0.35 \pm 3.32)\times10^{-4}$	$(5.1 \pm 2.1)\times10^{-2}$	$(0.31 \pm 5.1)\times10^{-4}$
	median	1.3×10^{-4}	3.5×10^{-5}	3.7×10^{-2}	3.1×10^{-5}
	max.	–	2.0×10^{-4}	6.6×10^{-2}	–
	min.	–	-2.7×10^{-4}	3.6×10^{-2}	–
	n	1	2	3	1
Ln-Ac(III)	mean ± σ	1.3 ± 2.1	1.2 ± 0.14	1.0 ± 0.4	2.1 ± 0.4
	median	8.9×10^{-2}	1.2	7.6×10^{-1}	2.1
	max.	3.8	1.3	1.5	–
	min.	5.6×10^{-2}	1.1	7.5×10^{-1}	–
	n	3	2	3	1

Notes: For single meeasurements, uncertainty is given as an estimate based on radiometric counting statistics; entries given as ”n/a” in the table signify data “not available”.

Table 4-18. Measured sorption coefficients, R_d (m^3/kg) for fracture coating materials associated with Fracture Type F (KFM04A 414.20 m, KFM06A 770.69 m). Data are based upon the < 0.125 mm size fraction and a contact time of 180 days. The arithmetic mean (± standard deviation), median, minimum, maximum values are given for the specified numbers (n) of samples involved in the study.

Solute		Groundwater type			
		Marine	Saline	Fresh	Brine
Cs(I)	mean ± σ	$(1.3 \pm 0.6)\times10^{-2}$	$(2.2 \pm 1.7)\times10^{-2}$	$(1.7 \pm 0.6)\times10^{-1}$	n/a
	median	9.1×10^{-3}	1.0×10^{-2}	1.4×10^{-1}	n/a
	max.	2.2×10^{-2}	4.3×10^{-2}	2.6×10^{-1}	n/a
	min.	8.2×10^{-3}	9.3×10^{-3}	1.3×10^{-1}	n/a
	n	5	5	5	n/a
Sr(II)	mean ± σ	$(1.3 \pm 1.2)\times10^{-3}$	$(7.4 \pm 5.5)\times10^{-4}$	$(1.8 \pm 1.4)\times10^{-1}$	n/a
	median	2.0×10^{-3}	9.5×10^{-4}	1.1×10^{-1}	n/a
	max.	2.3×10^{-3}	1.3×10^{-3}	4.0×10^{-1}	n/a
	min.	-3.3×10^{-4}	-1.5×10^{-4}	6.9×10^{-2}	n/a
	n	5	5	5	n/a
Ln-Ac(III)	mean ± σ	$(8.6 \pm 6.7)\times10^{-1}$	1.4 ± 1.2	$(2.0 \pm 1.7)\times10^{-1}$	n/a
	median	1.1	1.5	1.1×10^{-1}	n/a
	max.	1.5	2.7	4.5×10^{-1}	n/a
	min.	1.0×10^{-1}	1.0×10^{-1}	5.5×10^{-2}	n/a
	n	5	5	5	n/a

Notes: For single meeasurements, uncertainty is given as an estimate based on radiometric counting statistics; entries given as ”n/a” in the table signify data “not available”.

Table 4-19. Measured sorption coefficients, R_d (m^3/kg) for fracture coating materials associated with Fracture Type G (KFM02A 118.25 m). Data are based upon the < 0.125 mm size fraction and a contact time of 180 days. The arithmetic mean (± standard deviation), median, minimum, maximum values are given for the specified numbers (n) of samples involved in the study.

Solute		Groundwater type			
		Marine	Saline	Fresh	Brine
Cs(I)	mean ± σ	$(4.3 \pm 0.42)\times10^{-1}$	n/a	5.8 ± 2.3	n/a
	median	4.3×10^{-1}	n/a	5.8	n/a
	max.	4.6×10^{-1}	n/a	–	n/a
	min.	4.0×10^{-1}	n/a	–	n/a
	n	3	n/a	1	n/a
Sr(II)	mean ± σ	$(2.2 \pm 0.2)\times10^{-3}$	n/a	$(9.5 \pm 1.5)\times10^{-2}$	n/a
	median	2.2×10^{-3}	n/a	9.5×10^{-2}	n/a
	max.	2.3×10^{-3}	n/a	–	n/a
	min.	2.0×10^{-3}	n/a	–	n/a
	n	3	n/a	1	n/a
Ln-Ac(III)	mean ± σ	1.6 ± 0.14	n/a	1.8 ± 0.5	n/a
	median	1.6	n/a	1.8	n/a
	max.	1.7	n/a	–	n/a
	min.	1.5	n/a	–	n/a
	n	2	n/a	1	n/a

Notes: For single meeasurements, uncertainty is given as an estimate based on radiometric counting statistics; entries given as ”n/a” in the table signify data “not available”.

Sorption properties of deformation zone materials

In the following tables the sorption properties of different deformation zone materials are presented. Measurement data are available for deformation zone structural elements Category 1 (Fault rock), Category 2 (sealed fracture networks) and Category 3 (Vuggy rock). Measurement data for Category 4 (oxidised wall rock is not currently available).

Table 4-20. Measured sorption coefficients, R_d (m^3/kg) for Category 1 ("Fault rock") material associated with deformation zones (Sample of ZFMA2 from borehole KFM01B 47.72 m). Data are based upon the 1–2 mm size fraction and a contact time of 180 days. The arithmetic mean (± standard deviation), median, minimum, maximum values are given for the specified numbers (n) of samples involved in the study.

Solute		Groundwater type			
		Marine	Saline	Fresh	Brine
Cs(I)	mean ± σ	n/a	$(4.5 \pm 0.2)\times10^{-2}$	$(3.3 \pm 0.6)\times10^{-1}$	n/a
	median	n/a	4.6×10^{-2}	3.2×10^{-1}	n/a
	max.	n/a	4.6×10^{-2}	3.9×10^{-1}	n/a
	min.	n/a	4.3×10^{-2}	2.8×10^{-1}	n/a
	n	n/a	3	3	n/a
Sr(II)	mean ± σ	n/a	$(7.5 \pm 24)\times10^{-5}$	$(8.1 \pm 1.9)\times10^{-2}$	n/a
	median	n/a	-3.0×10^{-7}	8.7×10^{-2}	n/a
	max.	n/a	3.4×10^{-4}	9.6×10^{-2}	n/a
	min.	n/a	-1.1×10^{-4}	6.0×10^{-2}	n/a
	n	n/a	3	3	n/a
Ln-Ac(III)	mean ± σ	n/a	4.5 ± 1.8	$(1.9 \pm 0.5)\times10^{-1}$	n/a
	median	n/a	5.2	2.2×10^{-1}	n/a
	max.	n/a	5.9	2.2×10^{-1}	n/a
	min.	n/a	2.5	1.4×10^{-1}	n/a
	n	n/a	3	3	n/a
Ra(II)	mean ± σ	n/a	$(6.1 \pm 0.2)\times10^{-2}$	$(3.6 \pm 2.6)\times10^{-1}$	n/a
	median	n/a	6.1×10^{-2}	2.4×10^{-1}	n/a
	max.	n/a	6.4×10^{-2}	6.6×10^{-1}	n/a
	min.	n/a	6.0×10^{-2}	1.9×10^{-1}	n/a
	n	n/a	3	3	n/a
Ni(II)	mean ± σ	n/a	$(2.8 \pm 0.6)\times10^{-1}$	$(3.0 \pm 1.0)\times10^{-1}$	n/a
	median	n/a	2.9×10^{-1}	2.5×10^{-1}	n/a
	max.	n/a	3.3×10^{-1}	4.1×10^{-1}	n/a
	min.	n/a	2.2×10^{-1}	2.4×10^{-1}	n/a
	n	n/a	3	3	n/a
Np(IV/V)	mean ± σ	n/a	$(2.2 \pm 0.23)\times10^{-3}$	$(4.4 \pm 0.5)\times10^{-3}$	n/a
	median	n/a	2.1×10^{-3}	4.6×10^{-3}	n/a
	max.	n/a	2.4×10^{-3}	4.7×10^{-3}	n/a
	min.	n/a	2.0×10^{-3}	3.9×10^{-3}	n/a
	n	n/a	3	3	n/a
U(IV/VI)	mean ± σ	n/a	$(2.0 \pm 0.4)\times10^{-2}$	$(1.0 \pm 0.2)\times10^{-3}$	n/a
	median	n/a	1.9×10^{-2}	1.1×10^{-3}	n/a
	max.	n/a	2.5×10^{-2}	1.2×10^{-3}	n/a
	min.	n/a	1.7×10^{-2}	8.6×10^{-4}	n/a
	n	n/a	3	3	n/a

Notes: Entries given as "n/a" in the table signify data "not available".

Table 4-21. Measured sorption coefficients, R_d (m^3/kg) for Category 2 (sealed fracture network) material associated with deformation zones (Sample of ZFMENE0401B from borehole KFM05A 611.68 m). Data are based upon the 0.063–0.125 mm size fraction and a contact time of 180 days. The arithmetic mean (± standard deviation), median, minimum, maximum values are given for the specified numbers (n) of samples involved in the study.

Solute		Groundwater type			
		Marine	Saline	Fresh	Brine
Cs(I)	mean ± σ	1.4×10^{-2}	$(1.8 \pm 0.07)\times10^{-2}$	$(2.1 \pm 0.14)\times10^{-1}$	n/a
	median	1.4×10^{-2}	1.8×10^{-2}	2.1×10^{-1}	n/a
	max.	1.4×10^{-2}	–	2.0×10^{-1}	n/a
	min.	1.4×10^{-2}	–	2.2×10^{-1}	n/a
	n	2	1	2	n/a
Sr(II)	mean ± σ	n/a	$(2.0 \pm 5.7)\times10^{-4}$	$(3.7 \pm 0.1)\times10^{-2}$	n/a
	median	n/a	2.0×10^{-4}	3.7×10^{-2}	n/a
	max.	n/a	–	3.7×10^{-2}	n/a
	min.	n/a	–	3.6×10^{-2}	n/a
	n	n/a	1	2	n/a
Ln-Ac(III)	mean ± σ	$(7.3 \pm 2.3)\times10^{-2}$	1.1 ± 0.1	$(7.6 \pm 0.01)\times10^{-1}$	n/a
	median	7.3×10^{-2}	1.1	7.6×10^{-1}	n/a
	max.	8.9×10^{-2}	–	7.6×10^{-1}	n/a
	min.	5.6×10^{-2}	–	7.5×10^{-1}	n/a
	n	2	1	2	n/a

Notes: For single meeasurements, uncertainty is given as an estimate based on radiometric counting statistics; entries given as ”n/a” in the table signify data “not available”.

Table 4-22. Measured sorption coefficients, R_d (m^3/kg) for Category 3 (vuggy rock) material associated with deformation zones (Sample of ZFM1189 from borehole KFM02A 275.22 m). Data are based upon the 1–2 mm size fraction and a contact time of 180 days. The arithmetic mean (± standard deviation), median, minimum, maximum values are given for the specified numbers (n) of samples involved in the study.

Solute		Groundwater type			
		Marine	Saline	Fresh	Brine
Cs(I)	mean ± σ	$(2.0 \pm 0.2)\times10^{-3}$	n/a	$(9.4 \pm 1.3)\times10^{-3}$	$(6.4 \pm 0.6)\times10^{-4}$
	median	2.1×10^{-3}	n/a	9.5×10^{-3}	6.7×10^{-4}
	max.	2.1×10^{-3}	n/a	1.1×10^{-2}	6.8×10^{-4}
	min.	1.8×10^{-3}	n/a	8.1×10^{-3}	5.8×10^{-4}
	n	3	n/a	3	3
Sr(II)	mean ± σ	$(2.8 \pm 5.4)\times10^{-4}$	n/a	$(7.0 \pm 0.6)\times10^{-3}$	$(-4.4 \pm 1.8)\times10^{-4}$
	median	1.3×10^{-5}	n/a	6.7×10^{-3}	-4.2×10^{-4}
	max.	9.0×10^{-4}	n/a	7.7×10^{-3}	-2.7×10^{-4}
	min.	-8.2×10^{-5}	n/a	6.5×10^{-3}	-6.3×10^{-4}
	n	3	n/a	3	3
Ln-Ac(III)	mean ± σ	1.4 ± 0.8	n/a	$(2.7 \pm 0.71)\times10^{-1}$	$(9.0 \pm 3.7)\times10^{-1}$
	median	1.4	n/a	2.8×10^{-1}	9.6×10^{-1}
	max.	2.2	n/a	3.3×10^{-1}	1.2
	min.	6.4×10^{-1}	n/a	1.9×10^{-1}	5.1×10^{-1}
	n	3	n/a	3	3

Notes: Entries given as ”n/a” in the table signify data “not available”.

4.4.5 Confirmatory studies of sorption

The retention data used in this model could be considered to be somewhat uncertain owing to the fact that the major mechanisms for radionuclide retention (i.e. diffusive uptake to the rock matrix and adsorption) are not studied interactively and are mainly addressed using crushed samples of geologic material. For partial validation of the material properties assessment it would be advantageous to be able to see if the retention parameters determined on a very small scale can be used to correctly predict radionuclide retention on larger scales.

To this end, two sets of experiments have been conducted where the retention properties of intact drill core samples have been assessed.

I. Studies of diffusive uptake and radionuclide sorption within intact drill cores.

II. Studies of Cs(I) sorption using an electromigration technique to hasten diffusive/sorptive equilibration of the rock matrix pore space.

Generally, the results obtained in these studies confirm the understanding of retention processes which form the basis of the retardation models described in this chapter. On balance, and considering the uncertainties already addressed in the sections describing the diffusivity and sorption data, no indications of any severe deviation of the data or evidence to contradict the conceptual model of sorption can be identified at least for the spatial scales investigated. Full details concerning these complementary investigations can be found the Retardation model background report /Byegård et al. 2008/.

4.5 Retardation model

In accordance with the general concept proposed by /Widestrand et al. 2003/, the site descriptive retardation model described in this chapter consists of tables in which the geological description is combined with selected transport parameters for each geological entity (i.e. the different geological structures where retardation of radionuclides can take place) in a fashion which allows direct application within transport models.

It should be noted that the proposed conceptual model described by /Widestrand et al. 2003/ implies a description of retardation occurring in fractures where discrete layers of altered material surround the fracture. It is also implicitly assumed that these layers are of a sufficient thickness that it should be possible to take samples and make laboratory determinations of, for example, diffusivity and sorption. The actual case for the Forsmark area is, however, that the fractures are mainly found to have a very thin fracture coating and the altered rock is found predominantly in deformation zones and not necessarily only localised in the immediate vicinity of the individual fractures. For this reason, the description and parameterisation of the Forsmark retardation model differs from the originally proposed retardation model concept.

The resulting retardation model description developed for SDM-Site Forsmark consists of three sections dealing with the major rock types, specific fracture types, and deformation zone structural elements, respectively.

The description of fracture types considers the material properties of the fracture coatings themselves as well as additional information concerning, for example, typical depths of hydrothermally altered material surrounding the fracture surfaces. Since the fractures can be hosted within different rock types (and are not necessarily specific to any given rock type), the transport properties of the fracture itself must be combined with the transport properties of the underlying rock matrix to give a full description of the transport properties of potential flowpaths through the rock comprising the HRD.

For deformation zones, the rock interspersed between the flow bearing fractures may consist of unusual fabrics and microstructures, which are not present to a great extent in the HRD. A number of typical deformation zone structural elements have therefore been described to account for differences in material properties between the rock encountered in the HRD and

HCD. For the deterministic deformation zones comprising the HCD, the description of fracture types can be combined with that of the deformation zone specific materials to give a full description of transport properties of flowpaths within the HCD.

In the first of the following sections (4.5.1), the prevalence of the major rock types and their "best estimate" material properties are described. The second section (4.5.2) provides a description of the retention properties of water-conducting fractures while in the third section (4.5.3) the properties of deformation zone structural elements are described. To avoid excessive repetition, data concerning the sorptivity of the various solutes investigated in the laboratory programme are referred to in the Retardation model tables by using pointers to the appropriate data tables already presented in section 4.4.4.

4.5.1 Retardation properties of the rock mass

A major difference between the geological model described in /Stephens et al. 2008/ and the transport properties laboratory programme /Byegård et al. 2008/ is that the geological model was based on the concept of rock domains, whereas the sampling for the transport programme was based instead on rock types with a primary focus on the major rock type, 101057 (granite to granodiorite, metamorphic, medium-grained) together with some of the minor rock types (listed below).

The sample set represents both fresh and slightly altered (mainly oxidized with faint to weak degree of alteration) samples of these rock types. The proportion of rock types within rock domains RFM029 (dominant) and RFM045 (subordinate) are presented in Table 4-23. These are the two rock domains that comprise the target volume. A few of the minor rock types investigated in the laboratory programme have been excluded from the retardation model since they constitute less than 2% of the rock types within RFM029 and RFM045, or are located in rock domains external to the present target area.

Rock types investigated in the transport laboratory programme and integrated in the retardation model are:

- 101057 (Granite to granodiorite, metamorphic, medium-grained); dominates strongly in the target volume.
- 101051 (Granodiorite, tonalite and granite, metamorphic, fine- to medium-grained); relatively frequent and regularly distributed in RFM029 and RFM045.
- 101058 (Aplitic granite); occurs as dykes and minor bodies that are commonly discordant to ductile deformation in older rocks. Frequent rock type in RFM045.
- 101061 (Pegmatite, pegmatic granite); small amounts regularly distributed in RFM029 and RFM045, primarily as dykes and minor bodies.
- 102017 (Amphibolite); occurs as dykes and irregular intrusions and is present in both RFM029 and RFM045.

Rock types which have been investigated within the transport laboratory programme, although to a lesser extent and not included in the retardation model are:

- 101054 (Tonalite to granodiorite, metamorphic); A minor rock type that dominates within rock domain RFM017, which is not included in the target volume.
- 111058 (Granite, fine- to medium-grained); Occurs as dykes and minor bodies, commonly discordant to ductile deformation in older rocks.
- 103076 (Felsic to intermediate volcanic rock, metamorphic).
- 101056 (Granodiorite, metamorphic).

Table 4-23. Proportions of different rock types in the two rock domains which constitute the target volume, RFM029 and RFM045. /SKB 2007b/.

Rock Code (SKB)	Rock type	RFM029 (dominant)	RFM045 (subordinate)
103076	Felsic to intermediate volcanic rock, metamorphic	0.4%	1.2%
102017	Amphibolite	4.4%	6.3%
101057	Granite (to granodiorite), metamorphic, medium-grained	73.6%	18.0%
101058	Granite, metamorphic, aplitic	1.2%	49.3%
101051	Granodiorite, tonalite and granite, metamorphic, fine- to medium-grained	4.6%	9.0%
101061	Pegmatitic granite, pegmatite	13.3%	13.9%
111058	Granite, fine- to medium-grained	1.5%	1.3%

In the Retardation model, it is implicitly assumed that the properties of flowpaths through the different rock domains can be represented in a statistical sense by consideration of the proportions of the various rock types of which the rock domains are thought to be comprised. It is noted that although this treatment does not give consideration to the possibility of preferential flowpaths involving specific rock types within the fracture domains, the approach is probably sufficiently accurate for the purposes of modelling within safety assessment since the material properties of the different rock types appear to be broadly similar (when considered together with their associated uncertainties). Further justification of this assumption may be required within safety assessment.

Representative, "best estimate" transport parameters for comparative purposes are given in Table 4-24 for the suite of rock types where a statistically significant data set exists.

Generally, it has not been possible to directly measure the diffusive properties of the (typically thin) layers of hydrothermally altered rock immediately adjacent to fracture surfaces hosted in otherwise unaltered host rock. Porosity ranges measured for this material (see Table 4-7), however, suggests only minor differences in "bulk" diffusive properties relative to the unaltered rock matrix. PMMA impregnation studies /Penttinen et al. 2006/, on the other hand, suggest a

Table 4-24. Representative, "best estimate" transport parameters for the main rock types (> 2%) within rock domains RFM029 and RFM045 intended for comparative purposes. Data are given for porosity, formation factor, BET-surface area, and cation exchange capacity (CEC) considering non-deformation zone rock (N) and deformation zone rock (DZ) where applicable.

	101051 N	101057 N	DZ	101058 N	101061 N	102017 N
Porosity (vol%)	0.23 ± 0.09	0.23 ± 0.11	1.0 ± 2.4	0.22	0.32	0.16 ± 0.1
Formation factor (*in situ*)[†]						
Unaltered rock	$(1.1 \pm 0.8)\times10^{-5}$	$(1.6 \pm 1.0)\times10^{-5}$	$(1.5 \pm 0.8)\times10^{-5}$	$(1.3 \pm 0.2)\times10^{-5}$	$(1.9 \pm 0.8)\times10^{-5}$	$(1.7 \pm 1.2)\times10^{-5}$
Altered rock	$(1.7 \pm 0.5)\times10^{-5}$	$(2.0 \pm 0.8)\times10^{-5}$	$(1.5 \pm 5.6)\times10^{-4}$	$(1.4 \pm 0.5)\times10^{-5}$	$(1.9 \pm 0.5)\times10^{-5}$	$(1.4 \pm 0.1)\times10^{-5}$
All rock	$(1.2 \pm 0.8)\times10^{-5}$	$(1.6 \pm 1.0)\times10^{-5}$	$(2.9 \pm 4.1)\times10^{-5}$	$(1.4 \pm 0.4)\times10^{-5}$	$(1.9 \pm 0.8)\times10^{-5}$	$(1.7 \pm 1.2)\times10^{-5}$
Formation factor (lab)						
	1.0×10^{-4}	$(1.6 \pm 1.5)\times10^{-4}$	$(1.1 \pm 1.0)\times10^{-4}$	1.8×10^{-4}	2.8×10^{-4} [(A)]	2.9×10^{-5}
CEC (cmol/kg)*	< 1.2	< 1	n/a	n/a	n/a	n/a

Notes: Entries given as "n/a" in the table signify data "not available".
[(†)] Formation factors derived from *in situ* measurements are empirically corrected for measurement bias and are for "rock matrix" (i.e. ≥ 0.5 m distant from the nearest mapped, open fracture).
[(*)] 1 cmol/kg = 1 meq/100 g.
[(A)] Based on laboratory resistivity measurement.
[(B)] Based on BET measurements of two samples which were identified as medium altered, which therefore can be suspected to give an overestimate of the general conditions for intact rock within deformation zones.

heterogeneous distribution of porosity over very short length scales and the possibility exists for increased diffusivity over a distance of some cm into the rock matrix from water bearing fractures. BET measurements indicate that the microporous surface area of altered rock could be as much as an order of magnitude higher than that of the unaltered rock, thereby suggesting an increased sorptivity in the first few cm of rock matrix immediately adjacent to fracture surfaces.

It should be noted that the possibly increased diffusivity and sorptivity of altered matrix rock adjacent to fracture surfaces is only established qualitatively at present and cannot be rigorously accounted for in the retardation model.

4.5.2 Retardation properties of fractures

According to the available data the presence of different fracture coatings cannot be related to specific rock types, rock domains, or fracture domains. Nevertheless, certain fracture types do tend to be associated with different fracture orientations and it could therefore be argued that the intensities of various fracture sets in different fracture domains in effect gives rise to a variation in the distribution of fracture types in different fracture domains. The statistical certainty with which this can be established, however, is sufficiently weak that for modelling radionuclide transport, the different fracture types may be assumed to occur in all regions of the rock roughly in the same proportions as described in the tables.

Retardation parameters for the identified fracture types are given in Table 4-25 to Table 4-32.

Table 4-25. Retardation model parameters for fracture type A.

	Fracture coating: *Chlorite* + *Calcite*
Thickness	≤ 0.5 mm
Porosity (vol%)	n/a
Formation factor	n/a
BET surface area (m^2/g)	0.49
CEC (cmol/kg)	n/a
Sorption, K_d (m^3/kg)	n/a
Percentage of all open fractures	34%
Percentage of transmissive fractures	38%
Transmissivity interval (m^2/s)	> 10^{-10} (no evidence for preferential transmissivity interval)
Preferred orientation	n/a
Altered rock surrounding the fracture	no

Notes: Entries given as ”n/a” in the table signify data “not available”.

Table 4-26. Retardation model parameters for fracture type B.

	Fracture coating: *Chlorite* + *Clay* ± *epidote* ± *prehnite* ± *calcite*
Thickness	≤ 1 mm
Porosity (vol%)	n/a
Formation factor	n/a
BET surface area (m^2/g)	10.3
CEC (cmol/kg)	15 ± 10
Sorption, K_d (m^3/kg)	See Table 4-15
Percentage of all open fractures	7%
Percentage of transmissive fractures	7%
Transmissivity interval (m^2/s)	> 10^{-10} (no evidence for preferential transmissivity interval)
Preferred orientation	horizontal to gently dipping
Altered rock surrounding the fracture	yes, ~1 cm

Notes: Entries given as ”n/a” in the table signify data “not available”.

Table 4-27. Retardation model parameters for fracture type C.

	Fracture coating: *Chlorite + hematite* ± *other*
Thickness	< 0.5 mm (0.1 mm)
Porosity (vol%)	n/a
Formation factor	n/a
BET surface area (m^2/g)	2.3 ± 0.6
CEC (cmol/kg)	n/a
Sorption, K_d (m^3/kg)	n/a
Percentage of all open fractures	2%
Percentage of transmissive fractures	1%
Transmissivity interval (m^2/s)	> 10^{-10} (no evidence for preferential transmissivity interval)
Preferred orientation	ENE–NW, steeply dipping
Altered rock surrounding the fracture	yes, ~0.5 mm

Notes: Entries given as ”n/a” in the table signify data “not available”.

Table 4-28. Retardation model parameters for fracture type D.

	Fracture coating: *Chlorite* ± *other*
Thickness	< 0.5 mm (0.1 mm)
Porosity (vol%)	n/a
Formation factor	n/a
BET surface area (m^2/g)	5.1 ± 2.2
CEC (cmol/kg)	n/a
Sorption, K_d (m^3/kg)	See Table 4-16
Percentage of all open fractures	14%
Percentage of transmissive fractures	12%
Transmissivity interval (m^2/s)	> 10^{-10} (no evidence for preferential transmissivity interval)
Preferred orientation	no
Altered rock surrounding the fracture	no

Notes: Entries given as ”n/a” in the table signify data “not available”.

Table 4-29. Retardation model parameters for fracture type E.

	Fracture coating: *Laumontite* ± *calcite* ± *chlorite*
Thickness	0.1–2 mm
Porosity (vol%)	n/a
Formation factor	n/a
BET surface area (m^2/g)	0.42 ± 0.02
CEC (cmol/kg)	18 ± 5
Sorption, K_d (m^3/kg)	See Table 4-17
Percentage of all open fractures	14%
Percentage of transmissive fractures	1%
Transmissivity interval (m^2/s)	> 10^{-10} (no evidence for preferential transmissivity interval)
Preferred orientation	ENE–NW, steeply dipping
Altered rock surrounding the fracture	yes, 1–5 cm

Notes: Entries given as ”n/a” in the table signify data “not available”.

Table 4-30. Retardation model parameters for fracture type F.

	Fracture coating: *Calcite* ± *quartz* ± *pyrite* ± *other*
Thickness	0.1–2 mm
Porosity (vol%)	n/a
Formation factor	n/a
BET surface area (m^2/g)	2.2 ± 1.1
CEC (cmol/kg)	n/a
Sorption, K_d (m^3/kg)	See Table 4-18
Percentage of all open fractures	15%
Percentage of transmissive fractures	19%
Transmissivity interval (m^2/s)	> 10^{-10} (no evidence for preferential transmissivity interval)
Preferred orientation	new fractures, horizontal to subhorizontal
Altered rock surrounding the fracture	no

Notes: Entries given as ”n/a” in the table signify data “not available”.

Table 4-31. Retardation model parameters for fracture type G.

	Fracture coating: *Clay* ± *other*
Thickness	1–5 mm
Porosity (vol%)	n/a
Formation factor	n/a
BET surface area (m^2/g)	4.3
CEC (cmol/kg)	n/a
Sorption, K_d (m^3/kg)	See Table 4-19
Percentage of all open fractures	3%
Percentage of transmissive fractures	3%
Transmissivity interval (m^2/s)	> 10^{-10} (no evidence for preferential transmissivity interval)
Preferred orientation	horizontal to gently dipping
Altered rock surrounding the fracture	yes, ≥ 5 cm

Notes: Entries given as ”n/a” in the table signify data “not available”.

Table 4-32. Retardation model parameters for fracture type H (material properties assumed to be same as for rock type 101057).

	Fracture coating: *no mineral*
Thickness	n/a
Porosity (vol%)	0.23 ± 0.11
Formation factor	(1.6 ± 1.0)×10^{-5}
BET surface area (m^2/g)	0.025 ± 0.015
CEC (cmol/kg)	< 1
Sorption, K_d (m^3/kg)	See Table 4-12 (i.e. unaltered rock type 101057)
Percentage of all open fractures	5%
Percentage of transmissive fractures	13%
Transmissivity interval (m^2/s)	> 10^{-10} (no evidence for preferential transmissivity interval)
Preferred orientation	horizontal to gently dipping
Altered rock surrounding the fracture	no

Notes: Entries given as ”n/a” in the table signify data “not available”.

4.5.3 Retardation properties of deformation zones

As described in section 4.2.1, deformation zones are usually characterised as consisting of a transition zone and a core. Transmissive fractures, if they are present, are often found in the transition zone, close to the wall rock. The deformation zone core is commonly found to have substantially reduced flow permeability in a direction normal to its orientation.

Independent of which conceptual model is adopted for use in transport calculations (e.g. see Figure 4-7), there are some simplifications which constitute a basis for parameterising the transport properties of deformation zones:

- Deformation zones at Forsmark often appear to have been reactivated during different periods throughout geological history and display a wide spectrum of brittle and ductile alteration which can also vary considerably between different borehole intercepts with the same deformation zone. Consequently, it is not possible to give specific retardation properties for every single deformation zone because of their internal microstructural complexity and the fact that this is usually only known from a small number of borehole intercepts. This also limits the possibility to describe any variations between different categories of deformation zones.
- The vast majority of the sections mapped with strong or medium oxidation, are found within deformation zones. In addition, three other categories of altered bedrock have been distinguished as recurrent structural elements within deformation zones (i.e. sealed fracture networks, vuggy rock, and fault rock as outlined in Table 4-3). Retardation parameters for these elements are given below in Table 4-33 to Table 4-36.
- Deformation zones have an increased fracture frequency compared to the host rock (both open and sealed), which is assumed to have some effect upon their retardation properties. Statistics of fracture frequency and fracture distribution in deformation zones are available. It is possible to parameterize most of the open fracture types found within the transition zones and core regions. Retardation parameters for these fracture types have been given previously in Table 4-25 to Table 4-32.
- Both the frequency and distribution of transmissive fractures vary between different deformation zones. Notwithstanding this, the transmissivity ranges are broadly similar for all the fracture types described in the retardation model and there is little evidence of preferential flow within specific fracture types.

Tables of retardation properties for the deformation zone structural elements are given in Table 4-33 to Table 4-36.

Table 4-33. Retardation model for Fault rock (strongly tectonised and partly incohesive material).

Mineral content	Altered rock fragment, mineralogy dependant on host rock. Generally, chlorite, saussurite and clay
Porosity (vol%)	10%
Formation factor	n/a
BET (m^2/g)	5.6 ± 2.3
CEC (cmol/kg)	9 ± 1
Sorption coefficient, K_d (m^3/kg)	See Table 4-20

Notes: Entries given as ”n/a” in the table signify data “not available”.

Table 4-34. Retardation model for Sealed fracture networks, (usually brecciated).

Mineral content	Due to mineral paragenesis: a) laumontite +calcite ±others b) epidote ±chlorite ±prehnite ±others c) chlorite ±others
Porosity (vol%)	3%
Formation factor	n/a
BET (m^2/g)	0.64
CEC (cmol/kg)	5.4 ± 2.4
Sorption coefficient, K_d (m^3/kg)	See Table 4-21

Notes: Entries given as ”n/a” in the table signify data “not available”.

Table 4-35. Retardation model for Vuggy rock.

Mineral content	K-feldspar +albite +Fe-oxides +chlorite ± quartz ± sericite ± calcite ± others
Porosity (vol%)	13±6%
Formation factor	$(1.2\pm0.8)\times10^{-2}$
BET (m^2/g)	1.58
CEC (cmol/kg)	< 0.4
Sorption coefficient, K_d (m^3/kg)	See Table 4-22

Table 4-36. Retardation model for oxidized (medium to strong alteration) wall rock.

Mineral content	Hydrothermally altered host rock. Red staining from small hematite grains, K-feldspar, saussurite, plagioclase, quartz, chlorite
Porosity (vol%)	2.5 ± 3.8%
Formation factor	n/a
BET (m^2/g)	0.77
CEC (cmol/kg)	n/a
Sorption coefficient, K_d (m^3/kg)	n/a

Notes: Entries given as ”n/a” in the table signify data “not available”.

4.6 Summary of main findings

4.6.1 On retardation properties of the rock mass

The limited data available indicate that there are probably no significant differences in the retardation properties of the rock types present in rock domain RFM029 that dominates the target volume. Furthermore, the range of variation of specific material property parameters within a particular rock type is found in many cases to be larger than the apparent difference between different rock types.

From the few samples that have been characterised the amphibolite (102017) has been found to have a lower porosity and, as a consequence, most likely also a lower formation factor than the other rock types. Samples of this rock type have also been found to have very low BET surface areas (below the detection limit).

Comparison of the metagranite (101057) rock type samples taken from deformation zones with non-deformation zone samples indicates that there are no significant differences for the main retention parameters, with the possible exception of BET surface area. As pointed out

in Table 4-24, however, the value is based on two measurements which happen to be medium altered, which therefore probably gives an overestimation of the average values of BET surface areas within the deformation zones. Nevertheless, the altered rock is more predominant within deformation zones and the result can be regarded as a qualitative conclusion that the increased alteration in deformation zones gives increased microporous surface areas and consequently also higher sorption capacities. Owing to the low number of measurements, however, this finding is not possible to quantify accurately.

The subordinate rock domain RFM045 within the target volume consists principally of the Granite, metamorphic, aplitic (101058) rock type. This rock domain was not identified until very late in the site investigation and consequently there is very little data from laboratory investigations for the dominant rock type. Based on the available data, however, there does not appear to be any significant differences between the sorption properties of this rock type and the others that have been investigated.

4.6.2 On retardation properties of fractures

Retardation models have been produced for each of the different fracture types. A thin layer of fracture coating has been identified within all of them with the exception of fracture type H ("no mineral"). Due to the limited thickness of the layers and their frequently friable nature, porosity and diffusion measurements were not possible to perform on these materials. Owing to their physical characteristics, however, it appears likely that these layers are characterised by a substantially higher porosity and therefore also a higher diffusivity (i.e. formation factor) than the underlying rock matrix. It therefore seems reasonable within safety assessment transport modelling to consider fracture coatings and filling materials as equilibrium storage capacities.

The measured BET surface areas of the fracture material have been measured to be significantly higher than corresponding BET surface areas of samples from the rock mass. They vary from 0.42 m^2/g to 10.3 m^2/g, which is roughly 20–500 times higher than the corresponding value for the unaltered 101057 rock type. This finding suggests that the fracture coatings most likely contribute positively to the overall retardation effect.

The large differences in the BET surface area of intact rock and fracture filling materials is not always accompanied by a comparable divergence in estimated K_d values. The K_d for sorption of Cs(I) on clay minerals characteristic of fracture Type G, for example, is approximately 14 times larger than the corresponding value for the intact metagranite rock (101057). The BET surface area of the fracture filling material, on the other hand, is nearly 170 times greater than that of the intact rock. In this particular case, however, the variability of the K_d values is in general agreement with the known ion-exchange behaviour of Cs(I) in association with clay minerals so this is not altogether unexpected. For solutes that sorb by way of a surface complexation mechanism we expect a closer agreement. Although there appears to be a clear correlation between BET surface area and sorptivity generally when comparing different size fractions of crushed rock, it is very difficult to observe a consistent correlation with surface area when comparing the sorptivity of matrix rock and fracture coating materials.

4.6.3 On retardation properties of deformation zone elements

The deformation zone structural elements for which retardation properties have been tabulated are all comparatively heterogeneous in their structure. The porosities are considerably higher (3–16%) than for intact rock, with the exception of oxidized wall rock which is only slightly more porous than the intact metagranite rock (101057). In general, it is expected that the high porosities should also be accompanied by an increased diffusivity (formation factor). However, this has only been demonstrated for the vuggy rock samples where a very high formation factor on the order of 1.5×10^{-2} has been measured. BET-surface areas and sorptivities are generally slightly higher for the deformation zone materials than for intact rock which indicates a slightly greater relative potential for retention than intact rock in the HRD.

4.6.4 Application of the retardation model

Table 4-23 and Table 4-24 provide a basis for the parameterisation of rock domains RFM029 and RFM045. This could range from the selection of a single parameter value for the dominant rock type in that domain to, for instance, flowpath averaging using data for different rock types.

The quantitative descriptions of the identified fracture types including the available retardation parameters are given in Table 4-25 to Table 4-32. The corresponding descriptions and data for deformation zones are presented in Table 4-33 to Table 4-36. It is intended that the different fracture types and deformation zone structural elements be used in a modular fashion for constructing integrated models of radionuclide transport along flow paths within the rock.

In this chapter, the material property data are characterised in the form of simplified summary statistics (i.e. mean standard deviation, median, maximum, minimum, and number of samples) for the measurement data which could be used as a basis for preliminary stochastic parameterisation of transport models.

This chapter should be regarded as a proposal for how to formulate a descriptive and semi-quantitative retardation model derived from the available material properties database. Recommendations for the selection of data are given, however, with acknowledgement of the qualitative and quantitative uncertainty of the retention parameters. This caveat implies that the model does not provide exact and detailed guidelines on how to "dress" the geological model with transport parameters using the retardation model tables. Nevertheless, in the opinion of the authors this is the best representation achievable with the available data. The retardation model should be viewed as an overview of the interpreted site-specific information on retardation parameters, intended to provide a basis for the formulation of alternative parameterisations or necessary simplifications within safety assessment modelling.

5 Solute transport

Coupling of the F-factor estimates from the hydrogeological modelling with the retardation model allows for the prediction of transport times for key radionuclides. As already discussed in the context of the flow related transport properties evaluation, radionuclide transport in the site descriptive modelling work is conceptualised to occur in a serially connected, three compartment system consisting of the non-engineered near field (NNF), the immediate far-field (IFF), and the distant far field (DFF) which in this analysis is taken to correspond to the HCD. In this chapter, we present calculations which have been used to quantify likely radionuclide transport times along typical transport paths from a canister deposition hole to the near surface.

5.1 Overview of modelled solute transport processes

The transport models described in this chapter consider advectively dominated flow and transport along a flowpath where the transported solutes can diffuse into and sorb upon micro-surfaces within the rock matrix. Here, we consider a flowpath to be a simple set of serially connected flow channels within the rock. In a full hydrogeological description of the transport problem as to be used in SR-Site, however, we would expect flowpaths to bifurcate and join with other flowpaths over different length scales giving rise to a distribution of F-factors and advective transport times (i.e. water residence times).

The transport model assumes that flow is fully mixed across the aperture and width of the flowpath and that hydrodynamic dispersive mixing can be neglected. This last assumption is reliant upon the observation that apparent dispersion is generally dominated by the difference in residence times of solutes transported along different flowpaths and therefore does not need to be treated on the level of individual flow channels /Neretnieks 1993/. The assumption of full mixing across the width of a flowpath depends on whether there is sufficient time for any lateral concentration differences to even out over the advective transport length. If the characteristic time for diffusion across the flowpath width is substantially smaller than the advective travel time, then fully mixed conditions can generally be assumed.

Depending upon the hydrogeological scenario under consideration, advective travel times can be expected to be on the order of a few to many tens of years. This could run to hundreds, or perhaps even thousands of years if hydraulic gradients are extremely low. For a 10 cm wide flow channel, the characteristic time for diffusion will be on the order of 50–100 days and therefore full mixing can usually be assumed for flow channels of this dimension (see Appendix I) even for very short advective travel times. As the transport aperture of a flowpath is typically very small (on the order of a few mm at most), diffusive mixing across the aperture can always be assumed on safety assessment timescales.

Radionuclides transported along flowpaths leading away from the repository may mix with un-contaminated water at intersections with other flowpaths giving dilution effects. The extent of mixing will depend upon the water residence time at the flow junction and the effective surface area for diffusive mixing between adjacent water streams in which the radionuclides are being transported (assuming laminar flow). Here, the relation between the characteristic time for diffusion and stream contact time gives an indication of whether full diffusive mixing is a reasonable assumption or not. Although it is difficult to assess mixing for unknown flow intersection geometries, typically two limiting cases are considered in modelling; full mixing at flowpath intersections, and no mixing at flowpath intersections (“flowpath routing”). As the calculations presented in this chapter consider a single hypothetical flowpath, this does not need

to be considered (although we note that the simulation of a single flowpath is conceptually indistinguishable to the assumption of transport in a multi-flowpath system with no mixing). For SA calculations, however, particle tracking provides a simple means of weighting the contributions of individually traced particles to the overall radionuclide release rate in a complex, multiple-flowpath system.

Although in some cases flow channels may be described as actual physical entities in the rock (such as in the case of conductive fracture intersections or flow conduits hosted in fault stepovers), they generally are dynamic in the sense that their existence and distribution is predicated by the externally imposed flow regime /Neuman 2005/. Flow distributions in variable aperture fractures are thought to be highly channelised and stagnant zones can potentially exist adjacent to these flow channels. On the scale of a single fracture, variable fracture aperture provides the possibility for in-plane flow channelling although the geometry and spatial distribution of active flow channels themselves varies as a function of the applied boundary conditions. On the basis of field observations it is thought that in-plane flow channels have widths typically in the range of a few cm to some tens of cm /Neretnieks 2004, Abelin et al. 1991, 1994/. For the calculations in this chapter we therefore assume a flow channel width of 10 cm as a main scenario.

A schematic view of the radionuclide transport problem is given in Figure 5-1. The figure illustrates the idea of advective flow through a flow channel of limited extent with stagnant zones flanking the main flowpath.

Scoping calculations (see Appendix B) indicate that for fractures with strongly variable apertures and surface asperity contacts, there could be effectively stagnant zones of substantial extent that afford additional surface area for the radionuclides to interact with the rock matrix. This is referred to as diffusion accessible surface (DAS) in the present report.

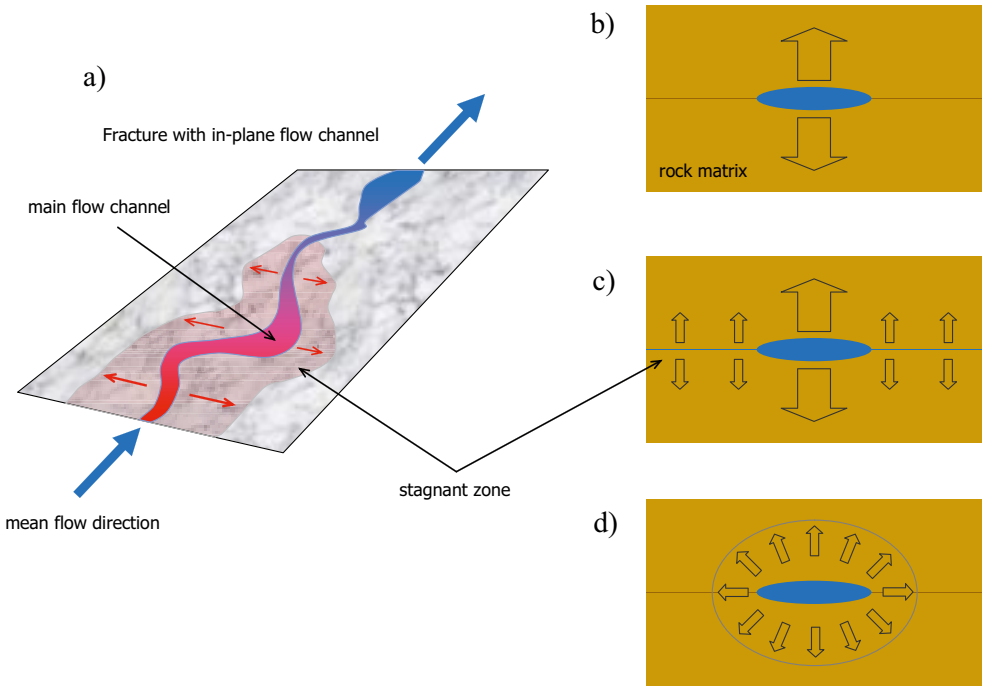

Figure 5-1. *The left-hand image (a) shows a schematic view of a fracture hosting an in-plane flow channel of limited width with stagnant zones flanking the main flowpath; The images on the right-hand side show conceptual illustrations of three different modes of mass transfer: b) diffusion directly to the rock matrix from the main flow channel; c) direct matrix diffusion coupled with diffusive uptake to the stagnant zone and subsequently into the rock matrix; d) mass transfer of solute described as a radial or pseudo-radial diffusion process when the penetration depth approaches the same size as the channel width.*

Figure 5-2 shows a typical simulation of a 10 m×10 m variable aperture fracture with a surface asperity contact of roughly 40% and an anisotropic, although spatially correlated aperture distribution. The open parts of the fracture have a mean aperture of 5×10^{-5} m and a standard deviation of the same size. The simulation considers a dipole line source/sink of 10 cm extent applied along the vertical (top images) and horizontal axis (bottom images) to demonstrate the dynamic nature of the flow channelling effect. As can be clearly appreciated from the figure, there are substantial regions of the fracture surface that are effectively stagnant although hydraulically accessible from the main flowpaths.

Provided flow channels are not isolated tubes hosted within annealed fractures (karstic porosity of this kind is thought to be unlikely for the Forsmark site although cannot be completely ruled out), these stagnant zones should be relatively well connected and accessible from the main flowpaths. It can be shown for single fractures that increasing contact of fracture surface asperities increases the degree of flow channelling significantly. Although this reduces the actual flow-wetted surface, large portions of the fracture must still stay open and hydraulically connected for the fracture to remain conductive at all. These hydraulically accessible, although non-flowing regions correspond to the stagnant zones illustrated in Figure 5-1.

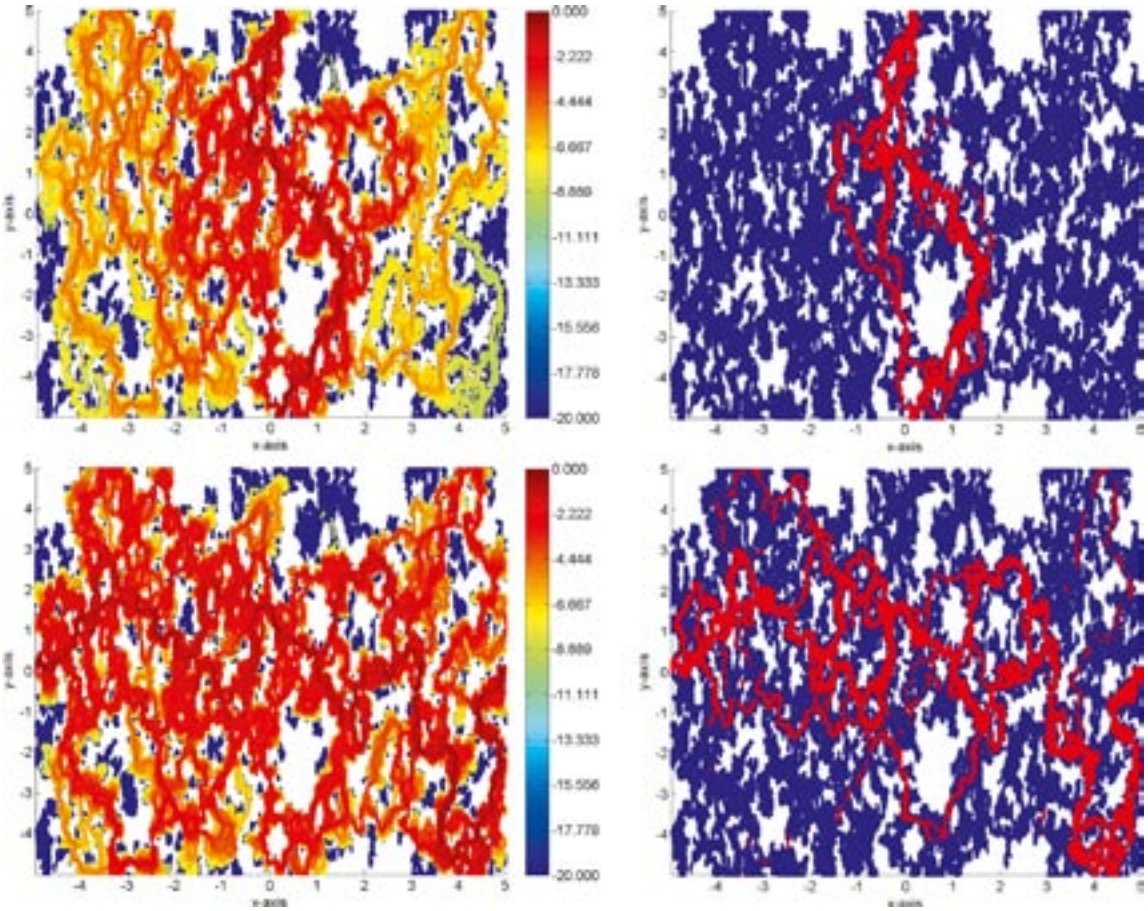

Figure 5-2. *Simulation of typical flow channels arising in a variable aperture fracture with a surface asperity contact of 40% and hydraulic gradient applied vertically (top) and horizontally (bottom) for a 0.1 m line source/sink dipole. Hydraulically inaccessible parts of the fracture are non-coloured. The left hand images indicate the actual simulated flow normalised by the maximum flow rate (log_{10}-units). The right-hand images show the dynamic nature of flow channels featuring flow > 1% (arithmetic units) of the maximum flowrate (red shading).*

In the calculations presented in this chapter we assume a stagnant zone width roughly 10 times greater than the channel width. This is referred to as a 10:1 stagnant zone in the present report. Therefore, for a flow channel of 10 cm width, the stagnant zone would be effectively 1 m wide. For a 1 cm wide channel, on the other hand, the stagnant zone would be only 10 cm wide. Furthermore, we assume that this stagnant zone only exists along one flanking side of the flowpath length. If we were to assume symmetric stagnant zones flanking the main flowpath, the retardation effect could be even greater.

If flow channels are narrow as expected, the 1D description of matrix diffusion customarily used in SA calculations is inaccurate and may grossly underestimate the potential radionuclide retardation. For this reason, we consider three main scenarios for radionuclide transport. These are:

1. (Base model) Advective flow coupled with 1D diffusion/sorption within the rock matrix.
2. (Model alternative 1) Advective flow in a narrow channel coupled with 1D diffusion/sorption in the rock matrix plus diffusion into a stagnant zone of limited extent and subsequent 1D diffusion/sorption within the rock matrix.
3. (Model alternative 2) Advective flow in a narrow channel coupled with 2D radial diffusion/sorption in the rock matrix.

Along flowpaths hosted within highly fractured rock there may be large numbers of open although stagnant fractures which intersect the flowpath. It is possible for transported radionuclides to diffuse into these regions and access additional surface area for mass transfer to the rock matrix. In the analysis of transport processes, we can therefore imagine two principal kinds of DAS; that comprising the in-plane stagnant zones and that belonging to incident, intersecting fractures. Since the in-plane DAS by definition follows the same trajectory as the flowpath itself, this is generally the dominant type of DAS. If the intensity of open, stagnant fractures is sufficiently high, however, the additional DAS residing in incident fractures may be substantial and give an additional retardation effect that is not insignificant. The impact of incident fracture DAS is somewhat complicated to describe as the mass fluxes from the different surfaces into the rock matrix will, in many cases, overlap and it is difficult to avoid double counting of the storage capacity of the rock. Further discussions concerning this issue can be found in Appendix I. In order to avoid the possibility of double counting and to improve modelling transparency, we shall not consider this additional effect in the transport calculations presented in this chapter.

For the assumed hydraulic gradients used in the estimation of the flow related transport properties, the flowpaths within the HRD appear to overwhelmingly dominate the aggregate F-factor for transport. Typical F-factors for temperate SA conditions in what we have termed the immediate far field (IFF) part of the HRD are estimated in section 3.6.2 to be on the order of about 10^6 y/m.

Typical F-factors for transport from individual canister positions (i.e. the non-engineered near field, NNF) could be significantly greater than the simplified estimates in section 3.6.1 suggest. Since there are many poorly qualified assumptions contained in the estimates of the F-factor for these initial pathways we do not take any additional credit for their hydrodynamic transport resistance and consider only the F-factors associated with typical flowpaths in the immediate far-field (IFF).

The transport resistance encountered in the gently dipping deformation zones within the HCD probably accounts for only about 1% of the total F-factor for a transport path from the repository to the surface according to the scoping calculations described in section 3.7. For transport via the less transmissive, steeply dipping zones the HCD probably accounts for no more than about 10% of the overall F-factor.

Based upon the above reasoning, we make the assumption that the transport model can be parameterised using data applicable for fractures and minor deformation zones found within the HRD. It is likely that this simplification is quite cautious since the increased hydrogeological and microstructural complexity found in the HCD should, on balance, give rise to substantially greater retardation properties if fully considered in the analysis.

Additionally, since fracture intersection zone (FIZ) conduits are assumed to contribute insignificantly to the overall F-factor for a transport path, we neglect these and only model the in-plane flow channels residing within fractures. It is noted, however, that the increased complexity of the FIZ intersections with possibly large stagnant zones (relative to their dimensions) flanking the main FIZ conduit are likely to make a non-negligible contribution to retardation in spite of their substantially lower flow-wetted surface. Although the calculations presented in this chapter do not directly consider FIZ, some discussion on how solute transport within these features may be modelled is given in Appendix I.

Using the site specific data for background fractures in the HRD at Forsmark implies a rock matrix microstructure featuring an alteration zone with material properties that do not differ significantly from the unaltered rock matrix. Most fracture types are also associated with thin coatings of secondary minerals that typically have enhanced sorption properties as compared with the unaltered rock matrix. Although we do not have diffusivity data for fracture coatings, they are sufficiently thin that they will not have a large impact upon the diffusive properties of the rock for F-factors characteristic of temperate SA conditions. We explore this issue further in section 5.4 by considering what impact fracture coatings may have on transport under the influence of different assumptions concerning their retention properties.

The impact of natural colloids upon retardation properties has not been investigated in this report as it is thought to be unlikely that these will exist in sufficient amounts at repository depth that they would detrimentally affect repository performance during temperate conditions /SKB 2006b/. In scoping calculations presented in Appendix K, it is shown that for the prevailing groundwater conditions at repository depth colloids should have an insignificant impact upon solute transport processes. This is, however, a phenomenon that is more fully investigated within safety assessment where scenarios can be conceived where colloids may have an unfavourable influence upon transport processes.

It has been suggested that the presence of microbial biofilms coating the fracture surfaces may detrimentally influence the retardation properties of the rock. This could occur by way of a reduced sorption capacity of the biofilm as compared to the rock matrix itself /Anderson et al. 2006, 2007/, as well as by way of the presence of microbes obstructing or blocking the micropores of the rock matrix immediately adjacent to the fracture surface /Charbonneau et al. 2006/. This is discussed in more detail in section 5.4.

An additional mechanism that could reduce the effective retardation of transported radionuclides is the presence of significant amounts of strong complexing agents called siderophores which are excreted by bacteria. Bacterial siderophores are strong complexing agents released by certain bacteria, usually under oxidising conditions (i.e. when Fe(III) availability is low) by those bacteria that use the Fe(II/III) redox couple as an oxidant. These complexing agents can also bind certain radionuclides very strongly, resulting in reduced sorption on geological materials.

5.2 Overview of base model with alternatives

In the calculations presented in this chapter we use the model for advective solute transport with matrix diffusion previously described in /Crawford 2006/ for simulations of the base model (BM) and model alternative 1 (MA1). The model is based upon an analytical solution in Laplace space with numerical inversion to obtain the solution in the time plane. The model is generalised to handle solute transport with mass transfer to the rock matrix including an arbitrary number of alteration layers. It also includes the possibility of simulating mass transfer to stagnant zones in the fracture plane with subsequent uptake to the rock matrix. The model can simulate equilibrium or diffusive mass transfer to fracture infilling material (fault gouge and breccia) and it is also feasible to simulate solute transport in features with non-symmetrical matrix properties as may be appropriate for modelling reactivated fractures and deformation zones featuring complex rock matrix microstructures.

For the simulations, the same set of solutes considered in the site investigation laboratory programme are used. These represent a broad range of sorption strengths from mildly sorbing in the case of strontium to strongly sorbing trivalent actinides/lanthanides. As the purpose of these calculations is to estimate typical travel times for solutes of differing sorption strengths, we do not consider radioactive decay. Although specific isotopes are not referred to in these calculations, it should be noted that the transport times calculated for some of the solutes are substantially greater than the half-lives of their radioactive counterparts. In this chapter the neglecting of decay is intentional as our aim is to highlight mechanistic aspects of solute transport relating to the interplay of material properties parameterisation and flow related transport properties at Forsmark. For safety assessment, on the other hand, the inclusion of radioactive decay for single solutes and decay chains for daughter nuclides is central to the estimation of far-field radionuclide release rates. The models presented here can be easily adjusted to simulate decay of single solutes and using the simplifications described by /Neretnieks 2006b/ they can be modified to simulate particular decay chains.

When considering the impact of an in-plane stagnant zone, a key variable is the ratio of diffusive surface area for uptake to the stagnant zone relative to the flow-wetted surface for diffusive uptake directly to the rock matrix. The ratio of diffusive surface area, R_s for a stagnant zone (with an effective aperture, δ_s) flanking the main flow channel is defined as:

$$R_s = \frac{\delta_s f_s}{2W_c} \tag{5-1}$$

For a flowpath featuring a single stagnant zone along 100% of its length, the parameter $f_s = 1$. If the stagnant zone can be assumed to be symmetrical and flanking both sides of the main flow channel, $f_s = 2$. The effective aperture, δ_s of the stagnant zone flanking the main flowpath is assumed to be 10^{-4} m in the analyses presented in this chapter. For a flow channel width of 0.1 m, this gives an R_s value of approximately 5×10^{-3} m^2/m^2 in the case of single stagnant zone. The reader should note that this is chosen purely for the sake of testing the consequences of the assumption of stagnant zones and the "true" aperture of actual stagnant zones may be greater than or less than this assumed value.

Although we do not consider intersecting stagnant fractures in this analysis, it is relevant to note that if these features were to be included, an additional stagnant zone flux term would need to be defined. This would be of most relevance for the HCD where open fractures can occur with sufficient frequency that the additional retardation effect might be non-negligible. More detailed discussion concerning the role of incident fractures can be found in Appendix I.

At very early times (i.e. in the limit as t→0), the diffusion of solute from the stagnant zone to the rock matrix can be neglected. In this case, the diffusive uptake terms can be approximated using the solution by /Crank 1975/ for diffusion into a semi-infinite slab. In the time plane and for a constant concentration boundary condition, the limiting fluxes to the rock matrix and the stagnant zone, respectively can be shown to be:

$$J_m(t) = \frac{C_0 D_e}{\sqrt{\frac{\pi D_e t}{\theta_m + K_{dm}\rho_{bm}}}} \tag{5-2}$$

$$J_s(t : t \to 0) \approx \frac{C_0 D_w}{\sqrt{\pi D_w t}} \tag{5-3}$$

Taking into account the different mass transfer surface areas for the rock matrix and stagnant zones, the overall rate of mass transfer to the stagnant zone relative to the rock matrix is then given by:

$$\frac{R_s J_s}{J_m}(t \to 0) = \frac{R_s\sqrt{D_w}}{\sqrt{D_e(\theta_m + K_{dm}\rho_{bm})}} = \frac{R_s}{\sqrt{F_f(\theta_m + K_{dm}\rho_{bm})}} \tag{5-4}$$

This approximation is useful for checking the results of the numerical models for very early times (section 5.3.2) as well as for interpreting the outcome of tracer tests (see section 6.3).

Simulations of the different model alternatives are made using the previously described Laplace space model (see also Appendix I). The 2D radially symmetric diffusion model is similar to that used for the Base Model (BM), although a different matrix uptake term is used. The modified matrix flux term is based upon a model presented in /Neretnieks 2006a/. This paper also contains a treatment of model alternative 1 (MA1) for a single layered rock matrix which is similar to that described in /Crawford 2006/. For the radial diffusion case (MA2) we make the approximation that a flow channel of limited width, W_c and transport aperture, δ_t can be approximately modelled as a cylinder of equivalent radius, a embedded in the rock /Rasmuson and Neretnieks 1986/. For an in-plane flow channel, the equivalent transport radius can then be shown to be /Johns and Roberts 1991/:

$$a = \frac{W_c + \delta_t}{\pi} \approx \frac{W_c}{\pi} \tag{5-5}$$

At very early times, the results predicted by the base model (BM) and model alternative 2 (MA2) are largely indistinguishable. It is only at later times when the penetration depth is roughly the same as the channel width that the results for the linear and radial cases begin to differ strongly.

5.3 Modelling results

Since sorption K_d values are highly dependent upon pore water compositions which can change significantly over time, simulation results are presented for the three transport model variants (BM, MA1, MA2) considering a range of sorption K_d values. These represent the range of sorption properties from weakly sorbing ($K_d = 10^{-5}$ m^3/kg) to strongly sorbing ($K_d = 1$ m^3/kg). To visualise the results in a enlightening fashion, we first present a series of figures where transport times are plotted against sorption K_d, for an assumed F-factor of 10^6 y/m and a formation factor of 1.6×10^{-5} which is the approximate mean value for rock type 101057 at the Forsmark site based upon *in situ* resistivity measurements (see Appendix H). These plots are made for a set of recovery fractions corresponding to 0.01%, 1%, 10%, and 50% of recovered solute, neglecting radioactive decay and assuming a maximum matrix depth of 2 m. In addition to the recovery time plots, full cumulative residence time distribution curves are given for $K_d = 10^{-4}$, 10^{-2}, and 10^{-1} m^3/kg as well as for a non-sorbing solute ($K_d = 0$) to aid interpretation of retardation mechanisms in the subsequent discussion.

In this chapter we show the results for saline groundwater. Results for fresh, marine, and brine groundwater can be found in Appendix I.

It should be noted that the choice of 2 m matrix penetration depth is purely an arbitrary modelling convenience and should not be taken to indicate a belief that the accessible matrix depth is only 2 m. It may be appropriate in safety assessment, for example, to assume a maximum matrix penetration depth substantially less than the theoretically available penetration depth (which could be many tens of metres) owing to the need to avoid "double counting" of matrix storage capacities for closely spaced flow channels. This is discussed in more detail in section 5.5. It should be clear from the results presented in the following sections that a penetration depth of 2 m is more than enough to provide a very substantial retardation effect for most sorbing radionuclides for the magnitude of the F-factor assumed in the calculations.

5.3.1 Typical transport times under contemporary groundwater conditions

The following figures show results for the BM, MA1, and MA2 transport models assuming saline groundwater chemistry and solute recovery fractions of 0.01%, 1%, 10%, and 50%. Transport times longer than 10^7 y (graduated, blue background shading) are considered to be

of minor interest and are only included here to illustrate the relative scaling of recovery times implied by the modelled retardation processes. In addition, to give an appreciation of the time scales involved, some significant events in Earth's geological history are indicated on the time axis of Figure 5-3. Approximate, illustrative time limits for quantitative and qualitative safety analysis are shown as the red, broken and unbroken, horizontal lines in the figures. These may not necessarily conform to safety assessment time limits considered in SR-Site, although are loosely based upon guidelines contained in /SSI 2005/.

To illustrate the combined impact of K_d uncertainty and model uncertainty for specific solutes, the span of transport times vs. K_d is plotted as a rectangular polygon in the figures. The lower left hand vertex is the transport time for the model giving the fastest breakthrough using the lowest reported K_d value, while the upper right hand vertex corresponds to the transport time for the model giving the slowest breakthrough time using the maximum reported K_d value.

It should be noted that the results presented in Figure 5-3 to Figure 5-6 assume constant groundwater conditions which will not necessarily be the case, particularly over the very long time spans indicated for the more strongly sorbing radionuclides. Since the K_d for specific solutes is often sensitive to changes in groundwater composition, the estimated transport times shown here should be regarded as being merely illustrative.

Provided the groundwater composition is relatively constant, the estimated transport times for the strongly sorbing trivalent Lanthanide-Actinide solutes (e.g. $K_d \geq 0.1$ m^3/kg) are so long that the solutes could be considered, for all practical purposes, immobile. In such cases, colloid and possibly bacterial siderophore transport mechanisms may dominate the release of these nuclides to the biosphere. For naturally occurring colloids, this will be particularly the case if sorption is deemed to be irreversible. In the case of reversible sorption, however, scoping calculations described in Appendix K indicate a negligible effect upon radionuclide transport for the natural colloid concentrations to be found in groundwater at repository depth.

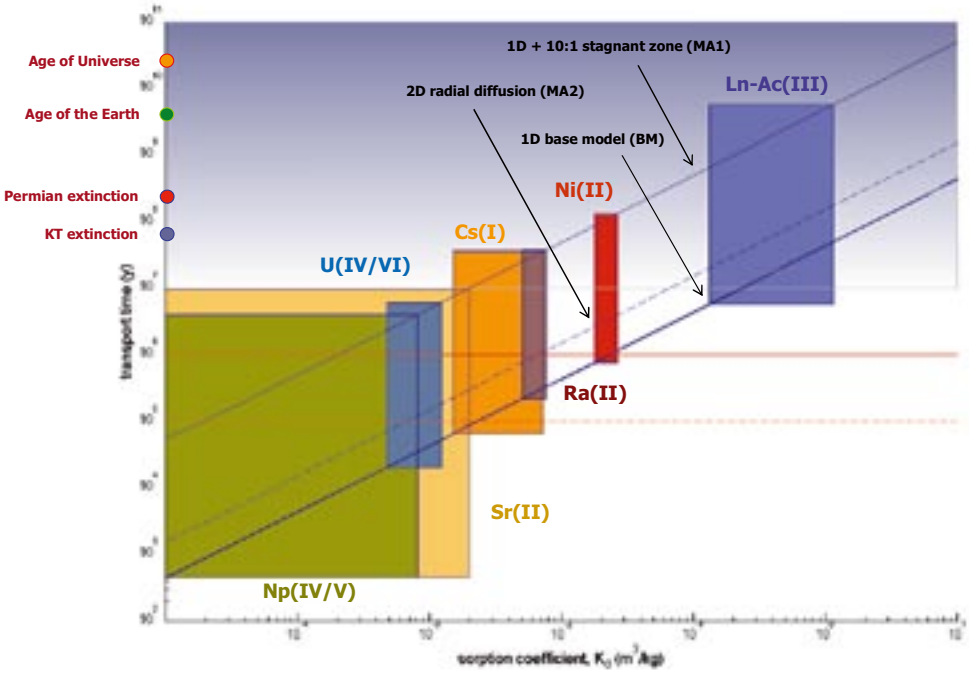

Figure 5-3. *Recovery times for solutes as a function of K_d for a recovery fraction of 0.01%, a fixed F-factor of 10^6 y/m, and formation factor of 1.6×10^{-5} (see text for detailed explanation). As an aid to appreciation of the relative time scales involved, some significant events in Earth's geological history are indicated on the time axis.*

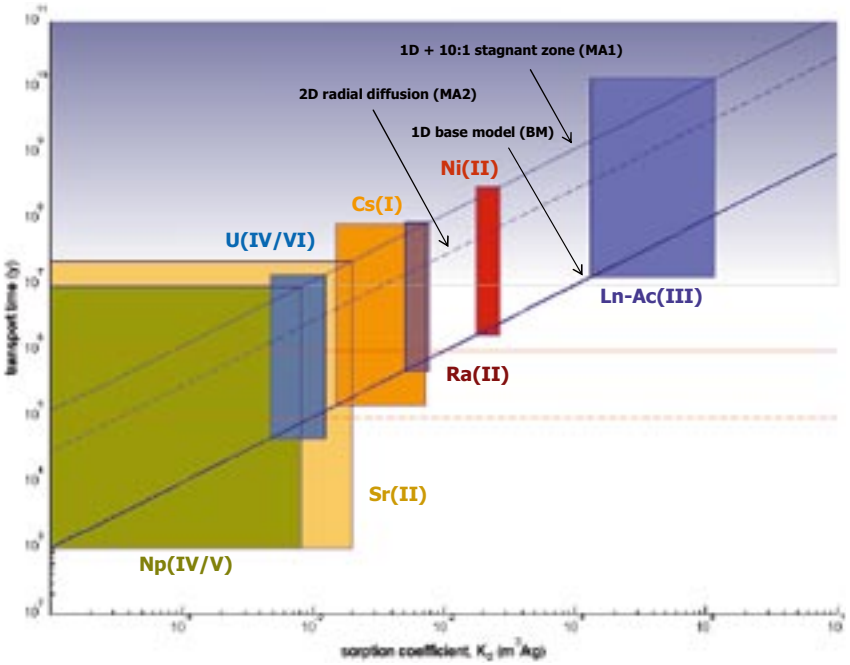

Figure 5-4. *Recovery times for solutes as a function of K_d for a recovery fraction of 1%, a fixed F-factor of 10^6 y/m, and formation factor of 1.6×10^{-5} (see text for detailed explanation).*

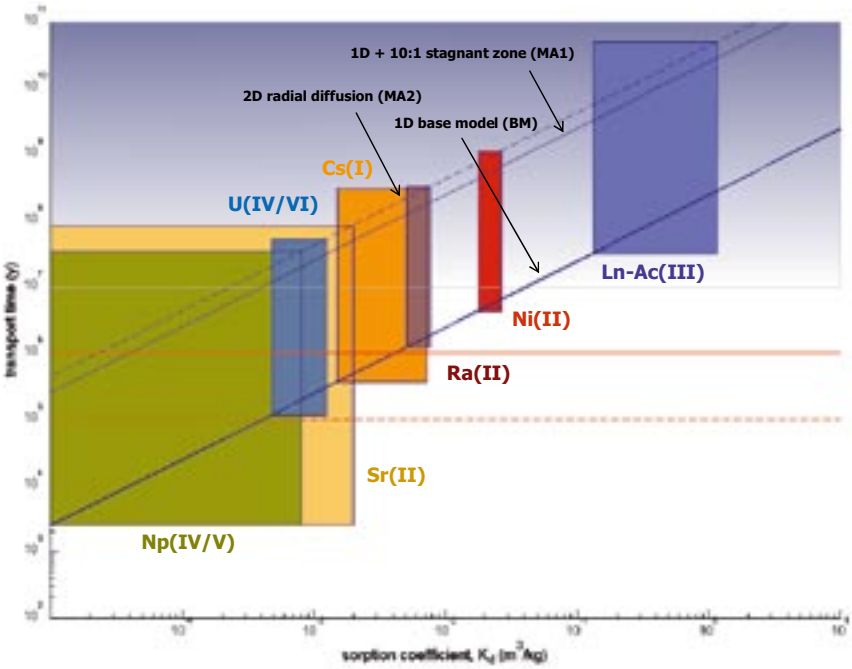

Figure 5-5. *Recovery times for solutes as a function of K_d for a recovery fraction of 10%, a fixed F-factor of 10^6 y/m, and formation factor of 1.6×10^{-5} (see text for detailed explanation).*

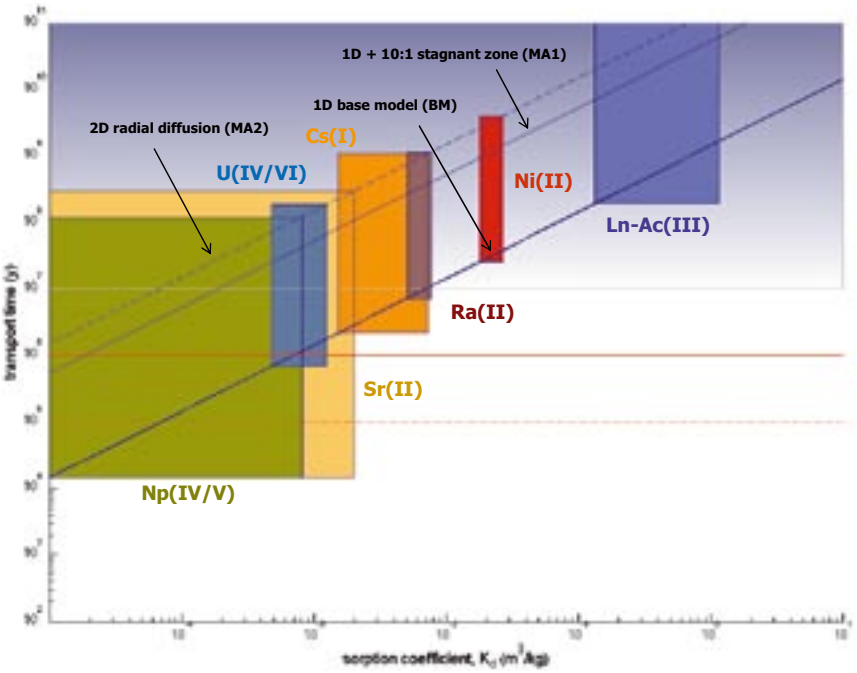

Figure 5-6. *Recovery times for solutes as a function of K_d for a recovery fraction of 50%, a fixed F-factor of 10^6 y/m, and formation factor of 1.6×10^{-5} (see text for detailed explanation).*

Here, by the term colloid we specifically mean "pseudocolloids" formed by the sorption of solutes on naturally occurring colloidal substrates. So-called "true" or "eigencolloids" formed by the microprecipitation of strongly hydrolysed actinides are not considered in the present report although may be relevant for safety assessment.

Bacteria capable of excreting siderophores have been cultivated from deep groundwater samples obtained at the Äspö HRL /Johnsson et al. 2006/, although it is not currently known whether there is a non-negligible background concentration of these complexing agents within the groundwater from repository depth at the Forsmark site (owing to the difficulty of directly identifying these by routine chemical analysis). Given that reducing conditions normally prevail at these depths, however, it is not thought that siderophores should be present in sufficient concentrations to detrimentally impact radionuclide sorption. Investigations at the Äspö HRL have confirmed that these substances are not present in the reducing groundwaters typically found at repository depth /Essén et al. 2007/.

The transport simulation results indicate a large spread in transport times for specific solutes with differing sorption properties. As expected from previous investigations /e.g. Neretnieks and Moreno 2003/ the advective travel time is very small compared with the retarded radionuclide residence time and therefore can be neglected for the radionuclide transport mechanisms considered here.

5.3.2 Residence time distributions for specific sorption strengths

In this section, results are given for the residence time distributions of solutes exhibiting different sorption strengths. Here, we compare the transport properties of typical solutes representing the categories: non-sorbing ($K_d = 0$), weakly sorbing ($K_d = 10^{-4}$), moderately sorbing ($K_d = 10^{-2}$), and strongly sorbing ($K_d = 10^{-1}$).

Non-sorbing solutes

Figure 5-7 shows the cumulative residence time distribution for a solute characterised as non-sorbing (K_d = 0 m³/kg). The following Figure 5-8 contains the same data although plotted on log-log axes to accentuate detail for early breakthrough. For comparison with the recovery times shown in Figure 5-3 to Figure 5-6, the recovery fractions 0.01%, 1%, 10%, and 50% are indicated by horizontal broken lines. Results are given for the case of an infinite rock matrix as well as a rock matrix of limited depth (here taken to be 2 m).

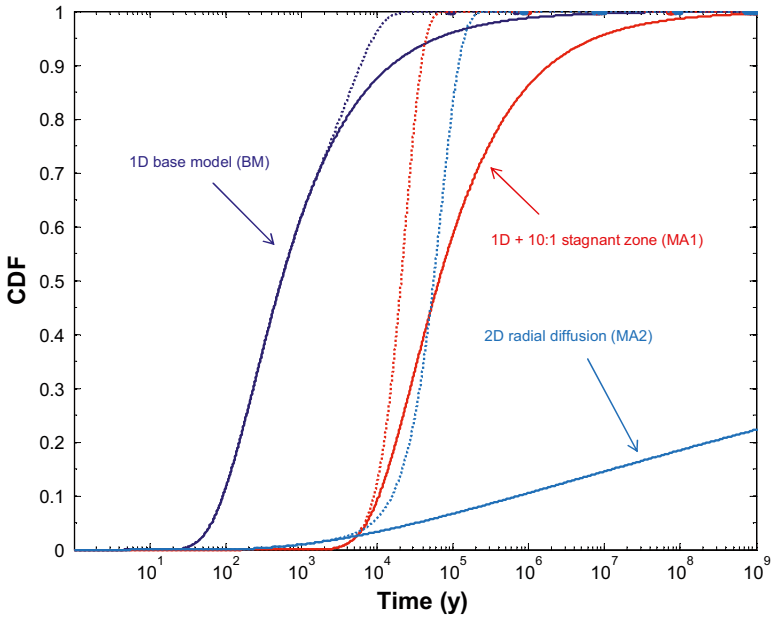

Figure 5-7. *Cumulative residence time distributions for BM, MA1, MA2 transport models for K_d = 0 m³/kg (non-sorbing), a fixed F-factor of 10^6 y/m, and formation factor of 1.6×10^{-5}. Unbroken lines show results for an infinite rock matrix, broken lines show results for a maximum matrix penetration depth of 2 m.*

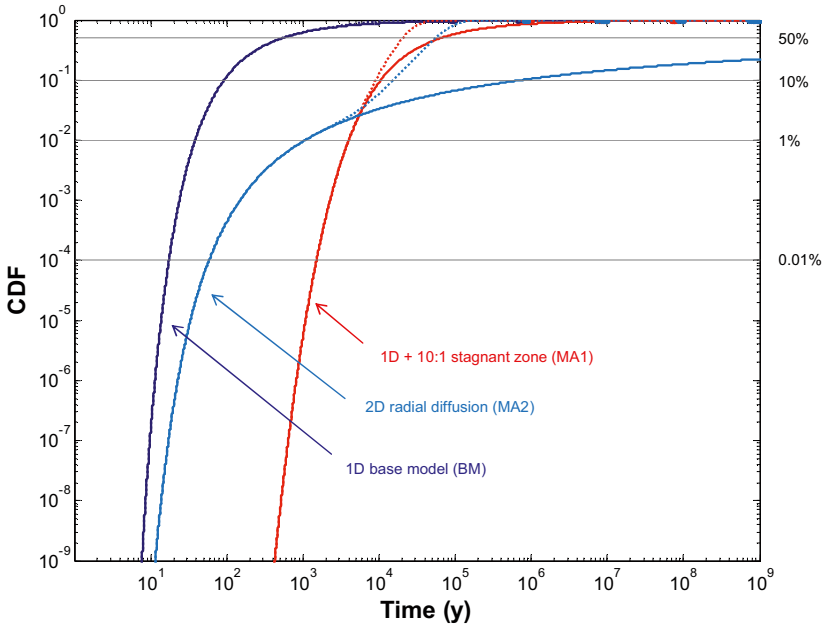

Figure 5-8. *Same results as above, although plotted on log-log axes. Horizontal broken lines indicate recovery fractions of 0.01%, 1%, 10%, and 50%.*

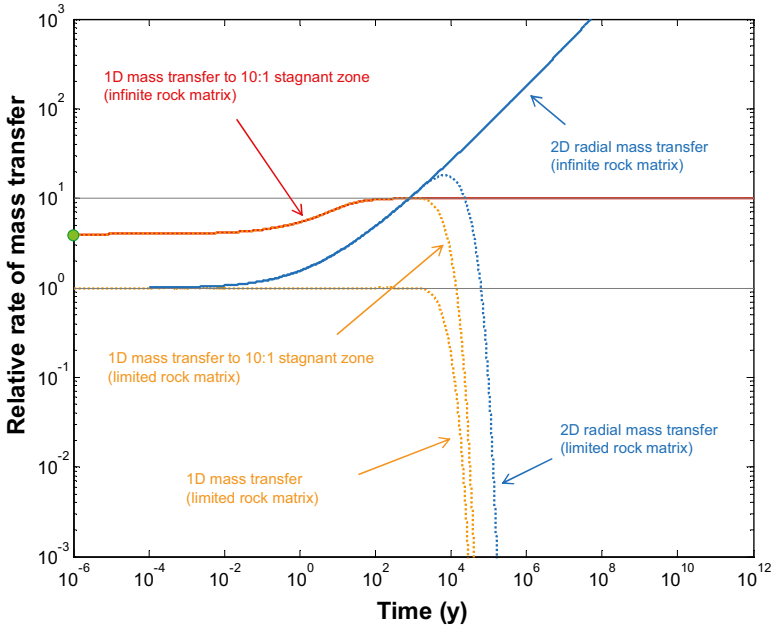

Figure 5-9. *Relative rates of mass transfer as compared to 1D direct uptake to a rock matrix of unlimited depth. The data are for K_d = 0 m^3/kg (non-sorbing) and a formation factor of 1.6×10^{-5}. Unbroken lines show results for an infinite rock matrix, broken lines show results for a maximum matrix penetration depth of 2 m. The green marker indicates limiting mass transfer rate to stagnant zone calculated using Equation 5-4.*

Figure 5-9 shows the rate of solute mass transfer for different systems relative to that calculated for 1D direct uptake to the rock matrix from a flow channel. Data are shown for the uptake rate to the stagnant zone with subsequent mass transfer as well as for 2D radial mass transfer.

For the assumed flow channel width and effective stagnant zone aperture, the initial (i.e. as $t\rightarrow0$) relative rate of mass transfer to the stagnant zone is given by Equation 5-4. For a non-sorbing solute, the limiting relative rate of mass transfer in this particular system is calculated to be 3.98 (indicated by the green marker in Figure 5-9). This means that for this particular solute, the rate of mass transfer to the stagnant zone is initially 3.98 times the rate of mass transfer directly to the rock matrix. As can be seen from the Figure, the location of the green marker agrees very closely with the limiting rate of mass transfer at early times predicted by the full numerical simulation curves.

As diffusion profiles start to develop within the rock matrix, the relative rate of mass transfer to the stagnant zone increases until it reaches its theoretical maximum where diffusive equilibrium can be assumed throughout the stagnant zone (upper, horizontal broken line). The lower, horizontal broken line indicates the limiting relative rate of mass transfer to the rock matrix from the main flow channel (which by definition is unity).

Weakly sorbing solutes

Figure 5-10 shows the cumulative residence time distribution for a solute characterised as weakly sorbing ($K_d = 10^{-4}$ m^3/kg). The following Figure 5-11 contains the same data although plotted on log-log axes to accentuate detail for early breakthrough. For comparison with the recovery times shown in Figure 5-3 to Figure 5-6, the recovery fractions 0.01%, 1%, 10%, and 50% are indicated by horizontal broken lines. Results are given for the case of an infinite rock matrix as well as a rock matrix of limited depth (here taken to be 2 m).

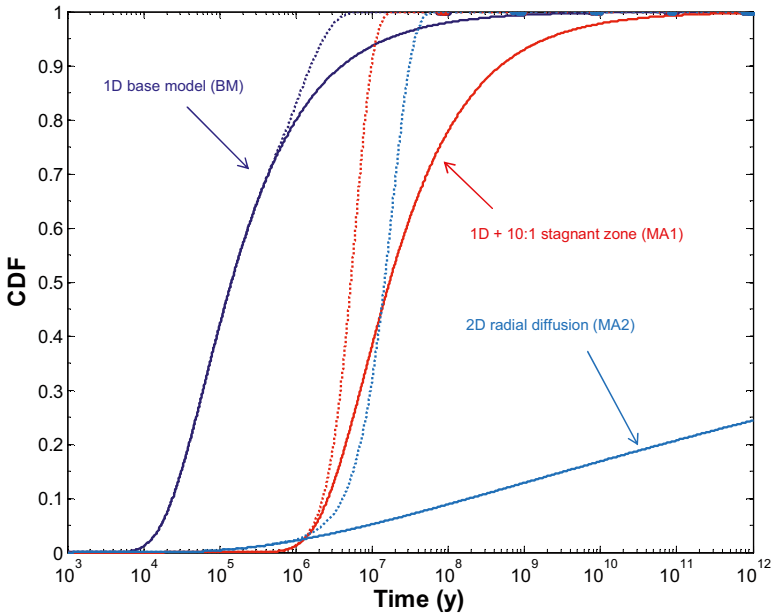

Figure 5-10. *Cumulative residence time distributions for BM, MA1, MA2 transport models for $K_d = 10^{-4}$ m³/kg (weakly-sorbing), a fixed F-factor of 10^6 y/m, and formation factor of 1.6×10^{-5}. Unbroken lines show results for an infinite rock matrix, broken lines show results for a maximum matrix penetration depth of 2 m.*

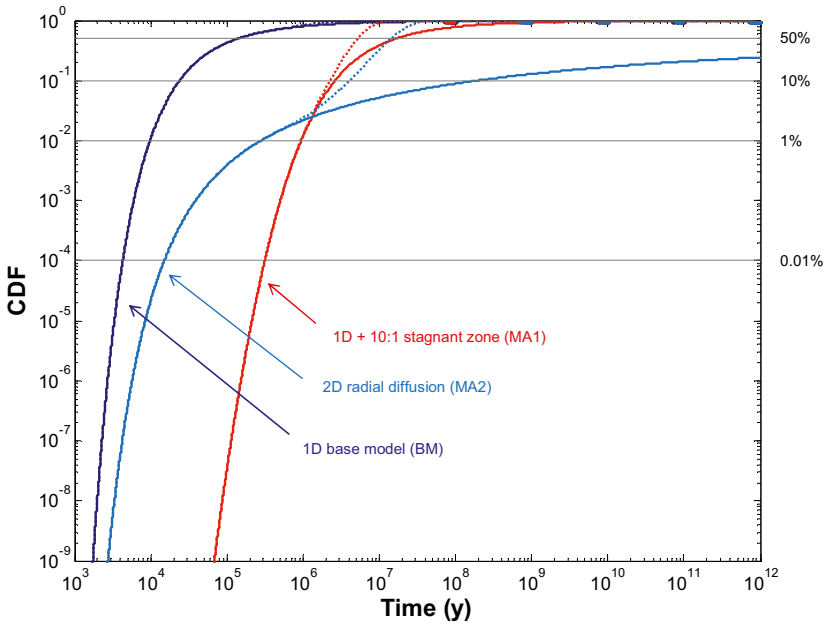

Figure 5-11. *Same results as above, although plotted on log-log axes. Horizontal broken lines indicate recovery fractions of 0.01%, 1%, 10%, and 50%.*

Figure 5-12 shows the rate of solute mass transfer for different systems relative to that calculated for 1D direct uptake to the rock matrix from a flow channel. Data are shown for the uptake rate to the stagnant zone with subsequent mass transfer as well as for 2D radial mass transfer.

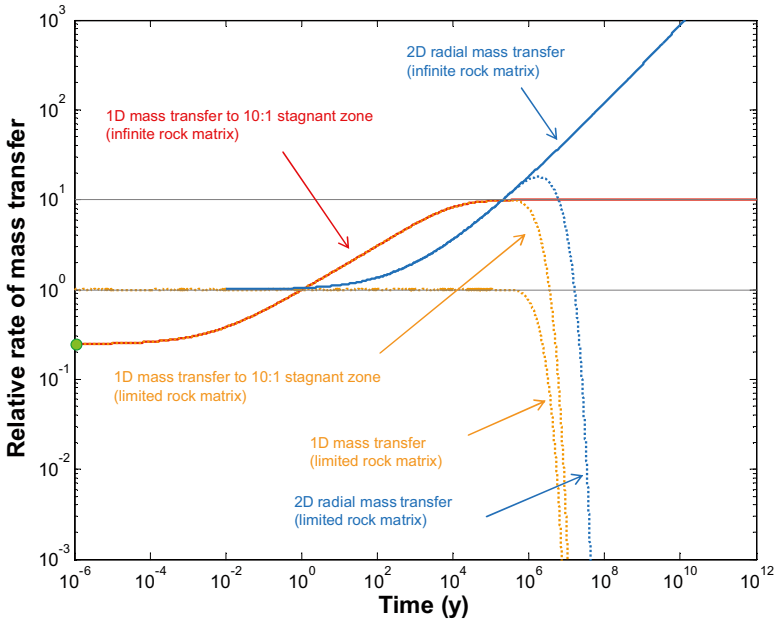

Figure 5-12. *Relative rates of mass transfer as compared to 1D direct uptake to a rock matrix of unlimited depth. The data are for $K_d = 10^{-4}$ m^3/kg (weakly-sorbing) and a formation factor of 1.6×10^{-5}. Unbroken lines show results for an infinite rock matrix, broken lines show results for a maximum matrix penetration depth of 2 m. The green marker indicates limiting mass transfer rate to stagnant zone calculated using Equation 5-4.*

For a weakly-sorbing solute, the limiting relative rate of mass transfer in this particular system is calculated using Equation 5-4 to be 0.25 (indicated by the green marker). This means that the initial rate of mass transfer to the stagnant zone is roughly 25% of the rate of mass transfer directly to the rock matrix. As previously, the location of the green marker coincides closely with the numerically simulated curves shown in the same figure.

As diffusion profiles start to develop within the rock matrix, the relative rate of mass transfer to the stagnant zone increases until it reaches its theoretical maximum where diffusive equilibrium can be assumed throughout the stagnant zone (upper, horizontal broken line). The lower, horizontal broken line indicates the limiting relative rate of mass transfer to the rock matrix from the main flow channel (which by definition is unity).

Moderately sorbing solutes

Figure 5-13 shows the cumulative residence time distribution for a solute characterised as moderately sorbing ($K_d = 10^{-2}$ m^3/kg). The following Figure 5-14 contains the same data although plotted on log-log axes to accentuate detail for early breakthrough. For comparison with the recovery times shown in Figure 5-3 to Figure 5-6, the recovery fractions 0.01%, 1%, 10%, and 50% are indicated by horizontal broken lines. Results are given for the case of an infinite rock matrix as well as a rock matrix of limited depth (here taken to be 2 m).

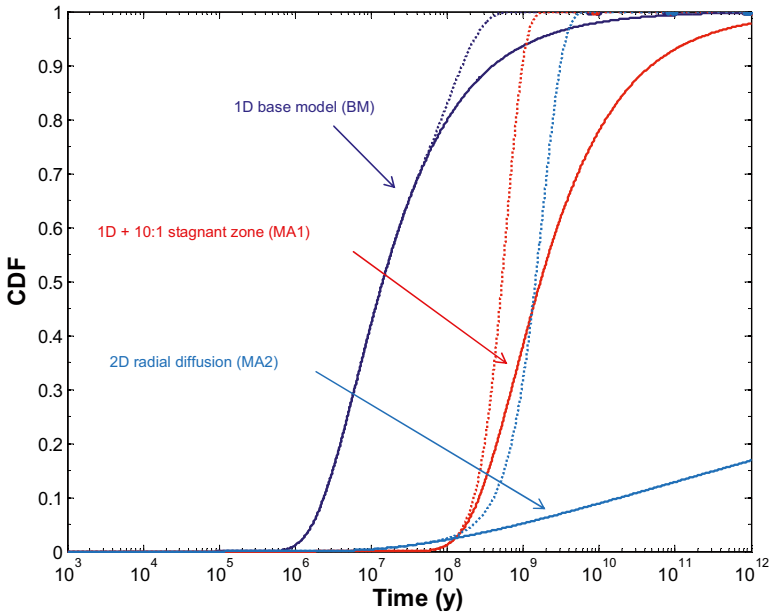

Figure 5-13. *Cumulative residence time distributions for BM, MA1, MA2 transport models for $K_d = 10^{-2}$ m³/kg (moderately-sorbing), a fixed F-factor of 10^6 y/m, and formation factor of 1.6×10^{-5}. Unbroken lines show results for an infinite rock matrix, broken lines show results for a maximum matrix penetration depth of 2 m.*

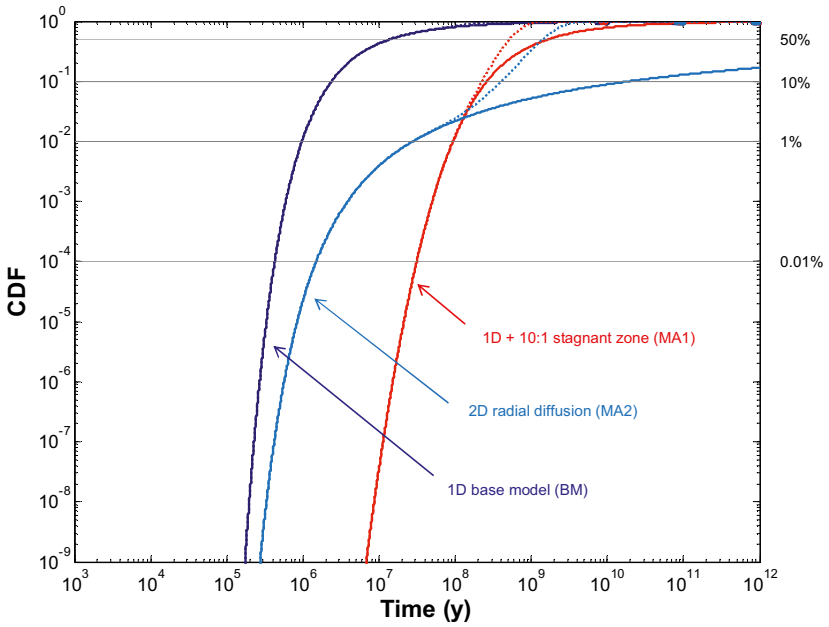

Figure 5-14. *Same results as above, although plotted on log-log axes. Horizontal broken lines indicate recovery fractions of 0.01%, 1%, 10%, and 50%.*

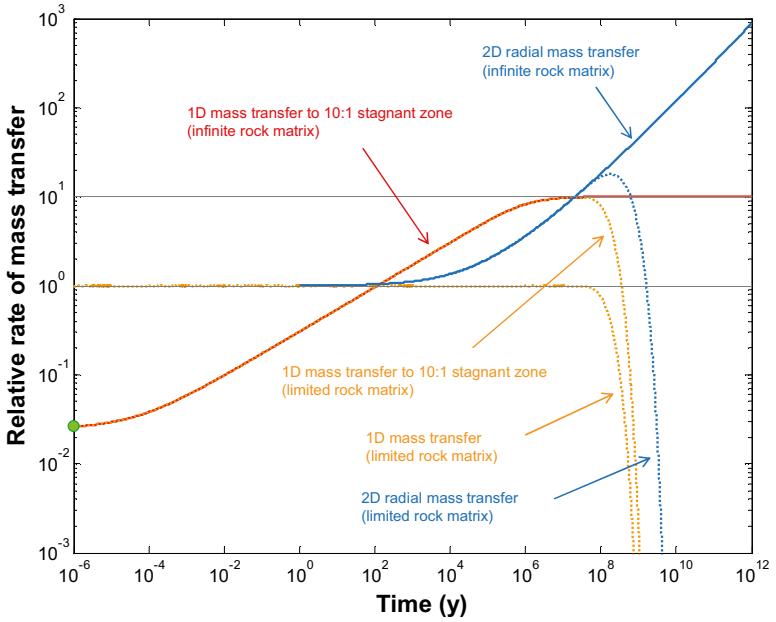

Figure 5-15. *Relative rates of mass transfer as compared to 1D direct uptake to a rock matrix of unlimited depth. The data are for $K_d = 10^{-2}$ m^3/kg (moderately-sorbing) and a formation factor of 1.6×10^{-5}. Unbroken lines show results for an infinite rock matrix, broken lines show results for a maximum matrix penetration depth of 2 m. The green marker indicates limiting mass transfer rate to stagnant zone calculated using Equation 5-4.*

Figure 5-15 shows the rate of solute mass transfer for different systems relative to that calculated for 1D direct uptake to the rock matrix from a flow channel. Data are shown for the uptake rate to the stagnant zone with subsequent mass transfer as well as for 2D radial mass transfer.

For a moderately-sorbing solute, the limiting relative rate of mass transfer in this particular system is calculated using Equation 5-4 to be 2.5×10^{-2} (indicated by the green marker). In this case, the initial rate of mass transfer to the stagnant zone is less than 2.5% of the rate of mass transfer directly to the rock matrix.

As diffusion profiles start to develop within the rock matrix, the relative rate of mass transfer to the stagnant zone increases until it reaches its theoretical maximum where diffusive equilibrium can be assumed throughout the stagnant zone (upper, horizontal broken line). The lower, horizontal broken line indicates the limiting relative rate of mass transfer to the rock matrix from the main flow channel (which by definition is unity).

Strongly sorbing solutes

Figure 5-16 shows the cumulative residence time distribution for a solute characterised as strongly sorbing ($K_d = 10^{-1}$ m^3/kg). The following Figure 5-17 contains the same data although plotted on log-log axes to accentuate detail for early breakthrough. For comparison with the recovery times shown in Figure 5-3 to Figure 5-6, the recovery fractions 0.01%, 1%, 10%, and 50% are indicated by horizontal broken lines. Results are given for the case of an infinite rock matrix as well as a rock matrix of limited depth (here taken to be 2 m).

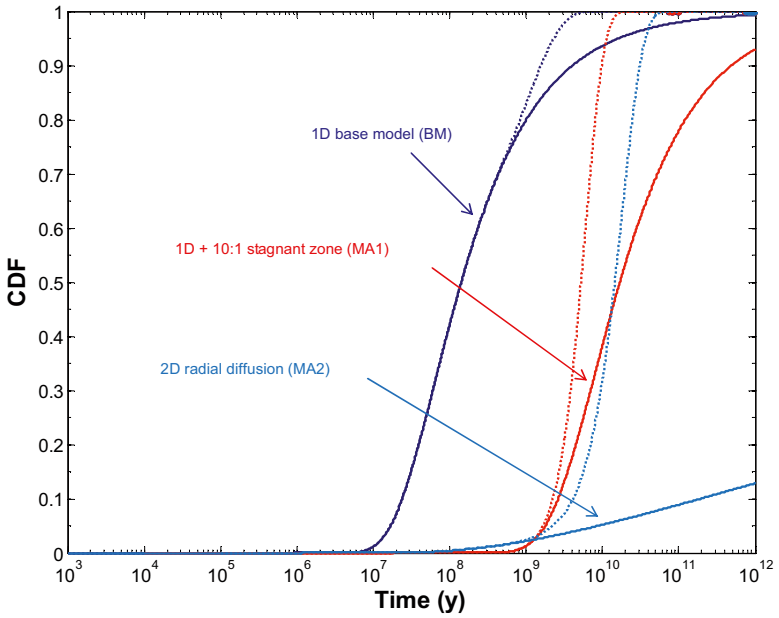

Figure 5-16. *Cumulative residence time distributions for BM, MA1, MA2 transport models for $K_d = 10^{-1}$ m^3/kg (strongly-sorbing), a fixed F-factor of 10^6 y/m, and formation factor of 1.6×10^{-5}. Unbroken lines show results for an infinite rock matrix, broken lines show results for a maximum matrix penetration depth of 2 m.*

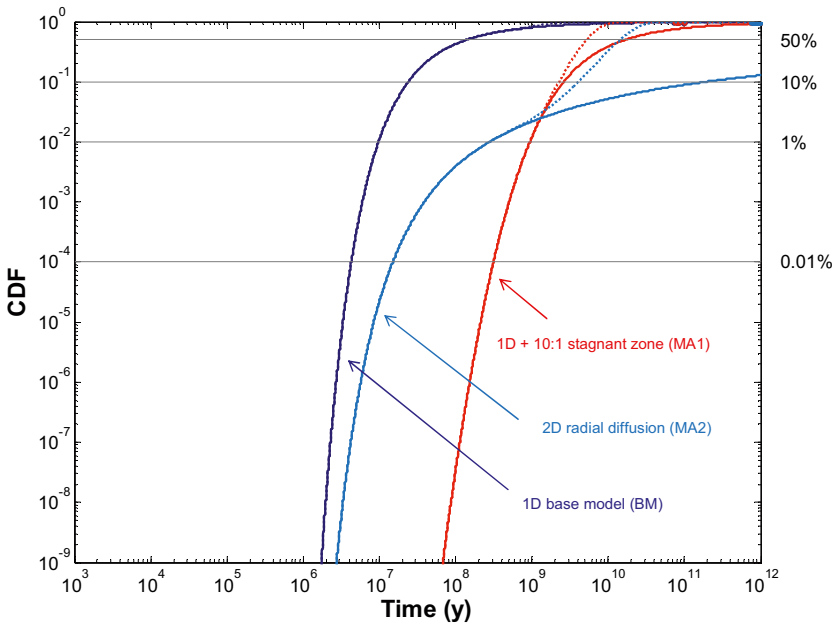

Figure 5-17. *Same results as above, although plotted on log-log axes. Horizontal broken lines indicate recovery fractions of 0.01%, 1%, 10%, and 50%.*

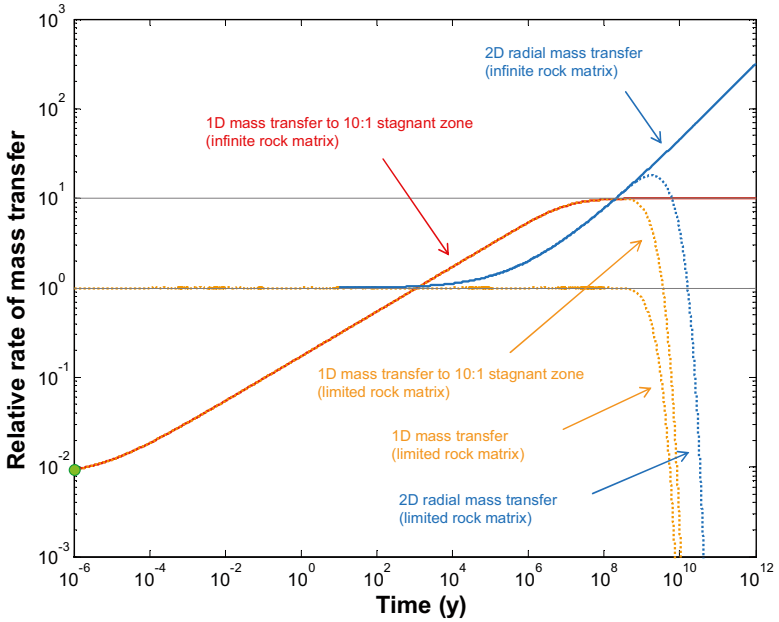

Figure 5-18. *Relative rates of mass transfer as compared to 1D direct uptake to a rock matrix of unlimited depth. The data are for $K_d = 10^{-1}$ m³/kg (strongly-sorbing) and a formation factor of 1.6×10^{-5}. Unbroken lines show results for an infinite rock matrix, broken lines show results for a maximum matrix penetration depth of 2 m. The green marker indicates limiting mass transfer rate to stagnant zone calculated using Equation 5-4.*

Figure 5-18 shows the rate of solute mass transfer for different systems relative to that calculated for 1D direct uptake to the rock matrix from a flow channel. Data are shown for the uptake rate to the stagnant zone with subsequent mass transfer as well as for 2D radial mass transfer.

For a strongly sorbing solute, the limiting relative rate of mass transfer in this particular system is calculated using Equation 5-4 to be 8×10^{-3} (green marker). The location of the green marker agrees to a high degree of accuracy with the numerically simulated curves, although a small discrepancy can be seen owing to the assumption that the subsequent diffusion to the rock matrix from the stagnant zone can be initially neglected.

As diffusion profiles start to develop within the rock matrix, the relative rate of mass transfer to the stagnant zone increases until it reaches its theoretical maximum where diffusive equilibrium can be assumed throughout the stagnant zone (upper, horizontal broken line). The lower, horizontal broken line indicates the limiting relative rate of mass transfer to the rock matrix from the main flow channel (which by definition is unity).

5.4 Impact of fracture coatings and biofilms

Although a small proportion of fractures do not have identifiable coatings, most fracture surfaces are thought to be associated with secondary mineral coatings of various kinds with a thickness of typically between 0.1–1 mm. The measurement data obtained in the laboratory programme and described in Chapter 4 suggests that these coatings, for the most part, have increased sorptivity and probably increased porosity as compared with the rock matrix. Owing to the difficulty of obtaining representative samples, however, there is no data concerning the effective diffusivity of these coatings. It is likely in many cases that the friable nature of these coatings may result in very high apparent diffusivities, which if considered together with the sorptivity data would suggest substantially improved retention properties compared to the rock

matrix. Many of the fractures at repository depth at Forsmark, however, feature chlorite coatings with very smooth and glossy textures. This hints at the possibility that slow shear movement of fracture surface over very long times could potentially "smooth out" the layers of clay mineral lamellae in such a way that they block the underlying rock matrix pores, thus decreasing the effective diffusivity of the surface coating relative to the rock matrix. It is also conceivable that paleo-oxidation processes may have resulted in the precipitation of ferric oxyhydroxides in the matrix pores very close to fracture surfaces also reducing the effective diffusivity.

If we make the assumption of a 10 times reduced sorptivity and diffusivity within the fracture coating, it is possible to calculate the residence time distribution of a solute using the extended transport model presented in /Crawford 2006/ which explicitly accounts for diffusion in a multi-layered rock matrix. The results of this analysis are shown in Figure 5-19 assuming a fracture coating thickness of 1 mm and a moderately sorbing tracer ($K_d = 10^{-2}$ m^3/kg). Although results are only given for a moderately sorbing tracer it can be shown that the simulated behaviour is general for all K_d values and the residence time distribution of the solute is influenced in a proportional manner.

At this time we do not have an extended model for the more complex, multilayer radial diffusion problem and therefore we only present results for the BM and MA1 transport models. The interpretation of the results, however, should apply equally well to the radial diffusion case as the thickness of the fracture coating is substantially less than typical flow channel widths and therefore radial diffusion will have a negligible impact upon the residence time distribution at very early times.

The reverse case of a 10 times increased sorptivity and diffusivity within the fracture coating is shown in Figure 5-20 for the same fracture coating thickness.

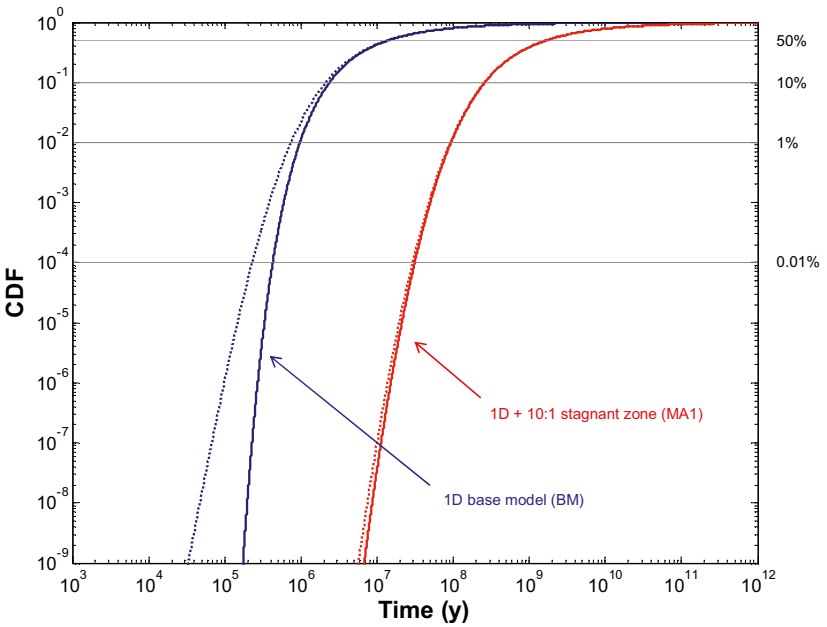

Figure 5-19. *Cumulative residence time distributions for BM and MA1 transport models for $K_d = 10^{-2}$ m^3/kg (moderately-sorbing), a fixed F-factor of 10^6 y/m, and formation factor of 1.6×10^{-5}. Unbroken lines show results for a rock matrix without fracture coating, broken lines show results for a 1 mm thick fracture coating with 10 times decreased sorptivity and effective diffusivity.*

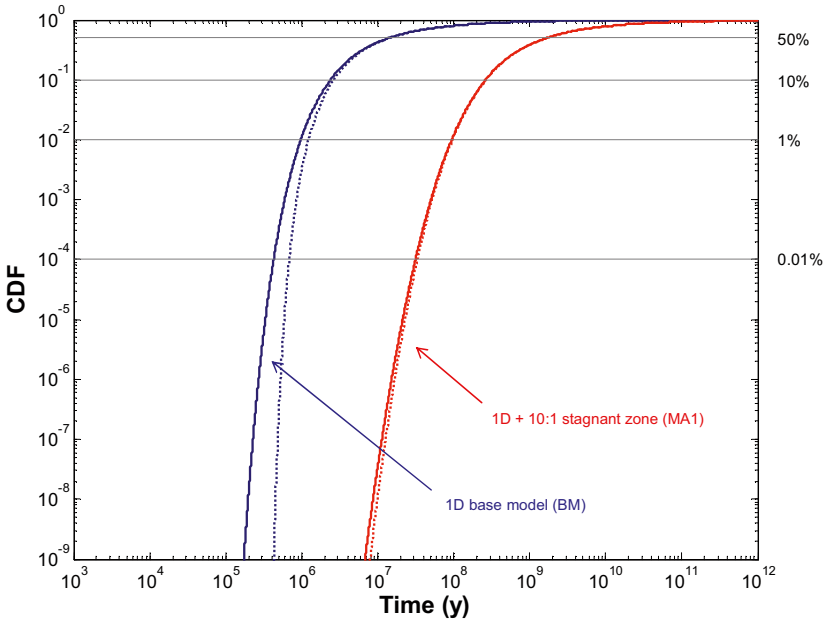

Figure 5-20. *Cumulative residence time distributions for BM and MA1 transport models for $K_d = 10^{-2}$ m³/kg (moderately-sorbing), a fixed F-factor of 10^6 y/m, and formation factor of 1.6×10^{-5}. Unbroken lines show results for a rock matrix without fracture coating, broken lines show results for a 1 mm thick fracture coating with 10 times increased sorptivity and effective diffusivity.*

As can be seen from the figures above, the presence of a 1 mm fracture coating has little impact upon the residence time distribution at later times and the effect is mostly seen for very early solute breakthrough. The retention properties of the fracture coating can be assessed by comparison of the material properties group, or *MPG* for the fracture coating as compared to the unaltered rock. The material properties group is defined as:

$$MPG = \sqrt{D_e\left(\theta_m + K_d\rho_b\right)} \qquad (5\text{-}6)$$

Although the *MPG* does not always uniquely specify the retention properties of the rock, it is still a good qualitative indicator of retention potential. Generally, a fracture coating with decreased *MPG* relative to the rock matrix gives slightly faster breakthrough for the leading edge of the solute residence time distribution, while a fracture coating with enhanced *MPG* gives slightly more retarded breakthrough. Given the very large variations in diffusivity/sorptivity considered here and the relatively thick fracture coating assumed for the calculation, the presence of a fracture coating should have an insignificant impact upon solute residence time distributions calculated under safety assessment conditions.

Although probably not important for safety assessment, it is noted that the presence or absence of a fracture coating is likely to have a large impact upon tracer test results owing to the limited solute penetration depth typically achieved in such experiments. This is discussed in more detail in section 6.3 where the results of field scale tracer tests carried out at Forsmark are analysed and interpreted.

Figure 5-21 and Figure 5-22, show the rate of mass transfer to the stagnant zone relative to the rock matrix in model variant MA1 for a moderately sorbing and non-sorbing solute, respectively. In Figure 5-21, the relative rate of mass flux at very early times cannot be always calculated for the full 2-layer matrix formulation owing to numerical problems involving the Laplace inversion. This has been previously discussed in /Crawford 2006/. The extrapolated broken curves, however, are based upon a single layer model assuming material properties of the fracture coating and can be seen to exactly match up with the full 2-layer formulation for contact times on the order of 0.01 y.

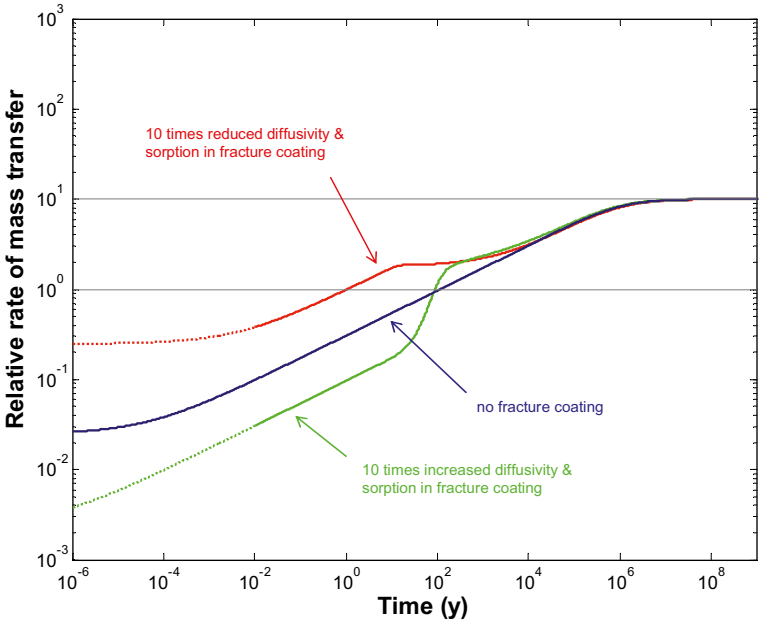

Figure 5-21. *Relative rates of mass transfer to the stagnant zone as compared to 1D direct uptake to a rock matrix of unlimited depth. The data are for $K_d = 10^{-2}$ m³/kg (moderately-sorbing) and a formation factor of 1.6×10^{-5}. Modelling results are shown for the case of no fracture coating as well as a 1 mm thick fracture coating with 10 times increased/decreased sorptivity and diffusivity relative to the rock matrix.*

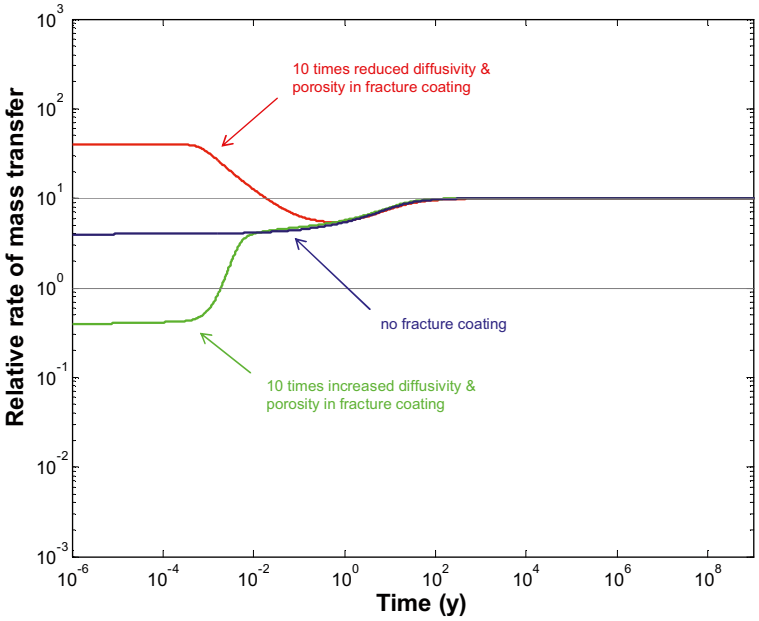

Figure 5-22. *Relative rates of mass transfer to the stagnant zone as compared to 1D direct uptake to a rock matrix of unlimited depth. The data are for $K_d = 0$ m³/kg (non-sorbing) and a formation factor of 1.6×10^{-5}. Modelling results are shown for the case of no fracture coating as well as a 1 mm thick fracture coating with 10 times increased/decreased storage porosity and diffusivity relative to the rock matrix.*

It is interesting to note that the asymptotic rate of mass transfer to the stagnant zone agrees with that predicted by Equation 5-4, assuming the fracture coating to be effectively infinite in depth over the timescale of the tracer test. This feature may be of some importance for the interpretation of field scale tracer tests as is discussed later in Chapter 6.

The possibility of the existence of biofilms has also been raised in section 5.1. Microbial biofilms in fractured rock are generally thought to consist of monolayers of bacterial cells embedded in thin, extracellular polysaccharidal matrices. Some studies have suggested that biofilms have reduced sorptivity for certain radionuclides of importance, although increased sorptivity for others /Anderson et al. 2006, 2007/. Measurement of the diffusive properties of biofilms has also proven difficult owing to the very small effects measured in laboratory experiments and non-uniqueness of modelling interpretations /Charbonneau et al. 2006/. Such biofilms could exist on the external surfaces of the fractures themselves as well as within the macro-pore space of the first few μm of the rock matrix. According to the literature /e.g. Stewart 1998/, the diffusivity of solutes in biofilms is relatively high (close to that for water) since they consist of sparsely distributed cells embedded in the volumetrically much larger extracellular polysaccharidal matrix. Although some reductions in sorptivity have been reported for biofilms in the references above, the thickness of biofilms is thought to be sufficiently small that this would not have a great impact upon the transport properties along a flowpath.

It is thought to be unlikely that microbes can exist within pores smaller than themselves which would restrict such growth to pore sizes greater than ~ 1μm /Pedersen and Karlsson 1995/. Whether microbes present in small pores would block diffusion is not known since this depends upon the extent to which they fill the pore space and whether the limited space is conducive to respiration and growth. It is thought, however, that ionic substances are excluded from the cells themselves /Stewart 1998/ which raises the theoretical possibility for some pore clogging to occur.

It is not clear what thickness such films could reach under normal growth conditions at repository depth in Forsmark as this is strongly dependent upon the availability of limiting nutrients and electron receptors. It is also not generally feasible to ascertain the presence or absence of biofilms from surface based site investigations, so we have chosen to handle this uncertainty by way of scoping calculations. Further work may need to be done, however, to establish the role of pore clogging by individual microbes during the construction phase of the repository.

Since monolayer colonies seem to be the norm, a biofilm thickness of 1 μm to perhaps a few tens of μm is probably not an unreasonable assumption for scoping calculations. If the same calculations are carried out as shown in Figure 5-19 and Figure 5-20 although for a biofilm thickness of 100 μm, no significant effect is seen. For the magnitude of F-factors considered in these calculations, it is therefore seems acceptable to disregard the impact of biofilms upon solute transport in safety analysis insofar as they might affect diffusive uptake to the rock matrix.

5.5 Discussion

The transport simulation results presented in section 5.3 indicate a large spread in transport times for specific solutes with differing sorption properties. Generally, the transport time for a solute can be shown to be proportional to both its K_d value and the square of the F-factor for the flowpath along which it is transported for a given effective matrix diffusivity. A 10 times increased K_d value therefore translates into a 10 times increase in the transport time. On the other hand, increasing the F-factor for a flowpath by a factor of 10 gives a 100 times increased transport time.

The range of variability of measured K_d values for specific solutes is about 1–2 orders of magnitude. Some solutes such as Ra(II) and Ni(II) have reduced ranges of apparent variability due to the lower numbers of samples. Other solutes such as Sr(II) have poorly constrained lower

K_d bounds owing to their generally weak sorption and relatively high measurement limits. Np and U are a special case owing to their sensitivity to redox conditions and the possibility that fully reducing conditions may not have been achieved in the laboratory. As already discussed in Chapter 4, this means that the lower measurement limits for U and Np may be biased by the presence of oxidised forms which may not necessarily be present under repository conditions at depth.

Additional variability in estimated transport times follows if further consideration is also given to the different assumptions made during transport modelling. The three different models presented in this chapter (BM, MA1, and MA2) represent hypothetical explorations of the consequences of some different modelling assumptions. It is not clear whether the assumption of a 10:1 in-plane stagnant zone in model alternative, MA1 is a reasonable estimate of the average stagnant zone width potentially existing along typical flowpaths within the rock. If the assumption is correct, this would give a factor of 121 increased transport time compared to the base case scenario (BM) lacking stagnant zones. The results for the MA1 model variant also suggest that at safety assessment timescales and for the F-factor considered (10^6 y/m), diffusion within the stagnant zone occurs sufficiently fast relative to the transport time that concentration equilibrium can be assumed between the main flow channel and the stagnant zone for most conceivable flow channel and stagnant zone widths.

If concentration equilibrium can be assumed as described above, it is not necessary to simulate the full problem involving diffusion into the stagnant zones. For a stagnant zone with a 10:1 width ratio it is sufficient to increase the flow-wetted surface of the channel by a factor of 11 for the same flowrate to obtain largely identical results. It is important to note that although this surface area is not strictly "flow-wetted surface" it is diffusion accessible on the time scale of transport. If roughly symmetric 10:1 stagnant zones exist on either side of the main flow channel, the total diffusion accessible surface area would be 21 times that of the flow channel, thus giving an overall increase in transport time of 441. A direct consequence of this observation is that the transport aperture, δ_s and mass transfer surface area ratio, R_s can be neglected in safety assessment and the effect approximated by incorporating the additional diffusion accessible surface into the flow-wetted surface without introducing significant errors for most of the residence time distribution envelope. This simplification is not valid for very short times as the advectively transported solute will not have had sufficient time to diffuse fully into the stagnant zone. The residence time distribution for the MA1 case therefore converges towards that for the BM case at very short timescales, suggesting that the transport time for the very first solute arrival is given correctly by the standard diffusion model (BM).

The simulation results are general for a given stagnant zone to flow channel width ratio and same hydraulic aperture. The transport time estimated for a 1 cm wide flow channel with a 10 cm wide stagnant zone, for example, is the same as for a 10 cm wide flow channel and 1 m wide stagnant zone, provided diffusive equilibrium is attained throughout the stagnant zone over the characteristic timescale of transport. Simulations show this to be a reasonable assumption for flow channels with width of up to about 20–30 cm and an F-factor of 10^6 y/m, although some deviation occurs for larger flow channel widths (or for lower F-factors). The deviation is greatest for very early solute breakthrough fractions. In such cases, the full diffusive formulation of the stagnant zone problem needs to be solved to obtain accurate results for the residence time distribution.

When radial diffusion from a flow channel of limited width is considered, the shape of the residence time distribution curve is very different to the base case model, BM or model alternative, MA1. At very early times (i.e. for low solute recovery fractions), the residence time distribution converges towards the base case model. In the limit as the recovery fraction approaches zero, the 1D and 2D radial formulations are indistinguishable. At later times when the effective solute penetration depth is on the order of the flow channel width or greater, the deviation becomes more apparent. The BM and MA2 models diverge strongly for recovery fractions in excess of 0.01%. It is important to note, however, that due to the much longer transport times associated with the MA1 and MA2 transport models, careful consideration of penetration depths must be

made, particularly for the radial diffusion case (MA2). In these cases, the transport times are sufficiently long that saturation to a matrix depth of 2 m is achieved relatively early in the residence time distribution curve (noting that by "early" we are speaking in terms of the recovery fraction rather than the transport time).

Although in this modelling work we make a strict demarcation between flowing and stagnant water volumes, in reality there will be a heterogeneous distribution of flow across fracture surfaces with variations in local advective velocities possibly spanning some orders of magnitude. In this work we operationally define flow channels to be pathways where "most flow" occurs. Under extreme in-plane flow channelling conditions with large portions of the fracture closed due to surface asperity contact it may be possible to find sparse flow channels and large regions of the fracture with stagnant water. For less extreme flow channelling situations, flow channels may occur with a greater spatial frequency, although there will still be large variations in the magnitude of the flows and possibly regions in between the channels that are for all practical purposes stagnant although still could be considered to be flowing.

Previous investigations /e.g. Painter 2006/ have suggested that the neglecting of heterogeneity on the level of single fractures may not have a large impact on solute transport as it is the fracture to fracture variability that has the largest impact upon the effective hydrodynamic resistance (F-factor) for the system and consequently also for solute transport times. This, however, is only true if diffusion between water volumes within the heterogeneous flow region is neglected (in the current discussion we refer to this as transverse diffusion).

As a general principle, flow will tend to seek out the path of least hydraulic resistance through a fracture and avoid low transmissive regions. In the case where there is no diffusive mixing between flow channels and stagnant regions, most of the solute will also follow these fast and possibly narrow flowpaths. If transverse diffusion is considered, however, this will result in a net transfer of solute from the main flowpaths to low velocity or stagnant regions of the fracture where additional interaction with the rock matrix can occur. This is mechanistically distinct from the notion of hydrodynamic transverse dispersive mixing as investigated by /Dershowitz et al. 2004/ which is an advective construct and scales differently to safety assessment timescales. It also differs from standard modelling approaches involving particle tracking within a heterogeneous flow field /e.g. Moreno et al. 1988, Nordqvist et al. 1992, Painter 2006/ as these typically do not consider diffusive exchange between flow trajectories. As discussed previously, the magnitude of the effect depends upon the F-factor of the main flowpath and the properties of the surrounding regions. If the F-factor is sufficiently large, then the solute may equilibrate diffusively across large portions of the low flow velocity regions of the fracture thus resulting in a substantial increase in solute transport times as suggested by the model alternative, MA1. This will have far reaching and important consequences for safety assessment if properly considered.

The combination of matrix diffusivity and sorptivity/storage parameters in the form of the lumped materials property group, MPG can be shown to be a unique descriptor of the retardation properties of the rock matrix for a single-layered, infinite rock matrix /Crawford 2006/. For the transport of solutes this means that rock with enhanced sorptivity/storage capacity and reduced diffusivity is indistinguishable from the case where the rock has decreased sorptivity/storage capacity and increased diffusivity, provided both cases are characterised by identical MPG values. While this is generally true for an infinite, single layer medium, it is not true for a limited matrix diffusion depth where saturation effects may occur, nor is it generally true for a rock matrix with multiple alteration layers[5]. The consequence of this is that systems featuring depth-limited or layered rock matrices with different effective diffusivities will saturate at different recovery fractions giving rise to measurably different residence time distributions although the MPG is the same in each case (except in certain limiting cases as demonstrated in Appendix J).

[5] The author notes that this was stated incorrectly in /Crawford 2006/ where it was suggested that this would generally apply for multi-layered systems (for a full discussion of this issue see Appendix J).

As previously discussed in /Crawford 2006, Löfgren et al. 2007/, when the solute residence time is dominated by rock matrix retardation rather than advective travel time or equilibrium sorption on fracture surfaces, it can be shown that the effective penetration depth associated with solute retardation is proportional to the F-factor of the flowpath and the effective diffusivity of the solute, but independent of the sorptivity/storage capacity of the rock. This also means that for a given effective diffusivity, solutes featuring different sorptivities will start to experience saturation effects at exactly the same point on the residence time distribution (i.e. for the same recovery fraction although at different absolute times). This principle is illustrated clearly in section 5.3.2 where the residence time distributions are simply translated proportionally in time (on a logarithmic scale) due to differing sorptivities, although always exhibit saturation effects at exactly the same relative recovery fraction.

It should also be noted that owing to the non linear nature of the radial diffusion formulation (model variant, MA2), the MPG value for the rock does not uniquely describe the transport properties of the system even for a single-layer rock matrix parameterisation and the sorptivity/storage capacity and diffusivity must be specified separately in such cases. At very short times, however, the radial diffusion model converges towards the same residence time distribution as that predicted by a 1D diffusion model (BM or MA1).

For material properties variation along the direction of flow within a flowpath, it is possible to directly calculate a flowpath average value which gives identical results to simulations made for a continuously, or piecewise variable system assuming a 1D matrix diffusion process in a single layer rock matrix of infinite depth. This was shown formally in /RETROCK 2004/ to be equal to the path-length weighted average of the variable material properties group (MPG). For a rock matrix featuring multiple alteration layers or continuously variable material properties extending into the rock matrix from the fracture surface, this is not possible although approximate results are still obtainable under certain asymptotic conditions. This is also the case for a rock matrix of limited depth which varies locally along a flowpath and also for the model variants MA1 and MA2, where the matrix uptake terms are non-linear functions of the effective diffusivity, D_e and volumetric storage capacity parameter, $\theta_m + K_d \rho_b$.

Flow path averaging of material properties assumes that the specified parameter variability is indeed an intrinsic material property variability and not a measurement uncertainty range. It is not clear whether the large ranges of sorption variability measured in the laboratory programme are of the former kind and there is good reason to suspect that the measured variability actually falls into the latter category. For this reason we consider it imprudent to make prognoses of flow-path averaged material properties in this report with regard to sorption. If we assume the measured range of *in situ* formation factors to roughly represent the spatial variability of effective diffusivity, however, the flowpath average will tend towards the arithmetic mean of the distribution.

Although in this investigation we have made scoping simulations for an assumed limited matrix depth of 2 m, this should not be interpreted in any way as a physically motivated choice relating to matrix porosity connectivity. As already discussed in previous chapters, there is now a substantial body of evidence that the porosity of the rock matrix should be connected over considerable distances into the rock. The reason for consideration of limited matrix penetration depths, however, is more prosaic and relates to the need to avoid "double counting" of the rock matrix storage capacity. Typically in safety assessment the maximum matrix depth is chosen to be either half the average spatial separation between flowing features /e.g. SKB 2006c/, or by assuming a much more limited depth by appealing to notions of conservativeness. The first of these implicitly assumes the rock matrix to be connected over large distances, whereas the second assumes a fixed, and usually low physical depth of matrix connectivity.

In many cases, flowpaths will be sufficiently well spaced that saturation effects will not be observed in transport calculations. When there are flowpaths in close proximity, such as flow channels within the plane of a fracture or within complex fractures of the type considered by /e.g. Mazurek et al. 2003/, saturation effects will invariably occur (see Figure 5-23). The assumption of a limited matrix depth equal to half the average separation distance is, however, only physically meaningful if both flowpaths have identical F-factors and inlet concentration boundary conditions. If the F-factors differ by some amount then results may not be correct since each flow channel will have a different concentration-time history. Clearly the limited rock matrix depth between each flowpath must be proportioned in such a way that each path reaches a saturation condition simultaneously thereby preserving the requirement for a reflection boundary condition at their interface. It is necessary for this situation to be handled correctly if the approximated composite system is to reflect the true physics of a two-path, parallel flow system.

Since, in this case there are no nearby flow channels residing on the outside of the complex flowpath, the outlying rock matrix for each path can be effectively assumed to be substantially larger (or as in the case illustrated in Figure 5-23, infinite). If the flow paths are very close together and the F-factors for both paths are sufficiently high and roughly equal, the rock matrix in between could be modelled as an equilibrium storage capacity (like a large piece of breccia). In other cases, for example, if the F-factor in one channel differs by perhaps an order of magnitude or more, then it may even be feasible to neglect the less transmissive flowpath altogether without introducing significant errors. The simulation of rock matrices featuring asymmetrical penetration depths as described above is relatively easy to handle in transport calculations and only requires minor modifications to the governing equation for transport (see /Crawford 2006/). The simulation results for the composite system, however, should be treated with caution owing to the lack of a phenomenologically consistent reflection boundary.

We note here that a proper treatment of solute transport in closely spaced flow channels actually requires full consideration of diffusive mass exchange between the channels (possibly via stagnant interspaces) and the recommendations given here are only rough approximations. Such coupling is not possible to achieve in a simple fashion in the current generation of transport models used in safety assessment which assume flow paths to be fully independent. This deficiency becomes particularly acute if we consider sparsely distributed in-plane flow channels separated by very low flow or stagnant regions as illustrated in Figure 5-24.

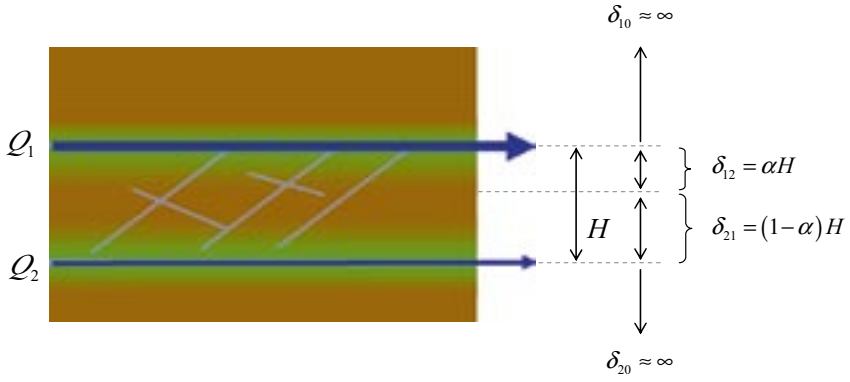

Figure 5-23. *Conceptual illustration of approach to assigning matrix depths for transport calculations involving two closely spaced flow channels as may exist in a complex fracture /e.g. Mazurek et al. 2003/. The limited matrix depth between the channels is usually assumed to be half the separation distance (α = 0.5) although the physical basis for this choice is rarely rationalised.*

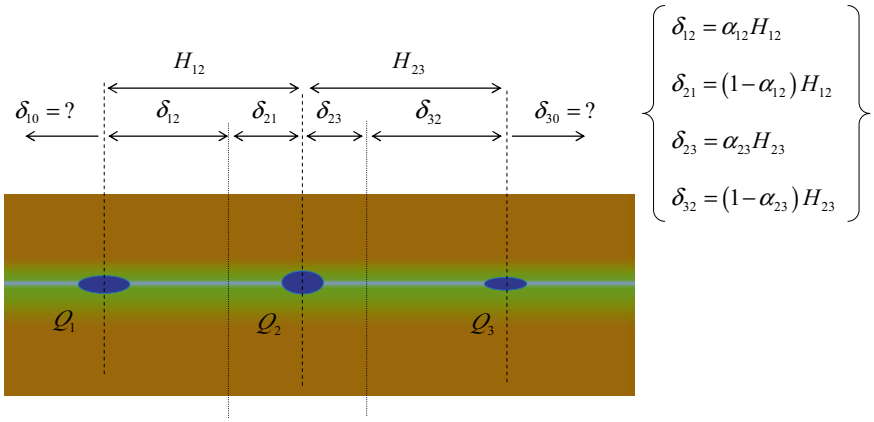

Figure 5-24. *Conceptual illustration of zone width assignment problem for transport calculations involving multiple, closely spaced flow channels as may exist in a fracture hosting a heterogeneous flow distribution.*

In this case, if we wish to account for the diffusion accessible surface area of the stagnant zones residing between the flow channels it is necessary to proportion the width of stagnant zones for each channel in a fashion that preserves the appropriate reflection boundary conditions where they interact. For extreme situations where flow channels are far apart, this may not have a large impact on results over the timescales of interest. For fractures featuring many, closely spaced, parallel flowpaths with only slightly differing F-factors, on the other hand, simulation of the composite system becomes difficult to achieve without introducing additional assumptions that are difficult to justify a priori. A further complication is the splitting and joining of individual flowpaths within a fracture and the spatially variable distance separating them. In many cases it is probable that simplified approaches give acceptable results. In some situations, for example, the consideration of one or two dominant flowpaths within a fracture and the assumption that everything else is a stagnant zone may be defensible. From inspection of the equations governing mass transfer it is clear that the matrix depth and stagnant zone width terms are non-linear and cannot be averaged over a flowpath in a similar fashion to the material properties of the rock matrix (see Appendix I). This makes the spatially variable nature of stagnant zone width (and also matrix depth) problematic. As mentioned previously, this treatment is only very approximate and full consideration of diffusive fluxes between adjacent flow channels should be made to obtain results which represent the physics of the system correctly.

5.6 Summary of main findings

In summary, the key findings of this chapter include:

- Given the many assumptions inherent in the description of the low transmissive initial pathways connecting individual deposition holes with “typical” major flowpaths within the hypothetical repository volume at Forsmark, no credit was taken for the hydrodynamic transport resistance accumulated in this part of the flow system. Only the major flowpaths in the repository volume were considered. Furthermore, since the hydrodynamic transport resistance in the deterministic deformation zones (HCD) were found in the scoping calculations to contribute as little as 1–10% of the overall F-factor, the material properties of the rock adjacent to the flowpaths was assumed to be the same as that to be found within fracture domain FFM01 at repository depth. An overall F-factor on the order of 10^6 y/m was therefore selected as being cautiously realistic for the hypothetical repository volume at Forsmark and representative of the major transport paths for the transport calculations made in this chapter.

- Since advective travel times are highly uncertain, a water residence time of 1 y was chosen as a base case. This was based loosely upon the ranges of values given in Table 3-14 for the hypothetical repository volume at Forsmark. A limited rock matrix depth of 2 m was chosen for the calculations. This does not in any way reflect an assumption concerning the depth of connected rock matrix porosity and is only a modelling convenience used here to illustrate some of the effects of matrix saturation.
- Since site specific K_d values for specific solutes are not well constrained, scoping calculations of radionuclide transport have been made for a hypothetical repository at Forsmark assuming a range of K_d values ranging from non-sorbing ($K_d = 0$ m^3/kg) to strongly sorbing ($K_d \geq 0.1$ m^3/kg). The site specific Formation factor of the rock matrix was assumed to be 1.6×10^{-5} which is approximately representative for the metagranite (101057) rock type based upon the *in situ* resistivity measurement data (see Appendix H).
- Three different modelling alternatives have been considered in this chapter for the estimation of transport times for radionuclides of interest along "typical" transport paths. These were intended to explore some of the consequences of flow channelling in a forward modelling perspective; i.e. how the existence of flow-channelling can be expected to influence modelled solute transport. The models used in the calculations were:
  a) A standard model of advective flow coupled with 1D matrix uptake which is commonly used in safety assessment studies (referred to as the base model, BM).
  b) A model similar to the above although with the inclusion of a single, flanking stagnant zone 10 times larger in width than the narrow central flow channel. Subsequent diffusive uptake from the stagnant zone to the rock matrix is a key feature of this model (referred to as model alternative, MA1 with a 10:1 stagnant zone).
  c) A model of advective flow coupled with 2D radially symmetric matrix uptake from a flow channel of limited width (referred to as model alternative, MA2 for radial diffusion).
- In parity with previous investigations it was found that the transport time of individual radionuclides is proportional to the sorption partitioning coefficient, K_d and the effective diffusivity, D_e. More generally, it is also possible to say that transport time is proportional to the square of the F-factor if matrix saturation effects are excluded. A 10 times increase in the F-factor can then be expected to give approximately a 100 times increase in the transport time for a solute.
- Scoping calculations detailed in Appendix B indicate that there should be extensive low flow (effectively stagnant) zones within fractures if there is significant in-plane flow-channelling. These stagnant zones should be accessible by diffusion from the main flow channel and provide additional surface area for solute uptake to the rock matrix. The high *in situ* normal stresses and sparsity of flowing features identified at repository depth suggests that flow is possibly strongly channelised within this rock volume at the Forsmark site.
- The presence of stagnant zones was found to greatly increase the retardation of transported solutes when included in transport simulations. For certain ranges of F-factors and flow channel/stagnant zone widths, the diffusive equilibration of the stagnant zone occurs sufficiently fast that the effect can be approximately modelled by simply upscaling the flow wetted surface to include the extra diffusion accessible surface (DAS). For the specific case considered in this chapter, this means an 11 times effective increase in the F-factor which implies a roughly two order of magnitude increase in transport times. This approximation appears to be valid down to solute recovery fractions on the order of 10^{-9} (or less) for the simulated F-factor assumed in this report without the risk of overestimating the retardation effect.
- Radial diffusion is particularly important for very narrow flow paths and can give very large increases in radionuclide transport time. Since flow is thought to be highly channelised within the repository volume at Forsmark, this could have an overall beneficial effect. The additional retardation effect is more pronounced at later times (radionuclide recovery fraction $\geq 0.01\%$). At short recovery times, however, the transport of radionuclides roughly matches the breakthrough modelled using the base model, BM.

- For the assumed F-factor of 10^6 y/m (considered representative for a repository at Forsmark), the advective travel time is vanishingly small in comparison to the matrix residence time and therefore does not strictly need to be considered for sorbing solutes ($K_d > 10^{-4}$ m^3/kg), provided matrix saturation does not occur.
- Since there is currently little data concerning the presence or absence of biofilms on fracture surfaces at Forsmark, scoping calculations have been used to investigate possible effects on transport. It is found that the presence of biofilms of thickness 1–10 μm should not have a discernable impact upon solute travel times on SA timescales when simulated using a range of assumed values for reduced sorptivity and diffusivity compared to the rock matrix.
- Fracture coatings on the order of 1 mm in thickness may have a positive or negative impact upon retardation at SA timescales depending upon their retention properties. The impact is, however, small for reasonable ranges of material property variability. It appears from the transport properties evaluation of site specific geologic material described in Chapter 4 that fracture skins of secondary mineralisation are most likely to enhance radionuclide retardation for the very leading edge of the radionuclide breakthrough at early times.
- Matrix saturation effects may or may not be important depending upon the permitted maximum depth of matrix penetration and transport model used. Relict porewater signatures at Forsmark /Laaksoharju et al. 2008/ imply the existence of a connected matrix porosity over at least some tens of metres and the depth of accessible matrix can therefore be assumed to be effectively unbounded. The consideration of shorter maximum depths of penetration, however, may be necessary to avoid double counting of matrix storage capacities during safety assessment modelling.
- The material properties group (MPG) which combines the sorptive and diffusive properties of the rock in a single parameter group only uniquely describes the transport properties of the rock under certain limiting conditions. In other situations (in particular for radial diffusion formulations such as model alternative, MA2), the sorptive and diffusive properties of the rock matrix need to be specified separately.
- Flowpath averaging of material properties gives an exact representation of radionuclide retardation only for certain limiting cases (i.e. the base model with an unlimited matrix penetration depth). In other situations, it is not possible to calculate a flowpath average that is valid for the entire residence time distribution envelope. In such cases, however, it is still feasible to calculate meaningful flowpath averages that are realistic for low to medium recovery fractions as most of the deviation appears to occur in the tail of the distribution and is related to saturation effects.
- Given that the largest material properties uncertainty appears to be related to the sorption partitioning coefficient, K_d a flowpath average of this parameter is likely to give a reasonably accurate indication of radionuclide transport time for the system if the variation in K_d is interpreted as an intrinsic material properties variability. If the reported variation is ascribed to measurement uncertainty, on the other hand, the uncertainty in arrival time is not reducible by flowpath averaging of material properties. Since the largest component of K_d variability is thought to be related to groundwater composition, flowpath averages need to be calculated with consideration given to groundwater chemistry evolving with time along a flowpath.
- The overall magnitude and proportioning of solute fluxes between stagnant zones and that for mass transfer direct to the rock matrix from a flow channel is different for solutes with differing sorptivity/diffusivity at the short times characteristic of tracer tests. It is also strongly dependent upon the properties of the fracture coatings and biofilms. These processes are shown to have fundamentally different characteristics under site characterisation and safety assessment conditions. Results from tracer tests carried out for partial validation of retardation models should therefore be interpreted with care (see also /Löfgren et al. 2007/). This is discussed in more detail in the following chapter.

6 Field scale tracer tests

An important element of the site descriptive modelling at Forsmark has been the integration of field scale testing within the modelling work. By “field scale” testing we specifically mean forms of hydrogeologic and tracer migration testing performed on site with the aim of directly characterising the properties of the system and on macroscopic scales larger than that typically considered in laboratory experiments.

These kinds of tests serve a multitude of functions for the different topic areas of interest. For hydrogeology, the incorporation of data in the form of pressure responses in interference tests, point water heads measured in rock and soil, groundwater compositions and paleo-hydrogeological information is instrumental in calibration of flow models and for validation of interpretations in the development of the hydrogeological site descriptive model. A large number of tracer dilution tests have also been carried out with the aim of characterising the hydrogeological properties of features with flow rates below the detection limit of direct measurement methods such PFL and PPS. Large scale, conservative tracer tests are also used to verify connectivity in the system which is used for confidence building with regard to the flow models.

For transport properties site descriptive modelling, tracer tests are used to verify connectivity as well as to demonstrate retention and retardation of transported solutes. In this chapter we discuss the tracer tests which have been carried out within the Forsmark site investigation and attempt to make interpretations of the results which have been obtained and what these mean for safety assessment. Here we focus upon the tracer tests that have most relevance for the transport properties site descriptive modelling. These consist of multiple well tracer tests and a series of single well injection withdrawal tests (SWIW). Results of tracer dilution tests are not discussed in this chapter as they have already been dealt with in section 3.3.

6.1 Multiple well tracer tests

Two multiple well tracer tests have been performed at Forsmark and reported /Wass and Andersson 2006, Lindquist et al. 2008a/. A third large-scale tracer test has been performed /Lindquist et al. 2008b/, although it was not fully reported at the time of preparation of this report and is not included in the discussions. Data obtained from this third tracer test, although not reported here, will form a direct input to SR-Site. The first test took the form of a large scale pumping test with non-sorbing tracer release from packed off sections in three boreholes in an approximately radially converging flow configuration. The other tracer test was made in a two-well, weak dipole configuration over a substantially shorter distance within zone ZFMA2 using a mix of both sorbing and non-sorbing tracers. The main purpose of the former investigation was to test connectivity of the fracture zone for validation of the hydrogeological flow model. The second tracer test was also intended to partially validate the hydrogeological model over the Forsmark candidate area, but also was intended to test the transport characteristics of the rock for comparison with data obtained from the laboratory transport properties investigations using drill core material.

6.1.1 Tracer test at drill site 1

This tracer test was performed in June and July of 2005 and was carried out in conjunction with a hydraulic interference test /Wass and Andersson 2006, Gokall-Norman et al. 2005/. This test involved injection of three different non-sorbing tracers in boreholes HFM02, HFM15, and KFM01A with pumping and sampling carried out in HFM01. The configuration of the tracer test was as indicated in Figure 6-1.

Figure 6-1. *Map of tracer test configuration in relation to the Forsmark site investigation area. The positions of the boreholes included in the test are shown as well as areas corresponding to 500 m and 1,000 m radius (concentric circles) from HFM01. (Figure taken from /Wass and Andersson 2006/).*

The tracer release took the form of passive, decaying pulse injections in the circulated, packed-off borehole sections indicated above. The withdrawal rate in HFM01 was 89 L/min and samples were taken continuously for detection of tracer breakthrough. Owing to the time schedule for other investigations at the site it was only possible to sample under undisturbed conditions for 380 hours after which the test was halted. The relevant tracer test parameters are given in Table 6-1.

No recovery of tracer was obtained from the tracers injected in HFM15 or KFM01, although about 3.4% of the tracer injected in HFM02 was recovered in the pumped borehole HFM01 (0–200 m). Since only a partial recovery of tracer was obtained, it was only possible to make a very rough fit of the breakthrough data with a one-dimensional advection dispersion (AD) equation assuming a 20 m dispersivity (9% of the travel distance of 222 m). The breakthrough data along with the model fitted by visual inspection is shown in Figure 6-2.

Based upon the approximate model fit /Wass and Andersson 2006/, the water residence time was estimated to be on the order of 500–1,000 hours which implies a kinematic porosity on the order of 0.1 (i.e. over the test section interval) assuming a linear flowpath between injection and recovery boreholes and a zone transmissivity of 10^{-4} m^2/s. For a radial flow assumption, on the other hand, the kinematic porosity would be roughly 0.03.

Table 6-1. Data for the tracer test performed at drill site 1.

Borehole section	Section interval (m)	Distance from HFM01 (m)	Head difference (m)	Tracer
HFM02:2	38–48	222	24.2	Amino-G acid
HFM15:1	85–95	325	25.0	Rhodamine WT
KFM01A:5	109–130	144	24.0	Uranine

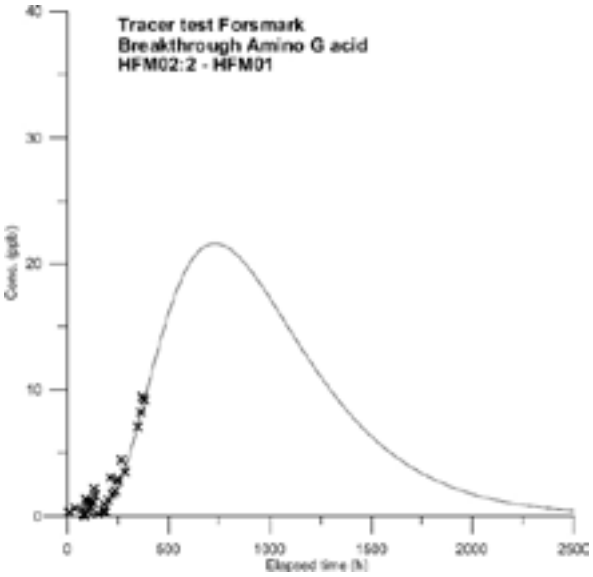

Figure 6-2. *Tracer breakthrough in HFM01 from passive injection in HFM02:2 (Amino G acid). A theoretical fit to the rising part of the residence time distribution was made by visual inspection and assuming a 1D advection-dispersion model. (Figure taken from /Wass and Andersson 2006/).*

6.1.2 Tracer test at drill site 2

The second tracer test was performed at drill site 2 and took the form of a weak dipole (1:100) test involving injection of tracer in a packed off section in borehole KFM02A with withdrawal in a section of KFM02B /Lindquist et al. 2008a/. The packed off sections were chosen so that the test would probe the transport characteristics of the ZFMA2 zone which is intersected by both boreholes. A cross-section of the zone showing the configuration of the tracer test is shown in Figure 6-3.

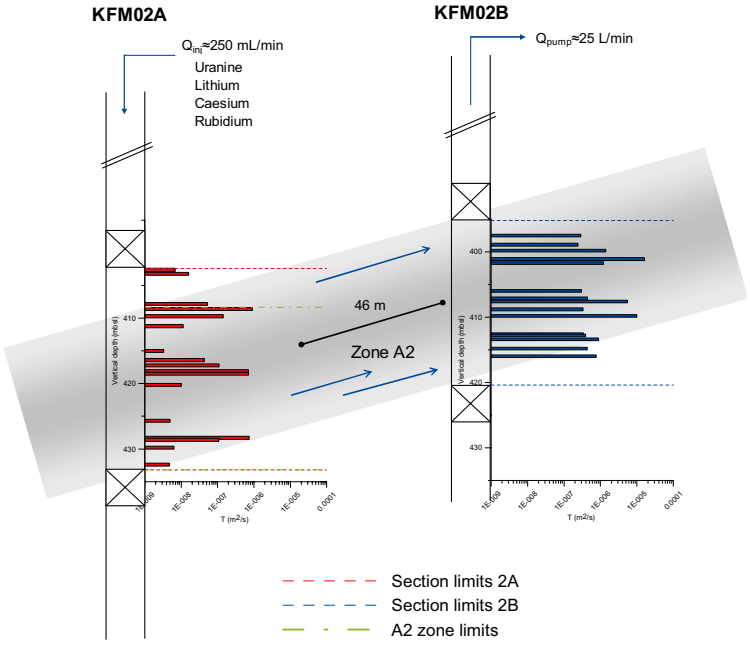

Figure 6-3. *Cross-section of zone ZFMA2 showing injection (KFM02A) and recovery wells (KFM02B) for the tracer test performed at drill site 2. The transmissivity distributions measured by PFL in the injection and recovery borehole sections are visualised as a horizontal bar graph next to each borehole. (Figure taken from /Lindquist et al. 2008a/).*

The test campaign consisted of a number of preliminary hydraulic tests in addition to the tracer tests. These included groundwater flow measurements under natural and pumped conditions using the tracer dilution measurement technique (using uranine) as well as a pumping and interference test with monitoring both in KFM02A and a number of surrounding HFM boreholes. In all these tests, pumping was performed in a packed off section of KFM02B (408.5–434.0 m).

The equipment used for the tracer tests was the same as that employed for tracer dilution measurements although with some minor additions and modifications. The tracers were mixed in a large 5 m^3 tank at the borehole and injected with a slight overpressure giving a weak dipole flow regime. The ratio of injection to pumping well flow was 1:100 and the dipole stability was maintained during the entire test period by injection of a synthetic groundwater chaser after the main tracer pulse. Regulation of carbonate concentrations and redox conditions in the traced water was achieved by continuous dosing with bicarbonate and Fe(II) stock solutions during tracer injection. The reason for this was to avoid CO_2 degassing and possible precipitation problems during the initial purging of the synthetic groundwater with N_2 gas which was performed in order to reduce the concentration of dissolved oxygen in the injection solution. Samples were collected continuously from the injection and withdrawal sections using a discrete sampling technique.

Two tracer tests were performed. The "pre-test" was initiated after six days of pumping and used Rhodamine WT as a tracer. This was intended as a trial to check the equipment configuration and verify transport connectivity over the time scale to be used for the subsequent main test. After approximately two weeks of pumping the main test was initiated. The main test consisted of the tracers uranine, Li^+, Cs^+, and Rb^+ at concentrations considered appropriate for the prevailing groundwater chemistry and estimated dilution during the test. The maximum tracer concentrations at injection were roughly 607 ppm, 39.3 ppm, and 146 ppm, respectively. The corresponding natural background concentrations were 57 ppb, 1.9 ppb, and 58 ppb. Other ionic tracers were considered during the design stage although rejected owing to their high background concentrations in the groundwater and in some cases due to concerns of solubility limitations. To avoid significant changes in ionic strength or groundwater density, the injection solutions were prepared using synthetic groundwater, replacing the natural Na^+ concentration for the Li^+ tracer.

Tracer breakthrough was obtained for all tracers in both the pre-test and main tracer test. In the pre-test the first arrival of Rhodamine WT was 16 h (pumping rate 19.8 L/min), whereas in the main test, first arrival times of 11 h for uranine and Li^+, 50 h for Cs^+, and 26 h for Rb^+ were observed (pumping rate 24.8 L/min). It should be noted that the reported first arrival times were not based upon a strict evaluation method, but were estimated based upon a subjective judgement of the first point at which the breakthrough concentrations were clearly higher than the background levels and therefore may be associated with some uncertainty.

The tracer injection and recovery curves for the pre-test using Rhodamine WT are shown in Figure 6-4. Since the pumping rate was increased at the conclusion of the pre-test, the results are given in terms of flow-normalised, elapsed time (for details see /Lindquist et al. 2008a/).

The tracer injection curves for the main tracer test using the uranine, Li^+, Cs^+, Rb^+ cocktail are shown in Figure 6-5. Owing to equipment problems the pump stopped on several occasions during the tracer injection as well as during the chaser fluid injection. These stops correspond to the large dips in the injection curves.

The tracer recovery curves for the main tracer test are given in Figure 6-6.

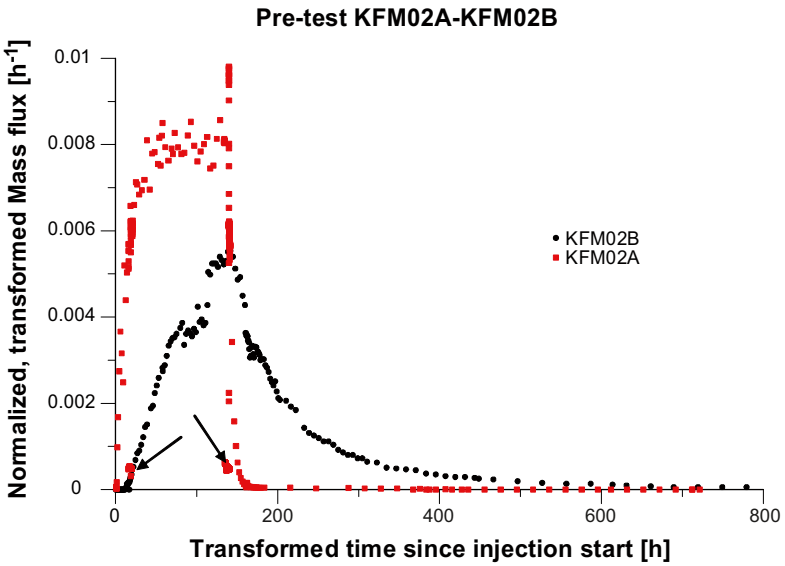

Figure 6-4. *Tracer (Rhodamine WT) injection in KFM02A:5 (red markers) and recovery in KFM02B (black markers). The data are given as injection mass normalised flux vs. flow-normalised elapsed time. The arrows in the figure indicate injection pump stops. (Figure taken from /Lindquist et al. 2008a/).*

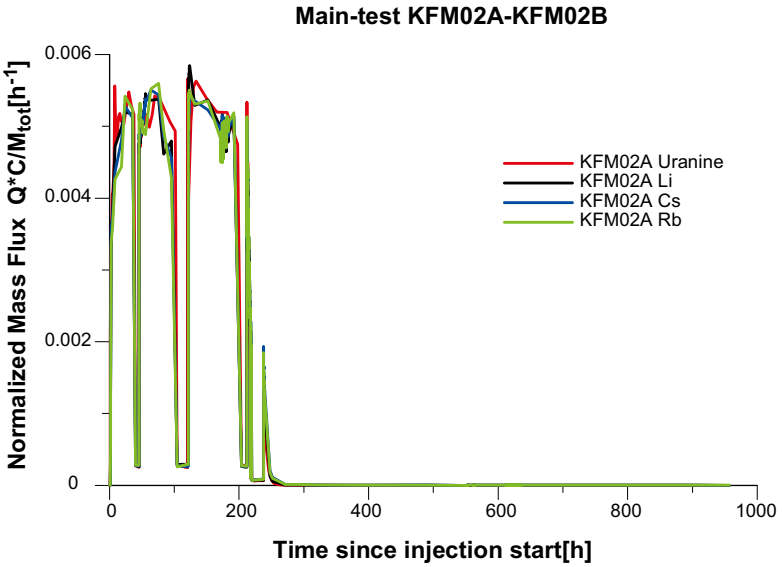

Figure 6-5. *Tracer injection curves for main tracer test in KFM02A:5. The data are given as injection mass normalised flux vs. elapsed time. (Figure taken from /Lindquist et al. 2008a/).*

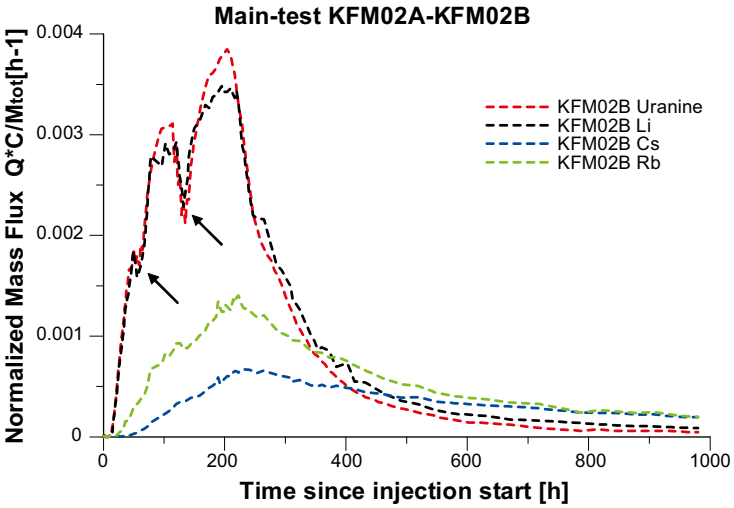

Figure 6-6. *Recovery of different tracers in KFM02B. The data are given as normalised transformed mass flux vs. elapsed time. The arrows indicating apparent notches in the uranine and Li^+ recovery curves correspond to injection pump stops. (Figure taken from /Lindquist et al. 2008a/).*

Three different modelling approaches were used to evaluate the tracer recovery data; these were:

- (AD-1) Single path, 1D advection-dispersion-sorption equation.
- (AD) Multi-path, 1D advection-dispersion-sorption equation.
- (AD-MD) Single path, 1D advection-dispersion-sorption model with matrix diffusion/sorption.

The tracer breakthrough data were evaluated using each of the above models and an inverse modelling procedure to estimate model parameters. The method was based upon a non-linear least squares regression technique using the Marquardt-Levenberg method (for details see /Lindquist et al. 2008a/). The multi-path, AD model generally failed to give convergent results with reasonable parameter values and so is not reported here.

The modelling results for the pre-test are given in Figure 6-7.

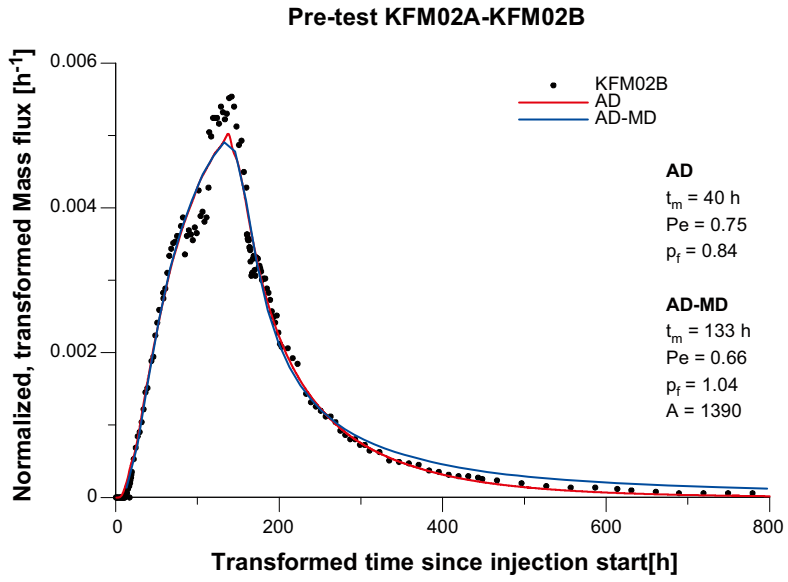

Figure 6-7. *Visualisation of model fit to experimental data using the AD-1 and AD-MD models for the pre-test (Rhodamine WT). Parameter values for the models are indicated in the figure (taken from /Lindquist et al. 2008a/).*

The transport parameters fitted in the modelling procedure were the final recovery fraction (p_f), the Péclet number for longitudinal dispersivity (Pe), water residence time (t_w), and the matrix interaction parameter (A) for the AD-MD model. The A-parameter is a lumped parameter representing the sorptive and diffusive properties of the rock matrix and is defined as /Moreno and Neretnieks 1983/:

$$A = \frac{(\delta_t/2) R_a}{\sqrt{D_e (\theta_m + K_d \rho_b)}} \qquad (6\text{-}1)$$

Where $\delta_t/2$ is the transport half-aperture, R_a is the retardation factor for equilibrium sorption along the flowpath, and the denominator is the material properties group for the rock matrix. If the depth of solute penetration is very low or the material properties of the fracture surface do not differ significantly from the underlying rock matrix, the R_a term can be neglected and subsumed into the denominator (i.e. as an effective material properties group for the sampled rock).

For the non-sorbing tracer used in the tracer test it is difficult to ascertain which model gives a better fit since the AD-1 model slightly under-predicts the tailing of the breakthrough curve at late times, whereas the fitted AD-MD model tends to over-predict the tailing (matrix interaction) effect. In both cases, the amount of dispersion as given by the estimated Péclet number is substantial. In the modelling report /Lindquist et al. 2008a/, the large difference in water residence times estimated for each model was partially ascribed to a shift in the centre of mass for the recovery curve as simulated using the two models and also due to a difference in model boundary conditions that was thought to be of some importance at low Péclet numbers.

Typical modelling results for the main tracer test are given in Figure 6-8 for the single path, advection-dispersion-sorption (AD-1) model.

The results shown in Figure 6-8 were obtained by first fitting the AD-1 model to the recovery curve for uranine, thus fixing the values for water residence time and the Péclet number ($R_a \approx 1$ for uranine). Using these parameters, fits were then obtained for each of the sorbing tracers by adjusting the retardation term (R_a) and tracer recovery (p_f) in succession. The recovery factors fitted using this procedure were found to be different for each tracer. The model fit to the tracer recovery data is reasonable, although with a noticeable underestimation of tailing at later times. It was noted in the modelling report that if the tracers were forced to have equal recovery at infinite time, the model fit to the experimental data was considerably poorer with a strong underestimation of the long-time tailing effect.

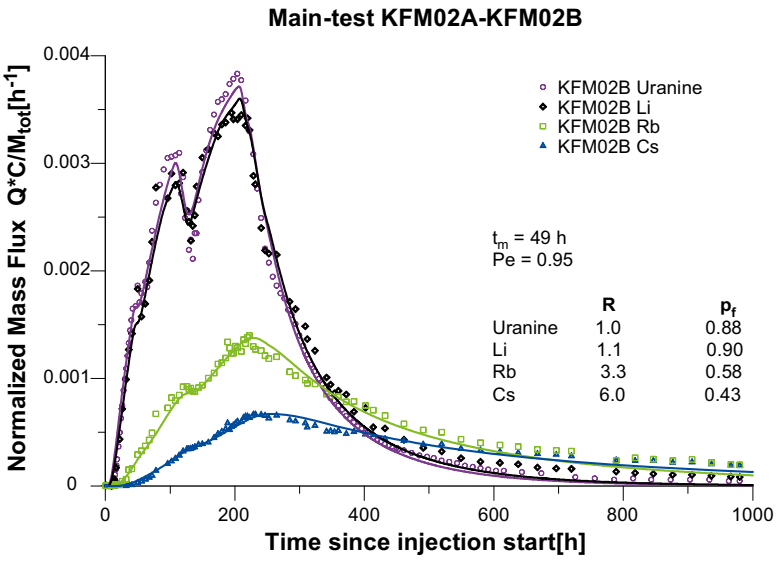

Figure 6-8. *Visualisation of model fit to experimental data using the single path, advection-dispersion-sorption model for the main tracer test. Parameter values for the model are indicated in the figure (taken from /Lindquist et al. 2008a/).*

Typical modelling results for the main tracer test are given in Figure 6-9 for the single path, advection-dispersion-sorption model with matrix diffusion/sorption (AD-MD).

The results shown in Figure 6-9 are based upon a simultaneous fit of all tracers. In the simulations, the water residence time (t_w), infinite recovery fraction (p_f), and Péclet number (Pe) were forced to be the same for all tracers while the equilibrium sorption (R_a) and matrix interaction (A) parameters were fitted for each tracer (assuming $R_a \approx 1$ for uranine). The AD-MD model was found to give a good fit to all tracers although there is a slight tendency of the fitted model to overestimate long-time tailing of uranine and slightly underestimate that of the sorbing tracers. As was found in the evaluation of the pre-test results, the fitted Péclet number was low for both the AD-1 and AD-MD model evaluations indicating a strong dispersion effect along the flowpath.

A summary of the main results of the modelling evaluation is given in Table 6-2 for the AD-MD model.

A summary of hydrogeologically derived parameters for the main tracer test is given in Table 6-3.

Table 6-2. Evaluated transport parameters from inverse modelling of tracer tests using the AD-MD.

Tracer	t_w (h)	p_f (–)	R_a (–)	A ($s^{-½}$)	Pe (–)
Rhodamine WT	133	1.04	1.0	1,390	0.66
Uranine	120	1.0	1.0	2,770	0.92
Li^+			1.1	2,880	
Cs^+			2.7	600	
Rb^+			3.4	310	

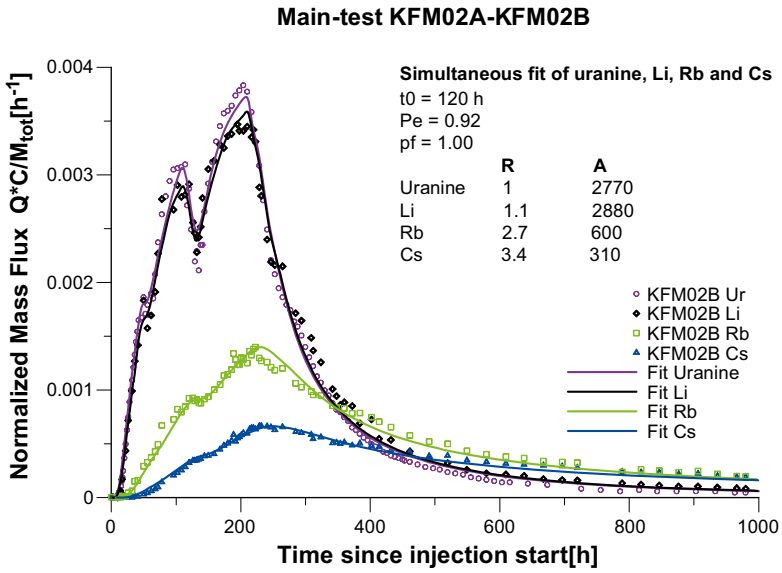

Figure 6-9. *Visualisation of model fit to experimental data using the single path, advection-dispersion-sorption model with matrix diffusion/sorption for the main tracer test. Parameter values for the model are indicated in the figure (taken from /Lindquist et al. 2008a/).*

Table 6-3. Data for the main tracer test performed at drill site 2.

Parameter	Value
Distance (m)	46.4
Mean head differential (m)	2.63
Hydraulic conductivity of zone (m/s)	6.7×10^{-3}
Equivalent fracture aperture, δ_t (m)	2.6×10^{-2}
Flow porosity, θ_f (–)	2.5×10^{-4}

6.2 Single well injection withdrawal tests (SWIW)

A number of single well injection-withdrawal (SWIW) tests have been performed in various borehole locations during the site investigation at Forsmark. These are also commonly referred to as "push-pull" tests in the scientific literature since the method involves a chased, pulse injection of a tracer into a well followed by pumping withdrawal in the same well. The technique is attractive for the purposes of the site investigation since it can be used to perform tracer tests within transmissive structures found at repository depth in which it would be very difficult to perform standard dipole or multiple well tracer tests from the surface. An additional advantageous feature of the SWIW technique is that the reversal of flow during the experiment theoretically reduces the impact of advective dispersion and flow dimension upon the residence time distribution of recovered tracer, thereby potentially simplifying mechanistic interpretation. The equipment used for performing the SWIW tests is illustrated in Figure 6-10.

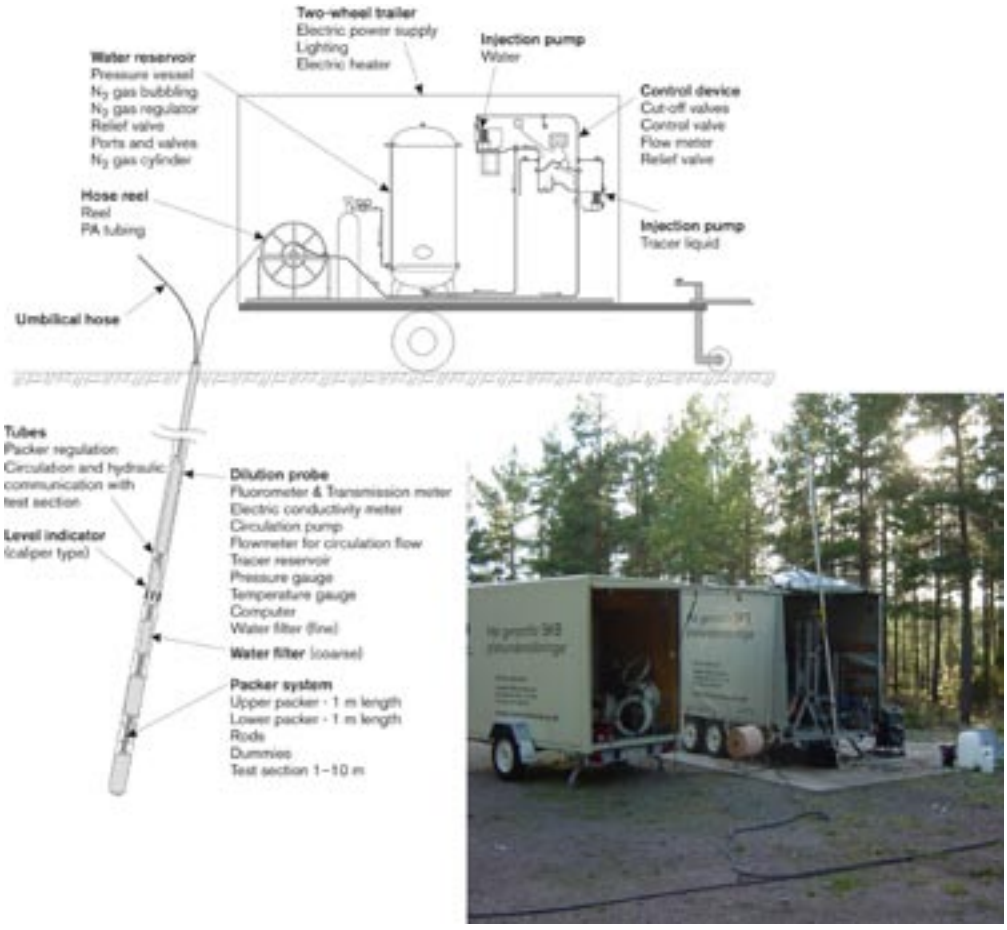

Figure 6-10. *Schematic of SWIW test equipment connected to the borehole dilution probe (left) and photograph of actual equipment used installed next to a borehole (right). (Schematic image is taken from /Gustafsson et al. 2005/).*

The procedure used for the SWIW tests carried out within the site investigation is described in detail in /Gustafsson et al. 2005/ as well as in the background feasibility study reports /Nordqvist and Gustafsson 2002, 2004/. It comprises the following phases and typical timescales:

1. pumping and storage of groundwater from the selected fracture for subsequent injection,
2. pre-injection of accumulated water to establish steady state hydraulic conditions (2–3 h),
3. active injection of one or more tracers within the packed-off borehole section (1 h),
4. injection of groundwater (chaser fluid) after cessation of tracer injection (12–14 h),
5. waiting phase, or "shut-in" period (< 1 h),
6. tracer recovery phase (withdrawal of water under active pumping, 100–200 h).

The tracer breakthrough data that is subsequently used in data evaluation is obtained from the recovery phase. The injection of a chaser fluid has the effect of pushing the tracer outwards in a ring in the formation surrounding the tested section /Nordqvist 2008/, the advantage being that both the ascending and descending parts of the breakthrough curve can then be well resolved. During the waiting phase there is no injection or withdrawal of fluid. The purpose of this is to increase the time available for diffusion and sorption within the formation so that these may be more easily evaluated from the tracer recovery data. An extended waiting period, however, suffers from the disadvantage that it increases sensitivity to background hydraulic gradients which can have a significant detrimental impact upon results.

A disadvantage of the technique as compared with multiple well tracer tests is that there is no easily discernable reference length scale associated with the test /Becker and Shapiro 2003/. In the evaluation of the test we have very little information concerning how far out into a fracture system the tracer pulse actually propagates since the arrival time of the returning pulse tends to be governed by the time schedule of the different test phases /Tsang and Doughty 2007/ rather than the kinematic porosity of the system as might be the case in a dipole tracer test. On the other hand, the peak concentration of the recovered tracer, its apparent spread and long-time tailing are largely dependent upon hydrodynamic dispersion (rather than advective dispersion) and retention processes which may include diffusion and sorption.

Since the tracer arrival time does not directly depend upon the kinematic porosity in a SWIW test, the combined impact of dispersivity and porosity are usually not possible to separate in a rigorous fashion and it is customary to fit a dimensionless lumped dispersion parameter, τ /Gelhar and Collins 1971/. This parameter is defined as:

$$\tau = \frac{\alpha_L^2 \delta_t}{V_{inj}} \tag{6-2}$$

Where α_L (m) is the dispersion length, δ_t (m) transport aperture, and V_{inj} (m^3) is the total injected water volume.

Using data for the injected flow volumes from the individual tests carried out at Forsmark and a range of plausible transport apertures, the magnitude of the radial travel distance is estimated to be on the order of about 5–20 m assuming relatively homogenous radial flow conditions /Nordqvist 2008/. If the flow is highly fingered or channelised the penetration distance may be somewhat greater than this.

In total, six SWIW tests have been performed at the Forsmark site in different types of structure, at different depths and transmissivity ranges with the aim of characterising the transport properties of a variety of flowing features typical of that which might be encountered in the vicinity of a repository. A summary of the individual tests is given in Table 6-4.

Table 6-4. Summary of basic features of SWIW tests performed at the Forsmark site.

Borehole	Elevation (m)	T (m^2/s)	Type	Rock and fracture coating description
KFM02A	–407	9.5×10^{-7}	DZ (1–3 flowing features)	101057 no fracture minerals slightly altered
KFM03A	–633	2.5×10^{-6}	MDZ (3 flowing features)	101057 clay, hematite, chlorite, calcite strongly altered
KFM08A	–340	1.0×10^{-8}	3 fractures	101057 chlorite, clay, calcite no visible alteration
KFM04A	–355	8.9×10^{-9}	1–2 open fractures in a sealed network of a DZ	501061 / 101057 zeolites, calcite, chlorite, quartz no visible alteration
KFM01D	–300	3.2×10^{-7}	1 fracture	101051 chlorite slightly altered
KFM01D	–342	1.0×10^{-6}	1 fracture	101051 chlorite slightly altered

Numerical simulations of SWIW tests in the presence of background hydraulic gradients were previously made by /Nordqvist and Gustafsson 2002/ where it was shown that they could have a significant impact upon the shape of the tracer recovery curve. For this reason, preceding each of the SWIW tests, the ambient groundwater flow through the borehole section was measured by means of a tracer dilution test using uranine to ensure that background flows were within an acceptable range. The measured natural flowrates through the test well sections are given in Table 6-5 along with the flowrates characterising the various phases of the tests themselves.

Although the ambient flow and the rates of injection and pumping during the SWIW tests are not strictly comparable owing to the different geometry of applied boundary conditions, the assumption that background gradients did not influence the test results does not appear unreasonable from the relative magnitudes of the flows reported.

The “run” parameters for each of the SWIW tests including recoveries of the different tracers are given in Table 6-6.

Table 6-5. Natural background flows through SWIW test well sections (as measured by tracer dilution prior to each SWIW test) and flows characterising the different phases of the tests themselves.

Borehole	Elevation (m)	Natural flow (dm^3/h)	SWIW injection flow (dm^3/h)	SWIW pumping flow (dm^3/h)	Total injected volume (dm^3)	Natural flow during “shut-in” (dm^3)
KFM02A	–407	0.0017	5.5–11.8	12.4	201	n/a
KFM03A	–633	0.010	9.9	8.0	126.8	0.014
KFM08A	–340	0.006	2.44	2.3	172.2	n/a
KFM04A	–355	0.001	2.2–2.4	2.3	158.0	n/a
KFM01D	–300	0.005	13.4–13.8	13.8	100.8	0.0025
KFM01D	–342	0.010	3.8–4.2	3.8	101.4	0.001

Table 6-6. Summary of run parameters for SWIW tests.

Borehole	Elevation (m)	Total injected water (dm^3)	Injection+chaser duration (h)	Waiting phase (h)	Recovery (%)		
					uranine	Cs^+	Rb^+
KFM02A	–407	201	15.2	0	86.9	83.3	n/a
KFM03A	–633	127	12.7	1.4	78.6	44.3	n/a
KFM08A	–340	172	75.2	0	81.1	50.1	42.4
KFM04A	–355	177	75.3	0.1	42.6	53.9	32.8
KFM01D	–300	113	8.3	0.1	104	92	68
KFM01D	–342	112	8.6	0.5	102	87	90

In some of the cases above, the tracer recovery was truncated due to the limited time allocated for each test and the recovery estimates are possibly lower than what would have been obtained if pumping were to continue until background values were reached. It should also be noted that the recovery for uranine is occasionally greater than 100% indicating a non-negligible contribution of the background concentration of uranine (principally from residual drilling fluid) to the tracer mass balance.

In the initial site investigation reports dealing with the SWIW tests /Gustafsson et al. 2005, 2006ab, Thur et al. 2007/, the recovery data were modelled using the SUTRA simulation code /Voss and Provost 2002/. The fracture system in which the SWIW test was performed was simulated as a 2D homogeneous domain. Since the SUTRA programme was originally designed to simulate porous media, the domain was parameterised with hydraulic properties chosen to be equivalent to the fracture being studied and centred upon a central injection and recovery well. The tracer injection at the central well was simulated as a continuously stirred tank reactor (with volume reducer "dummies") thereby giving a modified, extended tracer pulse input.

Additional consideration was also given to sorption upon the walls of the borehole, tracer residence times in the well recirculation system including stagnant zones, and dispersion effects in the tubing between the injection section and the equipment at the surface to ensure that the modelled tracer injection was physically realistic. It was found in scoping simulations that the effect of dispersion within the tubing would have a negligible impact. This was also considered for the sampling of solute (i.e. between the test well and the surface sampling equipment) where it was found that neither the residence time nor dispersion in the sampling system should leave a significant imprint upon the solute breakthrough curve.

The modelling procedure involved making an initial simulation for the tracer injection and fluid chaser step, and then using the resulting distribution of solute within the 2D domain as the starting condition for the pumping stage of the test. In the first round of modelling which was reported in the initial site investigation P-reports dealing with the SWIW tests /Gustafsson et al. 2005, 2006ab/, the recovery data were modelled using the Advection-Dispersion (AD) equation with retardation due to linear equilibrium sorption on fracture surfaces. Parameters characterising the transport of solute were estimated by the same inverse modelling technique described in section 6.1. The lumped dispersivity parameter, τ and retardation factor, R_a for the sorbing solutes were fitted simultaneously for uranine and the sorbing tracers Cs^+ and Rb^+ (where appropriate).

The actual tracer recovery data and the best fit model taken from the simulations are shown in Figure 6-11 for uranine and Cs^+ and in Figure 6-12 for uranine and Rb^+. Owing to poor uranine mass recovery, no results are reported here for KFM04A. In the modelling evaluation /Gustafsson et al. 2006b/ it was suggested that this possibly could have been due to a hydraulic short-circuit with the borehole itself.

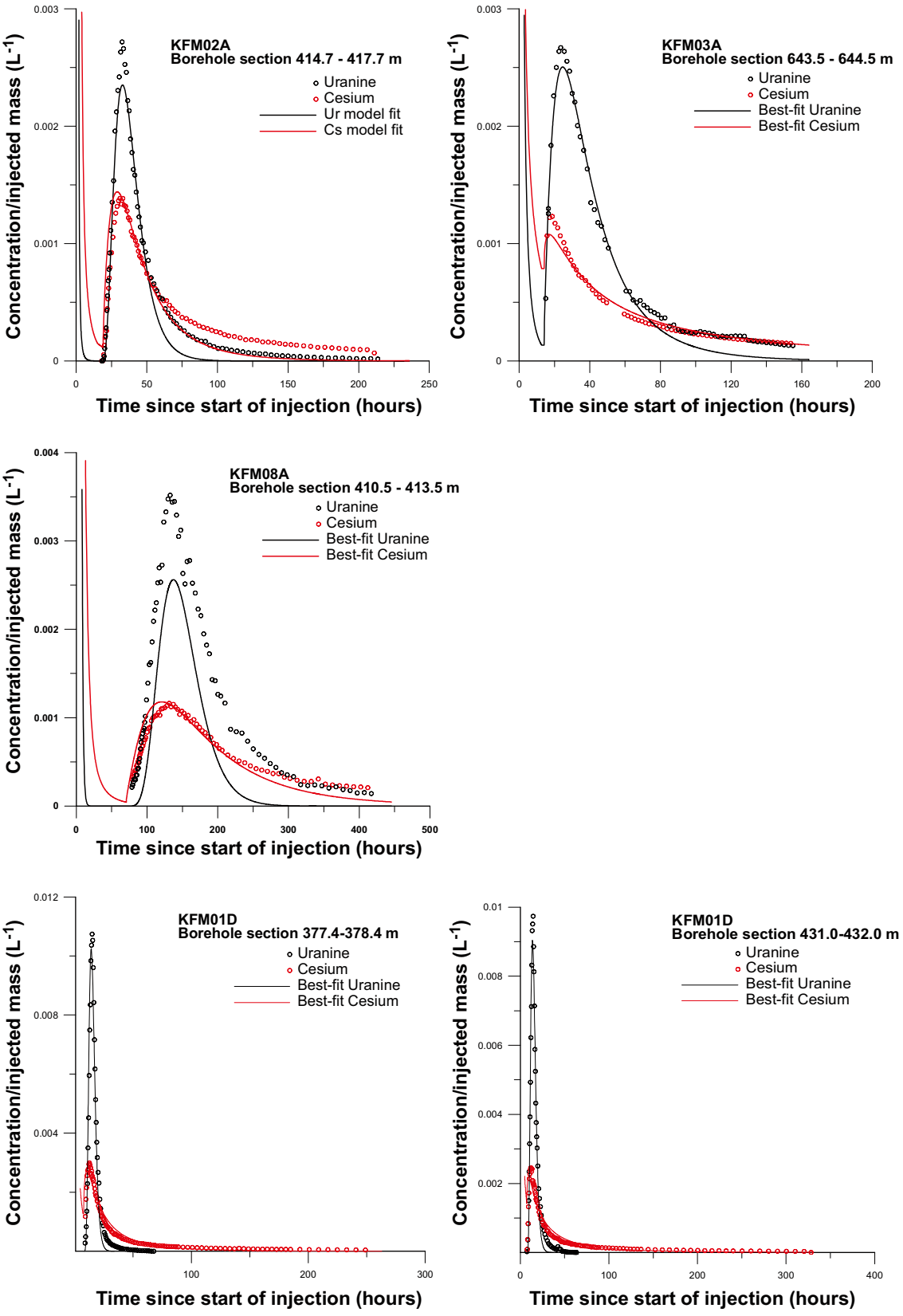

Figure 6-11. *Visualisation of model fit to uranine and Cs^+ recovery data for the radially symmetric, AD model with retardation simulated using SUTRA. (Figures taken from /Nordqvist 2008/).*

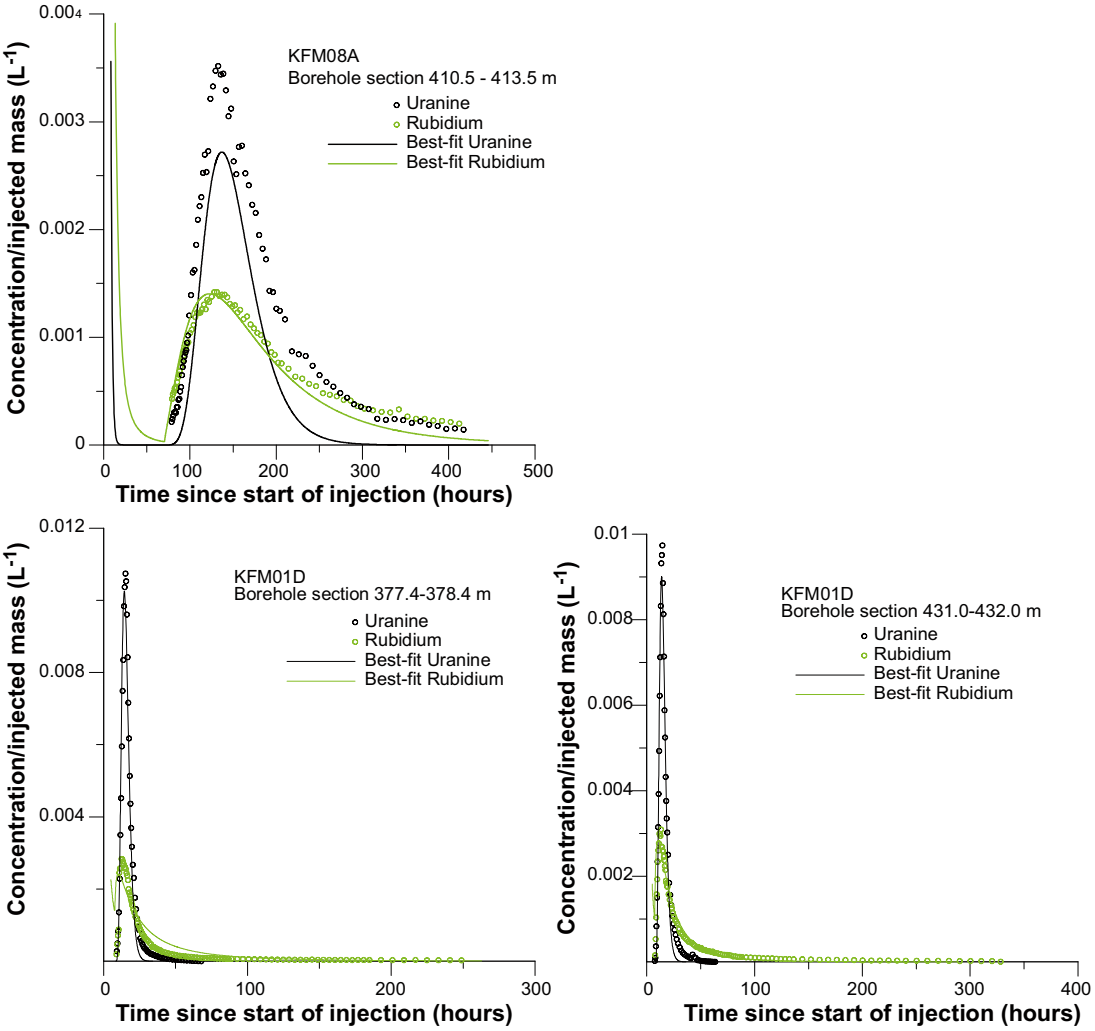

Figure 6-12. *Visualisation of model fit to uranine and Rb^+ recovery data for the radially symmetric, AD model with retardation simulated using SUTRA. (Figures taken from /Nordqvist 2008/).*

Although the simulation results indicate that it is possible to obtain a rough fit to the experimental data using the AD equation with linear sorption, close inspection of the curves indicates that there is consistent under-prediction of the long time tailing of the breakthrough curve for uranine. The results for the sorbing tracers Cs^+ and Rb^+ are mixed; in some cases late time tailing is under-predicted while in other cases it is over predicted.

In a second round of modelling /Nordqvist 2008/, the tracer recovery data were modelled using an advection-dispersion-sorption model coupled with matrix diffusion/sorption (AD-MD) in an attempt to better resolve the long time tailing behaviour. Consideration was also given to the influence of the background concentration of tracers and breakthrough data were corrected to account for this effect prior to modelling. In this case, instead of a surface retardation constant, R_a we attempt to fit the matrix interaction parameter, A as defined in Equation 6-1. The modelling procedure was based upon an extension of the SUTRA model used for the initial modelling efforts, although with the addition of a rock matrix 20 cm in extent. The rock matrix was implemented in the model by defining a zone with very low hydraulic conductivity adjacent to the flow domain. The stagnant zone was assigned a matrix porosity and pore diffusivity appropriate for the rock matrix. Parameters characterising the transport of solute were estimated by the same inverse modelling technique described previously (and in section 6.1).

The results of the extended evaluation using the AD-MD model are shown in Figure 6-13. Owing to problems in obtaining simultaneous fits for both uranine and sorbing tracers in KFM08A, only the uranine recovery curve was evaluated on this case.

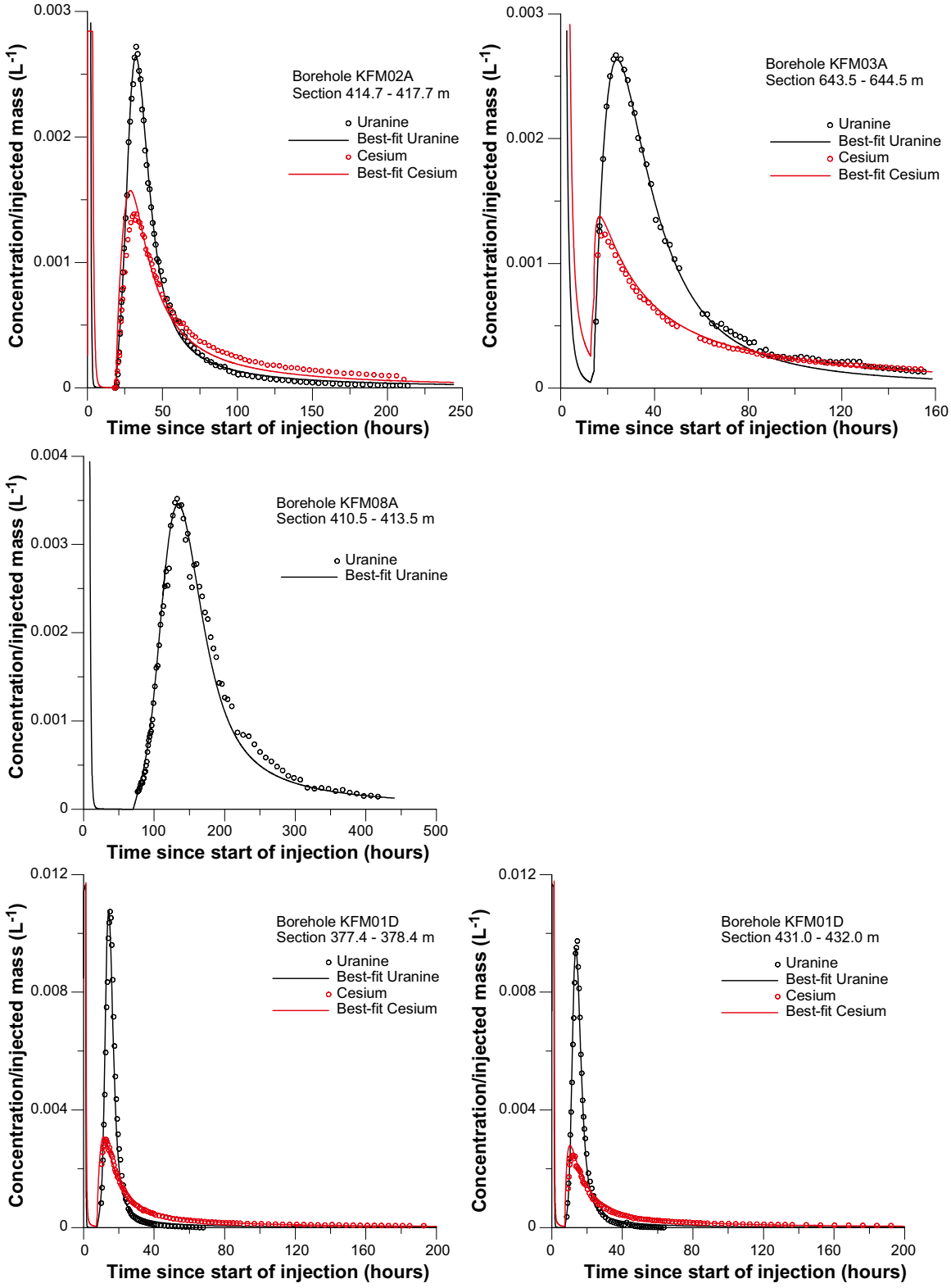

Figure 6-13. *Visualisation of model fit to uranine and Cs^+ recovery data for the radially symmetric, AD-MD model simulated using SUTRA. (Figures taken from /Nordqvist 2008/).*

The evaluation using the matrix diffusion model was found to give much improved fit to the experimental data, particularly for the long time tailing behaviour of uranine. For the SWIW tests carried out in KFM01D, the model fits are only marginally better than those obtained with the AD model with surface retardation. For KFM02A and KFM03A a substantially better fit to the main peak height and tailing behaviour was achieved, although for KFM02A the long time tailing was still slightly under-predicted.

Table 6-7. Summary of best fit parameter estimates for the AD model (linear sorption on fracture surfaces).

Borehole	Elevation (m)	Dimensionless dispersivity, τ (–)	Retardation factor, R_a (–)	
			Cs^+	Rb^+
KFM02A	–407	1.3	11	n/a
KFM03A	–633	12	73	n/a
KFM08A	–340	0.23	34	20
KFM04A	–355	n/a	n/a	n/a
KFM01D	–300	0.17	535	930
KFM01D	–342	0.29	918	238

Table 6-8. Summary of best fit parameter estimates for the AD-MD model (matrix diffusion and linear sorption within matrix porosity).

Borehole	Elevation (m)	Dimensionless dispersivity, τ (–)	Matrix interaction parameter, A ($s^{-½}$)	matrix retardation factor, R_m (Cs^+)
KFM02A	–407	0.09	282	1.6
KFM03A	–633	2.7	377	426
KFM08A [1)]	–340	0.08	741	n/a
KFM04A [2)]	–355	n/a	n/a	n/a
KFM01D	–300	0.05	382	1,890
KFM01D	–342	0.03	420	530

1) This section was only partly evaluated owing to ambiguity regarding uranine concentrations.
2) This section was not evaluated owing to incomplete uranine recovery.

Assuming that the sorbing tracer, on average, "samples" the same rock matrix as the non-sorbing tracer, the effective pore diffusion retardation factor, R_m for cesium can be roughly estimated from the A-parameter calculated for each solute and their known free phase diffusivities using the following relation:

$$R_m^{Cs^+} = \frac{D_w^{uranine}}{D_w^{Cs^+}} \left(\frac{A_{uranine}}{A_{Cs^+}} \right)^2 \qquad (6\text{-}3)$$

A summary of results from the modelling evaluation using the AD model is given in Table 6-7 and for the AD-MD model in Table 6-8.

6.3 Interpretation of modelling results and consequences for safety assessment

There are a number of processes which occur during the transport of solutes that can cause spreading of a tracer pulse injected into a heterogeneous flow system. Although these are customarily lumped together under the general term "dispersion", they may have very different origins and scale very differently depending upon the experimental flow configuration and timescale of a tracer test. Proper understanding of retention processes observed during a tracer test is dependent upon the ability to separate hydrodynamic dispersive effects from the effects of matrix diffusion and sorption upon geologic materials.

One of the major problems encountered when evaluating multiple well tracer tests is the occurrence of advective dispersion which can have a considerable impact upon modelling evaluation. Advective dispersion is the name given to the tracer spreading that occurs by way of the injected mass of tracer being transported along multiple, although mostly independent, flowpaths with differing fluid velocities /e.g. Neretnieks 1983/. Essentially, advective dispersion is a direct consequence of flow-channelling which has already been discussed at length in previous chapters. This is considered separately to "ordinary" hydrodynamic dispersion in that it cannot be described mathematically as a mixing process. Ordinary hydrodynamic dispersion is usually referred to in the literature as Fickian or Gaussian dispersion owing to the symmetric impact it has upon both early and late arriving solute. Indeed, while ordinary hydrodynamic dispersion is thought to behave in a Gaussian manner with a constant dispersivity as a function of flowpath length, advective dispersion gives a dispersivity that increases with observation distance. The apparent increase in dispersivity with increasing length scales has been discussed by a number of reviewers and is well known in the scientific literature /e.g. Gelhar et al. 1992, Neuman 1995, Berkowitz and Scher 1995/.

This is problematic since the advection-dispersion equation (with or without added matrix diffusion) implicitly assumes dispersion to be Gaussian, meaning that any non-Gaussian effects are typically assumed to be evidence of diffusive uptake to the rock matrix or stagnant zones adjacent to the flowpath /e.g. Becker and Shapiro 2000, 2003, Shapiro 2001/. The distinction between the effects of advective dispersion and matrix diffusion along flowpaths featuring differing F-factors, however, is difficult to assess since advective tailing cannot easily be distinguished from breakthrough tailing arising due to matrix diffusion. The situation is complicated even further if additional consideration is given to possible multiple timescales of mass transfer arising due to heterogeneous material properties and different types of immobile zones /e.g. Haggerty and Gorelick 1995/. Modelling interpretation of data from multiple-well tracer tests therefore remains a contentious issue which has not yet been fully resolved /e.g. Zhou et al. 2005/.

SWIW tests, on the other hand, are thought to be much less sensitive to the effects of advective dispersion and flowpath dimensionality /e.g. Becker and Shapiro 2003, Tsang and Doughty 2007/. If there is no background hydraulic gradient, no matrix diffusion, and no hydrodynamic dispersion in the radiating flow channels, we would expect an injected pulse of solute to be recovered exactly as it was injected /Neretnieks 2007/. This is because solute travelling along fast flowpaths travels further into the formation than solute residing in slow flowpaths, the distance being proportional to the flow velocity and the flow injection time. Under the assumption of purely advective transport it can be shown that the flow reversal exactly counteracts the advective spreading of the pulse regardless of the total injection and pumping flowrates. In practice, however, along a heterogeneous flowpath there is always a residual component of local hydrodynamic dispersion which is irreversible /Becker and Shapiro 2003/.

Given the various dispersive effects which can influence the residence time distribution of a tracer, we must be very careful in our interpretation of what the results represent in order to make physically justified pronouncements concerning the up-scaling of transport properties to safety assessment timescales and flow configurations.

If we accept, for the moment, the hypothesis of a diffusive sequestering mechanism for the long time tailing observed in a tracer test then the question remains as to what diffusive process or mix of processes this represents. Here we implicitly assume that the assumption of Gaussian hydrodynamic dispersion is correct and can therefore be separated from diffusive effects. As discussed previously, the strength of presumed matrix interaction in the modelling evaluations is given in terms of a lumped parameter, A which includes the effects of the effective F-factor for the transport path, the matrix effective diffusivity and sorptivity. If the average porosity of the system is reasonably well constrained it is possible to estimate the "apparent" formation factor, F_f^* observed in a tracer test if we also have information about the mean transport aperture, δ_t of the system:

$$F_f^* = \frac{1}{4 D_w \theta_m} \left(\frac{\delta_t}{A} \right)^2 \qquad (6\text{-}4)$$

For a sorbing tracer, we have instead:

$$F_f^* = \frac{1}{4D_w\left(\theta_m + K_d\rho_b\right)}\left(\frac{R_a\delta_t}{A}\right)^2 \qquad (6\text{-}5)$$

In this case, we additionally need to know something about the sorptivity of the tracer in order to constrain the apparent formation factor, since the estimated A-parameter lumps the effects of sorptivity and diffusivity together. It should be noted that we include the additional retardation term R_a here only because it is already utilised to obtain fitted values of A as given in /Lindquist et al. 2008a/. If mass transfer is modelled purely as a matrix diffusion process this extra parameter is not necessary. It should also be remembered that the F-factor characterising the tracer test is given by twice the quotient of the advective travel time and transport aperture (Equation 3-10) and so is implicitly included in the evaluation when both these entities are known or can be estimated.

The transport aperture is usually not well known since it is not necessarily related to the hydraulic aperture of the system in a simple fashion. This has already been discussed at some length in section 3.8. For the dipole test performed in ZFMA2, however, a value for the equivalent fracture aperture has been reported in the modelling evaluation /Lindquist et al. 2008a/. This estimate, however, is based upon a radial flow assumption in a single fracture and therefore may underestimate the true flow-wetted surface to flow ratio characterising the tracer test. It is easy to appreciate that if the same total transport aperture was instead to be divided amongst, say n parallel fractures the flow-wetted surface would be consequently n times greater for the same total flow.

In fact, using the reported transport aperture (2.6×10^{-2} m) for the ZFMA2 dipole test together with Equation 6-4 implies an apparent effective diffusivity much greater than for free diffusion in water which is not physically possible. In order to obtain physically realistic estimates of F_f^* the transport aperture needs to be at least an order of magnitude less than the figure reported. For the same kinematic porosity this is possible if transport occurs within an array of parallel flowpaths (or a flowpath filled with particulates) featuring a total flow-wetted surface 10 times greater than that for a single fracture.

For the SWIW tests, on the other hand, an assumed value for the transport aperture is used throughout the simulations using the SUTRA simulation code /Nordqvist 2008/. Since these values are already internalised in the evaluation of the A-parameter, it is these values which are most appropriate to use for further analysis using Equation 6-4 or 6-5. This is because the ratio δ_t/A negates the effect of the unknown transport aperture in the evaluation provided the same value is used as that utilised in obtaining the initial fitted estimate of the A-parameter. This, however, does not mean that the fracture aperture gives a correct representation of the flow-wetted surface encountered by tracer during the test and it is not difficult to imagine complex fracture sets that could give larger surface areas for diffusive uptake and thus anomalously large apparent matrix interaction effects.

In the analysis presented here, we revisit the SWIW tracer test data for non-sorbing tracers and compare the apparent formation factor derived using Equation 6-4 with the appropriate recommended value obtained from the retardation model. For sorbing tracers we use recommended K_d values from the retardation model in conjunction with Equation 6-5 to estimate an apparent formation factor. This then gives us an indication of the amount of diffusive mass transfer enhancement that we observe in the tracer experiment compared to that which we would expect on the basis of data derived from laboratory measurements. It also allows us to compare the apparent matrix diffusive properties of both sorbing and non-sorbing tracers from the same experiment in a semi quantitative fashion. In making these calculations we need to make some basic assumptions about the rock volume being tested. These assumptions are listed in Table 6-9.

Table 6-9. Additional modelling assumptions used in extended evaluation of SWIW tracer test data.

Tracer test	Parameter	Value	Comments
SWIW test KFM02A (–407 m):			
all tracers	F_f (reference)	5.2×10^{-5}	assumed for rock type 101057 (DZ)
uranine	K_d (m^3/kg)	0	non-sorbing
Cs^+	K_d (m^3/kg)	1.5×10^{-3}–7.3×10^{-3}	saline value range for "fresh rock" on account of no fracture minerals present
SWIW test KFM03A (–633 m):			
all tracers	F_f (reference)	5.2×10^{-5}	assumed for rock type 101057 (DZ)
uranine	K_d (m^3/kg)	0	non-sorbing
Cs^+	K_d (m^3/kg)	1×10^{-3}–5×10^{-1}	saline/marine K_d range for all fracture coatings
SWIW test KFM08A (–340 m):			
all tracers	F_f (reference)	1.2×10^{-4}	assumed for rock type 101057 (non-DZ)
uranine	K_d (m^3/kg)	0	non-sorbing
SWIW test KFM01D (–300 m):			
all tracers	F_f (reference)	1×10^{-4}	assumed for rock type 101051 (non-DZ)
uranine	K_d (m^3/kg)	0	non-sorbing
Cs^+	K_d (m^3/kg)	1×10^{-3}–5×10^{-1}	saline/marine K_d range for all fracture coatings
SWIW test KFM01D (–342 m):			
all tracers	F_f (reference)	1×10^{-4}	assumed for rock type 101051 (non-DZ)
uranine	K_d (m^3/kg)	0	non-sorbing
Cs^+	K_d (m^3/kg)	1×10^{-3}–5×10^{-1}	saline/marine K_d range for all fracture coatings

Using the modelling assumptions given above, the ratio of apparent and recommended formation factor can be compared. The apparent diffusive mass transfer enhancement factor calculated in this fashion is shown in Figure 6-14 for the various SWIW tests carried out at the Forsmark site. Since SWIW tests are not associated with a well-defined observation distance, we plot the results against the transmissivity of the tested fracture system/zone. It is noted, however, that although there may be correlation with observation scale, there appears to be no meaningful correlation between transmissivity and mass transfer evident in Figure 6-14.

The results of this analysis indicate that there is an apparent enhancement of mass transfer to the immobile zone that is considerably larger than what we can justify on the basis of uncertain laboratory derived measurement values. Even making allowances for very large increases in formation factors and sorption coefficients at the fracture surfaces or in association with fault gouge or breccia material does not appear to satisfactorily explain the degree of enhancement. This is qualitatively consistent with previous experiences from the TRUE-1 project /Winberg et al. 2000/. An alternative explanation for the enhanced mass transfer is that transport occurs within a complex fracture with substantially greater flow-wetted surface than the single fracture plane assumed in the SUTRA simulations. The increase in flow-wetted surface required, however, seems larger than what is realistic for the flow structures considered.

An interesting feature of the tracer test data reinterpretation presented here is that the diffusive mass transfer enhancement factor seems to be larger for non-sorbing tracers than for sorbing tracers. The difference is considerable and consistent across all tracer tests evaluated. It cannot readily be explained away as a result of uncertainty concerning the sorption K_d value used in the evaluation since the stronger the sorption at the fracture surface, the larger the apparent discrepancy appears to be (as indicated by the error bars for K_d uncertainty where the high end of the sorptivity range corresponds to the lower end of the error bar).

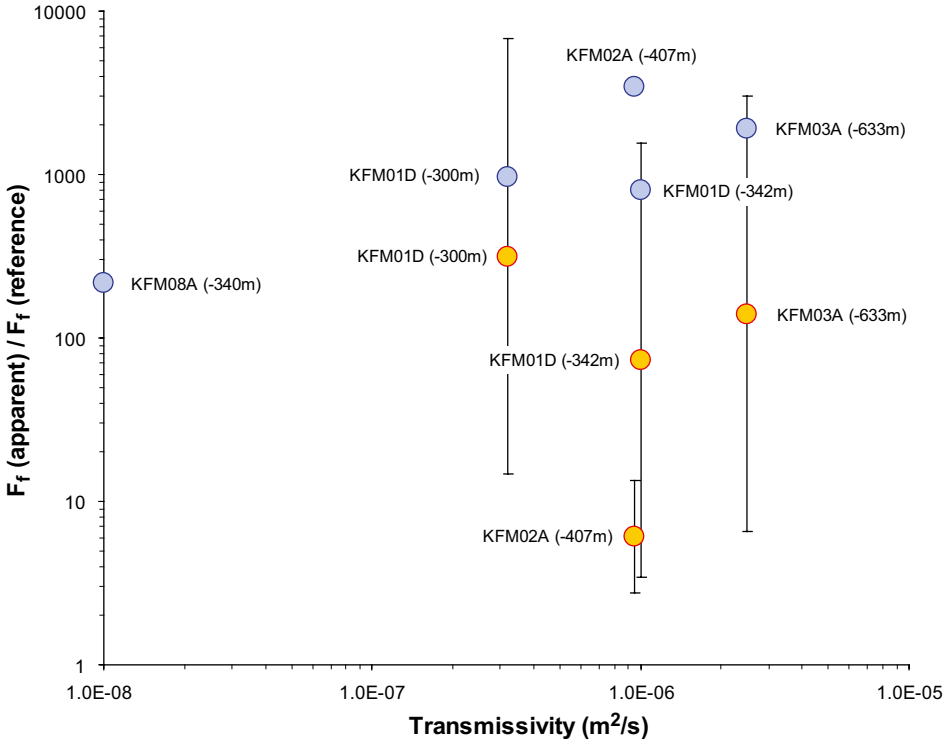

Figure 6-14. *Apparent diffusive mass transfer enhancement factors for SWIW tracer tests carried out at Forsmark plotted against transmissivity of the tested flowpath. Data are shown for both Cs^+ (orange shaded symbols) and non-sorbing uranine tracer (blue shaded symbols). The plotted data are geometric means with error bars where min-max ranges of possible K_d values have been considered.*

It should be noted that apparent enhancement of "diffusive" mass transfer as shown in Figure 6-14 does not imply that the "overall" rate of mass transfer to the immobile zone is greater for a non-sorbing tracer than a sorbing tracer. The former is based upon comparison of apparent Formation factors derived from a tracer test while the latter is based upon comparison of the apparent material properties group (MPG) for the solute in which sorptive and diffusive effects are lumped together. Since the material properties group is inversely proportional to the fitted *A*-parameter (e.g. Equation 6-1) it is easy to show that the overall rate of mass transfer for sorbing solutes is greater than that of the non-sorbing solutes.

Superficially these results would appear to be evidence for the existence of stagnant zones along the transport paths sampled in the tracer tests since this is actually what we predict from first principles using Equation 5-4. It also suggests that tracers with differing sorptive properties, probe different parts of the immobile zone. The mass transfer of non-sorbing tracers, for example, appears to be dominated by diffusion within the stagnant zones, while the mass transfer of sorbing tracers is dominated by mass transfer directly to the rock matrix (or fracture coating) at the flow-wetted surface of the advective flowpath. In short, sorbing tracers only "see" the flow-wetted surface, while non-sorbing tracers only "see" the stagnant water volume adjacent to the flowpath.

Diffusion of tracer into stagnant zones was also considered by /Neretnieks 2002/ in order to explain the anomalous mass transfer enhancement observed in the TRUE-1 tracer tests. In the modelling interpretations of the TRUE-1 tests described by /Cvetkovic et al. 2007/ where apparent dimensionless sorption coefficients of different solutes were compared with laboratory derived data it was found that there was a stronger enhanced retention for poorly-sorbing solutes than for sorbing solutes. This is consistent with stagnant zone diffusion, although in /Cvetkovic et al. 2007/ the effect is interpreted as being largely related to enhanced retention within the alteration rim.

Even though it is tempting to take the results directly as a confirmation of the existence of effectively stagnant zones of the kind hypothesised in Chapter 5, it is necessary to further test this notion to see if it gives reasonable values for the R_s factor (i.e. the ratio of stagnant zone mass transfer surface area and flow-wetted surface) and also to check that alternative explanations can be ruled out.

In /Neretnieks 2007/, the main entity governing the parallel rate of mass transfer from a flow channel to the rock matrix and stagnant zone (after replacing relevant variable names with those used in Chapter 5) can be shown to be:

$$\frac{\delta_t}{A} = R_s\sqrt{D_w} + \sqrt{D_e\left(\theta_m + K_d\rho_b\right)} = R_s\sqrt{D_w} + MPG_m \qquad (6\text{-}6)$$

From inspection of Equation 6-6 it is evident that the right-hand side of the equation is simply the sum of the mass flux, pre-factor terms describing mass transfer (for short contact times) as defined by the numerator and denominator of Equation 5-4. The second term on the right hand side of the equation is the material properties group, MPG_m for the rock matrix.

By analogy, it is easy to include additional parallel mass flux terms as deemed appropriate. For example, we could easily include an additional parallel mass flux to a gouge material (or breccia) by writing:

$$\frac{\delta_t}{A} = R_s\sqrt{D_w} + R_g \cdot MPG_g + MPG_m \qquad (6\text{-}7)$$

Where the term R_g is the ratio of gouge (or breccia) flow-wetted surface to "true" flow-wetted surface /Crawford 2006/ and MPG_g is simply the corresponding material properties group for the gouge/breccia particles. It should be noted that this treatment corresponds to the early time asymptotic limit for mass transfer before saturation effects begin to play a role.

If we only consider the impact of matrix diffusion and a hypothetical stagnant zone, rearrangement of Equation 6-6 gives R_s explicitly.

$$R_s = \frac{\delta_t}{A\sqrt{D_w}} - \sqrt{F_f\left(\theta_m + K_d\rho_b\right)} \qquad (6\text{-}8)$$

Using recommended values for the materials property data in the tracer tests it is now possible to make an estimate of the R_s factor and to compare this value to what would seem reasonable for an "average" flow channel. In this analysis we focus upon the SWIW test data as we know these to be less influenced by advective dispersion which may have biased the results for the dipole test given that the data evaluation in /Lindquist et al. 2008a/ considered a single flowpath with Gaussian dispersion.

If we assume that the stagnant zone is symmetric on either side of the main flow channel, the flow channel width can be calculated from the estimated value of the transport aperture using the relation (see Equation 5-1 assuming $f_s = 2$):

$$W_c = \frac{\delta_t}{R_s} \qquad (6\text{-}9)$$

The results of these calculations are given in Table 6-10.

Table 6-10. Estimated flow channel widths estimated from SWIW test data assuming multiple rates of mass transfer to a stagnant zone and to the rock matrix (parallel fluxes).

Tracer test	Tracer	R_s (m^2/m^2)	W_c (m)
KFM02A (–407 m):	uranine	0.039	5×10^{-3}
	Cs^+	0.018–0.036	6×10^{-3}–1×10^{-2}
KFM03A (–633 m):	uranine	0.029	7×10^{-3}
	Cs^+	0.36–0.6	3×10^{-4}–6×10^{-4}
KFM08A (–340 m):	uranine	0.015	1.4×10^{-2}
KFM01D (–300 m):	uranine	0.03	7×10^{-3}
	Cs^+	0.92–1.3	1.6×10^{-4}–2.2×10^{-4}
KFM01D (–342 m):	uranine	0.026	8×10^{-3}
	Cs^+	0.26–0.60	3×10^{-4}–8×10^{-4}

It is evident from the estimated flow channel widths in Table 6-10 that the assumption of mass transfer to a stagnant zone as discussed above may be an incorrect interpretation of the SWIW test results. These flow channel widths appear to be far too narrow to be considered realistic for the flow channels likely to be encountered during a SWIW test. It is also interesting to compare the difference in the value of R_s (5×10^{-4}) used in the calculations presented in Chapter 5 to the somewhat larger values estimated here.

To properly resolve this issue it is necessary to revisit some basic assumptions in the formulation of the solute transport problem for the timescales characteristic of a SWIW tracer test. While we believe that the advective dispersion component acquired during the injection and chaser phase of the test should be counteracted by the flow reversal during the pumping phase, we do not have a very clear picture of the nature of the irreducible hydrodynamic dispersion and whether this can be assumed to be a Gaussian process. Since the evaluation models presuppose this to be the case a priori, the assumption may not be safe.

There are many salient issues involved in the analysis of hydrodynamic dispersion that are too numerous to discuss in this report. We can, however, with some justification make the statement that these are largely diffusion mediated processes. This has been implicitly recognised by /Berkowitz and Scher 1995/ in their mechanistic description of solute transport in terms of a continuous time random walk (CTRW) process which assembles all advection-diffusion-dispersion processes together under a single mathematical framework. For these diffusion mediated processes to approach Gaussian behaviour requires the length and timescales characterising the tracer test to be such that the transported solutes diffusively sample all of flow space structure in an uncorrelated manner /Bryant and Thompson 2001/.

The most elemental form of hydrodynamic dispersion that can occur within a flow channel is Taylor-Aris dispersion /Taylor 1953, Aris 1956/. This arises due the existence of a parabolic velocity profile across the aperture of a flow channel for a fluid undergoing viscous, laminar flow. If the fluid contains a dissolved solute, streamlines near the centre of the velocity profile move faster than those near the edges and carry any dissolved solute at a faster rate. Diffusion between these streamlines attempts to even out the differences in concentration and the combined effect is similar to the existence of an enhanced molecular diffusivity along the direction of flow. The key assumption in this analysis is that the "contact time" is presumed to be sufficiently long that the dispersion asymptotically approaches a Gaussian limit. For the flow conditions characteristic of most tracer tests and for typical fracture apertures encountered in granitic rock, this is usually a reasonable assumption since diffusive equilibrium is attained in a matter of minutes across a typical fracture aperture. The longitudinal dispersivity is customarily estimated from the equation for infinite parallel plates which can be found in /Bird et al. 2002/:

$$\frac{D_L}{D_w} = \left(1 + \kappa_l \mathrm{Pe}^2\right) \tag{6-10}$$

Where the constant $\kappa_l = 1/210$ and the dimensionless Péclet number, Pe is defined as:

$$\mathrm{Pe} = \frac{u_w \delta_t}{D_w} \tag{6-11}$$

Analogous, asymptotic results have also been obtained for homogeneous flow in a radial flow field /Stone and Brenner 1999/.

It has been suggested by /Neretnieks 2007/ that a flow channel with a profile tapering towards the edges may give rise to a Taylor-Aris dispersion effect in the transverse direction spanning the channel width. This could potentially be much larger than the effect arising due to the velocity profile across the fracture aperture. In many recent studies it has been found that heterogeneous fractures hosted in rock have a spatially correlated aperture distribution often described as being self affine in nature /e.g. Brown 1995, Glover et al. 1998a/. Based upon these observations it would seem very likely that most flow channels hosted within fractures will exhibit tapering effects of this kind.

Hydrodynamic dispersion in flow channels with tapered edges has been studied extensively in the field of microfluidics owing to its relevance for laminar mixing in lab-on-a-chip applications /e.g. Dutta et al. 2006/. For tapered flow channels with regular geometry the "long-time" longitudinal dispersivity can be shown to be /Ajdari et al. 2006/:

$$\frac{D_L}{D_w} = \left(1 + \kappa_l \mathrm{Pe}_w^2\right) \tag{6-12}$$

Where the constant κ_l is a function of the non-dimensional geometric shape of the flow channel cross-section and Pe_w is the Péclet number based upon flow channel width:

$$\mathrm{Pe}_w = \frac{u_w W_c}{D_w} \tag{6-13}$$

The parameter κ_l has been calculated by /Ajdari et al. 2006/ using Aris's method of moments /Aris 1956/ and the lubrication approximation /Bird et al. 2002/. For high aspect ratios ($W_c \gg \delta_t$), κ_l values of 0.0052 (triangular profile), 0.0031 (parabolic profile), and 0.022 (ellipsoidal profile) have been estimated as well as more general results for "quasi-rectangular" profiles. It has also been shown by the above authors that, for flow channels characterised by high aspect ratios, hydrodynamic dispersion is generally controlled by the channel width rather than its aperture in agreement with the hypothesis proposed by /Neretnieks 2007/.

At short timescales (the so-called "ballistic regime") where the transported solute has had sufficient time to mix across the channel aperture, although not enough time to fully sample the width of the channel, the longitudinal dispersivity is given instead by:

$$\frac{D_L}{D_w} = \left(1 + \kappa_s \mathrm{Pe}_w^2 \left(\frac{D_w t}{W_c^2}\right)\right) \tag{6-14}$$

As can be seen from Equation 6-14, the short time dispersivity is time dependent and therefore increases with observational distance. The crossover time, t_{xo} where the ballistic regime undergoes the transition to the asymptotic Gaussian form is found by equating the variance of the solute residence time distributions estimated for short (Equation 6-12) and long contact times (Equation 6-14) and solving for t, assuming $\mathrm{Pe}_w \gg 1$. This gives:

$$t_{xo} = \kappa_{xo} \frac{W_c^2}{D_w} \tag{6-15}$$

The constant κ_{xo} is generally found to be in the range of 0.03–0.04 for some regular cross-section shapes featuring high aspect ratios (e.g. triangular, parabolic, ellipsoidal) /Ajdari et al. 2006/. For a 10 cm wide flow channel with tapered edges, we would therefore expect the crossover time to be on the order of 40–400 h depending upon the free diffusivity of the tracer.

Although real flow channels hosted in fractures are expected to feature substantially greater heterogeneity than this analysis assumes, it is very significant that even simple, cross-sectional channel profiles give rise to non-Gaussian behaviour at the timescales characteristic of a SWIW tracer test. It is noted, however, that the heterogeneous variation of flowpath width and aperture in a real fracture may actually hasten the transition to Gaussian behaviour and decrease longitudinal dispersion by inducing additional rotational and extensional flows that are absent in a smooth flow channel (depending upon the aspect ratio of the flow channel). This principal has actually been exploited to design optimised microfluidic mixing devices that induce chaotic axial mixing flows while minimising longitudinal dispersion /Stroock et al. 2002, Lauga et al. 2004/.

The above discussion suggests that the continuous convergence and divergence of flowpath widths and apertures within correlated structures gives rise to effects that are difficult to predict without detailed knowledge of the pore space structure. Locations where flow channels branch and join up with other channels may also play a significant role in determining dispersive behaviour.

It is not clear how this analysis would translate to radial flow and flow-reversal situations, although we have good reason to believe that dispersion incurred during such flow regimes will also be perceptibly non-Gaussian. Most numerical simulation codes are able to simulate these processes in principal. The inclusion of realistic flow field heterogeneity, however, is likely to be too coarse to capture all significant aspects of the hydrodynamic dispersion and streamline diffusion processes that are active on the timescale of the tracer test. For these effects to be captured correctly would probably require models with substantially higher spatial resolution than is typically considered in such investigations.

The consequence of non-Gaussian dispersion is that it is indistinguishable from matrix diffusion or diffusion into stagnant zones flanking a flow channel as these all give rise to long time tailing behaviour. This is a very important result with relevance for scale up of model derived results to safety assessment. It is highly possible that the enhanced diffusive uptake of uranine observed in the tracer tests could be dominated by non-Gaussian dispersion thus giving rise to the unrealistic values of R_s and the effective channel width, W_c calculated in Table 6-10. Over longer timescales and lower flowrates characteristic of safety assessment, non-Gaussian hydrodynamic dispersion effects should vanish since the transverse Taylor-Aris dispersion is asymptotically Gaussian.

Although we consider that non-Gaussian streamline diffusion is the most likely culprit for the apparently anomalous diffusive uptake of uranine in the SWIW tests, it should be recognised that there are other potential explanations that we have not fully explored. One of these is that the background concentration of uranine has not be correctly accounted for in the tracer recovery curve thereby giving a biased interpretation of long time tailing of this tracer. Although the effect has been accounted for to the full extent possible, it cannot be fully discounted in the analysis of the results.

Flow bypass effects (i.e. where the relatively low transmissive test section feeds into a strongly transmissive fracture at some distance from the borehole) may also give apparently anomalous retardation characteristics for uranine that would not necessarily be observed for cesium owing to its reduced range of mobility in the fracture system.

Whatever the case may be, it is relatively safe to say that if reduced peak height or long-time tailing in a non-Gaussian dispersion regime is used to infer matrix interaction properties in the form of a field calibrated material property group or multirate, sub-grid parameters for use in codes, simulation results may be incorrect as the matrix-diffusive and hydrodynamic dispersion components scale very differently to safety assessment flow situations and timescales. Having said this, the retardation of sorbing tracers appears to be less influenced by hydrodynamic effects and so derived material property parameters may be more reliable than the results for non-sorbing tracers. A direct consequence is that the anomalous behaviour of uranine should probably not be used to fix dispersive parameters governing the transport of sorbing solutes (i.e. in simultaneous breakthrough curve fitting) since they may not necessarily be subject to the same mass transfer processes at short timescales.

The present analysis suggests that breakthrough data for sorbing tracers can be used to estimate the material properties of fracture coatings governing the first arrival of similarly sorbing solutes under safety assessment conditions, provided a bias is not introduced by using non-sorbing tracer breakthrough data to fix hydrodynamic dispersion parameters. It should be remembered, however, that owing to the limited depth of rock matrix sampled during the tracer test, the estimated material properties will not have relevance for retardation processes at later times when the more deeply lying rock matrix plays a much more significant role.

On a slightly different note, although related to up-scaling of material properties, it should be remembered that typical numerical implementations of the multirate model of /Haggerty and Gorelick 1995/ consider parallel diffusive uptake into multiple immobile zones of different geometries and limited dimensions, but are usually not formulated to handle series-coupled resistances that may arise, for example, upon consideration of multiple alteration layers adjacent to a fracture surface or diffusion into a stagnant zone followed by uptake to the rock matrix. Moreover, the late time slope measured in a tracer test which is used for conditioning of multirate models can only provide information about the mass transfer processes which occur on the timescale of the tracer test and cannot sense boundaries or changes in material properties that occur at greater penetration distances than that probed by the tracer. In a typical tracer test we would expect the effective depth of solute penetration to be no more than about 10 μm to perhaps 100 μm which may not be representative of the rock which gives rise to the bulk of the retardation effect expected at safety assessment timescales. Great care must therefore be exercised when using parameters abstracted using multirate or CTRW /Berkowitz et al. 2001, Berkowitz and Scher 2001/ approaches to ensure that abstracted parameters are phenomenologically capable of being scaled up to safety assessment applications.

Another up-scaling effect that stands out from this analysis and the calculations presented in Chapter 5 is that the R_s parameter and the aperture of the stagnant zone, δ_s are only strictly relevant at short timescales before diffusive equilibrium is attained in the stagnant zone. As demonstrated in Chapter 5, at longer times and for F-factors characteristic of safety assessment, only the width of the stagnant zone is important and the parameters R_s and δ_s (which govern the apparent kinetics of exchange with the stagnant zone) can be shown to have little impact upon solute residence times.

6.4 Summary of main findings

In summary, the key findings of this chapter include:

- In general, the tracer tests carried out in support of transport property site descriptive modelling give indications of diffusive effects and retardation of sorbing solutes that are consistent with our conceptual model of solute transport within the fractured rock at Forsmark. Furthermore, the lumped parameters obtained from the modelling evaluation allow us to speculate on a range different physical phenomena that could have influenced the observed tracer transport. It is clear that tracer retention is generally enhanced relative to that predicted on the basis of independent laboratory data. Although this may be due in part to enhanced retention in the rim zone of fractures, detailed analysis of the results suggests that there may be other effects at play which are difficult to distinguish from true matrix retention processes, particularly for non-sorbing solutes.
- The various tracer test data obtained from Forsmark can be considered to support level A ("Confirmation of flow connectivity"), B ("Qualitative confirmation of retention"), and C ("Confirmation of process understanding") criteria as described in /Löfgren et al. 2007/ concerning the utility of tracer tests in site characterisation. The modelling evaluations also support Level D criteria ("Abstraction of lumped transport parameters") with the caveat that the retardation processes observed may not scale simply to safety assessment timescales;

- Although tracer tests performed in multiple well, dipole configurations exhibit signs of sorptive and diffusive retention, it is difficult to make detailed analyses of their magnitude owing to the presence of advective dispersion which has a similar impact upon the residence time distribution of solute as matrix diffusion (i.e. a tailing effect). In principle it is possible to evaluate the breakthrough of different tracers simultaneously to separate these processes and estimate a probability density function for the distribution of advective pathways /e.g. Cvetkovic et al. 2007/. The evaluations described in the Forsmark site modelling reports, however, had great difficulty in achieving this goal and the reported modelling results are generally based upon the advection-dispersion equation with matrix diffusion and sorption within an assumed single flow path.
- SWIW tracer tests are less sensitive to the impact of advective dispersion owing to the reversal of the flow field which partially reforms the injection pulse. The SWIW tests carried out at Forsmark gave strong indications of sorptive and diffusive retardation of transported solutes. Detailed evaluation of the modelling results also indicate that the enhancement of diffusive mass transfer was possibly greater for non-sorbing solutes than sorbing solutes. Although the overall effect could be explained by diffusive exchange with a stagnant zone, the results require unrealistic flow channel aspect ratios to explain the magnitude of the mass transfer enhancement and this can be probably ruled out. Other effects that might give rise to this behaviour include streamline diffusion (giving rise to non-Gaussian dispersion indistinguishable from matrix diffusion), faulty correction for background tracer concentrations, and so-called "flow bypass" effects. It is speculated that these phenomena may have a greater impact upon the interpretation of non-sorbing tracer transport and hence data for sorbing solutes may be more reliable. Fitting of hydrodynamic dispersion parameters and matrix formation factors by simultaneous interpretation of sorbing and non-sorbing tracer data may therefore contain unintended biases. Additional modelling work with more detailed consideration of hydrodynamic processes on the timescale of tracer tests may need to be done if the issue is deemed to warrant further resolution.
- Material property data derived from tracer tests, even if fully corrected for the effects outlined above, should be interpreted with care since the depths of solute penetration typically achieved may not be representative of the rock that is expected to give the bulk of the retardation effect operating at safety assessment timescales.

7 Overall summary and conclusions

In this report we have examined the transport properties of the bedrock at the Forsmark site with the intention of creating a site descriptive model (SDM) that can function as an input to safety assessment. Since the aim of this work is to give a detailed overview of the properties of the site rather than making specific recommendations for conservatively chosen parameter values to be used in safety assessment, the actual choice of which data to use in safety assessment calculations will be made later in the SR-Site data report for transport properties. This report serves in a supporting role for the final data selection.

From the flow-related transport properties modelling described in Chapter 3, we can say that the bulk of the potential hydrodynamic transport resistance (F-factor) appears to reside in the hydraulic rock domain (HRD). The scoping calculations suggest typical F-factors for major flowpaths within the proposed repository volume on the order of 10^6 y/m for a reference hydraulic gradient of 1%. For radionuclide release at –450 m elevation within deterministic deformation zones and the same reference hydraulic gradient, typical F-factors for transport to the near surface (assumed –100 m elevation) are estimated to be about 10^3 y/m for gently dipping deformation zones and as much as 10^5 y/m for steeply dipping zones. These predictions, however, are dependent upon underlying assumptions in the compartmentalised scoping calculations and deviations from this forecast are likely if full consideration of the integrated flow system is made. In particular, ECPM simulations of the integrated flow system made using ConnectFlow suggest that local hydraulic gradients may be low in certain deterministic deformation zones which comprise the hydraulic conductor domain (HCD). The regional scale simulations also suggest that hydraulic gradients in the repository volume are very low which can give much higher F-factors and advective travel times than those estimated in the scoping calculations.

For the transport calculations described in Chapter 5, the depth interval of fracture domain FFM01 below –400 m elevation has been taken to be representative of the target volume for a hypothetical repository for spent nuclear fuel. The typical major flowpaths encountered within this rock volume appear to be associated with sufficiently high F-factors that retardation of radionuclide transport is relatively strong. Additional hydrodynamic transport resistance will be available if credit is also taken for the poorly transmissive flow paths connecting individual canister positions with the major flowpaths in the repository fracture domain. Since the calculations of F-factors for these initial flowpaths are associated with significant uncertainties owing to underlying assumptions related to repository design, we have not considered them to contribute significantly to the transport retardation of radionuclides.

Since the hydrodynamic transport resistance accumulated in the deterministic deformation zones appeared to contribute no more than 1–10% of the overall flowpath F-factor in the scoping calculations, these were not included in the radionuclide transport simulations. However, it is noted that the increased microstructural complexity of the HCD, on balance, is likely to be associated with an elevated degree of transport retardation than the F-factor for these zones would appear to indicate at face value. The same can be probably be said for flow channels of limited extent hosted within fault step-overs or formed at the intersection of crossing or terminating fracture intersections (referred to in this report as conductive fracture intersection zones, or FIZ).

Six different sub-classes of flow channelling have been considered in this investigation as being relevant for the Forsmark site. It appears that their existence can be at least partially accounted for using information internalised in the geological and hydrogeological site descriptive models. The impact of these phenomena can be reasonably well bounded using scoping calculations of the kind described in this report. Although there is a risk that extreme flow channelling may lead to censoring of borehole data leading to the biasing of the hydrogeological properties description, we believe that the flow space is sufficiently hydraulically well-connected that most major

flow channels hosted in fracture planes should be identifiable from borehole investigations. Full resolution of this issue, however, will not be possible until the construction of an underground tunnel at the site since many aspects of flow channelling cannot be properly quantified from a surface based site investigation. When flow channelling effects are considered in the simulation of radionuclide transport they can often have a very positive effect on the retardation of radionuclide migration.

A retardation model has been developed which describes the material properties of the rock, various fracture types characteristic of the Forsmark site, and a number of recurring deformation zone structural elements. The retardation model describing the properties of various sub-structures within the rock can be assembled in a modular fashion and combined with hydrogeological models to create integrated models for the prediction of radionuclide transport. Generally, altered rock has stronger sorptive retention than unaltered rock types. It has been found that the main metagranite rock type (101057) residing in deformation zones can have slightly lower diffusivities than rock outside deformation zones (with the exception of vuggy rock which is characterised by very high diffusivities). The differences between the different rock types, however, are very small and it is not possible to discriminate between them statistically given the small sample sizes.

Three different alternative models of radionuclide transport have been considered in this report to study the impact of flow channelling for the transport of solutes representing a broad range of sorption properties from very poorly sorbing in the case of Sr(II) to very strongly sorbing in the case of the trivalent lanthanides or actinides. The base case model is a simple description of advective flow coupled with 1D matrix diffusion and sorption typically used in safety assessment calculations. The second model considers as an additional process, the diffusion of solutes into stagnant zones and subsequent uptake to the rock matrix. The third model assumes 2D radially symmetric matrix uptake from flow channels of very narrow width.

The estimated F-factors obtained from the flow related transport modelling were combined with sorption data from the retardation model to make predictions of typical solute transport times. It was found that when transport occurs in highly channelised flow within partially closed fractures containing regions of practically stagnant water, the diffusion of solute into stagnant zones followed by uptake to the rock matrix can give a considerably enhanced retardation effect compared to the base case model where this transport mechanism is not considered. In a similar fashion, when 2D radially symmetric matrix diffusion from narrow flow channels is considered, the retardation of solutes can be enhanced considerably over that predicted by the base case model.

A number of confirmatory tracer tests have been carried out at Forsmark with the aim of studying retention processes in situ. With regard to the transport properties site descriptive modelling, the main purpose of these tests was partial validation of the conceptual models of transport and material property data obtained from laboratory investigations using bore core samples. The results were found to be generally consistent with the conceptual models of solute transport used in safety assessment which consider a coupled sorptive-diffusive retention mechanism and strong retardation effects were also observed for sorbing solutes. While the retardation of sorbing solutes appears to be dominated by sorptive interaction with the rim zone of fracture surfaces, the diffusion mediated retardation of non-sorbing or poorly sorbing solutes seems to be more strongly influenced by what could be transverse diffusion between flow streamlines in variable aperture flow channels featuring tapered edges. Other experimental artefacts and processes, however, could give rise to similar effects during the tracer tests so this is only suggested as a speculative explanation for the apparently anomalous retention of uranine.

8 Nomenclature

This section contains explanations of the various variable names referred to in this report. Some variable names are used by more than sub-discipline in different contexts and therefore are defined multiple times in the following list as appropriate (i.e. with separate meanings referenced to different sections, or specific equations where first used in the report). More common variable names that are used consistently with the same meaning throughout the text, however, are not referenced to any specific section or equation.

a	(–)	Empirical parameter in transmissivity distribution function (Table 3-1).
a	(m)	Lower reference elevation for applied hydraulic gradient in (Figure 3-14).
a	(m)	Equivalent flow channel radius for 2D radially symmetric diffusion model (Equation 5-5).
a_i	(m)	Correlation length in variogram model (Figure H-1).
A	($s^{-½}$)	Matrix interaction parameter.
a'	(m)	Solute release elevation in deformation zone analytical model (Figure 3-14).
A_{BET}	(m^2/g)	Specific surface area measured using the BET method.
$A_{colloid}$	(m^2/g)	Specific surface area of colloidal material.
A_{EXT}	(m^2/g)	Specific external surface area of a crushed rock particle.
A_F	(m^2/m)	Flow-wetted surface per unit length of flow channel.
A_{INT}	(m^2/g)	Specific surface area of internal microsurfaces within the particle or rock matrix.
A_m	($s^{½}/m$)	Matrix interaction parameter.
a_R	(m^2/m^3)	Specific flow-wetted surface normalised with respect to rock volume.
a_t	($s^{½}$)	Proportionality constant in macroscopic quadratic equation relating transport aperture and transmissivity.
A_{xs}	(m^2)	Cross-sectional area of a stream tube.
A_0	(m^2/g)	Specific surface area of analogue mineral used to represent natural groundwater colloid.
b	(m)	Radial extent of limited rock matrix (Appendix I).
b	(–)	Empirical parameter in transmissivity distribution function (Table 3-1).
b	(m)	Upper reference elevation for applied hydraulic gradient (Figure 3-14).
b	(–)	Flow source “extent” in GRF flow equation (Appendix B).
b_x	(m)	Radial extent of stagnant zone formed by an incident fracture crossing a flow channel of narrow width.
c_i	(–)	Constant in variogram model (Figure H-9).
C	(m^2/s)	Flow channel conductance (Appendix A).
CDF	(–)	Cumulative distribution function.
C_f	(mol/m^3)	Solute concentration in an advective flow channel given as a function of position and time.
$\tilde{C}_f$	(mol/m^3)	Laplace transformed function describing solute concentration in an advective flow channel as a function of position and time.
C_{FF}	(m^{-1})	Conductive flowing fracture frequency.
C_{FIZ}	(m^2/s)	Conductance of fracture intersection zone, FIZ.

C_{ij}	(m^2/s)	Conductance of channel members in channel network model.
C_p	(–)	Correction factor for fracture set orientation.
C_{sc}	(mol/m^3)	Concentration of solute bound to colloidal particles).
C_0	(mol/m^3)	Assumed constant concentration of diffusing solute in advective flow channel.
D	(–)	Ratio of upper and lower transmissivity distribution bounds for deterministic deformation zone transmissivity, T_{max}/T_{min}.
D_a	(m^2/s)	Apparent diffusivity of rock matrix.
D_e	(m^2/s)	Effective diffusivity of rock matrix.
D_L	(m^2/s)	Longitudinal dispersivity.
d_p	(m)	Characteristic particle size of crushed rock.
D_p	(m^2/s)	Pore diffusivity of rock matrix.
D_w	(m^2/s)	Free diffusivity of solute at infinite dilution.
D_{Cl-}	(m^2/s)	Free diffusivity of chloride ion at infinite dilution in water.
D_{Na+}	(m^2/s)	Free diffusivity of sodium ion at infinite dilution in water.
D_{NaCl}	(m^2/s)	Free diffusivity of NaCl ion pair at infinite dilution in water.
F	(y/m)	F-factor.
f_c	(–)	Fracture asperity, surface area contact fraction.
F_{DFF_0}	(y/m)	F-factor for distant far field (DFF) flow paths under reference hydraulic gradient conditions.
F_f	(–)	Rock matrix formation factor.
F_f^*	(–)	"Apparent" rock matrix formation factor.
F_{IFF_0}	(y/m)	F-factor for immediate far field (IFF) flow paths under reference hydraulic gradient conditions.
F_{NNF_0}	(y/m)	F-factor for non-engineered near field (NNF) flow paths under reference hydraulic gradient conditions.
F_{PLTR}	(y/m)	F-factor for global path of least transport resistance.
F_{fs}	(–)	Formation factor of fracture coating (Appendix J).
F_{fm}	(–)	Formation factor of rock matrix (Appendix J).
f_s	(–)	Symmetry parameter for stagnant zone mass transfer (Equation 5-1).
FWS	(m^2)	Flow-wetted surface of flowpath.
fws_i	(m^2)	Flow-wetted surface of flowpath segment.
g_c	(m/s^2)	Acceleration due to gravity.
h	(m)	Distance parameter in semi-variogram (Figure H-9).
h_i	(m)	Hydraulic head (Figure C-1 and Figure D-9).
H	(m)	Hurst exponent.
h_a	(m)	Hydraulic head at lower deformation zone boundary.
h_b	(m)	Hydraulic head at upper deformation zone boundary.
h_w	(m)	Borehole drawdown (head).
h_0	(m)	Undisturbed head at the radius of influence of a borehole hydraulic test.
i	(m/m)	Hydraulic gradient.
I_i	(–)	Modified Bessel function of the first kind (order i).
i_0	(m/m)	Reference hydraulic gradient.
i_{NNF}	(m/m)	True hydraulic gradient for non-engineered near field (NNF).
i_{FFF}	(m/m)	True hydraulic gradient for immediate far field (IFF).

i_{DFF}	(m/m)	True hydraulic gradient for distant far field (DFF).
J_m	(mol/m²s)	Diffusive mass flux to rock matrix.
$\tilde{J}_m$	(–)	Laplace transformed diffusive mass flux into the rock matrix.
J_s	(mol/m²s)	Diffusive mass flux to stagnant zone.
$\tilde{J}_s$	(–)	Laplace transformed diffusive mass flux into the stagnant zone.
k	(–)	Deformation zone transmissivity model parameter.
k_+	(–)	Proportionality constant in Equation 3-11.
k	(–)	Proportionality constant in Equation L-10 (Archie's law).
K	(m/s)	Hydraulic conductivity of flow pipe in Hagen-Poiseuille relation (Equation F-3).
K_a	(m)	Surface area normalised sorption coefficient.
K_d	(m³/kg)	Linear equilibrium sorption coefficient.
$K_d^{colloid}$	(kg/m³)	Partitioning coefficient for pseudocolloid sorption.
K_d^0	(kg/m³)	Partitioning coefficient for sorption on colloid analogue mineral.
K_{dg}	(m³/kg)	Partitioning coefficient for sorption in fracture filling material.
K_{ds}	(m³/kg)	Partitioning coefficient for sorption in fracture coating.
K_{ds}^*	(m³/kg)	Volumetric capacity factor of the fracture coating (Equation J-7).
K_{dm}	(m³/kg)	Partitioning coefficient for sorption in rock matrix.
K_{dm}^*	(m³/kg)	Volumetric capacity factor of the rock matrix (Equation J-8).
K_f	(m/s)	Hydraulic conductivity of the flow system.
k_h	($m^{-1}s^{-1}$)	Proportionality constant in Hagen-Poiseuille relation for parallel plate flow (Equation F-1).
K_m	(m/s)	Mean hydraulic conductivity.
k_r	(–)	Shape parameter (exponent) in power-law distribution.
K_i	(–)	Modified Bessel function of the second kind (order i).
L	(m)	Length of deformation zone from lower to upper reference elevations.
L_{bh}	(m)	Length of tested borehole interval.
L_c	(m)	Flow channel length.
L_p	(m)	Path length.
L_p	(m)	Length of cylindrical tube in Hagen-Poiseuille relation (Equation F-1).
L_x	(m)	Correlation length with respect to principal axis (x-axis).
L_y	(m)	Correlation length with respect to secondary axis (y-axis).
L_z	(m)	Depth of channel network simulation volume (Appendix C, Equation C-2).
m	(–)	Deformation zone transmissivity model parameter.
m_c	(kg/m³)	Mass concentration of colloidal material in groundwater.
MPG_g	($m/s^{½}$)	Material properties group for gouge/breccia particles.
MPG_m	($m/s^{½}$)	Material properties group for the rock matrix.
n	(–)	Exponent in Equation 3-11.
n	(–)	Exponent in GRF flow equation (Equation B-5).
n	(–)	Number of parallel fractures in flow system.
n	(–)	Power law exponent in Equation L-10 (Archie's law).
P_{con}	(–)	Percolation probability.
Pe	(–)	Péclet number for longitudinal dispersivity.
Pe_w	(–)	Péclet number based upon flow channel width.
p_f	(–)	Final recovery fraction in tracer test.

p_m	(–)	Recursive Laplace-space function describing diffusion/sorption properties of multiple layer rock matrix.
$P_{10,PFL}$	(m^{-1})	Linear intensity of flowing features identified by PFL testing in a borehole.
P_{10cof}	(m^{-1})	Linear intensity of connected, open fractures identified along a borehole and corrected for orientation bias.
P_{10}^{DAS}	(m^{-1})	Linear intensity of stagnant open fractures.
P_{21}^{DAS}	(m/m^2)	Areal intensity of linear traces for intersection of diffusive fractures with an advective flow channel.
P_{32}	(m^2/m^3)	Volumetric areal intensity of fractures (equal to half the specific flow-wetted surface).
$P_{32target}$	(m^2/m^3)	Target volumetric areal intensity of fractures in Hydro-DFN realisations.
P_{32}^0	(m^2/m^3)	Volumetric areal intensity of fractures truncated to the size range, $r \geq r_0$.
Q	(m^3/s)	Flow.
Q_i	(m^3/s)	Flow (Figure D-9).
r	(m)	Fracture radius.
R_i	(m)	Resistance (Figure D-9).
R_a	(–)	Effective retardation coefficient for instantaneous equilibrium sorption within an advective flow channel.
r_{bh}	(m)	Borehole radius.
R_d	(m^3/kg)	Apparent partitioning ratio for radionuclide sorption.
R_F	(–)	Ratio of "apparent" and actual F-factor used to assess the impact of pseudocolloid sorption on radionuclide transport.
R_g	(m^2/m^2)	Ratio of gouge/breccia flow-wetted surface to "true" flow-wetted surface.
R_m	(–)	Effective pore diffusion retardation factor.
$R_n(0,1)$	(–)	Random normal deviate with zero mean and unit variance.
R_s	(m^2/m^2)	Ratio of mass transfer surface area for uptake to a stagnant zone relative to true flow-wetted surface of an advective flow channel.
r_{min}	(m)	Minimum fracture radius.
r_{max}	(m)	Maximum fracture radius.
r_0	(m)	Radius of influence of hydraulic test (Equation 3-24).
r_0	(m)	Location parameter in power-law distribution (Equation D-1).
R_0^1	(–)	Uniform random deviate in the interval [0,1].
s	(m)	Drawdown.
s	(–)	Laplace variable.
S	(–)	Storativity of the pipe.
S_s	(m^{-1})	Specific storage.
t	(y)	Time.
T	(m^2/s)	Transmissivity.
T	(K)	Groundwater temperature (Appendix L).
T_{eff}	(m^2/s)	Effective transmissivity of deformation zone.
T_f	(m^2/s)	Fracture or flow channel transmissivity.
T_h	(m^2/s)	Apparent transmissivity.
T_{max}	(m^2/s)	Maximum transmissivity trend curve for exponential decay model of deformation zone transmissivity vs. elevation.
T_{mean}	(m^2/s)	Mean transmissivity trend curve for exponential decay model of deformation zone transmissivity vs. elevation.

T_{min}	(m^2/s)	Minimum transmissivity trend curve for exponential decay model of deformation zone transmissivity vs. elevation.
T_s	(–)	Laplace space stagnant zone property parameter for in-plane flow channels.
T_{xs}	(–)	Laplace space stagnant zone property parameter for incident flow channels.
T_0	(m^2/s)	Transmissivity of uncompressed fracture.
T_0	(K)	Reference temperature (Appendix L).
t_{50}	(y)	Transport time corresponding to 50% recovery of transported solute.
t_{ref}	(y)	Reference transport time.
t_w	(y)	Advective travel time.
t_{xo}	(s)	Crossover time for transition from non-Gaussian to Gaussian asymptotic behaviour for Taylor-Aris dispersion.
u_w	(m/s)	Advective water velocity.
V	(m^3)	Volume of a flowpath.
V_{inj}	(m^3)	Total injected water volume in a SWIW test.
V_p	(m^3)	Volume of stream tube.
w_m	(–)	Recursive Laplace-space function describing diffusion/sorption properties of multiple layer rock matrix.
W_{bh}	(m)	Flowpath width (assumed same as borehole diameter).
W_c	(m)	Flow channel width.
x	(m)	Horizontal spatial coordinate (WE axis in hydrogeological model).
y	(m)	Horizontal spatial coordinate (NS axis in hydrogeological model).
I_i	(–)	Modified Bessel function of the first kind (order i).
Y_i	(–)	Bessel function of the second kind (order i).
z	(m)	Vertical spatial coordinate in numerical simulations (elevation above sea level in hydrogeological model according to the RHB 70 standard).
z_c	(m)	Elevation of the flow channel midpoint relative to the lower system boundary.
Z_i	(–)	Charge number of diffusing ion, i.

Greek symbols:

α	(–)	Exponent in Equation 3-16.
α	(–)	Ratio of flow resistances in the parallel branches of a bifurcating flowpath (Figure D-9).
α	(–)	Aspect ratio (i.e. ratio of minor and major axis lengths, used in Appendix B).
α	(m^2/s)	Hydraulic diffusivity (Equation F-7).
α	(–)	Storage capacity (Equation L-7).
α_{corr}	(–)	Correction factor for flow distortion in borehole dilution test.
α_L	(m)	Dispersion length.
α_n	(–)	Is the surface area of the unit hypersphere in n-dimensions.
β	(–)	Parameter in Equation B-8.
β_g	(m^3/m^3)	Relative void fraction of fracture occupied by particulate filling material.
β_p	(m^2/N)	Compressibility of fracture flow space.
β_w	(m^2/N)	Compressibility of water.
γ	(–)	Semivariance.
$\Gamma\left(\frac{n}{2}\right)$	(–)	Gamma function with argument n/2 used to calculate the area of a unit hypersphere in n dimensions.

δ	(–)	Rock matrix pore constrictivity.
δ_c	(m)	Diameter in Hagen-Poiseuille relation for a cylindrical pipe.
δ_f	(m)	Initial mean aperture of uncompressed fracture.
δ_{fs}	(m)	Thickness of fracture coating.
δ_h	(m)	Apparent hydraulic aperture of a fracture.
δ_s	(m)	Effective aperture of stagnant zone.
δ_t	(m)	Transport aperture of a fracture (also referred to as “mechanical aperture”).
$\overline{\delta}_t$	(m)	Mean transport aperture for a composite flowpath.
δ_{xs}	(m)	Mean transport aperture of incident stagnant fractures.
δ_0	(m)	“True” hydraulic aperture of a fracture.
Δh	(m)	Hydraulic potential difference.
ζ	(m)	Dummy length variable.
ζ	(–)	Transmissivity enhancement factor for flow in fracture intersection zone (FIZ).
ζ	(–)	Constant in Equation L-1.
η	(m)	Solute penetration depth.
$\overline{\eta}$	(m)	Mean solute penetration depth.
θ	(rad)	Deformation zone dip angle.
θ'	(rad)	Univariate Fisher distributed polar angle.
θ_f	(–)	Kinematic (or flow) porosity.
θ_g	(m^3/m^3)	Water saturation porosity of fracture filling material (gouge/breccia).
θ_m	(–)	Water saturation porosity of rock matrix.
θ_p	(–)	Transport porosity of rock matrix.
θ_s	(–)	Water saturation porosity of fracture coating.
κ	(–)	Dispersion parameter in univariate Fisher distribution.
κ_l	(–)	Constant in Equation 6-12.
κ_r	(S/m)	Electrical conductivity of brine saturated rock.
κ_s	(–)	Constant in Equation 6-14.
κ_w	(S/m)	Electrical conductivity brine pore water.
κ_{xo}	(–)	Constant in Equation 6-15.
λ	(m^2/m^2)	Mean surface roughness of crushed rock particles defined as the ratio of the external surface area of a crushed rock particle to that of a sphere containing the same mass of material (Equation 4-7).
λ	(s^{-1})	Radioactive decay constant (Equation I-4).
λ_y	(m)	Crossover dimension in y-direction.
λ_x	(m)	Crossover dimension in x-direction.
μ	(–)	Log_{10} mean transmissivity for HRD transmissivity distribution function.
μ_a	(–)	Log_{10} mean channelconductance at the lower system boundary.
μ_b	(–)	Log_{10} mean channel conductance at the upper system boundary.
μ_c	(–)	Log_{10} mean channel conductance at elevation of flow channel midpoint.
μ_{Ff}	(–)	Log_{10} mean of formation factor.
μ_F	(–)	Log_{10} mean of F-factor accumulated in the HCD.
μ_w	(Pa.s)	Viscosity of groundwater.
μ_θ	(–)	Log_{10} mean of rock matrix porosity.
ρ	(–)	Correlation coefficient in covariance matrix (Equation L-11).

ρ_{bg}	(kg/m^3)	Bulk density of fracture filling particulate material.
ρ_{bs}	(kg/m^3)	Bulk density of fracture coating.
ρ_{bm}	(kg/m^3)	Bulk density of the rock matrix.
ρ_w	(kg/m^3)	Density of groundwater (Equation F-2).
ρ_w	(Ω/m)	Electrical resistivity of brine pore water (Equation H-2).
ρ_r	(Ω/m)	Is the electrical resistivity of brine saturated rock.
σ	(–)	Log_{10} standard deviation for HRD transmissivity distribution function.
σ_c	(–)	Log_{10} standard deviation of flow channel conductance.
σ_f	(m)	Standard deviation of uncompressed fracture aperture distribution.
σ_{Ff}	(–)	Log_{10} standard deviation of formation factor.
σ_F	(–)	Log_{10} standard deviation of F-factor.
σ_g^2	(–)	Logarithmic (natural log) fracture aperture variance.
σ_p	(–)	Population standard deviation.
σ_T	(–)	Standard deviation of lateral variability in depth dependent deformation zone transmissivity distribution.
σ_x	(–)	Standard deviation of normally distributed random variable, R_1 (Equation L-11).
σ_y	(–)	Standard deviation of normally distributed random variable, R_2 (Equation L-11).
σ_θ	(–)	Log_{10} standard deviation of porosity.
τ	(–)	Dimensionless hydrodynamic dispersion parameter.
τ^2	(–)	Rock matrix pore tortuosity.
ϕ	(–)	"Shifted" Laplace space variable.
ϕ'	(rad)	Uniformly distributed azimuthal angle with respect to principal orientation vector.
ψ_m	(–)	Laplace-space, matrix flux parameter.
ψ_s	(–)	Laplace-space, stagnant zone linear flux parameter.
ψ_{xs}	(–)	Laplace-space, stagnant zone radial flux parameter.
ω	(–)	Laplace space parameter defined by Equation I-22.

9 References

Abelin H, Birgersson L, Widén H, Ågren T, Moreno L, Neretnieks I, 1990. Channeling experiment. Stripa Project, Technical Report 90-13, Svensk Kärnbränslehantering AB.

Abelin H, Birgersson L, Moreno L, Widén H, Ågren T, Neretnieks I, 1991. Large scale flow and tracer eperiment in granite. II. Results and interpretation. Water Resour. Res., 27(12), pp. 3119–3135.

Abelin H, Birgersson L, Moreno L, Widén H, Ågren T, Neretnieks I, 1994. Channeling experiments in crystalline fractured rocks. J. Cont. Hydrol., 15, pp. 129–158.

Ajdari A, Bontoux N, Stone H, 2006. Hydrodynamic dispersion in shallow microchannels: the effect of cross-sectional shape. Anal. Chem., 78, pp. 387–392.

Alexander W, Smith P, McKinley I, 2003. Modelling radionuclide transport in the geological environment: a case study from the field of radioactive waste disposal. Ch.5, pp. 109–146. In: E.M.Scott (Ed), Modelling Radioactivity in the Environment, Elsevier, Amsterdam, The Netherlands.

Anderson C, Pedersen K, Jakobsson A-M, 2006. Autoradiographic comparisons of radionuclide adsorption between subsurface anaerobic biofilms and granitic host rocks. Geomicrobiol. J., 41, pp. 830–836.

Anderson C, Jakobsson A-M, Pedersen K, 2007. Influence of in situ biofilm coverage on the radionuclide adsorption capacity of subsurface granite. Environ. Sci. Technol., 41, pp. 830–836.

Andersson J, Hermanson J, Elert M, Moreno L, Selroos J-O, 1998. Derivation and treatment of the flow-wetted surface and other geosphere parameters in the transport models FARF31 and COMP23 for use in safety assessment. SKB R-98-60, Svensk Kärnbränslehantering AB.

Aris R, 1956. On the dispersion of a solute in a fluid flowing through a tube. Proc. R. Soc. London. Series A, Mathematical and Physical Sciences. 235(1200), pp. 67–77.

Atkins P, 1999. Physical Chemistry, 6 ed. Oxford University Press.

Auradou H, Drazer G, Boschan A, Hulin J-P, Koplik J, 2006. Flow channelling in a single fracture induced by shear displacement. Geothermics, 35, pp. 576–588.

Axe L, Trivedi P, Anderson P, 2002. Diffusion at oxide and related surfaces. In: Encyclopedia of Surface and Colloid Science (A. Hubbard ed.), pp. 1447–1457, Marcel Dekker.

Barker J, 1988. A generalized radial flow model for hydraulic tests in fractured rock. Water Resour. Res., 24(10), pp. 1796–1804.

Becker M, Shapiro A, 2000. Tracer transport in fractured crystalline rock: Evidence of nondiffusive breakthrough tailing. Water Resour. Res., 36(7), pp. 1677–1686.

Becker M, Shapiro A, 2003. Interpreting tracer breakthrough tailing from different forced-gradient tracer experiment configurations in fractured bedrock. Water Resour. Res., 39(1), 1024, pp. 1–13.

Berglund S, Selroos J-O, 2003. Transport properties site descriptive model. Guidelines for evaluation and modelling. SKB R-03-09, Svensk Kärnbränslehantering AB.

Berkowitz B, Scher H, 1995. On characterization of anomalous dispersion in porous and fractured media. Water Resour. Res., 31(6), pp. 1461–1466.

Berkowitz B, Scher H, 2001. The role of probabilistic approaches to transport theory in heterogeneous media. Transport Porous Med., 42, pp. 241–263.

Berkowitz B, Kosakowski G, Margolin G, Scher H, 2001. Application of continuous time random walk theory to tracer test measurements in fractured and heterogeneous porous media. Ground Water, 39(4), pp. 593–604.

Berkowitz B, 2002. Characterizing flow and transport in fractured geological media: A review. Adv. Water. Resour., 25, pp. 861–884.

Bertetti F, Pabalan R, Turner D, Almedarez M, 1996. Neptunium(V) sorption behaviour on clinoptilolite, quartz and montmorillonite. In: Murphy W, Knecht D, (eds.), Scientific Basis for Nuclear Waste Management XIX, Mat. Res. Soc. Symp. Proc., 412, pp. 631–638.

Bertetti F, Pabalan R, Almedarez M, 1998. Neptunium(V) sorption behaviour on quartz, clinoptilolite, montmorillonite, and α-alumina. In: Jenne, ed., Adsorption of Metals by Geomedia – Variables, Mechanisms, and Model Applications, Academic Press, New York, pp. 131–148.

Bidaux P, Tsang C-F, 1991. Fluid Flow Patterns Around a Well Bore or an Underground Drift With Complex Skin Effects. Water Resour. Res., 27(11), pp. 2993–3008.

Bird R, Stewart W, Lightfoot E, 2002. Transport phenomena, 2 ed., Wiley, New York.

Birgersson L, Widén H, Ågren T, Neretnieks I, 1992. Stripa Project. Tracer migration experiments in the Stripa mine 1980–1991. SKB Stripa Project Report 92-25, Svensk Kärnbränslehantering AB.

Black J, Hodgkinson D, 2005. Äspö Task Force on modelling of groundwater flow and transport of solutes. Review of Task 6C. SKB R-05-33, Svensk Kärnbränslehantering AB.

Black J, Barker J, Woodman N, 2007. An investigation of 'sparse channel networks'. Characteristic behaviours and their causes. SKB R-07-35, Svensk Kärnbränslehantering AB.

Boadu F, 2000. Predicting the transport properties of fractured rocks from seismic information: numerical experiments. J. Appl. Geophys., 44, pp. 103–113.

Bonnet E, Bour O, Odling N, Davy P, Main I, Cowie P, Berkowitz B, 2001. Scaling of fracture systems in geological media. Rev. Geophys., 39(3), pp. 347–383.

Bouchaud E, 2003. The morphology of fracture surfaces: A tool for understanding crack propagation in complex materials. Surf. Rev. Lett., 10(5), pp. 797–814.

Brace W, Walsh J, Frangos W, 1968. Permeability of granite under high pressure. J. Geophys. Res., 73(6), pp. 2225–2236.

Bradbury M, Green A, 1986. Investigations into the factors influencing long range matrix diffusion rates and pore space accessibility at depth in granite. J. Hydrol., 89, pp. 123–139.

Bradbury M, Baeyens B, 1997. A mechanistic description of Ni and Zn sorption on Na-montmorillonite. Part II: modelling. J. Contam. Hydrol., 27, pp. 223–248.

Bradbury M, Baeyens B, 2005. Experimental measurements and modelling of sorption competeition on montmorillonite. Geochim. Cosmochim. Acta, 69(17), pp. 4187–4197.

Brantberger M, Zetterqvist A, Arnbjerg-Nielsen T, Olsson T, Outters N, Syrjänen P, 2006. Final repository for spent nuclear fuel Underground design Forsmark, Layout D1. SKB R-06-34, Svensk Kärnbränslehantering AB.

Brown S, Scholz C, 1985. Broad bandwidth study of the topography of natural rock surfaces. J. Geophys. Res., 90(B14), pp. 12,575–12,582.

Brown 1987. Fluid flow through rock joints: The effect of surface roughness. J. Geophys. Res., 92(B2), pp. 1337–1347.

Brown S, 1995. Simple mathematical model of a rough fracture. J. Geophys. Res., 100(B4), pp. 5941–5952.

Brown S, Stockman H, Reeves S, 1995. Applicability of the Reynolds equation for modeling fluid flow between rough surfaces. J. Geophys. Res. Lett., 22(18), pp. 2537–2540.

Bruines P, 2003. Laminar ground water flow through stochastic channel networks in rock. Ph.D. Thesis. ENAC School of Architecture, Civil and Environmental Engineering, École Polytechnique Fédérale de Lausanne, Switzerland.

Brunauer S, Emmet P, Teller E, 1938. Adsorption of gases in multimolecular layers. J. Am. Chem. Soc., 60, pp. 309–319.

Bryant S, Thompson K, 2001. Theory, modelling and experiment in reactive transport in porous media. Curr. Opin. Colloid Interface Sci., 6, pp. 217–222.

Byegård J, Larsson N-Å, 2004. Metodbeskrivning för batchsorptionmätning. SKB MD 540.002. Version 1.2, Svensk Kärnbränslehantering AB.

Byegård J, Selnert E, Tullborg E-L, 2008. Site descriptive modelling of transport properties. Retardation model Forsmark 2.3. SKB R-08-98, Svensk Kärnbränslehantering AB.

Börjesson S, Gustavsson E, 2005. Forsmark site investigation. Laboratory data from the site investigation programme for the transport properties of the rock. Data delivery for data freeze Forsmark 2.1. SKB P-05-109, Svensk Kärnbränslehantering AB.

Börner F, 2006. Complex conductivity measurements. In: Groundwater Geophysics (Kirsch ed.), pp. 119–153, Springer.

Caine J, Evans J, Forster C, 1996. Fault zone architecture and permeability structure. Geology, 24(11), pp. 1025–1028.

Carlsson A, Ohsson T, 1977. Water leakage in the Forsmark tunnel, Uppland, Sweden. Sveriges geologiska undersökning, Ser. C, No.734, Stockholm.

Carslaw H, Jaeger J, 1959. Conduction of heat in solids, 2ed. Oxford University Press.

Charbonneau A, Novakowski K, Ross N, 2006. The effect of a biofilm on solute diffusion in fractured porous media. J. Contam. Hydrol., 85, pp. 212–228.

Cheng H, Cvetkovic V, Selroos J-O, 2003. Hydrodynamic control of retention in heterogeneous rock fractures. Water Resour. Res., 39(5), pp. 1130–1139.

Comsol, 2005. FEMLAB v3.0, Multiphysics modelling. Comsol AB, Stockholm Sweden.

Contardi J, Turner D, Ahn T, 2001. Modeling colloid transport for performance assessment. J. Contam. Hydrol., 47, pp. 323–333.

Coppin F, Berger G, Bauer A, Castet S, Loubet M, 2002. Sorption of lanthanides on smectite and kaolinite. Chem. Geol., 182, pp. 57–68.

Coppin F, Castet S, Berger G, Loubet M, 2003. Microscopic reversibility of Sm and Yb sorption onto smectite and kaolinite: Experimental evidence. Geochim. Cosmochim. Acta, 67(14), pp. 2515–2527.

Cormen T, Leiserson C, Rivest R, Stein C, 2001. Introduction to Algorithms, 2ed. MIT Press and McGraw-Hill.

Cosgrove J, Standfors R, Röshoff K, 2006. Geological characteristics of deformation zones and a strategy for their detection in a repository. SKB R-06-39, Svensk Kärnbränslehantering AB.

Crank J, 1975. The mathematics of diffusion, 2 ed. Oxford University Press, Oxford, UK.

Crawford J, 2006. Modelling in support of bedrock transport property assessment. Preliminary site description. Laxemar subarea – version 1.2. SKB R-06-28, Svensk Kärnbränslehantering AB.

Crawford J, Neretnieks I, Malmström M, 2006. Data and uncertianty assessment for radionuclide K_d partitioning coefficients in granitic rock for use in SR-Can calculations. SKB R-06-75, Svensk Kärnbränslehantering AB.

Cvetkovic V, Selroos J-O, Cheng H, 1999. Transport of reactive tracers in rock fractures. J. Fluid Mech., 378, pp. 335–356.

Cvetkovic V, Painter S, Outters N, Selroos J-O, 2004. Stochastic simulation of radionuclide migration in discretely fractured rock near the Äspö Hard Rock Laboratory. Water Resour. Res., 40 (W02404), pp. 1–14.

Cvetkovic V, Cheng H, Widestrand H, Byegård J, Winberg A, Andersson P, 2007. Sorbing tracer experiments in a crystalline rock fracture at Äspö (Sweden): 2 Transport model and effective parameter estimation. Water. Resour. Res., 43 (W11421), pp. 1–16.

Cvetkovic V, Cheng H, 2008. Sorbing tracer experiments in a crystalline rock fracture at Äspö (Sweden): 3. Effect of microscale heterogeneity. Water Resour. Res., in press (doi:10.1029/2007WR006797).

Cvetkovic et al. (in prep.). Transport and retention from single to multiple fractures in crystalline rock at Äspö (Sweden): 2. Fracture network flow simulations and global retention properties.

Darcel C, Davy P, Bour O, De Dreuzy J-R, 2006. Discrete fracture network for the Forsmark site. SKB R-06-75, Svensk Kärnbränslehantering AB.

De Hoog F, Knight F, Stokes A, 1982. An improved method for numerical inversion of Laplace transforms, SIAM J. Sci. Stat. Comput., 3, pp. 357–366.

de Marsily G, 1986. Quantitative Hydrogeology: Groundwater Hydrology for Engineers, Academic Press, Inc., Orlando Florida.

Degueldre C, Ulrich H, Silby H, 1994. Sorption of Am-241 onto Montmorillonite, Illite and Hematite Colloids. Radiochim. Acta, 65, pp. 173–179.

Dershowitz W, Klise K, 2002. Äspö Hard Rock Laboratory. TRUE Block Scale project. Evaluation of fracture network transport pathways and processes using the Channel Network approach. SKB IPR-02-34, Svensk Kärnbränslehantering AB.

Dershowitz W, Lee G, Foxford T, 2004a. FracWorks XP Discrete Fracture Modeling Software, User Documentation. Golder Associates, Redmond, WA.

Dershowitz B, Shuttle D, Klise K, Outters N, Hermanson J, 2004b. Transverse dispersion in heterogeneous fractures. SKB R-04-52, Svensk Kärnbränslehantering AB.

Drazer G, Koplik J, 2000. Permeability of self-affine rough fractures. Phys. Rev. E., 62(6), pp. 8076–8085.

Drazer G, Koplik J, 2002. Transport in rough self-affine fractures. Phys. Rev. E., 66(026303), pp. 1–9.

Dutta D, Ramachandran A, Leighton D, 2006. Effect of channel geometry on solute dispersion in pressure-driven microfluidics systems. Microfluidics and Nanofluidics, 2, pp. 275–290.

EPA, 2002. A lexicon of cave and karst terminology with special reference to environmental karst hydrology. EPA/600/R-02/003, US Environmental Protection Agency, Office of Research and Development, Washington DC.

Essén S, Johnsson A, Bylund D, Pedersen K, Lundström U, 2007. Siderophore production by Pseudomonas stutzeri under anaerobic conditions. Appl. Environ. Microbiol., 73(18), pp. 5857–5864.

Fisher R, 1953. Dispersion on a sphere. Proc. Roy. Soc. London Ser. A., 217, pp. 295–305.

Follin S, Ludvigson J-E, Levén J, 2006a. A comparison between standard well test evaluation methods used in SKB's site investigations and the Generalised Radial Flow concept. SKB P-06-54, Svensk Kärnbränslehantering AB.

Follin S, Stigsson M, Svensson U, 2006b. Hydrogeological DFN modelling using structural and hydraulic data from KLX04. Preliminary site description Laxemar subarea – version 1.2. SKB R-06-24, Svensk Kärnbränslehantering AB.

Follin S, Levén J, Hartley L, Jackson P, Joyce S, Roberts D, Swift B, 2007a. Hydrogeological characterisation and modelling of deformation zones and fracture domains, Forsmark modelling stage 2.2. SKB R-07-48, Svensk Kärnbränslehantering AB.

Follin S, Johansson P-O, Hartley L, Jackson P, Roberts D, Marsic N, 2007b. Regional hydrogeological modelling for Forsmark stage 2.2: Conceptual model development and numerical modelling using CONNECTFLOW. SKB R-07-49, Svensk Kärnbränslehantering AB.

Follin S, Hartley L, Joyce S, Marsic N, 2008. Regional hydrogeological modelling for Forsmark stage 2.3: Conceptual model development and numerical modelling using CONNECTFLOW. SKB R-08-23, Svensk Kärnbränslehantering AB.

Fox A, La Pointe P, Hermanson J, Öhman J, 2007. Site descriptive modeling Forsmark, stage 2.2. Statistical geological discrete fracture network model for the Forsmark site, version 2.2. SKB R-07-46, Svensk Kärnbränslehantering AB.

Ge S, 1997. A governing equation for fluid flow in rough fractures. Water Resour. Res., 33(1), pp. 53–61.

Geier J, Axesson C, Hässler L, Benabderrahmane A, 1992. Discrete fracture modelling of the Finnsjön rock mass, Phase 2. SKB TR-92-07. Svensk Kärnbränslehantering AB.

Gelhar L, Collins M, 1971. General analysis of longitudinal dispersion in non-uniform flow. Water Resour. Res., **7**(6), pp. 1511–1521.

Gelhar L, Welty C, Rehfeldt K, 1992. A critical review of data on field-scale dispersion in aquifers. Water Resour. Res., 28(7), pp. 1955–1974.

Gelhar L, 1993. Stochastic subsurface hydrology. Academic Press, 385 pp.

Gimeno M, Auqué L, Gómez J, Acero P, 2008. Water-rock interaction modelling and uncertainties of mixing modelling. SKB R-08-86, Svensk Kärnbränslehantering AB.

Glamheden R, Fredriksson A, Persson L, Röshoff K, Karlsson J, Bohlin H, Lindberg U, Hakami H, Hakami E, Johansson M, 2007. Rock mechanics. Site descriptive modeling. Forsmark stage 2.2. SKB R-07-31, Svensk Kärnbränslehantering AB.

Gleich D, 2006. Matlab BGL v2.0 (users guide). Stanford University, Institute for Computational and Mathematical Engineering.

Glover P, Matsuki K, Hikima R, Hayashi K, 1998a. Synthetic rough fractures in rocks. J. Geophys. Res., 103(B5), pp. 9609–9620.

Glover P, Matsuki K, Hikima R, Hayashi K, 1998b. Fluid flow in synthetic rough fractures and application to the Hachimantai geothermal hot dry rock test site. J. Geophys. Res., 103(B5), pp. 9621–9635.

Gokall-Norman K, Svensson T, Ludvigson J-E, 2005. Forsmark site investigation. Single-hole injection tests in borehole KFM07A. SKB P-05-133, Svensk Kärnbränslehantering AB.

Gokall-Norman K, Ludvigson J-E, 2007. Forsmark site investigation. Hydraulic interference test in borehole HFM14. SKB P-06-196, Svensk Kärnbränslehantering AB.

Guimera J, Carrera J, 2000. A comparison of hydraulic and transport parameters measured in low-permeability fractured media. J. Cont. Hydrol., 41(3-4), pp. 261–281.

Gurban I, 2008. Forsmark Site: M3 modelling and 2D visualisation of the hydrochemical parameters in Forsmark groundwater data 2.2 and 2.3. In: B. Kalinowski (ed), 2008, SKB R-08-87, Svensk Kärnbränslehantering AB.

Gustafson G, Franson Å, 2005. The use of the Pareto distribution for fracture transmissivity assessment. Hydrol. J., 14, pp 15–20.

Gustafsson E, Nordqvist R, Thur P, 2005. Forsmark site investigation. Groundwater flow measurements in boreholes KFM01A, KFM02A, KFM03A, KFM03B and SWIW tests in KFM02A, KFM03A. SKB P-05-77, Svensk Kärnbränslehantering AB.

Gustafsson E, Nordqvist R, Thur P, 2006a. Forsmark site investigation. Groundwater flow measurements and SWIW test in borehole KFM08A. SKB P-06-90, Svensk Kärnbränslehantering AB.

Gustafsson E, Nordqvist R, Thur P, 2006b. Forsmark site investigation. Groundwater flow measurements and SWIW test in borehole KFM04A. SKB P-06-141, Svensk Kärnbränslehantering AB.

Gylling B, 1997. Development and applications of the channel network model for simulations of flow and solute transport in fractured rock. Ph.D. Thesis. Dept. of Chemical Engineering and Technology, Royal Institute of Technology (KTH), Stockholm.

Haggerty R, Gorelick S, 1995. Multiple-rate mass transfer for modelling diffusion and surface reactions in media with pore-scale heterogeneity. Water Resour. Res., 31(10), pp. 2383–2400.

Hakami E, Larsson E, 1996. Aperture measurements and flow experiments on a single natural fracture. Int. J. Rock Mech. Min. Sci. & Geomech. Abstr., 33(4), pp. 395–404.

Hallbeck L, Pedersen K, 2008. Explorative analysis of microbes, colloids and gases. SKB R-08-85, Svensk Kärnbränslehantering AB.

Hedin A, 2005. An analytic method for estimating the probability of canister/fracture intersections in a KBS-3 repository. SKB R-05-29, Svensk Kärnbränslehantering AB.

Hjerne C, Ludvigsson J-E, Harrström J, 2008. The impact of interpreted flow regimes during constant head injection tests on the estimated transmissivity from injection tests and difference flow logging. SKB R-08-XX, Svensk Kärnbränslehantering AB.

Hollenbeck K, 1998. INVLAP.M: A matlab function for numerical inversion of Laplace transforms by the de Hoog algorithm. The Mathworks Inc., Mathtools Online Link Exchange for the Technical Computing Community (http://www.mathtools.net/).

IUPAC, 1997. Compendium of Chemical Terminology, 2nd ed. (the "Gold Book"). Compiled by A. D. McNaught and A.Wilkinson. Blackwell Scientific Publications, Oxford.

Jacobsson L, 2007. Forsmark site investigation. Boreholes KFM01A and KFM02B. Microcrack volume measurements and triaxial compression tests on intact rock. SKB P-07-93, Svensk Kärnbränslehantering AB.

Jakobsson A-M, 1999. Measurement and modelling using surface complexation of cation (II to IV) sorption onto mineral oxides. Ph.D. Thesis, Chalmers University of Technology, Dept. of Nuclear Chemistry, Gothenburg, Sweden.

Johns R, Roberts P, 1991. A solute transport model for channelized flow in a fracture. Water Resour. Res., 27(8), pp. 1797–1808.

Johnsson A, Arlinger J, Pedersen K, Ödegaard-Jensen A, Albinsson Y, 2006. Solid-aqueous phase partitioning of radionuclides by complexing compounds excreted by subsurface bacteria. Geomicrobiol. J., 23, pp. 621–630.

Keller A, 1997. High resolution CAT imaging of fractures in consolidated materials. Int. J. Rock Mech. & Min. Sci., 34(3-4), pp. 358–375.

Kesten H, 1980. The critical probability of bond percolation on the square lattice equals ½. Comm. Math. Phys., 74(1), pp. 41–59.

Kirkpatrick S, 1973. Percolation and conduction, Rev. Mod. Phys., 45, pp. 574–588.

Konzuk J, Kueper B, 2004. Evaluation of cubic law based models describing single-phase flow through a rough-walled fracture. Water Resour. Res., 40(W02402), pp. 1–17.

Kosakowsi G, Berkowitz B, 1999. Flow pattern variability in natural fracture intersections. Geophys. Res. Lett., 26(12), pp. 1765–1768.

Koyama T, 2007. Stress, Flow and Particle Transport in Rock Fractures. Ph.D. Thesis. Dept. Land and Water Resource Engineering, Royal Institute of Technology, Stockholm, Sweden.

Koyama T, Neretnieks I, Jing L, 2008. A numerical study on the differences in using Navier-Stokes and Reynolds equations for modeling the fluid flow and particle transport in single rock fractures with shear. Int. J. Rock Mech. Min. Sci., 45(7), pp. 1082–1101.

Laaksoharju M, Smellie J, Tullborg E-L, Gimeno M, 2008. Hydrogeochemistry Forsmark, Site descriptive modelling. SDM-Site Forsmark. SKB R-08-47, Svensk Kärnbränslehantering AB.

Lage J, Antohe B, 2000. Darcy's experiments and the deviation to non-linear flow regime. J. Fluids Eng., 122, pp. 619–625.

Langmuir D, 1997. Aqueous Environmental Geochemistry, Prentice Hall, New Jersey.

Lauga E, Stroock A, Stone H, 2004. Three-dimensional flows in slowly varying planar geometries. Phys. Fluids. 16(8), pp. 3051–3062.

Li Y-H, Gregory S, 1974. Diffusion of ions in sea water and in deep-sea sediments. Geochim. Cosmochim. Acta., 38, pp. 703–714.

Lichtner P, 1996. Continuum formulation of multicomponent-multiphase reactive transport. In: Lichtner P, Steefel C, Oelkers (eds.), Reactive transport in porous media. Reviews in Mineralogy, Vol. 34, pp. 1–79. Mineralogical Society of America.

Liedberg L, 2006. Forsmark site investigation. Borehole KFM01A, KFM01C, KFM01D, KFM04A, KFM05A, and KFM06A. Determination of porosity by water saturation and density by buoyancy technique. SKB P-06-234, Svensk Kärnbränslehantering AB.

Lindquist A, Hjerne C, Nordqvist R, Byegård J, Walger E, Ludvigson J-E, Wass E, 2008a. Forsmark site investigation. Confirmatory hydraulic interference test and tracer test at drill site 2. SKB P-08-13, Svensk Kärnbränslehantering AB.

Lindquist A, Hjerne C, Nordqvist R, Wass E, 2008b. Forsmark site investigation. Large-scale confirmatory multiple-hole tracer test. SKB P-08-59, Svensk Kärnbränslehantering AB.

Liu L, Neretnieks I, 2005. Analysis of fluid flow and solute transport in a fracture intersecting a canister with variable aperture fractures and arbitrary intersection angles. Nucl. Technol., 150, pp. 132–150.

Liu L, Neretnieks I, 2006. Analysis of fluid flow and solute transport through a single fracture with variable apertures intersecting a canister: Comparison between fractal and Gaussian fractures. Phys. Chem. Earth., 31, pp. 634–639.

Lu N, Triay I, Cotter C, Kitten H, Bentley J, 1998. Reversibility of sorption of plutonium-239 onto colloids of hematite, goethite, smectite, and silica. A milestone final report of YMP. LA-UR-98-3057, LANL Los Alamos National Laboratory.

Löfgren M, 2001. Formation factor logging in igneous rock by electrical methods. Licentiate Thesis. Dept. of Chemical Engineering and Technology, Royal Institute of Technology (KTH), Stockholm.

Löfgren M, Neretnieks I, 2002. Formation factor logging *in situ* by electrical methods. Background and methodology. SKB TR-02-27, Svensk Kärnbränslehantering AB.

Löfgren M, Neretnieks I, 2003. Formation factor logging by electrical methods. Comparison of formation factor logs obtained *in situ* and in the laboratory. J. Contam. Hydrol., 61, pp. 107–115.

Löfgren M, 2004. Diffusive properties of granitic rock as measured by *in situ* electrical methods. Ph.D. Thesis. Dept. Chemical Enginerring and Technology, Royal Institute of Technology, Stockholm, Sweden.

Löfgren M, Neretnieks I, 2005. Forsmark site investigation. Formation factor logging by in situ electrical methods in KFM01A and KFM02A. SKB P-05-29, Svensk Kärnbränslehantering AB.

Löfgren M, Neretnieks I, 2006. Through-electromigration: A new method of investigating pore connectivity and obtaining formation factors. J. Cont. Hydrol., 87, pp. 273–252.

Löfgren M, 2007. Forsmark site investigation. Formation factor logging by *in situ* electrical methods in KFM01D and KFM08C. SKB P-07-138, Svensk Kärnbränslehantering AB.

Löfgren M, Crawford J, Elert M, 2007. Tracer tests – possibilities and limitations. Experience from SKB fieldwork: 1977–2007. SKB R-07-39, Svensk Kärnbränslehantering AB.

Löfgren M, Sidborn M, 2008. Statistical analysis of results from the quantitative mapping of fracture minerals in Forsmark. Site descriptive modelling –complemenetary studies. SKB R-08-XX, Svensk Kärnbränslehantering AB.

Marcotte D, 1996. Fast variogram computation with FFT. Comput. Geosci., 22(10), pp. 1175–1186.

Mathworks, 2005. Matlab & Simulink (Release 14, SP3). The Mathworks Inc.

Mazurek M, Jakob A, Bossart P, 2003. Solute transport in crystalline rocks at Aspö – I: geological basis and model calibration. J. Contam. Hydrol., 61(1-4), pp. 157–174.

McKinley I, Scholtis A, 1993. A comparison of radionuclide sorption databases used in recent performance assessments. J. Contam. Hydrol., 13(1-4), pp. 347–363.

Miller I, Lee G, Dershowitz W, 2002. MAFIC matrix/fracture interaction code with heat and solute transport. User Documentation, Version 1.6, Golder Associates Inc., Redmond, WA.

Missana T, García-Gutiérrez M, Alonso Ú, 2004. Kinetics and irreversibility of cesium and uranium sorption onto bentonite colloids in a deep granitic environment. Appl. Clay Sci., 26, pp. 137–150.

Moreno L, Neretnieks I, 1983. Evaluation of some tracer tests in the granitic rock at Finnsjön. SKBF-KBS Technical Report 83-38, Svensk Kärnbränslehantering AB.

Moreno L, Tsang Y, Tsang C-F, Hale F, Neretnieks I, 1988. Flow and tracer transport in a single fracture: a stochastic model and its relation to some field observations. Water Resour. Res., 24(12), pp. 2033–2048.

Moreno L, Neretnieks I, 1993. Fluid flow and solute transport in a network of fractures, J. Contam. Hydrol., 14(3-4), pp. 163–192.

Moreno L, Gylling B, Neretnieks I, 1997. Solute transport in fractured media – the important mechanisms for performance assessment. J. Contam. Hydrol., 25, pp. 283–298.

Mourzenko V, Thovert J, Adler P, 1995. Permeability of a single fracture; validity of the Reynolds equation. J. Phys. II France, 5(3), pp. 465–482.

Mourzenko V, Thovert J, Adler P, 2004. Macroscopic permeability of three-dimensional fracture networks with a power-law size distribution. Phys. Rev. E., 69(6), pp. 1–13.

Mourzenko V, Thovert J, Adler P, 2005. Percolation of three-dimensional fracture networks with power-law size distribution. Phys. Rev. E., 72(3), pp. 1–14.

Munier R, Stenberg L, Stanfors R, Milnes A-G, Hermanson J, Triumf C-A, 2003. Geological Site Descriptive Model. A strategy for the model development during site investigations. SKB R-03-07, Svensk Kärnbränslehantering AB.

Munier R, 2004. Statistical analysis of fracture data, adapted for modelling Discrete Fracture Networks-Version 2. SKB R-04-66, Svensk Kärnbränslehantering AB.

Munier R, Hökmark H, 2004. Respect distances. Rationale and means of computation. SKB R-04-17, Svensk Kärnbränslehantering AB.

Möri A, Mazurek M, Adler M, Schild M, Siegesmund S, Vollbrecht A, Ota K, Ando T, Alexander W, Smith P, Haag P, Bühler Ch, 2003. Grimsel Test Site Investigation Phase IV (1994–1996): The Nagra-JNC in situ study of safety relevant radionuclide retardation in fractured crystalline rock IV: The in situ study of matrix porosity in the vicinity of a water conducting fracture. Nagra Technical Report NTB 00-08. Nagra, Wettingen.

NEA, 1999. Confidence in models of radionuclide transport for site-specific assessment, Workshop Proceedings, Carlsbad, New Mexico, USA, 14–17 June, 1999. OECD-NEA Radioactive Waste Management, GEOTRAP Project.

Neretnieks I, 1980. Diffusion in the rock matrix: An important factor in radionuclide retardation. J. Geophys. Res., 85(8), pp. 4397–4379.

Neretnieks I, 1983. A note on fracture flow dispersion mechanisms in the ground. Water Resour. Res., 19(2), pp. 364–370.

Neretnieks I, 1993. Solute transport in fractured rock – applications to radionuclide waste repositories. In: Flow and Contaminant Transport in Fractured Rock, Bear, Tsang and Marsily (eds.), Academic Press Inc., San Diego.

Neretnieks I, 1994. Nuclear waste repositories in crystalline rock – An overview of nuclide transport mechanisms. In: Proc. XVIIIth Int. Symp. on the Scientific Basis for Nuclear Waste Management, pp. 24–26. Mat. Res. Soc., Kyoto, Japan.

Neretnieks I, 2002. A stochastic multi-channel model for solute transport – analysis of tracer tests in fractured rock. J. Cont. Hydrol., 55, pp. 175–211.

Neretnieks I, Moreno L, 2003. Prediction of some in situ tracer tests with sorbing tracers using independent data. J. Cont. Hydrol., 61, pp. 351–360.

Neretnieks I, 2004. Predicting solute transport in fractured rocks-processes, models and some concerns. In: Coupled Thermo-Hydro-Mechanical-Chemical Processes in Geo-Systems – Fundamentals, Modelling, Experiments and Applications. Elsevier Geo-Engineering Book Series, Vol. 2, pp. 19–30.

Neretnieks I, 2006a. Channeling with diffusion into stagnant water and into a matrix in series. Water Resour. Res., 42(W11418), pp. 1–15.

Neretnieks I, 2006b. Fast method for simulation of radionuclide chain migration in dual porosity fracture rocks. J. Cont. Hydrol., 88, pp. 269–288.

Neretnieks I, 2007. Single well injection withdrawal tests (SWIW) in fractured rock. Some aspects on interpretation. SKB R-07-54, Svensk Kärnbränslehantering AB.

Neuman S, 1995. On advective transport in fractal permeability and velocity fields. Water Resour. Res., 31(6), pp. 1455–1460.

Neuman S, 2005. Trends, prospects and challenges in quantifying flow and transport through fractured rocks. Hydrogeol. J., 13, pp. 124–147.

Nielsen U, Ringgaard J, 2003. Geophysical borehole logging in borehole KFM01A, HFM01 and HFM02. SKB P-03-103, Svensk Kärnbränslehantering AB.

Nolte D, Pyrak-Nolte L, Cook N, 1989. The fractal geometry of flow paths in natural fractures in rock and the approach to percolation. Pure Appl. Geophys., 131(1-2), pp. 111–138.

Nordgulen Ø, Saintot A, 2006. Forsmark site investigation. The character and kinematics of deformation zones (ductile shear zones, fault zones and fracture zones) at Forsmark – report from phase 1. SKB P-06-212, Svensk Kärnbränslehantering AB.

Nordqvist A, Tsang Y, Tsang C-F, Dverstorp B, Andersson J, 1992. A variable aperture fracture network model for flow and transport in fractured rocks. Water Resour. Res., 28(6), pp. 1703–1713.

Nordqvist R, Gustafsson E, 2002. Single-well injection-withdrawal tests (SWIW). Literature review and scoping calculations for homogeneous crystalline bedrock conditions. SKB R-02-34, Svensk Kärnbränslehantering AB.

Nordqvist R, Gustafsson E, 2004. Single-well injection-withdrawal tests (SWIW). Investigation of evaluation aspects under heterogeneous crystalline bedrock conditions. SKB R-04-57, Svensk Kärnbränslehantering AB.

Nordqvist R, 2008. Evaluation and modelling of SWIW tests performed within the SKB site characterisation programme. SKB R-08-104, Svensk Kärnbränslehantering AB.

Nordqvist R, Gustafsson E, Andersson P, Thur P, 2008. Groundwater flow and hydraulic gradients in fractures and fracture zones at Forsmark and Oskarshamn. SKB R-08-103, Svensk Kärnbränslehantering AB.

Nover G, 2005. Electrical properties of crustal and mantle rocks – a review of laboratory measurements and their explanation. Surv. Geophys., 26, pp. 593–651.

NRC, 1996. Rock fractures and fluid flow. Contemporary understanding and applications. Committee on Fracture Characterization and Fluid Flow, National Research Council, National Academy Press, Washington DC.

Oda M, 1985. Permeability tensor for discontinuous rock masses, Geothechnique, 35(4), pp. 483–495.

Ogilvie S, Isakov E, Glover P, 2006. Fluid flow through rough fractures in rocks. II: A new matching model for rough rock fractures. Earth Planet. Sc. Lett., 241, pp. 454–465.

Ohlsson Y, Neretnieks I, 1995. Literature survey of matrix diffusion theory and of experiments and data including natural analogues. SKB TR-95-12, Svensk Kärnbränslehantering AB.

Ohlsson Y, Neretnieks I, 1998. Some evidence for surface ion mobility in rock. J. Contam. Hydrol., 35, pp. 91–100.

Ohlsson Y, 2000. Studies of ionic diffusion in crystalline rock. Ph.D. Thesis. Dept. Chemical Enginerring and Technology, Royal Institute of Technology, Stockholm, Sweden.

Olin M, Valkiainen M, Aalto H, 1997. Martix diffusion in crystalline rocks: coupling of anion exclusion, surface diffusion and surface complexation. Posiva 96-25. Posiva OY, Finland. ISBN 951-652-024-3.

Olofsson I, Simeonov A, Stephens M, Follin S, Nilsson A-C, Röshoff K, Lindberg U, Lanaro F, Fredriksson A, Persson L, 2007. Site descriptive modelling Forsmark, stage 2.2: Presentation of a fracture domain concept as a basis for the statistical modelling of fractures and minor deformation zones, and interdisciplinary coordination. SKB R-07-15, Svensk Kärnbränslehantering AB.

Oron A, Berkowitz B, 1998. Flow in rock fractures: The local cubic law assumption reexamined. Water Resour. Res., 34(11), pp. 2811–2825.

Outters N, Shuttle D, 2000. Sensitivity analysis of a discrete fracture network model for performance assessment of Aberg. SKB R-00-48, Svensk Kärnbränslehantering AB.

Outters N, 2003. A generic study of discrete fracture network transport properties using FracMan/MAFIC. SKB R-03-13, Svensk Kärnbränslehantering AB.

Pabalan R, Turner D, Bertetti F, Prikryl J, 1998. Uranium(VI) Sorption onto Selected Mineral Surfaces – Key Geochemical Parameters. In: Jenne, ed., Adsorption of Metals by Geomedia – Variables, Mechanisms, and Model Applications, Academic Press, New York, pp. 100–128.

Painter S, Cvetkovic V, 2005. Upscaling discrete fracture network simulations: An alternative to continuum transport models. Water Resour. Res., 41(W02002), pp. 1–10.

Painter S, 2006. Effect of singe-fracture aperture variability on field-scale transport. SKB R-06-25, Svensk Kärnbränslehantering AB.

Park Y-J, Lee K-K, Kosakowski G, Berkowitz B, 2003. Transport behaviour in three-dimensional fracture intersections. Water Resour. Res., 39(8), pp. 1215–1224.

Parkhomenko E, 1967. Electrical properties of rocks. Plenum Press.

Pedersen K, Karlsson F, 1995. Investigations of subterranean microorganisms. Their importance for performance assessment of radioactive waste disposal. SKB TR-95-10, Svensk Kärnbränslehantering AB.

Penttinen L, Siitari-Kauppi M, Ikonen J, 2006. Forsmark Site Investigation. Determination of porosity and micro fracturing using the 14C-PMMA technique in samples taken from Forsmark area. SKB P-06-60, Svensk Kärnbränslehantering AB.

Peyré G, 2004. Matlab tips and tricks (A list of useful tips and tricks with concise piece of code and comments). The Mathworks Inc., White Papers and Articles on-line archive, http://www.mathworks.com/.

Polak A, Elsworth D, Liu J, Grader A, 2004. Spontaneous switching of permeability changes in a limestone fracture with net dissolution. Water Resour. Res., 40(W03502), pp. 1–10.

Poteri A, Billaux D, Cvetkovic V, Dershowitz B, Gómez-Hernández J-J, Hautojärvi A, Holton D, Medina A, Winberg A, 2002. TRUE Block Scale Project. Final Report – 3. Modelling of flow and transport. SKB TR-02-15, Svensk Kärnbränslehantering AB.

Power W, Tullis T, 1991. Euclidean and fractal models for the description of rock surface roughness. J. Geophys. Res., 96(B1), pp. 415–424.

Power W, Tullis T, 1992. The contact between opposing fault surfaces at Dixie valley, Nevada and implications for fault mechanics. J. Geophys. Res., 97(B11), pp. 15,425–15,435.

Prikryl J, Jain A, Turner D, Pabalan R, 2001. Uranium(VI) sorption behaviour on silicate mineral mixtures, J. Contam. Hydrol., 47, pp. 241–253.

Rabung T, Pierret M, Bauer A, Geckeis H, Bradbury M, Baeyens B, 2005. Sorption of Eu(III)/Cm(III) on Ca-montmorillonite and Na-illite. Part 1: Batch sorption and time resolved laser fluorescence spectroscopy experiments. Geochim. Cosmochim. Acta, 69(23), pp. 5393–5402.

Rasmuson A, Neretnieks I, 1986. Radionuclide transport in fast channels in crystalline rock, Water Resour. Res., 22(8), pp. 1247–1256.

RETROCK, 2004. RETROCK Project: Treatment of geosphere retention phenomena in safety assessments: Scientific basis of retention processes and their implementation in safety assessment models (WP2). SKB R-04-48, Svensk Kärnbränslehantering AB.

Revil A, Glover P, 1997. Theory of ionic-surface electrical conduction in porous media. Phys. Rev. B., 55(3), pp. 1757–1773.

Rhén I, Follin S, Hermanson J, 2003. Hydrological Site Descriptive Model – a strategy for its development during Site Investigations. SKB R-03-08, Svensk Kärnbränslehantering AB.

Robinson P, 1984. Connectivity, flow and transport in network models of fractured media. Ph.D. Thesis, St Catherine's College, Oxford University, Ref TP 1072.

Rouhiainen P, Pöllänen J, 2003. Forsmark site investigation. Difference flow logging of borehole KFM01A. SKB P-03-28, Svensk Kärnbränslehantering AB.

Rouhiainen P, Sokolnicki M, 2005. Difference flow logging in borehole KFM06A. SKB P-05-15, Svensk Kärnbränslehantering AB.

Ruffet C, Darot M, Guéguen Y, 1993. Surface conductivity in rocks: A review. Surv. Geophys., 16, pp. 83–105.

Sahimi M, 1998. Non-linear and non-local transport processes in heterogeneous media: from long-range correlated percolation to fracture and materials breakdown. Phys. Rep., 306. pp. 213–395.

Sandström B, Tullborg E-L, 2006. Fracture mineralogy. Results from KFM06B, KFM06C, KFM07A, KFM08A, KFM08B. Forsmark site investigation. SKB P-06-226, Svensk Kärnbränslehantering AB.

Sandström B, Tullborg E-L, Smellie J, MacKenzie A, Suksi J, 2008. Fracture mineralogy of the Forsmark site. SDM-Site Forsmark. SKB R-08-102, Svensk Kärnbränslehantering AB.

Sawada A, Uchida M, Shimo M, Yamamoto H, Takahara H, Doe T, 2000. Non-sorbing tracer migration experiments in fractured rock at the Kamaishi mine, northeast Japan. Eng. Geol., 56, pp. 75–96.

Sawada A, Shimo M, Yamamoto H, Takahara H, Doe T, 2001. Anisotropy, reversibility and scale dependence of transport properties in single fracture and fractured zone – Non-sorbing tracer experiment at the Kamaishi mine. SKB TR-01-24, Svensk Kärnbränslehantering AB.

Selnert E, Byegård J, Widestrand H, 2008. Forsmark site investigation. Laboratory measurements within the site investigation programme for the transport properties of the rock. SKB P-07-139, Svensk Kärnbränslehantering AB.

Serco Assurance, 2007. NAPSAC Release 9.5. Technical summary document. SA/ENV/CONNECTFLOW/12, Serco Ltd.

Shapiro A, 2001. Effective matrix diffusion in kilometre-scale transport in fractured crystalline rock. Water Resour. Res., 37(3), pp. 507–522.

Siitari-Kauppi M, 2002. Development of ^{14}C-polymethylmethacrylate method for the characterisation of low porosity media. Ph.D. Thesis. Laboratory of Radiochemistry, Dept. of Chemistry, University of Helsinki, Finland.

Silliman S, 1989. An interpretation of the difference between aperture estimates derived from hydraulic and tracer tests in a single fracture. Water Resour. Res., 25(10), pp. 2275–2283.

Sisavath S, Al-Yaarubi A, Pain C, Zimmerman R, 2003. A simple model for deviations from the cubic law for a fracture undergoing dilation or closure. Pure Appl. Geophys., 160, pp.1009–1022.

Skagius K, Neretnieks I, 1982. Diffusion in Crystalline Rocks of Some Sorbing and Nonsorbing Species, KBS Teknisk Rapport, 82-12. Svensk Kärnbränsleförsörjning AB.

Skagius K, Neretnieks I, 1986. Diffusivity measurements and electrical resistivity measurements in rock samples under mechanical stress. Water. Resour. Res., 22(4), pp. 570–580.

SKB, 2004. Preliminary site description. Forsmark area – version 1.1. SKB R-04-15, Svensk Kärnbränslehantering AB.

SKB, 2005a. Preliminary site description. Forsmark area – version 1.2. SKB R-05-18, Svensk Kärnbränslehantering AB.

SKB, 2005b. Preliminary safety evaluation for the Forsmark area. Based on data and site descriptions after the initial site investigation stage. SKB TR-05-16, Svensk Kärnbränslehantering AB.

SKB, 2006a. Site descriptive modelling. Forsmark stage 2.1. Feedback for completion of the site investigation including input from safety assessment and repository engineering. SKB R-06-38, Svensk Kärnbränslehantering AB.

SKB, 2006b. Geosphere process report for the safety assessment SR-Can. SKB TR-06-19, Svensk Kärnbränslehantering AB.

SKB, 2006c. Data report for the safety assessment SR-Can. SKB TR-06-25, Svensk Kärnbränslehantering AB.

SKB, 2007a. Fud-program 2007. Program för forskning, utveckling och demonstration av metoder för hantering och slutförvaring av kärnavfall. Svensk Kärnbränslehantering AB.

SKB, 2007b. Geology Forsmark. Site descriptive modeling Forsmark stage 2.2. SKB R-07-45, Svensk Kärnbränslehantering AB.

Slater L, 2007. Near surface electrical characterization of hydraulic conductivity: From petrophysical properties to aquifer geometries – A review. Surv. Geophys., 28, pp. 169–197.

SSI, 2005. Statens strålskyddsinstituts allmänna råd om tillämpning av föreskrifterna (SSI FS 1998:1) om skydd av människors hälsa och miljön vid slutligt omhändertagande av använt kärnbränsle och kärnavfall. SSI FS 2005:5, Statens strålskyddsinstituts författningssamling.

Steefel C, Lasaga A, 1994. A coupled model for transport of multiple chemical species and kinetic precipitation/dissolution reactions with application to reactive flow in single phase hydrothermal systems. Am. J. Sci., 294, pp. 529–592.

Stein D, Kruithof M, Dekker C, 2004. Surface-charge-governed ion transport in nanofluidic channels. Phys. Rev. Lett., 93(3), pp. 1–4.

Stephens M B, Fox A, La Pointe P R, Isaksson H, Simeonov A, Hermanson J, Öhman J, 2007. Geology – Site descriptive modelling Forsmark stage 2.2. SKB R-07-45, Svensk Kärnbränslehantering AB.

Stephens M, Simeonov A, Isaksson H, 2008. Bedrock geology Forsmark Modelling stage 2.3. Implications for and verification of the deterministic geological models based on complementary data. SKB R-08-64, Svensk Kärnbränslehantering AB.

Stewart P, 1998. A review of experimental measurements of effective diffusive permeabilities and effective diffusion coefficients in biofilms. Biotechnol. Bioeng., 59(3), pp. 261–272.

Stober I, Bucher K, 2007. Hydraulic properties of the crystalline basement. Hydrogeology Journal, 15, pp 213–224.

Stone H, Brenner H, 1999. Dispersion in flows with streamwise variations of mean velocity: Radial flow. Ind. Eng. Chem. Res., 38, pp. 851–854.

Stroock A, Dertinger S, Ajdari A, Mezić I, Stone H, Whitesides G, 2002. Chaotic mixer for microchannels. Science, 295, pp. 647–651.

Stråhle A, 2001. Definition och beskrivning av parametrar för geologisk, geofysisk och bergmekanisk kartering av berget. SKB R-01-19, Svensk Kärnbränslehantering AB.

Stumm W, Morgan J, 1996. Aquatic Chemistry: Chemical Equilibria and Rates in natural Waters, 3 ed., Wiley, New York.

Sundberg J, Wrafter J, Ländell M, Back P E, Rosén L, 2008. Thermal properties Forsmark. Modelling stage 2.3: Complementary analysis and verification of the thermal bedrock model. SKB R-08-65, Svensk Kärnbränslehantering AB.

Taylor G, 1953. Dispersion of soluble matter in solvent flowing slowly through a tube. Proc. R. Soc. London. Series A, Mathematical and Physical Sciences, 219(1137), pp. 186–203.

Terzaghi R, 1965. Sources of error in joint surveys. Geotechnique 15(3), pp. 287–304.

Thunehed H, 2005a. Forsmark site investigation. Resistivity measurements on samples from KFM01A and KFM02A. SKB P-05-26, Svensk Kärnbränslehantering AB.

Thunehed H, 2005b. Forsmark site investigation. Resistivity measurements on samples from KFM03A, KFM04A and KFM05A. SKB P-05-76, Svensk Kärnbränslehantering AB.

Thunehed H, 2007a. Forsmark site investigation. Resistivity measurements on samples from KFM01A, KFM01B, KFM02A, KFM05A and KFM06A. SKB P-07-51, Svensk Kärnbränslehantering AB.

Thunehed H, 2007b. Forsmark site investigation. Complementary resistivity measurements on samples from KFM01A, KFM02A, KFM06A, KFM08A, KFM08C and KFM09A. SKB P-07-137, Svensk Kärnbränslehantering AB.

Thur P, Nordqvist R, Gustafsson E, 2007. Forsmark site investigation. Groundwater flow measurements and SWIW tests in borehole KFM01D. SKB P-07-52, Svensk Kärnbränslehantering AB.

Torstenfelt B, Ittner T, Allard B, Andersson K, Olofsson U, 1982. Mobilities of radionuclides in fresh and fractured crystalline rock. SKB TR-82-26, Svensk Kärnbränslehantering AB.

Tsang Y, Tsang C-F, 1989. Flow channeling in a single fracture as a two-dimensional strongly heterogeneous permeable medium. Water Resour. Res., 25(9), pp. 2076–2080.

Tsang Y, 1992. Usage of "equivalent apertures" for rock fractures as derived from hydraulic and tracer tests. Water Resour. Res., 28(5), pp. 1451–1455.

Tsang C-F, Neretnieks I, 1998. Flow channelling in heterogeneous fractured rocks. Rev. Geophys., 36(2), pp. 275–298.

Tsang C-F, Doughty C, 2007. Some insights from simulations of SWIW tests on a complex fracture. SKI-INSITE TRD-07-06, Statens Kärnkraftinspektion.

Turner D, Pabalan R, 1999. Abstraction of mechanistic sorption model results for performance assessment calculations at Yucca Mountain, Nevada. Waste Manage., 19(6), pp. 375–388.

Uchida M, Doe T, Dershowitz W, Andrev T, Wallmann P, Sawada A, 1994. Discrete-fracture modeling of the Äspö LPT-2, large scale pumping and tracer test. SKB International Cooperation Report ICR-94-09, Svensk Kärnbränslehantering AB.

Valkiainen M, Aalto H, Lehikoinen J, Uusheimo K, 1996. The effect of thickness in through-diffusion experiments. Technical Research Center of Finland. VTT Research notes 1788. ISBN 951-38-4983-X.

Verberg R, Ladd A, 2002. Simulation of chemical erosion in rough fractures. Phys. Rev. E., 65(056311), pp. 1–6.

Vilks P, Caron F, Haas M, 1998. Potential for the formation and migration of colloidal material from a near-surface waste disposal site. Appl. Geochem., 13, pp. 31–42.

Vilks P, 2007. Forsmark site investigation. Rock matrix permeability measurements on core samples from borehole KFM01D. SKB P-07-162, Svensk Kärnbränslehantering AB.

Voss C, Provost A, 2002. SUTRA. A model for saturated-unsaturated, variable-density ground-water flow with solute or energy transport. U.S. Geological Survey, Water-Resources Investigations Report 02-4231, Reston Va.

Waber H, Smellie J, 2005. Borehole KFM06A: Characterisation of pore water. Part I: Diffusion experiments. Forsmark site investigation. SKB P-05-196, Svensk Kärnbränslehantering AB.

Waber H, Smellie J, 2007. Forsmark site investigation. Boreholes KFM01D, KFM08C, KFM09B. Characterisation of pore water. Part 1. Diffusion experiments and pore-water data. SKB P-07-119, Svensk Kärnbränslehantering AB.

Walsh J, 1981. Effect of pore pressure and confining pressure on fracture permeability. Int. J. Rock Mech. Min. Sci. & Geomech. Abstr., 18, pp.429–435.

Wass E, 2006. Forsmark site investigation. Groundwater flow measurements in permanently installed boreholes. Test campaign no. 1, 2005. SKB P-06-59, Svensk Kärnbränslehantering AB.

Wass E, Andersson P, 2006. Forsmark site investigation. Groundwater flow measurements and tracer tests at drill site 1. SKB P-06-125, Svensk Kärnbränslehantering AB.

Wass E, 2007. Forsmark site investigation. Groundwater flow measurements in permanently installed boreholes. Test campaign no. 2, 2006. SKB P-07-50, Svensk Kärnbränslehantering AB.

Wass E, 2008. Forsmark site investigation. Groundwater flow measurements in permanently installed boreholes. Test campaign no. 3, 2008. SKB P-08-32, Svensk Kärnbränslehantering AB.

Widestrand H, Byegård J, Ohlsson Y, Tullborg E-L, 2003. Strategy for the use of laboratory methods in the site investigation programme for the transport properties of the rock. SKB R-03-20, Svensk Kärnbränslehantering AB.

Winberg A, Andersson P, Hermanson J, Byegård J, Cvetkovic V, Birgersson L, 2000. Äspö Hard Rock Laboratory. Final report of the first stage of the tracer retention understanding experiments. SKB TR-00-07, Svensk Kärnbränslehantering AB.

Yasuhara H, Elsworth D, Polak A, Liu J, Grader A, Halleck P, 2006. Spontaneous switching between permeability enhancement and degradation in fractures in carbonate: Lumped parameter representation of mechanically- and chemically-mediated dissolution. Transport Porous Med., 65, pp. 385–409.

Zhang S, Tullis T, 1998. The effect of fault slip on permeability and permeability anisotropy in quartz gouge. Tectonphysics, 295, pp. 41–52.

Zhang S, Tullis T, Scruggs V, 1999. Permeability anisotropy and pressure dependency of permeabilityin experimentally sheared gouge materials. J. Struct. Geol., 21, pp. 795–806.

Zhou Q, Liu H, Molz F, Zhang Y, Bodvarsson G, 2005. Field-scale effective matrix diffsuin coefficient for fractured rock: Results from literature survey. Report LBLNL-57368, Lawrence Berkeley National Labortatory, Berkeley, CA.

Zimmerman R, Kumar S, Bodvarsson G, 1991. Lubrication theory analysis of the permeability of rough-walled fractures. Int. J. Rock Mech. Min. Sci. & Geomech. Abstr., 28(4), pp. 325–331.

Zimmerman R, Chen D-W, Cook N, 1992. The effect of contact area on the permeability of fractures. J. Hydrol., 139, pp. 79–96.

Zimmerman R, Bodvarsson G, 1996. Hydraulic conductivity of rock fractures. Transport Porous Med., 23, pp. 1–30.

Zimmerman R, Al-Yaarubi A, Pain C, Grattoni C, 2004. Non-linear regimes of fluid flow in rock fractures. Int. J. Rock Mech. Min. Sci., 41(3), pp. 1–7.

Appendix A

Flow channelling at open fracture intersections

Author: James Crawford

In previous chapters it has been suggested that the intersections at crossing or terminating fractures may constitute fast flowpaths through the rock if they are open and hydraulically unobstructed. In this report these have been referred to as fracture intersection zones, or FIZ.

If we consider a fracture intersection formed by two equi-dimensioned fracture planes, there may be a conduit with enhanced hydraulic conductivity along the line of fracture intersection as illustrated in Figure A-1.

The most common type of flow conduit formed in this manner is likely to be intersecting fractures where the effective aperture of the flow channel is defined by the apertures of the flanking fracture planes. Such intersections are referred to in this report as simple FIZ of subtype A. In some situations, shear movement or spheroidal weathering processes may lead to a significant enlargement of the fracture intersection. Such FIZ are referred to as subtype B and C, respectively.

Since FIZ of subtype A are thought to be ubiquitous throughout the rock volume (occurring wherever open fractures intersect), it is important to assess what effect they may have on the transport properties of the rock. To investigate this effect, the Multiphysics program (formerly known as FEMLAB /Comsol 2005/) was used to simulate laminar flow in 3D flow conduits formed by hypothetical, intersecting smooth fractures. The program solves the Navier-Stokes equations for steady-state flow using a finite element method.

For the flow problem where a hydraulic gradient is applied along the axis of fracture intersection, it is only necessary to solve the reduced portion of the fracture intersection corresponding to the shaded polygons in Figure A-1 owing to considerations of symmetry. The appropriate viscous and "slip" boundary conditions for the reduced flow volume are illustrated in Figure A-2.

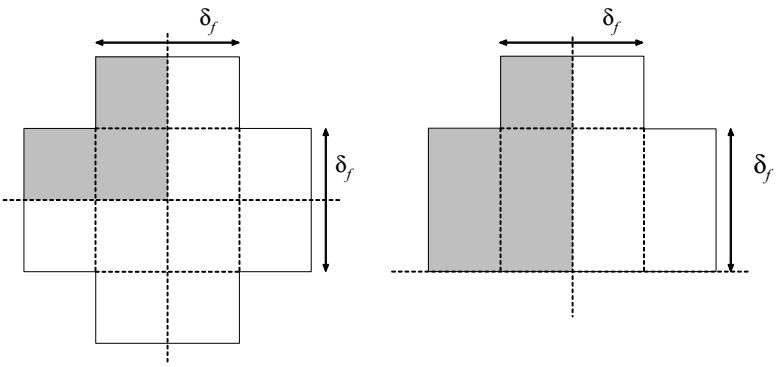

Figure A-1. *Illustration of crossing (left) and terminating (right) fracture intersections of sub-type A. Although the fractures are depicted as having the same aperture, this is not necessarily the case. The axis of enhanced transmissivity is normal to the cross sectional profiles in the illustration. The shaded polygons indicate the reduced region of symmetry for definition of the viscous flow problem.*

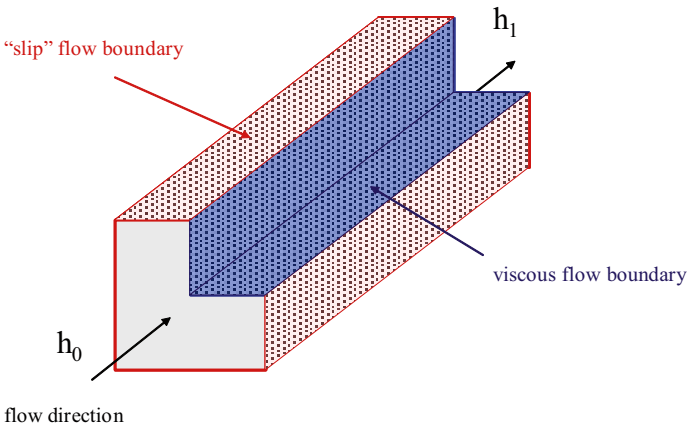

Figure A-2. *Schematic illustration of applied boundary conditions for reduced 3D flow problem.*

To reduce the computational overhead it is desirable to reduce the length of the discretised flow volume as much as possible, while ensuring that a steady-state flow velocity distribution is obtained. For laminar flow in a cylindrical tube, a steady-state fluid velocity profile is attained after approximately two aperture lengths along the tube axis according to /Bird et al. 2002/. Preliminary simulations were therefore performed to check for steady state flow conditions using a conduit length of two and four aperture lengths, respectively. It was found that there was essentially no difference in the velocity profiles for these two systems, indicating that steady state flow conditions were achieved after approximately two fracture aperture lengths.

The flow problem was simulated using equi-dimensioned fracture apertures ranging from 10^{-3} to 10^{-6} m for both crossing and terminating fracture intersections. Some examples of the simulated flow velocity profiles are shown in Figure A-3.

Over the range of fracture apertures tested, the mean flow velocity at a crossing fracture intersection was found to be about four times that calculated for parallel plate laminar flow in a fracture of the same aperture. For a terminating fracture intersection, the mean flow velocity was found to be roughly double that for parallel plate laminar flow. It is also interesting to note that in these simple cases, the region of the enhanced velocity profile extends roughly 1/4 of an aperture length into the flanking fracture planes.

Although the Darcy velocity at fracture intersections may be somewhat greater than within fracture planes hosting them, they do not necessarily conduct large amounts of flow owing to their limited dimensions (i.e. cross-sectional area for flow). One way of comparing the flow capacity of in-plane and FIZ flow channels is to consider their conductance.

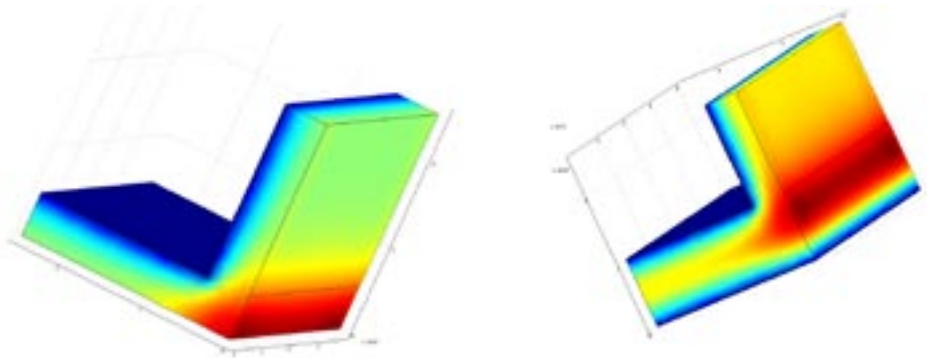

Figure A-3. *Simulation results for a conduit formed by the intersection of two fractures with aperture 10^{-5} m and an arbitrary hydraulic gradient parallel to the line of intersection. Regions of high relative fluid velocity are shaded red; regions of low relative velocity are shaded blue. Profiles are for a crossing fracture (left) and a terminating fracture (right).*

in-plane fracture channels

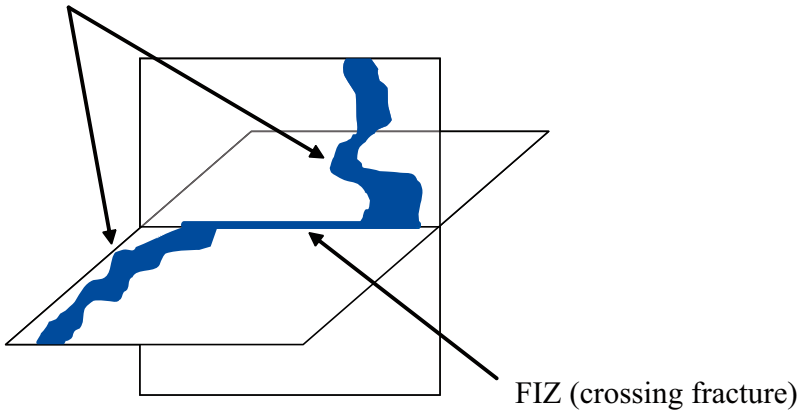

Figure A-4. *Illustration of two fracture flow channels linked by a narrow flow conduit formed at the intersection of two crossing fractures (referred to as a conductive fracture intersection zone, or FIZ).*

The conductance of a flow channel is defined as:

$$C = Q/\Delta h \tag{A-1}$$

Where C (m^2/s) is the conductance, Q (m^3/s) is the flow rate, and Δh is the hydraulic potential difference. For an in-plane flow channel of width W_c (m) and length L_c (m), the conductance can be shown to be:

$$C = T_f \frac{W_c}{L_c} \tag{A-2}$$

Where T_f (m^2/s) is the transmissivity of the flow channel.

Given that the increased relative flow velocity at the fracture intersection corresponds to an enhanced transmissivity for a given fracture aperture, δ_t (m) we can write for a FIZ flow channel:

$$C_{FIZ} = \zeta\ T_f \frac{\delta_t}{L_c} \qquad (2 \le \zeta \ge 4) \tag{A-3}$$

The ratio of conductances for an in-plane and FIZ flow channel can then be given as:

$$\frac{C}{C_{FIZ}} = \zeta \left(\frac{W_c}{\delta_f} \right) \tag{A-4}$$

To highlight the difference in conductance of in-plane and FIZ flow channels, we consider an in-plane flow channel with a hydraulic aperture of 10^{-4} m as an example. The transmissivity of such a flow channel is on the order of 6×10^{-7} m^2/s. If the hypothetical channel were 0.1 m wide and 1 m in length, its conductance would be 6×10^{-7} m^2/s. A FIZ flow channel of similar length, formed at the intersection of two such fractures would have a maximum conductance of 2.4×10^{-10} m^2/s even though its effective transmissivity, ζT_f could be as much as four times that of the in-plane flow channel. In terms of flow, this means that the FIZ flow channel can conduct 1/4,000 times less flow than the in-plane flow channel for the same hydraulic potential difference. Although the Darcy velocity within the FIZ flow channel is 2–4 times greater than in the fracture, such flow channels only conduct very small total flows and therefore cannot contribute considerably to far-field release rates.

Appendix B

In-plane flow channelling effects

Author: James Crawford

Theoretical aspects and background

In-plane flow channelling is one of the main classes of flow channelling that has been proposed to be active within the fractured rock at the Forsmark site. It describes the tendency for preferential flowpaths to develop within the plane of individual fractures due to the spatially variable aperture of the void space comprising the kinematic porosity.

Generally, we infer the existence of in-plane flow channels from the mathematical-statistical description of the kinematic porosity which has been investigated in many studies and is well described in the literature /e.g. Brown and Scholz 1985, Hakami and Larsson 1996, NRC 1996, Tsang and Neretnieks 1998/. Occasionally it is possible to observe in-plane flow channels more, or less directly at inflows to tunnels and drifts constructed in fractured rock as shown in Figure B-1.

The variable apertures observed in natural fractures typically arise due to the shear displacement of mated, although rough fracture surfaces. The spatial variability of the aperture is closely related to the composite topology formed by the opposing, mismatched surfaces and the amount of shear displacement. An important feature of this process is the anisotropy of the transmissivity field arising due to the shear displacement as studies have shown that the transmissivity is highest for flow perpendicular to the vector of shear displacement and lowest along it /Auradou et al. 2006/.

Generally it is thought that the flow porosity of real fractures can be represented in a statistical sense by the specification of (1) a probability density for the aperture distribution and (2) the auto-covariance function or some equivalent measure such as a power spectrum which describes the spatial correlation structure /Brown and Scholz 1985, Sahimi 1998, Power and Tullis 1991/.

Studies of excavated fractures suggest that the surface roughness distribution and composite surface topography of the pore space can often be well described by a log-normal distribution /e.g. Hakami and Larsson 1996, NRC 1996, Keller 1997/. Commonly it is also found that fracture surfaces in crystalline rock exhibit self-affine (i.e. fractal) scaling properties characterised by a Hurst exponent typically in the range of 0.75–0.85 /Drazer and Koplik 2000, Bouchaud 2003/.

Figure B-1. *Possible in-plane flow channels observed in the Bolmen tunnel as indicated by iron oxide precipitates at in-flow locations. Image taken from /Neretnieks 2006a/.*

The two opposing surfaces of a shear fracture are usually closely matched at long wavelengths although mismatched at short wavelengths. As a consequence, the aperture field is characterised by a decaying power law spectrum which tends to flatten out at long wavelengths /Brown and Scholz 1985, Power and Tullis 1991, Sahimi 1998/. The location on the power spectrum curve that this occurs is variously referred to in the literature as the "crossover dimension" or "cut-off frequency". Similar properties have also been observed for minor fault zones of considerable microstructural complexity /Power and Tullis 1992/.

In many studies a standard geostatistical covariance function with a specified correlation length is assumed for the spatial variation of the fracture aperture (or, more typically the transmissivity) /e.g. Moreno et al. 1988, Tsang and Tsang 1989, Liu and Neretnieks 2005, 2006/. In this context, the correlation length has essentially the same meaning as the crossover dimension; i.e. the length scale at which the aperture variation can be considered to be spatially non-correlated. This approach, however, does not necessarily capture the fine detail of the aperture spatial variation at small length scales.

Other approaches such as /Brown 1995, Glover et al. 1998ab, Ogilvie et al. 2006/ are based upon a direct spectral representation of the aperture field featuring some specified crossover dimension. In the calculations presented in this appendix we adopt the model proposed by /Brown 1995/ owing to the ease with which it can be numerically implemented. Although not necessarily as accurate as the approach described by /Ogilvie et al. 2006/, for the purpose of the scoping calculations presented here this model is thought to capture the most significant details of the aperture spatial structure. The model is the same as that used by /Liu and Neretnieks 2005, 2006/.

In the scoping calculations we are particularly interested in identifying the impact of surface asperity contact in fractures subjected to *in situ* normal stresses. Characterising the properties of fractures under these conditions is important as it is suspected that substantial portions of the fracture surface may be inaccessible owing to the need for the fractures to be in close physical contact to transmit stress. Studies of the impact of flow-channelling arising due to variable aperture distribution typically assume fractures to be hydraulically open across their entire surface and there are relatively few studies which explicitly examine the impact of asperity contact. If asperity contact areas are large, flow channels in individual fractures may be hydraulically isolated from the fracture as a whole and may be missed in borehole investigations due to their small dimensions. If this is the case, statistics of flowing features identified in boreholes and used to calibrate the Hydro-DFN models may seriously underestimate the true frequency of flowing features in high stress regions of the rock at repository depth.

Scoping calculations of in-plane flow channelling

In the scoping calculations, we simulate a pumping test for estimation of fracture transmissivity within a variable aperture fracture featuring different amounts of surface asperity contact.

First, an initial fracture aperture distribution is generated using a spectral synthesis method based on a Fast Fourier Transform (FFT) inversion procedure and implemented in Matlab. It is the same model described by /Liu and Neretnieks 2005, 2006/. For the purposes of these calculations, a self-affine distribution of fracture apertures is created on a 10 m×10 m square domain discretised into a 512×512 pixel map. Different extents of surface asperity contact are approximated in a rudimentary fashion by subtracting fixed amounts from the aperture map as a whole (i.e. effectively compressing the fracture surfaces inwards). Any overlaps between the adjacent surfaces in the form of negative apertures are assumed to be in contact and there the aperture is truncated to zero as shown schematically in Figure B-2. By doing this it is implicitly assumed that the contact points deform elastically in a simple fashion without changing the properties of the adjacent pore space.

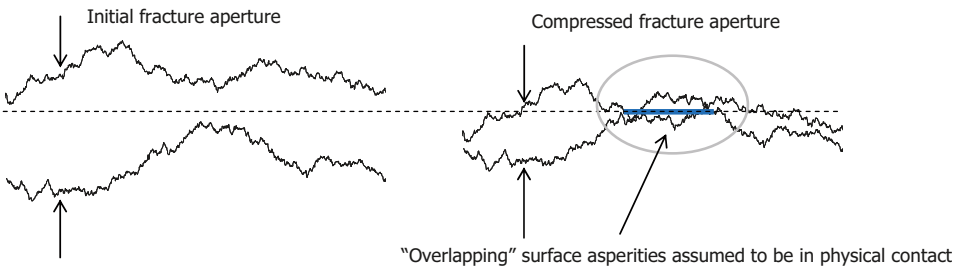

Figure B-2. *Schematic of fracture aperture cross-section. Asperity contact is approximated by compressing opposing surfaces and setting any overlapping regions (i.e. the blue line indicated in the figure) to zero aperture.*

Although this approach is an inexact representation of how fractures undergo deformation, it should be sufficient to give an indication of the overall effect that fracture aperture closure has upon in-plane flow channelling and how this relates to frequencies of flowing features identified in boreholes. For this reason we contemplate asperity contact à priori without any additional consideration of how this relates to magnitudes of normal or shear stresses. A full discussion of different hydrological-mechanical coupling phenomena of relevance for fracture deformation is beyond the scope of what we are trying to achieve by these calculations and is dealt with in more detail elsewhere /e.g. Koyama 2007/.

A summary of the basic parameters used to generate the anisotropic, self-affine aperture field is given in Table B-1. In the first set of simulations presented here, an anisotropy factor of 3 is arbitrarily assumed for the crossover dimension along the x- and y-axes. Although the assumption of anisotropy has some bearing upon the magnitude of the flows and connectivity of the fracture along the different axes, it is found to make little difference to the overall conclusions reached in the analysis provided the support scale of the simulation is larger than the maximum correlation length/crossover dimension for aperture variation.

The initial, self-affine fracture aperture map assuming no surface contact is shown in Figure B-3.

To simulate a pumping test, the aperture map is converted to an equivalent 2D channel network with orthogonal channel elements in an analogous fashion to the method described in /Moreno et al. 1988/. The conductances of individual channels are calculated assuming the local cubic law (LCL) and based upon the harmonic mean of their end node apertures which are interpolated in 2D from the initial aperture map. The pumping test is simulated by applying a 1 m head differential across the system. To achieve this, network nodes in the vicinity of the pumping well at a radius of 3.8 cm are assigned a hydraulic head of zero, while those at a radius of 5 m are assigned a 1 m hydraulic head. The hydrologic flow problem to find the head field is solved by way of analogy with electric networks (i.e. Kirchoff's current law) and is described in more detail in /Moreno and Neretnieks 1993/.

Table B-1. Summary of basic simulation parameters for hydraulic well-test scoping calculations.

Parameter	Value
Mean fracture aperture, δ_f	1.0×10^{-4} m
Standard deviation fracture aperture, σ_f	5.0×10^{-5} m
Hurst exponent, H	0.85
Crossover dimension in y-direction, λ_y	1.0 m
Crossover dimension in x-direction, λ_x	0.3 m

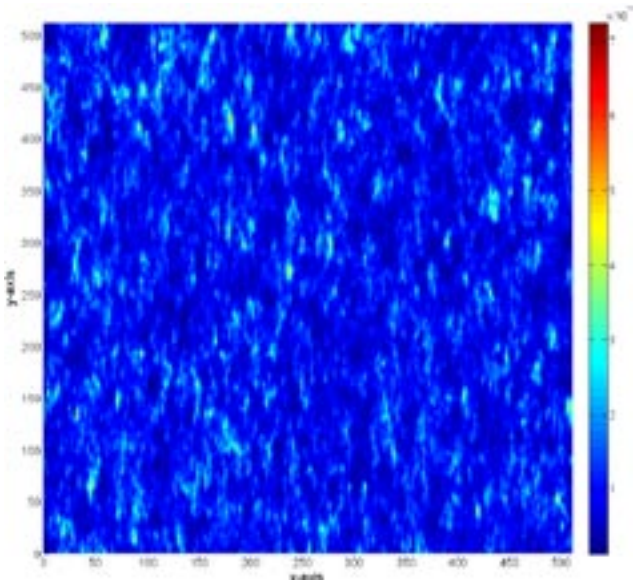

Figure B-3. *Initial aperture map of test fracture. The apertures are assumed to be lognormally distributed with a self-affine correlation structure and 3:1 anisotropy (i.e. 3 times greater correlation length along the y-axis than the x-axis).*

The channel network occupancy and flow distribution are shown in Figure B-4 for the base case where there is no surface contact. The pumping well is shown as a red marker at the centre of the image and the outer hydraulic boundary for the channel network is shaded green.

The total flowrate in the simulation was found to agree to within 16% of the theoretical flowrate assuming a radial flow configuration, the macroscopic cubic law (MCL) and the geometric mean aperture of the fracture.

Subsequent simulations considering surface contact generally lead to the formation of hydraulically isolated channels or clusters of isolated channels in the network. These invariably give rise to singular matrices when attempting to solve the hydrologic problem. An iterative algorithm was therefore developed to identify and remove hydraulically isolated channels and network nodes thus avoiding singularities.

Simulation results for surface contact fractions in the range 25%–48% are shown in Figure B-5 to Figure B-9.

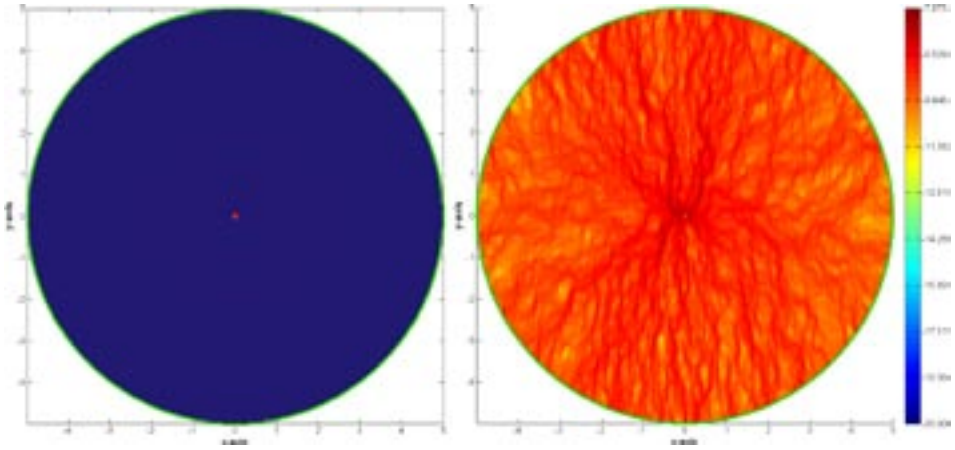

Figure B-4. *Channel network occupancy (left) and simulated flow magnitudes (right) for the base case where there is no surface contact. The blue shading in the left-hand image indicates hydraulically connected regions of the fracture directly accessible from the central borehole. Flows (m^3/s) are indicated in log10- units.*

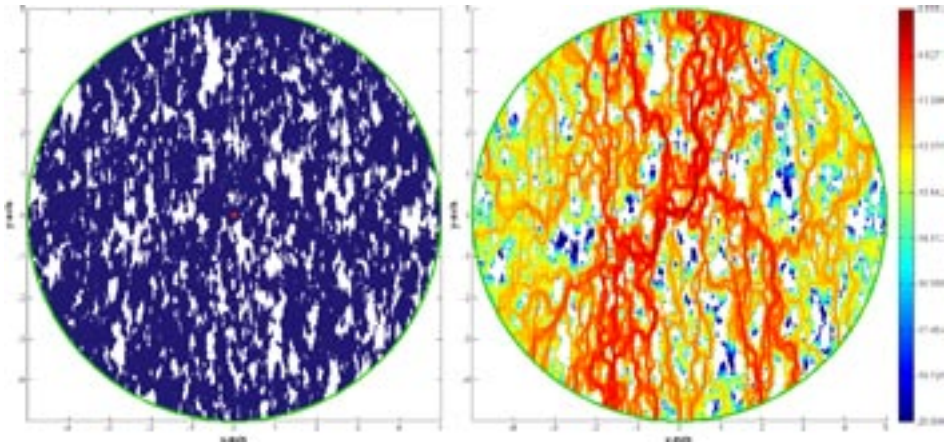

Figure B-5. *Channel network occupancy (left) and simulated flow magnitudes (right) for a surface contact fraction of 25%. The blue shading in the left-hand image indicates hydraulically connected regions of the fracture directly accessible from the central borehole. Flows (m^3/s) are indicated in log10- units.*

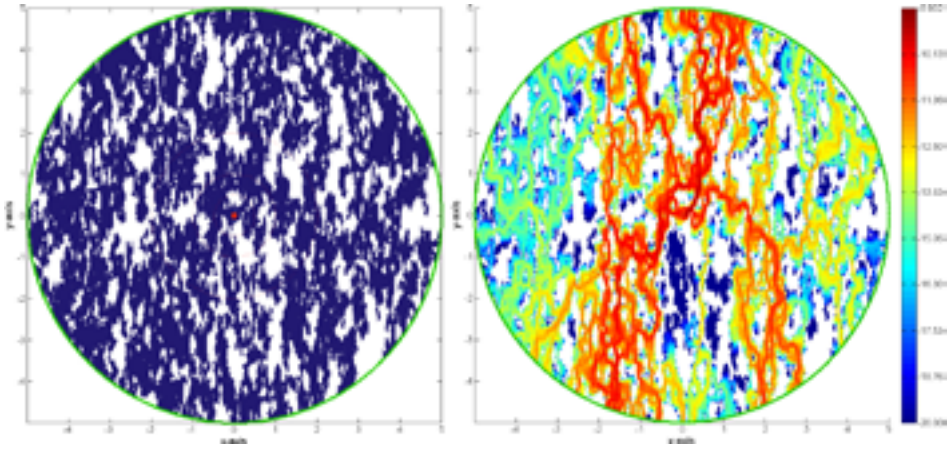

Figure B-6. *Channel network occupancy (left) and simulated flow magnitudes (right) for a surface contact fraction of 35%. The blue shading in the left-hand image indicates hydraulically connected regions of the fracture directly accessible from the central borehole. Flows (m^3/s) are indicated in log10- units.*

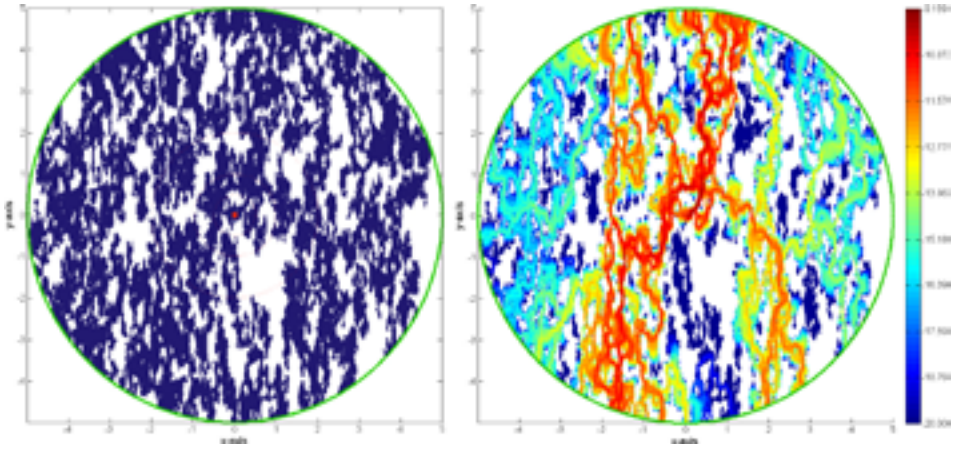

Figure B-7. *Channel network occupancy (left) and simulated flow magnitudes (right) for a surface contact fraction of 39%. The blue shading in the left-hand image indicates hydraulically connected regions of the fracture directly accessible from the central borehole. Flows (m^3/s) are indicated in log10- units.*

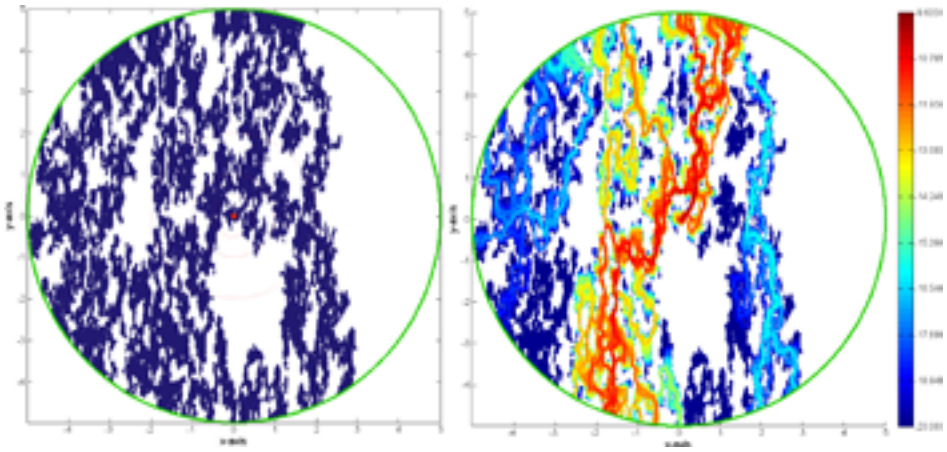

Figure B-8. *Channel network occupancy (left) and simulated flow magnitudes (right) for a surface contact fraction of 44%. The blue shading in the left-hand image indicates hydraulically connected regions of the fracture directly accessible from the central borehole. Flows (m^3/s) are indicated in log10- units.*

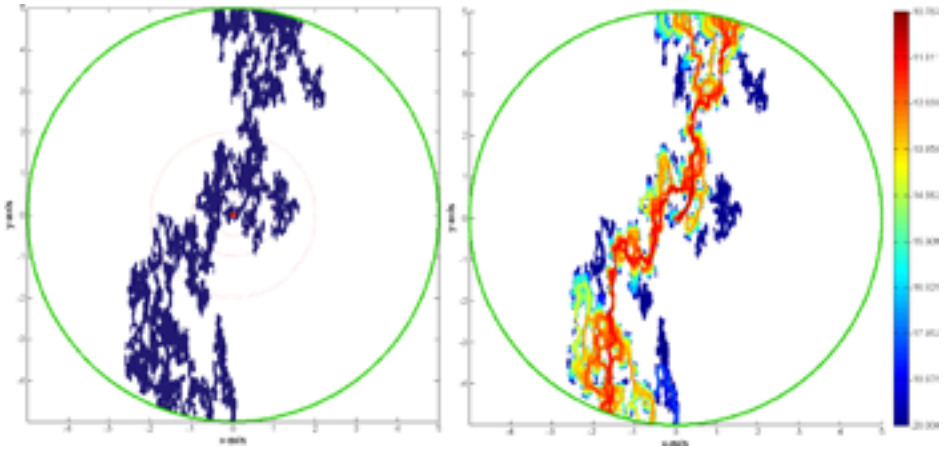

Figure B-9. *Channel network occupancy (left) and simulated flow magnitudes (right) for a surface contact fraction of 48%. The blue shading in the left-hand image indicates hydraulically connected regions of the fracture directly accessible from the central borehole. Flows (m^3/s) are indicated in log10- units.*

As can be seen from the figures above, even with relatively high contact area fractions the flow is perceptibly radial in character in spite of strong flow channelling. The impact of the flow anisotropy is also clearly evident by the preferential orientation of the main flow conductors in the figures. It is also interesting to note that there are clear indications of compartmentalisation in Figure B-8 and Figure B-9 where large regions of the fracture surface are not directly accessible from the central borehole. This, however, only appears to occur at high contact area fractions, close to the percolation threshold.

Generalised radial flow analysis of PSS (pipe string system) hydraulic responses in 58 packed off borehole sections in borehole KFM06A at Forsmark suggest that most flowing features (70–80%) are associated with flow dimensions greater than about 1.5, although a significant fraction (on the order of 20–30%) exhibit smaller flow dimensions symptomatic of approximately linear flow channelling /Follin et al. 2006/.

Although we have not tested the dimensionality of the hypothetical flow systems illustrated in the above figures by simulating transient well tests, the results appear to be qualitatively consistent with the GRF interpretations reported by /Follin et al. 2006/ for the Forsmark site.

It should be noted that the simulations shown above consider a fixed head boundary at a radial distance of 5 m from the borehole and could therefore have an in-built bias due to this fact.

To address this issue, further simulations of flow were made with applied boundary conditions in a roughly point to point configuration over a 10 m distance (see, for example, Figure 5-2). The extended simulations indicate that provided the "point" boundary conditions are applied as line sinks of realistic size (e.g. a few cm to dm in extent) the results are largely similar provided the surface contact fraction is not too high (i.e. < 40%). It was also found that the choice of a simple, self-affine fracture model such as that used here does not give substantially different results to those that would be obtained using a standard geostatistical treatment based upon a Gaussian, spherical, or exponential correlation model. Finally, the choice of correlation length or cut-off dimension does not appear have a large impact on the results provided it is significantly less than the characteristic scale of the test (i.e. less than the 5 m radius of influence in the cases presented here).

Additional simulations of flow were made to stochastically assess the impact of different contact area fractions. In this case, however, an isotropic fracture aperture map has been assumed (i.e. $\lambda_x = \lambda_y = 1$ m) as we are mostly interested in the overall effects of compression rather than anisotropy. The results of these calculations are shown in Figure B-10 for the main case of $\sigma_f / \delta_f = 0.5$, as well as a smaller number of realisations for the case studies $\sigma_f / \delta_f = 0.1$ and $\sigma_f / \delta_f = 1$. In the figure we calculate the apparent transmissivity of the tested fracture under compression assuming radial flow (Equation B-1) and compare this to the transmissivity of the uncompressed fracture by plotting the ratio T/T_0 as a function of surface contact area, f_c.

The initial discontinuity at $f_c = 0$ in Figure B-10 arises due to the fact that the initial aperture distribution needs to be compressed by a certain amount before first surface contact occurs. Results are only shown for $f_c > 0$ so data for compressed, although not yet contacting fractures are absent from the figure.

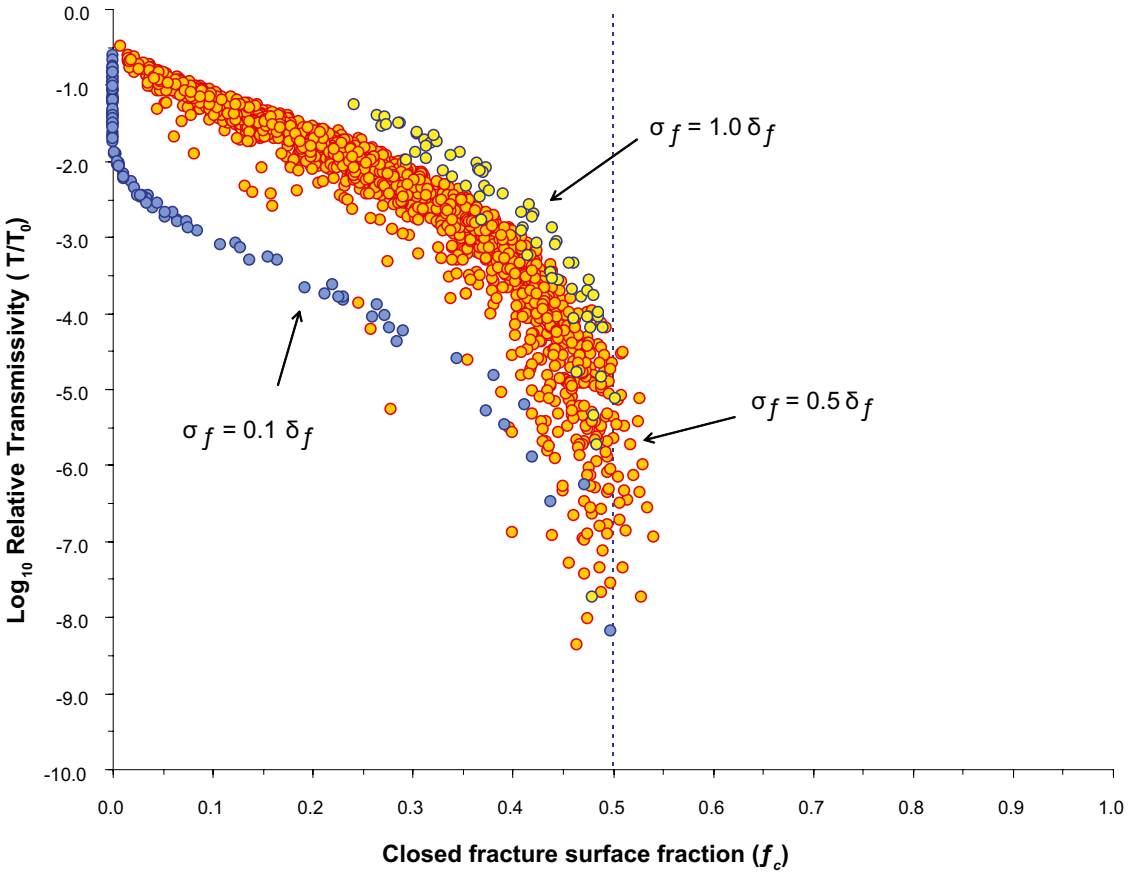

Figure B-10. *Results of stochastic simulations (3,748 realisations) showing simulated transmissivity relative to transmissivity of the fracture in an uncompressed state. The vertical broken line at $f_c = 0.5$ indicates the theoretical bond-percolation limit. Orange, yellow, and blue markers indicate different case studies for aperture variance as labelled in the figure.*

As can be seen from the figure, the relative transmissivity of the fracture decays rapidly with increasing surface contact area and very few realisations exhibit any kind of hydraulic connectivity for $f_c > 0.5$. This result is consistent with expectations based upon percolation theory for a square lattice /Kesten 1980/.

It is interesting to note that the initial, uncompressed fracture aperture in the simulations corresponds to a hydraulic transmissivity of 6.6×10^{-7} m^2/s. From Figure B-10 we can see that for a roughness factor of $\sigma_f/\delta_f = 0.5$, such a fracture could be compressed up to a contact fraction of 30–40% before falling below the approximate detection limit of the PFL method. For very smooth fractures, on the other hand, the transmissivity decays rapidly to below the detection limit for very small contact area fractions (10% or less). The opposite occurs for rough fractures and these can accommodate relatively large contact area fractions before becoming effectively non-transmissive.

Implications for Hydro-DFN modelling

Flow censoring effects

Specifically, there are two issues related to this form of flow channelling that are potentially problematic for the synthesis of Hydro-DFN models (referred to as Type 1 and Type 2 flow censoring effects). These are:

Flow channels may be completely missed owing to their limited dimensions, the low probability of a direct borehole intersection and the possibility of flow compartmentalisation;

Those flow channels that are identified may appear to be less transmissive than they really are owing to the low permeability of structures in which they are hosted (i.e. a flow bypassing effect).

Although dominant flow channels can be very narrow and only occupy a small fraction of the total wetted surface, it appears that fractures with a surface contact fraction of up to 40% are sufficiently well connected across their extent that hydraulic testing should, in principle, result in a positive detection of a flowing feature provided the borehole intersects an open part of the fracture somewhere in the immediate vicinity of the flow channel. If the flow channels were hydraulically isolated from the rest of the fracture, on the other hand, they may not be detected by a borehole randomly intersecting the fracture. This appears more likely for fractures with surface contact fractions above 40% and approaching the percolation threshold where flow compartmentalisation can occur.

A precondition for the borehole to identify a flowing feature is, of course, that it intersects the fracture in a mechanically open region. For a surface contact fraction of, say 40%, about the same percentage of flowing features will not be identified due to the random intersection of the borehole with closed regions. This means that the "true" frequency of conducting fractures will be about 1.6 times that estimated from the borehole data. This is likely to be an overestimate, however, as a borehole can partially intersect an open region and still register a positive detection of a flowing feature. The actual measurement bias will depend upon the effective correlation length for aperture variation in relation to the borehole diameter and could potentially be estimated more accurately by simulation. Although considered unlikely for Forsmark, we note that this analysis does not rule out more exotic, wormhole-like flow channels existing in otherwise annealed fractures. It is doubtful that such features would be detected by borehole hydraulic tests unless they were directly intersected.

As this implies, the detection of a flowing feature if not directly intersected by the borehole is also predicated on the intervening fracture flow space having a sufficiently high permeability that flow can be detected. Although the flow connectivity as shown in Figure B-4 to Figure B-9 suggests that most of the flow space should be accessible "in principle", this does not necessarily mean that the observed flow will be greater than the limit of detection (which is frequently only 1–2 orders of magnitude less than the mean fracture transmissivity). While this means that

pipe-like flow conduits embedded in tight or annealed fractures may not be detected, it is possible that the "normal" in-plane flow channels most affected by this are also those least likely to feature high transmissivities (since the probability of this occurring increases inversely with decreasing flow transmissivity). In compressed fractures featuring surface asperity contact fractions less than about 20–30% it seems that this form of flow censoring effect (Type 1) should not be an overwhelming issue unless there is a considerable accumulation of low permeable fracture filling materials plugging the pore space.

It is interesting to note that in transient analysis of constant head injection tests at Forsmark reported by /Hjerne et al. 2008/, only a very small proportion of tested sections gave indications of constant head boundary characteristics. Since such behaviour would be suggestive of strongly transmissive flow channels hosted in otherwise poorly transmissive fractures, it is possible to conclude that flow censoring effects characterised as Type 2 are not evident in the available hydrogeological data set and can probably be ruled out.

The impact of flow dimensionality on hydraulic transmissivity estimates

Transmissivity as a physical parameter describing flow in a fracture can be a confusing concept since its apparent numerical value depends upon a number of assumptions made in its estimation. A number of different forms of the steady state flow equation are given below for various flow dimensions typically assumed:

$$Q = \frac{2K_f L_s W_c}{r_0 - r_{bh}} \Delta h \qquad \text{(1D)} \qquad \text{(B-1)}$$

$$Q = \frac{2\pi K_f L_s}{\log\left(r_0 / r_{bh}\right)} \Delta h \qquad \text{(2D)} \qquad \text{(B-2)}$$

$$Q = \frac{4\pi K_f}{\left(\frac{1}{r_{bh}} - \frac{1}{r_0}\right)} \Delta h \qquad \text{(3D)} \qquad \text{(B-3)}$$

Here, Q (m^3/s) is the flowrate, K_f (m/s) is the hydraulic conductivity of the flow system, r_{bh} (m) is the borehole radius, r_0 (m) is the radius of influence of the test, and Δh (m) is the hydraulic potential difference (i.e. the difference between the borehole drawdown and the undisturbed head at the radius of influence of the test, $\Delta h = h_{bh} - h_0$).

For a borehole interval of length L_{bh} (m), the transmissivity T_f (m^2/s) of the flowing feature is related to the hydraulic conductivity by way of the relation:

$$T_f = K_f L_{bh} \qquad \text{(B-4)}$$

For intermediate, so-called "fractional" flow dimensions a more general flow equation is given by /Barker 1988/ as:

$$Q = \frac{\alpha_n (2-n) K_f b^{3-n}}{\left(r_0^{2-n} - r_{bh}^{2-n}\right)} \Delta h \qquad (n\text{-D}) \qquad \text{(B-5)}$$

Where, α_n is the surface area of the unit hypersphere in n-dimensions:

$$\alpha_n = \frac{2\pi^{n/2}}{\Gamma\left(\frac{n}{2}\right)} \qquad \text{(B-6)}$$

The parameter b in Equation B-5 describes the extent of the flow source, which has different meanings for different flow dimensionalities.

In Posiva Flow Log (PFL) tests, the transmissivity is typically assessed under steady-state conditions using Thiem's Equation (B-2) /de Marsily 1986/. A radial flow geometry is typically assumed in PFL analysis owing to the fact that the entire borehole is held at a constant head with no strong gradients along the borehole. Since the radius of influence is poorly known in a steady-state test this usually needs to be assumed. In the PFL tests carried out at Forsmark, a value of $r_0/r_{bh} = 500$ is arbitrarily chosen /e.g. Rouhiainen and Pöllänen 2003/ which is numerically convenient as it gives a geometric factor close to unity. For true radial flow, the uncertain radius of influence does not have a large impact on the order of magnitude of the estimated transmissivity since the value of r_0/r_{bh} can be varied within a considerable range and gives only relatively small changes to the estimated transmissivity. Given that the undisturbed head is usually not known, it is also customary to perform the test at two different drawdowns and eliminate the unknown background head from the flow equation.

Although the average flow dimension for flow converging towards the borehole as a whole can probably be safely assumed to be radial (since the entire borehole is pumped), the flow dimension on the level of individual fractures may not be, particularly if there are very strong channelling effects. If the fundamental assumption of radial flow geometry is incorrect on the level of individual fractures, this could bias the resulting transmissivity distribution estimated for the population of flowing fractures.

It is noted that this does not directly impact the Hydro-DFN described in Chapter 3 since the transmissivity distribution is conditioned iteratively to give the same flowrates as observed in the PFL testing (i.e. the transmissivity distribution estimated from borehole data is never used directly).

In spite of this, it is still interesting to consider the flow dimension of well tests to ascertain whether transmissivity estimates are biased and if so how much of the bias is due to incorrect assumptions of flow geometry. The understanding of flow dimensionality effects is particularly important if we wish to apply borehole transmissivity data directly to flow and transport calculations as we have done for the deterministic deformation zones in section 3.2.3.

Small deviations from true radial flow probably do not have a very large impact upon the estimated transmissivity even considering the additional uncertainty of unknown radius of influence. Flow dimensions close to unity, however, give apparent transmissivities that underestimate the true flow channel transmissivity by as much as two or more orders of magnitude depending upon actual flow channel width and radius of influence. Considering a linear flow channel of width 0.1 m and a radius of influence of 20 m, for example, Thiem's equation (i.e. Equation B-2 for radial flow) underestimates the true transmissivity by a factor of 100.

Although such underestimates of flow channel transmissivity could be a problem for pipe like flow channels, it seems unlikely that this would be the case for "normal" in-plane flow channels hosted in variable aperture fractures owing to the bifurcating nature of the flowpaths (at least those with low levels of surface asperity contact say, $f_c \leq 30\%$). In the generalised radial flow analysis reported by /Follin et al. 2006/, GRF transmissivities and "best choice" transmissivity values reported in Sicada exhibit an approximate 1:1 correspondence (to a precision of about an order of magnitude) with only a few exceptions. These features were generally found to have low flow dimensions, n in the range 0.1–1.25.

The impact of space filling effects on hydraulic transmissivity estimates

Transmissivity estimates derived from borehole hydraulic testing can also be influenced by space filling effects in addition to the considerations of flow dimension discussed in the previous section. By "space filling effects" we mean phenomena related to both the proportion of the fracture pore space actually occupied by flow as well as tortuosity/constrictivity effects in compressed, variable aperture fractures.

Consider for a moment, the hypothetical case of an in-plane flow channel radiating outwards from the borehole with a ¼ pie segment like geometry. In this case, a transient analysis would clearly indicate a radial flow system, although the actual fracture area occupied by flow is only

25% of that assumed in Thiem's equation. The transmissivity estimated by Thiem's equation would then underestimate the true transmissivity of the flow channel by a factor of four. In more realistic cases, we can easily conceive of situations where islands of surface asperity contacts reduce the available area that can be occupied by flow. For an isotropic distribution of contact points, the flow geometry would appear to be radial, although the transmissivity estimated by Thiem's equation would still underestimate the transmissivity of the available flow space.

A number of researchers have proposed means of correcting estimated fracture transmissivity (or permeability) for the presence of surface asperity contacts. One of the first attempts to do this for fracture flow is attributed to /Walsh 1981/ who proposed a simple formula based upon Maxwell's technique for calculating the effective permeability of a medium containing circular inclusions. The following expression defines the correction factor in terms of the apparent and true hydraulic aperture of the fracture:

$$\frac{T_h}{T} = \frac{\delta_h^3}{\delta_0^3} \approx \frac{(1 - f_c)}{(1 + f_c)} \tag{B-7}$$

Here, δ_h is the apparent hydraulic aperture of the fracture with surface contacts, and δ_0 is the "true" hydraulic aperture of the flow channels residing in the fracture. Since transmissivity is related to the cube of fracture hydraulic aperture, Equation B-7 also gives the relation between the apparent (T_h) and true transmissivity (T) of the flow space. Although an elegant approach, the derived expression is somewhat limited as it assumes an isotropic array of spatially separate inclusions without any structural correlation and it also fails to predict the onset of percolation. An additional limitation is that it makes no account of the variable aperture of the non-contacting parts of the fracture, which means that it also fails to predict form drag effects at the tapered edges of the flow porosity. The correction factor therefore approximately accounts for 2D tortuosity and constrictivity effects in the plane of the fracture, but does not properly account for variable aperture (nor out of plane tortuosity due to long wavelength undulations of the mean fracture plane).

This result was extended by /Zimmerman et al. 1992/ to account for elliptical shaped inclusions with aspect ratio α (i.e. ratio of minor and major axis lengths):

$$\frac{T_h}{T} = \frac{\delta_h^3}{\delta_0^3} \approx \frac{(1 - \beta f_c)}{(1 + \beta f_c)} \qquad \text{where, } \beta = (1 + \alpha)^2 / 4\alpha \tag{B-8}$$

In their paper it was also shown using stochastic simulations that the result could be extended to randomly distributed, irregular asperities provided an approximate aspect ratio is used that preserves the average perimeter to surface area of the contact area "obstacles" in the fracture.

An alternative approach was suggested by /Zimmerman et al. 1996/ based upon earlier work by /Kirkpatrick 1973/ involving bond percolation in resistor networks. In this case, the correction factor is defined as:

$$\frac{T_h}{T} = \frac{\delta_h^3}{\delta_0^3} \approx (1 - 2 f_c) \tag{B-9}$$

Although very simple, Equation B-9 is interesting as it implicitly predicts the existence of a percolation limit at $f_c = 0.5$, which is what was observed in the simulations in Figure B-10.

It should be noted that the correction factors implied by Equations B-7 to B-9 are relatively small for contact area fractions less than about 20–30% and possibly less than the overall uncertainty inherent in the interpretation of borehole measurement data.

As noted previously, it is also of some relevance to remember that the correction factor only considers simple in-plane tortuosity/constrictivity effects and doesn't consider the additional effect of form drag within the compressed pore spaces. For very narrow flow constrictions and flow channels featuring tapered edges, these effects could give additional biasing effects that although relatively easy to simulate are difficult to relate to individual measurements of transmissivity made in borehole hydraulic testing.

Appendix C

Correlation of hydraulic gradient and transmissivity

Author: James Crawford

In response to the empirical observations of correlation between apparent hydraulic gradient and transmissivity described in section 3.3, a number of hypothetical simulations have been made using a simple channel network model. This has been done to ascertain whether the correlation may be attributed to an artefact of data handling or whether it is something that can be expected on the grounds of mechanistic reasoning.

Calculations for a hypothetical 3D system

For these calculations we use a 3D channel network model that is based on the concept developed by /Moreno and Neretnieks 1993/ and implemented in Matlab. It is essentially a 3D extension of the 2D channel network model used for the simulations of HCD flow related transport described in section 3.7 and Appendix E. Figure C-1 shows the geometry of the modelled volume.

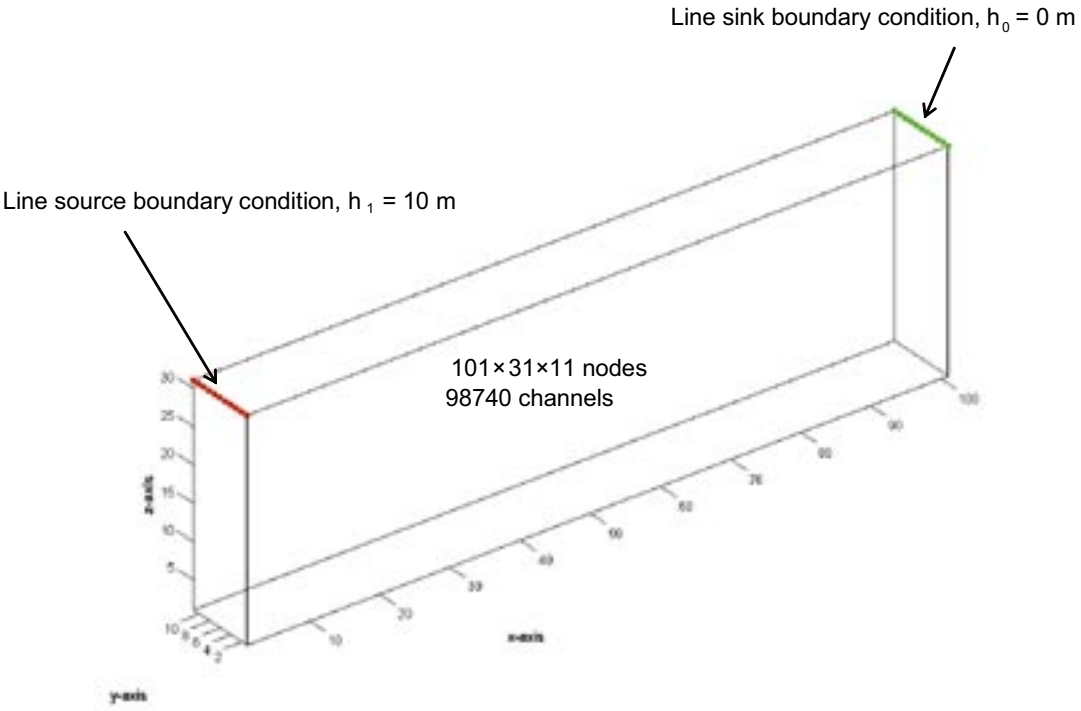

Figure C-1. *Visualisation of modelled volume. The flow system is modelled as a simple orthogonal network of 10 m channels with 6-channel intersection mixing nodes as described in /Moreno and Neretnieks 1993/. Note that the axes are labelled by node coordinates rather than distance. Transmissivities of individual flow channels are assigned from a lognormal distribution with and without depth correlation. Node locations where the hydraulic head boundary conditions are applied are indicated in red (upper boundary) and green (lower boundary).*

Each member of the channel network is assigned a hydraulic conductance. The conductance is defined by analogy with electrical networks where it is the reciprocal of resistance. Here, the flow may be expressed as the channel conductance multiplied by the hydraulic head difference between its ends. In the current model, we assume that the conductances of the channel members are lognormally distributed with a characteristic mean, μ_c and standard deviation, σ_c. The conductance of individual channel members is assigned from the equation:

$$\log_{10} C_{ij} = \mu_c + R_n(0,1) \times \sigma_c \qquad \text{(C-1)}$$

Where $R_n(0,1)$ is a random normal deviate with mean zero and unit variance. In cases where an exponentially decaying correlation between depth and transmissivity is simulated, μ_c is defined by a simple linear equation:

$$\mu_c(z) = \mu_a + \frac{(\mu_b - \mu_a)}{L_z} z_c \qquad \text{(C-2)}$$

Here, μ_a and μ_b are the values for the geometric mean conductances at the lower and upper system boundaries, L_z is the depth of the simulation volume (300 m) and z_c is the elevation of the flow channel midpoint relative to the lower system boundary. In the simulations presented in this Appendix chapter, a transmissivity depth trend spanning three orders of magnitude is assumed which is roughly the same as the depth trend characterising deformation zone transmissivities at Forsmark (see section 3.2.3).

Since conductances are linearly proportional to transmissivity (see Appendix A), relative conductances normalised by the maximum stochastic conductance is the same as the corresponding measure involving transmissivity.

The results of two realisations for $\sigma_c = 0.5$ and $\sigma_c = 2.0$ are shown in Figure C-2 and Figure C-3 for the case of non-spatially correlated (i.e. fully isotropic) transmissivities.

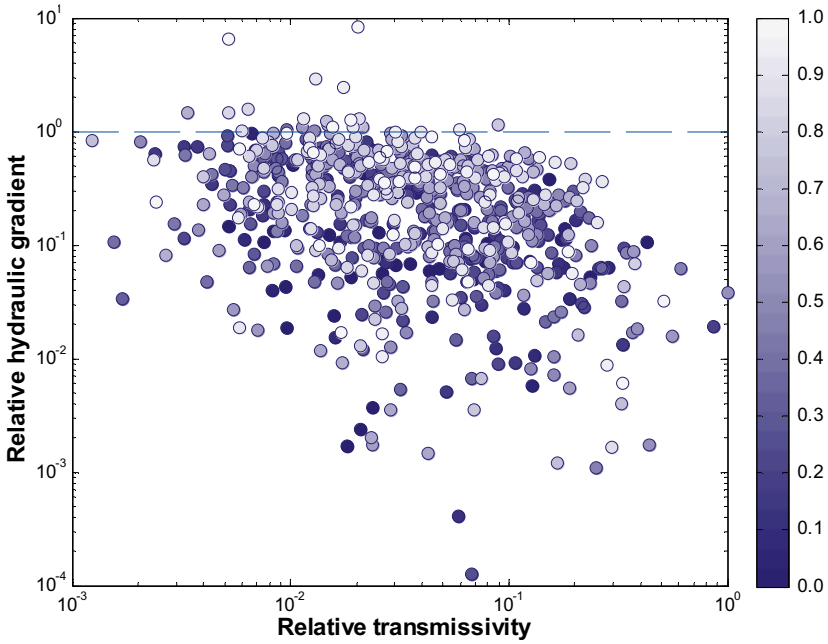

Figure C-2. *Simulation results for 3D channel network without depth correlation and $\sigma_c = 0.5$. Results are shown for the relative hydraulic gradient (normalised with respect to the overall gradient for the system) plotted against relative transmissivity. Markers correspond to 1,000 randomly selected nodes shaded according to depth (shading from light to dark with increasing depth).*

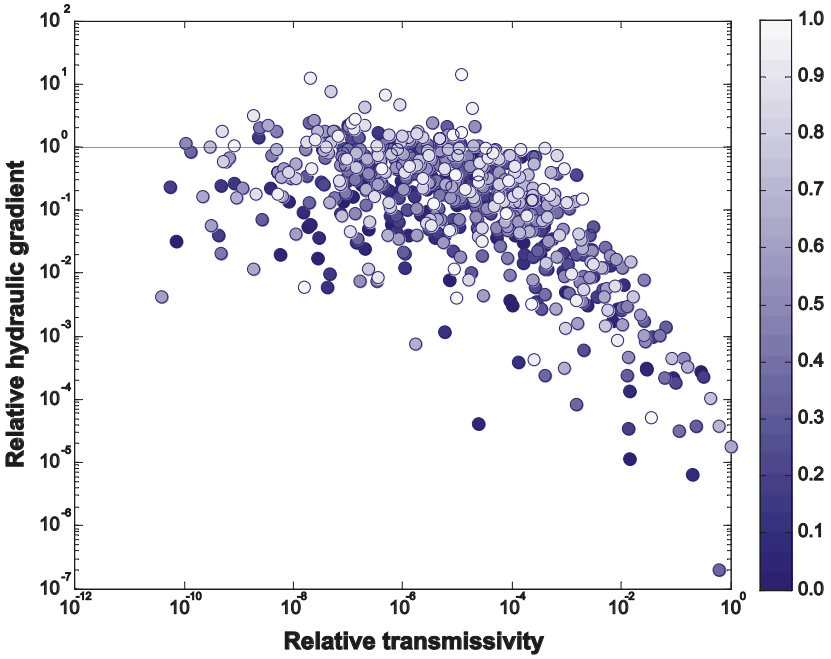

Figure C-3. *Simulation results for 3D channel network without depth correlation and σ_c = 2.0. Results are shown for the relative hydraulic gradient (normalised with respect to the overall gradient for the system) plotted against relative transmissivity. Markers correspond to 1,000 randomly selected nodes shaded according to depth (shading from light to dark with increasing depth).*

As can be seen from Figure C-2, there appears to be very little correlation between hydraulic gradient and transmissivity for the relatively homogeneous distribution of flow transmissivities implied by σ_c = 0.5. Here, roughly 65% of the flow channels have a transmissivity range that spans about an order of magnitude. For the more heterogeneous case shown in Figure C-3 (σ_c = 2.0), on the other hand, there is a clear tendency for the local hydraulic gradient to be inversely correlated with transmissivity at least within the top half of the transmissivity range. In this case, 65% of the flow channels have a transmissivity range that spans four orders of magnitude. In neither case does there appear to be a correlation between hydraulic gradient and depth.

The results of two realisations for σ_c = 0.5 and σ_c = 2.0 are shown in Figure C-4 and Figure C-5 for the case of a spatially-correlated depth transmissivity relation (i.e. isotropic channel transmissivities with an exponentially decaying depth trend).

Similarly to the spatially non-correlated example, the simulation results for the homogeneous case shown in Figure C-4 (σ_c = 0.5) exhibit no correlation between hydraulic gradient and transmissivity. The depth trend for channel transmissivity is, however, quite clear in the image as can be seen from the distribution of shaded markers. As previously, we also see a clear inverse trend for the correlation between local hydraulic gradient and transmissivity in the upper half of the transmissivity distribution in the heterogeneous case depicted in Figure C-5. Once again there is no apparent correlation between hydraulic gradient and depth in either case. It is interesting to note in Figure C-5 that the heterogeneity of the transmissivity distribution is sufficiently large that it tends to swamp the depth trend for the central tendency of the μ_c parameter. In all cases simulated the local hydraulic gradient is rarely more than a factor 10 greater than the overall applied hydraulic gradient (as indicated by the horizontal broken line in the figures). In these simulations, the channel length is 1/100 of the major axis length of the simulation volume so in the most extreme case the maximum theoretically achievable local hydraulic gradient is 100 times the overall hydraulic gradient applied across the simulation volume.

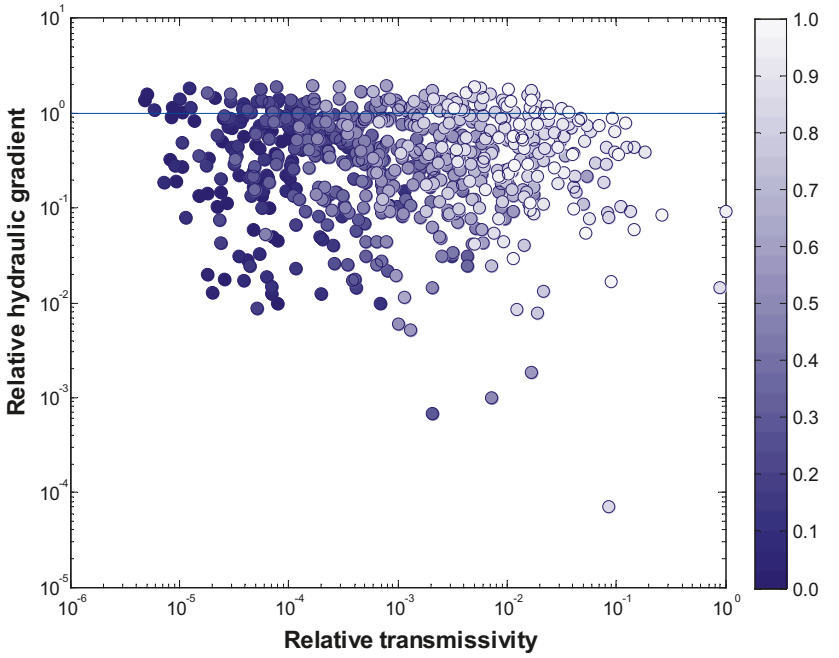

Figure C-4. *Simulation results for 3D channel network with depth correlation and σ_c = 0.5. Results are shown for the relative hydraulic gradient (normalised with respect to the overall gradient for the system) plotted against relative transmissivity. Markers correspond to 1,000 randomly selected nodes shaded according to depth (shading from light to dark with increasing depth).*

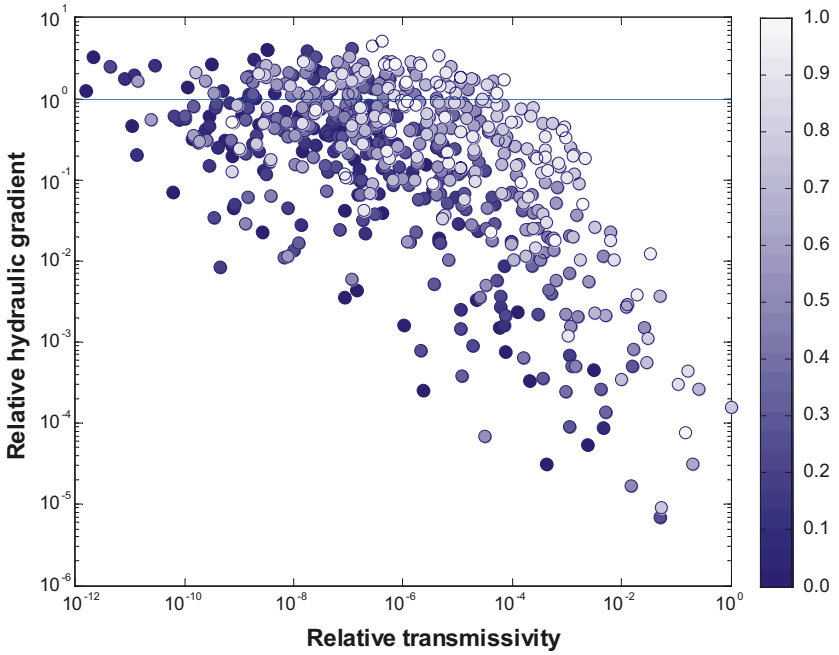

Figure C-5. *Simulation results for 3D channel network with depth correlation and σ_c = 2.0. Results are shown for the relative hydraulic gradient (normalised with respect to the overall gradient for the system) plotted against relative transmissivity. Markers correspond to 1,000 randomly selected nodes shaded according to depth (shading from light to dark with increasing depth).*

Calculations for a hypothetical 2D system

In the calculations presented here, we use the 2D version of the channel network model which was previously used for the estimation of HCD flow related transport properties. For the particular case shown in this section, we take the model for gently dipping zones which is loosely based on the hydraulic properties and orientation of ZFMA2. Here, we specifically consider the case of an isotropic, Gaussian spatial correlation structure with a 20 m correlation length overlaid on an exponentially decaying transmissivity trend. The simulated transmissivity and flow distribution are shown in Figure C-6.

The corresponding plot of relative hydraulic gradient against relative transmissivity is shown in Figure C-7.

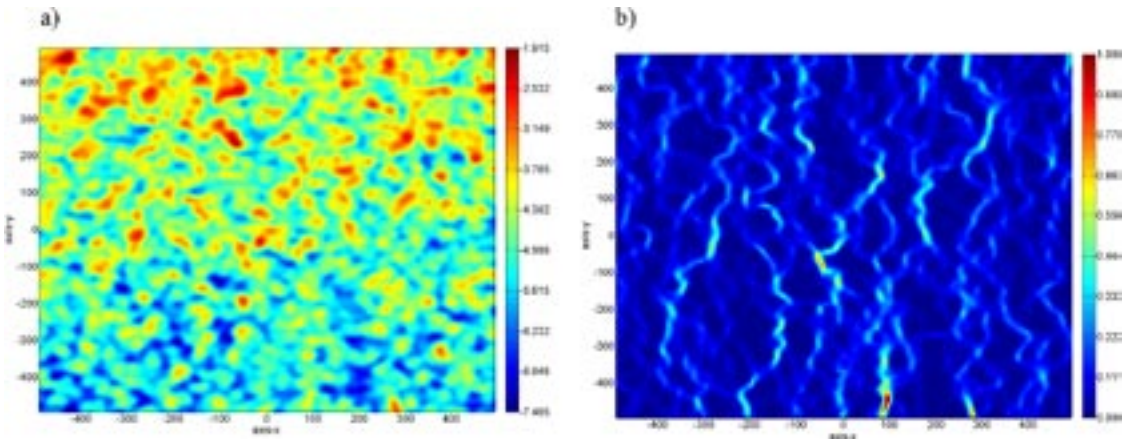

Figure C-6. *a) lognormally distributed transmissivity field for a gently dipping zone with an isotropic, Gaussian spatial correlation and exponential depth trend (20 m correlation length). The data are given as log_{10} values projected onto a 2D plane; b) corresponding flow field (normalised arithmetic values) simulated with a 2D channel network model.*

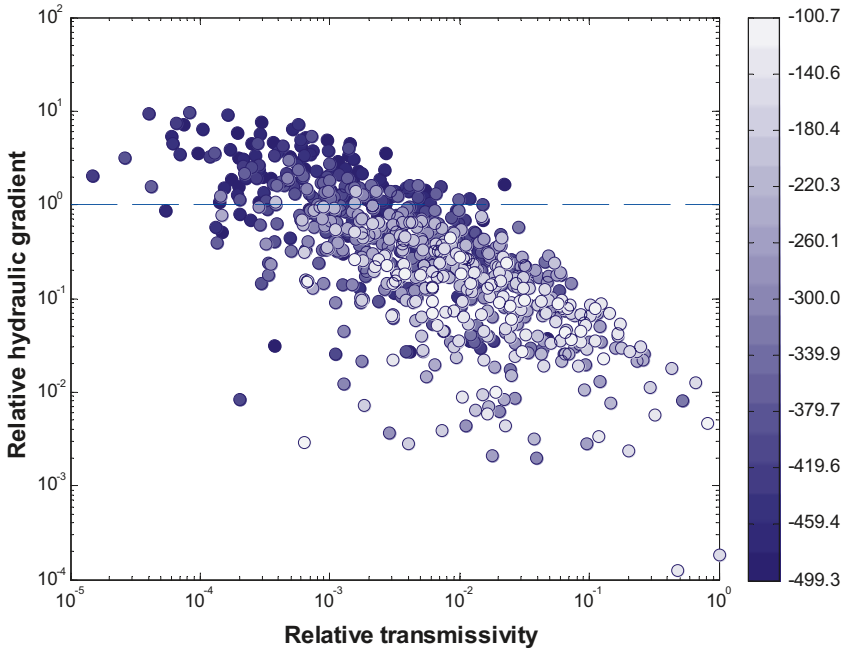

Figure C-7. *Simulation results for 3D channel network with depth correlation and σ_c = 2.0. Results are shown for the relative hydraulic gradient (normalised with respect to the overall gradient for the system) plotted against relative transmissivity. Markers correspond to 1,000 randomly selected nodes shaded according to depth (shading from light to dark with increasing depth).*

In the simulations made for the 2D system, there appears to be a much stronger inverse relation between local hydraulic gradient and transmissivity than for the 3D cases. This is at least partly because flow in a channel network tends to take the path of least resistance and 2D channel networks possess fewer alternative routes than 3D networks. For a purely 1D flow system, we would expect an even stronger inverse relation between gradient and transmissivity since all resistances are connected in series (this can be readily appreciated by consideration of Ohm's law for series coupled resistors in an electric circuit). Interestingly in this case, we do see a depth trend for the local hydraulic gradient with proportionally larger numbers of channels at greater depths exhibiting high local gradients relative to the overall gradient for the system. In this case too we do not see local gradients much larger than about an order of magnitude larger than the overall hydraulic gradient. Here, the channel length is 1/240 times the major axis length so in the most extreme case, the maximum theoretically achievable local hydraulic gradient is 240 times the overall hydraulic gradient applied.

On the basis of these simple scoping calculations we can therefore conclude that some kind of inverse correlation between hydraulic gradient and transmissivity can be expected in the measurement data for mechanistic reasons related to the propagation of hydraulic head in heterogeneous networks of flow channels. The existence per se of an empirical inverse relation between hydraulic gradient and transmissivity therefore does not appear to be an artefact of data handling. It is noteworthy, however, that it is very rare to encounter local hydraulic gradients that are more than an order of magnitude greater than the overall hydraulic gradient for the system, at least for the channel networks studied here. The fact that the estimated local hydraulic gradients based upon the site data interpretation (see Figure 3-10) appear to be as much as three orders of magnitude greater than the approximate regional hydraulic gradient of 1% appears curious in this respect.

Appendix D

Flow-related transport properties of the HRD

Author: James Crawford

Simulation results for FFM01c (< –400 m)

Detailed description of modelling procedure

Owing to the very sparse nature of the fracturing within FFM01c (< –400 m), it was found to be highly ineffective to make Hydro-DFN simulations using Napsac/ConnectFlow for the hypothetical 100 m simulation voxels considered in the conceptual model of transport described in section 3.4.2. To circumvent this problem a novel simulation tool was developed to make estimates of F-factors for "typical" flowpaths within this fracture sub-domain. Since over 95% of DFN realisations were found to be not hydraulically connected over a distance of 100 m, a rapid means of generating and discriminating the connectivity status of DFN networks was required.

To this end a Matlab program was created which would automatically generate large numbers of realisations of fracture networks and determine their connectivity over a range of distances spanning the simulation volume and along the different principal axis directions (North-South, West-East, and vertical). The simulations were sufficiently numerically intensive that a set of 1,000 realisations could take many days to process, therefore the need for this to occur in a relatively unsupervised manner.

As a first step, the program generates fracture centres, sizes, and orientations until a specified target areal intensity ($P_{32target}$) is obtained for each of the five pre-defined fracture sets in Table 3-3. The $P_{32target}$ is defined for the size interval [r_{min}, r_{max}] using the equation for the truncated power law distribution as given by /Follin et al. 2007a/:

$$P_{32\text{target}}\left[r_{\min}, r_{\max}\right] = P_{32}^{0}\left[r > r_0\right]\left(\frac{r_{\min}^{2-k_r} - r_{\max}^{2-k_r}}{r_0^{2-k_r}}\right) \tag{D-1}$$

Fracture centres are defined assuming a Poissonian distribution within a bounding box volume chosen to be sufficiently large to avoid "thinning" of the fracture population towards the edges of the inner box defining the actual simulation volume.

Fracture sizes are generated using the simulation procedure described by /Hedin 2005/:

$$r = \frac{r_{\min}}{R_0^1\left(\left(\frac{r_{\min}}{r_{\max}}\right)^{k_r} - 1\right)^{\frac{1}{k_r}}} \tag{D-2}$$

Where, R_0^1 is a uniform random deviate in the interval [0,1].

Fracture orientations are defined using a univariate Fisher distributed polar angle θ' and uniformly distributed azimuthal angle ϕ' with respect to a principal orientation vector /Hedin 2005/:

$$\theta' = \cos^{-1}\left(\frac{\log\left(\exp(\kappa) - R_0^1\left(\exp(\kappa) - \exp(-\kappa)\right)\right)}{\kappa}\right) \tag{D-3}$$

$$\phi' = 2\pi R_0^1 \tag{D-4}$$

Here, two independent uniform random deviates are required; one for the generation of θ' and one for ϕ'. The dispersion of the fracture pole distribution is defined by the Fisher κ parameter. The actual orientation of the stochastically generated fracture pole is then calculated by applying a Cartesian roll rotation around the x-axis (defined by the plunge of the fracture set), followed by a yaw rotation around the z-axis (defined by the trend of the fracture set) to give the correct fracture orientation in an absolute reference frame.

In keeping with the Napsac standard, fractures are generated as square features rather than circles or ellipses. To avoid vertex orientation bias, the vertices of the fractures are randomised by applying a uniform random rotation around the fracture normal vector.

Each fracture set is composed in sequence using an iterative procedure where parcels of 1,000 fractures are generated at a time and added to a global array. If the cumulative P_{32} of the global array exceeds $P_{32target}$ for the fracture set, the excess fractures are discarded. To approach the $P_{32target}$ as closely as possible, the procedure is repeated iteratively until a global set is obtained that is within a user specified absolute tolerance of the required target. Since large fractures are more likely to be discarded towards the end of the fracture generation process as the set converges towards $P_{32target}$, there is a theoretical possibility that the simulated fracture set may exhibit a distribution of sizes that does not honour the original power law distribution defined for the fracture set. Random testing of the generated data sets revealed that this was not a significant problem for any of the DFN realisations examined.

The Matlab program used for generating fractures makes no consideration of fracture termination so it may be considered to be a somewhat simplified implementation of a DFN generating algorithm compared to other commercially available DFN simulation programs. We note, however, that this has also been neglected in the derivation of optimised Hydro-DFN parameters in the hydrogeology site descriptive model, and so the lack of this functionality is not relevant for the simulations described here which are based upon that model.

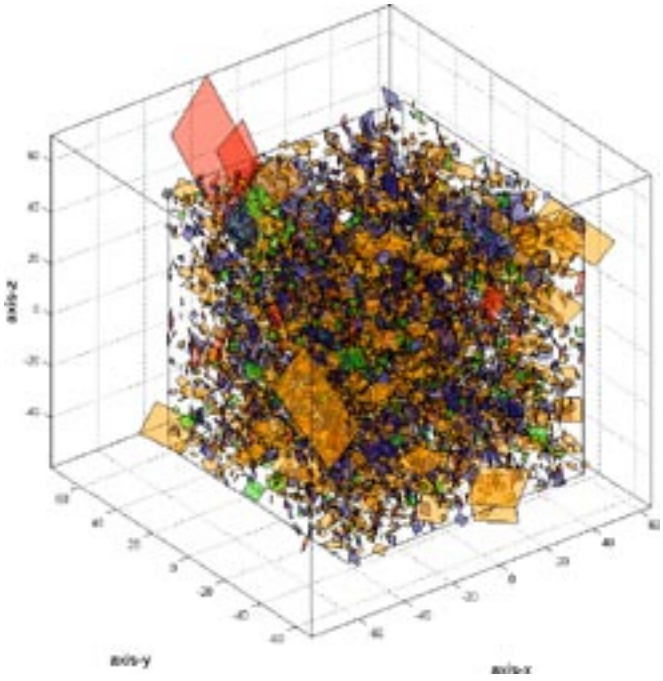

Figure D-1. *Typical realisation of a DFN for FFM01c (< –400 m) comprising the five fracture sets NS (blue), NE (red), NW (green), EW (mauve), HZ (orange) with parameters as defined in Table 3-2 for fracture size interval 1 m to 560 m radius.*

In addition to extensive internal checking within the program itself, a suite of external testing programmes was developed to ensure the quality of the stochastically generated DFN realisations. Essentially this involves taking a numerical "fingerprint" of the simulated DFN and comparing this to what was expected based upon the original fracture set definitions. This checking consisted of a number of procedures including:

- back-calculation of Fisher parameters to cross-check against the original parameters used to generate the fracture set,
- plotting of individual fracture pole clusters and mean orientation vector to visually check that the generated stochastic sets had correct orientation and dispersion,
- plotting the cumulative frequency of the simulated fracture sizes against the theoretical power law curve to visually check the extent to which the simulation algorithm honoured the pre-defined distribution,
- calculation of the local P_{32} within random 20 m×20 m×20 m sub-volumes of the simulation voxel to ascertain possible bias due to fracture set thinning at the edges of the simulation volume.

Generally it was found that the purpose written algorithms implemented within Matlab were capable of honouring the fracture set definitions to at least the same degree of accuracy achievable using Napsac/ConnectFlow (this was assessed by exporting stochastically generated DFN sets from Napsac and subjecting them to the same analysis).

To determine the connectivity of the simulated DFN, the pair-wise fracture intersections are first calculated for all fractures within the global fracture set. Although a time consuming process, it is possible to rule out a great many fracture-fracture combinations by simple geometric testing. If the mutual distance between the two fracture barycentres is greater than the sum of their effective radii (taking account of the fact that the fractures are not circular), then the fractures cannot physically intersect and no further calculation is required. If, however, the factures fall within a mutual sphere of influence then a computational geometry routine is used to identify if they intersect and the endpoints of their line of intersection if this is the case. An $n \times n$ sparse network adjacency matrix is then defined (where n is the total number of fractures), based upon the pair-wise connectivity of individual fractures. Connections are denoted by 1's in the appropriate row-column combinations corresponding to the intersecting fractures.

Since the DFN typically contains many thousands or even tens of thousands of fractures, the simplest method for calculating overall network connectivity by making use of the fill-in structure of successive powers of the adjacency matrix is not feasible. Instead it was found that a breadth first search algorithm implemented in the Matlab version of the Boost Graph Library /Gleich 2006/ was the most economical means of calculating the overall network connectivity. The overall network connectivity is recorded using a sparse connectivity matrix, also of size $n \times n$. This matrix contains 1's where pair-wise combinations of fractures are connected by any number of mutually intersecting intermediate fractures. The hydraulic connectivity of the DFN can then be ascertained by testing all fractures for mutual connections with the subset of fractures that additionally intersect the upper and lower boundary planes defining the hypothetical flow/transport control volume. This can be done by searching through the connectivity matrix using a simple masking routine to identify connections spanning the boundaries of the system.

Although comprising a relatively complex sequence of calculations, the results of the connectivity algorithm could be tested by importing the same fracture set into Napsac and cross-checking against the corresponding results obtained using Napsac. By and large, the Matlab algorithm gave identical results to Napsac. The only exceptions were a very small number of cases where rounding errors in the orientation of the fracture sets meant that the Matlab algorithm predicted mutual fracture intersections that were not identified by Napsac. This was due to the reduced number of significant figures included in the definitions of the fracture vertices in the gocad-formatted file used to import fracture definitions to Napsac. Generally, the exceptions were extreme cases involving fracture vertices just making contact with other fractures typically featuring intersection trace lengths on the order of microns.

An example of a typical outcome of a connectivity calculation is visualised in Figure D-2 where connected fractures are coloured blue and unconnected fractures are coloured red.

This particular realisation is somewhat unusual in that it is the only one out of 1,000 realisations that exhibits connectivity along all three principal axes (WE, NS, vertical) as shown in Figure D-3.

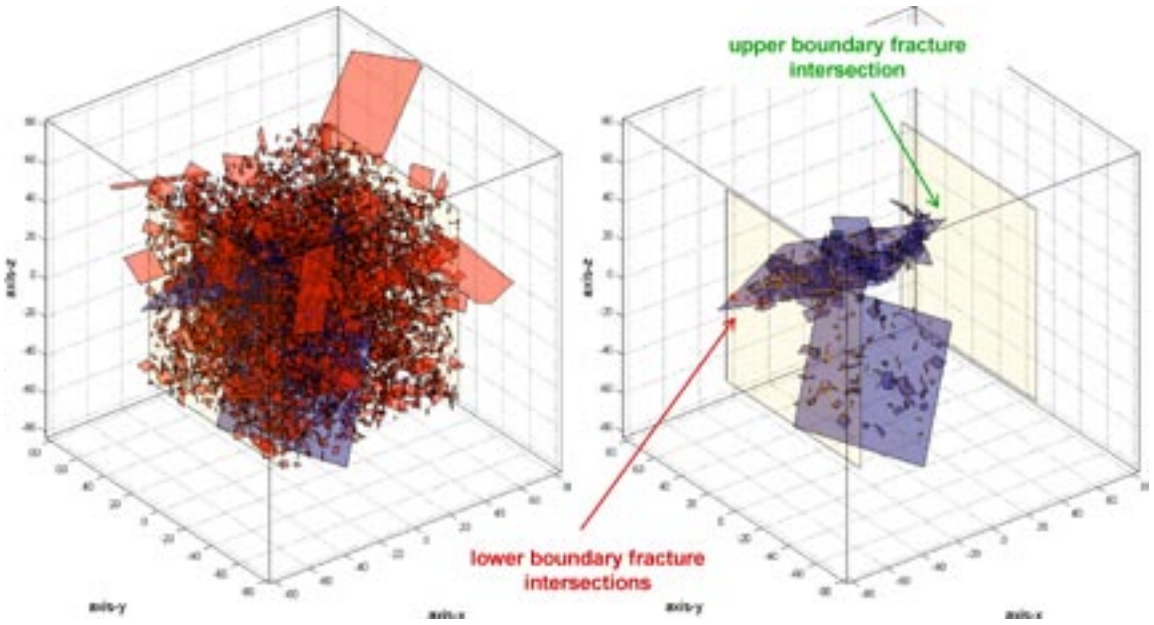

Figure D-2. *An example of a connectivity calculation result for a stochastically generated DFN (#242/1000). The connectivity is assessed for hypothetical flow along the WE direction (x-axis) between an upper (x = 50 m) and lower (x = –50 m) boundary plane. In the left-hand figure, connected fractures are coloured blue, whereas unconnected fractures are coloured red. The right-hand figure shows connected fractures only with fracture intersection traces coloured orange. Traces of intersection where the connected fractures cross the lower and upper boundaries are coloured red and green as indicated in the right-hand figure.*

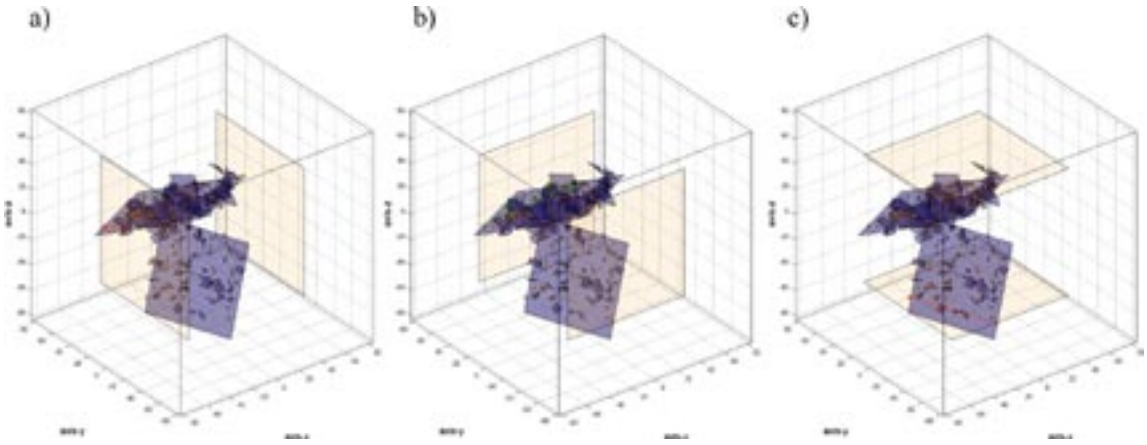

Figure D-3. *Example of connectivity calculation for the same DFN realisation as shown previously (#242/1000) for WE (x-axis), NS (y-axis), vertical (z-axis) flow. Only hydraulically connected fractures are visualised and it is clear that the same fracture cluster is responsible for connectivity along all three principal axes.*

If a DFN realisation possesses at least one fracture or fracture cluster that is connected between the upper and lower boundary planes of the system, then the DFN is considered to be hydraulically connected over the distance considered. Based upon the fraction of realisations that exhibit such connectivity relative to the total number of realisations, the probability of hydraulic connection can be calculated. This is referred to as the percolation probability in this report. The numerical results of the connectivity analysis have already been described in section 3.6.2, although the calculated percolation probability curve is shown again in Figure D-4 for illustrative purposes.

As can be seen from Figure D-4, there are very few DFN realisations that exhibit any kind of hydraulic connectivity over a distance of 100 m. The connectivity of FFM01c (< –400 m) has already been discussed in section 3.6.2 so will not be commented further here.

Having established the hydraulic connectivity status of a large number of stochastically generated DFN models, a number of possibilities exist for modelling flow in order to establish F-factors for typical flowpaths through the rock. One possibility was to import the connected fracture sets to make flow and particle tracking simulations using Napsac/ConnectFlow in a similar fashion to that done for the other fracture domains (FFM01a–b, FFM02, FFM03). The process of importing fracture sets to Napsac/ConnectFlow for a statistically significant number of realisations and carrying out simulations for different transport distances and along different axes of the simulation volume was found to be very tedious and not practical for the purposes of the site descriptive modelling. In addition, the program is not capable of making calculations involving conductive fracture intersection zones (FIZ) so is also less useful for assessing the impact of these conductive features on the hydrogeological properties of flowpaths through the rock.

Since it was not possible to use Napsac/ConnectFlow for these calculations, a simplified, "scoping calculation" approach to estimating the flow-related transport properties of the fracture networks was adopted. Overall the concept is similar to the pipe approximation technique used in PAWorks /Dershowitz et al. 2004/ although with some simplifications.

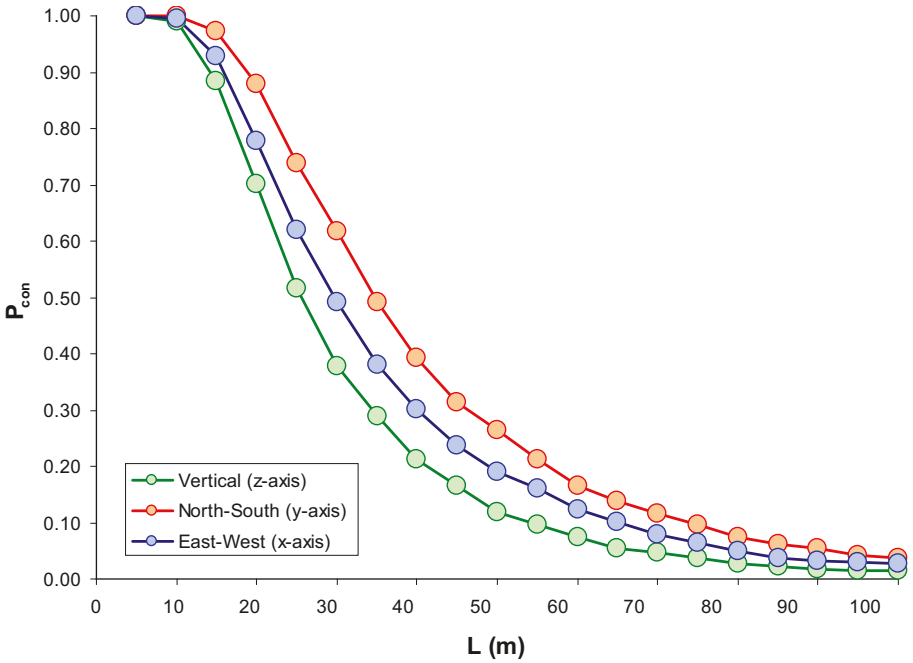

Figure D-4. *Results of connectivity analysis for FFM01c (< –400 m) based upon 1,000 stochastic realisations of the Hydro-DFN model. The percolation probability is plotted as a function of distance for the three principal axes of the model.*

For the case where fracture intersections are not considered to have high flow conductance, the midpoints of fracture intersections are assumed to be mixing nodes. For the cases where the fracture traces are considered to be highly transmissive (the FIZ-case), the mixing nodes are defined by the points of mutual closest approach between fracture traces. When considering all the possible pair-wise trace connections in a given fracture plane, this has the effect of leading to a somewhat larger number of mixing nodes in such cases. All mixing nodes internal to individual fracture traces are also linked by pipes. These pipes, however, are given an arbitrarily high conductance to simulate the properties of highly conductive FIZ. To avoid an excessive number of mixing nodes and pipes of trivial length in the resulting network description of the FIZ features, neighbouring nodes that reside within a certain critical distance (sub-millimetre) are merged thereby reducing the complexity of these features.

The pipe network analogue of the DFN is constructed by cycling through all connected fractures in sequence and successively building up an indexed list of 1D pipe elements representing pair-wise connections between all nodes residing in individual fracture planes. The conductance of a pipe element is proportional to the product of the transmissivity (i.e. of the fracture hosting the connection) and hypothetical flow channel width, and inversely proportional to the distance separating the end nodes of the pipe. This is the same relation as discussed in Appendix A (Equation A-2):

$$C_i = \frac{T_i W_i}{L_i} \qquad \text{(D-5)}$$

Additional nodes and pipes representing where fractures cross the notional upper and lower boundary planes are also included in the pipe network as starting and finishing points for flow and transport.

The main simplification inherent in this algorithm is that no consideration is given to the additional heuristic restrictions on pipe generation as employed in programs such as PAWorks (for more details concerning these heuristic rules see /Outters and Shuttle 2000/). This simplification essentially rules out the use of conventional particle tracking methods since the resulting F-factor distributions would give less a physically meaningful representation of the ensemble of flowpaths in the system. In spite of this, however, it is still possible to use the simplified pipe network topology to estimate a notional path of least resistance for the network using graph theory. Here, we are not so much interested in the distribution of F-factors arising due to flowpath heterogeneity, but rather what can we say about the most transmissive path through the system in a scoping calculation sense.

From the list of pipe elements, a weighted adjacency matrix is created based upon the pair-wise node connections where weights are assigned as the flow resistivity of the pipes (i.e. inverse of the pipe conductances). Finding the global path of least transport resistance involves first identifying the shortest weighted path from each source node on the lower boundary plane to any of the sink nodes resident on the upper boundary plane and then choosing the pathway that gives the lowest overall F-factor. The single-source, shortest path can be easily calculated using a suitable graph search algorithm in conjunction with the weighted adjacency matrix. For the calculations presented in this report, the implementation of Dijkstra's algorithm /Cormen et al. 2001/ in the Matlab Boost Graph Library /Gleich 2006/ was used. This gives the trajectory for least flow resistance through the network. Since the FIZ pipes are given arbitrarily high conductances, there is a tendency for the flow to seek out paths through these features if they exist.

Two hypothetical examples of a path of least resistance calculated in this fashion are illustrated in Figure D-5 for the case of neutrally conductive FIZ (left-hand image) and highly conductive FIZ (right-hand image) in a simple fracture cluster spanning two boundary planes along the x-axis.

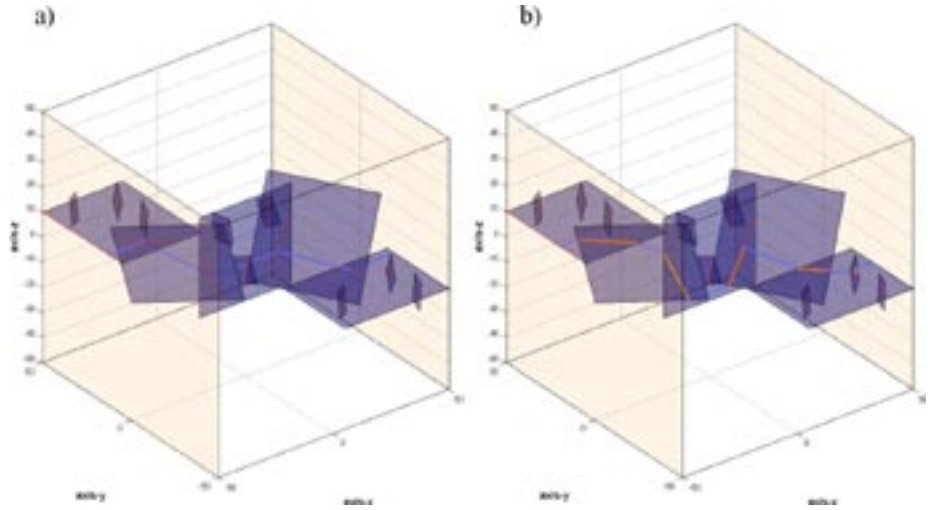

Figure D-5. *Simple example of a calculated path of least resistance for a hypothetical cluster of fractures featuring a) neutrally conductive FIZ, and b) highly conductive FIZ. The path of least resistance is shown as a light blue trajectory through the fracture network for in-plane flow pipes and coloured orange for FIZ flow pipe segments. Fracture traces of intersecting fractures are indicated as red lines. The upper and lower boundary planes for this simulation are visualised as lightly shaded polygons in the figure.*

The F-factor for the flowpath can be calculated for each single-source path by additionally assuming that it is the only feasible flowpath through the system. Although only a very rough approximation, this simplifies the problem to that of describing the properties of a single, although segmented and tortuous 1D flowpath connecting the upper and lower boundaries. By analogy with electrical networks, the total flow can be shown to be equal to the head differential of the terminal source and sink nodes, divided by the overall series resistance of the segments comprising the flowpath. Since FIZ pipes have negligible flow resistance, these can substantially reduce the overall flow resistance if they comprise a significant fraction of the total flow path length.

The flow-wetted surface in each pipe is taken to be proportional to the pipe length and width. Since the width of the flow pipe also determines the flow by way of the definition of the pipe conductance, the calculated F-factor is notionally independent of the width of the flow pipe. Therefore it makes no difference for the calculation of the F-factor what flow channel width is chosen. In the cases where flow and transport occurs via conductive FIZ pipes, on the other hand, we do need to specify the relative flow-wetted surface since they are assumed to have arbitrarily low flow resistance. Since we know very little about the geometry of the pore space within such feature we make the assumption that the flow-wetted surface per unit length of these features is no more than 1% of that for an in-plane flow pipe element. This would correspond to a pipe width of roughly 1 mm if the in-plane flow pipes are 10 cm in width. It should be noted that the aim of this exercise is to make scoping calculations of the possible impact of highly conductive FIZ, so the assumption of negligible flow resistance and much reduced flow-wetted surface could be considered very nearly a worst case scenario for conductive FIZ transport properties.

It should be noted that the “single flowpath approximation” described above is thought to always give lower F-factors than that which would be obtained if the full flow problem involving the entire pipe network is solved. This is because of the way the head field is distributed amongst the network nodes in a system comprising a combination of series and parallel resistances. The reliability of this assumption is discussed further as an addendum to this Appendix sub-chapter.

As mentioned previously, the global path of least transport resistance (PLTR) is obtained by choosing the lowest overall F-factor after making the same single source, shortest path calculation for each starting node resident on the lower boundary plane. This step gives the lowest F-factor for all identified pathways in the system where there may be multiple independent fracture clusters, each with different flow properties. A typical result of a path of least transport resistance calculated in this fashion is shown in Figure D-6 for neutrally conductive FIZ and Figure D-8 for highly conductive FIZ.

Using the simplified calculation procedure, the PLTR F-factor is found to be 2.8×10^6 y/m for the base case of neutrally conductive FIZ (Figure D-6) and 1.5×10^6 y/m for the highly conductive FIZ case (Figure D-7). Here, we have assumed the semi-correlated (SC) transmissivity model described in Table 3-2. In the highly conductive FIZ case the fraction of the flowpath length comprised of FIZ flow pipes is on the order of 46%, which in this particular case results in a decrease of the PLTR F-factor by about the same amount.

On the reliability of the single flowpath approximation

As discussed previously, the calculations to find the path of least transport resistance make the assumption that the identified flowpath represents the only viable flowpath through the system. This enables the description of flow and transport to be simplified considerably. An outstanding question, however, is whether this is a good measure of the "true" F-factor for the path of least transport resistance in the system and whether the measure given by this approximation is likely to give an overestimate of the F-factor for typical transport paths.

The first question is somewhat difficult to answer in a general sense as it is likely to vary substantially from realisation to realisation depending upon the complexity of the flow system. It is possible, however, to compare the results obtained using the full flow and particle tracking capabilities of Napsac/ConnectFlow for the same (imported) DFN realisation with those obtained using the approximate solution using 1D pipes (assuming a single flowpath through the system). This is shown in Figure D-8 for an early prototype based upon the Forsmark 1.2 Hydro-DFN model.

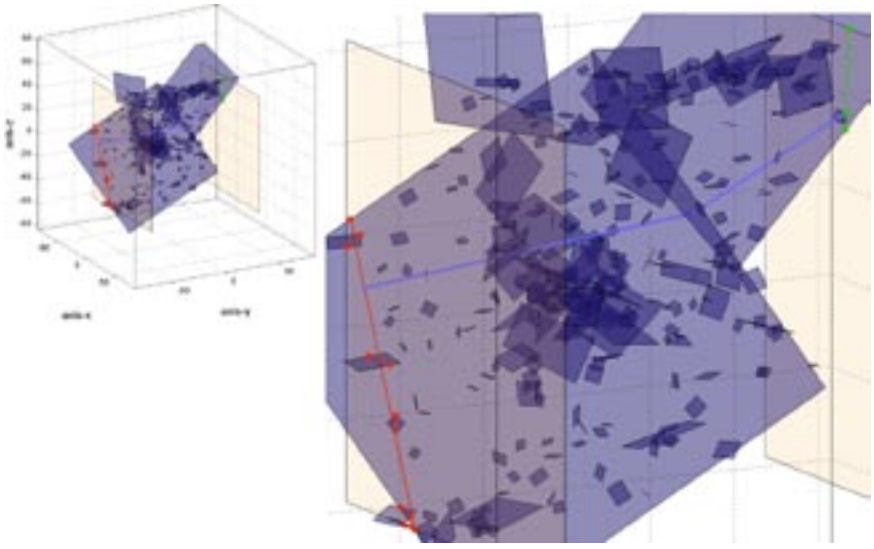

Figure D-6. *Trajectory of calculated path of least transport resistance, PLTR for a typical DFN realisation (#510/1000) of FFM01c (< 400 m) for the case of neutrally conductive FIZ. The PLTR is shown as a light blue trajectory through the fracture network and consists entirely of in-plane flow pipes. The upper and lower boundary planes for this simulation are visualised as lightly shaded polygons in the figure.*

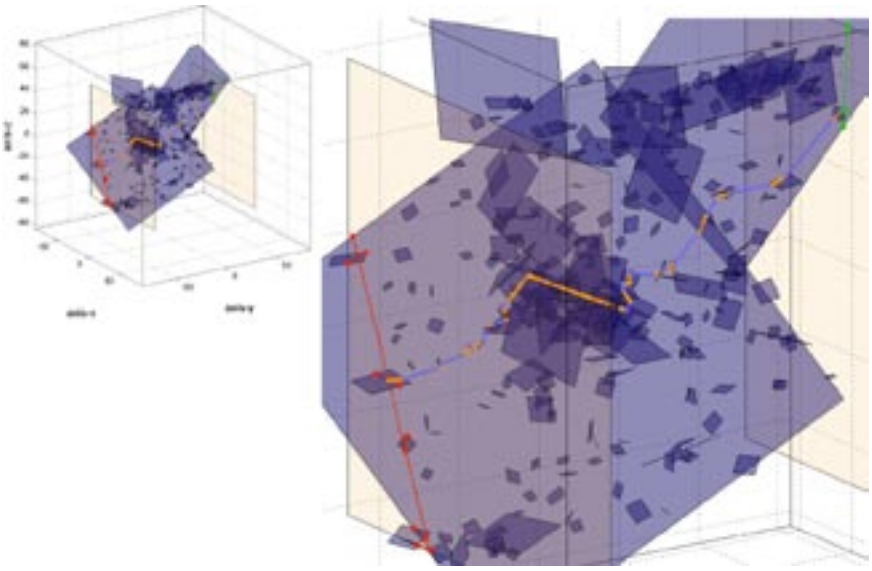

Figure D-7. *Trajectory of calculated path of least transport resistance, PLTR for a typical DFN realisation (#510/1000) of FFM01c (< 400 m) for the case of highly conductive FIZ. The PLTR is shown as a light blue trajectory through the fracture network for in-plane flow pipes and coloured orange for FIZ flow pipe segments. The upper and lower boundary planes for this simulation are visualised as lightly shaded polygons in the figure.*

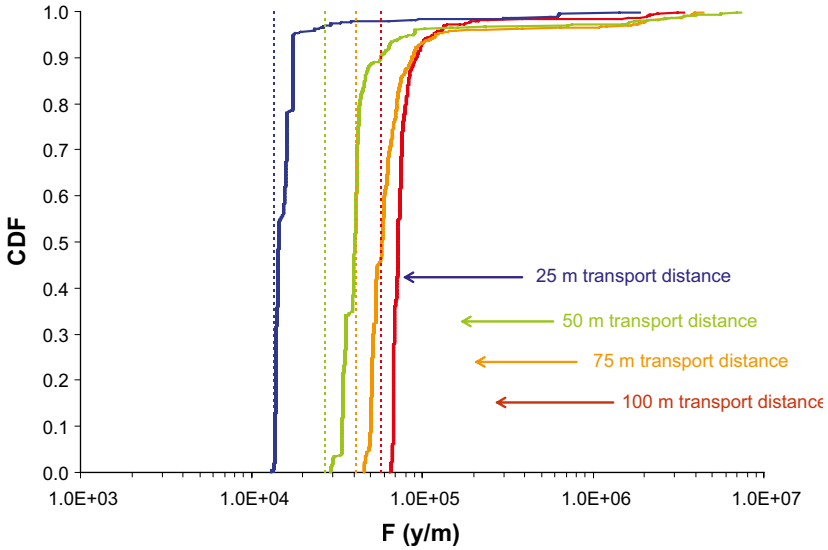

Figure D-8. *Comparison of cumulative F-factor distribution calculated using particle tracking within the Napsac/ConnectFlow program (solid curves) and the corresponding results obtained using the single flowpath approximation approach described in the text (vertical broken lines). Simulations are made for a connected fracture cluster over different transport distances.*

As can be seen from the figure above, the single flowpath approximation allows us to calculate a path of least transport resistance that predicts the leading edge of the F-factor distribution from the full flow and particle tracking simulation of a DFN network with reasonable accuracy. On the basis of this comparative simulation, the simplification afforded by the single flowpath approximation appears at face value to give a good estimate of the path of least transport resistance.

Although we do not have a formal proof for this in generalised, complex flow networks it is relatively straight-forward to demonstrate theoretically for the simplest of hydraulic systems consisting of one series and two parallel resistances as illustrated in Figure D-9.

If we were to treat the parallel connected flow system depicted in Figure D-9 as a "full" flow problem where we consider both branches of the circuit simultaneously, the path of least transport resistance would be given by:

$$\left.\begin{aligned} Q_1 &= \frac{(1+\alpha)\Delta H}{(1+2\alpha)R_1} \\ Q_2 &= \frac{\alpha}{(1+\alpha)}Q_1 \\ Q_3 &= \frac{1}{(1+\alpha)}Q_1 \end{aligned}\right\} F_{PLTR} = \frac{fws_1}{Q_1} + \min\left[\frac{fws_2}{Q_2}, \frac{fws_3}{Q_3}\right] \qquad \text{(D-6)}$$

Where fws_i is the flow-wetted surface of segment i, ΔH is the overall potential difference (i.e. head boundary condition), and α is the ratio of flow resistances in the parallel branches of the flowpath.

If, on the other hand, we were to treat path A and path B using the single flowpath approximation, the path of least transport resistance would instead be given by:

$$\left.\begin{aligned} Path\ A:\ Q_1 &= Q_2 = \frac{\Delta H}{2R_1} \\ Path\ B:\ Q_1 &= Q_3 = \frac{\Delta H}{(1+\alpha)R_1} \end{aligned}\right\} F_{PLTR} = \frac{fws_1}{Q_1} + \min\left[\frac{fws_2}{Q_2}, \frac{fws_3}{Q_3}\right] \qquad \text{(D-7)}$$

It can be shown numerically that the F-factor given by Equation D-7 will always be less than or equal to that given by Equation D-6 for all conceivable positive α. This is shown in Figure D-10 for α varied in the range 0.01–100 and an assumed constant flow-wetted surface in each segment.

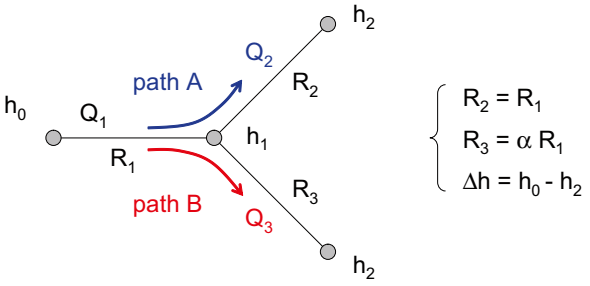

Figure D-9. *Hypothetical flow system containing a combination of series and parallel resistances. The estimated path of least transport resistance will always be less if the pathways A and B are considered as distinct and separate entities than if they are considered together as part of a parallel flowpath.*

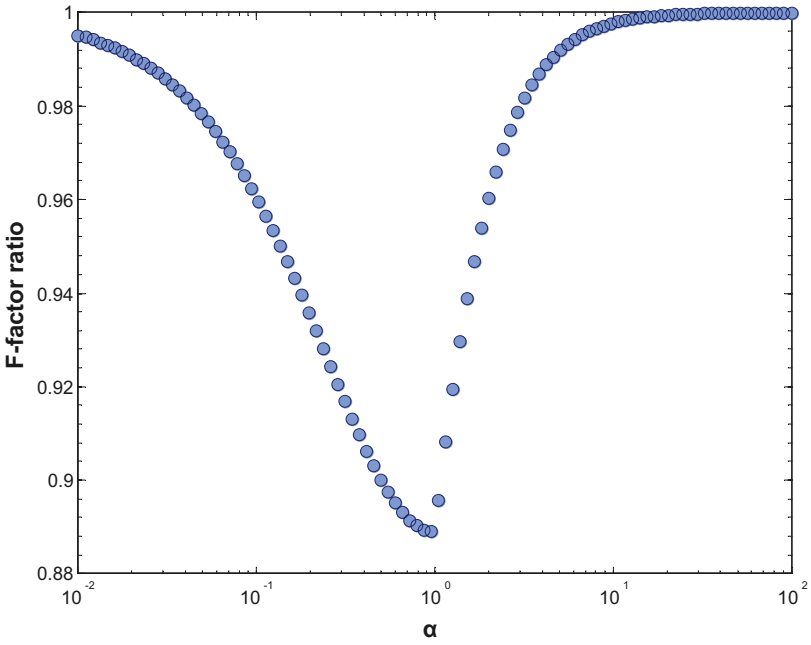

Figure D-10. *Ratio of F-factors calculated using Equation D-7 and D-6 for the path of least transport resistance. The results suggest that the single path approximation will always give a lower F-factor than if the whole flow system is solved as a conventional flow and transport problem.*

It should be noted that values of α outside of the range considered are trivial since the problem then effectively collapses to a single flowpath when one branch has a significantly larger resistivity than the other.

The calculations above indicate that the single flowpath approximation does not overestimate the F-factor for the identified PLTR flowpath which means that it should be cautiously realistic in a scoping calculation sense.

Modelling results for FFM01c (< –400 m)

The following sections contain a detailed account of the modelling results for FFM01c (< –400 m) considering transport along the different principal axes of the system and for different transport distances and transmissivity-size correlations.

Transport along the North-South axis

Results for PLTR F-factor scoping calculations assuming a semi-correlated (SC) transmissivity model are shown in Figure D-11.

Summary statistics for the cases illustrated in Figure D-11 are given in Table D-1.

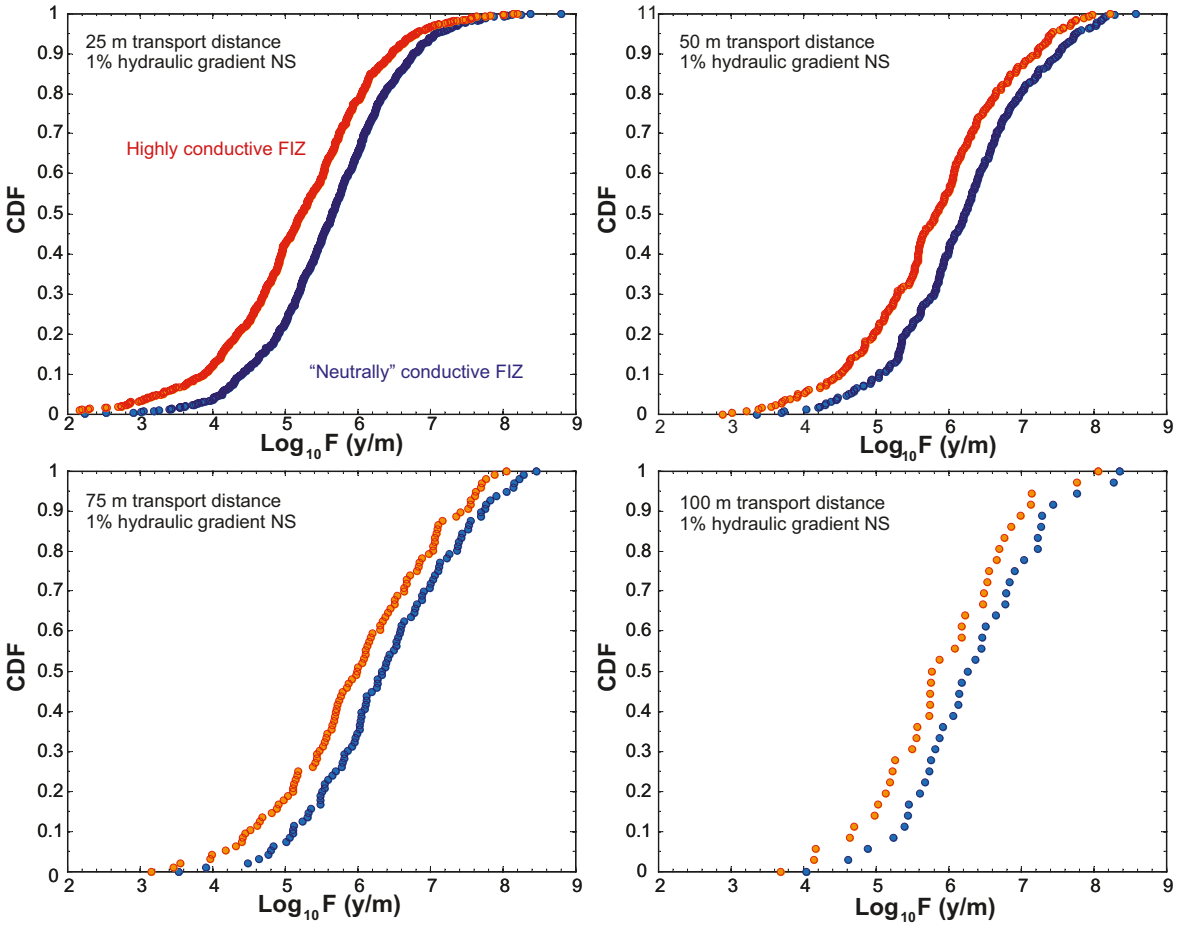

Figure D-11. *Typical F-factor ranges for paths of least transport resistance, PLTR in the immediate far field (IFF) based upon 1,000 realisations of the Hydro-DFN for FFM01c (< –400 m). The calculations consider different transport distances, an assumed hydraulic gradient of 1% applied along the North-South axis, and a semi-correlated fracture length-transmissivity (SC) model. Results are given for the case of neutrally conductive FIZ (blue markers) and highly conductive FIZ (orange markers) and are plotted as cumulative distribution probability curves.*

Table D-1. Summary statistics for the F-factor (log_{10} units) corresponding to the pooled particle residence time distribution data for FFM01c (< –400 m), different transport distances, and a hydraulic gradient of 1%. Results are given for both the neutrally conductive FIZ case and highly-conductive FIZ case.

	Neutrally conductive FIZ				Highly-conductive FIZ			
Semi-Correlated (SC)	**25 m**	**50 m**	**75 m**	**100 m**	**25 m**	**50 m**	**75 m**	**100 m**
Mean	5.64	6.22	6.38	6.32	5.14	5.80	5.97	5.90
Median	5.65	6.22	6.34	6.26	5.23	5.83	5.99	5.77
5th percentile	4.13	4.62	4.78	4.71	3.32	3.92	4.06	4.15
10th percentile	4.41	5.05	5.11	5.27	3.89	4.49	4.47	4.65
25th percentile	5.05	5.61	5.69	5.72	4.56	5.12	5.18	5.23
75th percentile	6.24	6.82	7.12	6.94	5.89	6.48	6.83	6.59
90th percentile	6.77	7.53	7.75	7.41	6.48	7.23	7.51	7.11
95th percentile	7.09	7.76	8.11	8.10	6.81	7.43	7.67	7.55
Std. deviation	0.93	0.94	1.01	0.95	1.32	1.03	1.09	0.99
Variance	0.86	0.89	1.03	0.91	1.73	1.05	1.18	0.98
Min value	2.24	3.36	3.54	4.04	–4.16	2.89	3.16	3.69
Max value	8.81	8.58	8.47	8.36	8.21	8.23	8.05	8.06
Connected fraction (%)	73.80	26.50	9.70	3.70	73.80	26.50	9.70	3.70

Results for PLTR F-factor scoping calculations assuming a fully-correlated (FC) transmissivity model are shown in Figure D-12.

Summary statistics for the cases illustrated in Figure D-12 are given in Table D-2.

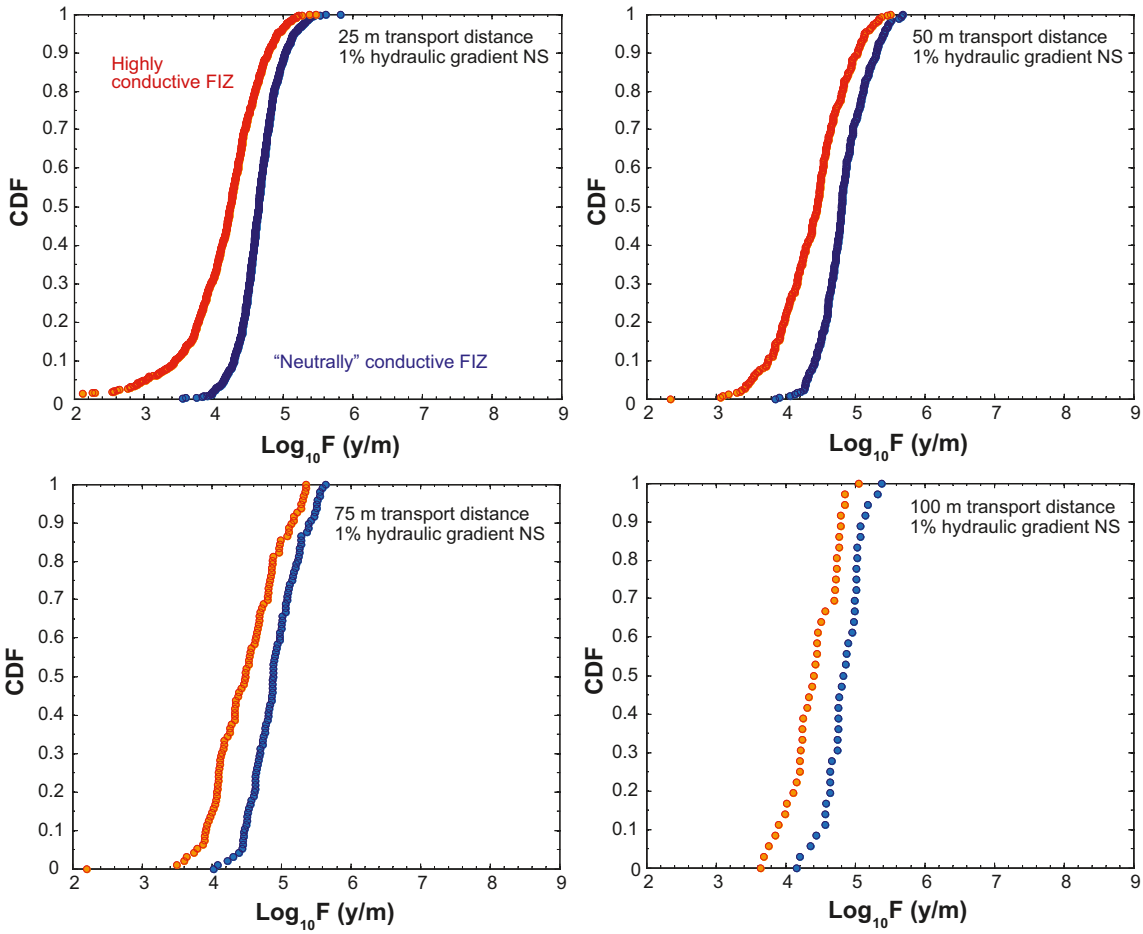

Figure D-12. *Typical F-factor ranges for paths of least transport resistance, PLTR in the immediate far field (IFF) based upon 1,000 realisations of the Hydro-DFN for FFM01c (< –400 m). The calculations consider different transport distances, an assumed hydraulic gradient of 1% applied along the North-South axis, and a fully-correlated fracture length-transmissivity (FC) model. Results are given for the case of neutrally conductive FIZ (blue markers) and highly conductive FIZ (orange markers) and are plotted as cumulative distribution probability curves.*

Table D-2. Summary statistics for the F-factor (log_{10} units) corresponding to the pooled particle residence time distribution data for FFM01c (< –400 m), different transport distances, and a hydraulic gradient of 1%. Results are given for both the neutrally conductive FIZ case and highly-conductive FIZ case.

	Neutrally conductive FIZ				Highly-conductive FIZ			
Fully-Correlated (FC)	**25 m**	**50 m**	**75 m**	**100 m**	**25 m**	**50 m**	**75 m**	**100 m**
Mean	4.66	4.84	4.91	4.83	4.11	4.40	4.48	4.39
Median	4.65	4.81	4.88	4.82	4.25	4.46	4.49	4.41
5th percentile	4.16	4.30	4.41	4.26	3.05	3.51	3.77	3.71
10th percentile	4.30	4.42	4.47	4.46	3.46	3.75	3.91	3.86
25th percentile	4.48	4.62	4.64	4.65	3.88	4.06	4.10	4.19
75th percentile	4.83	5.05	5.17	5.02	4.52	4.72	4.85	4.73
90th percentile	5.04	5.31	5.42	5.13	4.79	5.04	5.18	4.79
95th percentile	5.17	5.42	5.52	5.27	4.92	5.14	5.30	4.85
Std. deviation	0.30	0.33	0.35	0.28	0.92	0.50	0.51	0.36
Variance	0.09	0.11	0.12	0.08	0.84	0.25	0.27	0.13
Min value	3.56	3.86	4.03	4.16	–4.16	2.35	2.20	3.64
Max value	5.83	5.68	5.64	5.39	5.47	5.51	5.36	5.06
Connected fraction (%)	73.80	26.50	9.70	3.70	73.80	26.50	9.70	3.70

Results for PLTR F-factor scoping calculations assuming a non-correlated (NC) transmissivity model are shown in Figure D-13.

Summary statistics for the cases illustrated in Figure D-13 are given in Table D-3.

Table D-3. Summary statistics for the F-factor (log_{10} units) corresponding to the pooled particle residence time distribution data for FFM01c (< –400 m), different transport distances, and a hydraulic gradient of 1%. Results are given for both the neutrally conductive FIZ case and highly-conductive FIZ case.

	Neutrally conductive FIZ				Highly-conductive FIZ			
Non-Correlated (NC)	**25 m**	**50 m**	**75 m**	**100 m**	**25 m**	**50 m**	**75 m**	**100 m**
Mean	4.35	4.97	5.09	5.31	3.87	4.55	4.66	4.88
Median	4.33	5.03	5.15	5.33	3.92	4.51	4.67	4.81
5th percentile	2.89	3.59	3.74	3.93	2.20	2.82	2.98	3.48
10th percentile	3.24	3.89	4.07	4.16	2.70	3.40	3.44	3.72
25th percentile	3.78	4.50	4.63	4.72	3.30	3.96	4.13	4.14
75th percentile	4.94	5.51	5.62	5.68	4.55	5.19	5.24	5.31
90th percentile	5.47	6.03	6.11	6.50	5.13	5.74	5.91	6.04
95th percentile	5.82	6.30	6.42	7.32	5.48	6.01	6.09	6.99
Std. deviation	0.90	0.87	0.85	0.90	1.21	0.95	0.93	0.95
Variance	0.80	0.76	0.72	0.82	1.47	0.91	0.87	0.90
Min value	1.38	2.11	2.54	3.65	–4.16	1.52	2.08	3.26
Max value	7.55	7.79	7.54	7.40	7.25	7.60	7.29	7.05
Connected fraction (%)	73.80	26.50	9.70	3.70	73.80	26.50	9.70	3.70

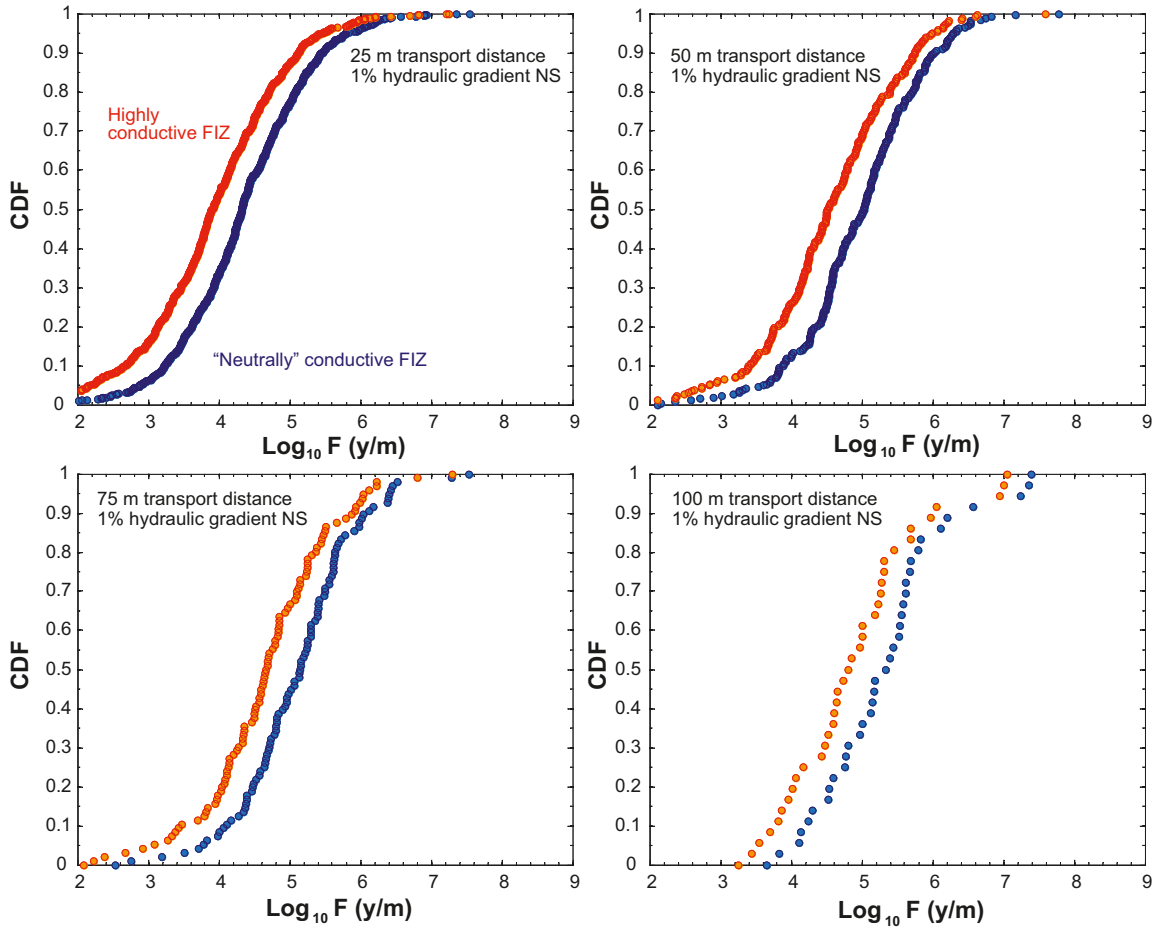

Figure D-13. *Typical F-factor ranges for paths of least transport resistance, PLTR in the immediate far field (IFF) based upon 1,000 realisations of the Hydro-DFN for FFM01c (< –400 m). The calculations consider different transport distances, an assumed hydraulic gradient of 1% applied along the North-South axis, and a non-correlated fracture transmissivity (NC) model. Results are given for the case of neutrally conductive FIZ (blue markers) and highly conductive FIZ (orange markers) and are plotted as cumulative distribution probability curves.*

Transport along the West-East axis

Results for PLTR F-factor scoping calculations assuming a semi-correlated (SC) transmissivity model are shown in Figure D-14.

Summary statistics for the cases illustrated in Figure D-14 are given in Table D-4.

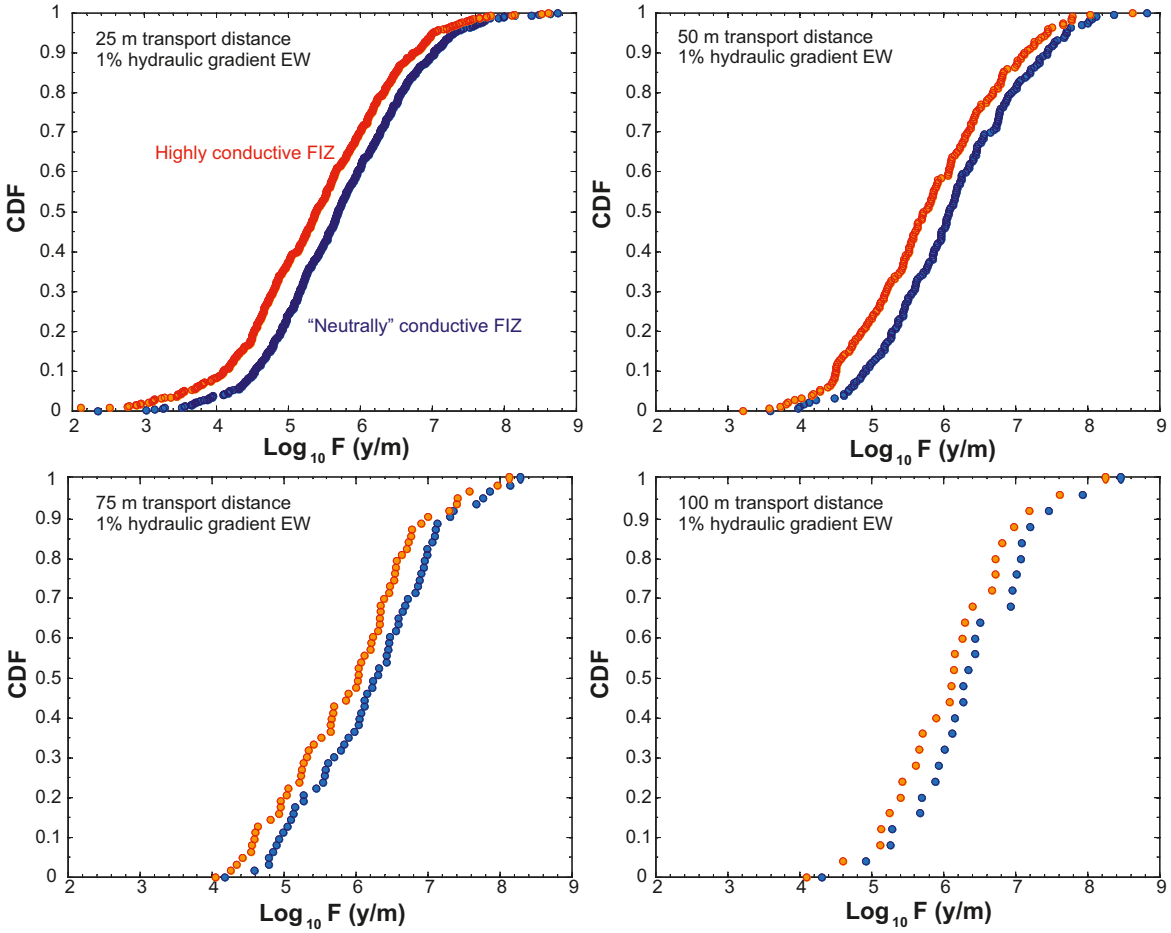

Figure D-14. *Typical F-factor ranges for paths of least transport resistance, PLTR in the immediate far field (IFF) based upon 1,000 realisations of the Hydro-DFN for FFM01c (< –400 m). The calculations consider different transport distances, an assumed hydraulic gradient of 1% applied along the West-East axis, and a semi-correlated fracture length-transmissivity (SC) model. Results are given for the case of neutrally conductive FIZ (blue markers) and highly conductive FIZ (orange markers) and are plotted as cumulative distribution probability curves.*

Table D-4. Summary statistics for the F-factor (log_{10} units) corresponding to the pooled particle residence time distribution data for FFM01c (< –400 m), different transport distances, and a hydraulic gradient of 1%. Results are given for both the neutrally conductive FIZ case and highly-conductive FIZ case.

	Neutrally conductive FIZ				Highly-conductive FIZ			
Semi-Correlated (SC)	**25 m**	**50 m**	**75 m**	**100 m**	**25 m**	**50 m**	**75 m**	**100 m**
Mean	5.74	6.13	6.22	6.37	5.37	5.79	5.91	6.09
Median	5.70	6.08	6.28	6.31	5.39	5.72	6.03	6.13
5th percentile	4.19	4.68	4.80	4.80	3.56	4.28	4.41	4.51
10th percentile	4.54	4.91	4.94	5.27	4.10	4.50	4.59	5.12
25th percentile	5.04	5.44	5.56	5.89	4.66	5.07	5.23	5.43
75th percentile	6.43	6.78	6.91	7.02	6.17	6.46	6.54	6.73
90th percentile	7.03	7.45	7.32	7.43	6.77	7.14	7.04	7.17
95th percentile	7.32	7.72	7.80	8.04	7.03	7.45	7.47	7.74
Std. deviation	0.99	0.96	0.92	0.92	1.24	1.01	0.94	0.92
Variance	0.99	0.93	0.85	0.85	1.55	1.01	0.89	0.84
Min value	2.36	3.59	4.18	4.31	–4.11	3.21	4.06	4.10
Max value	9.62	8.83	8.28	8.46	9.47	8.63	8.13	8.25
Connected fraction (%)	61.90	19.10	6.40	2.60	61.90	19.10	6.40	2.60

Results for PLTR F-factor scoping calculations assuming a fully-correlated (FC) transmissivity model are shown in Figure D-15.

Summary statistics for the cases illustrated in Figure D-15 are given in Table D-5.

Table D-5. Summary statistics for the F-factor (log_{10} units) corresponding to the pooled particle residence time distribution data for FFM01c (< –400 m), different transport distances, and a hydraulic gradient of 1%. Results are given for both the neutrally conductive FIZ case and highly-conductive FIZ case.

	Neutrally conductive FIZ				Highly-conductive FIZ			
Fully-Correlated (FC)	**25 m**	**50 m**	**75 m**	**100 m**	**25 m**	**50 m**	**75 m**	**100 m**
Mean	4.67	4.77	4.79	4.78	4.29	4.43	4.47	4.50
Median	4.64	4.76	4.71	4.74	4.34	4.44	4.38	4.47
5th percentile	4.12	4.29	4.30	4.21	3.52	3.81	3.87	3.78
10th percentile	4.28	4.38	4.41	4.40	3.74	3.98	3.99	3.94
25th percentile	4.47	4.58	4.54	4.59	4.04	4.16	4.20	4.33
75th percentile	4.86	4.92	5.06	4.92	4.64	4.64	4.79	4.76
90th percentile	5.16	5.22	5.27	5.24	4.93	4.99	5.03	4.99
95th percentile	5.28	5.41	5.55	5.30	5.11	5.23	5.27	5.05
Std. deviation	0.34	0.33	0.37	0.32	0.75	0.41	0.42	0.36
Variance	0.12	0.11	0.14	0.10	0.56	0.17	0.18	0.13
Min value	3.56	3.86	4.03	4.16	–4.11	3.20	3.55	3.74
Max value	6.11	5.82	5.81	5.49	5.84	5.58	5.53	5.22
Connected fraction (%)	61.90	19.10	6.40	2.60	61.90	19.10	6.40	2.60

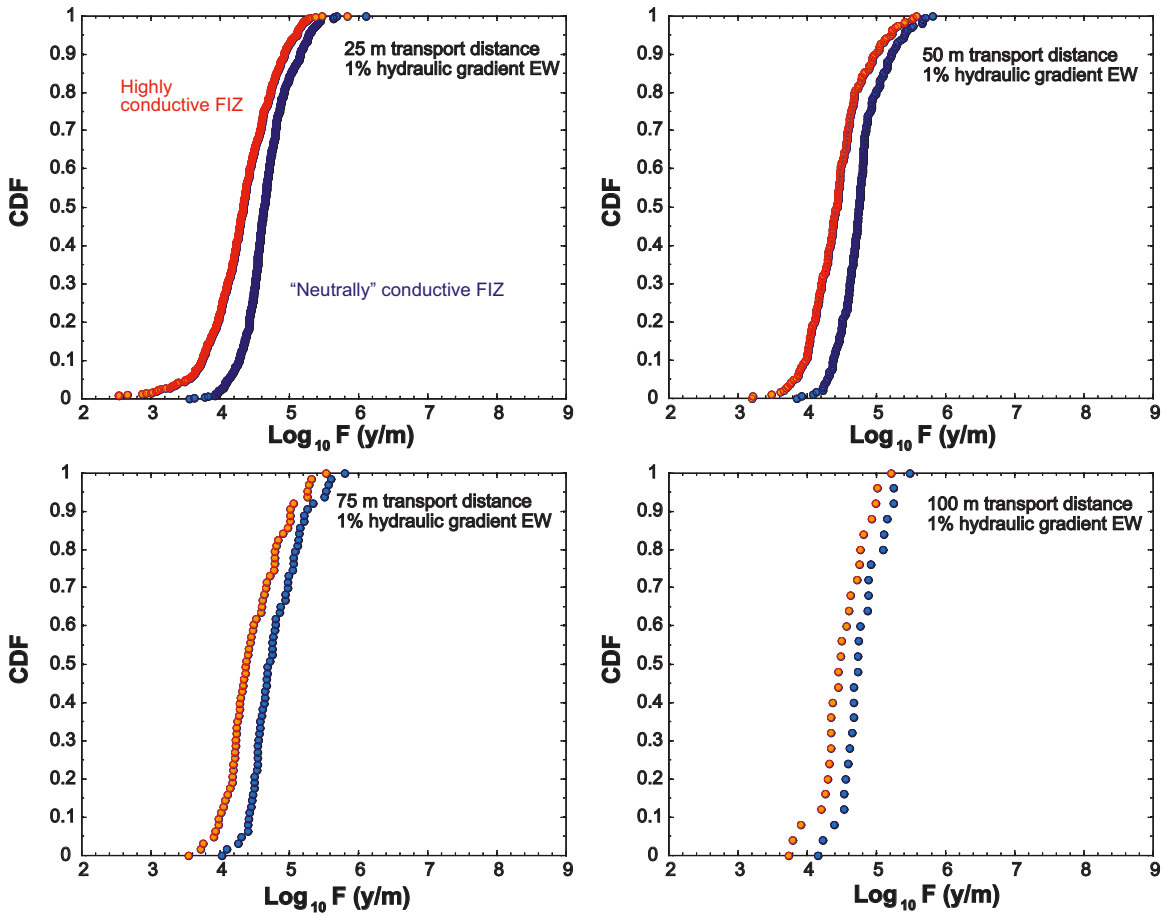

Figure D-15. *Typical F-factor ranges for paths of least transport resistance, PLTR in the immediate far field (IFF) based upon 1,000 realisations of the Hydro-DFN for FFM01c (< –400 m). The calculations consider different transport distances, an assumed hydraulic gradient of 1% applied along the West-East axis, and a fully-correlated fracture length-transmissivity (FC) model. Results are given for the case of neutrally conductive FIZ (blue markers) and highly conductive FIZ (orange markers) and are plotted as cumulative distribution probability curves.*

Results for PLTR F-factor scoping calculations assuming a non-correlated (NC) transmissivity model are shown in Figure D-16.

Summary statistics for the cases illustrated in Figure D-16 are given in Table D-6.

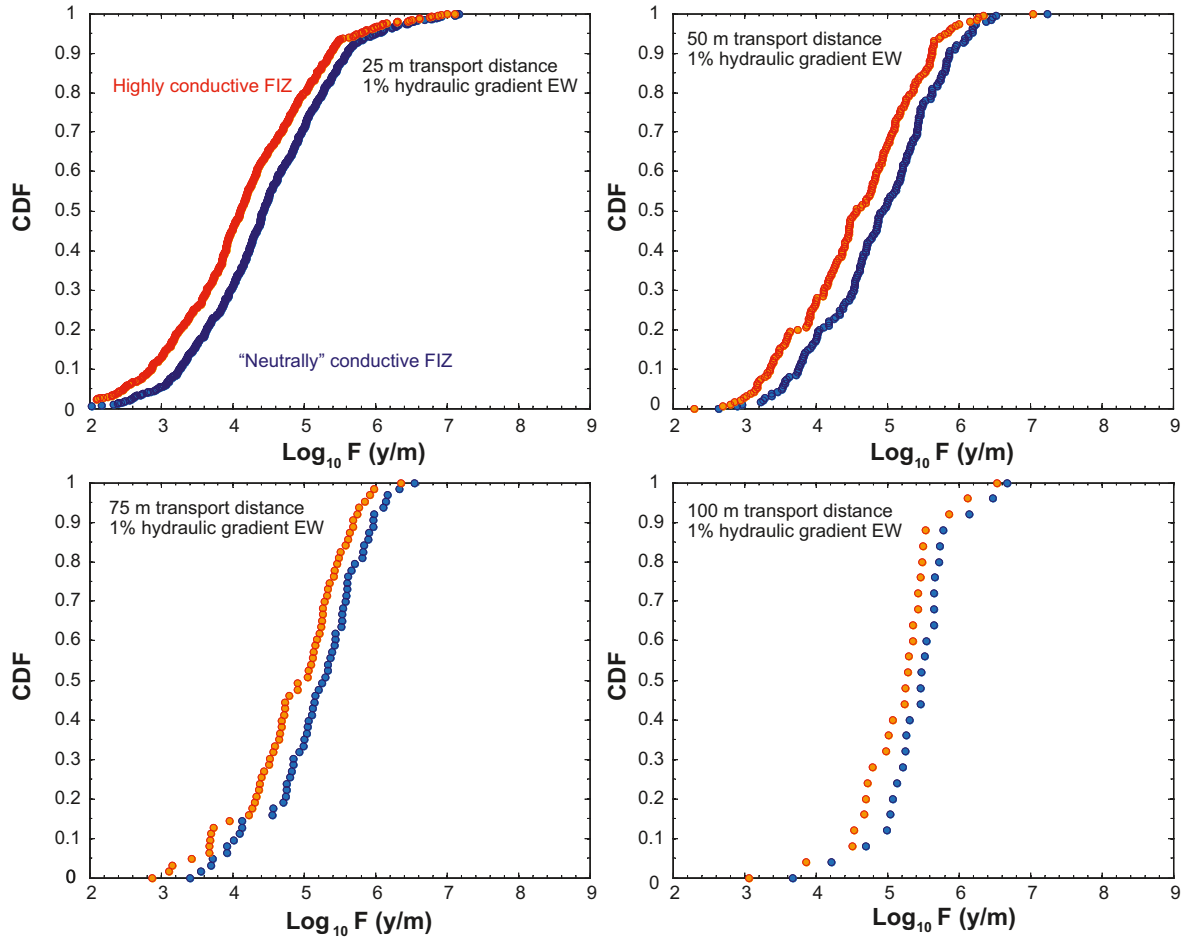

Figure D-16. *Typical F-factor ranges for paths of least transport resistance, PLTR in the immediate far field (IFF) based upon 1,000 realisations of the Hydro-DFN for FFM01c (< –400 m). The calculations consider different transport distances, an assumed hydraulic gradient of 1% applied along the West-East axis, and a non-correlated fracture transmissivity (NC) model. Results are given for the case of neutrally conductive FIZ (blue markers) and highly conductive FIZ (orange markers) and are plotted as cumulative distribution probability curves.*

Table D-6. Summary statistics for the F-factor (log_{10} units) corresponding to the pooled particle residence time distribution data for FFM01c (< –400 m), different transport distances, and a hydraulic gradient of 1%. Results are given for both the neutrally conductive FIZ case and highly-conductive FIZ case.

	Neutrally conductive FIZ				Highly-conductive FIZ			
Non-Correlated (NC)	**25 m**	**50 m**	**75 m**	**100 m**	**25 m**	**50 m**	**75 m**	**100 m**
Mean	4.46	4.90	5.16	5.41	4.11	4.56	4.84	5.12
Median	4.43	4.94	5.28	5.47	4.11	4.57	4.99	5.27
5th percentile	2.95	3.52	3.71	4.11	2.48	3.16	3.35	3.71
10th percentile	3.25	3.76	4.00	4.73	2.87	3.36	3.69	4.52
25th percentile	3.84	4.35	4.78	5.14	3.46	3.94	4.40	4.72
75th percentile	5.10	5.47	5.61	5.66	4.84	5.19	5.39	5.47
90th percentile	5.61	5.87	5.97	6.11	5.37	5.63	5.70	5.83
95th percentile	6.03	6.19	6.15	6.51	5.81	5.85	5.87	6.21
Std. deviation	0.96	0.84	0.72	0.61	1.15	0.86	0.76	0.68
Variance	0.92	0.70	0.52	0.38	1.32	0.75	0.58	0.47
Min value	0.37	2.64	3.41	3.68	–4.11	2.30	2.88	3.07
Max value	7.17	7.25	6.55	6.68	7.11	7.05	6.36	6.54
Connected fraction (%)	61.90	19.10	6.40	2.60	61.90	19.10	6.40	2.60

Transport along the vertical axis

Results for PLTR F-factor scoping calculations assuming a semi-correlated (SC) transmissivity model are shown in Figure D-17.

Summary statistics for the cases illustrated in Figure D-17 are given in Table D-7.

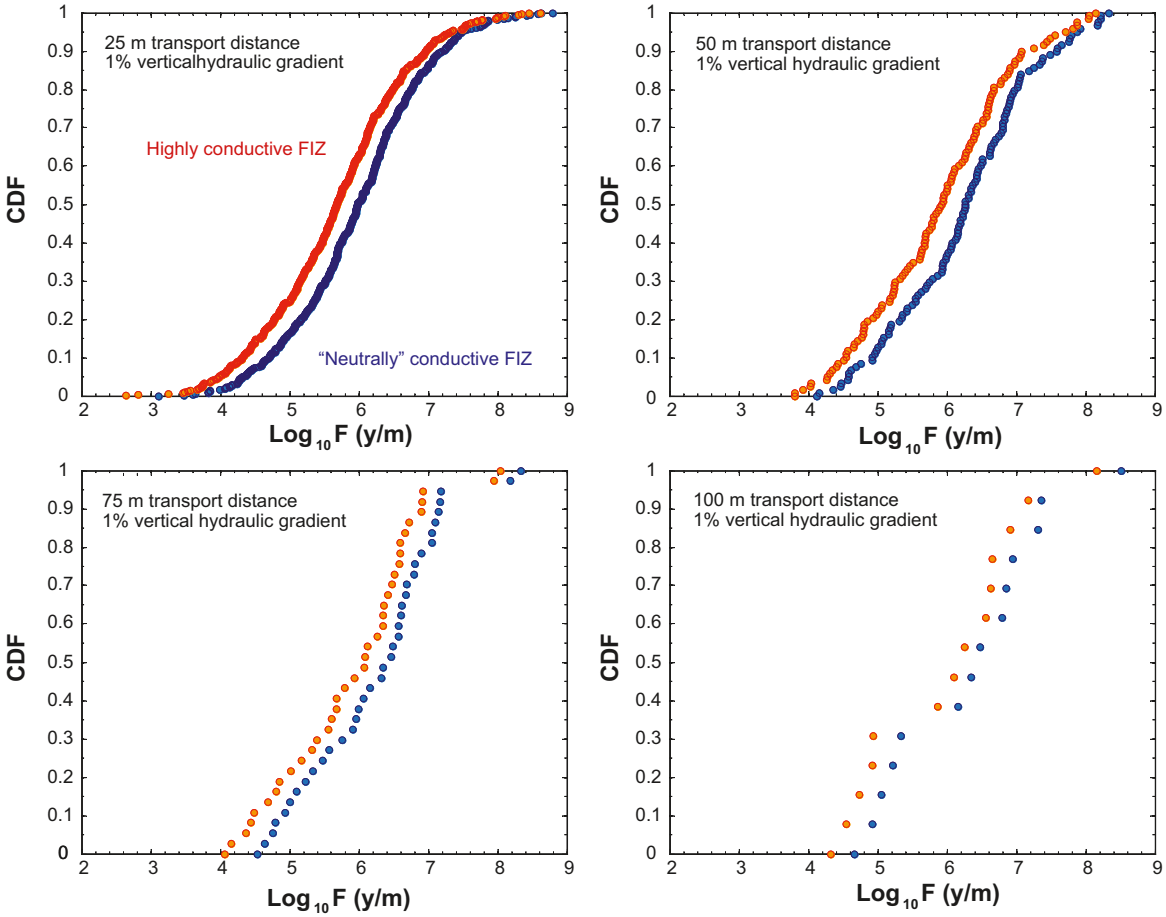

Figure D-17. *Typical F-factor ranges for paths of least transport resistance, PLTR in the immediate far field (IFF) based upon 1,000 realisations of the Hydro-DFN for FFM01c (< –400 m). The calculations consider different transport distances, an assumed hydraulic gradient of 1% applied along the vertical axis, and a semi-correlated fracture length-transmissivity (SC) model. Results are given for the case of neutrally conductive FIZ (blue markers) and highly conductive FIZ (orange markers) and are plotted as cumulative distribution probability curves.*

Table D-7. Summary statistics for the F-factor (log_{10} units) corresponding to the pooled particle residence time distribution data for FFM01c (< –400 m), different transport distances, and a hydraulic gradient of 1%. Results are given for both the neutrally conductive FIZ case and highly-conductive FIZ case.

	Neutrally conductive FIZ				Highly-conductive FIZ			
Semi-Correlated (SC)	**25 m**	**50 m**	**75 m**	**100 m**	**25 m**	**50 m**	**75 m**	**100 m**
Mean	5.98	6.24	6.22	6.28	5.65	5.89	5.89	5.98
Median	5.98	6.26	6.41	6.41	5.68	5.92	6.08	6.18
5th percentile	4.32	4.57	4.69	4.71	3.98	4.27	4.25	4.37
10th percentile	4.70	4.92	4.84	4.90	4.32	4.52	4.46	4.53
25th percentile	5.36	5.55	5.48	5.22	5.01	5.17	5.18	4.92
75th percentile	6.59	6.88	6.80	6.95	6.32	6.60	6.58	6.66
90th percentile	7.22	7.59	7.17	7.47	6.97	7.18	6.91	7.27
95th percentile	7.48	7.90	7.78	8.28	7.34	7.77	7.54	7.96
Std. deviation	0.96	0.99	0.94	1.12	1.10	1.02	0.98	1.14
Variance	0.92	0.97	0.88	1.25	1.21	1.05	0.95	1.30
Min value	3.11	4.13	4.54	4.66	–4.25	3.80	4.06	4.33
Max value	8.80	8.33	8.33	8.51	8.62	8.14	8.04	8.16
Connected fraction (%)	51.60	11.90	3.80	1.40	51.60	11.90	3.80	1.40

Results for PLTR F-factor scoping calculations assuming a fully-correlated (FC) transmissivity model are shown in Figure D-18.

Summary statistics for the cases illustrated in Figure D-18 are given in Table D-8.

Table D-8. Summary statistics for the F-factor (log_{10} units) corresponding to the pooled particle residence time distribution data for FFM01c (< –400 m), different transport distances, and a hydraulic gradient of 1%. Results are given for both the neutrally conductive FIZ case and highly-conductive FIZ case.

	Neutrally conductive FIZ				Highly-conductive FIZ			
Fully-Correlated (FC)	**25 m**	**50 m**	**75 m**	**100 m**	**25 m**	**50 m**	**75 m**	**100 m**
Mean	4.77	4.88	4.95	4.96	4.42	4.52	4.61	4.66
Median	4.74	4.79	4.94	4.90	4.48	4.45	4.61	4.63
5th percentile	4.24	4.38	4.52	4.63	3.61	3.86	3.85	4.09
10th percentile	4.34	4.46	4.55	4.67	3.81	3.99	4.05	4.22
25th percentile	4.53	4.62	4.72	4.69	4.16	4.28	4.34	4.38
75th percentile	4.98	5.12	5.23	5.05	4.76	4.79	4.83	4.79
90th percentile	5.28	5.36	5.42	5.47	5.03	5.17	5.27	5.21
95th percentile	5.38	5.48	5.60	5.60	5.19	5.26	5.36	5.33
Std. deviation	0.34	0.34	0.33	0.32	0.61	0.44	0.44	0.36
Variance	0.12	0.12	0.11	0.10	0.37	0.19	0.19	0.13
Min value	3.95	4.26	4.48	4.62	–4.25	2.96	3.73	4.06
Max value	5.85	5.67	5.65	5.64	5.61	5.51	5.41	5.36
Connected fraction (%)	51.60	11.90	3.80	1.40	51.60	11.90	3.80	1.40

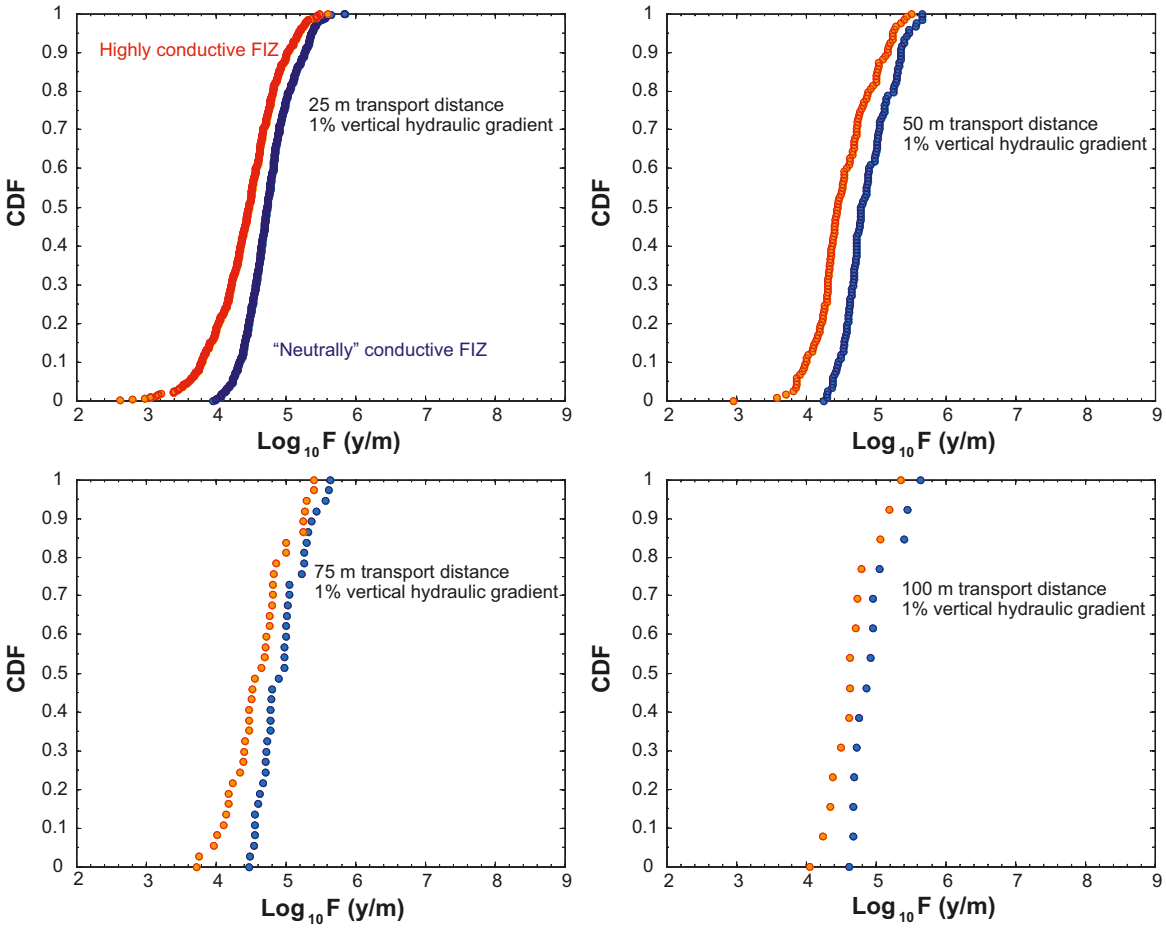

Figure D-18. *Typical F-factor ranges for paths of least transport resistance, PLTR in the immediate far field (IFF) based upon 1,000 realisations of the Hydro-DFN for FFM01c (< –400 m). The calculations consider different transport distances, an assumed hydraulic gradient of 1% applied along the vertical axis, and a fully-correlated fracture length-transmissivity (FC) model. Results are given for the case of neutrally conductive FIZ (blue markers) and highly conductive FIZ (orange markers) and are plotted as cumulative distribution probability curves.*

Results for PLTR F-factor scoping calculations assuming a non-correlated (NC) transmissivity model are shown in Figure D-19.

Summary statistics for the cases illustrated in Figure D-19 are given in Table D-9.

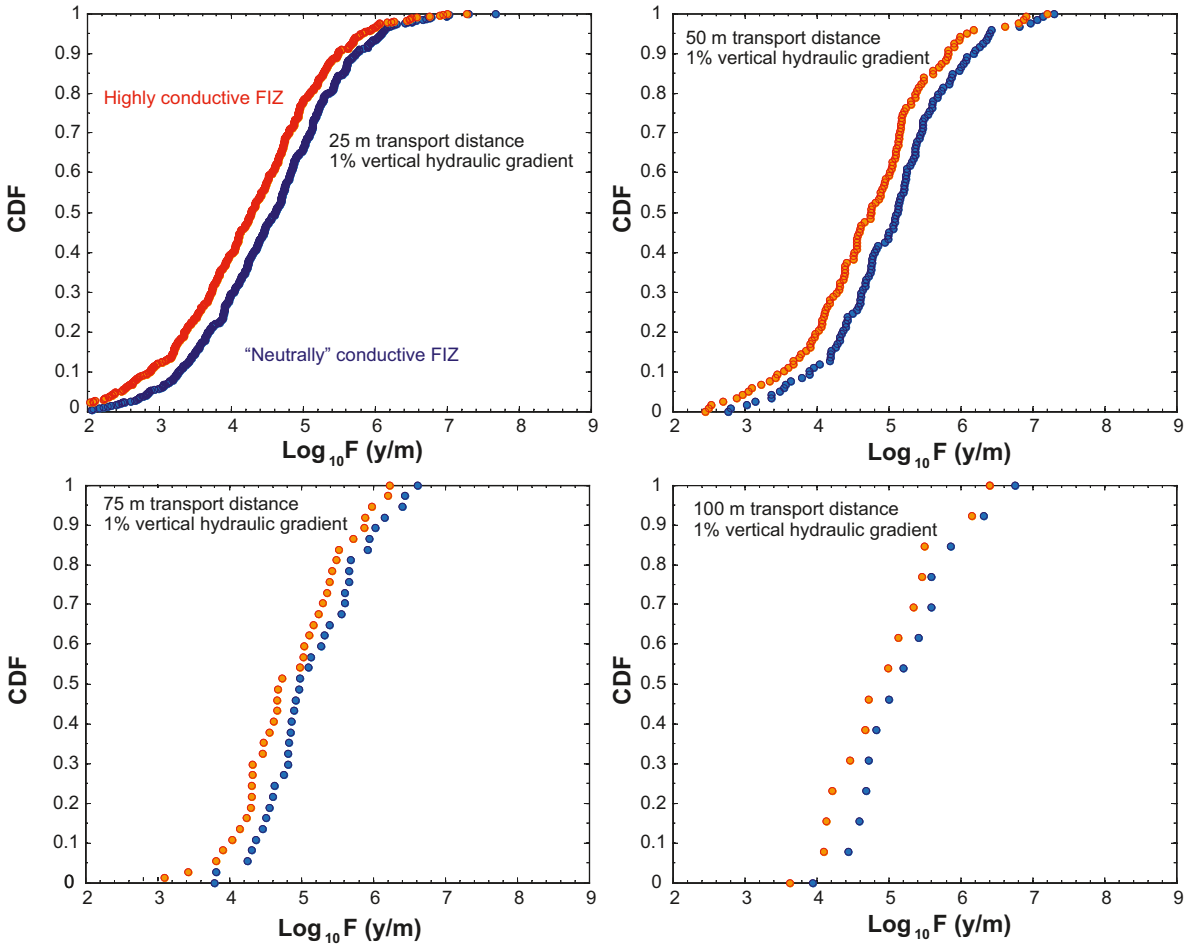

Figure D-19. *Typical F-factor ranges for paths of least transport resistance, PLTR in the immediate far field (IFF) based upon 1,000 realisations of the Hydro-DFN for FFM01c (< –400 m). The calculations consider different transport distances, an assumed hydraulic gradient of 1% applied along the vertical axis, and a non-correlated fracture transmissivity (NC) model. Results are given for the case of neutrally conductive FIZ (blue markers) and highly conductive FIZ (orange markers) and are plotted as cumulative distribution probability curves.*

Table D-9. Summary statistics for the F-factor (log_{10} units) corresponding to the pooled particle residence time distribution data for FFM01c (< –400 m), different transport distances, and a hydraulic gradient of 1%. Results are given for both the neutrally conductive FIZ case and highly-conductive FIZ case.

	Neutrally conductive FIZ				Highly-conductive FIZ			
Non-Correlated (NC)	**25 m**	**50 m**	**75 m**	**100 m**	**25 m**	**50 m**	**75 m**	**100 m**
Mean	4.55	5.05	5.15	5.21	4.23	4.71	4.84	4.93
Median	4.62	5.12	4.97	5.11	4.28	4.76	4.70	4.86
5th percentile	2.86	3.42	3.99	4.04	2.42	3.01	3.58	3.73
10th percentile	3.26	3.90	4.33	4.39	2.88	3.50	3.95	4.06
25th percentile	3.90	4.52	4.63	4.68	3.55	4.11	4.32	4.22
75th percentile	5.21	5.56	5.66	5.60	4.94	5.21	5.39	5.46
90th percentile	5.75	6.20	6.12	6.36	5.49	5.83	5.89	6.18
95th percentile	6.10	6.42	6.43	6.68	5.85	6.14	6.11	6.36
Std. deviation	0.98	0.90	0.70	0.77	1.09	0.94	0.75	0.80
Variance	0.95	0.81	0.49	0.59	1.19	0.88	0.56	0.64
Min value	1.97	2.77	3.79	3.94	–4.25	2.46	3.10	3.63
Max value	7.67	7.30	6.62	6.76	7.27	7.21	6.23	6.41
Connected fraction (%)	51.60	11.90	3.80	1.40	51.60	11.90	3.80	1.40

Appendix E

Flow-related transport properties of the HCD

Author: James Crawford

In this Appendix chapter we give detailed results for the HCD flow related transport properties calculations obtained using a 2D channel network model. The model is the same as that used for scoping calculations of borehole pumping tests described in Appendix B although with a slightly modified algorithm for direct assignment of channel transmissivities instead of local fracture aperture.

Although the F-factor can be estimated directly using the analytical expression given by Equation 3-9, additional numerical simulations have been performed to understand the impact that different assumptions of transmissivity spatial correlation may have upon typical F-factors calculated for deformation zones. For this purpose we use a standard geostatistical model for spatial correlation implemented in Matlab using a spectral synthesis technique. The method for generating spatially correlated transmissivities is the same as that previously used by /Liu and Neretnieks 2005, 2006/.

The seven different case studies for transmissivity spatial variation are:

1. log-normally distributed transmissivities with an isotropic Gaussian correlation structure and exponential depth trend
   (correlation lengths: L_x = 20 m, L_y = 20 m),
2. log-normally distributed transmissivities with an isotropic Gaussian correlation structure and exponential depth trend
   (correlation lengths: L_x = 5 m, L_y = 5 m),
3. log-normally distributed, spatially non-correlated transmissivities with exponential depth trend,
4. log-normally distributed transmissivities with an anisotropic Gaussian correlation structure and exponential depth trend
   (correlation lengths: L_x = 5 m, L_y = 20 m),
5. log-normally distributed transmissivities with an anisotropic Gaussian correlation structure and exponential depth trend
   (correlation lengths: L_x = 20 m, L_y = 5 m),
6. log-uniform distributed, spatially non-correlated transmissivities with exponential depth trend,
7. log-normally distributed transmissivities with an “extreme” anisotropic Gaussian correlation structure and exponential depth trend
   (correlation lengths: L_x = 10 m, L_y = 100 m).

In the following sections we demonstrate some typical results obtained using each of these model variants to show how they affect the estimated central tendency and variance of the F-factor distribution. Although only single realisations are visualised, the results are generally stable and multiple realisations tend to only exhibit minor differences. A possible exception is the case study #7 which considers an extreme anisotropic spatial correlation where the preferential flowrate through the particle release location can vary somewhat between different realisations. A statistical summary containing the mean and standard deviation of the simulated F-factor distributions for each of the seven case studies defined above is also given in the form of a table (based upon the outcome of 30 stochastic realisations).

Solute transport is simulated using a particle tracking technique based upon the method described in /Robinson 1984, Moreno 1988/. Many particles are introduced, one at a time into the simulated flow field at one or more locations. Particles arriving at a channel intersection node are distributed in the outlet channel members with a probability proportional to their flow rates. This is equivalent to assuming total mixing at the channel intersections. The case of no-mixing at channel intersections can be simulated as a special case where particles always choose an exit channel with the highest flowrate. This corresponds to the path of least flow resistance (PLFR) which may or may not necessarily be the same as the path of least transport resistance (PLTR).

The transport problem was defined in accordance with the conceptual model illustrated in Figure 3-14 with gently dipping and steeply dipping zones being modelled separately owing to their differing hydrogeological and orientation properties.

Simulation results for gently dipping zones

The results in this section are for gently dipping zones and are based upon the properties of ZFMA2 as a typical example. The transport distance is roughly 860 m from the particle release location at –450 m elevation to the recovery location at –100 m elevation. Solute particles are released as a line source 50 m in extent parallel to the x-axis on the 2D projection of the deformation zone. The local transmissivity of the line source feature is enhanced by a factor of 100 to avoid problems involving high transport resistance within the immediate vicinity of the injection section. A channel length of 5 m was assumed in the calculations.

Gently dipping zone – Case#1

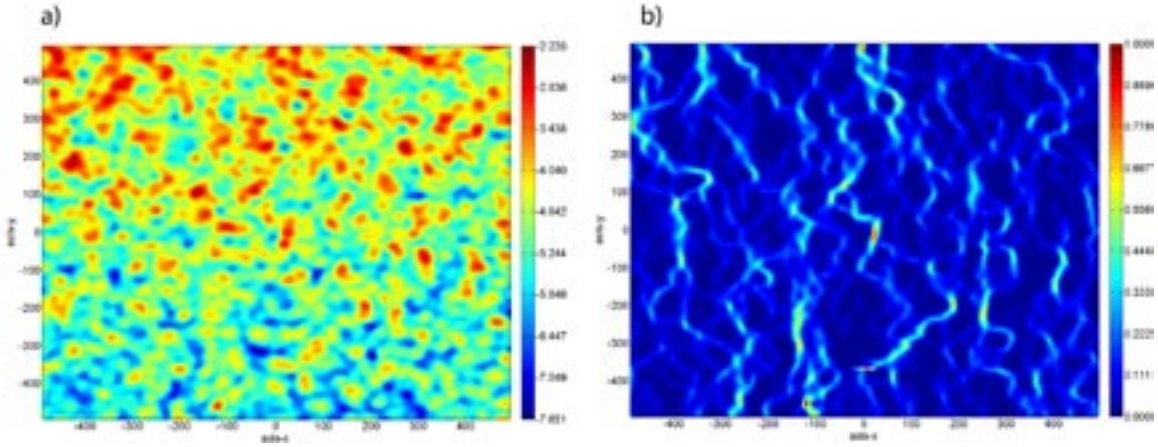

Figure E-1. *a) lognormally distributed transmissivity field for a gently dipping zone with an isotropic, Gaussian spatial correlation and exponential depth trend (L_x = 20 m, L_y = 20 m). The data are given as log_{10} values projected onto a 2D plane; b) corresponding flow field (normalised absolute values) simulated with a 2D channel network model.*

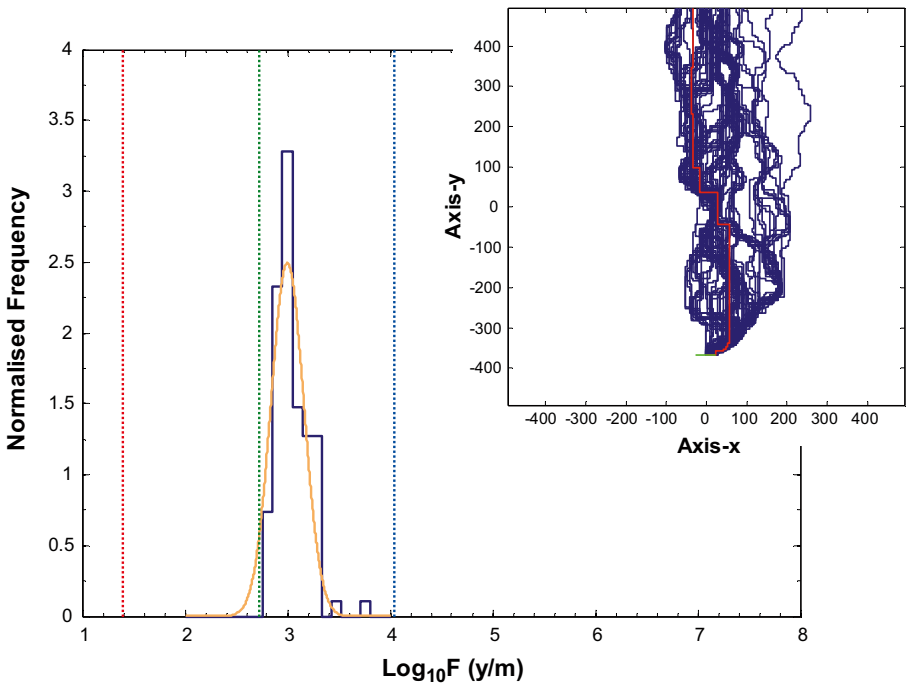

Figure E-2. *Simulated F-factor distribution calculated using 2D channel network model and (inset) trajectory of 100 particles released as a line source at –450 m elevation (the red trajectory corresponds to the path of least flow resistance). Vertical broken lines indicate analytically calculated F-factor for minimum (blue), mean (green), and maximum (red) transmissivity trend. The simulated data are shown as an outline histogram (blue curve) and fitted lognormal distribution (orange curve; μ = 3.00, σ = 0.16).*

Gently dipping zone – Case#2

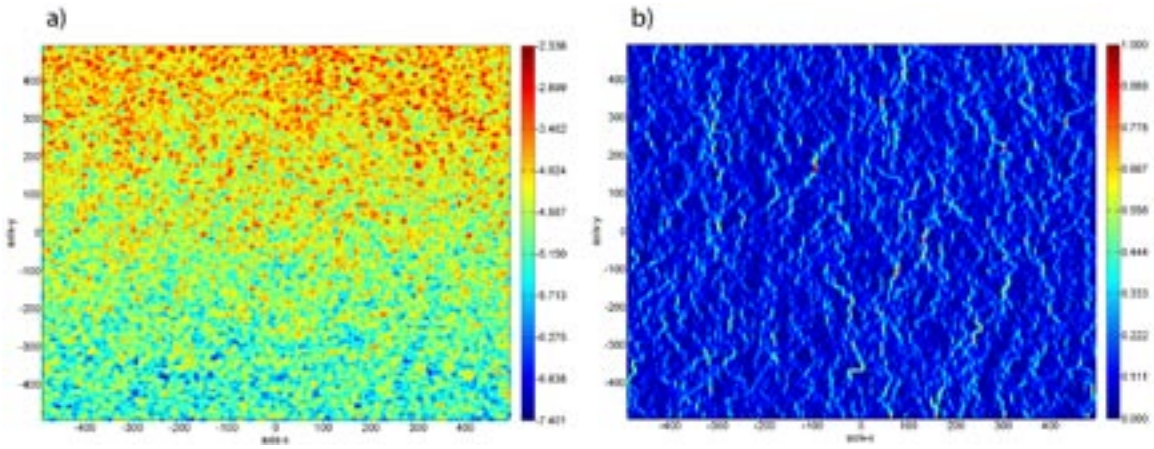

Figure E-3. *a) lognormally distributed transmissivity field for a gently dipping zone with an isotropic, Gaussian spatial correlation and exponential depth trend (L_x = 5 m, L_y = 5 m). The data are given as $\log_{10}$ values projected onto a 2D plane; b) corresponding flow field (normalised absolute values) simulated with a 2D channel network model.*

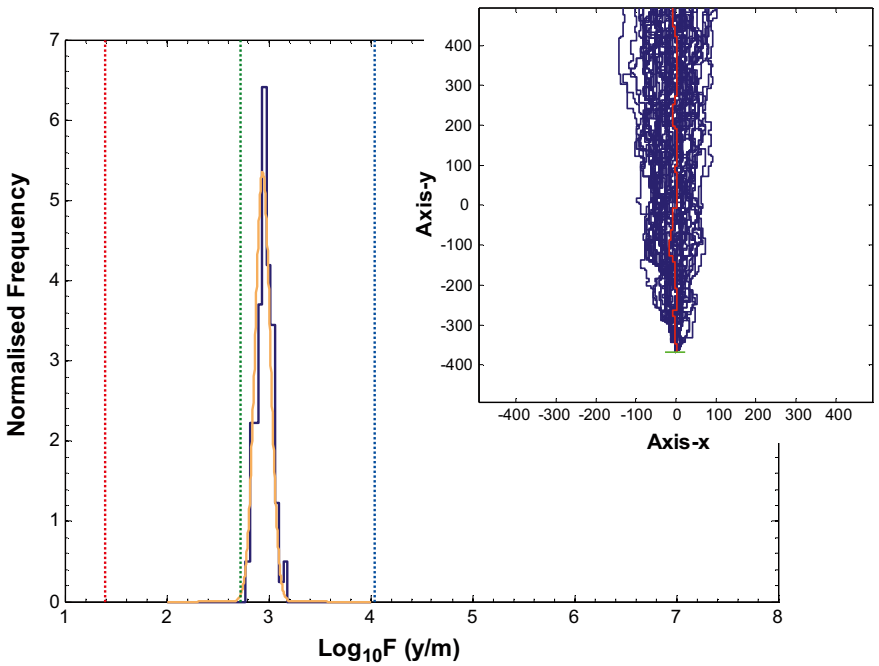

Figure E-4. *Simulated F-factor distribution calculated using 2D channel network model and (inset) trajectory of 100 particles released as a line source at –450 m elevation (the red trajectory corresponds to the path of least flow resistance). Vertical broken lines indicate analytically calculated F-factor for minimum (blue), mean (green), and maximum (red) transmissivity trend. The simulated data are shown as an outline histogram (blue curve) and fitted lognormal distribution (orange curve; μ = 2.94, σ = 0.08).*

Gently dipping zone – Case#3

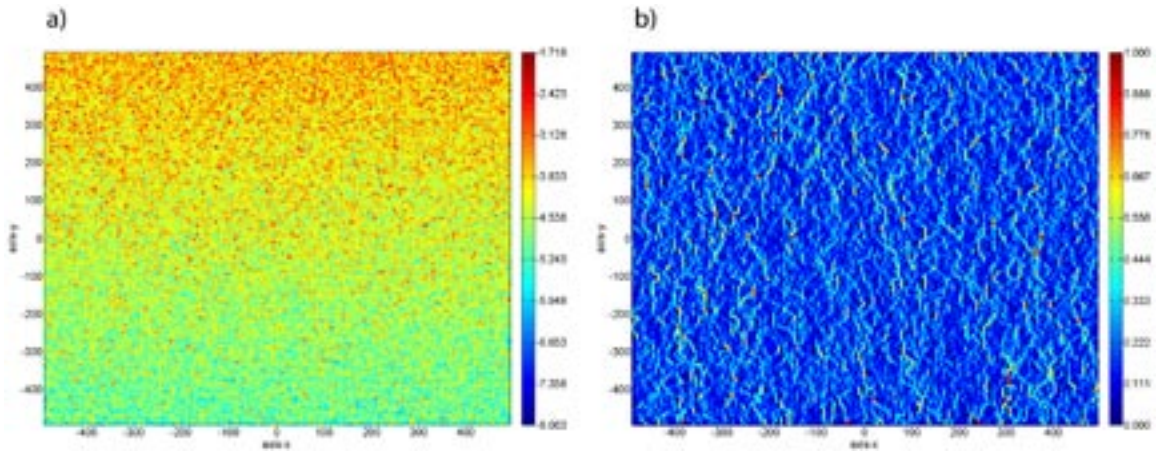

Figure E-5. *a) lognormally distributed transmissivity field for a gently dipping zone with an isotropic, non-correlated spatial structure and exponential depth trend. The data are given as log_{10} values projected onto a 2D plane; b) corresponding flow field (normalised absolute values) simulated with a 2D channel network model.*

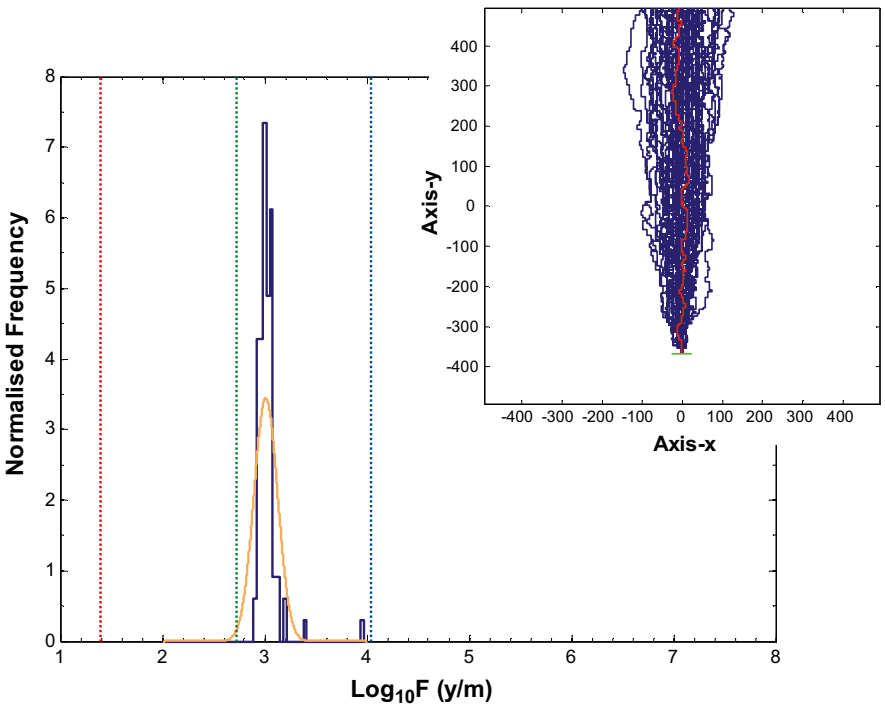

Figure E-6. *Simulated F-factor distribution calculated using 2D channel network model and (inset) trajectory of 100 particles released as a line source at –450 m elevation (the red trajectory corresponds to the path of least flow resistance). Vertical broken lines indicate analytically calculated F-factor for minimum (blue), mean (green), and maximum (red) transmissivity trend. The simulated data are shown as an outline histogram (blue curve) and fitted lognormal distribution (orange curve; μ = 3.01, σ = 0.11).*

Gently dipping zone – Case#4

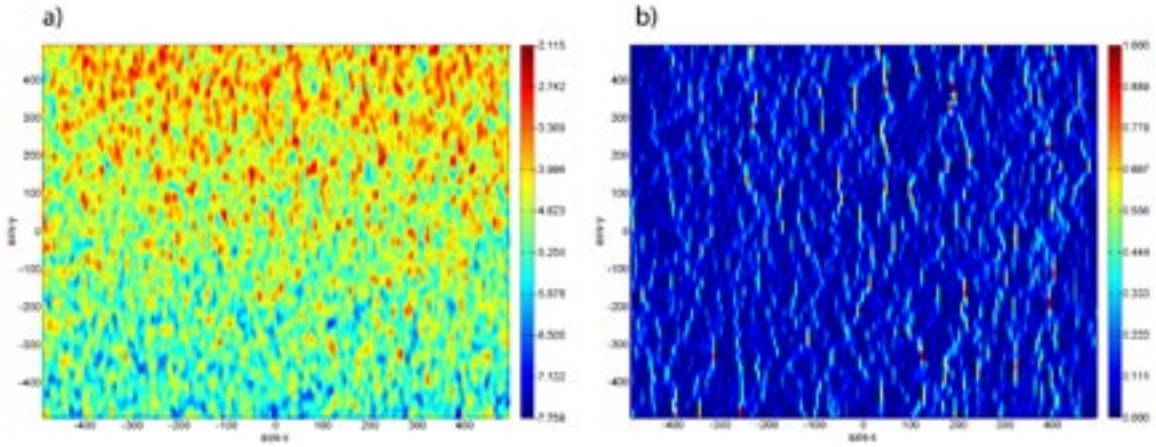

Figure E-7. *a) lognormally distributed transmissivity field for a gently dipping zone with an anisotropic, Gaussian spatial correlation and exponential depth trend (L_x = 5 m, L_y = 20 m). The data are given as log_{10} values projected onto a 2D plane; b) corresponding flow field (normalised absolute values) simulated with a 2D channel network model.*

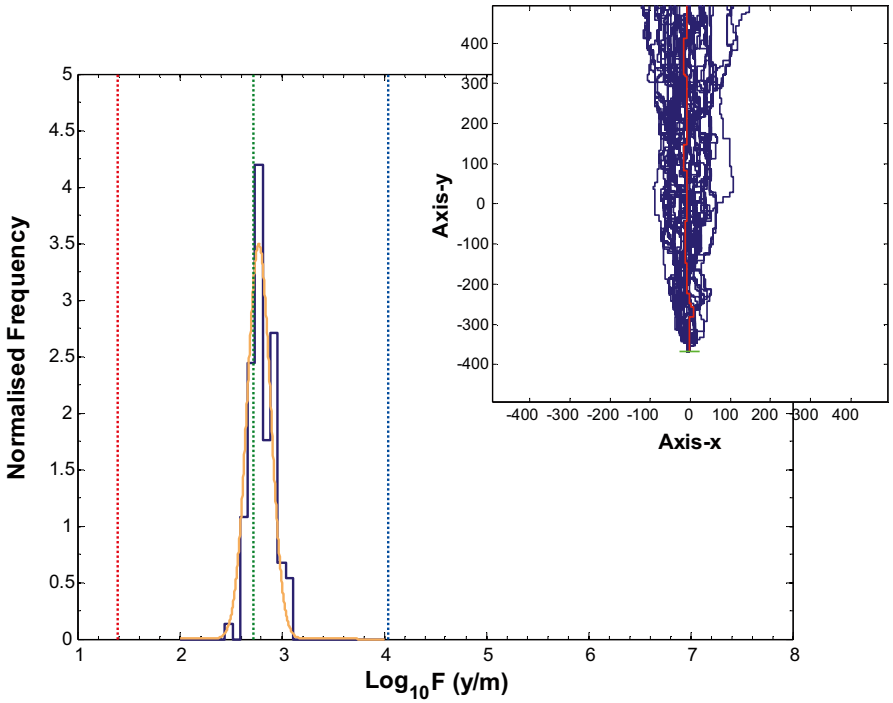

Figure E-8. *Simulated F-factor distribution calculated using 2D channel network model and (inset) trajectory of 100 particles released as a line source at –450 m elevation (the red trajectory corresponds to the path of least flow). Vertical broken lines indicate analytically calculated F-factor for minimum (blue), mean (green), and maximum (red) transmissivity trend. The simulated data are shown as an outline histogram (blue curve) and fitted lognormal distribution (orange curve; μ = 2.78, σ = 0.12).*

Gently dipping zone – Case#5

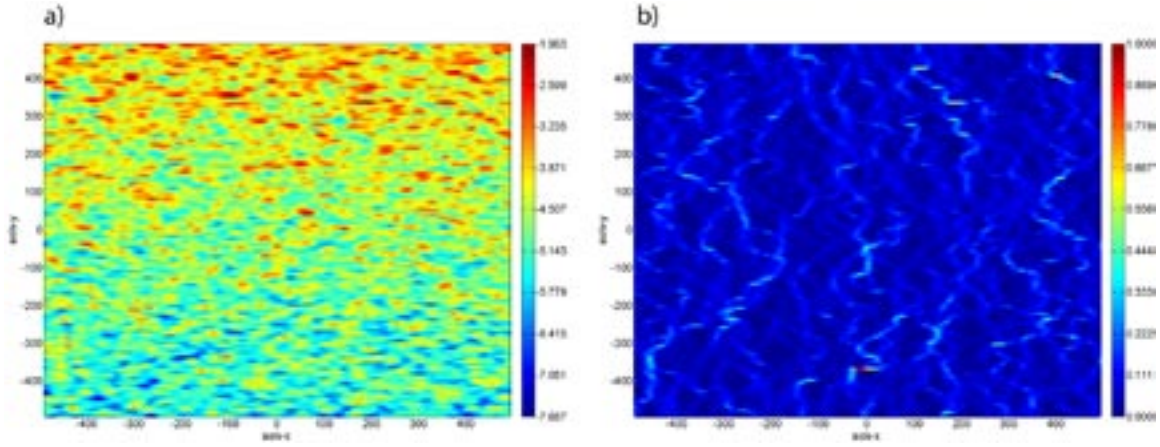

Figure E-9. *a) lognormally distributed transmissivity field for a gently dipping zone with an anisotropic, Gaussian spatial correlation and exponential depth trend (L_x = 20 m, L_y = 5 m). The data are given as log_{10} values projected onto a 2D plane; b) corresponding flow field (normalised absolute values) simulated with a 2D channel network model.*

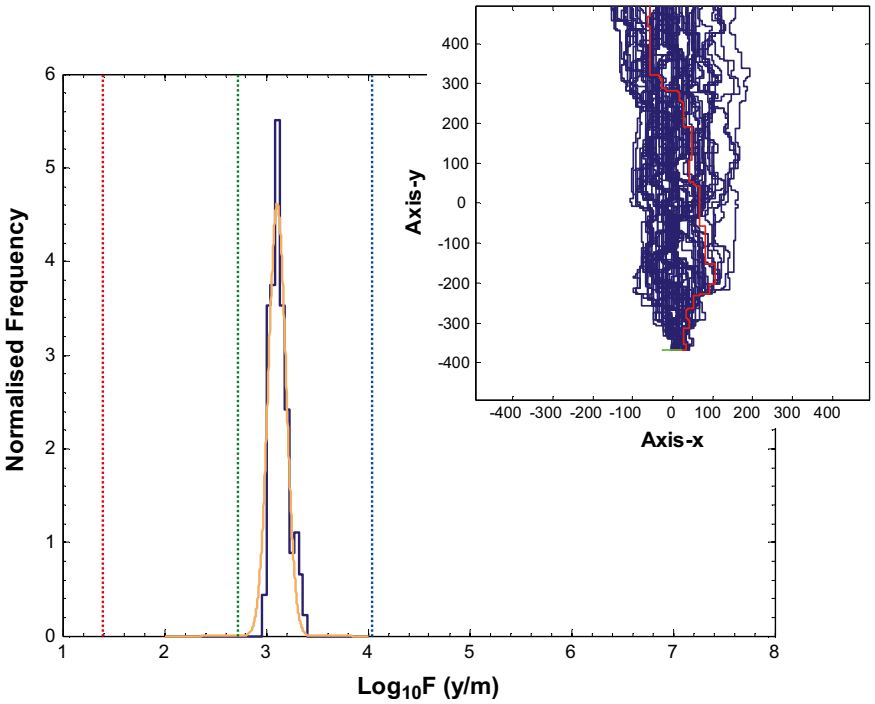

Figure E-10. *Simulated F-factor distribution calculated using 2D channel network model and (inset) trajectory of 100 particles released as a line source at –450 m elevation (the red trajectory corresponds to the path of least flow resistance). Vertical broken lines indicate analytically calculated F-factor for minimum (blue), mean (green), and maximum (red) transmissivity trend. The simulated data are shown as an outline histogram (blue curve) and fitted lognormal distribution (orange curve; $\mu = 3.11$, $\sigma = 0.09$).*

Gently dipping zone – Case#6

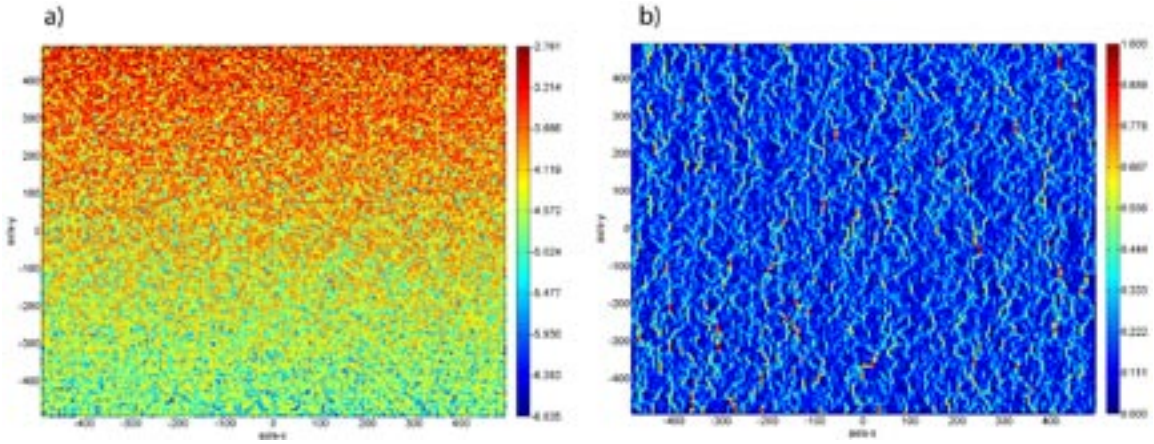

Figure E-11. *a) log-uniform distributed transmissivity field for a gently dipping zone with an isotropic, non-correlated spatial structure and exponential depth trend. The data are given as log_{10} values projected onto a 2D plane; b) corresponding flow field (normalised absolute values) simulated with a 2D channel network model.*

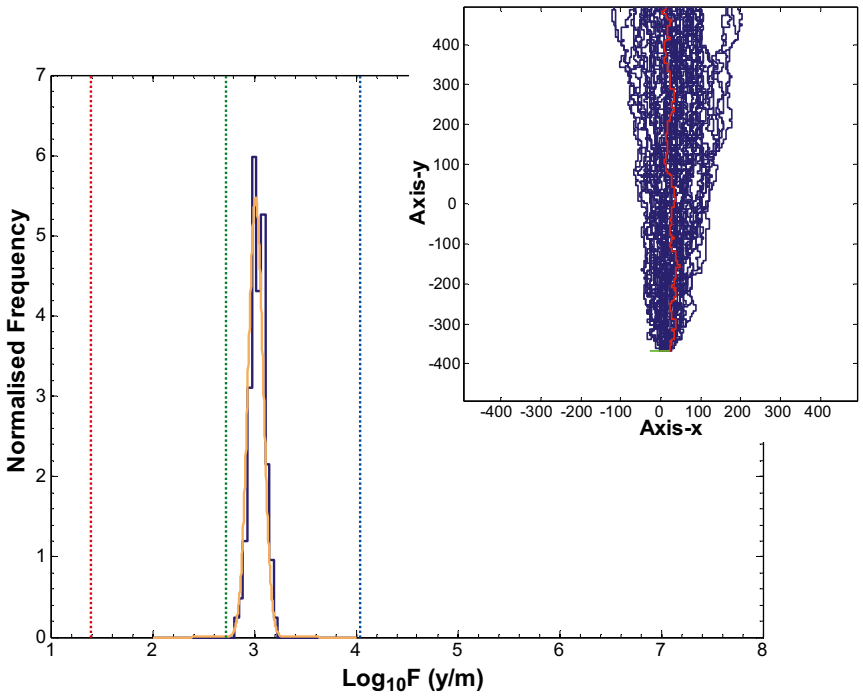

Figure E-12. *Simulated F-factor distribution calculated using 2D channel network model and (inset) trajectory of 100 particles released as a line source at –450 m elevation (the red trajectory corresponds to the path of least flow resistance). Vertical broken lines indicate analytically calculated F-factor for minimum (blue), mean (green), and maximum (red) transmissivity trend. The simulated data are shown as an outline histogram (blue curve) and fitted lognormal distribution (orange curve; μ = 3.01, σ = 0.07).*

Gently dipping zone – Case#7

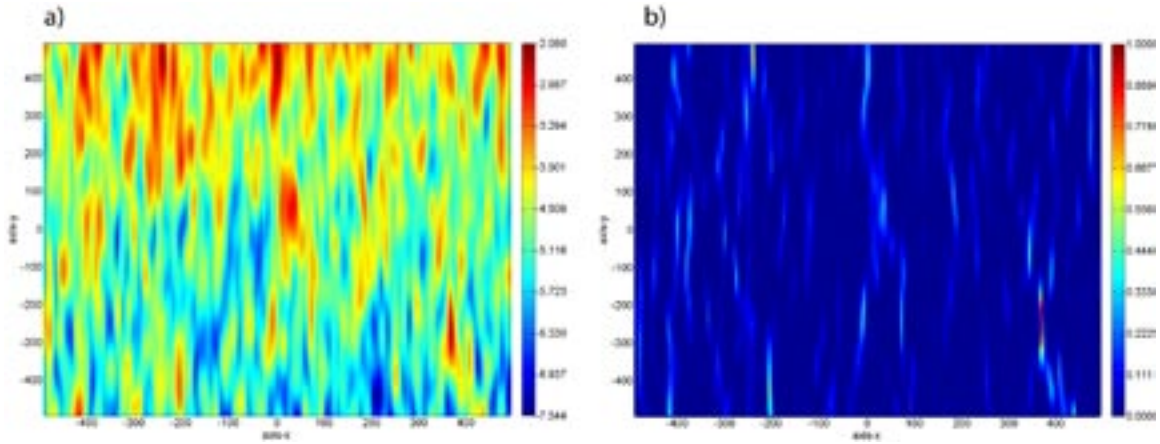

Figure E-13. *a) lognormally distributed transmissivity field for a gently dipping zone with an anisotropic, Gaussian spatial correlation and exponential depth trend (L_x = 10 m, L_y = 100 m). The data are given as $\log_{10}$ values projected onto a 2D plane; b) corresponding flow field (normalised absolute values) simulated with a 2D channel network model.*

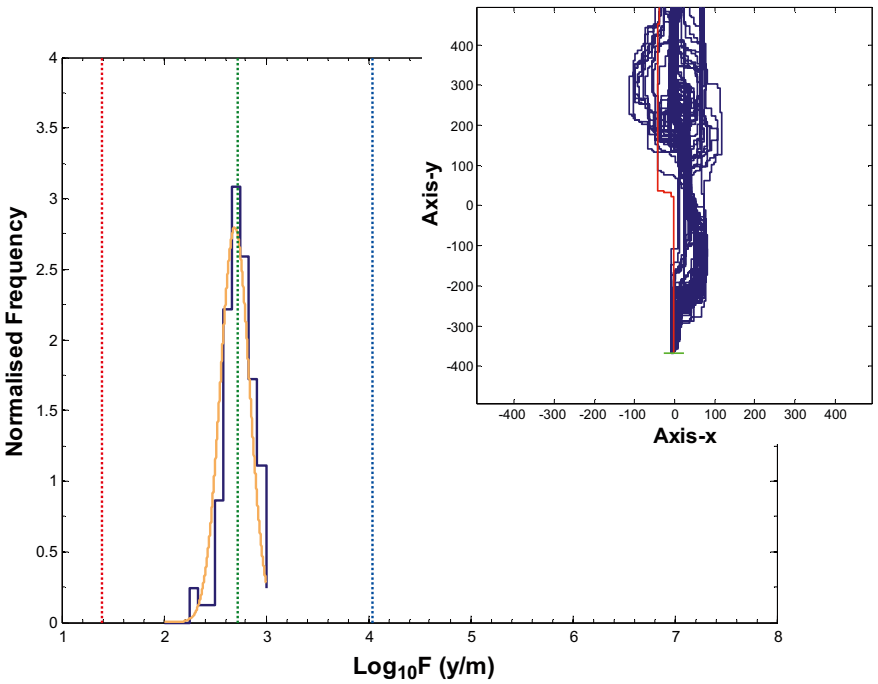

Figure E-14. *Simulated F-factor distribution calculated using 2D channel network model and (inset) trajectory of 100 particles released as a line source at –450 m elevation (the red trajectory corresponds to the path of least flow resistance). Vertical broken lines indicate analytically calculated F-factor for minimum (blue), mean (green), and maximum (red) transmissivity trend. The simulated data are shown as an outline histogram (blue curve) and fitted lognormal distribution (orange curve; μ = 2.70, σ = 0.14).*

A statistical summary of the central tendency (mean) and dispersion (standard deviation) of the estimated F-factor distributions is given in Table E-1. The calculated means and standard deviations are based upon the ensemble average of 100 released particles in each of 30 individual realisations. Variation of these statistical measures between realisations is represented by an error value which corresponds to the sample population standard deviation of the given statistic.

Simulation results for steeply dipping zones

The results in this section are for steeply dipping zones and are based upon the properties of ZFM0060A as a typical example. Here, the transport distance is roughly 350 m from the particle release location at –450 m elevation and the recovery location at –100 m elevation. Solute particles

Table E-1. Statistics for the central tendency (mean, μ_F) and dispersion (standard deviation, σ_F) of the F-factor distribution ($\log_{10}$ units) for gently dipping zones calculated in individual realisations for each case study. Variability between individual realisations is given as a standard error (± σ_p) for the population sample of 30 stochastic realisations.

Case Study #	μ_F	σ_F	L_x (m)	L_y (m)	Transmissivity model
Equation 3-9	2.7	1.4–4.0 §	n/a	n/a	Mean depth trend only
1	3.02 ± 0.08	(1.6 ± 0.6)×10^{-2}	20	20	Lognormal + depth trend
2	2.96 ± 0.03	(6.8 ± 1.6)×10^{-3}	5	5	Lognormal + depth trend
3	3.01 ± 0.01	(4.9 ± 1.1)×10^{-3}	0	0	Lognormal + depth trend
4	2.80 ± 0.04	(1.6 ± 0.5)×10^{-2}	5	20	Anisotropic lognormal + depth trend
5	3.12 ± 0.04	(7.8 ± 2.5)×10^{-3}	20	5	Anisotropic lognormal + depth trend
6	3.01 ± 0.02	(6.0 ± 1.2)×10^{-3}	0	0	Log-uniform + depth trend
7	2.67 ± 0.17	(3.8 ± 1.4)×10^{-2}	10	100	Anisotropic lognormal + depth trend

Notes: § for the analytical case, the span of possible F-factors is given as a min-max range.

are released as a line source 50 m in extent parallel to the x-axis on the 2D projection of the deformation zone. The local transmissivity of the line source feature is enhanced by a factor of 100 to avoid problems involving high transport resistance within the immediate vicinity of the injection section. Owing to the smaller size of the simulated deformation zone compared to the gently dipping cases, a channel length of 2 m was assumed in the calculations.

Steeply dipping zone – Case#1

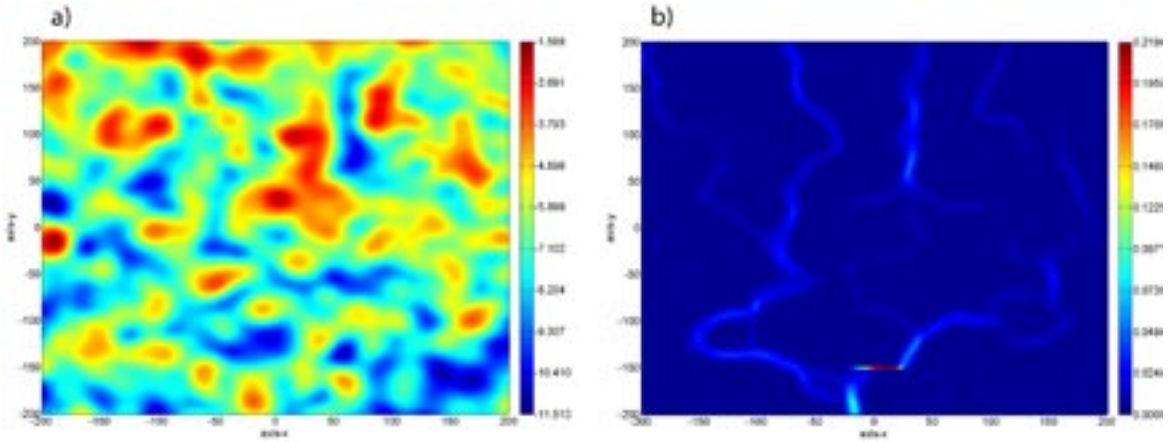

Figure E-15. *a) lognormally distributed transmissivity field for a steeply dipping zone with an isotropic, Gaussian spatial correlation and exponential depth trend (L_x = 20 m, L_y = 20 m). The data are given as log_{10} values projected onto a 2D plane; b) corresponding flow field (normalised absolute values) simulated with a 2D channel network model.*

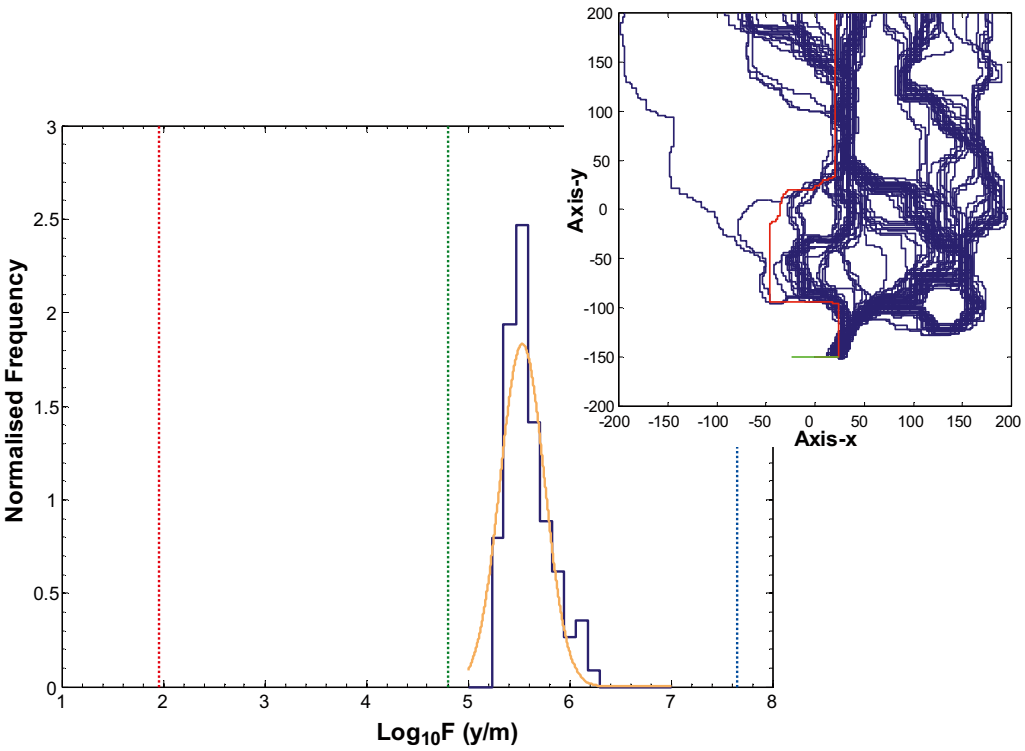

Figure E-16. *Simulated F-factor distribution calculated using 2D channel network model and (inset) trajectory of 100 particles released as a line source at –450 m elevation (the red trajectory corresponds to the path of least flow resistance). Vertical broken lines indicate analytically calculated F-factor for minimum (blue), mean (green), and maximum (red) transmissivity trend. The simulated data are shown as an outline histogram (blue curve) and fitted lognormal distribution (orange curve; μ = 5.54, σ = 0.22).*

Steeply dipping zone – Case#2

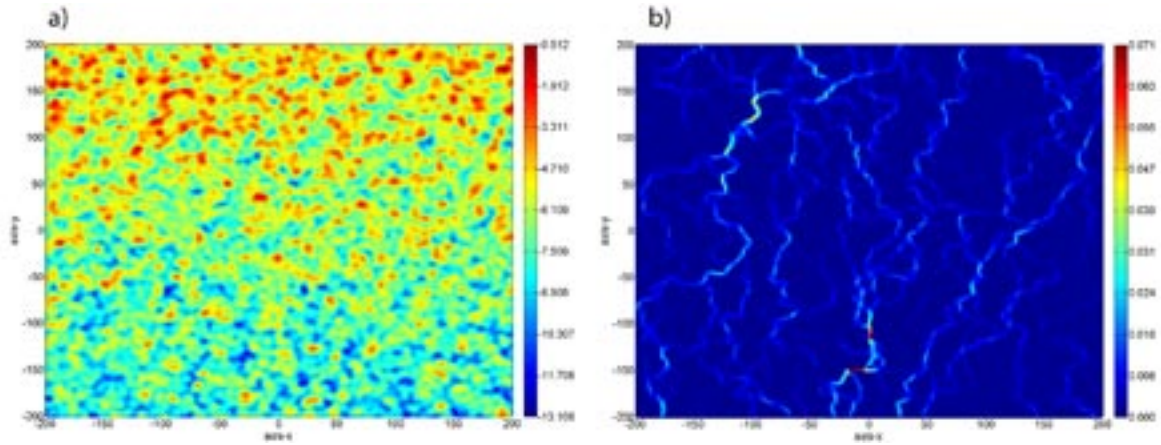

Figure E-17. *a) lognormally distributed transmissivity field for a steeply dipping zone with an isotropic, Gaussian spatial correlation and exponential depth trend (L_x = 5 m, L_y = 5 m). The data are given as log_{10} values projected onto a 2D plane; b) corresponding flow field (normalised absolute values) simulated with a 2D channel network model.*

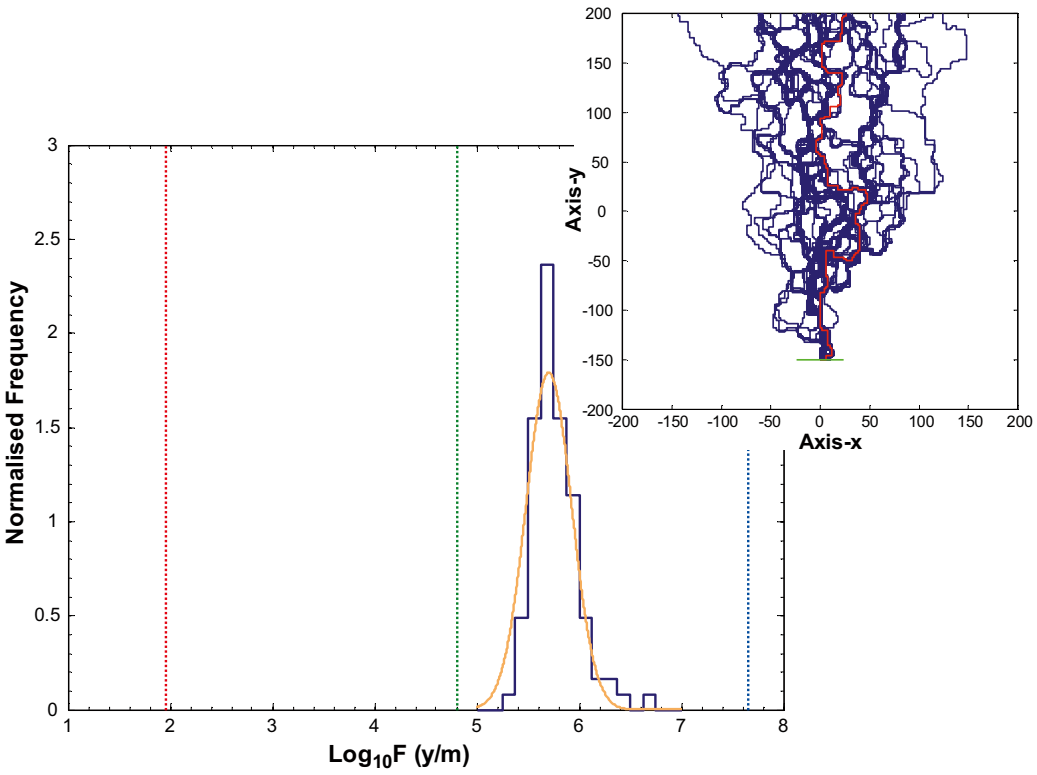

Figure E-18. *Simulated F-factor distribution calculated using 2D channel network model and (inset) trajectory of 100 particles released as a line source at –450 m elevation (the red trajectory corresponds to the path of least flow resistance). Vertical broken lines indicate analytically calculated F-factor for minimum (blue), mean (green), and maximum (red) transmissivity trend. The simulated data are shown as an outline histogram (blue curve) and fitted lognormal distribution (orange curve; μ = 5.70, σ = 0.22).*

Steeply dipping zone – Case#3

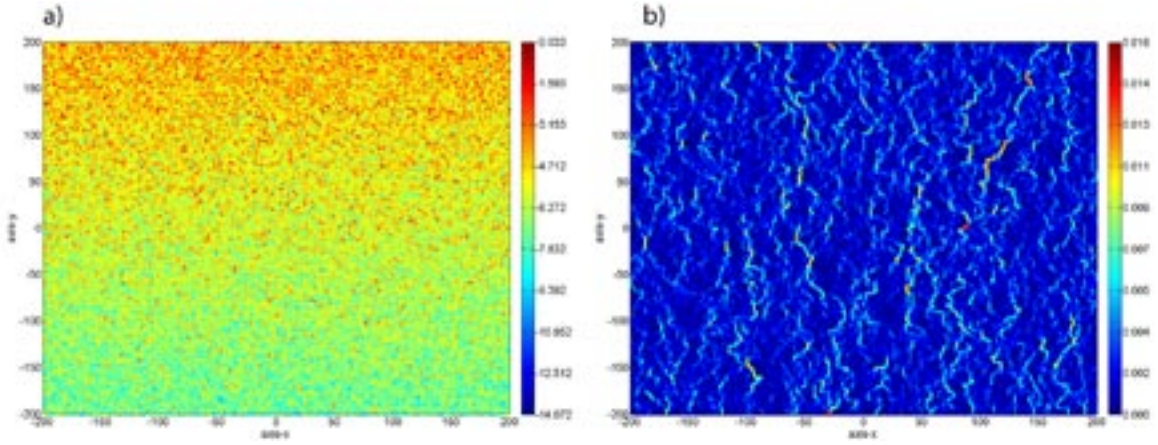

Figure E-19. *a) lognormally distributed transmissivity field for a steeply dipping zone with an isotropic, non-correlated spatial structure and exponential depth trend. The data are given as log_{10} values projected onto a 2D plane; b) corresponding flow field (normalised absolute values) simulated with a 2D channel network model.*

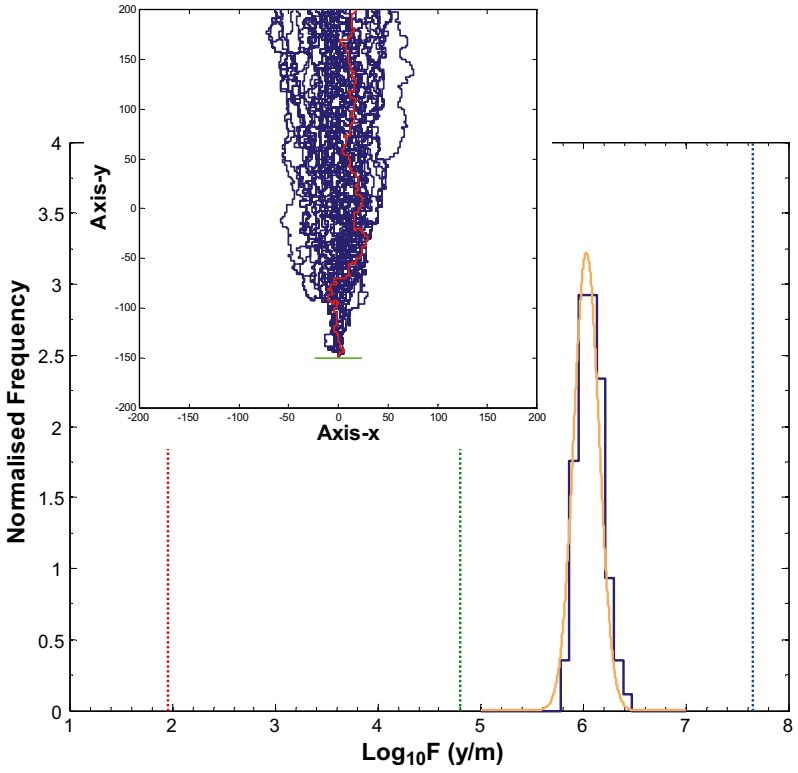

Figure E-20. *Simulated F-factor distribution calculated using 2D channel network model and (inset) trajectory of 100 particles released as a line source at –450 m elevation (the red trajectory corresponds to the path of least flow resistance). Vertical broken lines indicate analytically calculated F-factor for minimum (blue), mean (green), and maximum (red) transmissivity trend. The simulated data are shown as an outline histogram (blue curve) and fitted lognormal distribution (orange curve; μ = 6.03, σ = 0.13).*

Steeply dipping zone – Case#4

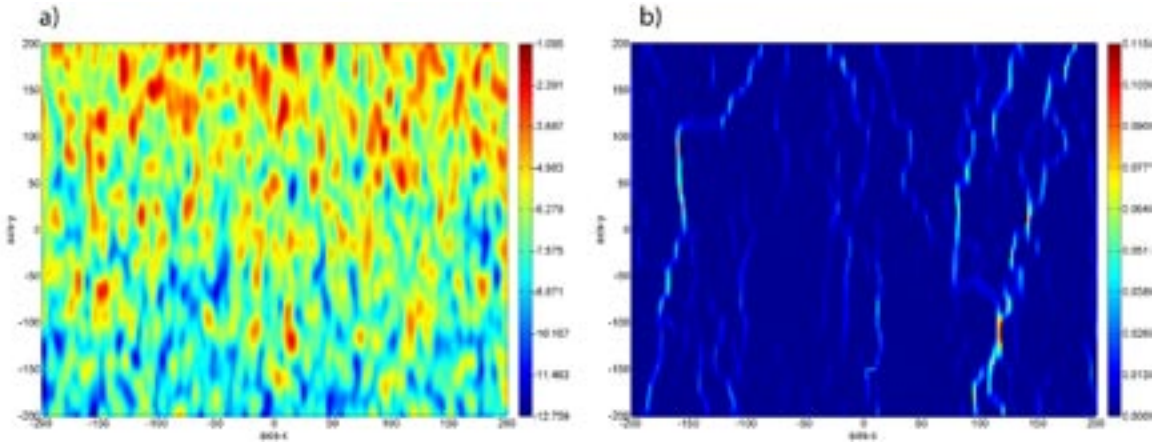

Figure E-21. *a) lognormally distributed transmissivity field for a steeply dipping zone with an anisotropic, Gaussian spatial correlation and exponential depth trend (L_x = 5 m, L_y = 20 m). The data are given as log_{10} values projected onto a 2D plane; b) corresponding flow field (normalised absolute values) simulated with a 2D channel network model.*

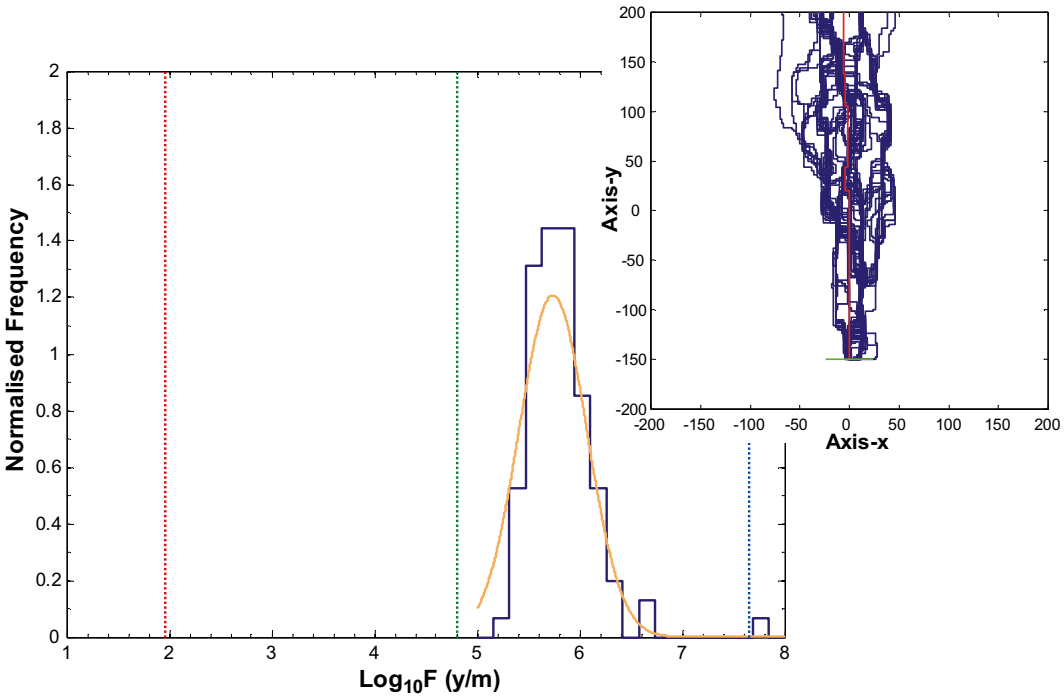

Figure E-22. *Simulated F-factor distribution calculated using 2D channel network model and (inset) trajectory of 100 particles released as a line source at –450 m elevation (the red trajectory corresponds to the path of least flow resistance). Vertical broken lines indicate analytically calculated F-factor for minimum (blue), mean (green), and maximum (red) transmissivity trend. The simulated data are shown as an outline histogram (blue curve) and fitted lognormal distribution (orange curve; μ = 5.74, σ = 0.33).*

Steeply dipping zone – Case#5

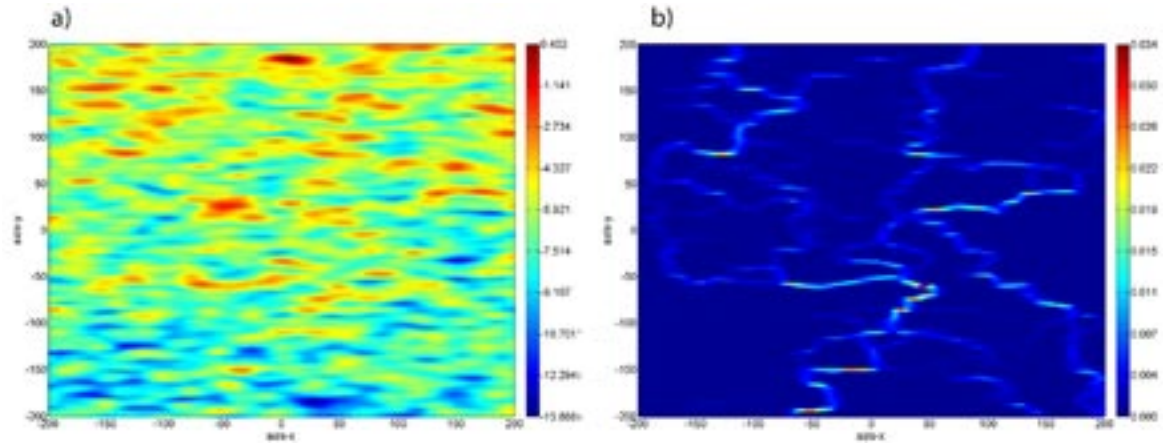

Figure E-23. *a) lognormally distributed transmissivity field for a steeply dipping zone with an anisotropic, Gaussian spatial correlation and exponential depth trend (L_x = 20 m, L_y = 5 m). The data are given as log_{10} values projected onto a 2D plane; b) corresponding flow field (normalised absolute values) simulated with a 2D channel network model.*

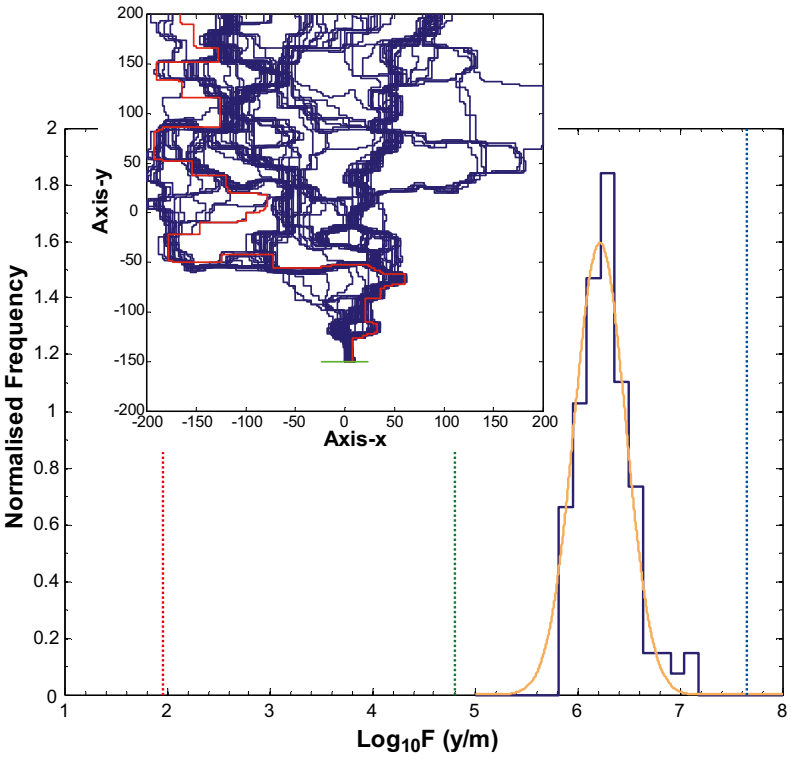

Figure E-24. *Simulated F-factor distribution calculated using 2D channel network model and (inset) trajectory of 100 particles released as a line source at –450 m elevation (the red trajectory corresponds to the path of least flow resistance). Vertical broken lines indicate analytically calculated F-factor for minimum (blue), mean (green), and maximum (red) transmissivity trend. The simulated data are shown as an outline histogram (blue curve) and fitted lognormal distribution (orange curve; μ = 6.22, σ = 0.25).*

Steeply dipping zone – Case#6

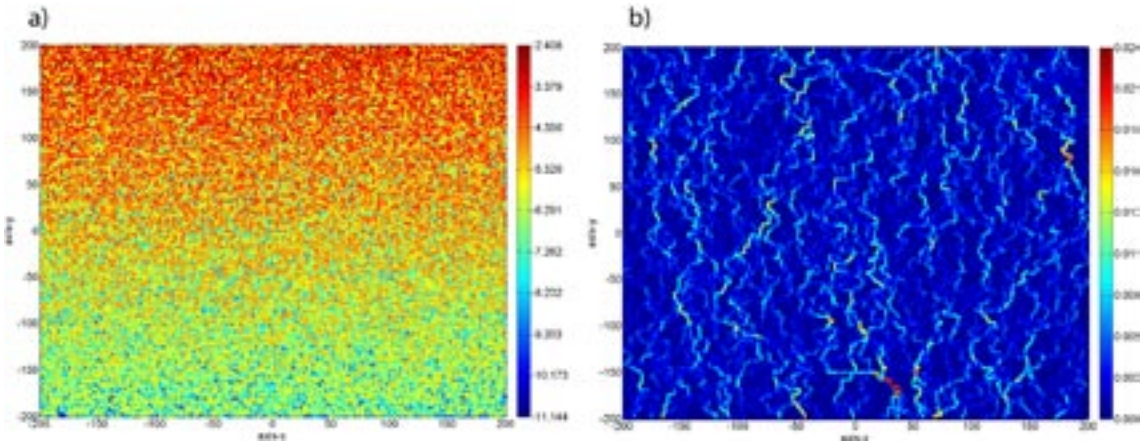

Figure E-25. *a) log-uniform distributed transmissivity field for a steeply dipping zone with an isotropic, non-correlated spatial structure and exponential depth trend. The data are given as log_{10} values projected onto a 2D plane; b) corresponding flow field (normalised absolute values) simulated with a 2D channel network model.*

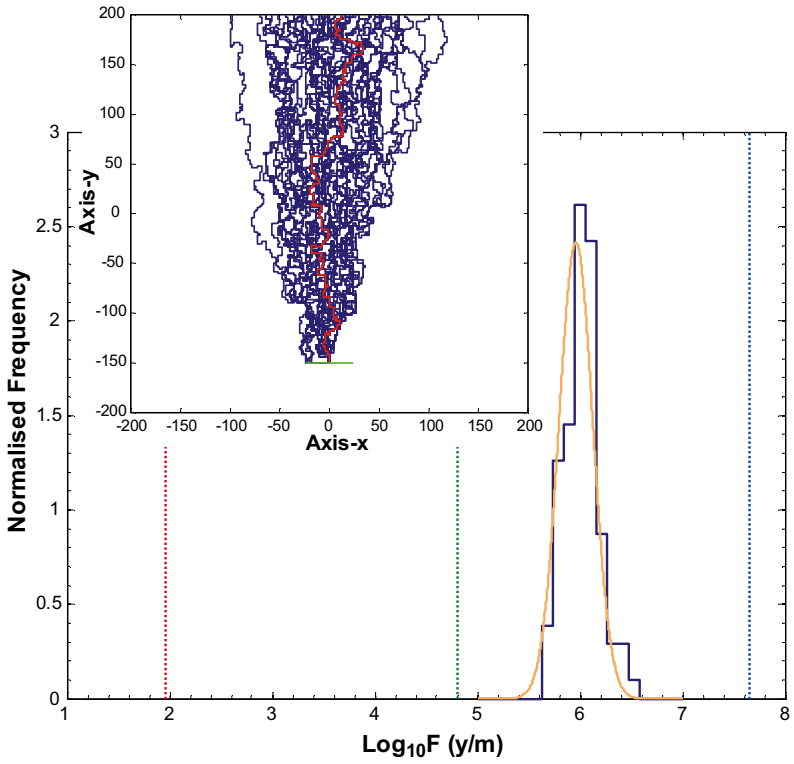

Figure E-26. *Simulated F-factor distribution calculated using 2D channel network model and (inset) trajectory of 100 particles released as a line source at –450 m elevation (the red trajectory corresponds to the path of least flow resistance). Vertical broken lines indicate analytically calculated F-factor for minimum (blue), mean (green), and maximum (red) transmissivity trend. The simulated data are shown as an outline histogram (blue curve) and fitted lognormal distribution (orange curve; $\mu = 5.96$, $\sigma = 0.17$).*

Steeply dipping zone – Case#7

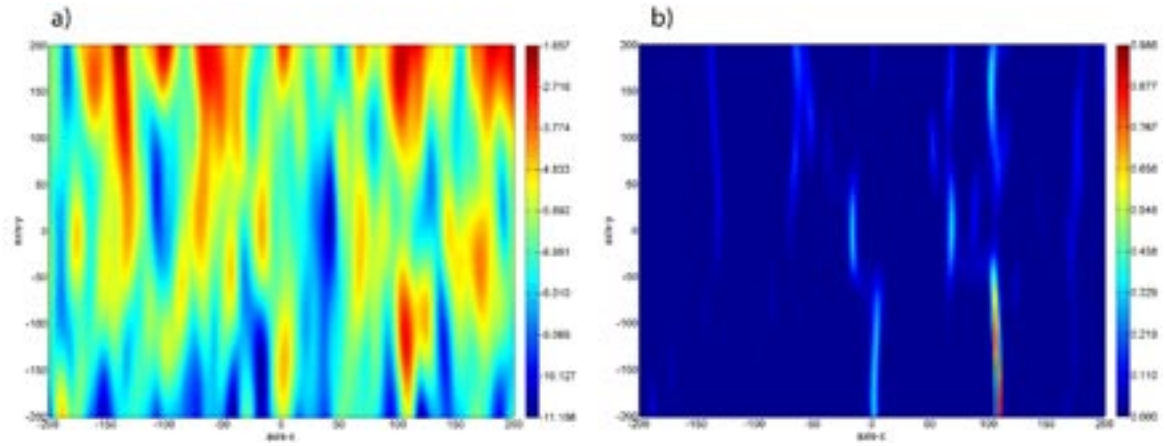

Figure E-27. *a) lognormally distributed transmissivity field for a steeply dipping zone with an anisotropic, Gaussian spatial correlation and exponential depth trend (L_x = 10 m, L_y = 100 m). The data are given as log_{10} values projected onto a 2D plane; b) corresponding flow field (normalised absolute values) simulated with a 2D channel network model.*

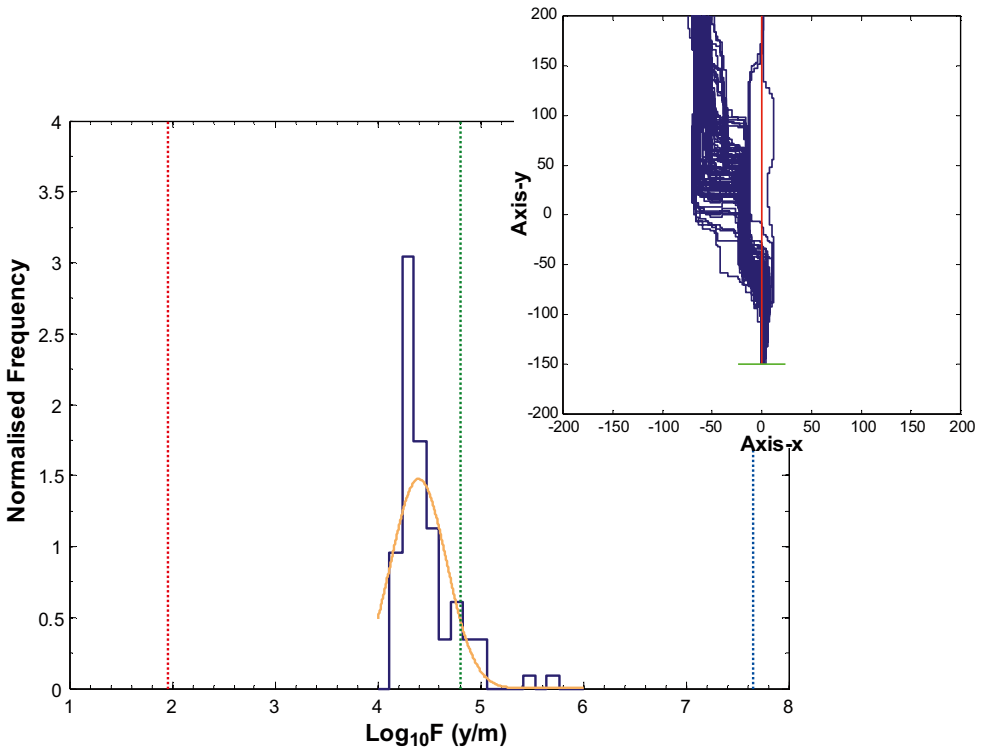

Figure E-28. *Simulated F-factor distribution calculated using 2D channel network model and (inset) trajectory of 100 particles released as a line source at –450 m elevation (the red trajectory corresponds to the path of least flow resistance). Vertical broken lines indicate analytically calculated F-factor for minimum (blue), mean (green), and maximum (red) transmissivity trend. The simulated data are shown as an outline histogram (blue curve) and fitted lognormal distribution (orange curve; μ = 4.40, σ = 0.27).*

Table E-2. Statistics for the central tendency (mean, μ_F) and dispersion (standard deviation, σ_F) of the F-factor distribution ($\log_{10}$ units) for steeply dipping zones calculated in individual realisations for each case study. Variability between individual realisations is given as a standard error (± σ) for the population sample of 30 stochastic realisations.

Case Study #	μ_F	σ_F	L_x (m)	L_y (m)	Transmissivity distribution
Equation 3-9	4.8	2.0–7.7 §	n/a	n/a	Mean depth trend only
1	6.0 ± 0.4	$(8.4 \pm 4.1)\times10^{-2}$	20	20	Lognormal + depth trend
2	5.9 ± 0.1	$(5.5 \pm 1.5)\times10^{-2}$	5	5	Lognormal + depth trend
3	6.1 ± 0.1	$(2.1 \pm 0.7)\times10^{-2}$	0	0	Lognormal + depth trend
4	5.3 ± 0.2	$(9.5 \pm 3.2)\times10^{-2}$	5	20	Anisotropic lognormal + depth trend
5	6.3 ± 0.2	$(5.9 \pm 2.2)\times10^{-2}$	20	5	Anisotropic lognormal + depth trend
6	6.0 ± 0.1	$(3.8 \pm 0.9)\times10^{-2}$	0	0	Log-uniform + depth trend
7	5.1 ± 0.7	$(1.5 \pm 1.1)\times10^{-1}$	10	100	Anisotropic lognormal + depth trend

Notes: § for the analytical case, the span of possible F-factors is given as a min-max range.

A statistical summary of the central tendency (mean) and dispersion (standard deviation) of the estimated F-factor distributions is given in Table E-2. The calculated means and standard deviations are based upon the ensemble average of 100 released particles in each of 30 individual realisations. Variation of these statistical measures between realisations is represented by an error value which corresponds to the sample population standard deviation of the given statistic.

Conclusions

As can be seen from the statistical summaries in Table E-1 and Table E-2, the simple analytical expression given by Equation 3-9 provides a reasonable estimate of the mean F-factor for both the gently and steeply dipping deformation zones in the HCD when compared against the simulated data. Case study #3 which assumes a spatially non-correlated, lognormal distribution of transmissivities is theoretically most similar to the conceptual model implied by the analytical estimate. The mean F-factor calculated for this case study is roughly double the analytical estimate (in arithmetic scale) for the gently dipping zones, although slightly more than an order of magnitude greater in the case of the steeply dipping zones. This is thought to be at least partly due to the more circuitous pathways taken by particles in the simulations using the 2D orthogonal channel network model.

The simulation results also indicate for the simple cases studied here, that spatial correlation and anisotropy have a relatively minor impact upon the overall magnitude of the F-factor, provided the correlation length is smaller than the dimensions of the transport path modelled. As would be expected, however, anisotropy giving preferential conductors along the axis of the applied hydraulic gradient gives lower F-factors than the isotropic cases. In a similar fashion, anisotropy giving preferential conductors normal to the axis of the applied hydraulic gradient gives higher F-factors than the isotropic cases. The results show that although the magnitude of the F-factor central tendency is only weakly influenced by the different assumptions of spatial correlation, the dispersion of the F-factor distribution for transported solute particles is more strongly influenced. In the isotropic cases, there is an almost linear relation between the assumed correlation length and the dispersivity of the F-factor distribution specified by σ_F.

Appendix F

On the relation between transmissivity and aperture

Author: James Crawford

"Pipe flow" along a single flowpath of constant aperture

Assuming the Hagen-Poiseuille relation for laminar flow in a cylindrical tube of length, L_p and diameter, δ_c we can write:

$$Q = \left(\frac{\pi \rho_w g_c}{128 \mu_w} \right) \delta_c^4 \frac{\Delta h}{L_p} = \left(\frac{3\pi}{32} k_h \right) \delta_c^4 \frac{\Delta h}{L_p} \tag{F-1}$$

Where,

$$k_h = \frac{\rho_w g_c}{12 \mu_w} \tag{F-2}$$

The flow can also be expressed in terms of the hydraulic conductivity of the pipe:

$$Q = K \left(\frac{\pi \delta_c^2}{4} \right) \frac{\Delta h}{L_p} \tag{F-3}$$

Where the hydraulic conductivity, K (m/s) is defined as:

$$K = \left(\frac{3\pi}{8} k_h \right) \delta_c^2 \tag{F-4}$$

The storativity, S of the pipe is defined as:

$$S = \rho_w g_c \left(\beta_p + \beta_w \right) \delta_c \tag{F-5}$$

This is related to the specific storage, S_s (m^{-1}) by way of the relation:

$$S_s = \frac{S}{\delta_c} \tag{F-6}$$

The hydraulic diffusivity, α (m^2/s) measured in a hydraulic test is defined as:

$$\alpha = \frac{T}{S} = \frac{K}{S_s} \tag{F-7}$$

The transmissivity of the pipe is thus:

$$T = K \frac{S}{S_s} = K \delta_c = \left(\frac{3\pi}{8} k_h \right) \delta_c^3 \tag{F-8}$$

The transmissivity and storativity of the pipe therefore vary with the pipe diameter (i.e. aperture) in the following way:

$$\left. \begin{array}{l} T \propto \delta_c^3 \\ S \propto \delta_c \end{array} \right\} \tag{F-9}$$

A direct consequence of Equation F-9 is:

$$S \propto T^{\frac{1}{3}} \tag{F-10}$$

The notion that storativity should vary with the square root of transmissivity therefore does not appear to hold for the case considered here. From Equation F-9 we can also say that:

$$\frac{T}{S} \propto \delta_c^2 \tag{F-11}$$

And consequently:

$$\frac{T}{S} \propto T^{\frac{2}{3}} \tag{F-12}$$

For a parallel-plate flow channel, the transmissivity and storativity vary in the same way as described by Equation F-9. We therefore conclude that transport in a pipe and a parallel plate flow channel are characterised by an identical dependency upon aperture. Confusion may arise when comparing flow in a pipe with a parallel plate flow channel if the width of the flow channel is not considered. The width of the flow channel enters implicitly into the equation for pipe flow, but is considered to be a separate and constant entity in the slit formulation.

For a single pipe, we therefore conclude that the empirically derived square root relation between hydraulic diffusivity and transmissivity /Uchida et al. 1994/ is not consistent with a pipe flow geometry.

Appendix G

Detailed ECPM modelling results

Author: James Crawford

This appendix contains a detailed examination of particle tracking results for a number of particles thought to be representative of potential transport paths from the hypothetical repository layout discussed in section 3.9 to surface discharge locations near the Singö deformation zone to the North-East.

Figure G-1 shows a visualisation of the whole set of particle release locations with some of the major deterministic deformation zones highlighted. The particular particles which are examined in this appendix are shown as light blue markers in Figure G-1. Since particle #228 has already been examined in detail in section 3.9.3, results here are given for particle #270, #866, and #1525. Only particle #270 is released within a conductive region of FFM01. The remaining two are given as typical examples of particles released directly to deformation zones.

Detailed profile of particle #270

The migration path for particle #270 is shown from a perspective view in Figure G-2.

The cumulative F-factor as a function of transport path length is shown in Figure G-3 where the different structural elements encountered by the particle are colour coded and labelled individually.

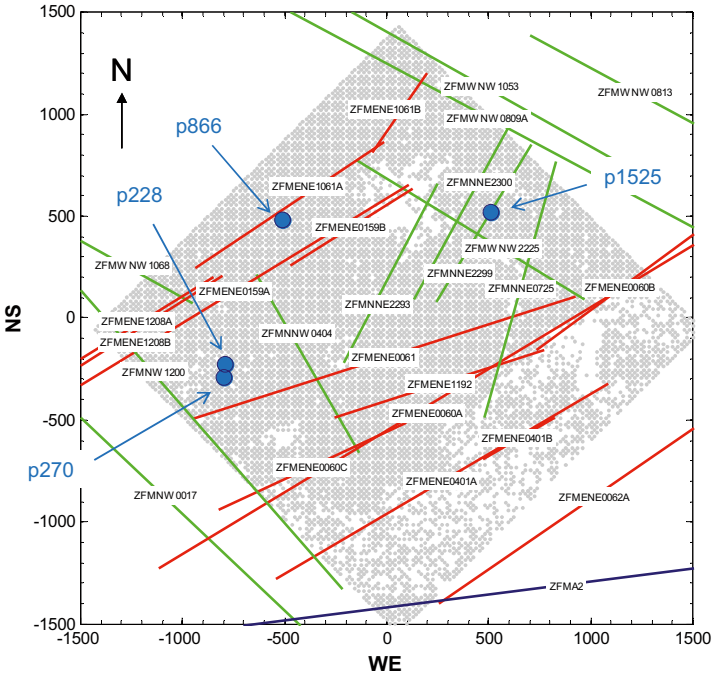

Figure G-1. *Visualisation of particle release locations (grey markers) where particles subject to detailed profiling in this report are highlighted (mauve blue markers). Major deformation zones with ENE strike are shown as red traces. Other significant deformation zones with NNE, WNW, NW orientation are indicated (green traces) as well as the gently dipping ZFMA2 zone (dark blue). The axis scaling is based upon a coordinate transformation with the origin at the centre of the particle release grid.*

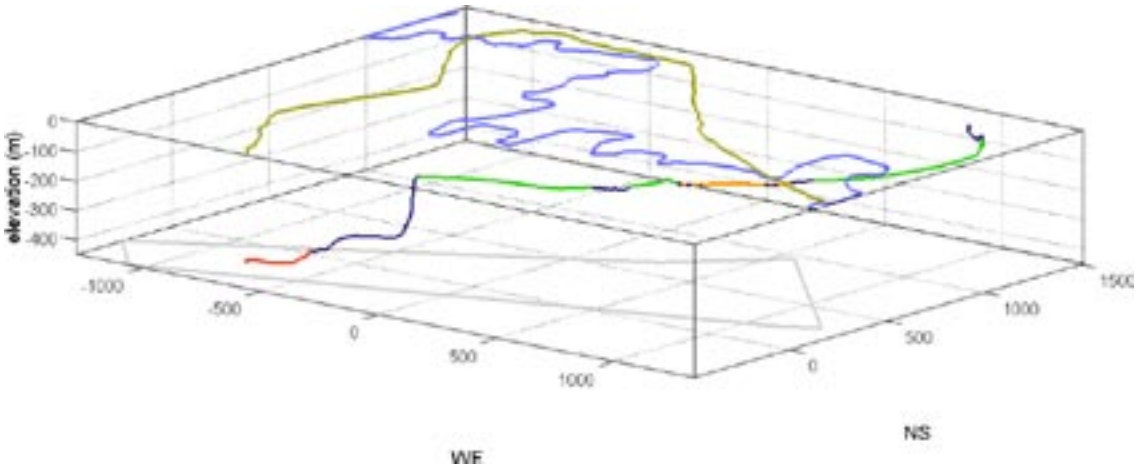

Figure G-2. *The transport path taken by particle #270 in perspective view looking NE. The path line is coloured with regard to structural elements that the particle encounters on its way to the surface exit location, i.e. red for fracture domain FFM01c (< –400 m), orange for upper levels of FFM01 and FFM06, dark blue for the various deterministic deformation zones, and green for near surface sheet joint features.*

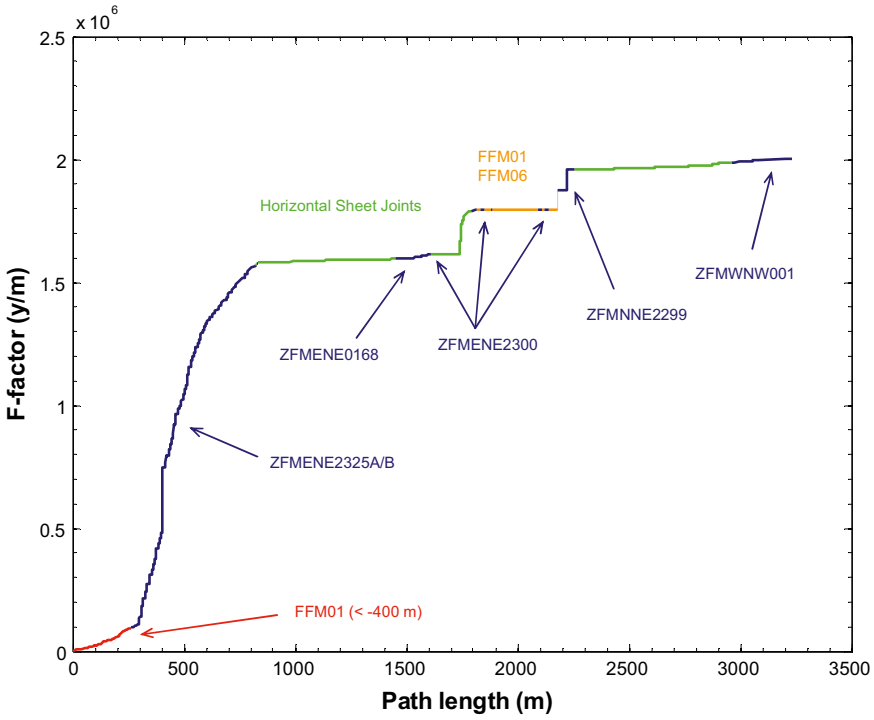

Figure G-3. *Cumulative F-factor (y/m) as a function of transport path length for particle #270.*

The cumulative advective travel time for the same particle is shown in Figure G-4.

Figure G-5 shows the local mean hydraulic conductivity encountered by the particle along its transport path plotted as a function of path length.

Figure G-6 shows the local hydraulic gradient experienced by particle #270 along its transport path. Figure G-7 immediately following shows a scatter plot of the hydraulic gradient plotted against the local mean hydraulic conductivity where the markers in the scatter plot are shaded with respect to elevation.

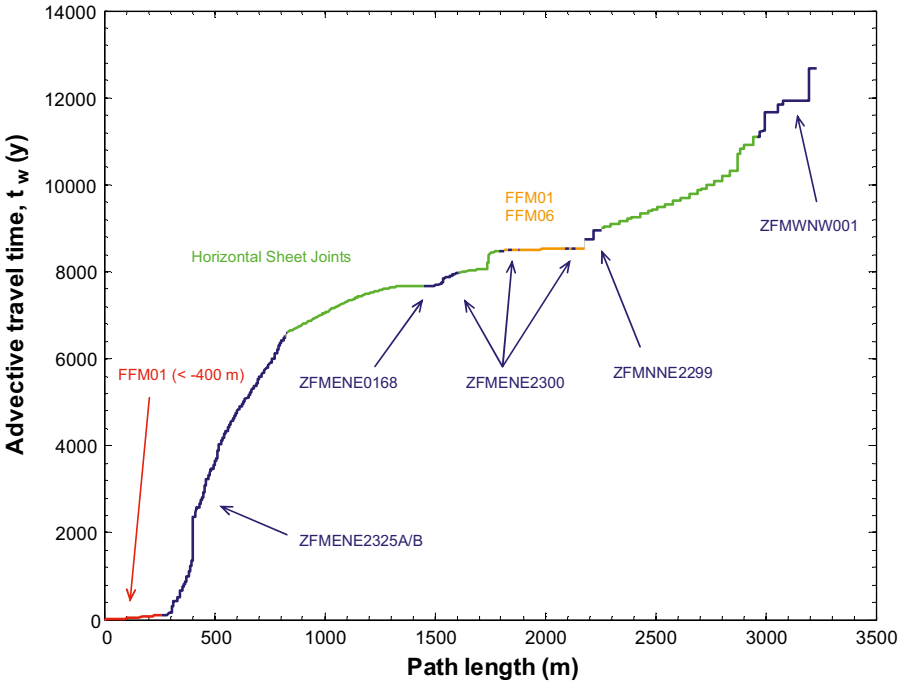

Figure G-4. *Cumulative advective transport time (y) as a function of transport path length for particle #270.*

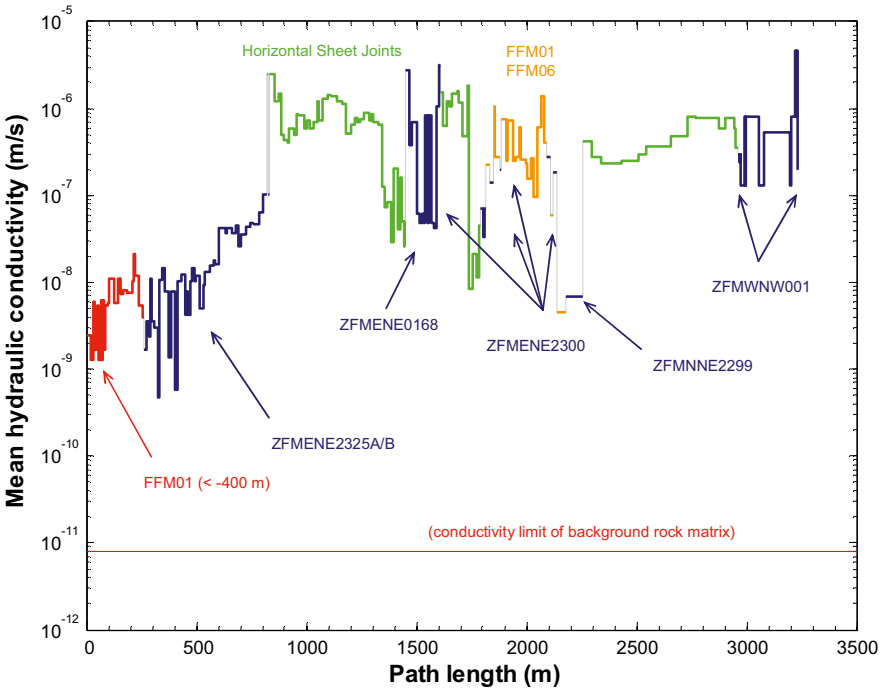

Figure G-5. *Local mean hydraulic conductivity (m/s) as a function of transport path length for particle #270. The broken horizontal line at the bottom of the figure represents the limit of hydraulic conductivity for the rock matrix itself assuming an in situ temperature of 12°C (this is defined as a permeability cut-off in ConnectFlow). The grey coloured segments represent discontinuities in the parameter value when the particle passes from one structural feature to another.*

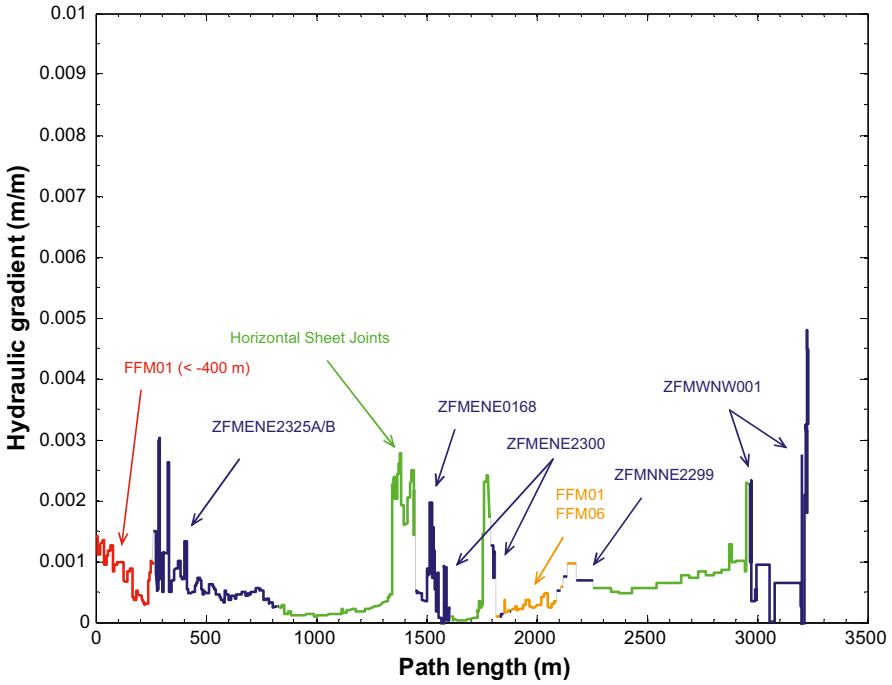

Figure G-6. *Local hydraulic gradient (m/m) plotted as a function of transport path length for particle #270.*

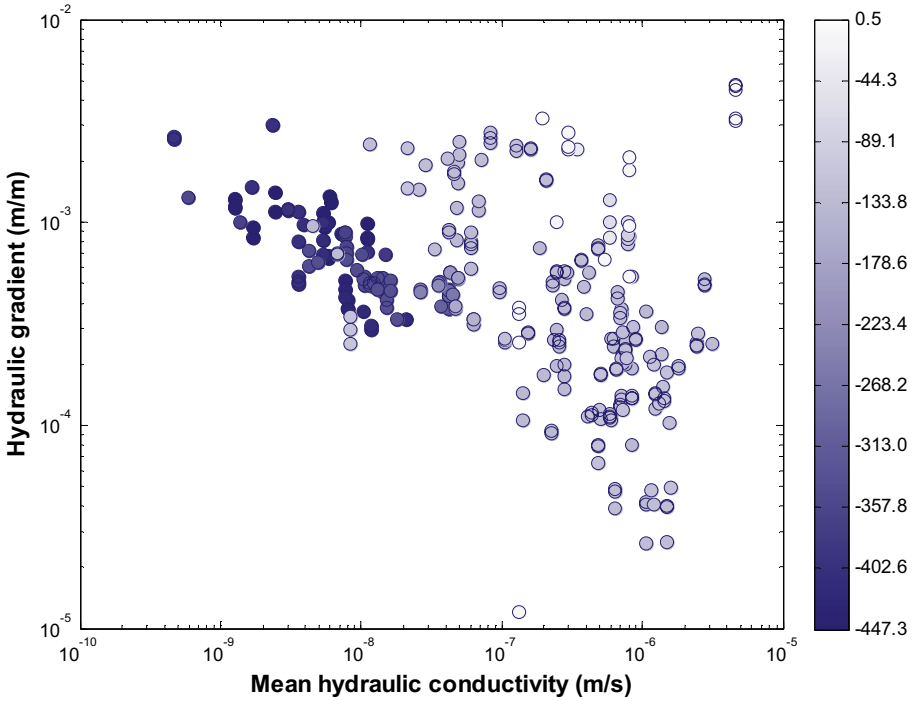

Figure G-7. *A scatter plot of the local hydraulic gradient (m/m) experienced by particle #270 along its transport path versus the mean hydraulic conductivity of the rock at that location. The symbols are shaded according to elevation (m) as specified in the colour bar to the right hand side of the figure.*

The specific flow-wetted surface used in the ECPM calculations is plotted in Figure G-8.

The local equivalent transport aperture (m) is given by the ratio of kinematic porosity and specific flow-wetted surface ($\delta_t = \theta_f / a_R$) and is shown in Figure G-9.

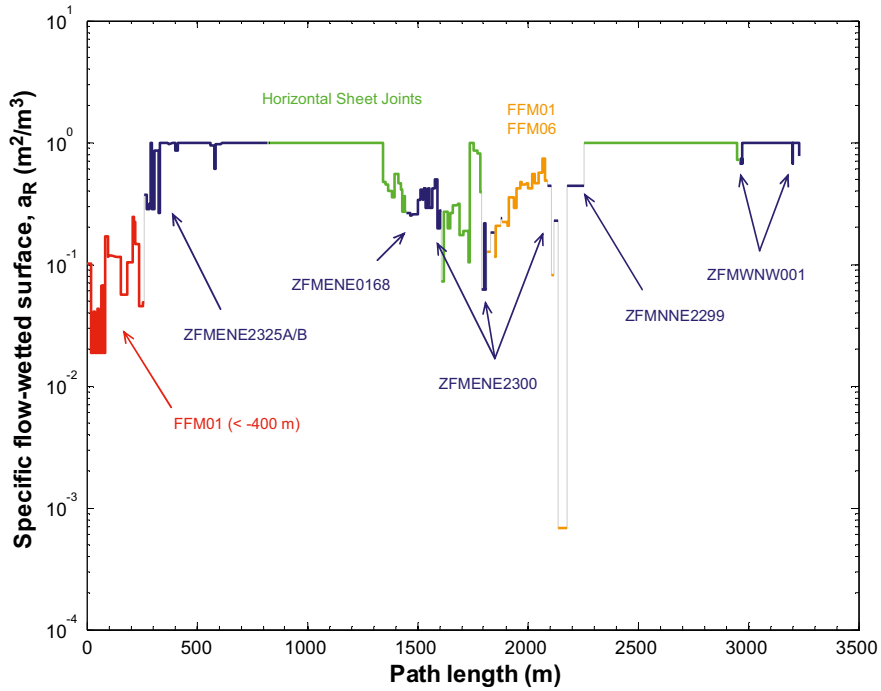

Figure G-8. *Local specific flow-wetted surface, a_R (m^2/m^3) encountered by particle #270 and plotted as a function of transport path length.*

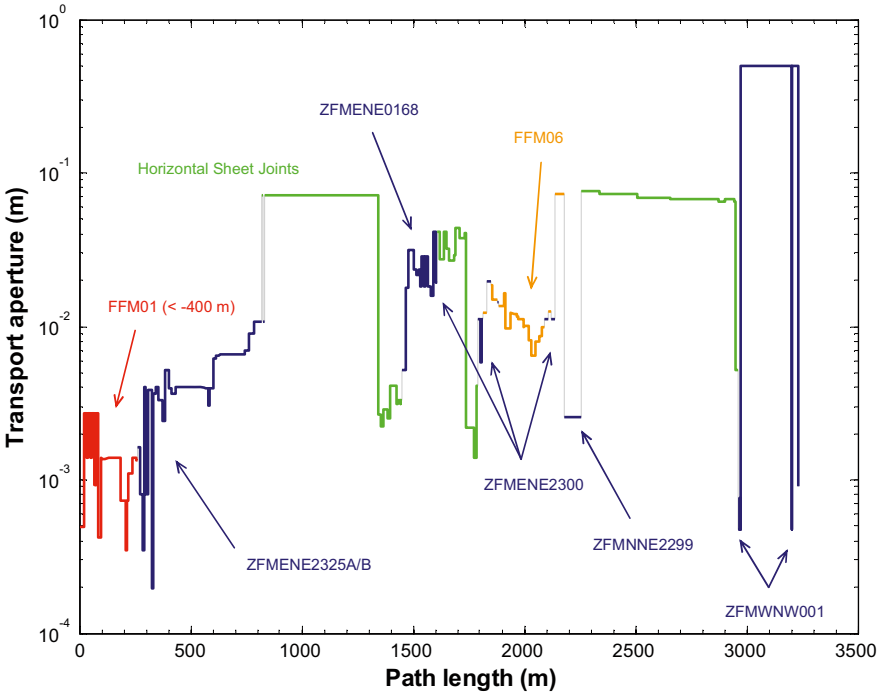

Figure G-9. *Local equivalent transport aperture (m), calculated as the ratio of kinematic porosity and specific flow-wetted surface, encountered by particle #270 and plotted as a function of transport path length.*

Interestingly, the F-factor accumulated within fracture domain FFM01c (< –400 m) for this particle is small in comparison to that subsequently accumulated during transport through deformation zones ZFMENE2325A and B. From the plots of the individual transport parameters it appears that the reason for this might be a much lower specific flow-wetted surface in FFM01 compared to the subsequent deformation zone, also combined with a hydraulic conductivity in the release location within FFM01 that is much higher than the expected average (see discussion in section 3.9.4) for this fracture domain elevation. Analogous behaviour is seen in the plot of cumulative advective travel time versus transport path length. This example possibly represents a more realistic transport path than that previously shown for particle #228 (section 3.9.3) since the particle is at no time observed to be transported advectively through the rock matrix.

The F-factor accumulated within the first 260 m after release in FFM01 is very low, and is approximately in the range of that predicted for the upper 5% of fast flowpaths in the scoping calculations for a 100 m voxel and the semi-correlated transmissivity model described in section 3.6.2.

The F-factor accumulated in the deformation zone ZFMENE2325A and B seems higher than what would be expected based upon comparison with the scoping calculation model described in section 3.7. This is thought to be partly due to a lower hydraulic gradient in the zone than assumed in the scoping calculations as well as a significantly higher specific flow-wetted surface implicit in the ConnectFlow simulations made using the ECPM.

Detailed profile of particle #866

The migration path for particle #866 is shown from a perspective view in Figure G-10. This particle is released within the deterministic deformation zone ZFMENE1061A to the North-West of release area, RA1 described in section 3.9 and is examined here as an example of a transport path starting from a large, deterministic deformation zone with an ENE strike.

The cumulative F-factor as a function of transport path length is shown in Figure G-11 where the different structural elements encountered by the particle are colour coded and labelled individually.

The cumulative advective travel time for the same particle is shown in Figure G-12.

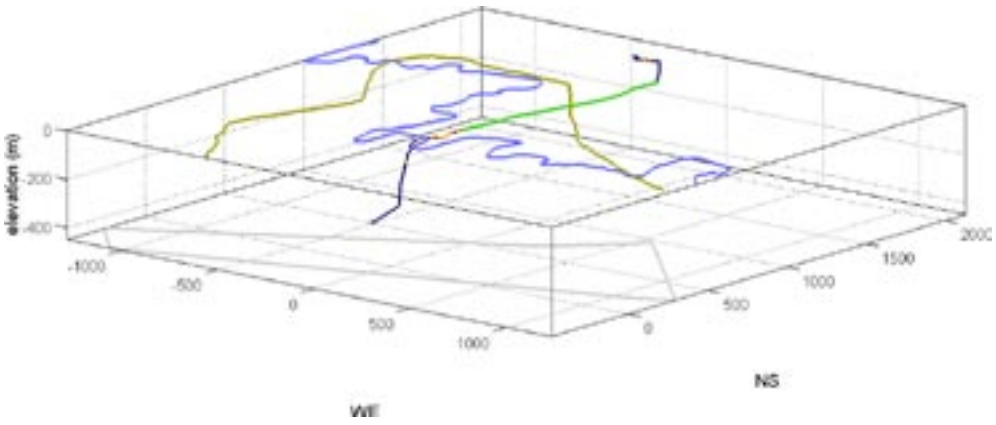

Figure G-10. *The transport path taken by particle #866 in perspective view looking NE. The path line is coloured with regard to structural elements that the particle encounters on it sway to the surface exit location, i.e. red for fracture domain FFM01c (< –400 m), orange for upper levels of FFM01 and FFM06, dark blue for the various deterministic deformation zones, and green for near surface sheet joint features.*

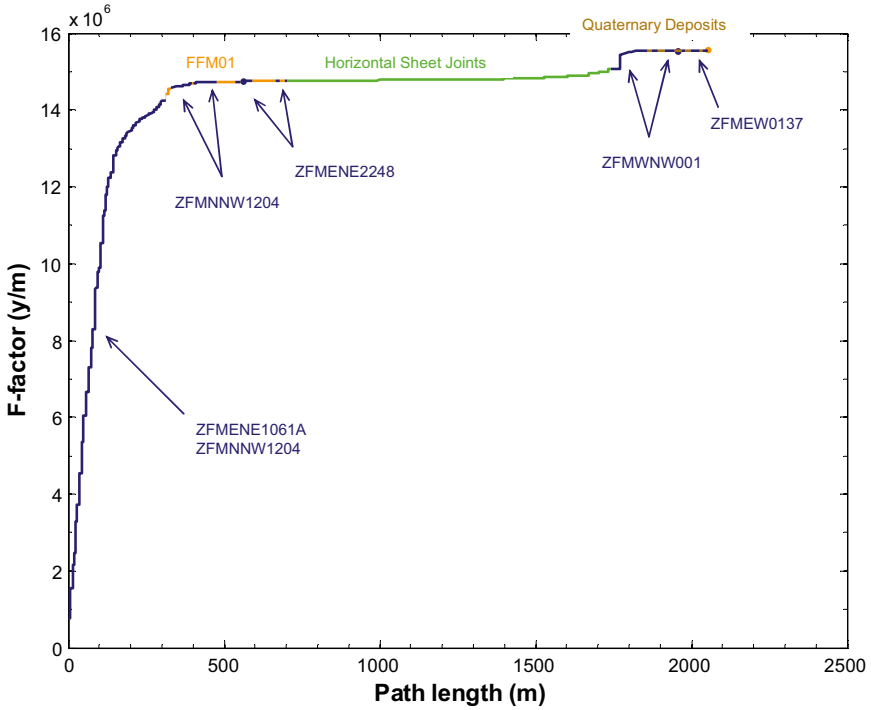

Figure G-11. *Cumulative F-factor (y/m) as a function of transport path length for particle #866.*

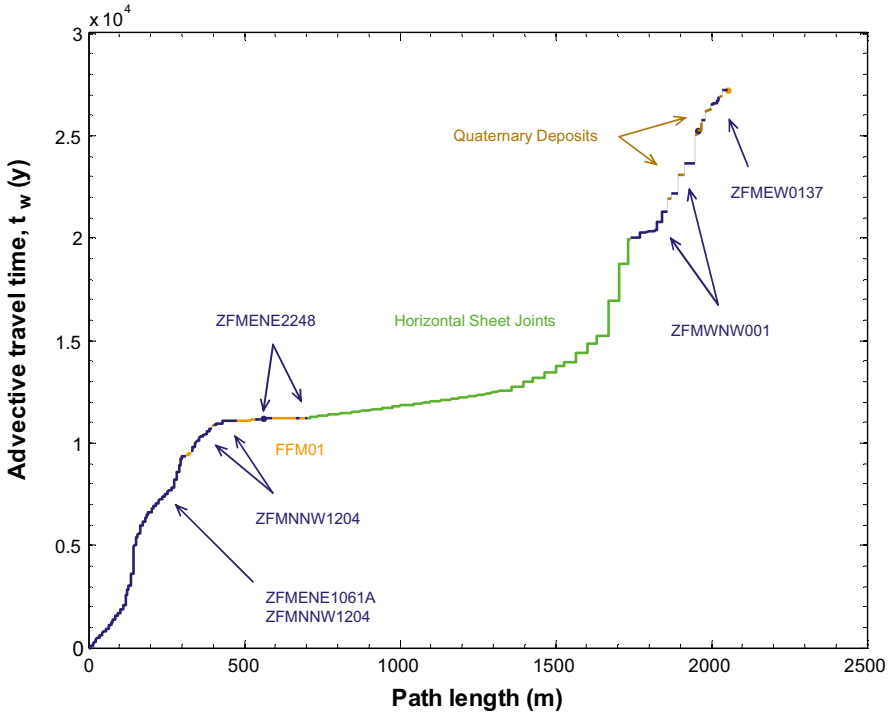

Figure G-12. *Cumulative advective transport time (y) as a function of transport path length for particle #270.*

Figure G-13 shows the local mean hydraulic conductivity encountered by the particle along its transport path plotted as a function of path length.

Figure G-14 shows the local hydraulic gradient experienced by particle #866 along its transport path. Figure G-15 immediately following shows a scatter plot of the hydraulic gradient plotted against the local mean hydraulic conductivity where the markers in the scatter plot are shaded with respect to elevation.

The specific flow-wetted surface used in the ECPM calculations is plotted in Figure G-16.

The local equivalent transport aperture (m) is given by the ratio of kinematic porosity and specific flow-wetted surface ($\bar{\delta}_t = \theta_f / a_R$) and is shown in Figure G-17.

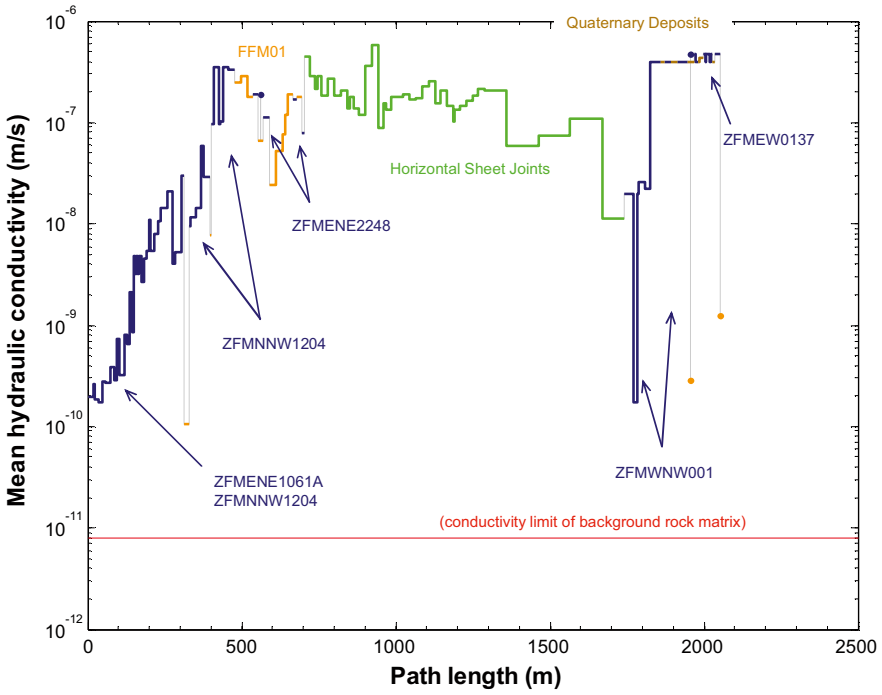

Figure G-13. *Local mean hydraulic conductivity (m/s) as a function of transport path length for particle #866. The broken horizontal line at the bottom of the figure represents the limit of hydraulic conductivity for the rock matrix itself assuming an in situ temperature of 12°C (this is defined as a permeability cut-off in ConnectFlow). The grey coloured segments represent discontinuities in the parameter value when the particle passes from one structural feature to another.*

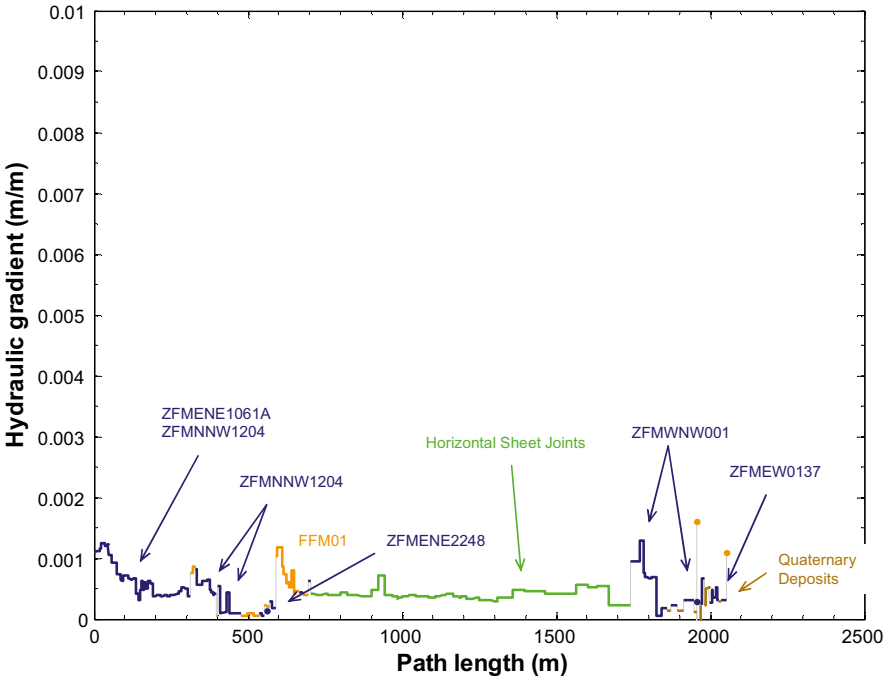

Figure G-14. *Local hydraulic gradient (m/m) plotted as a function of transport path length for particle #866.*

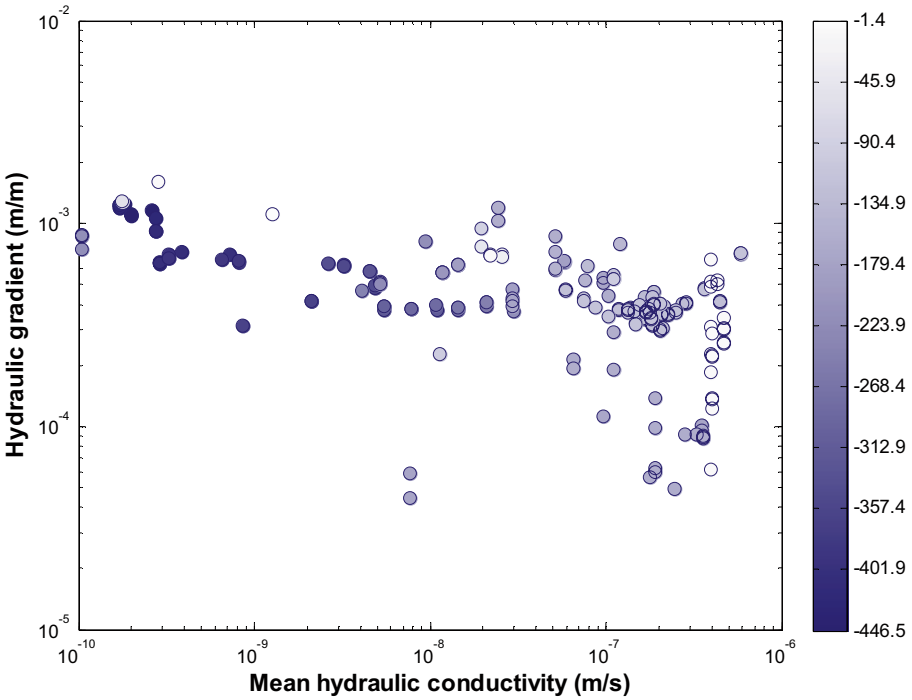

Figure G-15. *A scatter plot of the local hydraulic gradient (m/m) experienced by particle #866 along its transport path versus the mean hydraulic conductivity of the rock at that location. The symbols are shaded according to elevation (m) as specified in the colour bar to the right hand side of the figure.*

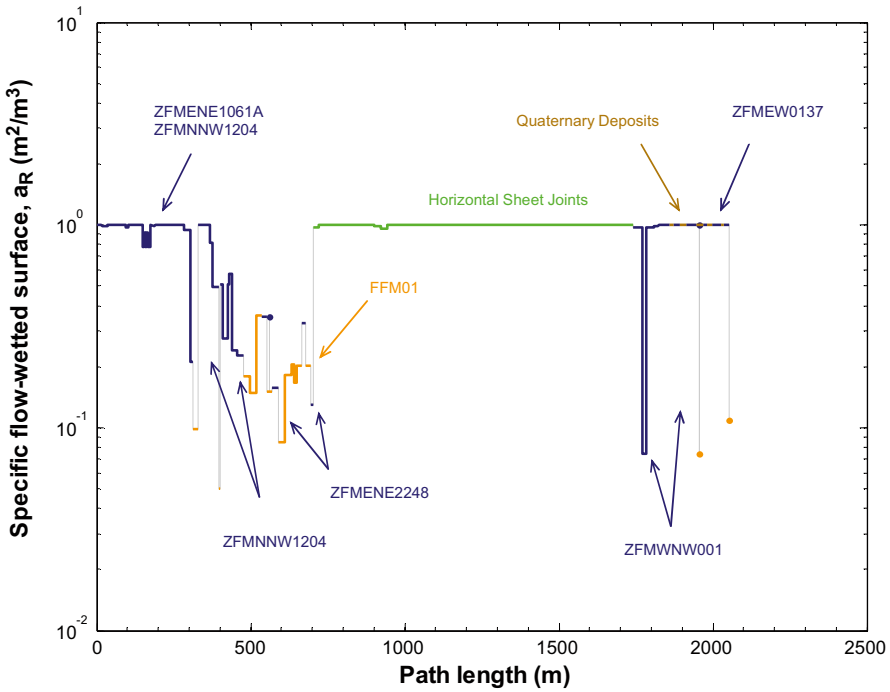

Figure G-16. *Local specific flow-wetted surface, a_R (m^2/m^3) encountered by particle #866 and plotted as a function of transport path length.*

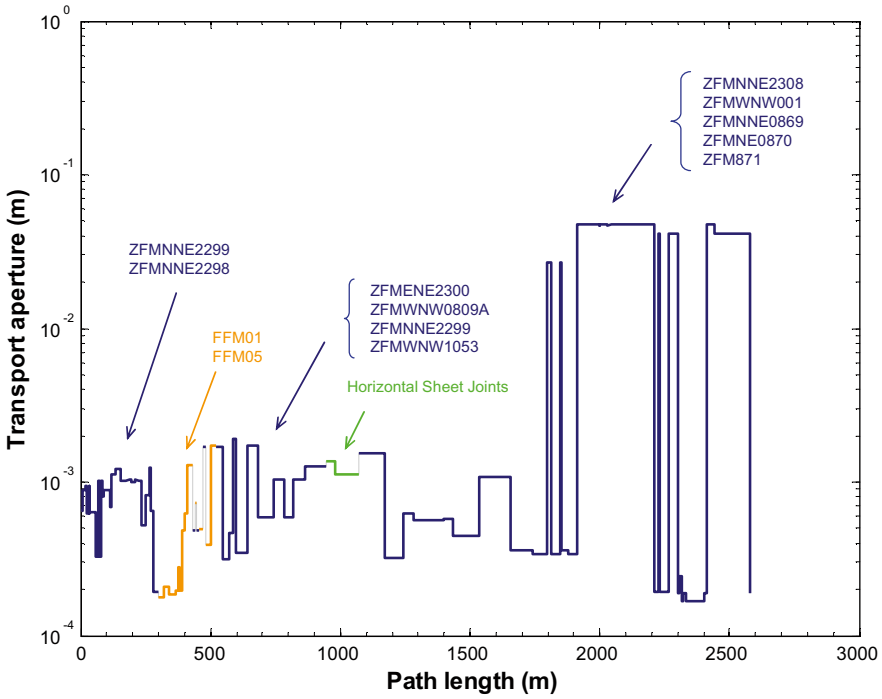

Figure G-17. *Local equivalent transport aperture (m), calculated as the ratio of kinematic porosity and specific flow-wetted surface, encountered by particle #866 and plotted as a function of transport path length.*

Detailed profile of particle #1525

The migration path for particle #1525 is shown from a perspective view in Figure G-18. This particle is released within the deterministic deformation zone ZFMNNE2299 (inside release area, RA1 as described in section 3.9) and is examined here as an example of a transport path starting from a large, deterministic deformation zone with a NNE strike.

The cumulative F-factor as a function of transport path length is shown in Figure G-19 where the different structural elements encountered by the particle are colour coded and labelled individually.

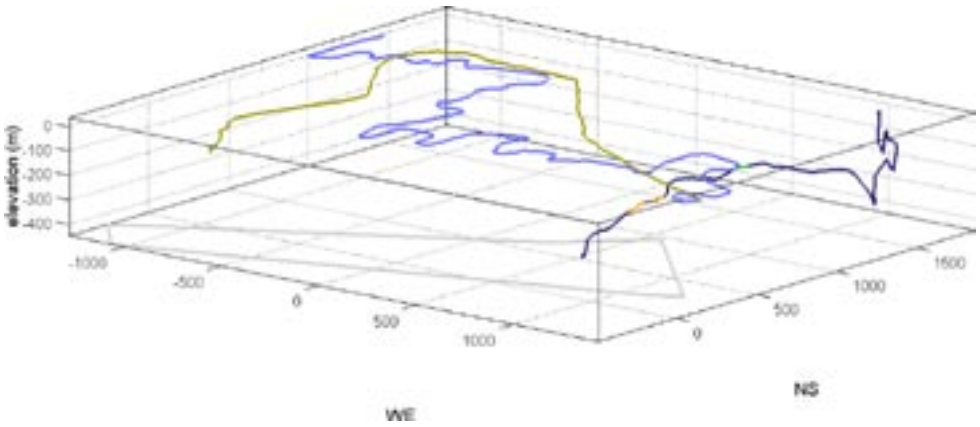

Figure G-18. *The transport path taken by particle #1525 in perspective view looking NE. The path line is coloured with regard to structural elements that the particle encounters on its way to the surface exit location, i.e. red for fracture domain FFM01c (< –400 m), orange for upper levels of FFM01 and FFM06, dark blue for the various deterministic deformation zones, and green for near surface sheet joint features.*

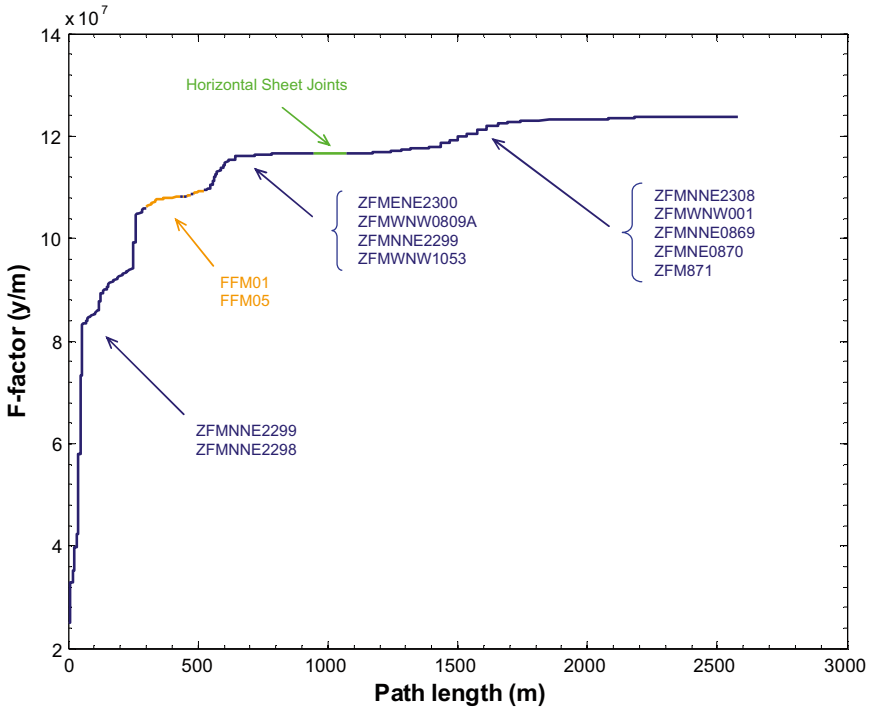

Figure G-19. *Cumulative F-factor (y/m) as a function of transport path length for particle #1525.*

The cumulative advective travel time for the same particle is shown in Figure G-20.

Figure G-21 shows the local mean hydraulic conductivity encountered by the particle along its transport path plotted as a function of path length.

Figure G-22 shows the local hydraulic gradient experienced by particle #1525 along its transport path. Figure G-23 immediately following shows a scatter plot of the hydraulic gradient plotted against the local mean hydraulic conductivity where the markers in the scatter plot are shaded with respect to elevation.

The specific flow-wetted surface used in the ECPM calculations is plotted in Figure G-24.

The local equivalent transport aperture (m) is given by the ratio of kinematic porosity and specific flow-wetted surface ($\bar{\delta}_t = \theta_f / a_R$) and is shown in Figure G-25.

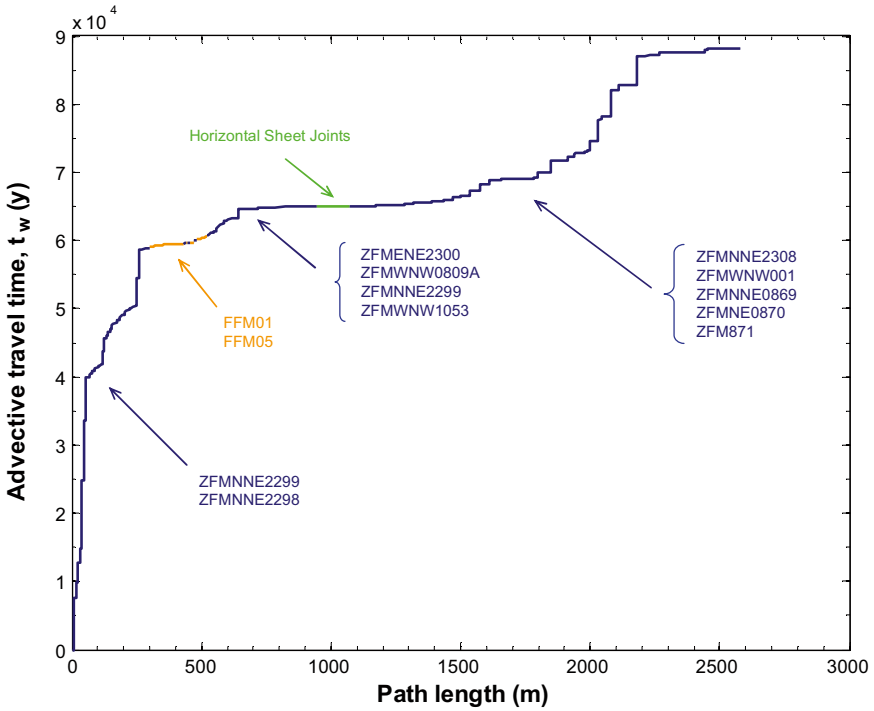

Figure G-20. *Cumulative advective transport time (y) as a function of transport path length for particle #1525.*

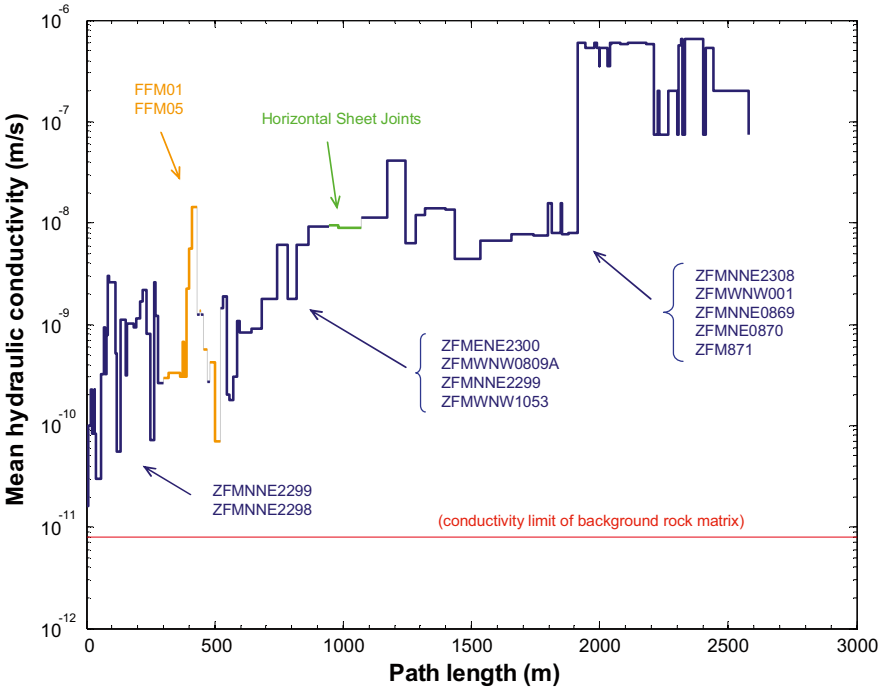

Figure G-21. *Local mean hydraulic conductivity (m/s) as a function of transport path length for particle #1525. The broken horizontal line at the bottom of the figure represents the limit of hydraulic conductivity for the rock matrix itself assuming an in situ temperature of 12°C (this is defined as a permeability cut-off in ConnectFlow). The grey coloured segments represent discontinuities in the parameter value when the particle passes from one structural feature to another.*

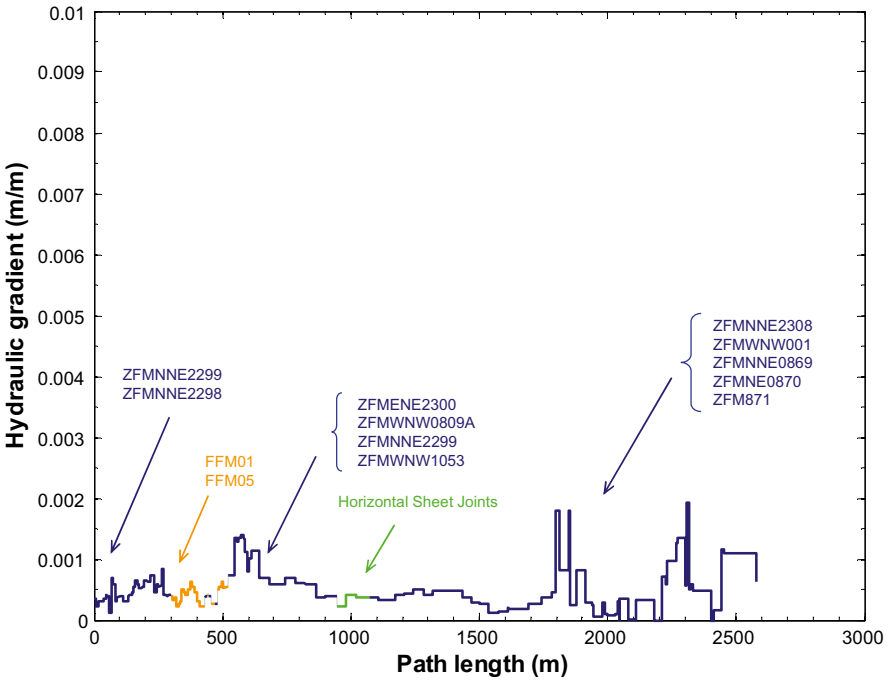

Figure G-22. *Local hydraulic gradient (m/m) plotted as a function of transport path length for particle #1525.*

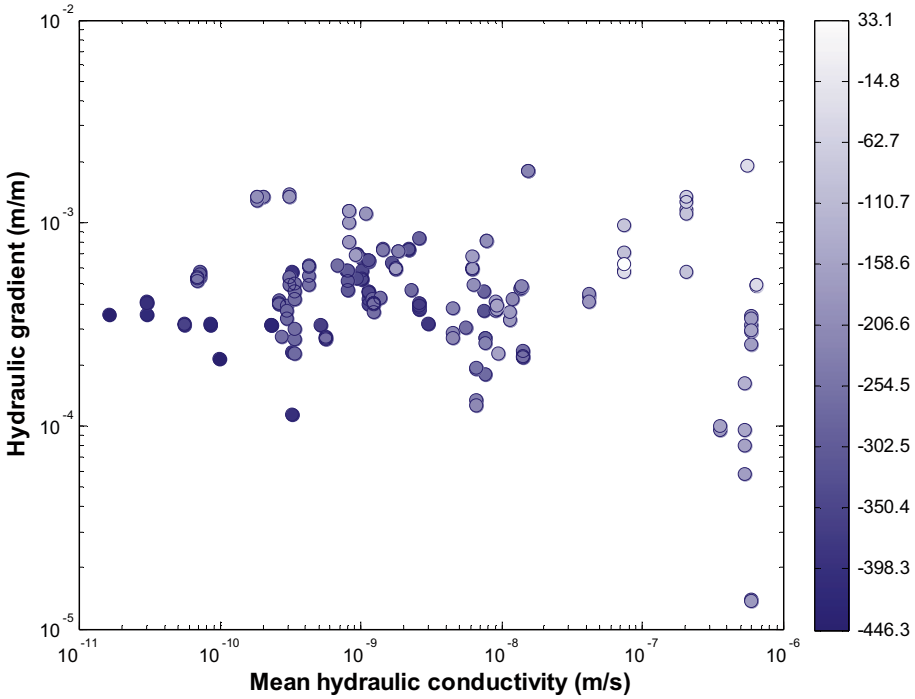

Figure G-23. *A scatter plot of the local hydraulic gradient (m/m) experienced by particle #1525 along its transport path versus the mean hydraulic conductivity of the rock at that location. The symbols are shaded according to elevation (m) as specified in the colour bar to the right hand side of the figure.*

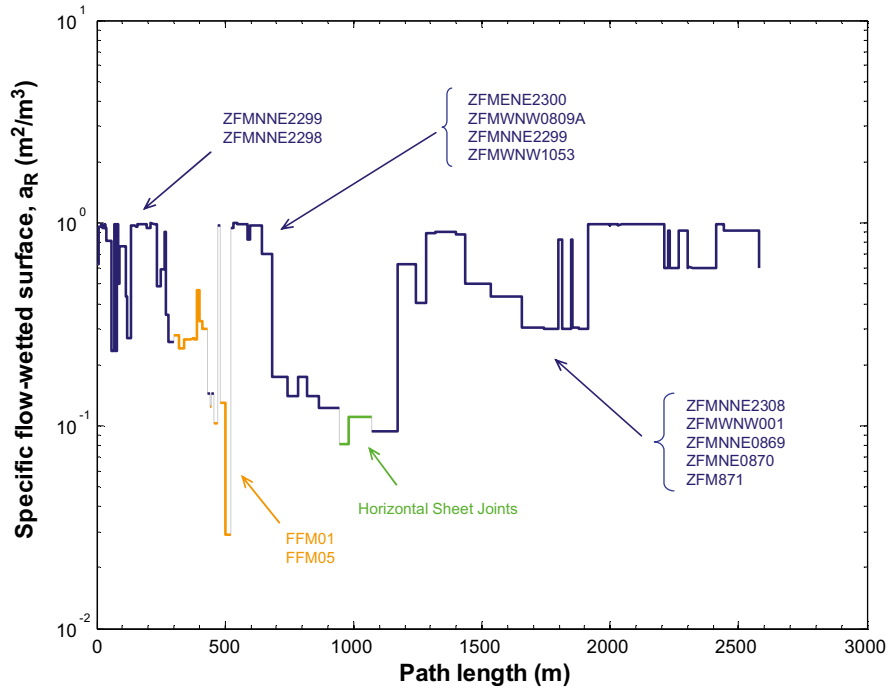

Figure G-24. *Local specific flow-wetted surface, a_R (m^2/m^3) encountered by particle #1525 and plotted as a function of transport path length.*

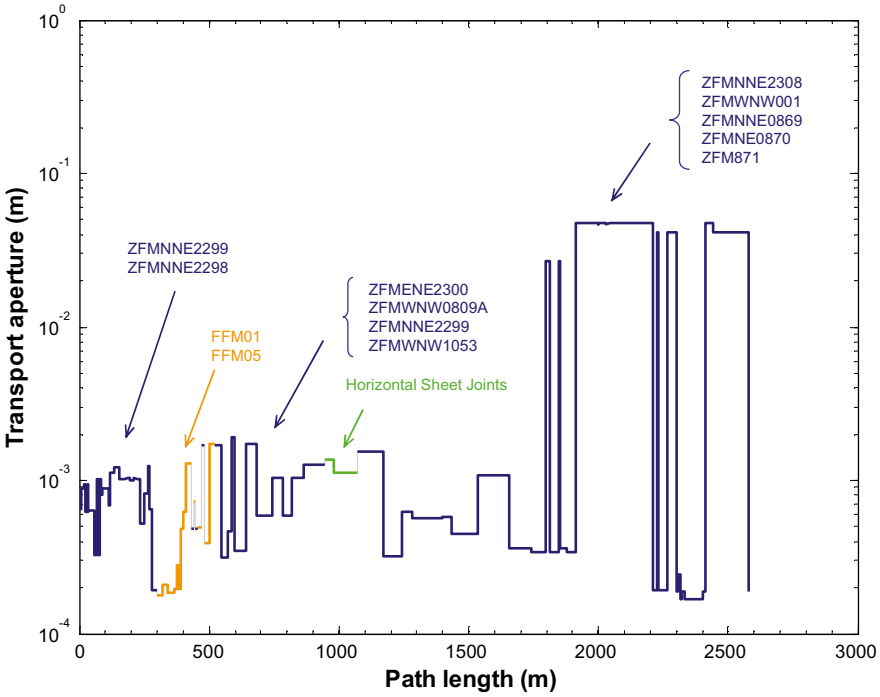

Figure G-25. *Local equivalent transport aperture (m), calculated as the ratio of kinematic porosity and specific flow-wetted surface, encountered by particle #1525 and plotted as a function of transport path length.*

Appendix H

On the use of *in situ* formation factors

Authors: James Crawford and Martin Löfgren

Introduction

In the transport calculations presented in this report, we base the effective matrix diffusivity upon formation factor data obtained *in situ* using electrical methods. We believe that this data may more accurately reflect the properties of the rock matrix at repository depth, compared to data obtained in the laboratory on drill core samples, which could be considerably affected by stress relaxation and mechanical damage. Before using estimated formation factors based upon *in situ* resistivity data, however, there are a number of issues which need to be considered. These are discussed in this Appendix chapter, which has the following outline:

Theory: A short description of the formation factor and its relation to key parameters underlying the electrical methods.

In situ rock resistivity measurements and data uncertainty: A short description of how the *in situ* rock resistivity is measured and issues of uncertainty related to such measurements.

Estimates of electrical conductivity of in situ pore water and data uncertainty: A short description of how the electrical conductivity (EC) of the *in situ* pore water is measured or estimated, and its associated uncertainty.

Evidence of pore connectivity: A discussion of the evidence for large-scale pore connectivity; a much debated issue that is of great importance for radionuclide retention and a prerequisite for the application of electrical methods *in situ*.

Effect of stress relaxation and mechanical damage: When comparing results from *in situ* and laboratory measurements the comparison is complicated by the fact that the core samples used in laboratory investigations have been subjected to a different degree of stress relaxation and mechanical damage than the *in situ* rock in the vicinity of a borehole.

Corrections required to account for differences between measurement methods: When comparing results obtained by electrical methods and traditional diffusion-based methods (whether in the laboratory or *in situ*) the comparison is complicated by the fact that the two methods do not utilise the same pore water species as a probe of migration. Therefore, corrections are needed to account for inherent mechanistic differences between the two approaches.

Representative results: After having discussed the above issues, which is a requirement for assessing the usefulness of the *in situ* method in comparison to the laboratory method, some representative results obtained by the *in situ* method are presented.

Theory

The effective diffusivity of the rock matrix is often given in terms of the formation factor, F_f as:

$$D_e = F_f D_w \qquad \text{(H-1)}$$

Where D_w is the diffusivity of the solute in free solution, often approximated by the diffusivity of the solute at infinite dilution. The formation factor is a purely geometric entity that is only dependent on the bulk geometrical properties of the micropore network and is independent of the identity of the diffusing species. Specifically, it accounts for the combined effects of porosity, tortuosity and constrictivity on the effective rate of diffusive transport in the rock.

A prerequisite for the formation factor to be genuinely independent of the identity of a diffusing solute species is firstly that the size of the solute is small compared to that of the pore diameter (or other appropriate characteristic length of the confined pore space). In crystalline rock this is not a major issue for most dissolved species owing to their small size relative to that of the pores. An issue that has not yet been satisfactorily examined and discussed within the scientific community is how to internalise influences of diffusive processes occurring in the vicinity of charged mineral surfaces into the formation factor (or, whether or not it is a good idea to do so). In safety assessment calculations a cautious approach is generally taken whereby effects lowering the effective rate of diffusive transport (anion exclusion) are internalised in the formation factor, whereas effects that may increase this (surface diffusion) are excluded.

Traditionally, the effective diffusivity of crystalline rock has been examined by allowing solutes, often in trace amounts, to diffuse through rock samples and to observe their apparent macroscopic diffusive flux. An alternative method, implemented within the SKB site investigation programme, allows solutes to migrate in the porous system under the influence of an electric potential. The undisputed fact that there is a mechanistic analogy between diffusion and electromigration has been known for about a century, the relation between the diffusivity and ionic mobility being formalised in the Einstein relation /e.g. Atkins 1999/.

A precondition for using the relation between electro-migration and diffusion in a porous system is that the matrix surrounding the water saturated pores (mineral grains in the case of crystalline rock) do not conduct current. This condition is fulfilled at Forsmark, as the principal minerals (e.g. plagioclase, quartz, etc) of the most common rock types have electrical conductivities orders of magnitude lower than that of the water saturated rock. Phase angle measurements on laboratory samples /e.g. Thunehed 2005ab, 2007ab/ also suggests that anomalous conductive properties of the rock matrix due to the presence of significantly conductive minerals (principally pyrite or magnetite) and membrane effects associated with clay minerals are not common for rock samples from Forsmark.

From the Einstein relation it is relatively straight-forward to deduce the relations between effective diffusivity, electrical current, electrical conductivity (EC), and resistance as has been previously shown in /e.g. Löfgren 2004/ for crystalline rock. The formation factor (F_f) can be defined in terms of either electrical resistivity or EC as:

$$F_f = \frac{\rho_w}{\rho_r} = \frac{\kappa_r}{\kappa_w} \qquad \text{(H-2)}$$

Here, the terms ρ_w and ρ_r are the electrical resistivity (Ωm) of the pore water and saturated rock respectively, while κ_w and κ_r are the corresponding terms for electrical conductivity (S/m).

By using Equations H-1 and H-2, the effective diffusivity *in situ* can be assessed if the *in situ* rock resistivity (which can be measured) and the EC of the *in situ* pore water (which can be either measured or estimated) are both known.

In-situ rock resistivity measurements and data uncertainty

Measuring the *in situ* rock resistivity by electrically based, geophysical methods has been commonplace for decades even in crystalline rock such as granite. In essence, an alternating electrical current is sent out into the rock matrix from a probe lowered down a borehole. The tool used in the SKB site investigations is a focused tool whereby the current is sent out in an orthogonal direction to the borehole. This minimizes the influence of the borehole itself on the results and also that of an adjacent zone of rock subjected to stress release and mechanical damage. Measurements are made at 10 cm intervals along the borehole which may be as much as 1,000 m in length. The resistivity tool and method used in the SKB site investigations are described in /e.g. Löfgren 2007/.

A problem that can potentially bias the data obtained using *in situ* measurements is the upper measurement limit of the resistivity probe which, for highly impermeable media, can result in truncation of the lower tail of the formation factor distribution. If not accounted for in the data interpretation, this can result in apparent formation factors higher than in actuality. The sensitivity of the resistivity probe used in the site investigations (Century 9072) varies according to the site specific conditions, although it is known to be quantitatively accurate to a rock resistivity of 50,000 Ωm and qualitatively accurate to roughly 80,000 Ωm with roughly 10% uncertainty /Löfgren and Neretnieks 2005/. The bulk of the resistivity data (80–90%) obtained in most boreholes at Forsmark are well within the range of the quantitative measurement limits of the resistivity probe used. For KFM01D and KFM08C, 93% and 96% respectively of the measurement data lie within the quantitative limits /Löfgren 2007/.

Estimates of electrical conductivity of *in situ* pore water and data uncertainty

A correct estimation of the formation factor requires an accurate knowledge of the EC of the pore water of the rock matrix. Within the SKB site investigation programme the composition of the pore water has for some boreholes been investigated by leaching drill core samples /e.g. Waber and Smellie 2007/. From the assessed concentration of the major groundwater constituent Cl^-, and the knowledge of the *in situ* temperature, the *in situ* EC of the pore water has been estimated /e.g. Löfgren 2007/. Such pore water EC data are shown in Figure H-1, for boreholes KFM01D (red filled circles) and KFM08C (blue filled circles).

In addition to estimating the EC of the *in situ* pore water by leaching of drill core samples, the EC of freely flowing groundwater has been directly measured *in situ*. This was done by isolating short sections around hydraulically conductive fractures, pumping for an extensive period of time, and measuring the EC of the groundwater flowing out from the fractures. These data points are shown as filled triangles in Figure H-1, for boreholes KFM01D (red) and KFM08C (blue).

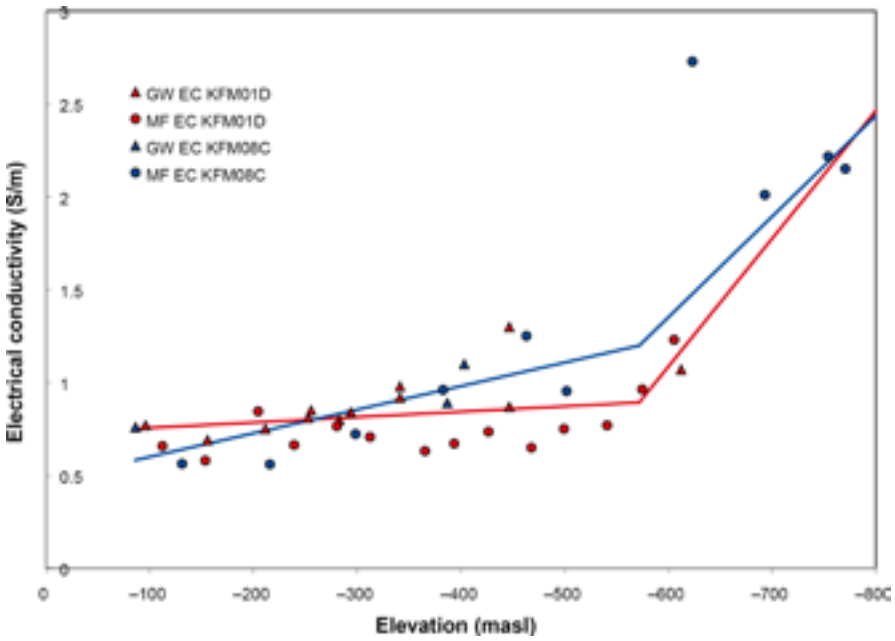

Figure H-1. *Groundwater (GW) and matrix porewater (MF) EC at in situ temperature in KFM01D and KFM08C. Figure taken from /Löfgren 2007/.*

As can be seen in Figure H-1, the data obtained by the different methods do not differ remarkably, considering that each method is associated with data uncertainties. Even when there is a wealth of such data as in KFM01D and KFM08C, which is not generally the case for the Forsmark boreholes, there is a need to interpolate between the data points. This is shown in Figure H-1 by the red and blue solid lines for KFM01D and KFM08C, respectively. Where there is a lack of data, the interpolation becomes somewhat subjective as can be seen, for example, around –600 m elevation in KFM08C and below –600 m in KFM01D.

There are a number of sources of error that give rise to data uncertainties associated with estimation of the EC from leached core samples. One is sample handling where samples taken to the surface are subject to stress release and mechanical damage. This could potentially result in their original pore water being diluted or altered in other ways. In /Waber and Smellie 2007/, however, it was found that although a certain amount of stress relaxation did occur either during or after bore core retrieval, there was no detectable borehole water contamination and these effects could be accounted for in a rigorous manner.

Another source of data uncertainty is that in order to calculate the original concentration of the pore water from the concentration of the leachate, the porosity of the core sample must be known. In addition to this, there are also data uncertainties associated with sample preparation and analysis. Even so, the estimated total data uncertainty of the pore water chloride concentration is only about 10% in /Waber and Smellie 2007/. A similar magnitude of uncertainty is likely to be introduced when estimating the EC at *in situ* temperature from this chloride concentration.

Sources of data uncertainty for the EC estimated from measurements of free flowing groundwater are the following:

- Under the influence of pumping, the groundwater may have flowed relatively quickly from another location and may not be representative of the rock matrix porewater in the locality where it is sampled.
- The sampled groundwater may have been diluted by the drilling fluid or other water flowing in the borehole.
- Even if the groundwater is representative for the location, it is not necessarily equilibrated with the pore water at some distance from the fracture within the rock matrix.

It is not an easy task to quantify the data uncertainty of the estimated pore water EC profile. If examining Figure H-1 between the elevations –100 m to –600 m below sea level, the total spread in the data is less than a factor of three. As this spread also includes natural variability, the true data uncertainty should be even lower. From about –600 m to –800 m, the density of data points is smaller and perhaps the estimated EC profile in this interval range is less well founded. Even so, the spread of data in this range is still not more than a factor of three.

An additional uncertainty associated with borehole *in situ* resistivities logged for Forsmark early-on in the site investigations was due to some electrical conductivities (used for estimating the EC profile) being reported at *in situ* temperature and some at 25°C. It is possible that the original formation factor data reported for borehole KFM01A, for example, /Löfgren and Neretnieks 2005/ may be biased downwards by a factor of as much as 50%, partly due to this reason (this has been accounted for in the following discussions with regard to Figure H-3).

Evidence of pore connectivity

The connectivity of the microporous system of crystalline rock is an issue that has been hotly debated within the scientific community for decades. The *in situ* rock resistivity tool used by SKB in the site investigations is claimed to emit a current many meters into the rock matrix. As the mineral grain resistivity of the rock is so large, the current should be propagated predominantly in the interstitial water of the microporous system. The fact that very reasonable formation factors are obtained with the *in situ* method indicates that the current indeed penetrates

the rock matrix on the scale of many metres. If only small scale connectivity existed, say on the scale of centimetres to a few decimetres, the rock resistivity would be much larger than what is actually measured and consequently, the obtained formation factors would be unreasonably low.

It has been questioned whether the concept of large-scale pore connectivity can be justified on the basis of the propagation of an alternating current, where the current-bearing ions only migrate over minute distances. In order to investigate this, the through-electromigration method was developed, where direct current is used to propagate ionic tracers through the rock /Löfgren and Neretnieks 2006/. In this investigation it was shown that the alternating current and direct current methods gave comparable results on drill core samples (from the Laxemar site) up to 12 cm in length.

Large-scale pore connectivity can also be inferred from *in situ* migration experiments where diffusion has been the only significant transport mechanism. An important example is the in-diffusion experiment performed at the Stripa mine /Birgersson et al. 1992/ where tracers were shown to have migrated to a depth of at least 40 cm into the undisturbed rock matrix; a distance consistent with the expected penetration depth on the time scale of the experiment. As mentioned previously in this report, the characterisation of porewater many tens of metres distant from known fractures shows relict indications of past climatic conditions and groundwater compositions /Laaksoharju et al. 2008/ that differ significantly from what would be expected if the porewater originated purely from initially existing fluid inclusions of formation water. This observation, in itself, is strong corroborating evidence for the existence of a connected microporosity in the rock.

It should be noted that dissolved species migrating in the microporous network, whether driven by a concentration gradient or an electrical potential gradient, do not discriminate pores based on their origin. Migration occurs in all connected porosity, including grain boundary pores, micro-fractures and sometimes sheet silicate pores. It is therefore not strictly necessary to make pronouncements on the relative proportions and distribution of micro-fracture versus grain boundary porosity *in situ* as discussed in section 2.2.1 to justify the use of *in situ* data derived from electrical resistivity measurements.

Effect of stress relaxation and drilling induced mechanical damage

Within the SKB site investigations, much effort has been spent on obtaining formation factors by using three different, although complementary methods. One is the traditional through-diffusion method using a concentration gradient as the driving force for migration, which is performed in the laboratory on short drill core samples /e.g. Widestrand et al. 2003/. The other is the *in situ* method that is the focus of attention for this appendix chapter. The third is a similar electrical method applied to drill core samples in the laboratory. All three methods are associated with their own specific data uncertainty issues, but there is one issue that deserves extra attention. This issue concerns drill core samples that are subjected to stress relaxation and drilling induced mechanical damage. In addition to this, short drill core samples of, say 10 mm length may also be significantly affected by sawing induced mechanical damage.

When a drill core sample is excavated and taken to the surface, the confining pressure it has been subjected to *in situ* is released. As a result, tension in the mineral grains may be released and different minerals may expand to different degrees, depending on their bulk moduli of expansion. This generally gives rise to increased porosity, which in turn gives rise to an increased formation factor. The increase in porosity may to some extent be reversed, by re-confining the rock sample in triaxial compression tests /e.g. Jacobsson 2007/, as discussed in section 2.2.1.

Within the site investigation programme, formation factor measurements in the laboratory have not been performed on re-confined samples. However, such measurements have been performed elsewhere and a reduction in the formation factor for crystalline rock samples under increasing applied confining stress is well known in the literature /e.g. Skagius and Neretnieks 1986, Brace et al. 1965/.

As already discussed in section 2.2.1 there is strong corroborating evidence that suggests a possible compression of pore spaces under *in situ* stress conditions. Specifically, porosity measurements made in triaxial compression tests /Jacobsson 2007/ and measurements from the matrix pore water characterisation /Waber and Smellie 2007/ give indications of this phenomenon. No strong depth trend for the *in situ* formation factor is perceptible at the Forsmark site, although this could be related to the high absolute magnitude of *in situ* stress /Glamheden et al. 2007/ observed throughout the boreholes at the Forsmark site. A tendency towards slightly increasing formation factors with increasing depth is seen in certain laboratory data sets, in particular the data reported for KFM01A (see Figure H-3), which could be interpreted as an indication of a drilling induced damage effect.

Partially corroborating evidence for the impact of the confining stress on the microporous system is available in the form of laboratory measurements of flow permeability. Permeability and effective diffusivity are very closely related since they are both highly dependent upon the geometry of the microporous structure in the rock. In /Siitari-Kauppi 2002/, for example, a near perfect linear correlation is found between the permeability of crystalline rock samples and effective diffusivity. As part of the site investigations, the permeability of drill core samples from KFM01D was measured at different confining pressures /Vilks 2007/. Although there are some additional issues associated with bore core damage and the creation of new micro-fractures in the small samples used in these experiments, a tendency for decreased permeability with increasing confining pressure is apparent in a number of the data sets (see Figure H-2).

There also appears to be a substantial amount of spatial variability and anisotropy in the permeability of the samples investigated. This may be related to the highly anisotropic nature of the *in situ* stress field within FFM01. It is also relevant to note that the maximum confining pressure used in these experiments is slightly less than half that existing at repository depth within FFM01.

Mechanical damage due to drilling or other sample preparation is an issue that should not be confused with the issue of stress relaxation. The degree of mechanical damage inflicted on the excavated sample depends on numerous factors such as the rock type, properties of the drill bit

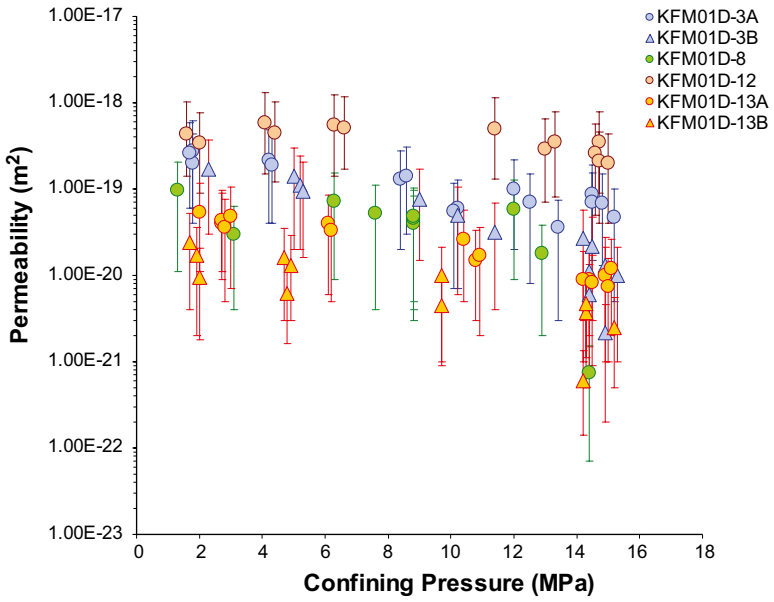

Figure H-2. *Results of laboratory permeability measurements on core samples from borehole KFM01D /Vilks 2007/. Data series labelled 3A/B and 13A/B are for samples from the same core sample, although measured parallel (A) and normal (B) to the core axis respectively.*

and sawing blade, the power applied in the drilling and sawing, percussive vibration, etc. The porosity induced as result of mechanical damage during the excavation process would most likely be best characterised as a tendency to increased intensity of micro-fracturing. We would expect this damage to increase slightly with depth as the mechanical force which needs to be applied during core drilling often tends to increase with depth. When excavating a sample and taking it to the laboratory, the increased porosity is due to both stress relaxation and mechanical damage. Predicted trends of increased porosity or formation factor in the laboratory compared to *in situ* values at different depths may also be masked by mechanical damage effects that are not directly related to the drilling process itself (i.e. sample sawing).

Stress relaxation most likely affects the entire core sample, whereas damage effects may be concentrated near the periphery of the sample. Since the damaged zone *in situ* forms a series resistance with outlying undamaged rock during resistivity logging, the *in situ* data will be only marginally affected by damage in the immediate vicinity of the borehole. Resistivity and through diffusion measurements performed on core samples in the laboratory, on the other hand, are typically made parallel to the core sample axis. In this configuration, the damaged zone will most likely form a parallel resistance which could have a larger impact upon laboratory based measurement results.

If it were not for the disturbance in porosity arising due to sample excavation, the formation factors obtained in the laboratory by electrical methods should be comparable to those obtained *in situ*. A prerequisite for this, of course, is that the *in situ* pore water EC is correctly estimated. If applying the best known EC profile for the pore water at Drill Site 1 (solid red line in Figure H-1) and the *in situ* rock resistivity data obtained in KFM01A /Nielsen and Ringgaard 2003/, the *in situ* formation factor log shown in Figure H-3 is obtained (green markers).

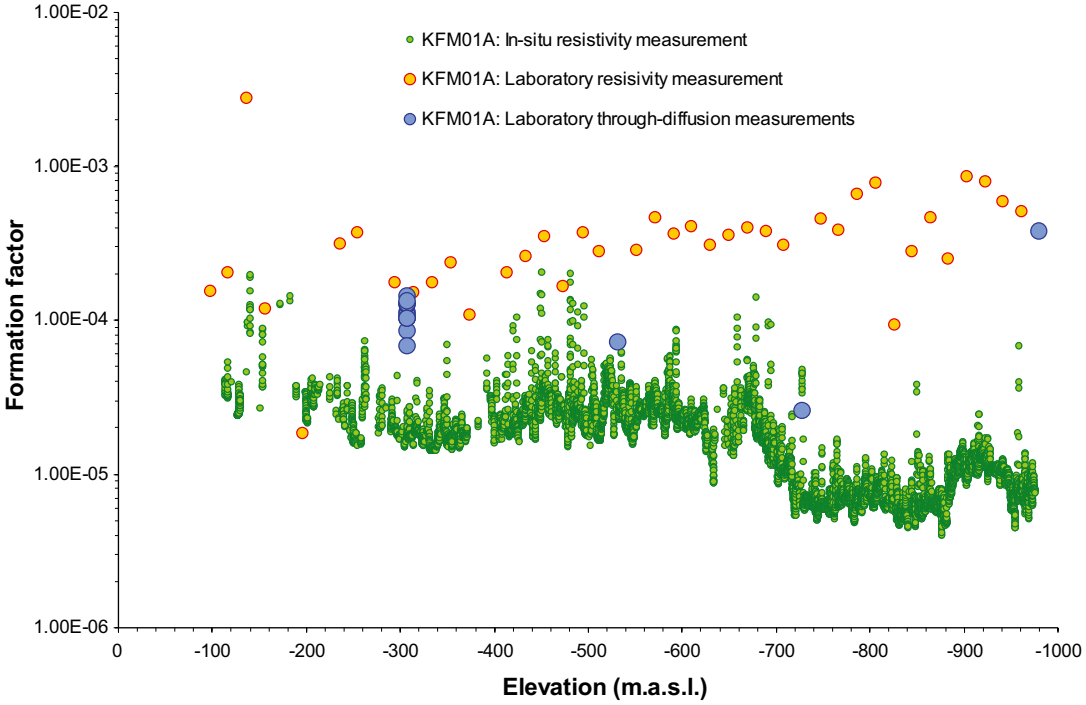

Figure H-3. *Comparison of formation factors derived from in situ resistivity measurements in KFM01A (green markers) with corresponding data measured on core samples in the laboratory (orange makers) also based upon electrical resistivity measurements. Laboratory measurements based upon the through-diffusion method using tritiated water are also shown for comparison (blue markers). The in situ data are based upon a re-interpretation of original borehole resistivity logs corrected to reflect current best estimate pore water compositions at Drill Site 1.*

If comparing this to the formation factors obtained by electrical methods in the laboratory on core samples from KFM01A /Thunehed 2005a, Löfgren and Neretnieks 2005/, as shown by orange coloured markers in Figure H-3, it becomes apparent that the latter is about one order of magnitude larger. It seems that such a large systematic deviation is unlikely to originate in uncertainty concerning the *in situ* pore water composition, nor any other known data uncertainty of the measurements. A more parsimonious explanation is that the porosity has been increased both by stress relaxation and induced mechanical damage in the process of excavating and preparing the samples for laboratory studies.

Corrections required to account for differences between measurement methods

As discussed in the theory part of this Appendix chapter, the formation factor by definition should only depend on the geometry of the porous system and not on the identity of the migrating solute. Also, by definition, the formation factor should be the ratio of the effective diffusivity D_e and the diffusivity in free solution D_w. However, for ionic solutes in crystalline rock, both of these requirements cannot be fulfilled, as the mineral surfaces surrounding the pores are generally negatively charged and can be expected to interact with the ionic solutes, thereby affecting their rate of migration.

As it is not yet settled within the scientific community how to handle this inconsistency, in the site description a pragmatic decision has been taken to avoid internalising processes as part of the formation factor that lead to an increase in the effective rate of diffusion. In practice, this means that enhanced migration at the mineral surfaces (by surface diffusion and surface conduction) is not internalised in the formation factor. Although this could well be considered to be an inconsistency in the data evaluation, it is motivated by the wish to avoid the possibility of overestimating the effective diffusivity of matrix diffusing solutes.

When comparing formation factors obtained by electrical methods and traditional diffusion methods, the comparison is complicated by the fact that the two methods do not utilise the same pore water species as a probe of migration. In through-diffusion measurements, a single tracer (or a defined set of tracers) diffuses through the porous system under a concentration gradient. The tracer being used within the site investigation is the non-charged, and hypothetically non-interacting molecule, tritiated water (HTO) /Byegård et al. 2008/. In supporting studies, the anionic tracers uranine and iodide have also be used /e.g. Ohlsson 2000, Löfgren and Neretnieks 2006/. In the electrical methods, all anionic and cationic solutes dissolved within the pore water propagate the current. In the laboratory programme of the site investigation, the solution used as pore water is 1 M NaCl. Rock resistivity measurements *in situ* is, by necessity, performed at the naturally existing pore water (with an ionic strength comparable to 0.1 M NaCl or higher).

A number of comparative studies have been performed in the laboratory using both electrical and through diffusion methods on the same samples /e.g. Byegård et al. 2008, Löfgren and Neretnieks 2006, Ohlsson 2000/. As expected, some deviation in the formation factors obtained by the different methods is found. Probable explanations for this deviation are that the methods do not utilise the same pore water species as a probe of migration, that they utilise analogue but not identical transport mechanisms, and that the different methods invoke different data uncertainties. The deviations found are generally a factor of about two in magnitude, where the electrical method gives enhanced formation factors compared to the through-diffusion method. Three processes have been identified as candidates for being responsible for (part) of this deviating factor of about two. These are surface conduction, anion exclusion, and capacitance effects.

Surface conduction

A process postulated to occur that would give a theoretically increased effective rate of diffusive transport (and therefore is not internalised in the formation factor) is diffusion in the electrical double layer (EDL). This process is also referred to as surface diffusion in the scientific literature /e.g. Olin et al. 1997/. Since cations are concentrated in the EDL due to electrostatic

attraction, this could potentially lead to higher concentration gradients close to the mineral surfaces and thus an enhanced rate of cation diffusion /e.g. Ohlsson and Neretnieks 1998/. Although the existence or non-existence of surface diffusion is a hotly debated topic in the field of transport modelling in fractured crystalline rock, no such controversy exists in the field of geophysics where the existence of charge conduction in the EDL has been used as a basis of petrophysical methods for many years /e.g. Ruffet et al. 1993, Nover 2005, Börner 2006, Slater 2007/. It should be noted that the conduction of electric charge in the EDL is primarily mediated by the movement of principal cations of the pore water, which are only loosely bound to the mineral surfaces, such as Na^+ or Ca^{2+}. This should be considered distinct from notions of surface diffusion involving more strongly bound, sorbing solutes which may have very different mobilities in the EDL /e.g. Axe et al. 2002/. An overview of the theory of surface conduction in porous media is given in /Revil and Glover 1997/.

When measuring the formation factor by electrical methods, surface conduction is a process that, if not corrected for, gives rise to enhanced formation factors. It has been noted in laboratory experiments that even at relatively high salinities (≈ 1 M NaCl) the apparent formation factors are roughly a factor of two times higher than those measured by through-diffusion using non-sorbing tracers on the same samples. This has been found to be the case for anionic solutes such as uranine /Ohlsson 2000/ and iodide /Löfgren and Neretnieks 2006/ and also for the non-charged tracer HTO /Byegård et al. 2008/.

The utilisation of the enhanced cation concentration at the mineral surfaces in the electrical methods could be responsible for at least part of the deviating factor of about two. However, it could be questioned whether the effect of surface conduction is that significant at salinities as high as 1 M NaCl. /Ohlsson and Neretnieks 1998/ measured the rock conductivity of a number of samples that were first saturated with low ionic strength pore water (> 0.001 M NaCl) and thereafter with high ionic strength pore water (1.0 M NaCl). The measured rock conductivity corresponding to the low ionic strength pore water can be assumed to represent the surface conductivity, in agreement with /e.g. Revil and Glover 1997/. Furthermore, it can be assumed that the surface conductivity does not significantly change with the pore water's ionic strength, in agreement with /Olin et al. 1997/. By comparing the measured rock conductivities at high and low ionic strength pore water, one can surmise that surface conduction should only contribute to about 5–10% of the overall rock conductivity if the sample is saturated with 1.0 M NaCl.

The surface conductivities obtained in /Ohlsson and Neretnieks 1998/ and later on in /Ohlsson 2000/ and /Löfgren 2004/ range between 6×10^{-6}–6×10^{-5} S/m. After accounting for differences in porosity and tortuosity-constrictivity between the different investigations, this is in excellent agreement with the detailed experimental and theoretical results obtained by /Stein et al. 2004/ in studies of surface charge transport in nano-fluidic channels (0.07–1.0 µm) fabricated on fused silica substrates.

Anion exclusion

Due to the presence of negatively charged mineral surfaces (which is counteracted by the cations in the EDL), part of the pore volume will be excluded for anionic migration. Such anion exclusion can be studied by comparing the matrix diffusion of anions and the non-charged tracer HTO. However, no such measurements have been performed within the site investigation programme or in supporting studies on Swedish rock. In studies on Finnish granite, through diffusion measurements utilising the tracers HTO and ^{36}Cl have been performed on the same samples, with the aim of investigating the effect of anion exclusion /Valkiainen et al. 1996, Olin et al. 1997/. In /Olin et al. 1997/ it was concluded that about one third of the pore space is restricted for anionic movement and that ion exclusion is not a (clear) function of the pore water's ionic strength. A number of different pore water salt solutions in the interval 0.001 M–0.5 M were used. In /Valkiainen et al. 1996/, effective diffusivity measurements were performed on three granite samples 2-6 cm in length. By comparing the D_e obtained by HTO and ^{36}Cl for each sample, it was found that the D_e obtained by HTO was on average six times larger. It should be noted that D_w for both ^{36}Cl and HTO is about the same (~ 2×10^{-9} m^2/s).

Anion exclusion may greatly contribute to the deviating factor of about two between formation factor obtained by electric methods and through diffusion measurements using uranine /Ohlsson 2000/ and iodide /Löfgren and Neretnieks 2006/ as tracers. It does not explain, however, the deviation in formation factors obtained with electrical methods and through diffusion measurements using HTO /Byegård et al. 2008/. Other possible reasons therefore need to be considered to explain this deviation.

Capacitance effects

It is well known within the field of geophysics that if the rock resistivity is measured with alternating current at too high frequency, the obtained apparent resistivity will be underestimated due to capacitance effects. For this reason the rock resistivity has been measured at different frequencies, ranging from 0.1–10^6 Hz /e.g. Löfgren 2001, Thunehed 2007a/. In addition, the rock resistivity has been measured using direct current /Löfgren and Neretnieks 2006/. What can be concluded is that measurement of the rock resistivity with alternating current at frequencies of a few Hz up to a few hundred Hz, the formation factor is overestimated by not more than a few (< 5%) percent.

Handling of correction factors in site investigations and the site descriptive model

As has been found within the site investigation and supporting studies, the formation factor obtained from electrical methods is a factor of about two times larger than those obtained in laboratory tracer tests. A factor of two is a small deviation compared to the formation factor variability and uncertainties in other transport parameters. Therefore, only very limited data uncertainty is introduced if, without further consideration, the formation factors obtained from electrical methods are (cautiously) decreased by a factor of two. An additional prerequisite for applying this correction to formation factors obtained *in situ* is that the deviating factor does not increase under conditions other than those used in the laboratory. Two conditions that may differ significantly are the sample size and the pore water ionic strength.

Concerning the sample size, /Löfgren and Neretnieks 2006/ compared formation factors obtained with the electrical resistivity methods and a tracer test method (the through-electromigration method) on samples from 1.5 cm up to 12 cm in length. It was concluded that the deviating factor of about two does not appear to change with increasing sample length. Also the fact that *in situ* formation factor measurements, where the effective sample size is on the scale of metres, gives reasonable formation factors lends weight to the notion that the factor is not dependant on sample size (as long as the sample length is significantly larger than the size of individual pores or microfractures). There are measurements made on very thin samples (≤ 1 cm) that indicate larger formation factors /e.g. Selnert et al. 2008/. For samples larger than a few centimetres, however, the formation factor seems unaffected by sample size /e.g. Skagius and Neretnieks 1982, Bradbury and Green 1986, Ohlsson 2000/.

Concerning the pore water ionic strength, the observations of the deviating factor of about two are all made at pore waters of high ionic strength (typically 1 M NaCl). It would be very valuable to observe that the factor does not significantly increase at pore waters relevant for the site (~ 0.1 M NaCl at repository depth). A supporting study has been initiated and is currently underway to better address this data uncertainty in SR-Site. It can be argued that the deviating factor should not increase significantly *in situ* for site specific pore waters, as neither the surface conductivity nor anion exclusion seems to be dependant on the ionic strength of the pore water within rock matrix samples similar to those found at Forsmark.

The importance of surface conductivity relative to the overall rock matrix conductivity, however, increases with decreasing ionic strength of the pore water /e.g. Skagius and Neretnieks 1982, Ohlsson and Neretnieks 1998/. When obtaining *in situ* formation factors within the site investigation programme, this has been handled by rejecting resistivity data where the EC of the pore

water is thought to be lower than 0.5 S/m. Above this EC, the majority of the current propagated through the rock should be carried by ions in the bulk pore water. This lower EC limit of 0.5 S/m is based on interpretation of Figure 3-8 in /Löfgren 2004/ for rock with a formation factor typical for the site.

It should be noted that the suggested correction factor of two is based purely upon the empirical observations described above and is not quantitatively related to any detailed theoretical reasoning. It may be so that this leads to an overestimation of the formation factor in the lower tail of the formation factor distribution. This, together with the limited measurement range of the *in situ* rock resistivity tool, may result in a truncation of the lower tail of the formation factor distribution. When averaged over a flowpath, however, the arithmetic mean of the formation factor distribution is certainly the most appropriate measure for calculating the flowpath effective matrix diffusivity. Uncertainties in the lower tail of the formation factor distribution should only make a small contribution to the overall uncertainty of the arithmetic mean calculated for the flowpath.

Further reflections on surface diffusion and surface conduction

It appears that the existence of increased concentrations of mobile cations in the EDL is non-controversial. On the other hand, the existence of increased concentration gradients in the EDL sufficiently large that they can significantly enhance the total diffusive flux through the porous system is still not entirely resolved.

Although part of a continuum of behaviour, the relative mobility of loosely bound cations in the EDL should be considered distinct to surface diffusion involving more strongly bound solutes. The diffusion of sorbing solutes is strongly influenced by the magnitude of the potentiometric energy well in which the solute sits when occupying sorption sites. Movement by surface diffusion in such cases is associated with a considerably greater activation energy for site transition and results in markedly different surface diffusivities for different solutes /e.g. Axe et al. 2002/. Experimentally derived results for surface diffusion of particular solutes therefore cannot be generally extrapolated to other solutes without specifically accounting for this effect.

Representative results

If we accept the arguments in favour of using formation factors derived from *in situ* electrical resistivity measurements, the most reliable data are most certainly those obtained in boreholes KFM01D and KFM08C. The data from borehole KFM01D is particularly valuable since it transects the target volume through fracture domain FFM01. A plot showing the variation of the formation factor with borehole elevation can be seen in Figure H-4 for the main rock type, 101057 (Granite to granodiorite, metamorphic, medium-grained granite).

Based upon the *in situ* measurements of formation factors at the Forsmark site we estimate the formation factor for intact, non-fractured matrix rock in fracture domain FFM01 (Rock type 101057) to be roughly -4.5 ± 0.1 in $\log_{10}$ units. By non-fractured, this means that any measurements closer than 0.5 m to an open or possible open fracture in the bore map are excluded. It is also interesting to note that there are a number of instances within the boreholes at the Forsmark site, where *in situ* formation factors are roughly equal to the site average although not a single open fracture has been mapped for up to 10–15 m. An excellent, although by no means unique, example of this can be found in the KFM01D borehole between an elevation of –576 m and 590 m as shown in Figure H-5.

As discussed in the previous sections, since the raw data formation factor is almost certainly biased by various measurement artefacts, the data values should be reduced by about a factor of 2 to give a realistic value for the true geometrical formation factor. The raw data histogram and the approximate fit to the lognormal distribution are shown in Figure H-6.

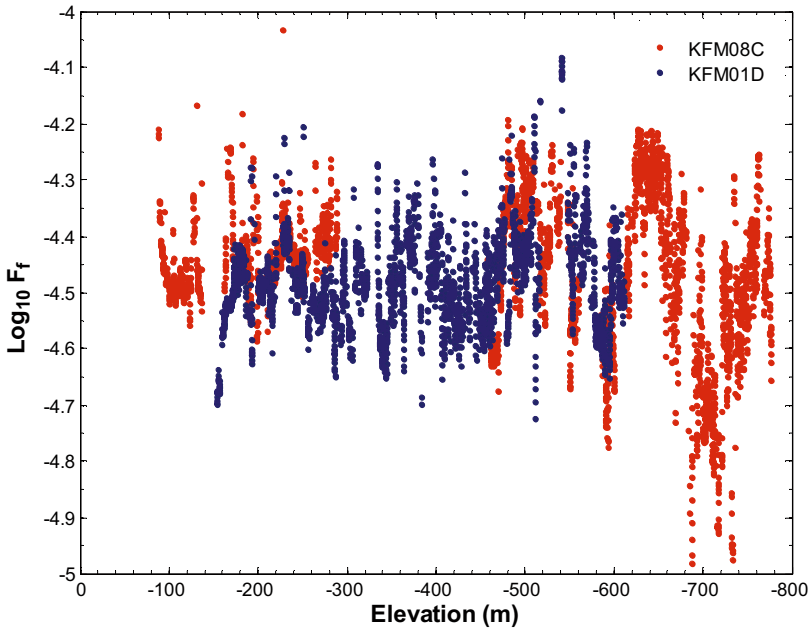

Figure H-4. *In-situ formation factors for rock type 101057, Granite to granodiorite, metamorphic, medium-grained granite within fracture domain FFM01 (data based on 5,897 point resistivity measurements in borehole KFM01D and KFM08C).*

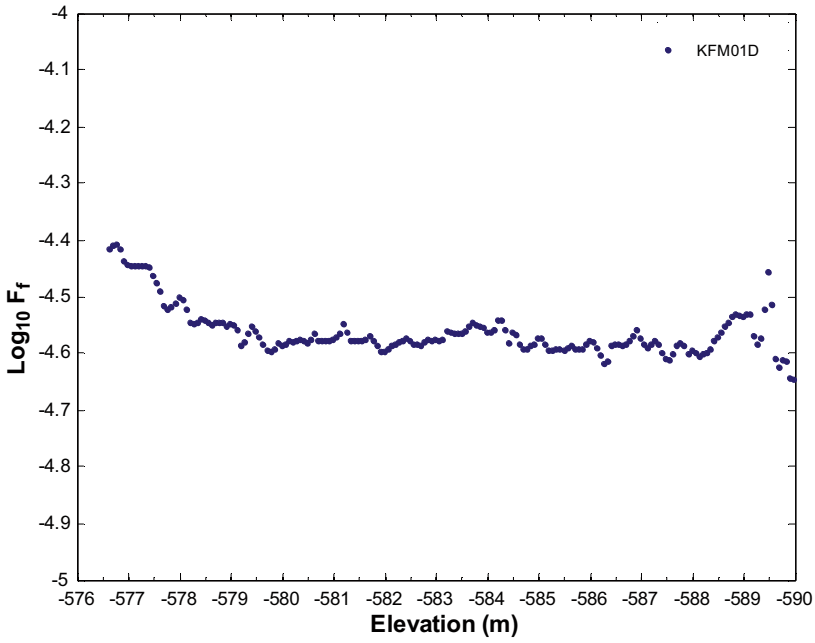

Figure H-5. *Close-up view of formation factors measured in the depth interval 576–590 m in borehole KFM01D where there are no fractures mapped as open for a stretch of roughly 15 m.*

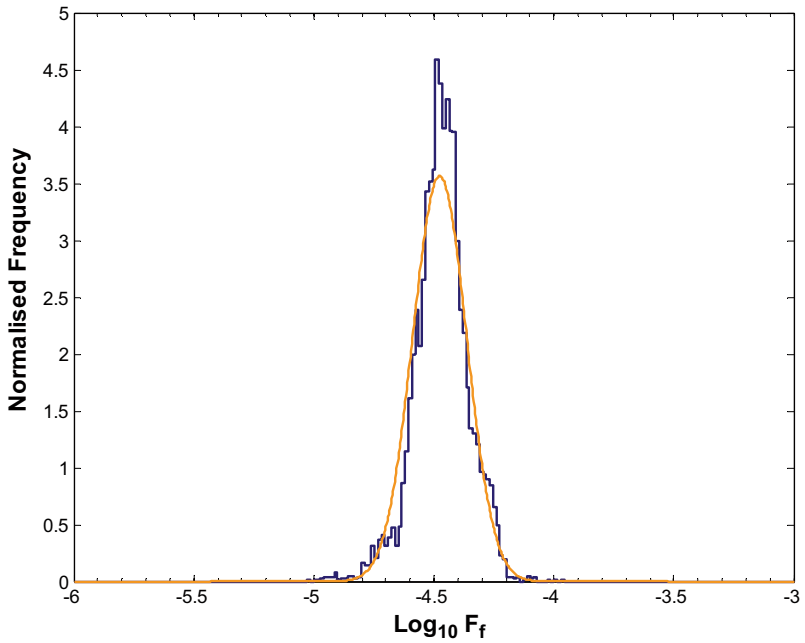

Figure H-6. *Raw data histogram of formation factor (uncorrected) and fit of data to lognormal distribution for rock type 101057, Granite to granodiorite, metamorphic, medium-grained granite within fracture domain FFM01.*

As can be seen from the figure, the data give a reasonable fit to the proposed lognormal distribution, although with a small tendency for negative skew apparent in the raw data histogram. In the light of the discussion concerning mechanical damage and pore compression stress effects, it is interesting to note that the effective diffusivities estimated for salt out-diffusion using large 12–19 cm long bore core samples from KFM01D /Laaksoharju et al. 2008/ imply formation factors (in the range 4.3×10^{-5} to 1.6×10^{-3}) which are roughly an order of magnitude greater than those based upon the *in situ* measurement data.

In order to derive information concerning the spatial correlation of the formation factor, the data was first de-trended assuming a linear trend and then subjected to a semi-variogram analysis using a fast Fourier Transform (FFT) based algorithm described by /Marcotte 1996/ and implemented in Matlab. The data from KFM01D exhibit an almost non-existent trend as can be seen from Figure H-7. Here, we concentrate mainly on the data from KFM01D as the more discontinuous character of the data in KFM08C renders it less suitable for geostatistical analysis.

Since the data are not exactly lognormally distributed, the data were normal-score transformed prior to computation of the semi-variogram to avoid biasing effects. The statistical Q-Q plot of the log-transformed data is shown in Figure H-8 showing the deviation from normality at the upper and lower tail end of the distribution which is consistent with the apparent skewness of the histogram (Figure H-6).

The resulting semi-variogram is shown in Figure H-9 together with a proposed 2-component exponential model for the spatial correlation (fitted visually).

As can be seen from the proposed variogram model in Figure H-9, roughly 20% of the variance occurs with a correlation length of roughly 1 m or less, while on the order of 80% is associated with a correlation length of about 5–7 m. It is noted that although we have used a 2-component semi-variogram model to explain the overall data variation, the smallest length scale considered is probably less than the effective length probed by the resistivity tool. The first component of the exponential model (i.e. corresponding to parameters a_1, c_1) can, for all practical purposes, be interpreted as a nugget effect accounting for about 20% of the variance.

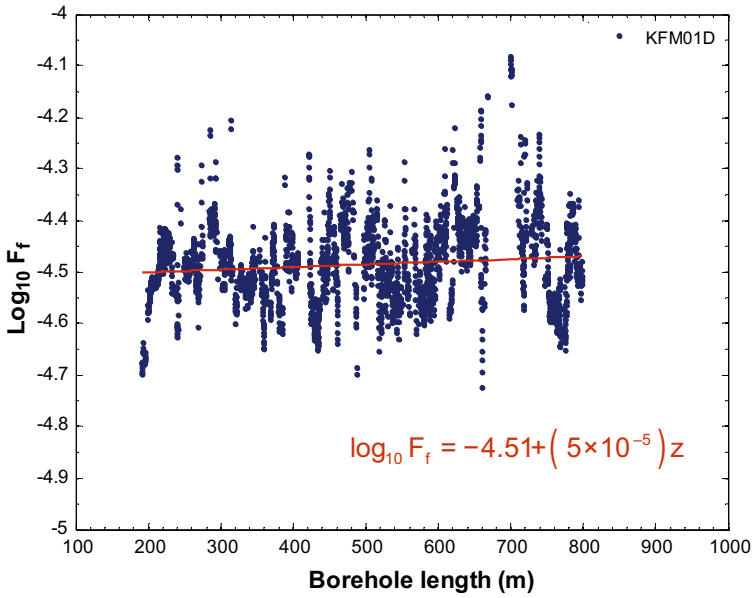

Figure H-7. *Trend line for depth variation of the mean formation factor in KFM01D plotted as a function of borehole length. The equation of the trend line is indicated in the figure and describes an almost negligible variation with borehole length.*

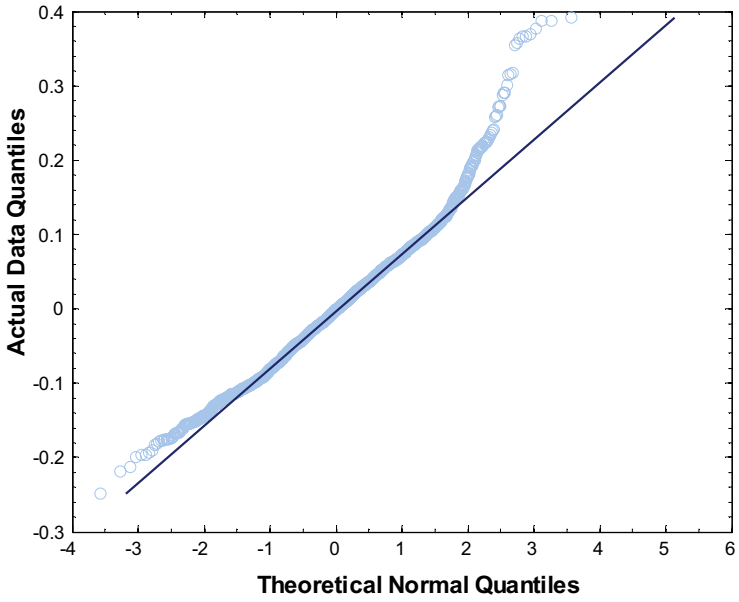

Figure H-8. *Q-Q Plot for log_{10}-transformed formation factor data derived from in situ electrical resistivity measurements borehole KFM01D.*

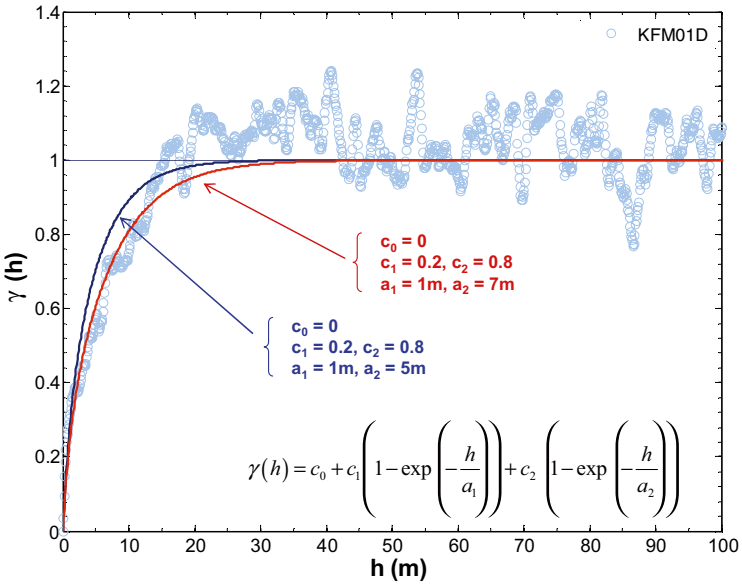

Figure H-9. *Semi-variogram for formation factor variation in KFM01D based upon in situ resistivity measurements. Two possible visual fits to a 2-component exponential variogram model are indicated in the figure.*

Statistical distributions of *in situ* formation factors for different rock types

Although we have only considered the main rock type (101057) in much of the discussion above, a cursory examination of the raw *in situ* data reported in the Sicada database can give us a rough indication of the relative properties of the different rock types to be found at the Forsmark site. Some representative data (uncorrected) is plotted in Figure H-10 for rock domain RFM029 which includes the fracture domains FFM01, FFM02, and FFM03.

As can be seen from the plotted data, there does not appear to be very large systematic differences between the different rock types; indeed the spread of data points within individual rock types tends to be greater than the differences between rock types. Furthermore, the dispersion observed in individual data sets could be more closely related to the size of the data set than an intrinsic difference in effective diffusivity. The main exception here is amphibolite (102017) which appears to have a large data spread in spite of the small sample size. On the basis of these observations and assuming that the data are roughly order of magnitude correct, a compelling argument could be made for the use of a single parameterisation representing all rock types at the Forsmark site.

A breakdown of the data for different rock types is given in the following tables for rock domain RFM029, considering rock resident in fracture domain FFM01–03 as well as all deformation zones encountered within this rock domain. The data are further classified according to alteration status and proximity to open fractures in the borehole fracture mapping.

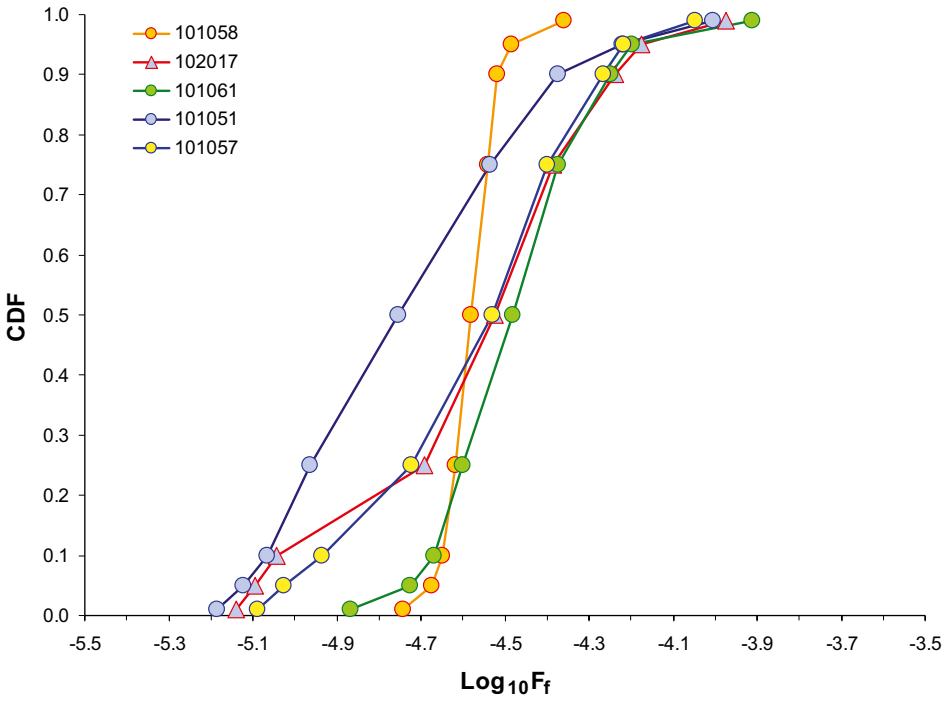

Figure H-10. *Empirical percentiles for in situ matrix formation factors, specified according to rock type within rock domain RFM029 (FFM01–03) and plotted as a cumulative distribution function, CDF. The data dispersion for individual rock types appears to be closely related to the size of the data set with the exception of amphibolite (102017) which seems to have a large intrinsic spread. Data are plotted for (unaltered) rock types 101057 (~ 34,000 data points), 101051 (3,591 data points), 101061 (1,353 data points), 102017 (567 data points), and 101058 (382 data points).*

Data for fracture domains FFM01, FFM02, and FFM03

Table H-1. Empirical percentiles for *in situ* matrix formation factors within RFM029 (FFM01–03). Data set is for rock classified as unaltered (measurement points less than 0.5 m distant from open fractures not included). Median and interquartile range are highlighted as red and blue text.

Quantiles	101051	101054	101056	101057	101058	101061	102017	103076	108019	111058
0.01	–5.19	–4.46	n/a	–5.09	–4.74	–4.87	–5.14	–4.54	–5.20	–5.09
0.05	–5.12	–4.46	n/a	–5.03	–4.67	–4.73	–5.09	–4.53	–5.19	–5.07
0.10	–5.07	–4.46	n/a	–4.94	–4.65	–4.67	–5.04	–4.53	–5.16	–5.05
0.25	–4.96	–4.44	n/a	–4.72	–4.62	–4.60	–4.69	–4.53	–5.09	–4.93
0.50	–4.75	–4.40	n/a	–4.53	–4.58	–4.48	–4.52	–4.50	–5.03	–4.67
0.75	–4.53	–4.34	n/a	–4.40	–4.54	–4.37	–4.38	–4.48	–4.98	–4.44
0.90	–4.37	–4.32	n/a	–4.27	–4.52	–4.25	–4.24	–4.39	–4.40	–4.13
0.95	–4.22	–4.32	n/a	–4.22	–4.49	–4.20	–4.17	–4.33	–4.33	–4.08
0.99	–4.01	–4.32	n/a	–4.05	–4.36	–3.91	–3.97	–4.33	–4.24	–4.03

Note: Entries given as “n/a” in the table signify data “not available”.

Table H-2. Empirical percentiles for *in situ* matrix formation factors within RFM029 (FFM01–03). Data set is for rock classified as altered – all alteration types and intensities (measurement points less than 0.5 m distant from open fractures not included). Median and interquartile range are highlighted as red and blue text.

Quantiles	101051	101054	101056	101057	101058	101061	102017	103076	108019	111058
0.01	–4.73	n/a	n/a	–4.74	–4.62	–4.76	–4.58	n/a	n/a	–4.85
0.05	–4.70	n/a	n/a	–4.70	–4.62	–4.74	–4.58	n/a	n/a	–4.83
0.10	–4.69	n/a	n/a	–4.68	–4.61	–4.72	–4.58	n/a	n/a	–4.81
0.25	–4.66	n/a	n/a	–4.58	–4.60	–4.44	–4.57	n/a	n/a	–4.64
0.50	–4.55	n/a	n/a	–4.45	–4.57	–4.39	–4.56	n/a	n/a	–4.52
0.75	–4.50	n/a	n/a	–4.31	–4.37	–4.37	–4.54	n/a	n/a	–4.23
0.90	–4.40	n/a	n/a	–4.23	–4.35	–4.35	–4.51	n/a	n/a	–4.16
0.95	–4.37	n/a	n/a	–4.16	–4.34	–4.35	–4.50	n/a	n/a	–4.16
0.99	–4.28	n/a	n/a	–3.93	–4.33	–4.24	–4.50	n/a	n/a	–4.15

Note: Entries given as “n/a” in the table signify data “not available”.

Table H-3. Empirical percentiles for *in situ* matrix formation factors within RFM029 (FFM01–03). Data set is for rock classified as unaltered (measurement points in proximity to open fractures included). Median and interquartile range are highlighted as red and blue text.

Quantiles	101051	101054	101056	101057	101058	101061	102017	103076	108019	111058
0.01	–5.18	–4.46	–4.32	–5.08	–4.74	–4.83	–5.12	–4.66	–5.20	–5.09
0.05	–5.10	–4.46	–4.32	–5.00	–4.70	–4.70	–5.03	–4.63	–5.19	–5.05
0.10	–5.04	–4.46	–4.30	–4.88	–4.65	–4.65	–4.87	–4.59	–5.15	–5.00
0.25	–4.92	–4.44	–4.27	–4.67	–4.62	–4.56	–4.64	–4.53	–5.09	–4.74
0.50	–4.69	–4.40	–4.25	–4.50	–4.57	–4.44	–4.47	–4.50	–5.03	–4.51
0.75	–4.50	–4.34	–4.16	–4.36	–4.53	–4.32	–4.25	–4.22	–4.97	–4.22
0.90	–4.32	–4.32	–4.15	–4.23	–4.44	–4.21	–4.08	–4.17	–4.47	–4.03
0.95	–4.14	–4.32	–4.14	–4.12	–4.37	–4.11	–3.91	–4.13	–4.33	–3.87
0.99	–3.72	–4.32	–4.14	–3.85	–4.28	–3.87	–3.43	–4.11	–4.24	–3.44

Note: Entries given as “n/a” in the table signify data “not available”.

Table H-4. Empirical percentiles for *in situ* matrix formation factors within RFM029 (FFM01–03). Data set is for rock classified as altered – all alteration types and intensities (measurement points in proximity to open fractures included). Median and interquartile range are highlighted as red and blue text.

Quantiles	101051	101054	101056	101057	101058	101061	102017	103076	108019	111058
0.01	–4.72	n/a	n/a	–4.73	–4.62	–4.76	–4.66	–4.11	n/a	–4.85
0.05	–4.68	n/a	n/a	–4.69	–4.61	–4.73	–4.62	–4.11	n/a	–4.80
0.10	–4.67	n/a	n/a	–4.65	–4.60	–4.56	–4.58	–4.11	n/a	–4.63
0.25	–4.60	n/a	n/a	–4.53	–4.58	–4.47	–4.55	–4.11	n/a	–4.52
0.50	–4.46	n/a	n/a	–4.39	–4.46	–4.39	–4.15	–4.11	n/a	–4.40
0.75	–4.30	n/a	n/a	–4.24	–4.36	–4.36	–3.97	–4.11	n/a	–4.15
0.90	–3.97	n/a	n/a	–4.03	–4.34	–4.28	–3.64	–4.11	n/a	–3.89
0.95	–3.87	n/a	n/a	–3.89	–4.31	–4.21	–3.53	–4.11	n/a	–3.78
0.99	–3.50	n/a	n/a	–3.45	–4.23	–4.04	–3.18	–4.11	n/a	–3.00

Note: Entries given as “n/a” in the table signify data “not available”.

Data for deformation zones resident in RFM029 (all deformation zones and possible deformation zones)

Table H-5. Empirical percentiles for *in situ* matrix formation factors within RFM029 (deformation zones). Data set is for rock classified as unaltered (measurement points less than 0.5 m distant from open fractures not included). Median and interquartile range are highlighted as red and blue text.

Quantiles	101051	101054	101056	101057	101058	101061	102017	103076	108019	111058
0.01	–4.80	n/a	n/a	–5.02	–4.61	–4.66	–4.79	–4.54	n/a	–4.71
0.05	–4.80	n/a	n/a	–4.91	–4.61	–4.65	–4.79	–4.53	n/a	–4.71
0.10	–4.80	n/a	n/a	–4.86	–4.61	–4.62	–4.78	–4.53	n/a	–4.70
0.25	–4.76	n/a	n/a	–4.76	–4.60	–4.56	–4.77	–4.53	n/a	–4.67
0.50	–4.71	n/a	n/a	–4.61	–4.58	–4.46	–4.77	–4.49	n/a	–4.48
0.75	–4.64	n/a	n/a	–4.46	–4.56	–3.98	–4.74	–4.35	n/a	–4.44
0.90	–4.43	n/a	n/a	–4.29	–4.54	–3.79	–4.02	–4.20	n/a	–4.29
0.95	–4.34	n/a	n/a	–4.16	–4.54	–3.74	–3.84	–4.18	n/a	–4.24
0.99	–4.19	n/a	n/a	–4.02	–4.54	–3.71	–3.68	–4.16	n/a	–4.19

Note: Entries given as “n/a” in the table signify data “not available”.

Table H-6. Empirical percentiles for *in situ* matrix formation factors within RFM029 (deformation zones). Data set is for rock classified as altered – all alteration types and intensities (measurement points less than 0.5 m distant from open fractures not included). Median and interquartile range are highlighted as red and blue text.

Quantiles	101051	101054	101056	101057	101058	101061	102017	103076	108019	111058
0.01	–4.78	n/a	n/a	–4.80	n/a	–4.66	–4.42	–4.45	n/a	n/a
0.05	–4.72	n/a	n/a	–4.76	n/a	–4.66	–4.42	–4.45	n/a	n/a
0.10	–4.69	n/a	n/a	–4.72	n/a	–4.64	–4.42	–4.45	n/a	n/a
0.25	–4.38	n/a	n/a	–4.62	n/a	–4.34	–4.38	–4.45	n/a	n/a
0.50	–4.36	n/a	n/a	–4.30	n/a	–4.17	–4.28	–4.45	n/a	n/a
0.75	–4.35	n/a	n/a	–3.63	n/a	–4.00	–4.16	–4.45	n/a	n/a
0.90	–4.34	n/a	n/a	–2.62	n/a	–3.99	–4.10	–4.45	n/a	n/a
0.95	–4.33	n/a	n/a	–2.44	n/a	–3.97	–4.10	–4.45	n/a	n/a
0.99	–4.32	n/a	n/a	–1.65	n/a	–3.97	–4.10	–4.45	n/a	n/a

Note: Entries given as “n/a” in the table signify data “not available”.

Table H-7. Empirical percentiles for *in situ* matrix formation factors within RFM029 (deformation zones). Data set is for rock classified as unaltered (measurement points in proximity to open fractures included). Median and interquartile range are highlighted as red and blue text.

Quantiles	101051	101054	101056	101057	101058	101061	102017	103076	108019	111058
0.01	–4.80	n/a	n/a	–5.02	–4.61	–4.82	–4.78	–4.61	n/a	–4.82
0.05	–4.80	n/a	n/a	–4.92	–4.61	–4.70	–4.77	–4.56	n/a	–4.74
0.10	–4.78	n/a	n/a	–4.84	–4.60	–4.67	–4.76	–4.55	n/a	–4.71
0.25	–4.74	n/a	n/a	–4.73	–4.57	–4.57	–4.67	–4.52	n/a	–4.60
0.50	–4.64	n/a	n/a	–4.51	–4.51	–4.44	–4.28	–4.41	n/a	–4.45
0.75	–4.36	n/a	n/a	–4.28	–4.36	–4.01	–4.03	–4.16	n/a	–4.28
0.90	–4.00	n/a	n/a	–4.06	–4.30	–3.80	–3.84	–3.95	n/a	–4.06
0.95	–3.72	n/a	n/a	–3.92	–4.16	–3.72	–3.71	–3.85	n/a	–3.89
0.99	–2.97	n/a	n/a	–3.57	–4.16	–3.20	–3.38	–3.57	n/a	–3.36

Note: Entries given as “n/a” in the table signify data “not available”.

Table H-8. Empirical percentiles for *in situ* matrix formation factors within RFM029 (deformation zones). Data set is for rock classified as altered – all alteration types and intensities (measurement points in proximity to open fractures included). Median and interquartile range are highlighted as red and blue text.

Quantiles	101051	101054	101056	101057	101058	101061	102017	103076	108019	111058
0.01	–4.80	n/a	n/a	–4.82	–3.84	–4.73	–4.39	–4.45	n/a	–4.72
0.05	–4.77	n/a	n/a	–4.74	–3.84	–4.63	–4.06	–4.45	n/a	–4.72
0.10	–4.72	n/a	n/a	–4.66	–3.84	–4.60	–3.96	–4.45	n/a	–4.71
0.25	–4.44	n/a	n/a	–4.48	–3.84	–4.39	–3.84	–4.24	n/a	–4.27
0.50	–4.35	n/a	n/a	–4.18	–3.84	–4.15	–3.69	–3.82	n/a	–4.18
0.75	–3.81	n/a	n/a	–3.71	–3.84	–3.93	–3.49	–3.48	n/a	–4.00
0.90	–3.33	n/a	n/a	–3.22	–3.84	–3.73	–2.91	–3.34	n/a	–3.50
0.95	–2.04	n/a	n/a	–2.42	–3.84	–3.66	–2.87	–3.34	n/a	–2.89
0.99	–1.90	n/a	n/a	–2.02	–3.84	–3.53	–2.84	–3.34	n/a	–2.52

Note: Entries given as ”n/a” in the table signify data “not available”.

Appendix I

Detailed solute transport modelling results

Author: James Crawford

Theoretical considerations concerning governing equations

The transport model considers advective flow and transport along a flowpath where solute can diffuse into and sorb upon micro-surfaces within the rock matrix. In a previous report /Crawford 2006/, a detailed account of the governing equation for transport in a flow channel with diffusion into a multilayered rock matrix has been given. In the model derivation, the rock matrix was considered to have piecewise constant material properties (K_d, θ_m, D_e) which can be used to model variable material properties within the rock matrix adjacent to the flowpath. The impact of mass transfer to a flanking stagnant zone accompanied by diffusive interaction with a multilayered rock matrix was also derived as a special case.

In the concept which was previously developed, the Laplace space solution for transport is formulated in terms of the F-factor for the flow channel and a number of parallel flux terms which account for mass transfer to the different immobile zones. Although the model was originally developed to deal with advective transport along in-plane flow channels, it can readily be adapted for simulation of diffusion in radial configurations such as may occur in narrow flow channels and at fracture intersection zones (FIZ). Some theoretical considerations related to this are summarised in the following sections.

The model assumes that flow is fully mixed across the width of the flowpath. As discussed previously in Chapter 5, we expect diffusive mixing across the flowpath width to occur over relatively short timescales compared to the advective travel time in the flow channel. For a flowpath F-factor of 10^6 y/m, we would expect the flow velocity in a channel to be roughly in the range 0.1–1 m/y depending upon the transport aperture. From penetration depth theory /e.g. Neretnieks 1980/, the characteristic time for diffusion across a flow channel of width W_c is:

$$t \approx \frac{\pi}{4D_w} W_c^2 \tag{I-1}$$

For a flow channel width of 10 cm, this implies a characteristic time for diffusion of about 50–100 days. In this time the advective flow will have travelled a distance of 2–20 cm. It is clear from this calculation that the assumption of diffusive equilibrium across a flow channel is not unreasonable given the time scale of advective flow which may be on the order of years. It is also noted that the rate of advective transport at the lower end of this estimate is close to the rate of free diffusion in water. When considered together with matrix interaction, however, solute transport times are sufficiently long that this need not be taken into account.

1D linear diffusion cases

Assuming advectively dominated flow, the mass balance for solute concentration in a flow channel is:

$$R_a \frac{\partial C_f}{\partial t} + v \frac{\partial C_f}{\partial x} = \frac{2J_m}{\delta_t} - \lambda C_f \tag{I-2}$$

Here, the term J_m is the diffusive flux into the rock matrix. If radioactive decay is neglected, the cumulative distribution function (CDF) for the residence time distribution of a solute along a flowpath is given in Laplace space as:

$$\tilde{C}_f = \frac{1}{\phi} \exp\left(-R_a t_w \phi\right) \exp\left(-F\psi_m\right) \tag{I-3}$$

Where ϕ represents a "shifted" Laplace space variable (see explanation following), t_w is the advective travel time, and F is the cumulative F-factor for the flowpath. The curly overbar notation represents a Laplace transformed variable; in this case the Laplace transform of the temporal CDF. In the equations given above, radioactive decay is subsumed into the parameter, ϕ which is defined in terms of the Laplace variable, s and the radioactive decay constant, λ (s^{-1}):

$$\phi = s + \lambda \tag{I-4}$$

The matrix flux parameter ψ_m is given by:

$$\psi_m = MPG_m \sqrt{\phi} \qquad \text{(for an infinite, simple matrix)} \tag{I-5}$$

$$\psi_m = MPG_m \sqrt{\phi} \tanh\left(A_m \delta_m \sqrt{\phi}\right) \qquad \text{(for a limited, simple matrix)} \tag{I-6}$$

$$\psi_m = MPG_{m(1)} \sqrt{\phi} \left(1 - \frac{2}{1 + \frac{w_m}{p_m}}\right) \qquad \text{(for a limited, complex matrix)} \tag{I-7}$$

Where, MPG_m is the material properties group for the single layer rock matrix and the parameter A_m is defined as:

$$A_m = \sqrt{\frac{\theta_m + K_{dm}\rho_{bm}}{D_e}} = \frac{1}{\sqrt{D_a}} \tag{I-8}$$

As previously, the apparent diffusivity, D_a (m^2/s) is the ratio of the effective diffusivity, D_e (m^2/s) and storage capacity of the rock:

$$D_a = \frac{D_p \theta_p}{\theta_m + K_{dm}\rho_{bm}} = \frac{D_e}{\theta_m + K_{dm}\rho_{bm}} \tag{I-9}$$

The parameters w_m and p_m in Equation I-7 are defined by recursive functions that depend upon the number of matrix layers and their properties (for details see /Crawford 2006/). It is noted that a typographical error in this previous report meant that the flux parameters were defined with incorrect sign. The definitions given by Equations I-5 to I-7 are the correct versions.

The Laplace space solution given in Equation I-3 can be extended to the case of a flanking stagnant zone, or any number of parallel fluxes to immobile zones with differing material properties:

$$\tilde{C}_f = \frac{1}{s} \exp\left(-R_a t_w \phi\right) \exp\left(-F\left(\sum_{i=1}^{n} R_i \psi_i\right)\right) \tag{I-10}$$

The R_i term within the summation is simply the ratio of mass transfer surface area of the particular immobile zone and the flow-wetted surface per unit length of the flow channel used in the definition of the F-factor. For the simple case of an in-plane flow channel of limited width with a flanking stagnant zone we define the surface area ratio, R_s as:

$$R_s = \frac{\delta_s f_s}{2W_c} \tag{I-11}$$

The constant f_s accounts for the existence of a partial stagnant zone within the flowpath. For a symmetric stagnant zone along 100% of the path length, for example, we would have $f_s = 2$. Uptake to asymmetric stagnant zones or an asymmetric rock matrix as might arise in a reactivated fracture can be handled simply by defining separate flux terms for each matrix subcomponent as described in /Crawford 2006/. This approach can also be used to simulate mass transfer processes in complex features such as deformation zones with different ultimate depths of penetration for different matrix subcomponents. This could be used to account for multiple rates of diffusive exchange within fault gouge, fracture splays, breccias, and so forth.

In the particular case of a single in-plane stagnant zone, Equation I-10 simplifies to:

$$\tilde{C}_f = \frac{1}{\phi}\exp\left(-R_a t_w \phi\right)\exp\left(F\left(\psi_m + R_s\psi_s\right)\right) \qquad \text{(I-12)}$$

The terms ψ_m and ψ_s are the mass transfer flux terms to the rock matrix and stagnant zones respectively.

The additional flux parameter, ψ_s for diffusive exchange within a stagnant zone including subsequent matrix diffusion is given by:

$$\psi_s = \sqrt{D_w T_s}\,\tanh\left(W_s\sqrt{\frac{T_s}{D_w}}\right) \qquad \text{(for a limited stagnant zone width)} \qquad \text{(I-13)}$$

Or,

$$\psi_s = \sqrt{D_w T_s} \qquad \text{(for an infinite stagnant zone width)} \qquad \text{(I-14)}$$

The variable T_s in Equation I-13 and I-14 is defined as:

$$T_s = R_a\phi + \frac{MPG_m}{\delta_s/2}\sqrt{\phi} \qquad \text{(for an infinite, simple matrix)} \qquad \text{(I-15)}$$

$$T_s = R_a\phi + \frac{MPG_m}{\delta_s/2}\sqrt{\phi}\,\tanh\left(A_m\delta_m\sqrt{\phi}\right) \qquad \text{(for a limited, simple matrix)} \qquad \text{(I-16)}$$

$$T_s = R_a\phi + \frac{MPG_{m(1)}}{\delta_s/2}\sqrt{\phi}\left(1-\frac{2}{1+\frac{w_m}{p_m}}\right) \qquad \text{(for a limited, complex matrix)} \qquad \text{(I-17)}$$

The mass flux to the stagnant zone, J_s and to the rock matrix from the main flow channel, J_m can also be calculated. In Laplace space, these are:

$$\tilde{J}_m = \psi_m\tilde{C}_f \qquad \text{(I-18)}$$

$$\tilde{J}_s = \psi_s\tilde{C}_f \qquad \text{(I-19)}$$

The Laplace space solutions are inverted numerically using the algorithm described by /de Hoog et al. 1982/ and implemented in the Matlab function developed by /Hollenbeck 1998/.

When simulating complex matrix microstructures it is important to take care not to "double count" matrix storage capacity since no account is made in the simplified mass balance model described above for the mutual interaction of diffusion profiles emanating from different surfaces. This is of particular importance if credit is to be taken for mass transfer via incident diffusive fractures that cross the main flow channel. For the simple cases considered in Chapter 5, however, this was not a problem as incident fractures were not considered.

Incident diffusive fractures can be accounted for in an approximate fashion by consideration of the intersecting trace length per unit area of the flow-wetted surface in the main flow channel. By assuming that the fractures "on average" intersect the flowpath orthogonally they can be accounted for using an additional stagnant zone flux term as defined by Equation I-13. This, however, only accounts for diffusive fractures that intersect the flow channel directly and no additional accounting is made for intersection of these fractures with the in-plane stagnant zone. Although possible, this would require a more complex formulation of Equation I-13 and I-14.

To simulate cases involving incident diffusive fractures, statistics of fracture intersection with the flow channel need to be calculated using the Hydro-DFN model with an upper size limit set at the smallest advective fracture considered in Hydrogeological simulations. For the fracture sets used as a basis for the calculations presented in Chapter 3, for example, a lower limit of r_{min} = 1 m was assumed for the smallest advective fracture radius. If the modeller wishes to include the additional diffusive uptake to these features, the appropriate range of diffusive fractures to consider would then be $< r_0, r_{min} >$ where r_0 is the lower cut-off size of the Hydro-DFN (r_0 = 0.04 m in this report). The approximate intensity of line traces, P_{21}^{DAS} (m/m^2) for intersection of diffusive fractures with the main flow channel can be obtained using the parameters of the Hydro-DFN directly. In a similar fashion, the average stagnant zone width of the diffusive fractures can also be obtained from the statistics of intersecting fractures. Figure I-1 illustrates the sequence of calculations that would be hypothetically necessary in order to achieve this.

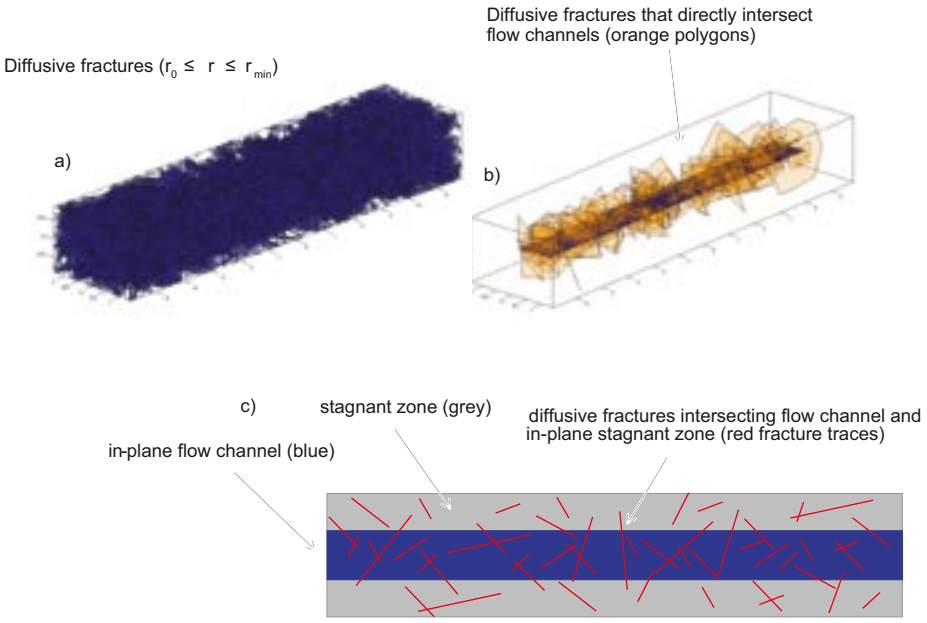

Figure I-1. *Conceptual illustration showing a) fracture network of small diffusive fractures in the relevant size range simulated within a control volume using the Hydro-DFN; b) identification of diffusive fracture subset that directly intersect the flow channel; and c) calculate P21 line traces for intersection of diffusive fractures with the main flow channel and flanking, in-plane stagnant zone.*

For fracture sets with a roughly isotropic and random orientation relative to the flowpath, it is possible to define the trace length intensity in terms of the linear intensity, P_{10}^{DAS} (m^{-1}) of stagnant open fractures using the relation:

$$R_{xs} = P_{21}^{DAS}\delta_{xs} \approx \frac{\pi}{2} P_{10}^{DAS}\delta_{xs} \qquad \text{(I-20)}$$

Here, δ_{xs} is the average transport aperture of the incident fractures and it is implicitly assumed that they terminate against the main fracture hosting the flowpath. When using this approximation, however, we do not know anything about the average size of the incident fractures, so this needs to be assumed or otherwise estimated from the fracture size distribution. This information is necessary to be able to say something about the width of the stagnant zone to be modelled.

Although the use of Equation I-20 in conjunction with an additional flux term is only strictly correct for very early times before diffusion fronts in the rock matrix begin to overlap and interact, it demonstrates that for incident fracture intensities, P_{10}^{DAS} on the order of 5 m^{-1} to 10 m^{-1}, the diffusive flux into incident fractures could be as much as that for an in-plane stagnant zone. This could have a considerable impact upon retention properties in deformation zones where the fracture intensity is much higher.

When modelling incident fractures it may be more physically accurate to assume a very limited depth of penetration from the incident fractures into the matrix in order to avoid double counting at later times. As an example, for a P_{10}^{DAS} of 10 m^{-1} and a limited penetration depth of 0.5 cm assumed for the incident fractures, the F-factor for direct matrix uptake should be reduced by about 10% (i.e. for every 90 cm of flowpath length, there are 10 incident fractures with a penetration depth of 0.5 cm on each side). This can be achieved by reducing the F-factor directly or by using an appropriately scaled R_i term in Equation I-10 (i.e. $R_m = 0.9$).

If the intensity of incident fractures is sufficiently high, it may be more computationally expedient to approximate the rock matrix containing embedded diffusive fractures as a bi-porous medium with two characteristic rates of diffusion (this can be derived by analogy with Equation I-13) or perhaps by simply estimating an effective diffusivity that approximately internalises the effect of such fractures.

2D radially symmetric diffusion cases

As already discussed in some detail in Chapter 5, for very narrow flow channels (or larger flow channels at long times) the physics of diffusive exchange with the rock matrix may be more accurately described by a 2D radial model of diffusion. If the solute diffusion can be described as an approximately radially symmetric process, it is possible to define a 1D flux term that allows us to simulate this case using Equation I-3. For a rock matrix of infinite extent, /Neretnieks 2006/ gives a solution based upon analogy with a heat conduction problem described by /Carslaw and Jaeger 1959/. The flux term for this case is defined as:

$$\psi_m = MPG_m\sqrt{\phi}\left(\frac{K_1(a\omega)}{K_0(a\omega)}\right) \qquad \text{(I-21)}$$

Where, K_0 and K_1 are modified Bessel functions of the second kind (order 0 and 1, respectively) and the parameter a is the equivalent radius for transport (which will be discussed later). The parameter ω is defined as:

$$\omega = \sqrt{\frac{\phi}{D_a}} \qquad \text{(I-22)}$$

For a rock matrix of limited radial extent, *b* the flux term is instead given by the more complex expression:

$$\psi_m = MPG_m\sqrt{\phi}\left(\frac{I_1(b\omega)Y_1(-ia\omega)-I_1(a\omega)Y_1(-ib\omega)}{iI_1(b\omega)Y_0(-ia\omega)+I_0(a\omega)Y_1(-ib\omega)}\right) \quad \text{(I-23)}$$

Here, I_0 and I_1 are modified Bessel functions of the first kind, while Y_0 and Y_1 are Bessel functions of the second kind (order 0 and 1, respectively).

As already discussed for the 1D linear case, if there is a high frequency of intersecting diffusive fractures, this could have a large impact upon effective rates of diffusion along a flowpath. For an orthogonally intersecting diffusive fracture of limited extent, b_x we can derive a stagnant zone radial flux term, ψ_{xs} as:

$$\psi_{xs} = D_w\omega\left(\frac{I_1(b_x\omega)Y_1(-ia\omega)-I_1(a\omega)Y_1(-ib_x\omega)}{iI_1(b_x\omega)Y_0(-ia\omega)+I_0(a\omega)Y_1(-ib_x\omega)}\right) \quad \text{(I-24)}$$

Where,

$$\omega = \sqrt{\frac{T_{xs}}{D_w}} \quad \text{(I-25)}$$

And,

$$T_{xs} = R_a\phi + \frac{MPG_m}{\delta_{xs}/2}\sqrt{\phi} \quad \text{(for an infinite, simple matrix)} \quad \text{(I-26)}$$

$$T_{xs} = R_a\phi + \frac{MPG_m}{\delta_{xs}/2}\sqrt{\phi}\tanh\left(A_{mx}\delta_{mx}\sqrt{\phi}\right) \quad \text{(for a limited, simple matrix)} \quad \text{(I-27)}$$

Once again it is very important to not double count matrix storage capacities as the multiple rate terms in Equation I-10 do not account for mutually interacting diffusion profiles. As described previously, this can be avoided by defining limited penetration depths for the subsequent diffusion to the rock matrix from the diffusive fracture while reducing the amount of flow-wetted surface available for the direct matrix uptake term. Other alternatives based upon the suggestions given for the 1D case are also possible for the 2D radial-symmetric case.

To calculate the approximate R_{xs} term to be used in Equation I-10, we could use the Hydro-DFN to estimate the trace length intensity of intersecting fractures on a cylinder of effective radius, *a* or the approximation given by Equation I-20 for a flow channel of width greater than a few cm. For very narrow, tube-like flow channels, however, the following relation which assumes orthogonally oriented diffusive fractures should be sufficiently accurate for scoping calculations:

$$R_{xs} \approx \frac{P_{10}^{DAS}\delta_{xs}}{2\pi a} \quad \text{(I-28)}$$

In-plane stagnant zones within the fracture hosting the flow path are also possible to simulate in the 2D radial-symmetric case using the previously defined flux terms given by Equation I-13 or I-14. In this situation, however, it is critical to avoid double counting of the storage capacity as the radial diffusion profile will always interact with the 1D matrix diffusion profile radiating from the in-plane stagnant zone. To avoid this, the modeller could define a limited depth of matrix diffusion associated with the in-plane stagnant zone. This would give reasonable results at short times, but may underestimate matrix uptake at later times as the limited matrix in the stagnant zone becomes equilibrated. Another possibility is to assume a relatively fast diffusive equilibrium throughout the stagnant zone and define an enhanced flow-wetted surface that

includes the additional matrix surface area accessible by diffusion from the main advective flow channel. This approach is probably most appropriate for fracture intersection zones, FIZ where the diffusion accessible surface in the extended stagnant zone may be far greater than the "actual" flow-wetted surface available in the advective flow channel. As discussed in the following sections, there may not always be a clear demarcation between the advective and diffusive zones for flow channels hosted within FIZ features.

Geometrical considerations concerning flow channel geometry

Although it is relatively straight-forward to define a radial matrix flux term for in-plane flow channels with relatively high W_c/δ_t aspect ratios, this is somewhat more difficult for flow channels of very narrow extent as might exist at fracture intersections. In such cases, the flow-wetted surface for direct matrix interaction is not well defined and is strongly influenced by assumptions made in its calculation. In these cases, choices made as to how in-plane flanking diffusive zones are conceptualised may have a large impact upon the outcome of transport calculations. In the F-factor calculations described in section 3.6.2, for example, the flow-wetted surface per metre flowpath length within conductive FIZ was simply assumed to be no more than 1% of that existing in a "normal" in-plane flow channel. For a 0.1 m wide standard in-plane flow channel, this means that FIZ flow channels would be no more than 1 mm in extent.

Although this is probably not an unreasonable assumption given that we seek to identify an upper limit to the effect that these zones have on the overall F-factor for a flowpath (where FIZ are assumed to not contribute significantly to the hydraulic resistance), it may unfairly bias transport calculations by not making any consideration of the enhanced retention that may be exhibited by these zones by way of increased rates of diffusive uptake. Some additional thoughts on this issue are summarised in the following paragraphs.

In-plane flow channels

For narrow flow channels residing within the plane of a fracture, solute transport may be more accurately described using a model of radial diffusion. Here we make the approximation that a flow channel of limited width (W_c) and aperture (δ_t) can be approximately modelled as a cylinder of equivalent radius (a) embedded in an infinite medium. The reliability of this assumption has been previously addressed by /Rasmuson and Neretnieks 1986/ and found to be a very good approximation. The geometry of the system under consideration is depicted in Figure I-2.

For solute uptake to the rock matrix, the equivalent radius is that of a circle with the same perimeter as the flow-wetted surface in the channel. It should be noted that this is a different definition to that used for hydraulic aperture for turbulent flow as used in engineering textbooks. It is also important to consider that the equivalent radius defined in this manner is purely a geometrical construct to simplify the formulation of the flux terms and is not the same as the transport half-aperture necessary to calculate the advective travel time, t_w. In /Johns and Roberts 1991/

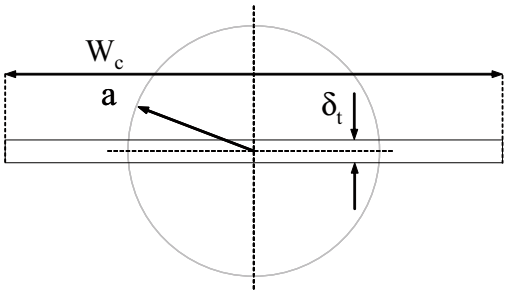

Figure I-2. *Schematic illustration of an in-plane channel where solute uptake to the rock matrix is approximated as a radially symmetric diffusion process in a cylinder of equivalent radius, a. For the case considered here, the flow channel has an aperture, δ_t and width W_c.*

this problem was circumvented by defining a "pseudo-porosity" to account for the larger cross-sectional area of the flow channel implied by mapping the flow-wetted surface to an equivalent cylindrical surface. It is not necessary to do this in the formulation described here, however, as the advective transport time enters as an independent parameter in Equation I-3 and I-10.

The width of narrow flow channels is thought to be in the range of a few cm to perhaps a few tens of cm, whereas for the fracture aperture a range of 10^{-3}–10^{-5} m is expected. For such large aspect ratios, the solute uptake at short times will be more accurately represented by the standard solution for a 1D, semi-infinite slab geometry. At a solute penetration depth on the order of the channel width itself and greater, however, the radial solution provides a more accurate account of solute mass transfer and can therefore be seen as a special asymptotic case of the more general, radially asymmetric solute uptake problem.

The flow-wetted surface per unit length of the flow channel is:

$$A_F = W_c \tag{I-29}$$

The equivalent transport radius can then be given as /Johns and Roberts 1991/:

$$a = \frac{W_c + \delta_t}{\pi} \approx \frac{W_c}{\pi} \tag{I-30}$$

Flow channels at fracture intersections (FIZ)

If we consider a joint intersection formed by two equidimensional, crossing fracture planes (i.e. FIZ subtype A), there will be a conduit with enhanced hydraulic conductivity at the line of fracture intersection as illustrated schematically in Figure I-3 for the non-terminating (left) and terminating (right) cases, respectively.

In the case where we assume flow to be restricted to the square duct formed by the actual fracture intersection, the flow-wetted surface per unit length of the conduit would simply be the perimeter of the central square duct.

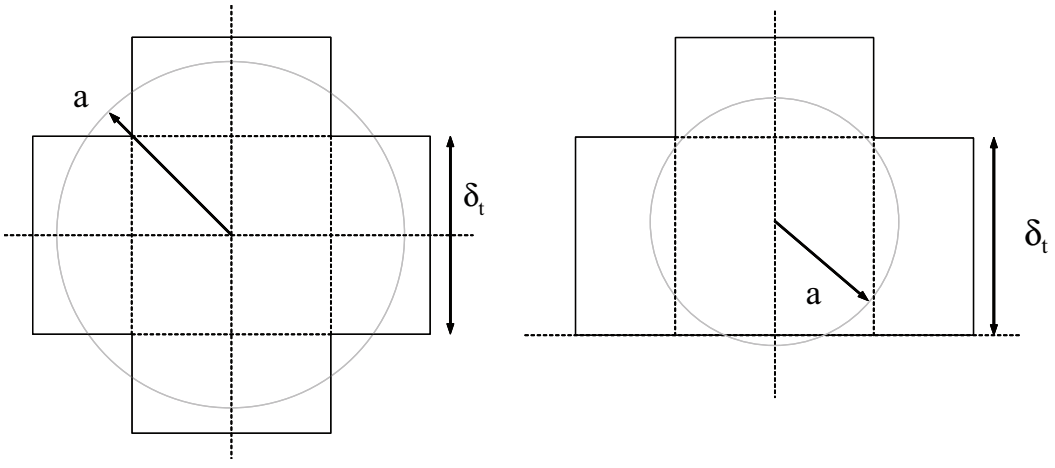

Figure I-3. *Schematic illustration of a joint intersection formed by two crossing fracture planes (FIZ subtype A, non-terminating and terminating variants). For the cases considered here, both fractures have the same aperture, δ_t and the effective transport radius of the flow conduit is a.*

A conceptual problem arises, however, if we wish to consider mass transfer to stagnant zones in the plane of non-terminating fractures as this would require the flow-wetted surface for the conduit itself to be zero. Since the region of the enhanced velocity profile at such an intersection extends a small distance into the bounding fracture planes (see Appendix A), it is possible to define this as part of the flow-wetted surface of the flow channel and thereby avoid the problem. In this case, the flow-wetted surface per unit length of the conduit would be roughly half of the square duct perimeter if we were to assume that the enhanced velocity profile extends roughly 1/4 of an aperture length into the flanking fracture planes.

Depending upon how the geometry of the advective flow conduit at the fracture intersection is defined, the flow-wetted surface per unit length of the flow channel could be anywhere in the range:

$$\sim \delta_t \leq A_F \leq \sim 6\delta_t \tag{I-31}$$

The equivalent transport radius can then be shown to be:

$$\sim \frac{\delta_t}{2\pi} \leq a \leq \sim \frac{3\delta_t}{\pi} \tag{I-32}$$

For the case of FIZ subtype B which may arise as a result of rock block rotation, the flow channel geometry may look something like that depicted in Figure I-4.

In this case, the flow-wetted surface of the flow conduit is somewhat better defined and we can write:

$$A_F \approx 4\left(\delta_t - \delta_s\right) \tag{I-33}$$

And for the equivalent transport radius:

$$a \approx \frac{4\left(\delta_t - \delta_s\right)}{\pi} \tag{I-34}$$

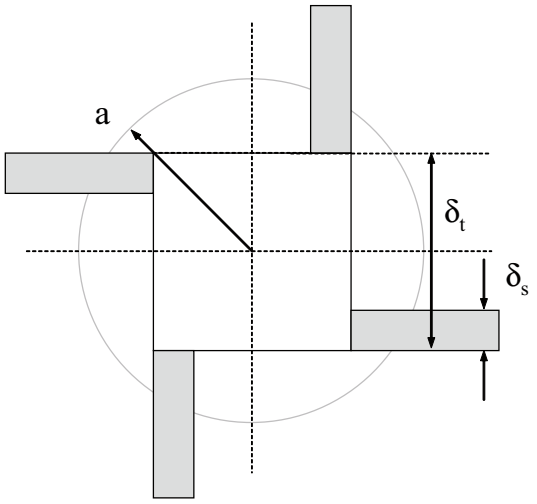

Figure I-4. *Schematic illustration of a joint intersection formed by rotated rock blocks (FIZ subtype B). For the case considered here, the flow conduit itself has an effective aperture, δt while the bounding fractures have aperture, δ_s. As previously, the effective transport radius of the flow conduit is a.*

Flow channels at fracture intersections (FIZ) with spheroidal weathering

If the fracture intersections have been subject to spheroidal weathering and erosion they may develop a cuspoid profile after some time (i.e. featuring rounded corners). In these cases, we consider the cross-sectional flow channel configuration as depicted in Figure I-5.

Here, we firstly consider the situation where flow is restricted to the intersection itself with no stagnant zone. The flow-wetted surface per unit length of the flow channel is:

$$A_F \approx \begin{cases} 4\delta_t + 2\pi r_{sw} & \text{(non-terminating fractures)} \\ 4\delta_t + (2+\pi) r_{sw} & \text{(terminating fractures)} \end{cases} \qquad \text{(I-35)}$$

The equivalent transport radius is then:

$$a \approx \begin{cases} \dfrac{2\delta_t}{\pi} + r_{sw} & \text{(non-terminating fractures)} \\ \dfrac{2\delta_t}{\pi} + \left(\dfrac{1}{\pi} + \dfrac{1}{2}\right) r_{sw} & \text{(terminating fractures)} \end{cases} \qquad \text{(I-36)}$$

If we consider the flanking fractures to comprise a diffusive zone, the flow-wetted surface per unit length of flow channel would instead need to be defined as:

$$A_F \approx \begin{cases} 2\pi r_{sw} & \text{(non-terminating fractures)} \\ \delta_t + (2+\pi) r_{sw} & \text{(terminating fractures)} \end{cases} \qquad \text{(I-37)}$$

We would then have for the equivalent transport radius:

$$a \approx \begin{cases} r_{sw} & \text{(non-terminating fractures)} \\ \dfrac{\delta_t}{2\pi} + \left(\dfrac{1}{\pi} + \dfrac{1}{2}\right) r_{sw} & \text{(terminating fractures)} \end{cases} \qquad \text{(I-38)}$$

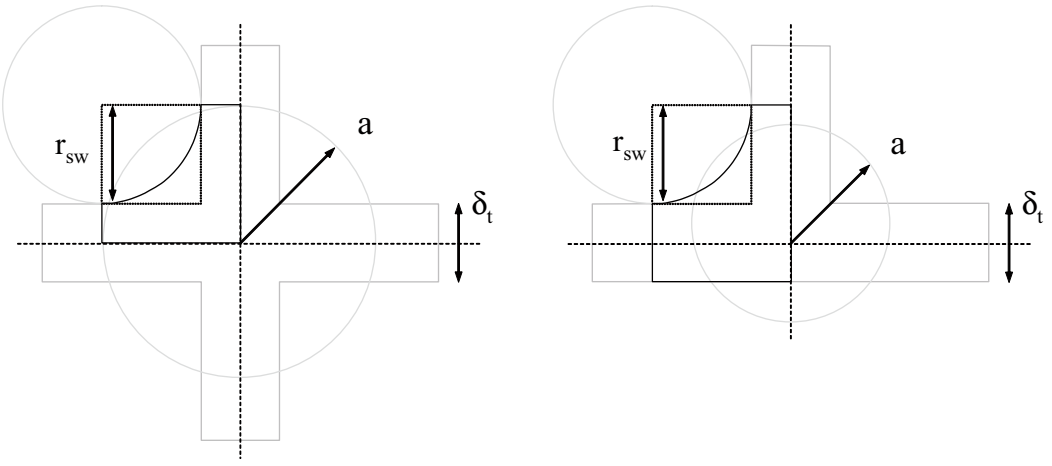

Figure I-5. *Schematic illustration of a joint intersection formed by two crossing fracture planes featuring spheroidal weathering at their intersection (FIZ subtype C, non-terminating and terminating variants). For the case considered here, both fractures have the same nominal aperture, δ_t. and weathered edge radius, r_{sw}. The effective transport radius of the flow conduit is a.*

In spite of these deliberations, it should be noted that the smooth geometry of FIZ features as described above is highly idealised and "actual" FIZ are likely to exhibit a considerable amount of surface roughness and aperture variability which makes such a strict analysis of their geometric properties questionable. Here, the aim is more to establish an envelope of flow-wetted surface values for such flow channels under some limiting assumptions. The flow-wetted surface of actual FIZ features is likely to be higher than these simple geometric cases suggest.

If we were to consider a "fringe" area of enlarged aperture that comprises the flow-wetted surface, the advective zone of a real FIZ feature may look something like that illustrated in Figure I-6.

As illustrated in the figure above, the increased microstructural complexity of a rough fracture intersection could potentially result in the formation of an advective fringe zone adjacent to the central flow conduit. Depending upon the dimensions of this fringe zone, the effective flow-wetted surface of the conductive fracture intersection may be many times larger than that calculated for the simple geometric cross-sections described previously. The additional diffusive surface area afforded by such flow channel configurations could substantially increase retardation.

It should also be noted that a conductive fracture intersection with an effective radius on the order of a few mm would only require a couple of cm of diffusion accessible surface in the flanking fracture planes to qualify as a 10:1 in-plane stagnant zone (as discussed previously for the 1D linear diffusion case).

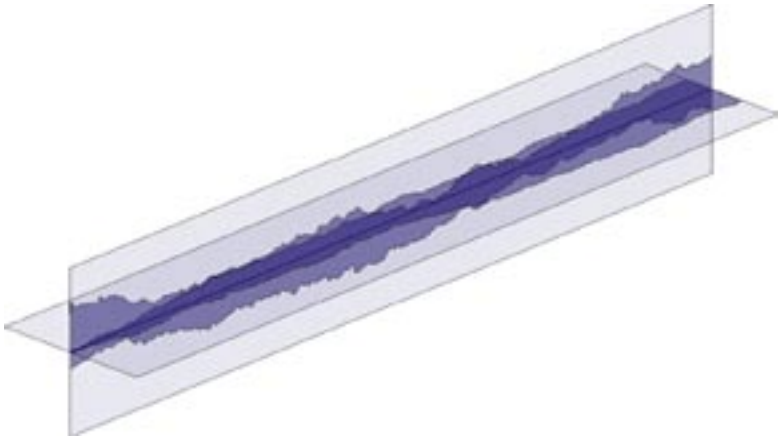

Figure I-6. *Schematic illustration of a rough joint intersection formed by two crossing fracture planes. In this case there is no well defined demarcation between the advective (dark shading) and diffusive zones (light shading).*

Detailed transport simulation results

In this section, detailed simulation results are given for the transport times of different solutes for the different representative groundwater compositions defined within the laboratory programme. Here we give results for fresh, marine, saline, and brine groundwater types. The results for saline conditions have already been presented in section 5.3.1 although are included again here to aid comparisons between the results for different groundwater types.

As discussed previously in Chapter 5, the simulation results are presented for the three transport model variants (BM, MA1, MA2) considering a range of sorption K_d values representing the spectrum of sorptivity from weakly sorbing ($K_d = 10^{-5}$ m^3/kg) to strongly sorbing ($K_d = 1$ m^3/kg). The three model variants are:

1. (BM) Advective flow coupled with 1D diffusion/sorption within the rock matrix.
2. (MA1) Advective flow in a narrow channel coupled with 1D diffusion/sorption in the rock matrix plus diffusion into a stagnant zone of limited extent and subsequent 1D diffusion/sorption within the rock matrix.
3. (MA2) Advective flow in a narrow channel coupled with 2D radial diffusion/sorption in the rock matrix.

Transport times for each model variant are plotted against sorption K_d for an assumed F-factor of 10^6 y/m and a formation factor of 1.6×10^{-5}. The formation factor is approximately the site average for rock type 101057 at Forsmark, as derived from *in situ* resistivity measurements (see Appendix G). The plots are made for a set of recovery fractions corresponding to 0.01%, 1%, 10%, and 50% of recovered solute, neglecting radioactive decay and assuming a maximum matrix depth of 2 m. Calculations based upon the MA1 model variant consider a single stagnant zone of width 10 times greater than the main advective flow channel (this is referred to as a 10:1 stagnant zone in the present report).

To illustrate the combined impact of K_d uncertainty and model uncertainty for specific solutes, the span of transport times vs. K_d is plotted as a rectangular polygon in the figures. The lower left hand vertex is the transport time for the model giving the fastest breakthrough using the lowest reported K_d value, while the upper right hand vertex corresponds to the transport time for the model giving the slowest breakthrough time using the maximum reported K_d value.

To set the results in a proper perspective, time limits for quantitative and qualitative safety assessment are indicated by the red broken and unbroken lines in the figure (loosely based upon guidelines in /SSI 2005/). Transport times longer than 10^7 years are considered to be of only academic interest and are included with the sole purpose of illustrating the relative scaling of transport times. It should be noted that although the upper end of the time axis, $\gg 10^7$ years is largely meaningless for safety assessment, the extrapolation to these timescales is a logical consequence of the physics of the simplified system as it is modelled without any additional consideration of geosphere stability. What this might mean in a safety assessment perspective is that the postulated retardation mechanism (i.e. transport of dissolved solute) may not be the major transport mechanism for very strongly sorbed solutes and alternative transport mechanisms such as pseudocolloid transport may be more important (i.e. transport of solute sorbed to naturally existing groundwater colloids).

Typical transport times for solutes under fresh (Type I) groundwater conditions

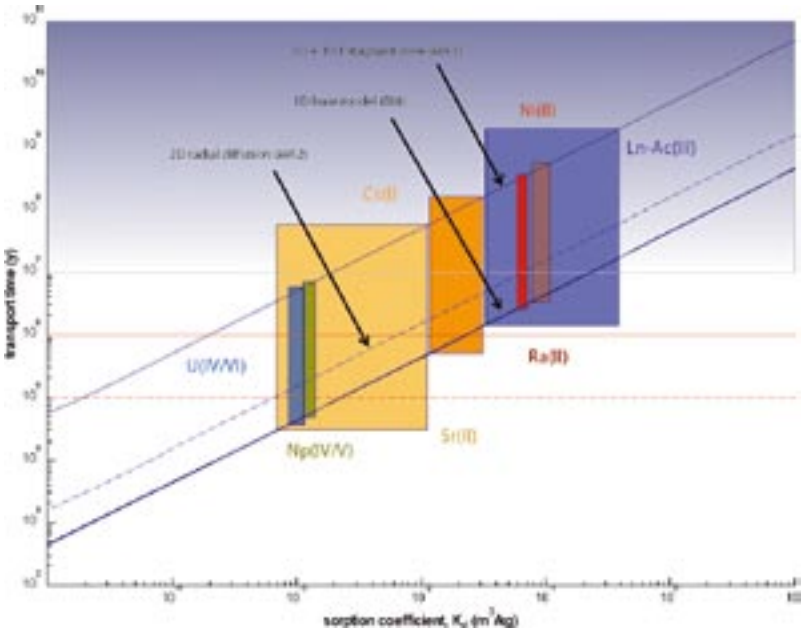

Figure I-7. *Recovery times for solutes as a function of K_d for a recovery fraction of 0.01%, a fixed F-factor of 10^6 y/m, and formation factor of 1.6×10^{-5}. Polygons represent approximate ranges of behaviour for indicated solutes under fresh (Type I) groundwater conditions.*

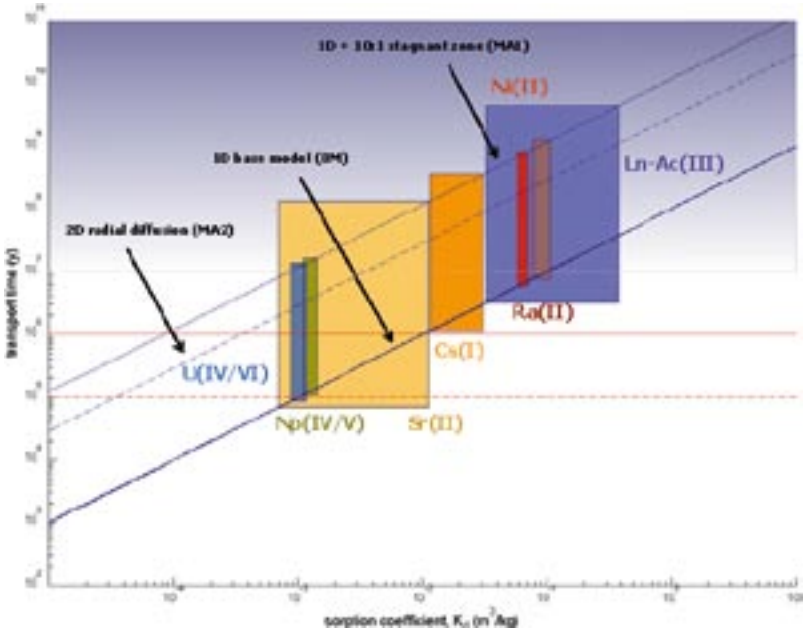

Figure I-8. *Recovery times for solutes as a function of K_d for a recovery fraction of 1%, a fixed F-factor of 10^6 y/m, and formation factor of 1.6×10^{-5}. Polygons represent approximate ranges of behaviour for indicated solutes under fresh (Type I) groundwater conditions.*

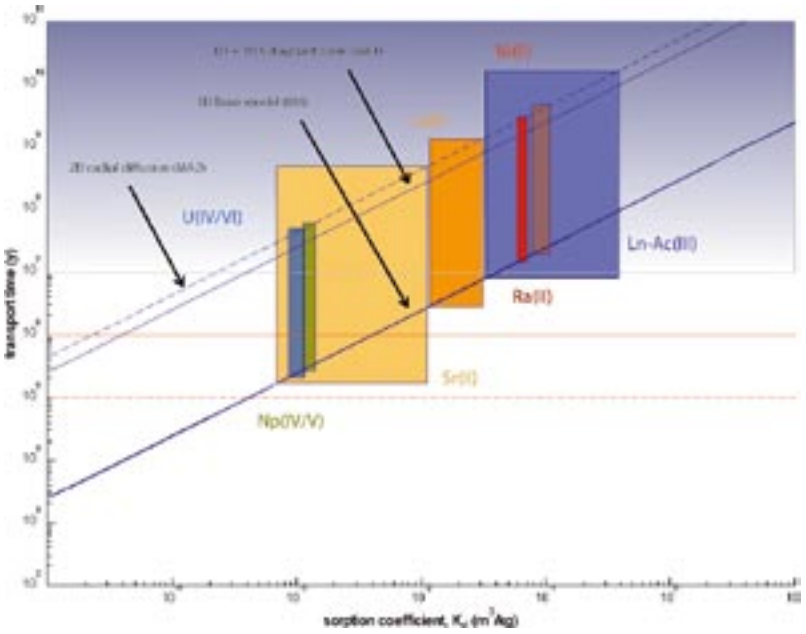

Figure I-9. *Recovery times for solutes as a function of K_d for a recovery fraction of 10%, a fixed F-factor of 10^6 y/m, and formation factor of 1.6×10^{-5}. Polygons represent approximate ranges of behaviour for indicated solutes under fresh (Type I) groundwater conditions.*

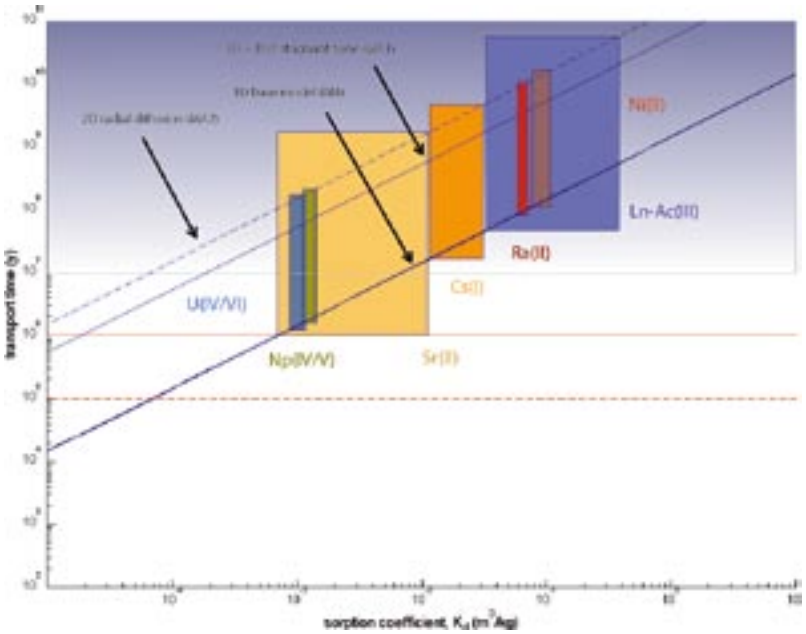

Figure I-10. *Recovery times for solutes as a function of K_d for a recovery fraction of 50%, a fixed F-factor of 10^6 y/m, and formation factor of 1.6×10^{-5}. Polygons represent approximate ranges of behaviour for indicated solutes under fresh (Type I) groundwater conditions.*

Typical transport times for solutes under marine (Type II) groundwater conditions

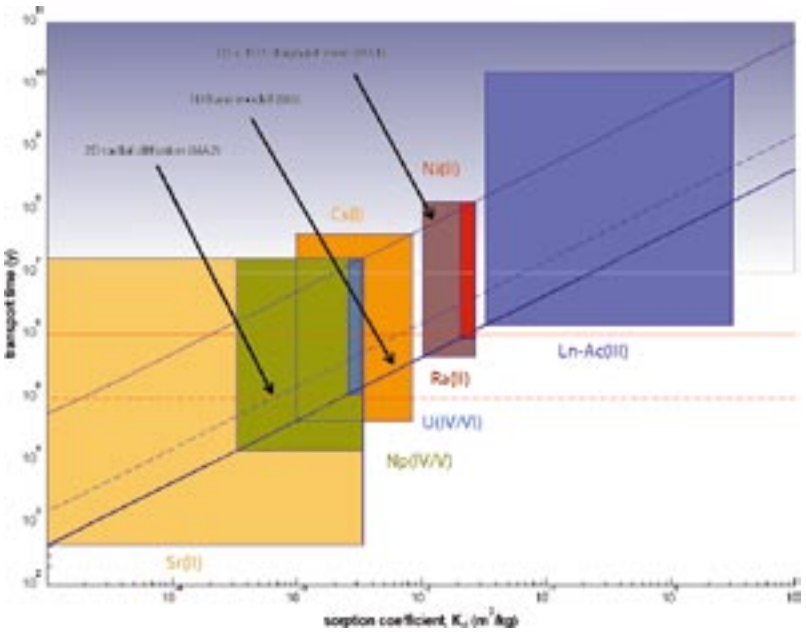

Figure I-11. *Recovery times for solutes as a function of K_d for a recovery fraction of 0.01%, a fixed F-factor of 10^6 y/m, and formation factor of 1.6×10^{-5}. Polygons represent approximate ranges of behaviour for indicated solutes under marine (Type II) groundwater conditions.*

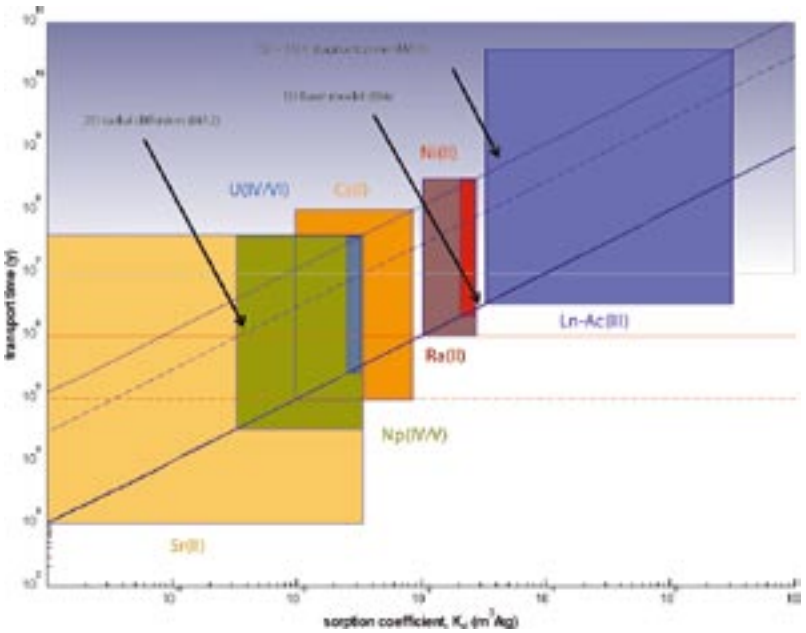

Figure I-12. *Recovery times for solutes as a function of K_d for a recovery fraction of 1%, a fixed F-factor of 10^6 y/m, and formation factor of 1.6×10^{-5}. Polygons represent approximate ranges of behaviour for indicated solutes under marine (Type II) groundwater conditions.*

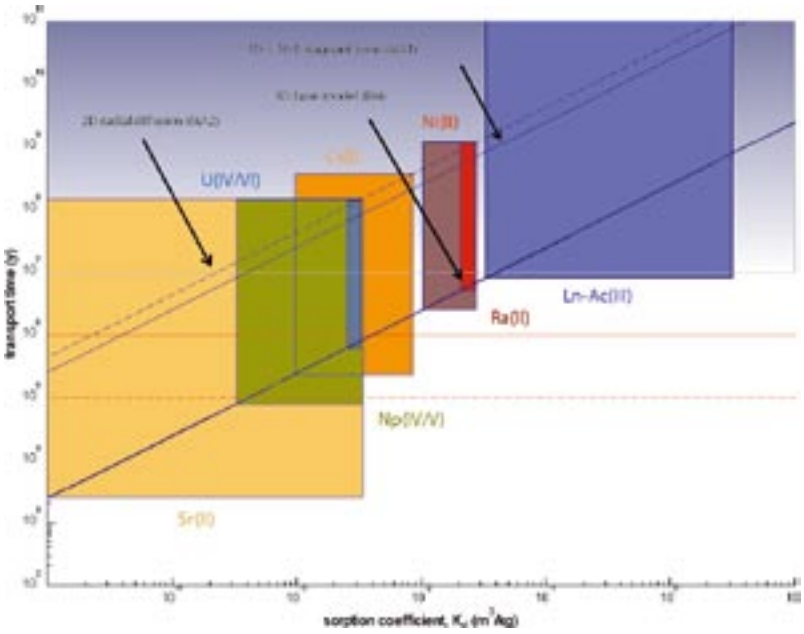

Figure I-13. *Recovery times for solutes as a function of K_d for a recovery fraction of 10%, a fixed F-factor of 10^6 y/m, and formation factor of 1.6×10^{-5}. Polygons represent approximate ranges of behaviour for indicated solutes under marine (Type II) groundwater conditions.*

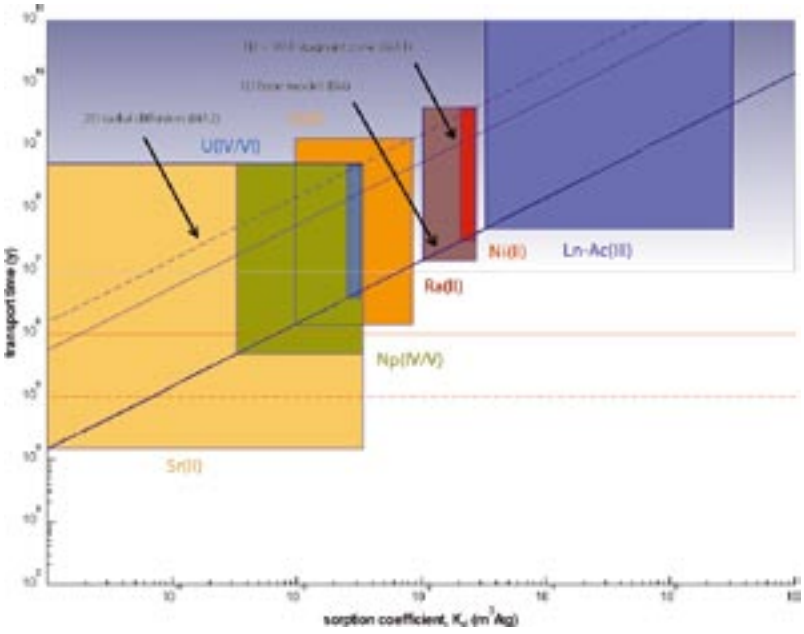

Figure I-14. *Recovery times for solutes as a function of K_d for a recovery fraction of 50%, a fixed F-factor of 10^6 y/m, and formation factor of 1.6×10^{-5}. Polygons represent approximate ranges of behaviour for indicated solutes under marine (Type II) groundwater conditions.*

Typical transport times for solutes under saline (Type III) groundwater conditions

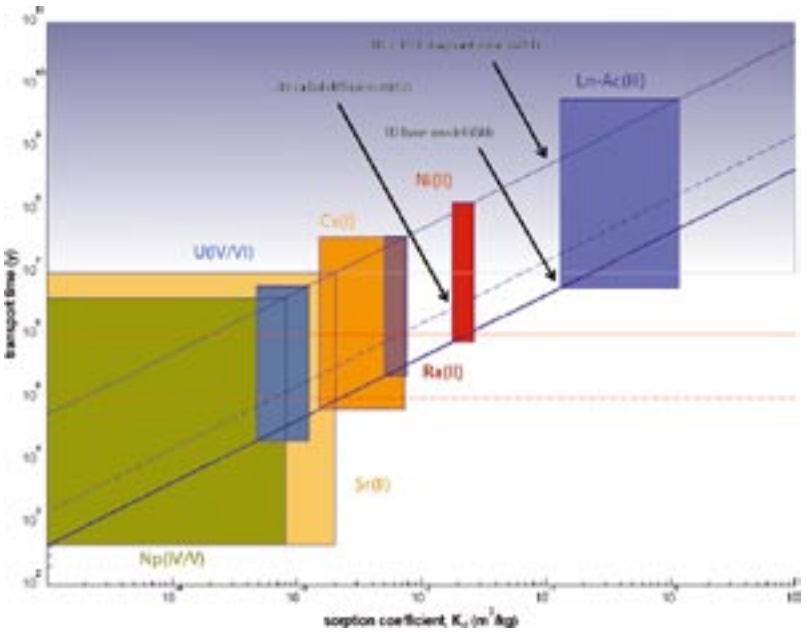

Figure I-15. *Recovery times for solutes as a function of K_d for a recovery fraction of 0.01%, a fixed F-factor of 10^6 y/m, and formation factor of 1.6×10^{-5}. Polygons represent approximate ranges of behaviour for indicated solutes under saline (Type III) groundwater conditions.*

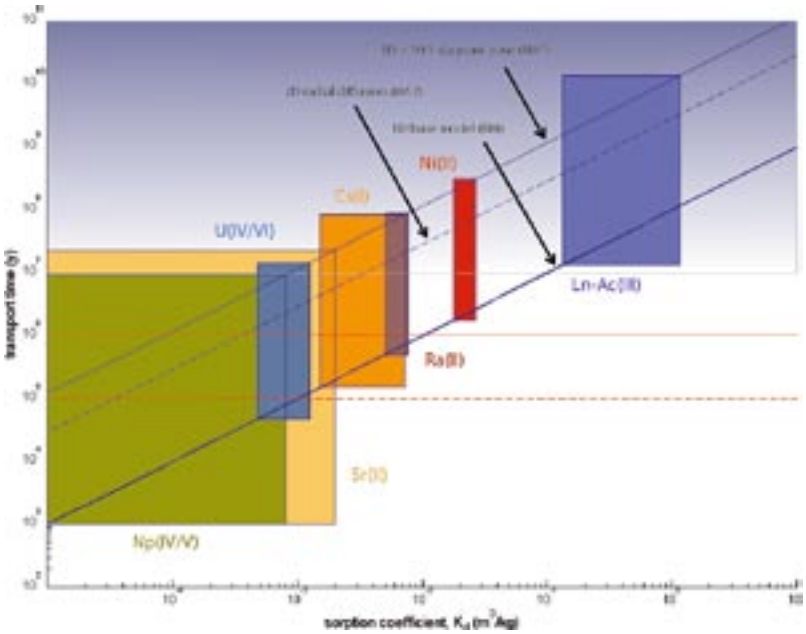

Figure I-16. *Recovery times for solutes as a function of K_d for a recovery fraction of 1%, a fixed F-factor of 10^6 y/m, and formation factor of 1.6×10^{-5}. Polygons represent approximate ranges of behaviour for indicated solutes under saline (Type III) groundwater conditions.*

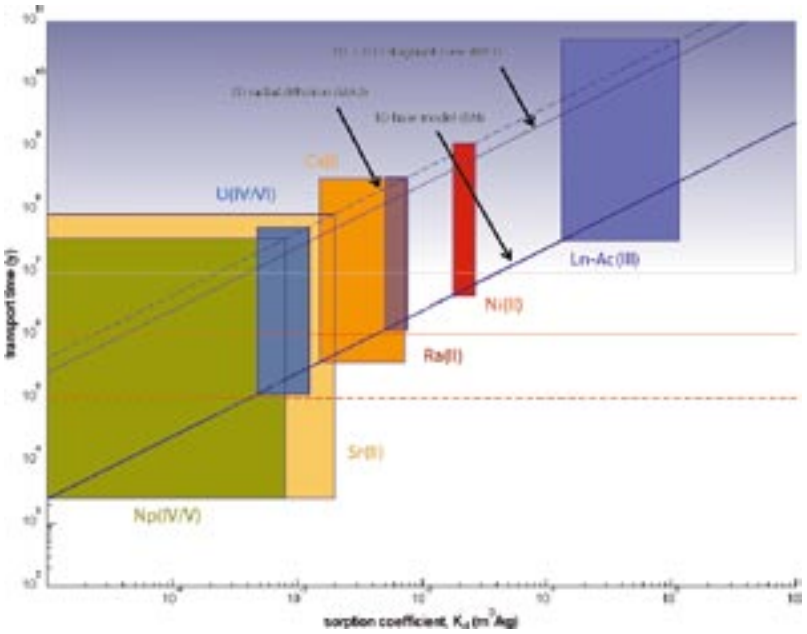

Figure I-17. *Recovery times for solutes as a function of K_d for a recovery fraction of 10%, a fixed F-factor of 10^6 y/m, and formation factor of 1.6×10^{-5}. Polygons represent approximate ranges of behaviour for indicated solutes under saline (Type III) groundwater conditions.*

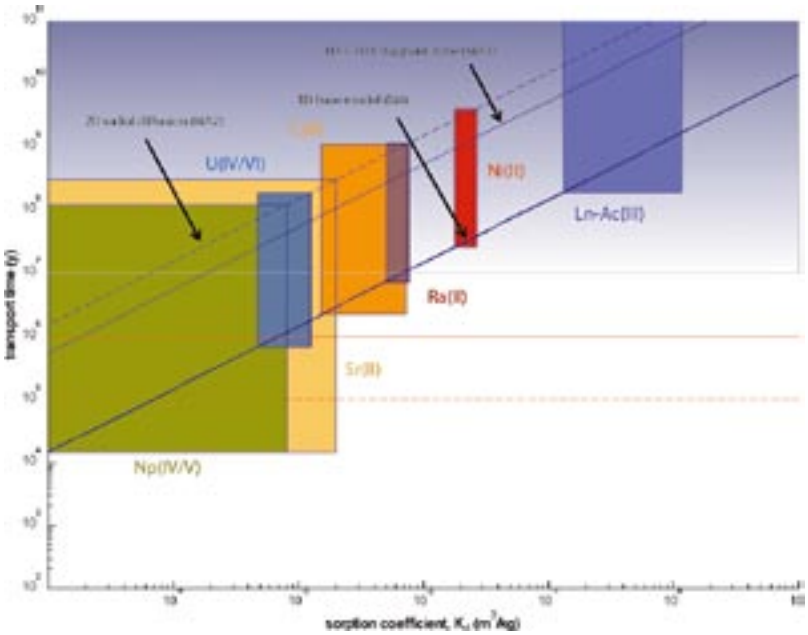

Figure I-18. *Recovery times for solutes as a function of K_d for a recovery fraction of 50%, a fixed F-factor of 10^6 y/m, and formation factor of 1.6×10^{-5}. Polygons represent approximate ranges of behaviour for indicated solutes under marine (Type III) groundwater conditions.*

Typical transport times for solutes under brine (Type IV) groundwater conditions

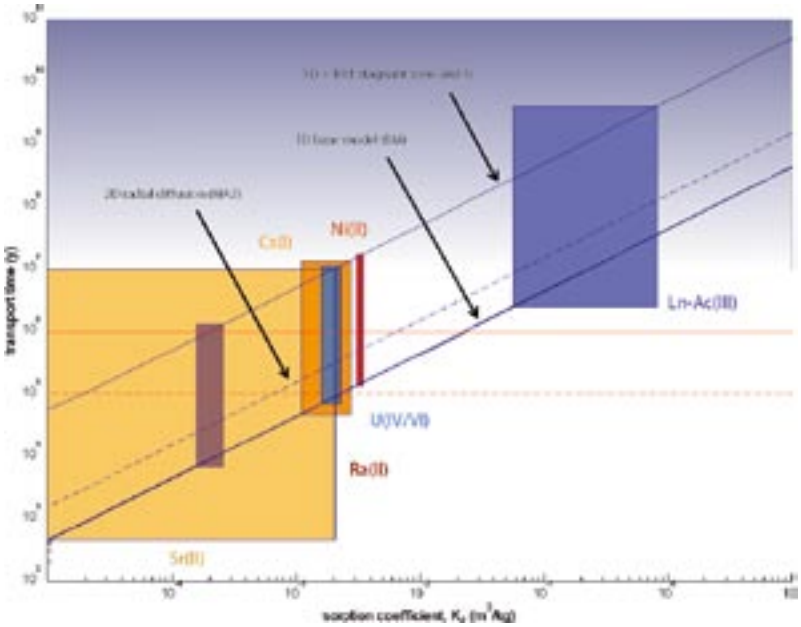

Figure I-19. *Recovery times for solutes as a function of K_d for a recovery fraction of 0.01%, a fixed F-factor of 10^6 y/m, and formation factor of 1.6×10^{-5}. Polygons represent approximate ranges of behaviour for indicated solutes under brine (Type IV) groundwater conditions.*

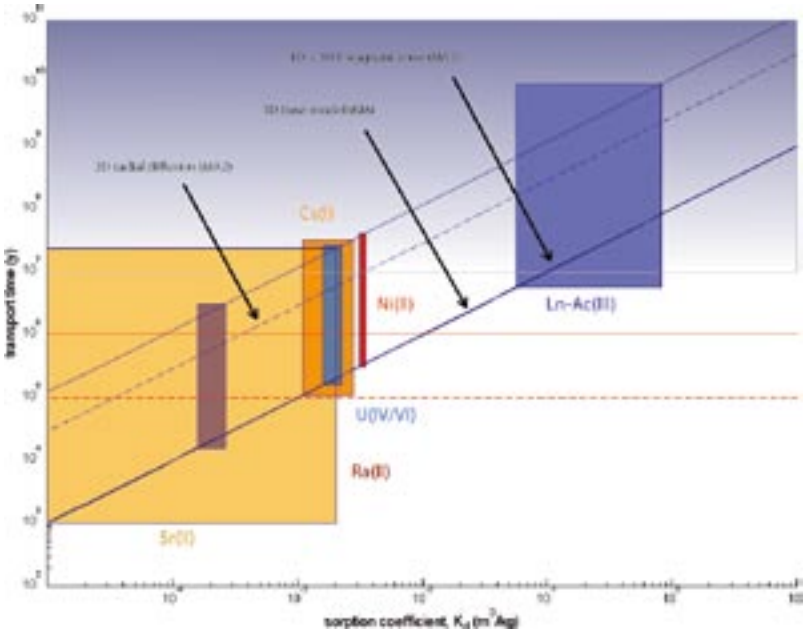

Figure I-20. *Recovery times for solutes as a function of K_d for a recovery fraction of 1%, a fixed F-factor of 10^6 y/m, and formation factor of 1.6×10^{-5}. Polygons represent approximate ranges of behaviour for indicated solutes under brine (Type IV) groundwater conditions.*

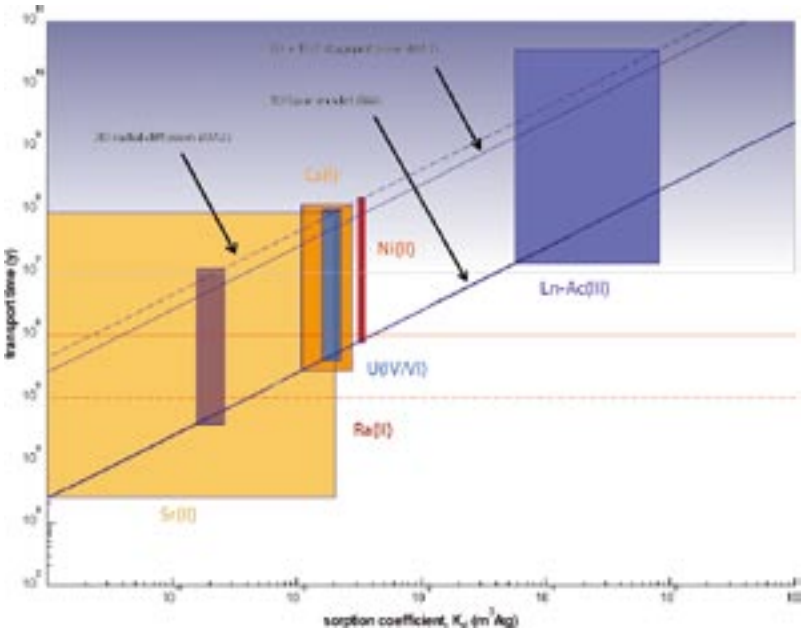

Figure I-21. *Recovery times for solutes as a function of K_d for a recovery fraction of 10%, a fixed F-factor of 10^6 y/m, and formation factor of 1.6×10^{-5}. Polygons represent approximate ranges of behaviour for indicated solutes under brine (Type IV) groundwater conditions.*

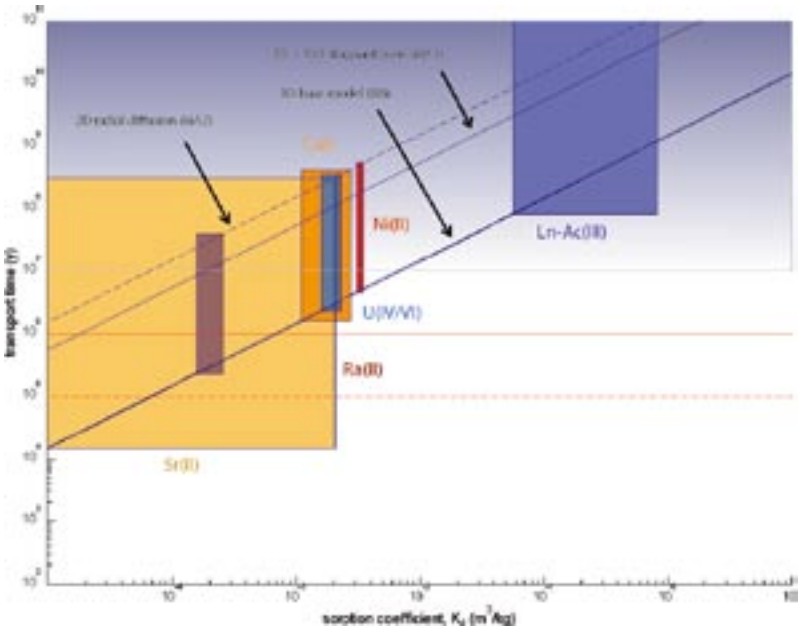

Figure I-22. *Recovery times for solutes as a function of K_d for a recovery fraction of 50%, a fixed F-factor of 10^6 y/m, and formation factor of 1.6×10^{-5}. Polygons represent approximate ranges of behaviour for indicated solutes under brine (Type IV) groundwater conditions.*

Appendix J

On flowpath averaging of material properties

Author: James Crawford

In section 5.5 the uniqueness of the description of rock material properties was discussed briefly. In this Appendix chapter we present calculations to demonstrate under what conditions the material properties group (MPG) can be assumed to be a unique descriptor of the transport properties of the rock matrix and when the storage capacity and diffusivity of the rock matrix need to be specified separately. This issue is of some importance when flowpath averaging is to be used as a means of describing the effective retention properties of a flowpath.

In general, for advective solute transport along a flow channel with mass transfer to a single-layered rock matrix of infinite extent, the MPG can be shown to be a unique descriptor of the retardation properties of the rock. This means that the case of rock matrix with reduced sorptivity and increased effective diffusivity should be indistinguishable from the case of increased sorptivity and decreased effective diffusivity, provided the MPG is identical in both cases (i.e. indistinguishable with regard to the residence time distribution of transported solute).

It is not clear when this was first stated explicitly, although it is a logical consequence of the solution given by /Neretnieks 1980/ and the analogous problem in heat conduction as described by /Carslaw and Jaeger 1959/. Furthermore, it can be shown /RETROCK 2004/ that the material properties of the rock as represented by the MPG can be integrated along a flowpath in a simple fashion to calculate a flowpath average. This considerably simplifies calculations involving material properties which exhibit spatial variability along a flowpath. In terms of the local differential F-factor, *dF(x)/dx* the path integrated form of Equation I-10 for spatially variable material properties (i.e. variation along the flowpath trajectory) can be written as:

$$\tilde{C}_f = \frac{1}{s}\exp\left(-\frac{t_w}{L_p}\int_0^{L_p} R_a(x)\,dx\right)\exp\left(-\int_0^{L_p}\left(\left(\frac{d}{dx}F(x)\right)\sum_{i=1}^{n} R_i(x)\psi_i(x)\right)dx\right) \quad \text{(J-1)}$$

For a segmented flowpath consisting of *m* segments with piecewise constant material and flow related transport properties, Equation J-1 could be written in the form:

$$\tilde{C}_f = \frac{1}{s}\exp\left(-\sum_{j=1}^{m} t_{w(j)} R_{a(j)}\right)\exp\left(-\sum_{j=1}^{m}\left(F_j \sum_{i=1}^{n} R_{i,j}\,\psi_{i,j}\right)\right) \quad \text{(J-2)}$$

If we were to consider a single matrix flux term and an infinite rock matrix, Equation J-1 simplifies to:

$$\tilde{C}_f = \frac{1}{s}\exp\left(-\bar{R}_a t_w\right)\exp\left(-\sqrt{\phi}\int_0^{L_p}\left(\frac{d}{dx}F(x)\right)MPG_m(x)\,dx\right) \quad \text{(J-3)}$$

Or, for a segmented flowpath:

$$\tilde{C}_f = \frac{1}{s}\exp\left(-\bar{R}_a t_w\right)\exp\left(-\sqrt{\phi}\sum_{j=1}^{m} F_j \cdot MPG_{m(j)}\right) \quad \text{(J-4)}$$

As can be seen from the form of Equation J-4 the summation term corresponds to a simple weighted average of the variable MPG based upon the local flowpath F-factor. For a flowpath without any diverging or converging flow mixing points, the term *dF(x)/dx* is a constant (i.e. the F-factor for the flowpath is proportional to distance travelled) and the summation term in Equation J-4 would then be the overall flowpath F-factor multiplied by the arithmetic mean MPG:

$$\overline{MPG} = \frac{1}{L_p}\int_0^{L_p} MPG_m(x)\,dx = \frac{1}{m}\sum_{j=1}^{m} MPG_{m(j)} \qquad \text{(J-5)}$$

For a rock matrix characterised by a limited depth of "permissible" penetration, multiple alteration layers or continuously variable material properties extending into the rock matrix from the fracture surface, it is not possible to calculate a simple, weighted flowpath average in this manner. If we take the matrix flux term for a limited penetration depth, for example, it is easy to see that the transcendental function containing the Laplace variable, ϕ cannot be broken out of the summation for the segmented path:

$$\tilde{C}_f = \frac{1}{s}\exp\left(-\overline{R}_a t_w\right)\exp\left(-\sqrt{\phi}\sum_{j=1}^{m} F_j \cdot MPG_{m(j)} \tanh\left(A_{m(j)}\delta_{m(j)}\sqrt{\phi}\right)\right) \qquad \text{(J-6)}$$

This is generally the case for all situations where the flux term contains non-separable functions of ϕ. Of course, in the limit where full saturation of the rock matrix occurs, Equation J-6 collapses to a trivial form and a simple average of the storage capacity along the flowpath can be shown to be the key parameter governing the residence time distribution (by way of a single retardation factor).

This attribute has an interesting consequence for simulations involving stagnant zones. As shown in Chapter 5, diffusive equilibrium can occur relatively quickly within a stagnant zone of limited width. Provided the assumption holds for the F-factor under consideration, these cases can be handled approximately by simply up-scaling the F-factor of the flowpath to include the diffusion accessible surface area as part of the flow-wetted surface. For the stagnant zone cases examined in Chapter 5 this corresponds to an increase of the F-factor by about an order of magnitude. In cases where mass transfer to the rock matrix (in both the flow channel and stagnant zone) is formulated as uptake to a single layer with unlimited penetration depth, it is also possible to use simplified flowpath averaging in an analogous fashion to Equation J-5. Although we do not have a formal proof of this, it is relatively straight forward to demonstrate using simulations where the full diffusive formulation of the stagnant zone with subsequent matrix uptake is implemented. Similarly to the simple case described above, this simplification does not apply when partial matrix saturation effects are tangible.

This discussion should not be taken to mean that for complex matrix microstructures it is not possible to calculate a meaningful average of material properties along a flowpath, but merely that a more complicated calculation needs to be performed based upon multiplication of transfer functions in Laplace space (i.e. Equation J-1 or J-2) or convolution of residence time distribution curves in the time plane. If only the early part of the residence time distribution is important, then the objection relating to limited penetration depth can be neglected as in many situations this only has an impact at much later times.

More importantly, however, for cases where a simple flowpath weighted average for the MPG cannot be calculated à priori, a direct consequence is also that the "average" MPG for the flowpath (however this is estimated) does not uniquely describe the retardation properties of the system. In such cases the diffusive and sorptive properties must always be specified separately rather than as a lumped parameter group.

Simulations for a single-layer rock matrix of limited extent

In the simulations presented here, we calculate the cumulative residence time distribution (CDF-RTD) for a moderately sorbing solute using the BM, MA1, and MA2 model variants.

To investigate the issue of uniqueness and by direct consequence, the flowpath "integratability" of the MPG, we calculate the CDF-RTD for three different cases where the partitioning coefficient, K_d and formation factor, F_f differ in each case although the MPG is identical throughout. For convenience we choose K_d values in a range where the matrix porosity makes no difference to the storage capacity of the rock and therefore can be neglected. The parameters used in the calculations are given in Table J-1.

The resulting cumulative solute residence time distributions are shown in Figure J-1 to Figure J-3.

As can be seen from the figures, the results are identical in all three cases for the BM and MA1 models when an infinite rock matrix is assumed. For a limited rock matrix, on the other hand, different matrix formation factors give rise to matrix saturation at different times on the residence time distribution curve. This behaviour is fully consistent with expectations for these cases based upon the previous discussions and demonstrates how the assumption of the uniqueness of the MPG breaks down in such situations. The results for the radial diffusion case, MA2 are particularly interesting in that the MPG gives non-unique results in all cases considered both for an infinite and a limited rock matrix. This is due to the non-linear form of the matrix flux term for radial diffusion.

Table J-1. Summary of material property parameters for scoping calculations involving a single layer rock matrix of limited depth.

Parameter	Case (a)	Case (b)	Case (c)
K_d (m^3/kg)	0.001	0.01	0.1
F_f (–)	1.6×10^{-4}	1.6×10^{-5}	1.6×10^{-6}
MPG (m/y½)	115	115	115
F-factor (y/m)	10^6	10^6	10^6

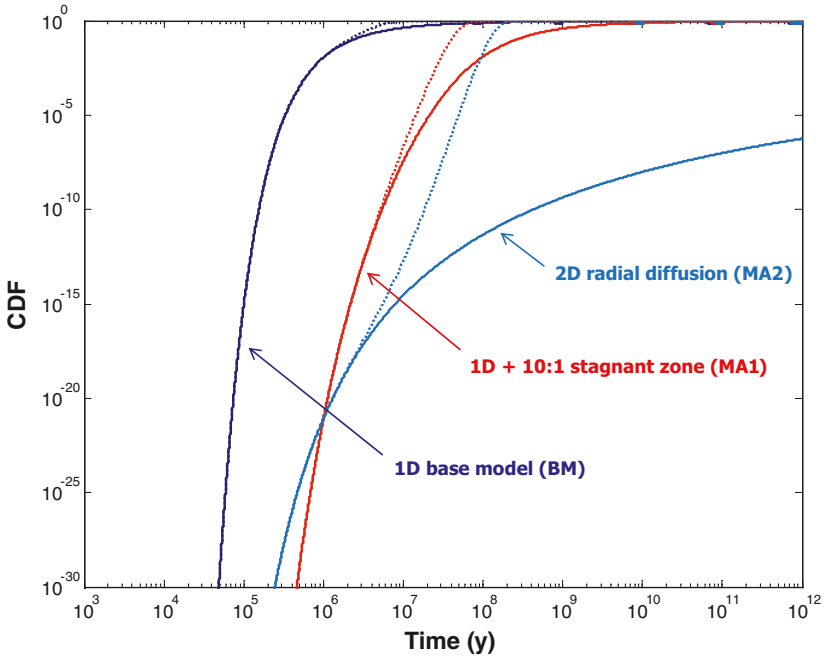

Figure J-1. *Cumulative residence time distributions for BM, MA1, MA2 transport models for Case (a). Unbroken lines show results for an infinite rock matrix, broken lines show results for a maximum matrix penetration depth of 2 m.*

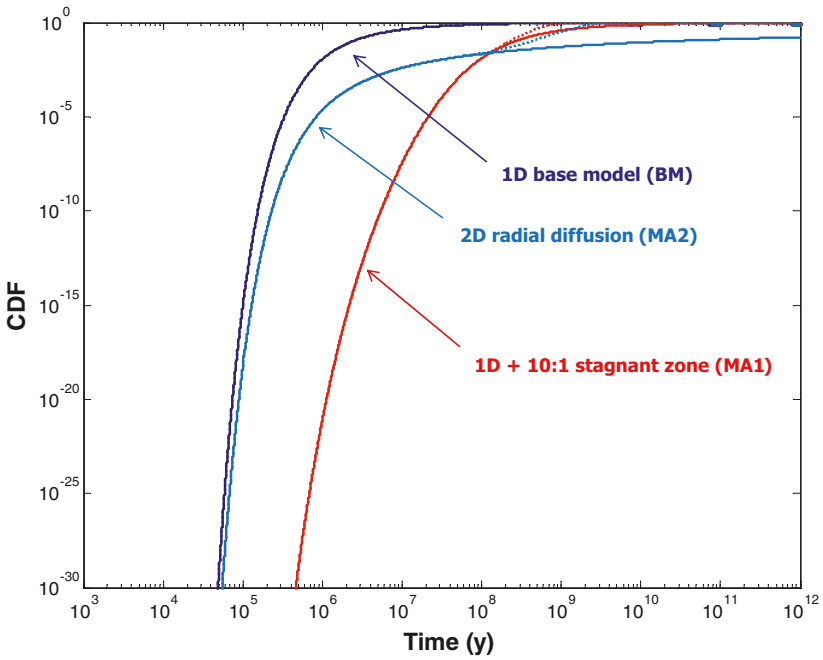

Figure J-2. *Cumulative residence time distributions for BM, MA1, MA2 transport models for Case (b). Unbroken lines show results for an infinite rock matrix, broken lines show results for a maximum matrix penetration depth of 2 m.*

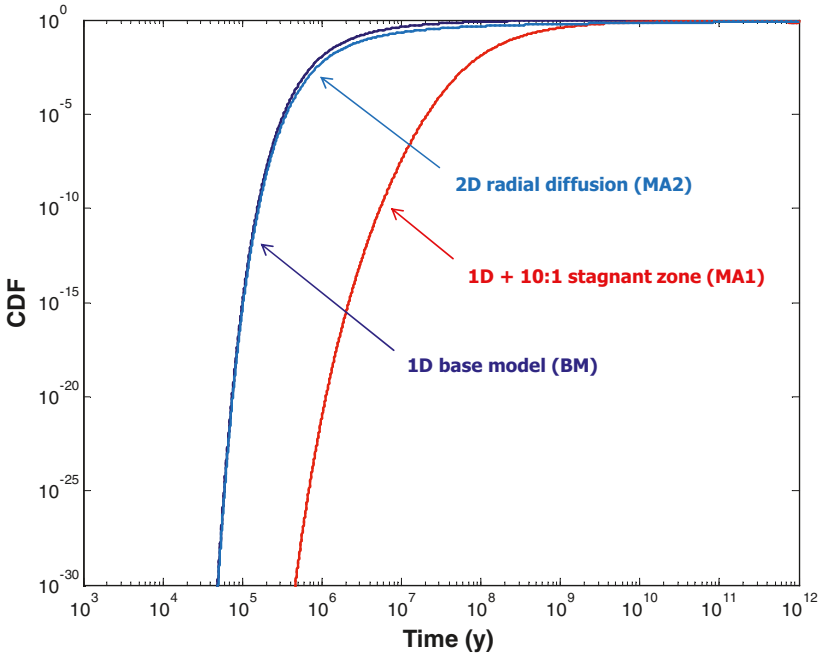

Figure J-3. *Cumulative residence time distributions for BM, MA1, MA2 transport models for Case (c). Unbroken lines show results for an infinite rock matrix, broken lines show results for a maximum matrix penetration depth of 2 m.*

Simulations for a two-layer rock matrix of limited extent

In this section we calculate the cumulative residence time distribution (CDF-RTD) for a moderately sorbing solute considering a two-layer rock matrix using the BM model. Here, the CDF-RTD is calculated for five different cases where the material properties of the surface layer and underlying, unaltered rock matrix are given in Table J-1.

In Table J-2 the alteration layer in cases (a) through (c) has the same MPG as the unaltered rock matrix although based upon different F_f and K_d combinations. Case (d) and (e) have enhanced retention in the surface layer although in case (d) this is due to an increased F_f, whereas in case (e) this is because of an increased sorption K_d. In addition to these five cases, a range of simulations were also performed where the F_f and K_d of the surface layer were varied systematically over two orders of magnitude relative to the unaltered rock matrix. The resulting response surfaces comparing the transport times for recovery of 1%, 10%, and 50% of released solute are shown in Figure J-4 to Figure J-6 together with results for the five cases specified in Table J-2.

It is noted by the author that a similar calculation was made in /Crawford 2006/ to investigate the question of MPG uniqueness. In this previous study, however, only the diagonal cases (corresponding to (a), (b), and (c)) were considered in the discussion and off-diagonal cases ((d) and (e)) were not examined. For this reason an incorrect conclusion was drawn concerning uniqueness of the MPG in multi-layer systems. This oversight is rectified in the current report by way of the deliberations presented here. In Figure J-4 to Figure J-6, the bulk storage capacity of the rock is defined in the following fashion:

$$K^*_{ds}\,\rho_{bs} = \theta_s + K_{ds}\,\rho_{bs} \tag{J-7}$$

$$K^*_{dm}\,\rho_{bm} = \theta_m + K_{dm}\,\rho_{bm} \tag{J-8}$$

Table J-2. Summary of material property parameters for scoping calculations involving a two-layer rock matrix of limited depth.

Parameter	Case (a)	Case (b)	Case (c)	Case (d)	Case (e)
Surface layer:					
K_{ds} (m^3/kg)	0.001	0.1	0.01	0.01	0.1
F_{fs} (–)	1.6×10^{-4}	1.6×10^{-6}	1.6×10^{-5}	1.6×10^{-4}	1.6×10^{-5}
MPG_s (m/y½)	115	115	115	362	362
Depth (m)	0.1	0.1	0.1	0.1	0.1
Matrix layer:					
K_{dm} (m^3/kg)	0.01	0.01	0.01	0.01	0.01
F_{fm} (–)	1.6×10^{-5}	1.6×10^{-5}	1.6×10^{-5}	1.6×10^{-5}	1.6×10^{-5}
MPG_m (m/y½)	115	115	115	115	115
Depth (m)	2	2	2	2	2
F-factor (y/m)	10^6	10^6	10^6	10^6	10^6

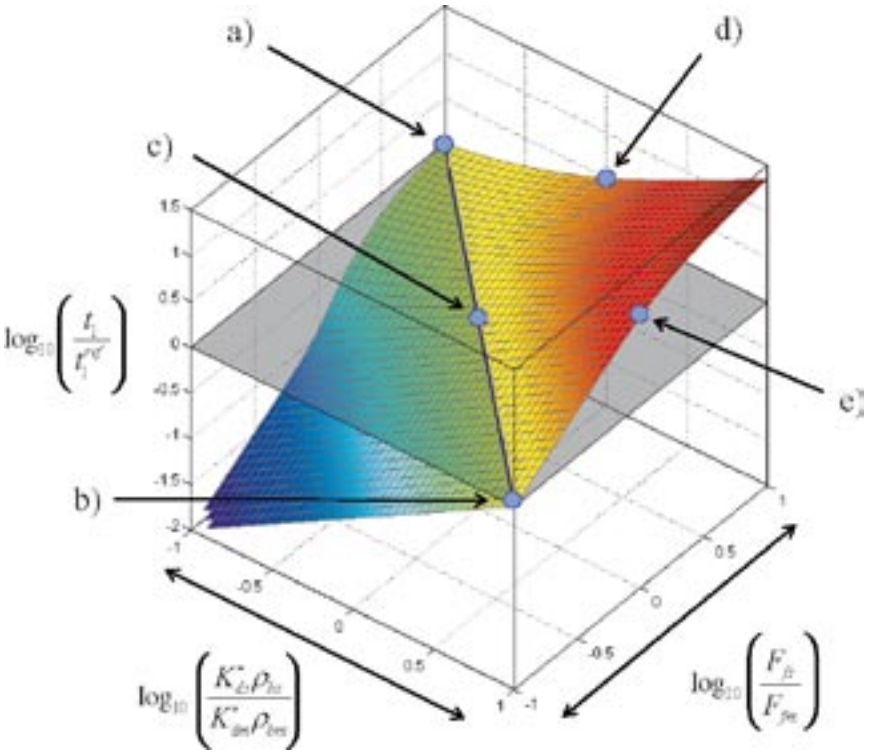

Figure J-4. *Response surface for solute transport with variable surface layer retention properties relative to unaltered rock matrix. The vertical axis shows the transport time in the 2-layer system relative to that for the 1-layer case for 1% recovery.*

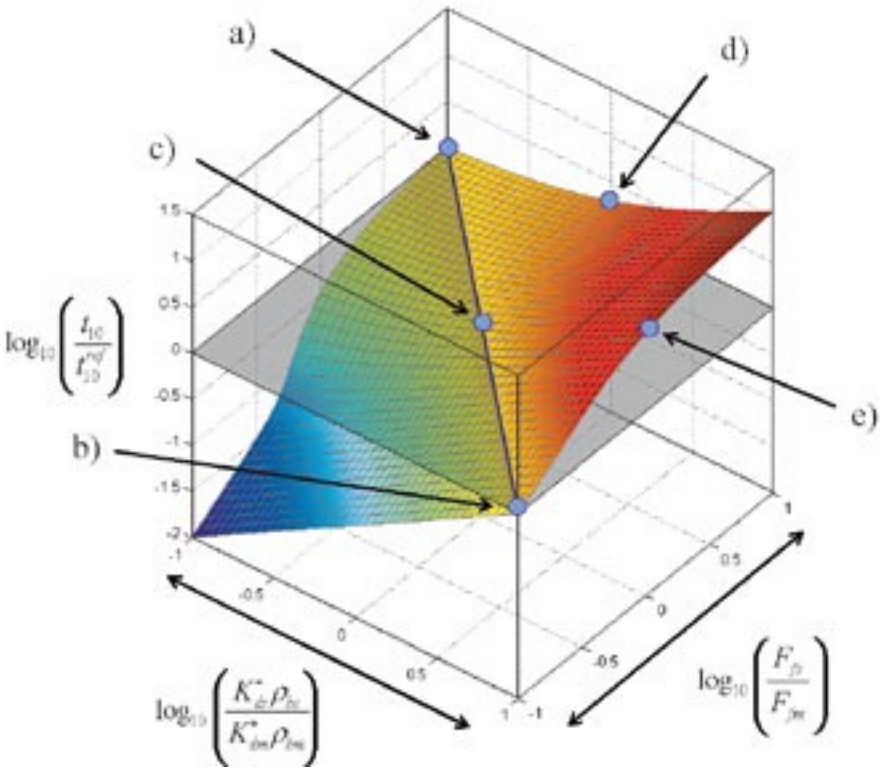

Figure J-5. *Response surface for solute transport with variable surface layer retention properties relative to unaltered rock matrix. The vertical axis shows the transport time in the 2-layer system relative to that for the 1-layer case for 10% recovery.*

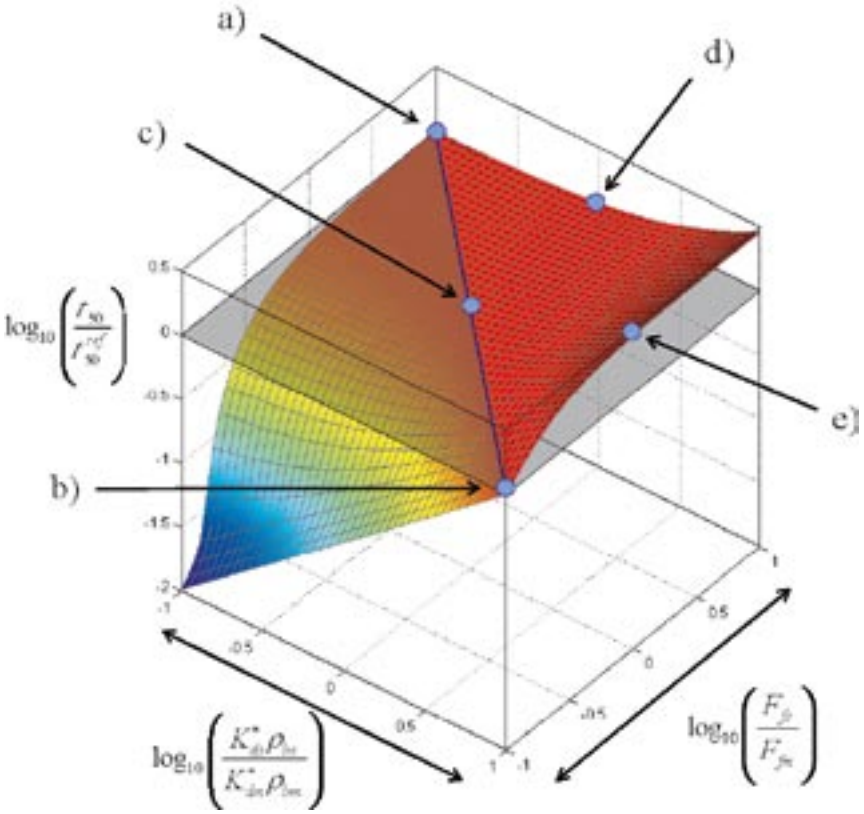

Figure J-6. *Response surface for solute transport with variable surface layer retention properties relative to unaltered rock matrix. The vertical axis shows the transport time in the 2-layer system relative to that for the 1-layer case for 50% recovery.*

Detailed results for the five particular cases described in Table J-2 are shown in Figure J-7 and Figure J-8.

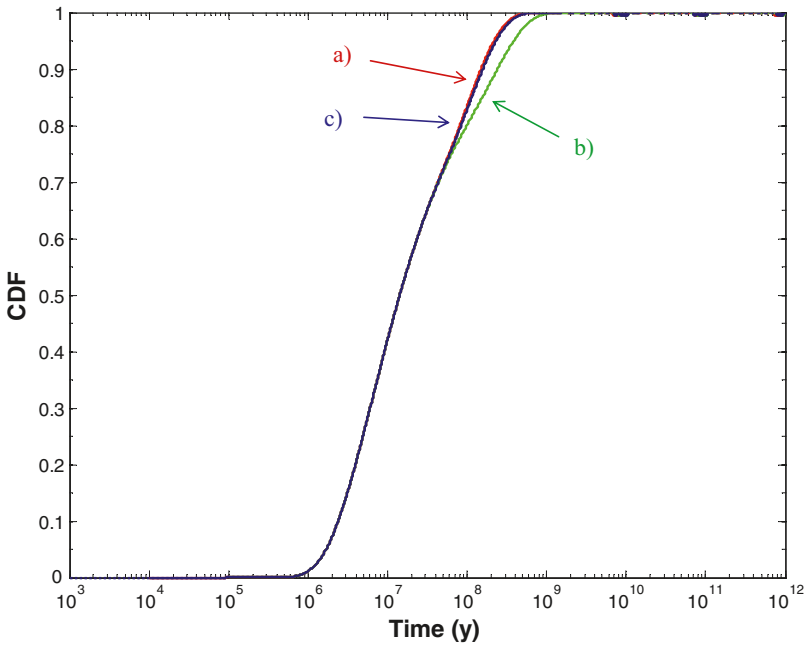

Figure J-7. *Cumulative residence time distributions for the BM transport model. Breakthrough curves are shown for Cases (a)–(c).*

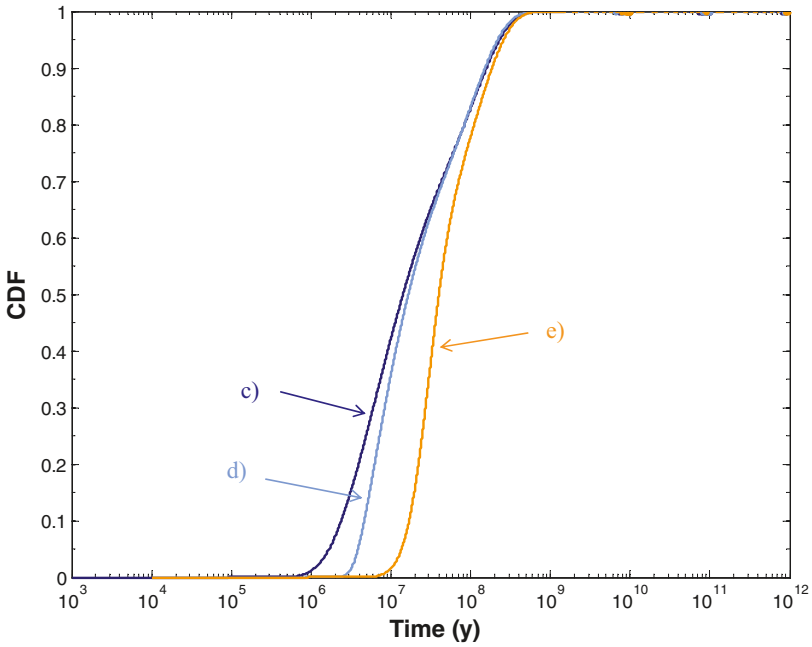

Figure J-8. *Cumulative residence time distributions for the BM transport model. Breakthrough curves are shown for Cases (c)–(e).*

As can be seen from the figures above, the trivial diagonal cases where the surface layer has the same MPG as the rock matrix although due to different F_f and K_d combinations are for the most part indistinguishable. The only deviation occurs at very long times where partial matrix saturation occurs at slightly different times for the cases (a), (b), and (c). For the off-diagonal cases (d) and (e), on the other hand, the different F_f and K_d combinations give rise to very different breakthrough behaviour even at very early times. In these cases it is clear that the MPG of the surface layer is non-unique and F_f and K_d must be specified separately.

Appendix K

Scoping calculations of the impact of natural colloids

Author: James Crawford

The unsteady, differential mass balance for advective transport of (both dissolved and colloidal bound) solute in a flow channel with diffusive uptake of solute can be written as:

$$R_a \frac{\partial C_f}{\partial t} + v\left(\frac{\partial C_f}{\partial x} + \frac{\partial C_{sc}}{\partial x}\right) = \frac{2J_m}{\delta_t} \qquad \text{(K-1)}$$

Where, C_f (mol/m^3) is the free aqueous concentration of solute, C_{sc} (mol/m^3) is the colloid bound concentration of solute, R_a (–) is the equilibrium retardation coefficient for equilibrium sorption on fracture outer surfaces, ν (m/s) is the advective velocity, δ_t (m) is the flow channel transport aperture, and J_m (mol/m^{2}s) is the diffusive flux to the rock matrix.

Since colloids[6] are frequently too large to participate in matrix diffusion, we only consider their carrying capacity as part of the advective transport term on the left-hand side of the Equation K-1. If we assume that sorption of solutes upon suspended colloids is an instantaneous and reversible equilibrium process, the concentration of solute bound to colloidal particles, C_{sc} (mol/m^3) can be given as:

$$C_{sc} = m_c K_d^{colloid} C_f \qquad \text{(K-2)}$$

Where, m_c (kg/m^3) is the suspended colloidal mass concentration which is assumed to be constant, and $K_d^{colloid}$ (kg/m^3) is the coefficient for sorption on the colloidal particles. For a constant colloid loading, we can then rewrite the mass balance as:

$$R_a \frac{\partial C_f}{\partial t} + v\left(1 + m_c K_d^{colloid}\right)\frac{\partial C_f}{\partial x} = \frac{2J_m}{\delta_t} \qquad \text{(K-3)}$$

In /Hallbeck and Pedersen 2008/ it was concluded that the natural colloidal particles identified in Forsmark groundwater sampled at repository depth are composed predominantly of iron and sulphur although with a minor fraction in the form of clay minerals (characterised as K-Mg-illite).

Provided the composition of the colloids is known, an approximate sorption K_d value for the colloidal particles can be estimated by scaling the K_d for an appropriate mineral analogue by the specific surface area ratio ($A_{colloid}/A_0$) of the colloidal material and analogue mineral:

$$K_d^{colloid} \approx \left(\frac{A_{colloid}}{A_0}\right) K_d^0 \qquad \text{(K-4)}$$

The form of Equation K-3 suggests that the impact of suspended colloidal material enters the transport equations by way of reducing the "apparent" F-factor for a transport flowpath. Here, we also make the assumption that the load of colloids is constant along a transport path and there is no adhesion to, or remobilisation from fracture surfaces. The ratio of the apparent and actual F-factor for a transport path including the effects of equilibrium sorption on colloids can then be given as:

$$R_F = \frac{F_{app}}{F} = \frac{1}{1 + m_c K_d^{colloid}} \approx \frac{1}{1 + m_c\left(\frac{A_{colloid}}{A_0}\right) K_d^0} \qquad \text{(K-5)}$$

[6] It should be noted that in this discussion the term colloid is used exclusively to refer to so-called "pseudo-colloids" formed where solute is reversibly adsorbed to naturally existing colloidal particles, rather than "eigen colloids" formed by agglomeration of strongly hydrolysed solute species in the groundwater.

It should be noted that this definition of the impact of colloids on radionuclide transport is different to the analyses presented by /Vilks et al. 1998/ and /Contardi et al. 2001/ since matrix diffusion effects were not considered in those studies. To the best knowledge of the author, scoping calculations equivalent to Equation K-5 (i.e. including matrix diffusion) have not been previously described in the literature.

In /Hallbeck and Pedersen 2008/ the average natural colloid concentration in Forsmark groundwater at repository depth was estimated to be roughly 58 ± 63 µg/L.

In the kind of scoping calculation implied by Equation K-5 it is probably most relevant to chose the most strongly sorbing radionuclides as this would give the largest impact upon transport. Of all the analogue minerals that we could choose to calculate an order of magnitude estimate for R_F using Equation K-5, the assumption of colloidal ferric oxyhydroxide or hematite would probably give the largest effect since K_d values are typically very high for these sorbents.

In /Degueldre et al. 1994/, for example, the K_d for Am(III) sorption on hematite was found to be in the range 345–9,330 m^3/kg at pH 8. Taking the upper limit of this range, we calculate R_F to be on the order of 0.47–0.65 depending upon the colloid concentration (and assuming $A_{colloid} \approx A_0$). This means that in the worst case scenario for the most strongly sorbing radionuclides we would expect a reduction in retardation equivalent to decreasing the F-factor by roughly 50%.

For other possible analogue minerals such as smectite clay, we calculate far smaller impacts upon radionuclide transport. The sorption K_d of trivalent lanthanides on smectite has been measured by /Coppin et al. 2002/ to be approximately in the range 0.5–100 m^3/kg. Taking the upper limit of this K_d range would give R_F values of 0.988 or greater.

If, on the other hand, we were to assume that the colloids are more similar in character to the chlorite fracture coatings sampled in the transport properties laboratory programme, we could use the data for fracture Type D described in Chapter 4 to make an estimate of R_F. The chlorite fracture coatings described in Chapter 4 were found to have a sorption K_d on the order of 2.4–2.8 m^3/kg for sorption of trivalent lanthanides. This gives an R_F value of over 0.99 for the transport of Am(III).

As the calculations above indicate, the impact of a given concentration of natural colloids depends upon which proxy mineral is used to represent their properties and the sorptivity of the transported solute under consideration. Since the trivalent Lanthanides, exemplified here by Am(III), are among the most strongly sorbing of the solutes of interest in safety assessment, these calculations give an upper limit to the impact of colloidal transport mechanisms under the prevailing groundwater conditions measured at Forsmark. For less strongly sorbing solutes featuring K_d values less than about 10–100 m^3/kg the impact is likely to be negligible.

The crucial assumption in this analysis is, of course, that the sorption of radionuclides on the colloids is macroscopically reversible over the timescale of transport. The status of sorption reversibility for key radionuclides on colloids is not conclusively established at present and there are conflicting pronouncements on this issue in the scientific literature.

Generally it is thought that the sorption of ion-exchanging solutes (and solutes that form outer sphere complexes) should be largely reversible owing to the absence of covalent chemical bonding /Coppin et al. 2003/. For solutes that form inner-sphere surface complexes, however, partial irreversibility and hysteresis effects are frequently observed /e.g. Lu et al. 1998, Coppin et al. 2003, Missana et al. 2004/. This is typically due to a slow rate of desorption as compared to the adsorptive uptake step and the limited observational timescale of experiments. Such behaviour could occur where there is a slow redistribution of solute sorbed initially in the form of outer sphere surface complexes to more stable inner-sphere surface complexes. Given sufficient time, however, the sorption should be reversible provided there is an absence of chemical reactions which might lead to incorporation of radionuclides in the structure of the colloids /Rabung et al. 2005/. Given the uncertainty associated with the reversibility of radionuclide sorption on colloids, however, further analysis of this will need to be undertaken within safety assessment.

Appendix L

Scoping calculations of salt penetration depths

Author: James Crawford

Absolute depths of salt penetration

In this section we make simplified scoping calculations of the expected penetration depth of saline water as a function of time. The intention here is to compare results based upon diffusivities estimated from *in situ* resistivity measurements and compare these to salt concentrations in matrix porewater characterised within the Hydrogeochemistry programme.

If we consider an infinite rock matrix, the solute penetration depth can be obtained from the solution to the 1D diffusion equation and is given by /Neretnieks 1980/ as:

$$\eta = \zeta \sqrt{D_a t} \tag{L-1}$$

Where, D_a is the apparent diffusivity, t is the contact time, and ζ is a parameter that depends upon the part of the solute diffusion profile upon which the calculation is based:

$\zeta = 3.64$ (depth corresponding to 1% of equilibrium concentration) (L-2)

$\zeta = 0.954$ (depth corresponding to 50% of equilibrium concentration) (L-3)

We can also define a hypothetical "mean penetration depth" as described in /Neretnieks 1980/. In this case the constant ζ would be:

$$\zeta = 2/\sqrt{\pi} \approx 1.13 \quad \text{(mean penetration depth)} \tag{L-4}$$

For a non-sorbing solute, we can write:

$$\eta = \zeta \sqrt{D_p t} = \zeta \sqrt{\frac{D_e t}{\alpha}} \tag{L-5}$$

The mean penetration depth would then be given by:

$$\overline{\eta} = 2\sqrt{\frac{D_p t}{\pi}} = 2\sqrt{\frac{D_e t}{\pi \alpha}} \tag{L-6}$$

Where, D_p is the pore diffusivity, D_e is the effective diffusivity, and α is the storage capacity. The storage capacity is simply the sum of the water saturation porosity of the rock, θ_m and the volumetric sorption capacity, $K_{dm}\rho_{bm}$:

$$\alpha = \theta_m + K_{dm}\rho_{bm} \tag{L-7}$$

Under ideal conditions we would expect the storage capacity of a non-sorbing solute to be equal to the water saturation porosity (i.e. $\alpha = \theta_m$). In the through-diffusion experiments reported in /Selnert et al. 2008/, however, the fitted storage capacity was found to be on average about 35% larger than the water saturation porosity.

The free diffusivities of Na^+ and Cl^- at 25°C and infinite dilution are given by /Li and Gregory 1974/ as:

$D_{Cl^-} = 2.03\times10^{-9}$ (m^2/s)

$D_{Na^+} = 1.33\times10^{-9}$ (m^2/s)

The diffusivities can be corrected for intrinsic and viscous temperature effects using the Stokes-Einstein relation /Li and Gregory 1974/:

$$D_w(T) = D_w(T_0) \times \left(\frac{\mu_w^{T_0}}{\mu_w^{T}} \right) \times \left(\frac{T}{T_0} \right) \qquad \text{(L-8)}$$

Where T (K) is temperature and μ_w (Pa.s) is the viscosity of water at the reference (T_0) and "actual" temperatures (T), respectively. The *in situ* temperature generally increases linearly with depth at Forsmark. For borehole KFM01D, for example, the temperature varies from about 7°C to 12°C over the borehole length interval –100 m to –700 m. For this temperature range, the temperature correction factor for *in situ* free diffusivity is reduced by a factor 0.6–0.7 relative to the value at 25°C.

For a concentrated salt diffusing into a dilute porewater we need to consider electrostatic effects on the binary component diffusion. The free diffusivity at infinite dilution is then given by:

$$D_{NaCl}(25°\mathrm{C}) = \frac{\left(|Z_{Na^+}| + |Z_{Cl^-}| \right) D_{Na^+} D_{Cl^-}}{|Z_{Na^+}| D_{Na^+} + |Z_{Cl^-}| D_{Cl^-}} = \frac{2 D_{Na^+} D_{Cl^-}}{D_{Na^+} + D_{Cl^-}} \approx 1.6 \times 10^{-9} \qquad \text{(L-9)}$$

Where Z_i is the charge number of the diffusing ion, i.

Based upon *in situ* measurements of formation factors at the Forsmark site we estimate the formation factor for intact matrix rock in fracture domain FFM01 (i.e. rock type 101057) to be –4.5 ± 0.1 in $\log_{10}$ units. Since there is evidence that the formation factors estimated using resistivity measurements may over-estimate the true geometric formation factor by about 50% owing to a measurement bias, we reduce the resistivity-based formation factors by a factor 2 before using them in transport calculations. This corresponds to an arithmetic mean formation factor of roughly 1.6×10^{-5}.

From the data contained in /Börjesson and Gustavsson 2005/, we can make an estimate of the rock matrix porosity for metagranite (rock type 101057) found in a number of core drilled boreholes at the Forsmark site (KFM01A, KFM01B, KFM02A–7A). In this case there are a number of samples in the upper part of the boreholes which are strongly altered and may not be representative of the porosities to be found at repository depth. If we consider only those measurements below –350 m elevation, we estimate the porosity to be roughly –2.66 ± 0.11 in $\log_{10}$ units. The raw data histogram and the fit to the lognormal distribution (neglecting a slight negative skew in the data) are shown in Figure L-1 along with a plot of the variation with sampling elevation.

It is difficult to obtain fully representative samples from bore cores owing to possible stress relaxation and mechanical damage incurred during core excavation and sample preparation. Both of these may result in the formation of additional micro-fractures that increase the porosity of samples used in laboratory measurements.

The actual extent of the bias introduced by stress release and mechanical damage is difficult to quantify and is complicated by the fact that the different methods for porosity measurement do not always give the same results. In the geology programme of the site investigation, for example, the porosity is measured using a water resaturation technique where the samples are first submerged in water for 7 days and then dried at 105°C for a further 6 days /Liedberg 2006/. The difference in weight of the saturated and dried sample then allows the porosity to be determined. Since samples used in the transport programme are frequently destined for other

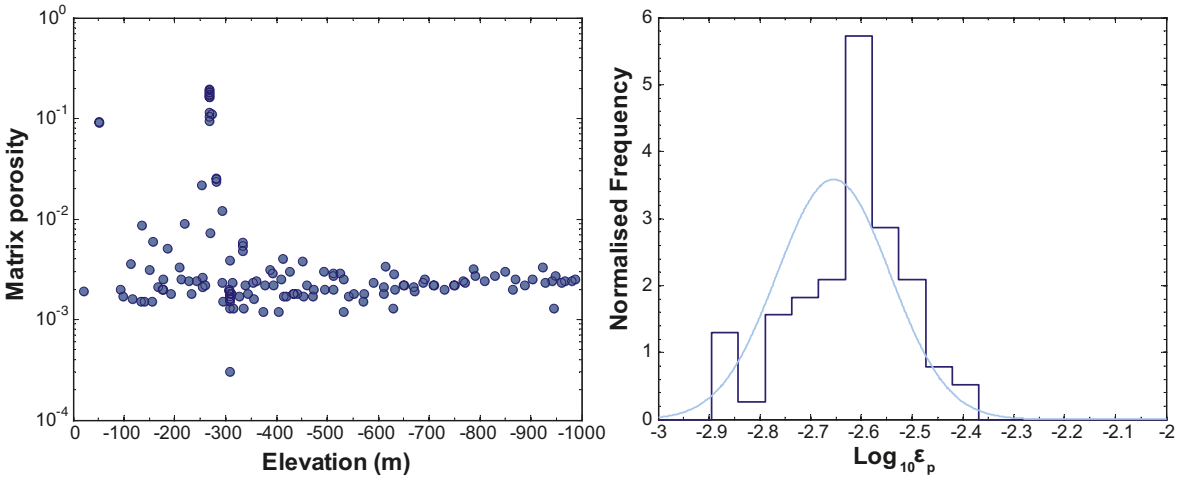

Figure L-1. *Laboratory determined matrix porosities for rock type 101057 at Forsmark (data based on 147 gravimetric water saturation measurements). The figure on the left shows porosity plotted against sampling elevation, while the right hand figure is the histogram and approximate lognormal fit to the data below –350 m.*

studies where an elevated temperature might accelerate undesirable weathering reactions, the drying step is carried out at a temperature of 70°C. The "water loss" technique used by /Waber and Smellie 2007/ is based upon a single drying step at 105°C until such time that stable weight conditions are obtained. Another method employed by /Waber and Smellie 2005, 2007/ is based upon a diffusive isotope dilution technique involving vapour phase exchange between a water vessel containing water with a known ^{18}O and ^{2}H composition and the pore water contained in the bore core sample. In the latter two methods, no preliminary resaturation step is performed and therefore care must be taken to ensure that the retrieved bore core sample does not desiccate in transit to the laboratory.

Generally, the water loss and isotope dilution methods give very similar results. In a comparison described in /Waber and Smellie 2007/ the resaturation technique was found to give porosities as much as three to four times larger than the water loss method suggesting a strong decompression of the pore space during or immediately after core retrieval. Another complicating factor is that the time allowed for both resaturation and drying in the water resaturation technique may not be sufficient since longer drying times were required to reach stable weight conditions in the work reported by /Waber and Smellie 2007/.

In another investigation where the volumetric strain response of bore core samples was measured during hydrostatic compression /Jacobsson 2007/, the volume dilation from roughly *in situ* stress conditions (20 MPa) was found to be as much as double that implied by the results of /Waber and Smellie 2007/.

If we neglect possible input data biases, we can calculate a likely range of penetration depths for "salt" in the rock matrix as a function of time at Forsmark sing the site-specific formation factor and porosity data. Since we cannot say with certainty how much the reported porosities are biased by stress release effects, we use the data "as is" although note that penetration depths could be greater than those estimated in the following calculations by as much as a factor of two or more. This is also complicated by the possible presence of anion exclusion and electrical double layer diffusion effects. For salt diffusing into an initially dilute porewater, we would

expect the cations to have an enhanced pore diffusivity, while anions would have a somewhat reduced pore diffusivity. If the effect is sufficiently strong, however, we would expect the binary component diffusivity for the salt to be less than that predicted in the absence of these electrostatic effects thereby complicating the impact of pore compression on penetration depth analyses.

In many studies the formation factor and porosity are thought to be correlated by Archie's law /Parkhomenko 1967/:

$$F_f = k\,\theta_m^n \tag{L-10}$$

Where n is an empirically established power law exponent and k is a proportionality constant. In the Forsmark site investigation, it has been found that the correlation between formation factor and bulk porosity is very poor at the low porosities typically encountered. For this reason, we use an alternative approach to introduce a partial correlation between these variables based upon a Monte Carlo method.

For the calculations in this paper, we generate correlated log-normally distributed random number pairs using the bivariate normal distribution and a covariance matrix:

$$\Sigma = \begin{bmatrix} \sigma_x^2 & \rho\sigma_x\sigma_y \\ \rho\sigma_x\sigma_y & \sigma_y^2 \end{bmatrix} \tag{L-11}$$

Where, ρ is the correlation coefficient, which can range from $\rho = 0$ for no correlation, to $\rho = 1$ for perfect positive correlation (we consider negative correlation to be not physically motivated for the current analysis and so this is not considered). For our purposes we generate normally distributed random deviates with a mean value of zero and a standard deviation of unity ($\mu_x = \mu_y = 0$, $\sigma_x = \sigma_y = 1$). The paired random deviates are then used to generate partially correlated values for formation factor and porosity assuming a lognormal distribution of values:

$$\log_{10}\left(F_f\right) = \mu_{Ff} + R_1\left(0,1\right)\sigma_{Ff} \tag{L-12}$$

$$\log_{10}\left(\theta_m\right) = \mu_\theta + R_2\left(0,1\right)\sigma_\theta \tag{L-13}$$

Using Equation L-6, the mean penetration depth can then be calculated. The results of these calculations are shown in the following figures (assuming an *in situ* temperature of 12°C) and different levels of simple correlation between porosity and effective diffusivity.

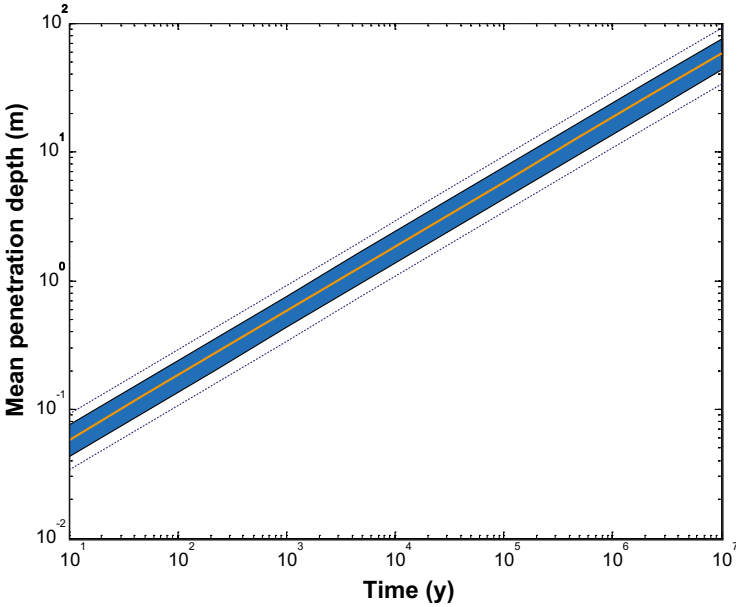

Figure L-2. *Estimated mean penetration depth as a function of time for non-correlated formation factor and porosity (ρ = 0) calculated using a simple Monte Carlo simulation method. The data are given as a mean value (orange curve), 5%–95% percentile range (shaded region), as well as minimum and maximum value (broken curves).*

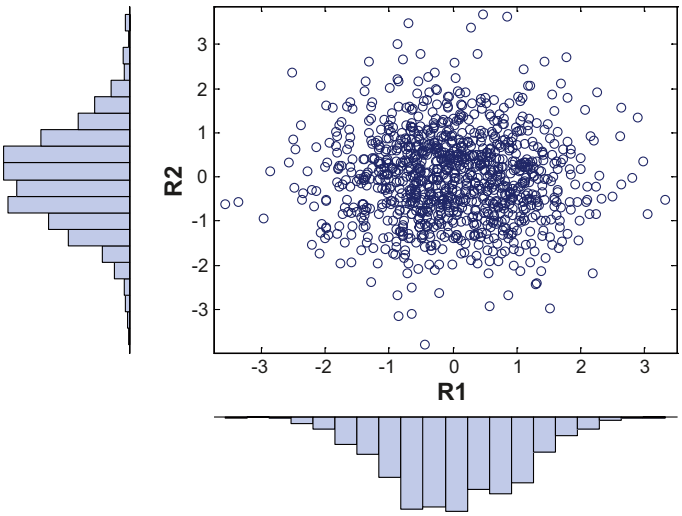

Figure L-3. *Cross-plot of random deviates R_1 and R_2 showing correlation for ρ = 0.*

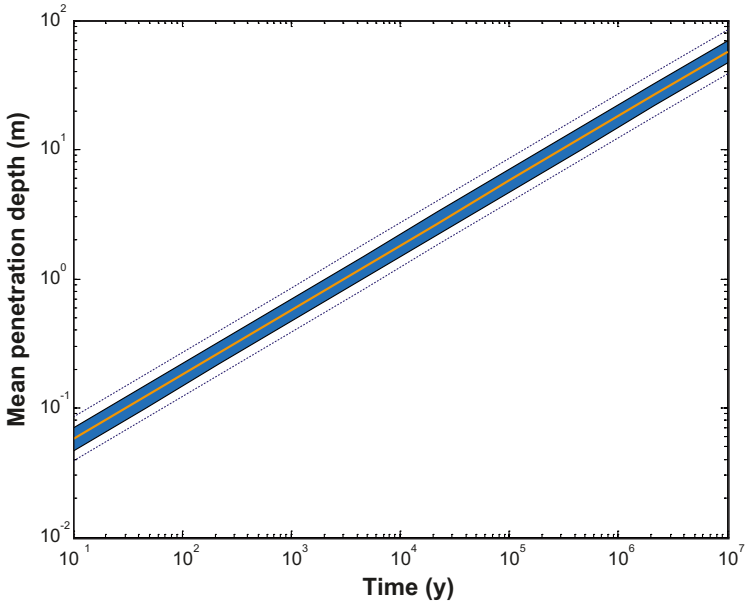

Figure L-4. *Estimated mean penetration depth as a function of time for partially-correlated formation factor and porosity (ρ = 0.5) calculated using a simple Monte Carlo simulation method. The data are given as a mean value (orange curve), 5%–95% percentile range (shaded region), as well as minimum and maximum value (broken curves).*

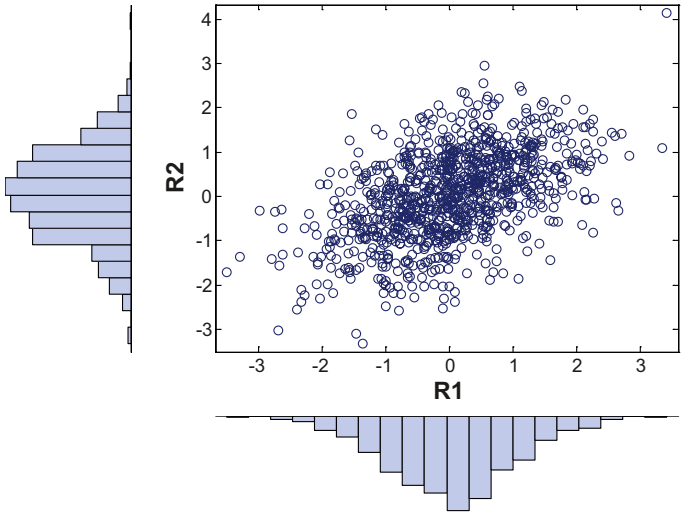

Figure L-5. *Cross-plot of random deviates R_1 and R_2 showing correlation for ρ = 0.5.*

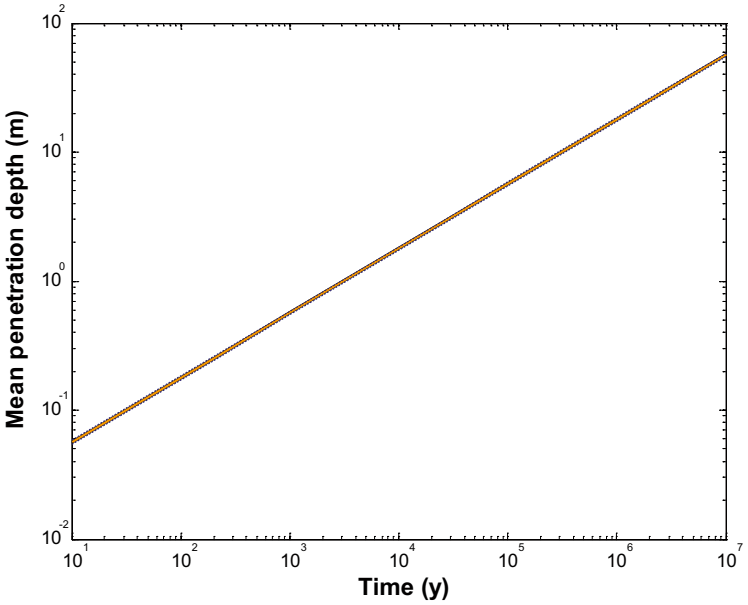

Figure L-6. *Estimated mean penetration depth as a function of time for perfectly-correlated formation factor and porosity (ρ = 1) calculated using a simple Monte Carlo simulation method. The data are given as a mean value (orange curve), 5%–95% percentile range (shaded region), as well as minimum and maximum value (broken curves).*

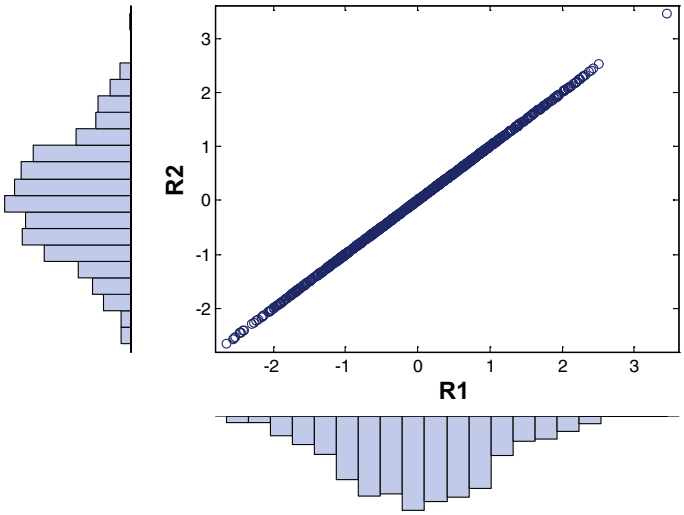

Figure L-7. *Cross-plot of random deviates R_1 and R_2 showing correlation for ρ = 1.*

From the figures above we calculate that the penetration depths are possibly quite low, on the order of 3–11 m with a mean of slightly less than 6 m over a 100 ky time period. Uncertainty in the actual pore diffusivity for a salt could cause this to vary significantly. If, for example, we were to use pore diffusivity data based upon laboratory through-diffusion tests we would calculate a mean penetration depth roughly 2–3 times greater for the central case. On the other hand, for the pore diffusivities reported in /Laaksoharju et al. 2008/ we would expect a mean penetration depth roughly 2–6 times larger.

Although it is possible that the laboratory derived data may be reasonable for diffusion in the immediate vicinity of flowing fractures where the rock is locally de-stressed and subject to a greater intensity of micro-fracturing, it is not clear whether this is appropriate for penetration distances into the rock greater than the first few cm. The wish to avoid overestimation of the rock matrix effective diffusivity is the main reason for using effective diffusivities based upon *in situ* resistivity measurements in the calculations of solute transport presented in this report.

For the very long contact times considered in salt penetration calculations, however, additional factors come into play. Chief among these is the possible presence of small diffusive fractures in the cm to metre size range. Such fractures do not have to be connected to the wider fracture network in order to have an appreciable impact upon rates of diffusion. Any solute being transported by diffusion through the rock matrix, upon encountering such a fracture, will be transported very quickly along its length relative to the rate of diffusion in the matrix porosity comprised of grain boundaries and micro-fractures. Solute transported in this fashion will also diffuse outwards from the fracture surfaces in a similar fashion to the notion of diffusion in a stagnant zone with subsequent mass transfer to the rock matrix discussed in Chapter 5.

Depending upon the intensity and size distribution of such background diffusive fractures, the coupling of different rates of mass transfer may give rise to an apparently non-Fickian diffusion profile over distances of more than a couple of metres. For this reason, any diffusion profile of haline or isotopic components that are associated with very long contact times may give apparently larger *in situ* diffusivities than would be recommended for transport calculations on the basis of independent laboratory or *in situ* measurement data.

It is noted that this effect will probably be more important for matrix porewater concentration profiles adjacent to deformation zones where a greater intensity of background fracturing is expected. In very fracture-poor sections of the target volume, for example, there may not be a sufficient intensity of background fracturing for this to be an issue.

If flow channels in the rock are very sparsely distributed and narrow in width, a radial diffusion model may be a more appropriate than the 1D model of semi-infinite diffusion typically assumed in penetration depth calculations. The solution to the radial diffusion equation is, however, not amenable to a simple analytical treatment as for the 1D cases so a numerical approach is necessary. With the aid of the Laplace-space model for 2D radial diffusion (described in Appendix I) it is possible to calculate the mean penetration depth using a mass balance approach. For a constant concentration boundary condition, the mean penetration depth is then given in terms of the time integrated matrix flux term, J_m (below assumed normalised with respect to boundary concentration):

$$\overline{\eta} = -a + \sqrt{a^2 + \frac{2a}{\theta_m}\int_0^t J_m(t)\,dt} \qquad \text{(L-14)}$$

Figure L-8 shows the mean penetration depth calculated for the central case (i.e. $F_f = 1.6\times10^{-5}$, $\theta_m = 2.2\times10^{-3}$) using Equation L-14 and assuming a 10 cm wide flow channel.

The calculations show clearly that the penetration depth for the radial case is less than that for the linear diffusion model by about a factor of 2 for a contact time of 100 ky.

In the light of these discussions it is relevant to point out that the apparent disequilibrium (chloride and $\delta^{18}O$) between matrix pore water and water flowing in fractures in the borehole elevation interval –300 m to –600 m is largely consistent with our understanding of matrix diffusion properties. We would expect salt penetration depths of a few metres to at most a few tens of metres over the timescales characteristic of glacial-interglacial cycles (e.g. 10–100 ky) depending upon the various assumptions in the calculation. This is approximately what is seen,

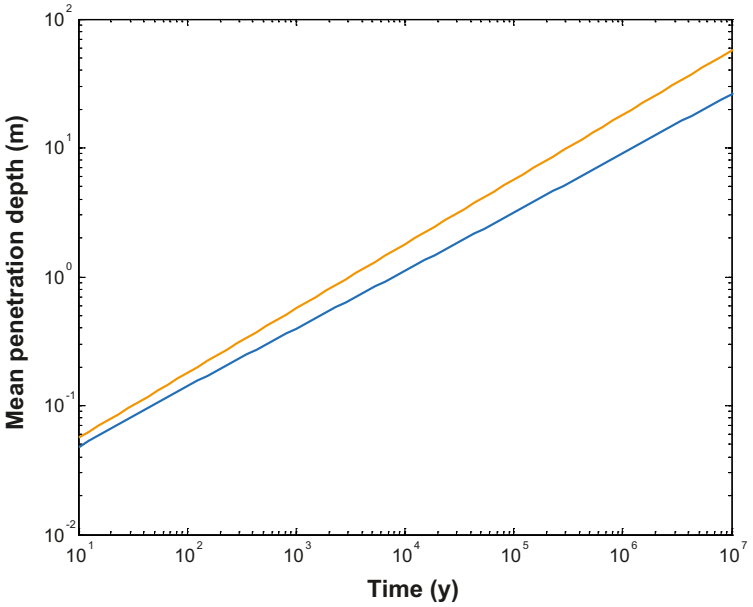

Figure L-8. *Comparison of mean penetration depth calculated using Equation L-6 (orange curve) and that calculated numerically using Equation L-14 for the radial diffusion case (blue curve).*

for example, in borehole KFM09B where an apparent salt diffusion front can be observed over a distance of about 10–15 m away from a highly transmissive section of the borehole around –572 m /Waber and Smellie 2007/. The apparent disequilibrium between groundwater and porewater at intermediate borehole elevations (–300 m to –600 m) within KFM01D, KFM02B, KFM06A and KFM08C as reported in /Laaksoharju et al. 2008/ also seems to be qualitatively consistent with expectations given the low frequency of conductive fractures at these depths and the possible timescale of saline fluctuations in the groundwater.

On the relation between advective travel time, penetration depth and solute residence time

Although on the timescale of 10–100 ky we might expect only limited, "absolute" penetration depths for a constant concentration of solute, it is important to bear in mind that this does not correspond to the "effective" depth of penetration experienced by radionuclides transported from repository depth to the surface.

It has previously been shown (under the assumption of unlimited 1D matrix diffusion and sufficiently high F-factor that the advective travel time can be neglected) that the effective depth of penetration associated with the average retardation of a Dirac pulse of solute transported along a flowpath can be given approximately by the relation /Crawford 2006/:

$$\overline{\eta} = \frac{D_e}{\sqrt{\pi}\ erfc^{-1}(0.5)} \cdot F \approx 1.18\, D_e F \qquad \text{(L-15)}$$

In the present context, "average" retardation is taken to mean the retardation effect associated with the centre of mass of the solute residence time distribution (i.e. the 50% recovery fraction).

For a formation factor of 1.6×10^{-5} and an F-factor of 10^6 y/m characterising a transport path, the effective depth of penetration would be roughly 0.66 m. For an F-factor of 10^8 y/m, on the other hand, we would expect an effective penetration depth of 66 m (i.e. 100 times greater). Noting that the effective diffusivity used in the ECPM calculations detailed in section 3.9 is 10^{-13} m^2/s (implying a formation factor, $F_f \sim 10^{-4}$), we calculate an effective depth of penetration of 3.7 m for an F-factor of 10^6 y/m. For an F-factor of 10^8 y/m this would grow to 370 m.

This is because the characteristic time during which the solute interacts with the rock matrix is related to the transport time of the solute along the flowpath and not the advective travel time. This is also why Equation L-15 implies the same effective penetration depth for all solutes regardless of sorptivity. Both the travel time and absolute penetration depth are related to the sorption K_d value. In the derivation of Equation L-15, however, they cancel out thereby giving the same depth of penetration for all transported solutes where the reference timeframe is the transport time itself.

Put simply, a pulse of a more strongly-sorbing solute will have a longer transport time, as compared to a pulse for a less sorbing solute. This additional time will allow the more strongly-sorbing solute, although having lower apparent diffusivity, to penetrate the rock matrix to the same depth as the less sorbing solute /Löfgren et al. 2007/. It should be noted, however, that many sorbing tracers have transport times that are significantly longer than their radioactive decay half-lives. This means that these sorbing tracers may never get an opportunity to diffuse more than a short distance into the rock before their activity decays to insignificant levels. Non-sorbing tracers with long half-lives relative to their transport time, on the other hand, can potentially diffuse to greater depths in the rock matrix for this reason.

If we were to consider a rock matrix of unlimited extent and the same transport parameters considered in the ECPM simulations described in section 3.9, the average residence time of a salt pulse, or for that matter any other non-sorbing environmental tracer, for an F-factor of 10^8 y/m would be /Crawford 2006, Löfgren et al. 2007/:

$$\overline{t} = t_w + \overline{t}_m \approx t_w + \frac{D_e \theta_m}{4\left(erfc^{-1}\left(0.5\right)\right)^2} F^2 \approx t_w + \left(6.1\times10^{-9}\right)F^2 \approx 1.3\times10^8 \text{ y} \qquad \text{(L-16)}$$

As can be seen from Equation L-16, the advective travel time t_w is for all practical purposes negligible in comparison to the average matrix residence time $\overline{t}_m$ of the solute if we were to consider unlimited matrix diffusion.

Since we know that the average spacing of fractures in the ConnectFlow simulation is somewhat less than 370 m for much of the transport path, this means that any solute transported from repository depth to the surface would most likely saturate the rock matrix for such a high F-factor. In this particular case it would not be appropriate to base the solute residence time calculation on the notion of unlimited matrix diffusion and it is more accurate to consider the retardation provided by equilibrium with a fully saturated depth of rock matrix. Based upon the relative storage capacity of the rock matrix as compared to the kinematic porosity, we would calculate an average travel time for a non-sorbing solute using:

$$\overline{t} = t_w + \overline{t}_m = R_d t_w = \left(1 + \frac{\left(1-\theta_f\right)}{\theta_f}\theta_m\right) t_w \approx 50\, t_w = 4\times10^6 \text{ y} \qquad \text{(L-17)}$$

As can be seen from the numerical value given in Equation L-17, the predicted travel time is roughly 32 times less than that calculated in the case of unlimited matrix diffusion.

This should not be taken as a general recommendation for the use of equilibrium retardation factors in safety assessment since a retardation factor only gives the mean arrival time for a transported solute assuming saturation of the rock matrix occurs. As shown in Chapter 5, the transient radionuclide breakthrough before the onset of equilibrium saturation is also important for calculation of far field fluxes in safety assessment, particularly at early times. The point of this calculation is merely to show that one must be careful with what is meant by penetration depth in the context of radionuclide transport from repository depth to the near surface. The calculations considered here consider an F-factor of 10^8 y/m. For F-factors on the order of 10^6 y/m, we would expect the effective penetration depth of solute to be 100 times less and therefore not an equilibrium process for the average flow channel separation implicit in the calculations (unless the matrix depth is specified as being less than this for other reasons).